# Photocontrol and Structural Analysis of Amyloid Fibril Formation Using Azobenzene and Novel Spiropyran Photoswitches

### **Dissertation**

zur Erlangung des Doktorgrades der Naturwissenschaften (Dr. rer. nat.)

der

Naturwissenschaflichen Fakultät II Chemie, Physik und Mathematik

der Martin-Luther-Universität Halle-Wittenberg

vorgelegt von

Herrn André Paschold

Gutachter: Prof. Dr. Wolfgang H. Binder

Univ.-Prof. Dr. Kerstin Blank

Verteidigung: 16.10.2025



"The supreme question about a work of art is out of how deep a life does it spring. Paintings of Moreau are paintings of ideas. The deepest poetry of Shelley, the words of Hamlet bring our mind into contact with the eternal wisdom; Plato's world of ideas. All the rest is the speculation of schoolboys for schoolboys."
"A man of genius makes no mistakes. His errors are volitional and are the portals of discovery."
James Joyce - Ulysses

#### Eigenständigkeitserklärung

Hiermit erkläre ich an Eides statt, dass ich die vorliegende Arbeit selbstständig und ohne fremde Hilfe verfasst habe. Andere als die angegebenen Quellen und Hilfsmittel wurden nicht benutzt und die den benutzten Werken wörtlich oder inhaltlich entnommenen Stellen wurden als solche kenntlich gemacht. Außerdem erkläre ich, die vorliegende Dissertation an keiner anderen wissenschaftlichen Einrichtung zur Erlangung eines akademischen Grades eingereicht zu haben.

Halle (Saale), den 12.05.2025

André Paschold

## Acknowledgements

First and foremost, I would like to express my deepest appreciation to Prof. Dr. Wolfgang H. Binder. He made this topic available and gave me the opportunity to work on it. I am sincerely grateful for his guidance and the many scientific and literary discussions.

I am also grateful to Dr. Maria Ott for being my mentor and for answering all my questions about peptide fibrillization with help and advice.

I would like to express my gratitude to all my colleagues from AG Binder who have supported me and without whom these years would not have been so enjoyable. I would especially like to thank Anke Hassi, the heart of our group, who reminded me of all the important dates, Julia Großert and Susanne Tanner, who kept our research going, and Dr. Anja Marinow, who was a great help to me. I'm grateful to Dr. Vico Adjedje, without whom I might not be writing these lines, and Philipp S. Hilgeroth, without whom Bergfeste would not have been the same.

I am also thankful to Dr. Vico Adjedje, Nicolas Schwalm, Dr. Justus F. Thümmler, Dr. Anja Marinow, and Dr. Zviadi Katcharava for the detailed corrections to this thesis.

Furthermore, I would also like to thank my co-operation partners, with whom I was able to produce and publish all these results together: Moritz Schäffler, Prof. Dr. Birgit Strodel, Dr. Henrike Lucas, Dr. Merle Röhr & group, and Prof. Dr. Henrike Heise & group for the good cooperation and their theoretical calculations that made our joint second paper possible. Prof. Dr. Jochen Balbach, Dr. Bruno Voigt and Dr. Shubra Sachan for providing me with their laboratory equipment and teaching me peptide fibrillization. Simone Fraas, Dr. Stephanie Krüger and Dr. Gerd Hause for the TEM recordings. Dr. Sven Rothemund for the countless peptides he synthesised for me, Dr. Tim Kohlmann for the introduction to photophysical measurements, and Dr. Dieter Ströhl and his team for the measurement of all NMR samples.

Finally, I would like to extend my sincere thanks to my family and all the lovely people out there who have put up with me during this time.

# **Contents**

Abstract  Zusammenfassung  1 Introduction  1.1 Azobenzenes
1 Introduction         1.1 Azobenzenes          1.1.1 History
1.1 Azobenzenes
1.1.1 History
1.1.2 Synthesis
1.1.3 Transition process in detail
1.1.4 Structure-activity relationship
1.1.5 Photoswitching of materials
1.2 Spiropyrans
1.2.1 History
1.2.2 Synthesis
1.2.3 Structure-activity relationship
1.2.4 Photoswitching of materials
1.3 Amyloidogenic proteins and peptides
1.3.1 Amyloids in nature
1.3.2 Structure, mechanism of aggregation and how to analyse
1.3.3 Parathyroid hormone
2 Aim of the thesis
3 Scientific concept
4 List of publications
[P1] Modulating the Fibrillization of Parathyroid-Hormone (PTH) Peptides: Azo-Switches
as Reversible and Catalytic Entities
[P2] Photocontrolled Reversible Amyloid Fibril Formation of Parathyroid Hormone-Derived
Peptides
[P3] Spiropyran as building block in peptide synthesis and modulation of photochromic properties

CONTENTS	iii

5	Con	clusion	82
	5.1	Photocontrol of azo-modified PTH <sub>25-37</sub> -derived peptides	83
	5.2	Co-fibrillization of azo-modified PTH $_{25-37}$ and PTH(-derived peptides)	86
	5.3	Novel spiropyran building blocks for SPPS	87
6	Syn	theses	89
	6.1	Azobenzenes	90
	6.2	Spiropyrans	92
	6.3	Solid-phase peptide synthesis	104
7	Refe	erences	105
Cı	ırricu	ılum Vitae	124
Aı	pend	iix	127

## List of abbreviations

 $A\beta$  amyloid- $\beta$ 

AFM atomic force microscopy

Ac acetyl

3,4'-AMPB 3-((4-(aminomethyl)phenyl)diazenyl)benzoic acid AMPP [3-(3-aminomethyl)phenylazo]phenylacetic acid

ATR attenuated total reflectance
Boc tert-butyloxycarbonyl
CD circular dichroism

CyHex cyclohexane
DCM dichloromethane
DMF dimethylformamide
DMSO dimethyl sulfoxide

EE ethyl acetate

EM electron microscopy

eq. equivalent Et ethyl

ESI electrospray ionization

FA formic acid

FASC 5'-amino-1',3',3'-trimethylspiro[chromene-2,2'-indoline]-

6-carboxylic acid

Fmoc fluorenylmethyloxycarbonyl

IR infrared

HPLC high-performance liquid chromatography

HR-MS high-resolution mass spectrometry

MALDI matrix-assisted laser desorption/ionization

MC merocyanine

MD molecular dynamics

Me methyl

MS mass spectrometry

NMR nuclear magnetic resonance

PSS photostationary state

PrP prion protein

PTH parathyroid hormone QS quorum sensing SAFC 6-amino-1',3',3'-trimethylspiro[chromene-2,2'-indoline]-

5'-carboxylic acid

SP spiropyran

SPPS solid-phase peptide synthesis

ssNMR solid-state nucleus magnetic resonance

Su succinimide TEA triethylamine

TEM transmission electron microscopy

THF tetrahydrofuran

TMFA thioflavin T-monitored fluorescence assay

ToF time-of-flight

UV ultraviolet radiation UV/Vis ultraviolet visible

WAXS wide-angle X-ray scattering

## **Abstract**

Amyloidogenic peptides are involved in many biological processes. Their self-organization, termed as amyloid formation, comprises of complex inter- and intramolecular interactions and is an efficient process to transform peptides from a soluble into an insoluble state. They play a crucial role in diseases such as Alzheimer disease or Parkinson disease or in physiological functionalities, like the storage of peptide hormones. Thus, the control of this process is a powerful tool to gain insight into the kinetics of fibrillization and the structural nature of the supramolecular assemblies. Furthermore, it promises the potential to develop novel medical treatments. Peptide hormones in particular, such as parathyroid hormone (PTH), are suitable candidates for the establishment of a model system due to their reversible fibril formation under physiological conditions.

In this work, various photoswitches were used to develop a model system based on PTH-derived peptides that is able to switch between a fibrillar and a non-fibrillar state by light. For this purpose, the respective building blocks were synthesised and incorporated into the fibril-forming sequence of the parathyroid hormone ( $PTH_{25-37}$ ) at different positions

Therefore, the azobenzene photoswitch 3-((4-(aminomethyl)phenyl)diazenyl)benzoic acid (3,4'-AMPB) was chosen and the novel spiropyran building blocks 5'-amino-1',3',3'-trimethylspiro[chromene-2,2'-indoline]-6-carboxylic acid (FASC) and 6-amino-1',3',3'-trimethylspiro[chromene-2,2'-indoline]-5'-carboxylic acid (SAFC) were designed, which can be incorporated into the peptide backbone. More than 20 peptides were produced using solid-phase peptide synthesis (SPPS) and their isomerisation behaviour, fibrillization behaviour and the morphology of the fibrils were studied.

The novel spiropyran building blocks are the first report of spiropyrans introduced in the backbone of peptides and thus, expand the toolbox of available switchable entities for modulating peptide behaviour. Solid-state nuclear magnetic resonance (ssNMR) and molecular dynamics (MD) studies of the unmodified PTH<sub>25-37</sub> and the azobenzene-containing derivatives allowed conclusions to be drawn about the structural details of the fibrils produced. While the unmodified peptide mainly forms fibrils consisting of parallel  $\beta$ -sheets, the fibrils of the 3,4'-AMPB containing peptides adopts an antiparallel arrangement. Furthermore, it was demonstrated that the isomeric conformations of the photoswitch modulated the fibrillization in a contrary way, which unlocked the control of the fibrillization. Thus, this is the first reversible (de)fibrillating peptide model and insights hereof, can be used as basis for further developments.

## Zusammenfassung

Amyloidogene Peptide sind an vielen biologischen Prozessen beteiligt. Ihre Selbstorganisation, die als Amyloidbildung bezeichnet wird, besteht aus komplexen inter- und intramolekularen Wechselwirkungen und ist ein effizienter Prozess, um Peptide von einem löslichen in einen unlöslichen Zustand zu überführen. Sie spielen eine entscheidende Rolle bei Krankheiten wie der Alzheimer- oder Parkinson-Krankheit oder bei physiologischen Funktionen wie der Speicherung von Peptidhormonen. Die Kontrolle über diesen Prozesses bietet daher eine einzigartige Möglichkeit, um Einblicke in die Kinetik der Fibrillierung und die strukturelle Beschaffenheit der supramolekularen Aggregate zu gewinnen. Darüber hinaus bietet sie das Potential neue medizinische Behandlungen zu entwickeln. Insbesondere Peptidhormone, wie das Parathormon, sind aufgrund ihrer reversiblen Fibrillenbildung unter physiologischen Bedingungen geeignete Kandidaten für die Etablierung eines Modellsystems.

In diesem Werk wurden verschiedene Photoschalter genutzt um ein Modellsystem auf Basis von PTH abgeleiteten Peptiden zu entwickeln, dass durch Licht in der Lage ist zwischen einem fibrillierenden und einem nicht fibrillierenden Zustand zu wechseln. Dazu wurden die jeweiligen Bausteine synthetisiert und in die fibrillenbildende Sequenz des Parathormons (PTH<sub>25-37</sub>) an verschiedenen Positionen eingebaut.

Die Grundlage dafür bildeten der Azobenzen-Schalter 3,4'-AMPB, sowie die neuartigen hierfür konzipierten Spiropyran-Bausteine FASC and SAFC, die in das Peptidrückgrat eingebaut werden können. Es wurden mehr als 20 Peptide mittels Festphasenpeptid-Synthese hergestellt und deren Isomerisierungsverhalten, Fibrillierungsverhalten, sowie die Morphologie der Fibrillen studiert.

Die hier entwickelten Spiropyran-Bausteine sind die erste Möglichkeit, Spiropyrane in das Rückgrat von Peptiden einzubauen und erweitern somit die Palette an schaltbaren Rückgratsmodifikationen zur Modulation des Peptidverhaltens. Festkörper-NMR und MD-Studien des unmodifizierten PTH $_{25-37}$  und der azobenzenhaltigen Derivate ließen Rückschlüsse auf strukturelle Details der erzeugten Fibrillen zu. Während das unmodifizierte Peptid hauptsächlich Fibrillen bildet, die aus parallelen  $\beta$ -Faltblättern bestehen, konnte gezeigt werden, dass eines der 3,4'-AMPB-haltigen Peptide eine antiparallele Anordnung annimmt. Darüber wiesen die isomeren Formen des Photoschalters gegensätzliche Effekte auf die Fibrillierung auf und es konnte demonstriert werden, dass es möglich ist zwischen einer fibrillierenden und einer nicht fibrillierenden Form reversibel zu wechseln. Dies ist somit der erste Bericht über ein reversibel (de)fibrillierendes Petidsystem und bietet damit eine Basis für weitere Entwicklungen.

## Introduction

The first process that takes places in the human body as we read these lines, is the a million times occuring phototriggered  $cis \rightarrow trans$ -isomerization of a 11-cis-retinal chromophore. The chromophore is attached to proteins called opsins, which are present in the rod and cone cells of the retina. <sup>1,2</sup> It is one of the most astonishing systems that we can find in nature concerning switching processes on a molecular level reacting to a external trigger. In general, molecular switches are molecules or entities of molecules, which can be activated through an external trigger in a directed manner between bistable or multistable states. <sup>3–5</sup> A plethora of stimulis exists to trigger the process: e.g. light, <sup>6,7</sup> temperature, <sup>8,9</sup> electric fields, <sup>10,11</sup> tunneling electrons, <sup>12,13</sup> changes in polatrity and pH, <sup>14,15</sup> and other chemical stimuli, <sup>16,17</sup> enable the manipulation of electronic properties, dipole moments, and molecular conformations. They can differ in their size from a small chemical entity inside a molecule <sup>6,18</sup> up to large macromolecules. <sup>19,20</sup>

The generic definition of molecular switches already indicates that the research in this field covers a broad scope and even more that it is a highly interdisciplinary field. The chemical and the physical aspects refer mostly to the structural motives of molecular switches and describe the isomerization process itself. In biological context switches are responsible for signal transduction<sup>21–23</sup> in living tissue and are a powerful tool in synthetic biology to control cellular processes.<sup>24</sup> In material sciences molecular switches are explored as molecular machines,<sup>25,26</sup> in displays,<sup>27,28</sup> and in smart materials.<sup>29</sup> For computer technology they are potential candidates to gain access to new materials like sensors and logical gates in molecular computers,<sup>30,31</sup> which could undergo the physical limits of silicon-based computer chips.<sup>32,33</sup>

As life on the earth is mainly fueled by the light energy of the sun, beneath some archaebacteria living under extreme conditions, their exist several behaviours of cells in reaction of changing light conditions. Beneath our ability of vision, described *vide supra*, the main purposes are: *e.g.* establishment of the circadian rythm, sensing different wavelengths of light, phototaxis,<sup>34</sup> and ATP synthesis.<sup>35</sup> Most of these processes are triggered by photochromic molecules, whereby photochromism describes the ability to undergo photoinduced isomerization reactions between stable and (meta)stable states.

Usually the chromophore is bound to a protein, e.g. G-proteine coupled receptor, ion channels,  $^{38,39}$  kinases,  $^{40}$  proton/ion pumps,  $^{35}$  or gene expression regulator. Absorption of a photon induces an isomerization process that leads to conformational change in the protein and starts a signal cascade. The chromophores can be seperated after their modes of action: retinal-based chromophores, bilin-based chromophores and cinnamic acid undergo a E/Z-isomerization, flavenoid-based chromophores and tryptophan change their electronic state. The deactivation of the protein, respectively the recovery of the photoswitch, can occur thermodynamically or accelerated via enzymes. In Table 1.1 a short

Table 1.1: Natural photoswitches and where they can be found. The changing bonds are highlighted in colour.

melanopsin <sup>36</sup> circadian ryrthm (blue)  rhodopsins¹ vision (visible)  neuropsin <sup>37</sup> circadian rythm (blue)  retinal-based  phototaxis  retinal-based  retina	Chromophor	Protein (organisms)	Function (light color)
retinal-based  retinal-based  retinal-based  retinal-based  (animals)  channelrhodopsin <sup>37</sup> (animals)  channelrhodopsin <sup>38</sup> (algae)  bacterial rhodopsins <sup>35,39</sup> (bacteria, archae)  phototaxis (green)  retinal-based  channelrhodopsins <sup>35,39</sup> (bacteria, archae)  phototaxis (green)  retinal-based  channelrhodopsins <sup>35,39</sup> (bacteria, archae)  phototaxis cell regulation (blue)  retinal-based  cyanobacteriochromes <sup>42</sup> (cyanobacteria)  retinal-based  retinal-based  collaboration (blue)  retinal-based  circadian rythm (blue)  circadian rythm (blue)  circadian rythm (blue)  collaboration (blue)  retinal-based  collaboration (blue)  retinal-based  collaboration (blue)  retinal-based  circadian rythm (blue)  circadian rythm (blue)  circadian rythm (blue)  collaboration (blue)  phototropin <sup>46</sup> (algae, plants)  chloroplast movement (UV and blue)			<u> </u>
retinal-based  Channelrhodopsin <sup>38</sup> (algae)  bacterial rhodopsins <sup>35,39</sup> (bacteria, archae)  Phototaxis (green)  phytochrome <sup>40,41</sup> (plants, bacteria, fungi)  Cyanobacteriochromes <sup>42</sup> (cyanobacteria)  phototaxis cell regulation (blue)  Cys-S-O-O-O-O-O-O-O-O-O-O-O-O-O-O-O-O-O-O-	\ /   onsin	-	
Cys   S   O		•	•
Cys-S  Cys-S  Chacteria indoopsins (bacteria, archae)  Cys-S  Cys-S  Chacteria, archae)  Cys-S  Cyanobacteriochromes (cyanobacteria)  Cyanobacteria)  Cyanobacteria  Cyan	retinal-based	_	_
Cys-S  O  Cys-S  O  Cys-S  O  Cyanobacteriochromes  (cyanobacteria)  (cyanobacteria)  (cyanobacteria)  (cyanobacteria)  (cyanobacteria)  (cyanobacteria)  (cyanobacteria)  (cyanobacteria)  (cyanobacteria)  (blue)  Cys-S  OH  xanthopsin <sup>43</sup> (bacteria)  (blue)  Cryptochrome  (blue)  Cryptochrome  (canimals)  (circadian rythm (blue)  (blue)  Chloroplast movement (algae, plants)  (chloroplast movement (uV and blue)  COOH  NH2  UVR8 <sup>47</sup> phototaxis			ATP synthesis
cyanobacteriochromes 22 phototaxis cell regulations (blue and green)  Cys-S-OH xanthopsin 43 unkwown (blue)  cinnamic acid  cryptochrome 44,45 (animals) circadian rythm (blue)  phototropin 46 (algae, plants) (UV and blue)  COOH  NH2 UVR8 47 phototaxis	0		cell regulation
xanthopsin <sup>43</sup> unkwown (blue)  cinnamic acid  cryptochrome <sup>44,45</sup> circadian rythm (blue)  quad phototropin <sup>46</sup> chloroplast movement (algae, plants) (UV and blue)  cooh  Vision (blue)  phototropin <sup>46</sup> (UV and blue)	Cys-S O		cell regulations
phototropin <sup>46</sup> chloroplast movement (algae, plants) (UV and blue)  COOH  NH <sub>2</sub> UVR8 <sup>47</sup> phototaxis	0	_	
phototropin <sup>46</sup> chloroplast movement (algae, plants) (UV and blue)  COOH  NH <sub>2</sub> UVR8 <sup>47</sup> phototaxis	N N O		· ·
NH <sub>2</sub> UVR8 <sup>47</sup> phototaxis	O		
tryptophan	N N N H		_

overview is given about known chromophores and examples of photoswitchable proteins, which occur in nature.

Occasionally, the first emergence of a photochromic behaviour is reported for Alexander III of Macedon, better known as Alexander the Great. 48,49 During his reign from 336–323 BC it was told, that his warriors used wristbands, changing their colour through the presence or absence of sunlight, to synchronize their military actions. It is not known if these should be taken seriously as it might be based on a play of words from an article in an American news magazine in 1961. It refers to the wristband as "Alexanders Rag Time Band", a homophonous word play to the song "Alexander's Ragtime Band" from Irvine Berlin.<sup>50</sup> However, the first "real" discovery of the photochromic effect was attributed to a German chemist in the second half of the nineteenth century. J. Fritsche reported the decolourization of an orange tetracene solution in the daylight and their recolourisation during the night.<sup>51</sup> In the following decades several similar phenomena were described<sup>52,53</sup> and the nowadays used term photochromism was introduced 1950 by Y. Hirshberg.<sup>54</sup> Light is a nearly perfect stimulus as it encodes information in wavelength and intensity. It exhibits a high resolution in space and time and does not permanently contaminate a treated sample. Furthermore, it does not cause undesired interactions as the photoisomerization is only triggered by light of specific wavelengths. This offers possibilities, like using two photoswitchable entities in a molecule, where each can be activated separatly, <sup>55</sup> or dual wavelength activation of initiators for polymerization reactions, which offer high spatial control.<sup>56</sup>

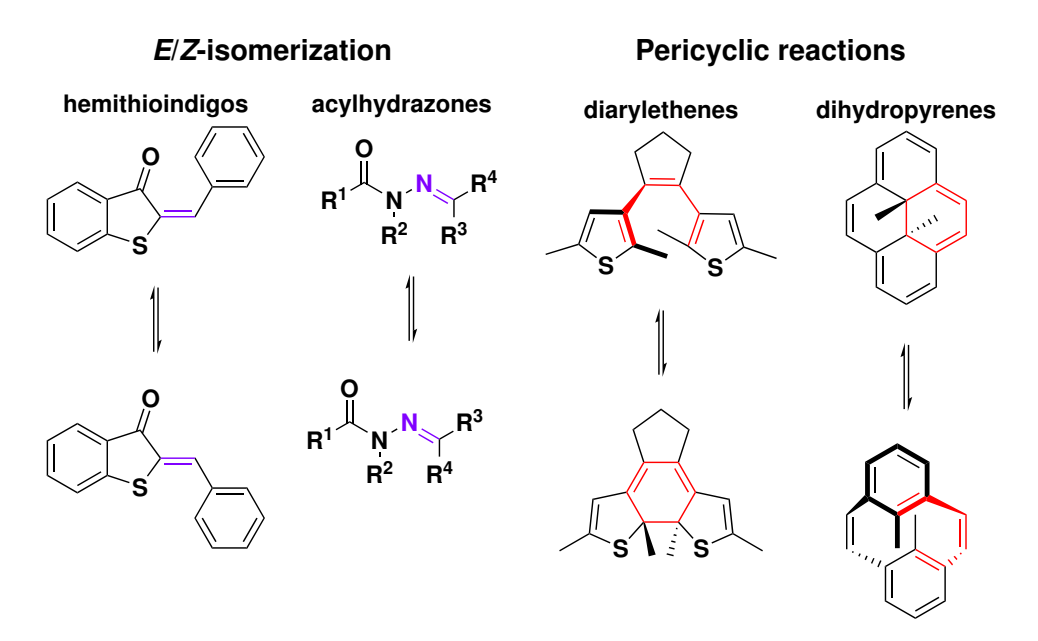


Figure 1.1: Selection of different types of synthetic photoswitches: (left) Photoswitches undegoing E/Z-isomerization. (right) Photoswitches undergoing pericyclic reactions.

Since Hirshberg introduced the term photochromism, several molecular structures were synthesised that possess this ability. However, for application in materials, they have to fulfill some requirements: large extinction coefficients, high quantum yields, a elevated ratio of the isomers in the respective photostationary state (PSS), low photobleaching, and facile synthesis and chemical functionalization.

Further requirements can occur in the different fields, e.g. in  $in\ vivo$  systems the switching wavelengths should be in the visible or far-red range to avoid ultraviolet radiation (UV) based cell damages.<sup>57</sup> Common photoswitchable entities can be divided into two groups (Figure 1.1):<sup>57–59</sup> The first group involves molecular entities, where the absorption of a photon causes E/Z-isomerization of a N=N, C=C or N=C double bond,  $e.\ g.$  stilbenes, hemithioindigos, overcrowded alkenes, acylhydrazones, and azobenzenes. While the second group undergoes pericyclic reactions (primary cyclization and ring opening), like diarylethenes, fulginimides, dihydropyrenes, and spiropyrans. In the following two sections we will gain further insights in the groups of azobenzenes, which exhibit E/Z-isomerization, and in the spiropyrans, which undergo cyclization/ring opening reactions.

#### 1.1 Azobenzenes

Azobenzenes are a class of molecules that represents a diazene (HN=NH) derivative, where both hydrogen atoms were replaced by arenes. The eponymous functionality is the azo-bridge (highlighted in Figure 1.2 in purple), two nitrogen atoms connected through a double bond. Similarly to stilbenes,  $^{60}$  the analogs with a carbon-carbon double bond, azobenzenes can exist in two isomeric forms. According to the arrangement of the arenes in relation to the double bond, we have either a *trans*-isomer, also called E-, or a *cis*-isomer, also called Z-. (Figure 1.2). In the further oeuvre exclusivly the *trans*-/*cis*-nomenclature will be used for the azobenzenes.

Figure 1.2: The simplest representative of the azobenzenes in it's isomeric forms: *trans*-azobenzene and *cis*-azobenzene.

Both forms can undergo isomerization to generate the other isomer. The isomerization process in both direction can be accessed *via* irradiation with light of different wavelengths. Further possible external triggers are mechanical stress<sup>61</sup> or electrostatic stimulation.<sup>62,63</sup> In general, the *trans*-isomer is the thermodynamically favoured state and therefore the metastable *cis*-form isomerizes spontaneously in the dark. Their beneficial switching properties and the facile synthetic access made them one of the most used and best studied photoswitches.<sup>64–67</sup>

#### **1.1.1 History**

The discovery of azobenzene occured in 1834 by E. Mitscherlich (Figure 1.3).<sup>68</sup> He described a red compound, which was obtained by heating nitrobenzene in the prescence of aqueous KOH-solution. After more than twenty years A. Nobel was the first who reported a method that could produce azobenzenes on an industrial scale, <sup>69</sup> which marks the beginning of the succes story of azobenzenes. He adapted the Bechamp modification of the Zinin's procedure, an actual procedure to reduce nitrobenzol to aniline with iron and acetic acid. 70 Two years afterwards P. Griess reported the diazotation reaction. 71 It is the nowadays singularly most used reaction in the synthetic dyes industry, <sup>72</sup> as azo dyes represent almost 70% of dyes used in industry. The textile industry, growing through the industrial revolution, 74 had an increasing demand of dyes. The first commercial azobenzene dye Aniline Yellow was reported by C. Mene in 1861.<sup>76</sup> Closely afterwards, in 1863 Bismarck Brown Y was introduced by C. A. von Martius.<sup>72</sup> It is the first bis azo dye and was synthesised through allowing nitrous acid to act on 1,3-phenylendiamine, an diazotation reaction followed by an azo coupling. Even though azobenzene had been known for more than thirty years, A. Kekulé reported the correct molecular formula C<sub>12</sub>H<sub>10</sub>N<sub>2</sub> for the first time in 1866.<sup>77</sup> A further application for azobenzenes was reported 1935 by G. Domagk, <sup>78</sup> who showed that sulfamidochrysoidine, a prodrug for sulfanilamide and better known under it's trade name "Prontosil", possesses an antibiotical activity against various bacteria. He was awarded for his achievement 1939 with the Nobel prize in physiology and medicine. The next significant step was

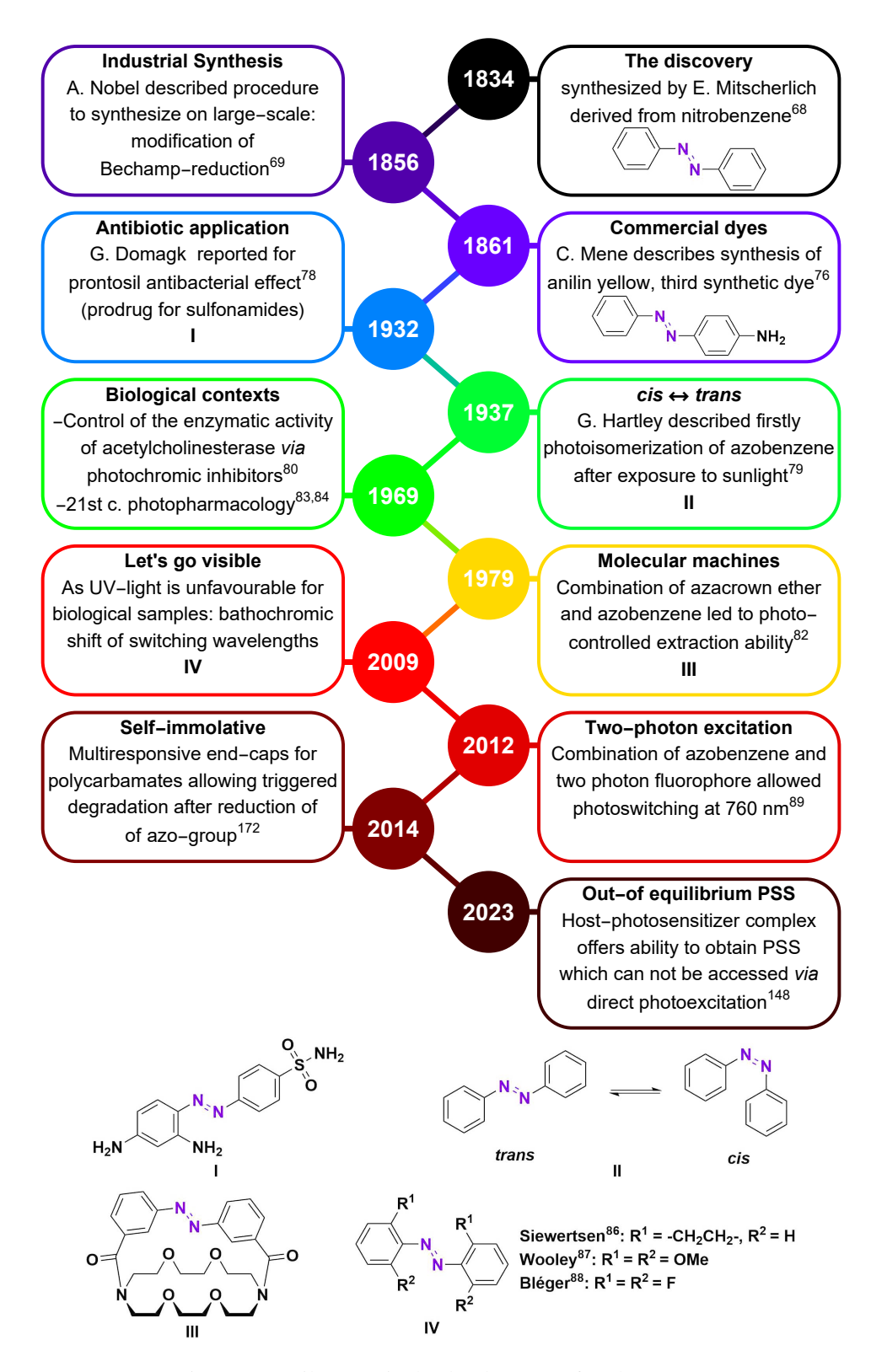


Figure 1.3: Milestones in the development of azobenzenes.

made by G. S. Hartley in 1937, when he observed a lack of reproducibility in solubility experiments upon exposure to light. His conclusions led him to the discovery of the photochemical *cis-trans*-isomerization.<sup>79</sup> This result offered another possible application for azobenzenes. Beneath the industrial use as a dye, azobenzenes could also be used as photoswitchable entities to control properties of materials. Major achievements are the first use in a biological example, which was in 1969,<sup>80</sup> the induced photochemically alignment of a liquid crystal phase in 1971,<sup>81</sup> or the first report of a molecular machine based on an azobenzene.<sup>82</sup> In the last two decades the field of photopharmacology emerged, where pioneering research was contributed by the groups of Trauner, Krahmer, and Feringa based on azobenzene photoswitches.<sup>83,84</sup> Even nowadays azobenzenes are the most used photoswitches in this field,<sup>85</sup> as they possess the most suitable properties especially for *in vivo* use. This correlates with another trend, which started at the end of the first decade of this century: the red-shifting of the azobenzene-switching.<sup>86–89</sup>

#### 1.1.2 Synthesis

In the almost 200 years that have passed since the discovery of azobenzenes, a plethora of synthetic methods have been described to obtain them. 90,91 Five main approaches have emerged (Figure 1.4):

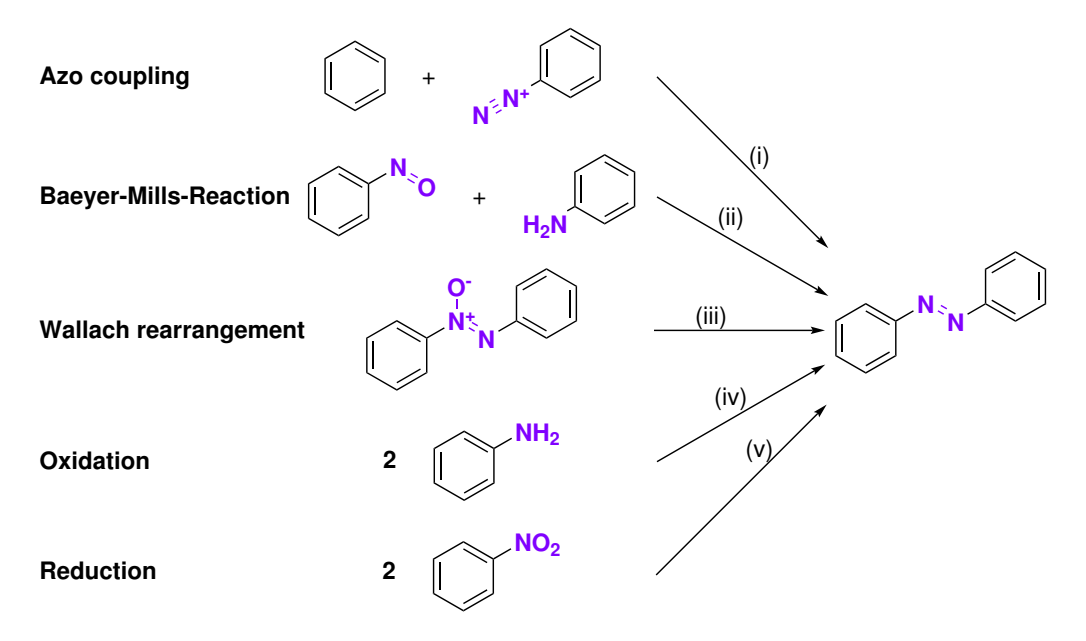


Figure 1.4: Synthetic methods towards azobenzenes.

- (i) The azo coupling reaction, discovered by the victorian brewer P. Griess, is still the most used chemical reaction to synthesize azobenzene derivates. It is based on the initial formation of the diazonuium-salt, from an aromatic amine, which then reacts with an electron-rich aromatic compound, e.g. aromatic amines or phenols.  $^{92}$
- (ii) The Bayer-Mills reaction is based on the condensation reaction between a nitroso compound and an aniline derivate. It was first published by A. Baeyer in 1874<sup>93</sup> and further investigated by C. Mills.<sup>94</sup>

- (iii) A chemoselective deoxygenation reaction of N-oxides, named after the German chemist O. Wallach, who discovered the reaction in 1890. The Wallach-rearrangement describes the transformation of azoxybenzenes into hydroxyazobenzene. The reaction is promoted by strong acids and dependent of the substituents in position 4 of the phenyl rings. It can lead either to 2-hydroxy or 4-hydroxy products.  $^{96,97}$
- (iv) The latest discovered of these methods is the oxidation of aromatic amines to obtain azobenzenes. The first chemical oxidation was reported in 1953<sup>98</sup> and the first electrolytical oxidation in 1972.<sup>99</sup> There exist various metallic and non-metallic oxidation reagents, which lead to symmetrical azobenzenes.
- (v) The reduction of nitro compounds was the first method discovered to synthesize azobenzenes (see 1.1.1).<sup>68</sup> It was the first method to obtain azobenzenes on an industrial scale and, like the oxidation of anilines, it leads to symmetrical azobenzenes.

#### 1.1.3 Transition process in detail

Azobenzenes belong to the group of photoswitches, which undergoes trans/cis-isomerization of a N=N double bond. The trans-isomer is the thermodynamically favoured one and adopts a planar conformation with  $C_{2h}$  symmetry,  $^{100}$  while the cis-isomer is distorted in the planarity and posseses  $C_2$  symmetry.  $^{101}$  The energy difference  $\Delta G$  between two isomers is  $\sim 56 \, \text{kJ/mol}^{102}$  and the thermal barrier between both isomers  $\Delta G^*$  is approximately  $100 \, \text{kJ/mol}$  in heptane  $^{103}$  and benzene.  $^{104}$  The  $trans \rightarrow cis$ -isomerization is achieved by the irradiation of UV light, while the opposing  $cis \rightarrow trans$ -isomerization proceeds thermally or is triggered by the irradiation of visible light. Beneath altering the shape, the isomerization process has two main impacts: Change in the dipole moment  $^{105}$  and in the end-to-end distance of the carbon atoms at the para-position of the rings (Figure 1.5A).  $^{106}$  While the trans-configuration has a dipole moment near zero and an end-to-end distance of  $\sim 9 \, \text{Å}$ , the dipole moment increases in the cis-form to  $\sim 3 \, \text{D}$  and the end-to-end distance is decreased to  $\sim 5.5 \, \text{Å}$ .

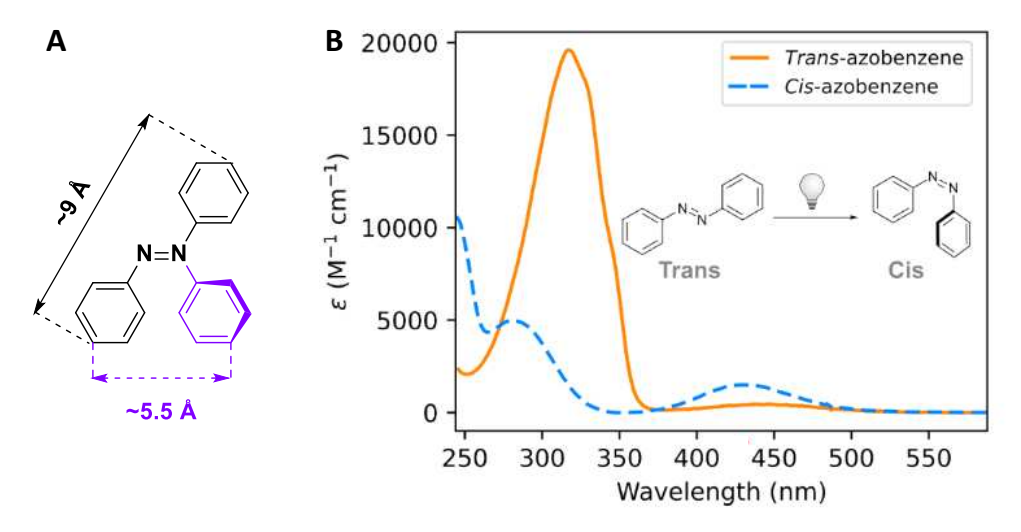


Figure 1.5: (A) Distance of the carbon atoms in the *para*-postions of the unsubstituted azobenzene. Black - structure of the *trans*-isomer. Purple - corresponds to the phenylring in *cis*-configuration. (B) Ultraviolet visible (UV/Vis)-absorption spectra of the isomers of unsubstituted azobenzene. Reprinted with permission from the Beilstein-Institute, copyright ©2024 (open access).<sup>107</sup>

In Figure 1.5B the extinction coefficients of the unsubstituted trans- and cis-azobenzene are shown. In both spectra we can observe two well seperated bands.<sup>66</sup> In the UV region we observe for the trans-azobenzene a band at 320 nm and for the cis-isomer a band at 270 nm, which both correspond to the symmetry allowed  $\pi \to \pi^*$  transition. The weaker band in the visible region, for both isomers the maximum is ~440 nm, corresponds to the symmetry forbidden  $n \to \pi^*$  transition. <sup>108</sup> As the *cis*-isomer is slightly distorted in the planarity, the  $n \to \pi^*$  transition absorbs more strongly than the one for the trans-isomer. While the  $\pi \to \pi^*$  transition excites the molecule to the  $S_2(\pi\pi^*)$  state, the  $n \to \pi$ transition excites the molecule to the  $S_1(n\pi^*)$  state. In stilbene *cis/trans*-photoisomerization occurs only via a rotational pathway,  $^{109}$  whereby the sum of the quantum yields of photoinduced  $cis \rightarrow trans$ and  $trans \rightarrow cis$ -isomerization equals one. However, in azobeneze the sum of the quantum yields does not, <sup>110</sup> which suggests, that the photoisomerization can occur *via* different mechanisms (Figure 1.6): in the rotation mechanism (upper mechanism), a cleavage of the  $\pi$  bond between the two nitrogens allows a free out-of-plane rotation of the dihedral angle of C-N-N-C, whereby the angle of N-N-C remains fixed. 100 In the inversion mechanism (lower mechanism) an inversion occurs in the plane. It corresponds to a transition state with linear geometry, where one of the nitrogen is sp hybridized.<sup>111</sup> One of the N=N-C angles is increased to 180°, while the C-N=N-C dihedral angle remains unchanged. Further possible mechanisms are the concerted inversion of both phenyl rings or the inversion supported rotation.66

Figure 1.6: Changes in the configuration of unsubstituted azobenzene from the thermostable *trans*-isomer to the metastable *cis*-isomer through irradiation with UV light. Shown here are, as examples: The rotation, an out of plane torsion of the C-N-N-C dihedral angle, and the inversion, which corresponds to an in plane inversion of the N=N-C angle between the azo moiety and the adjacent carbon atom of the phenyl ring.

For the  $trans \rightarrow cis$ -isomerization it has been proposed that excitation with UV (upper mechanism), which leads to the high-energy  $S_2(\pi\pi^*)$  state, causes a cleavage of the  $\pi$  bond between the two nitrogens. This allows a free out-of plane rotation of the C-N-N-C dihedral angle, whereby the N-N-C angle remains fixed. The excitation with visible light (lower mechanism), which excites in the  $S_1(n\pi^*)$  state, should therefore proceed via an in-plane inversion. However, a few years later investigations of the isomerization process after excitation in the  $S_2(\pi\pi^*)$  state revealed that the  $S_2$  state quantitatively relaxes in the  $S_1$  state and isomerization occurs uniformly from this state. Up to today it is not completely

clear by which pathway  $trans \rightarrow cis$  isomerization occurs, independent of the excitation wavelength. While computational analysis indicates a more rotational mechanism, ultra-fast time-resolved techniques tend to show a relaxation mechanism dominated by inversion with a rotational part. <sup>66</sup> For the reversed  $cis \rightarrow trans$ -isomerization we have a thermal and a photomediated process. Both are less investigated than the photostimulated trans-process. For the photoisomerization computational analysis, e.g. dynamic simulations<sup>114</sup> and ab initio calculations, <sup>115</sup> rather indicate a mechanism dominated by rotation. The half-life time of *cis*-isomer is ~two days. 104 As mechanism in solution rotation and inversion are possible mechanisms, <sup>116,117</sup> while the inversion pathway seems to be the dominant one in liquid crystals<sup>118</sup> and under high pressure.<sup>119</sup> While the rate of thermal isomerization is independent of solvent polarity<sup>120,121</sup> and solvent viscosity, it is dependent on temperature and accelerated by acids. 122 As well for the photoisomerization processes solvent viscosity does not have an effect. For solvent polarity, the situation is different: Although it does not show an effect on the  $\pi \to \pi^*$  excitation, the quantum yield of the trans  $\rightarrow$  cis-photoisomerization following the  $n \rightarrow \pi^*$  is increased and for the reversed photoisomerizaion it is decreased with increasing solvent polarity.<sup>66</sup> It was assumed that, only one exited state, the  $n\pi^*$  state itself, or a state more easily reachable from the  $n\pi^*$  than from the  $\pi\pi^*$ state, is responsible for the phototriggered isomerization process. 110

As the *trans* -isomer is thermally more stable, the equilibrium is strongly shifted towards it. Under ambient temperature and in the dark more than 99.9% of the *trans*-isomer are possible.<sup>65</sup> The photoisomerization process, however, is incomplete. At the optimal wavelength of 313 nm, 90% of the *cis*-isomer can be obtained, while in the reversed isomerization process 80% of the *trans*-form can be generated using light with a wavelength of 436 nm.<sup>123</sup> The reason is observable in the UV/Vis spectra (Figure 1.5B): Both, the UV band and the band in the visible region, overlap for the isomers.

#### 1.1.4 Structure-activity relationship

The photophysical properties of azobenzenes are highly dependent on the substitution pattern. Especially, the electron withdrawing/donating propensity and the position of the substituent have a great influence on the switching behaviour. Derivates bearing substituents, e.g. alkyl,  $^{130}$  halides,  $^{131}$  carboxylic acids,  $^{132}$  amides,  $^{133}$  esters,  $^{134}$  carbonyl, nitrile, and nitro  $^{135}$  in the 3/3'/4/4'-positions as well as 3/3'-alkoxy  $^{136}$  and -amino  $^{137}$  have in common, that the UV/Vis spectra resemble mostly the spectra of unsubstituted azobenzene, whereby the  $\pi\pi^*$  transistion band is slightly red-shifted, but both transition bands are well seperated (Table 1.2). They possess a shorter half-life of the cis-isomer as the substituents decrease the energy barrier for thermal isomerization. This effect correlates with the electron-withdrawing propensity of the substituents,  $^{138}$  e.g. carboxylic acid and nitro-containing azobenzenes exibit a rather fast thermal isomerization.

Electron-donating substituents with a +M effect (amino, N-amides, hydroxy, and alkoxy) in the 4/4'-position have a stronger effect on the absorption spectra. The  $\pi\pi^*$  transition is red-shifted and overlaps with the  $n\pi^*$  transition. This effect is minor for the weaker donors of electron density, N-amides<sup>125</sup> and alkoxy substituents, <sup>136</sup> and the two transition bands are still observable. For stronger electron-donating substituents, e.g. hydroxy or amino groups, both transition bands are overlapping partially or completely. <sup>125,139</sup> While in the latter case both transition bands lie in the range of visible

Table 1.2: Substituent effect on  $\pi\pi^*$  transition in the *trans*-isomer and on the half-life time  $\tau_{1/2}$  of *cis*-isomer in 4/4' modified azobenzenes.

# R¹ R² 
$$\tau_{1/2,cis}$$
 (solvent)  $\lambda_{\pi\pi^*,trans}$  [nm] Ref.

- H H 2880 min 320 [107]
1 Cl Cl 430 min (CyHex) 331 [124]
2 Me Me 401 min (CyHex) 330 [124]
3 H OMe 221 min (CyHex) 357 [124]
4 OMe OMe 221 min (CyHex) 353 [124]
5 NC(O)CH<sub>3</sub> NC(O)CH<sub>3</sub> 159 min (-) ~370 [125]
6 H NO<sub>2</sub> 94 min (CyHex) 330 [124]
7 H NEt<sub>2</sub> 69 min (CyHex) 330 [124]
8 NH<sub>2</sub> NH<sub>2</sub> 2 min (-) 420 [125]
9 H OH 31 min (toluene) 205 ms (ethanol) ~350 [126]

push-pull azobenzenes

10 NO<sub>2</sub> OH 4.6 ms (EtOH) - [127]
11 N(Me)<sub>2</sub> NO<sub>2</sub> 5 ms (DMSO) 450 [128, 129]

light, the overlapping of the transition states hampers the correct assignment of them and lowers the photoisomerization yield (Table 1.2). A different tendency can be observed in thermal  $cis \rightarrow trans$ -isomerization. N-amides and alkoxy substituents reduce the half-life time moderately, as they increase the electron density in the  $\pi^*$  orbital and thus lower the energy barrier of isomerization. However, the introduction of tautomerisable amino and hydroxy groups cause a significant decrease. Despite increasing the electron density in the  $\pi^*$  orbital the even greater influence arises from the resonance structures formed or from the tautomerization in the case of hydroxy groups (Figure 1.7). <sup>125,139</sup> These effects favour a hydrazone like-distribution with a N-N bond, which enables a rotation pathway to easily isomerize to the trans-isomer. The thermal isomerization is significantly affected by solvent polarity: in case of 4,4'dihydroxyazobenzene the half-life time increases by four orders of magnitude in toluene compared to ethanol. <sup>126,140</sup> Furthermore, in the case of amino groups we can observe a dependence of the pH value. Below the p $K_a$  value a protonated form of the azobenzene exists, where the  $n\pi^*$  transition is red-shifted to  $\sim$ 680 nm and therefore, both transition bands are seperated again. Unfortunately, the hydrazone-tautomer is in this case the preferred one, which disables the photoisomerization. <sup>141</sup>

If both electron-donating and electron-withdrawing substituents are present in the 4,4'-positions, it's called a push-pull-system (Figure 1.7). In general, the  $\pi\pi^*$  transition is red-shifted and can as well overlap with the  $n\pi^*$  transition band. The *cis*-isomer is less stable and therefore the half-life time is significantly reduced and can be in the range of milliseconds or microseconds (Table 1.2). A reason

Figure 1.7: Transition states increasing the thermal rate for *cis→trans*-isomerization.

hereby is again the formation of resonance structures, which enables the rotation around the azo-bond. The half-life time is furthermore dependend on the solvent polarity, whereby a increase of the rate constant about  $10^5$ -fold is possible for polar solvents over non-polar, because the isomerization occurs *via* a highly polar charge-separated transition state. <sup>129</sup>

Table 1.3: Substituent effect on  $n\pi^*$  transition in both isomers and on the half-life time  $\tau_{1/2}$  of *cis*-isomer in *ortho*-modified azobenzenes.

#	$\mathbf{R}^1$	$\mathbf{R}^2$	$ au_{1/2,cis}$ (solvent)	$\lambda_{n\pi^*,trans}$ [nm]	$\lambda_{n\pi^*,cis}$ [nm]	Ref.
-	Н	Н	2880 min	440	440	[107]
1	Н	Me	10 h (hexane)	460	439	[142, 143]
2	Me	Me	-	462	454	[142]
3	Cl	Cl	20.7 h	455	443	[144]
4	H	F	11 h (MeCN, 60°C)	448	420	[145]
5	F	F	~700 d (MeCN)	458	416	[88]
6	H	OMe	1.9 h (DMSO)	474 (calc.)	472 (calc.)	[87]
7	OMe	OMe	14 d (DMSO)	480	444	[87]

While the *para*-substitution has an effect on the electronic properties of the azobenzene, spatial and steric effects play a role if substituion occurs in *ortho*-position. Alkyl subtituents do not alter the electronic properties significantly. While *para*-alkyl subtituents cause for the *trans*-isomer a slight red-shift of the  $\pi\pi^*$  and a slight blue-shift of the  $n\pi^*$  transition, *ortho*-alkyl substituents cause an opposite effect, a slight blue-shift of  $\pi\pi^*$  and red-shifting of  $n\pi^*$  (Table 1.3). This effect is further

intensified with the number and size of the substituents and is steric in nature, as it causes a twisting of the phenyl rings. It results from the repulsion of the *ortho*-substituent and the distant lone-pair of the azo-nitrogen. Therefore, the effect is stronger for tetra-alkylated compared to dialkylated compounds, as in the second case the azobenzene can adopt a conformation, where the substituent does not interfere with the lone-pair. The same effect occurs for the *cis*-isomer. Interestingly, the dialkylated compund has a larger separation of the  $n\pi^*$  transition between both isomers than the tetralkylated one, as the transition is not shifted for the *cis*-isomer. Compared to unsubstituted azobenzene the half-life time of the *cis*-isomer is reduced. Half-life time of the *cis*-isomer is reduced. Half-life time of the cis-isomer is reduced. Half-life time

To achieve higher PSS ratios a further separation of the  $n\pi^*$  transition is necessary, which can be achieved with either ortho-methoxy or ortho-fluoro substituents. While a disubstitution with orthomethoxy groups only cause a significant red-shift, but not a separation of the transition bands, the tetramethoxy substituted derivate has a large separation of 36 nm. 87 This allows a PSS of 80% cis-isomer in dimethyl sulfoxide (DMSO) with 530-560 nm and 85% trans-isomer with 450-460 nm. Additionally, a strong increase of the half-life time was observed (2 d for the unsubstituted vs. 14 d for tetramethoxy substituted). Again this effect results from a large sterical repulsion, which brings the trans-isomer in a highly twisted conformation, compared to nearly planar unsubstituted or 4/4'-substituted azobenzenes. This brings the HOMO, which is located at the lone-pair of the nitrogen close to the electron-rich oxygen and therefore raises the relative energy of the HOMO. Photoisomerization in the cis-form relieves this interaction. Another approach, which nearly maintains the planarity, is the introduction of fluorine-atoms in the *ortho*-position. 88 Instead of the repulsion effect of the lone-pairs of nitrogen and oxygen, the fluorine, as a  $\sigma$ -electron withdrawing group, reduces the *n*-electron density in the azo-bond and therefore lowering the n-orbital energy. As the planarity is not distorted, the  $\pi\pi^*$ -transition is only slightly blue-shifted. Furthermore, it's causing a separation of the  $n\pi^*$  transition bands by 42 nm. Light of wavelengths above 450 nm leads to a PSS of 91% cis-isomer and light of 410 nm leads to 86% trans-isomer. The most exceptional property, however, is the thermal stability of the cis-isomer with a half-life time of more than two years. Further research with the fluorine-substituents showed, that if only the 2/2'-positions is substituted the effect on the switching behavior is diminished and the half-life time is reduced. 145

Despite, the shown effects of substitution patterns, there exist a plethora of different azobenzene compounds. Some with more exotic behavior can be seen in Figure 1.8: *e.g.* introduction of an ethylen bridge in the *ortho*-positions leads to an highly twisted *trans*-isomer, which is thermodynamically disfavoured compared to the *cis*-conformer, with an half-life time of 4.5 h in hexane. Furthermore the distortion of the planarity causes a separation of the  $n\pi^*$  bands of 95 nm, which enables a isomerization yield of >90% *trans*-isomer with light between 370–400 nm and 100% *cis*-isomer with green light (480–550 nm).

An *ortho*-hydroxy group<sup>139</sup> leeds to a similar behavior like a *para*-hydroxy group. It favours an hydrazone like structure and therefore possesses a half-life time below a second. In contrary to the

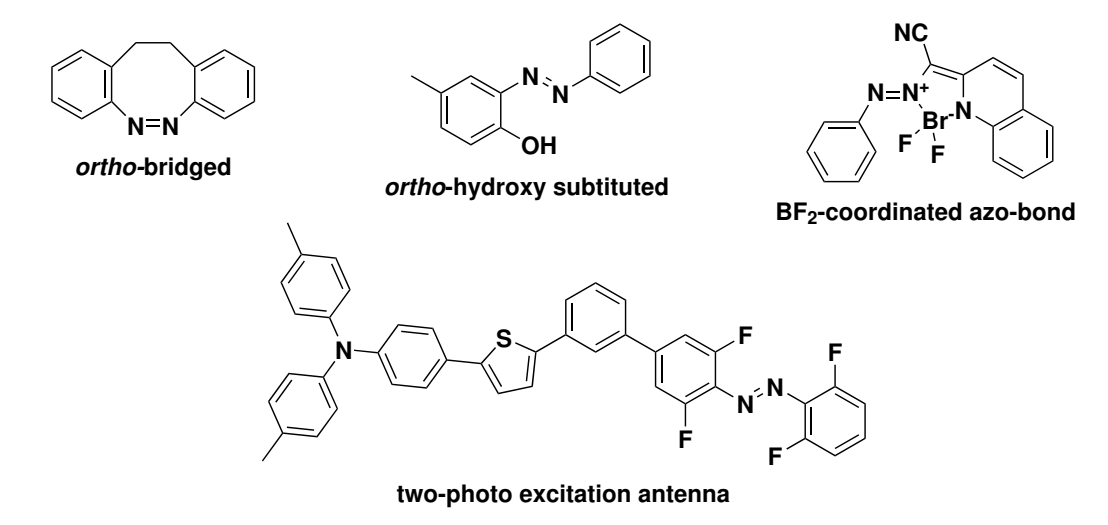


Figure 1.8: Further examples of rather exotic azobenzenes with interesting properties

para-position the ortho-position enables this behavior independently of the solvent.

The complexation of a BF<sub>2</sub>-unit with the nitrogen lone-pair, coupled with an extended  $\pi$ -electron system, alternates the energy of the  $n\pi^*$  and  $\pi\pi^*$  transition and leads to well separated transitions bands for both isomers of the latter in the visible range. <sup>146</sup>

The last example shows an *ortho*-F<sub>4</sub>-azobenzene with a conjugated "antenna". The antenna is able to harvest low energy light in the near-infrared (IR) region (750 nm), which is used for  $cis \rightarrow trans$ -isomerization triggered by two-photon excitation. In contrast, the reverse isomerization occurs with green light (510 nm). Recent research also showed that two-photon isomerization with near-IR excitation is possible *via* intermolecular Förster resonance energy transfer. 89

Another approach is the use of photosensitizers and cage-like structures. While the photosensitizer enables the use of different wavelengths, the cage has a significantly higher binding ability towards the *trans*-isomer. This enables a PSS out-of-equilibrium of nearly 100%, which is not achievable under normal photoisomerization conditions. 148

#### 1.1.5 Photoswitching of materials

From the myriad of photoswitches, azobenzenes offer currently the largest range of switching wavelengths and stabilities of photoactivated states. Therefore, they are widely distributed in material science. The Web of Science<sup>TM</sup>-database counts more than 18.000 entries for the keyword "azobenzene" (effective 11.05.2025). There exists a plethora of reviews covering the different applications, *i.e.* movable materials, <sup>149</sup> optical materials, <sup>150,151</sup> energy storage, <sup>152</sup> polymers for biological use, <sup>153</sup> or in biological systems, respectively, in biomimetical systems. <sup>85,154,155</sup>

The scientific discipline of investigating ways to influence the biologic ability of synthetic compounds is termed "photopharmacology". 85 To obtain photocontrol of proteins or peptides in particular, the photoresponsive entity has to stabilize or destabilize their interacting conformation. Thus, several approaches exist for photoswitches to achieve this for the protein of interest (Figure 1.9):

#### (i) Incorporation into ligand or inhibitor

- (ii) Attachment in the side-chain or at the N-terminal/C-terminal end
- (iii) Incorporation in the backbone

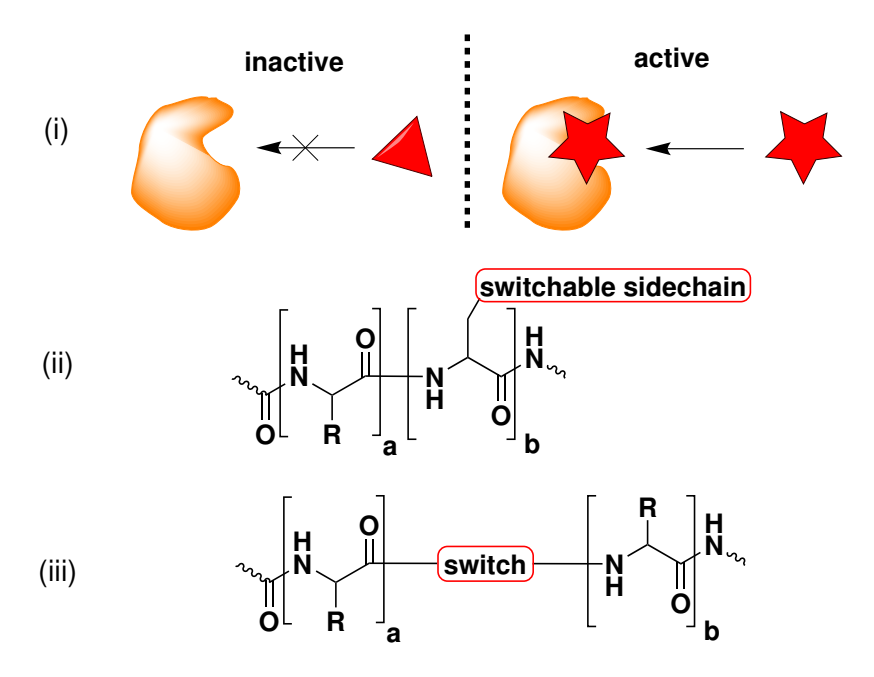


Figure 1.9: Approaches to achieve photocontrol of protein of interest. (i) Photochromic ligand switching between active (triangle) and inactive form. (ii) Photoswitch is attached to side chain. (iii) Photoswitch is introduced as a backbone modification.

In the first approach (i) the azobenzene is incorporated into the structure of a ligand or an inhibitor of a protein. These are usually smaller molecules and the azobenzene is introduced during the synthesis process. One of the azobenzene isomers forms the active molecule, while the other isomer forms an inactive form. The first use of azobenzenes in proteins is an example therefore (Table 1.4 #1). A reversible inhibitor of acetylcholin esterase was synthesised bearing an azobenzene moiety. As both azobenzene isomers possess different effectivity, it was possible to modulate the activity of the enzyme over several switching cycles *in vitro* with UV light and sunlight.

The molecule ShuBQX-3 (Table 1.4 #2) is a derivate of an antagonist of the AMPA receptor. <sup>156</sup> AMPA receptors are transmembrane receptors for glutamate and play a crucial role in excitatory neurotransmission. It could be shown that ShuBQX-3 was able to reduce selectively the activity of AMPA receptors *in vivo* with the *trans*-form as the active one. Interestingly, interaction of the photoswitchable antagonist and the receptor caused a red-shift of the  $\pi\pi^*$  band and therefore enabled isomerization to the inactive *cis*-form with blue light.

The third example (Table 1.4 #3) acts in the regulation of quorum sensing (QS) in bacteria. QS describes a process to detect cell density and synchronize gene expression *via* extracellular signal molecules. The combination of such an azobenzene and a signal molecule, an *N*-acyl homoserine lactone, enabled control over this process and therefore QS-related gene expression. <sup>157</sup> The *trans*-form was inactive, while the *cis*-isomer, generated with light of 365 nm wavelength, induces the production of luminescent molecules in an *E. coli* strain.

For the second approach (ii) the azobenzene is attached to the side-chains or at one of the terminal ends. Therefore, the protein can change spatial distances in the target molecule or between the target molecule and an attached structure. In this case the azobenzene is usually introduced after the proteine was synthesised. Therefore, it has to bear moieties which can be linked to the protein. An example for that is azo-modified poly(L-lysine) (Table 1.4 #4). The azobenzene was attached at the amino groups of the lysine side chain via a sulfonamide group. It was demonstrated that in mixtures of organic solvents, the conformation of photoresponsive polypeptides could be switched between a rather random coil and higher  $\alpha$ -helical content with light of 340 nm and 417 nm wavelength.

Ionotropic glutamate receptors (iGluR) are ligand-gated ion channels responding to glutamate. A engineered iGluR was modified with the reaction of the thiol residue of cysteine with a maleinimide bearing an azobenzene and a tethered glutamate residue (Table 1.4 #5). The *trans*-isomer is the inactive form as it seperates the glutamate entity from the binding site of the receptor, while the *cis*-isomer brings the glutamate close to the binding site. In *ex vivo* experiments the receptor was activated after irradiation with light of 380 nm wavelength and turned off with light of 500 nm wavelength.

Table 1.4: Selected examples of azobenzene modified materials

#	Structure	Target/construct	Ref.
1	N N CI	acetylcholin esterase in vitro	[80]
2	O N CF <sub>3</sub> O N N N N	AMPA receptor ex vivo	[156]
3	O H N N	quorum sensing in vivo	[157]

#	structure	target/construct	Ref.
4	O N N N N N N N N N N N N N N N N N N N	poly(L-lysine) in vitro	[158]
5	O H N O H O H O H O H O H O O H O O O O	iGluR ex vivo	[159]
6	DDDIVFE-C FARQRL C-GMKDD	β-adaptin ex vivo	[160]
7	F N VHLRKS-C(O)NH <sub>2</sub> NH  H <sub>2</sub> N-SARA	WDR5 in vitro	[161]
8	SWTWE N N N N N N N N N N N N N N N N N N N	Trp-zipper in vitro	[162]

#	structure	target/construct	Ref.
9	$ \begin{array}{c c}  & N \\  & A \\$	Aβ in vitro	[163]
10	HN N N O	neuronal NO synthase in vitro	[164]

Another linker strategy involving the thiol residue is based on the nucleophilic substitution of alkyl halides. In Table 1.4 #6 an endocytosis process was turned on and off via protein-protein interaction with  $\beta$ -adaptin. The azobenzene bearing two para-chloroacetamido groups was attached by reaction with two cysteine residues in the designed peptides. Furthermore, the azobenzene possesses two meta-sulfonate groups to increase solubility. The resulting peptides were cell-permeable and taken up by various cell lines. The cis-isomer induced an  $\alpha$ -helical conformation, generated by light of 380 nm, while the trans-isomer favors a random coil conformation, generated by light of 500 nm. The  $\alpha$ -helical conformation binds the  $\beta$ -adaptin and inhibits the endocytosis process in ex vivo experiments.

The last approach (iii) comprises azobenzenes, which are incorporated into the protein backbone. Therefore, the azobenzene has to bear an amino and a carboxy moiety. In general standard SPPS technics are sufficient to integrate the switch directly in the peptide. However, if groups are not stable under standard SPPS conditions, *i.e. ortho*-fluoro groups can undergo nucleophilic substitution reactions, <sup>161</sup> chemical ligation of peptides acts as an alternative synthetic route. <sup>165</sup> For the azobenzene in Table 1.4 #7 the chemical ligation was used to introduce the photoswitch into a peptidomimetic, which interacts with WDR5. <sup>161</sup> WDR5 is essential for the histone-methyltransferase activity of MLL1. The novel peptidomimetics showed affinity to WDR5, but the configuration of the azo double bond showed only a minor impact. This was the first attempt of incorporating visible light switchable *ortho*-fluoro azobenzenes into peptides.

The AMPP ([3-(3-aminomethyl)phenylazo]phenylacetic acid) photoswitch is designed to link two peptide chains. <sup>166</sup> Therefore it bears the necessary groups in the *meta*-position linked through a methylene group. The  $\beta$ -hairpin is the smallest known structural motif consisting of short  $\beta$ -strands. However, they are only marginally stable and are more difficult to characterize. In Table 1.4 #8 the AMPP was incorporated into the known  $\beta$ -hairpin forming Trp-zipper motif. <sup>162</sup> The *meta*-, *meta*-substitution has proven to be suitable in the *cis*-form to stabilize the  $\beta$ -hairpin. In contrary, the *trans*-form preferred a disordered structure.

Based on this the AMPP switch was introduced in amyloid- $\beta$  (A $\beta$ , Table 1.4# 9)<sup>163</sup> to test the hypothesis whether turn nucleation affects self-assembly of A $\beta$ . They replaced three amino acids in the turn region by the AMPP switch and were able to show that the *trans*-isomer self-assembles into

aggregates, while the *cis*-isomer only forms amorphous structures.

Another used azobenzene is the 3,4'-AMPB switch, which bears the carboxy group in the *meta*-position and the amino group with an methylene linker in the *para*-position. <sup>167</sup> For example in Table 1.4 # 10, the 3,4'-AMPB entity was included into the internal recognition motif of neuronal NO synthase. <sup>164</sup> The peptidomimic is a cyclic petide that adopts in the *cis*-form a  $\beta$ -finger, an internal  $\beta$ -hairpin, which activates the enzym. The *trans*-isomer, however, showed almost no binding.

Figure 1.10: Applications of azobenzene degradation. (A) The sulfasalazin prodrug is metabolized through bacterial azoreductases to active compounds 5-amino salicylic acid and sulfapyridin. (B) Self-immolative polymers: reduction of azobenzene group causes depolymerization. The elipsoids represent the monomeric units. Reprinted and adapted with permission from the American Chemical Society, copyright ©2014. 172

It has to be taken into consideration, that in *in vivo* and *ex vivo* experiments reduction reactions and reductive environments in cells can limit the availability of the respective molecule. The main

degradation pathways are the NADPH dependent reduction *via* azoreductases to anilines<sup>168</sup> and the glutathion mediated reduction to hydrazines.<sup>169</sup> In other contexts, however, this can be a desired property, *i.e.* prodrugs,<sup>170</sup> mycel based drug release,<sup>171</sup> or in self-immolative polymers.<sup>172,173</sup> In medicine for example the 1935 discovered Prontosil, serves as a prodrug that is metabolized to sulfanilamide. Sulfasalazin (Figure 1.10A) is metabolized in the colon through bacterial azoreductases and the metabolites sulfapyridin and 5-amino salicylic acid serve as anti-rheumatic agents against inflammatory diseases.<sup>170</sup> The sensitivity to reducing agents can also be used in polymer science as a trigger for self-immolative polymers. In Figure 1.10B the schematic structure of a self-immolative polycarbamate with a single azobenzene end-cap is shown.<sup>172</sup> Upon reduction, including hydrazine and dithiothreitol to hydrazobenzene, an 1,6-elimination reaction occurs followed by depolymerization of the polymer.

1.2. SPIROPYRANS 21

#### 1.2 Spiropyrans

Another class of widely used photoswitches are the spiropyrans. These photoswitches belong in contrast to the azobenzene to the second group of photoswitches, which undergo isomerization through pericyclic reactions. In the case of spiropyrans, irradiation with UV light generates the coloured merocyanine (MC)-isomer *via* ring-opening and visble light regenerates the colourless spiropyran (SP)-form through cyclization (Figure 1.11). The MC-form is a hybrid of its two resonance structures, the quinoidal and the zwitterionic MC. As a chemist the term spiropyran is somewhat misleading: from nomenclature aspects spiropyran would refer to all pyran-isomers, where the protons at one position are replaced by a spiro functionality, a second ring system linked to the carbon atom. However, nowadays it is associated with indolino-benzospiropyrans, a 2H-pyran-isomers bearing an indole as the second ring (Figure 1.11), <sup>174–176</sup> and we will focus on this type in the following section.

Figure 1.11: Isomerization process of spiropyrans: (left) spiropyran-form (SP), (right) resonance structures of the merocyanine-form (MC). The ring system participating in isomerization is highlighted in red.

What makes spiropyrans special compared to most other photoswitches are the strongly different properties of the SP- and the MC-form. Furthermore, beneath the photoisomerization there exist several further triggers: *e.g.* solvent polarity, <sup>177</sup> metal ions, <sup>178</sup> acidity/basicity, <sup>179</sup> temperature, <sup>180</sup> redox potential, <sup>181</sup> and mechanical force. <sup>182</sup> This enables, dependent of the environmental properties both positive, the colourization under UV light, and negative photochromism, the decolourization under visible light.

#### 1.2.1 History

The story of spiropyrans begun more than 70 years after the discovery of azobenzenes in the year 1908. The first description is attributed to H. Decker and H. Felser, who synthesised dipheno-spiropyran (IUPAC: 2,2'-spirobi[chromene], Figure 1.12) starting from dicumarketon, the aldol condensation product of one equivalent (eq.) acetone and two eq. salicylaldehyde. Spiropyrans first attracted attention when their thermochromism was reported. Three articles appeared in 1926 describing, that dinaptho-spiropyrans, colourless in solution and as solid, turn to a violet-blue colour simply by heating. Furthermore, they assumed the formation of a zwitter ionic species. During the following

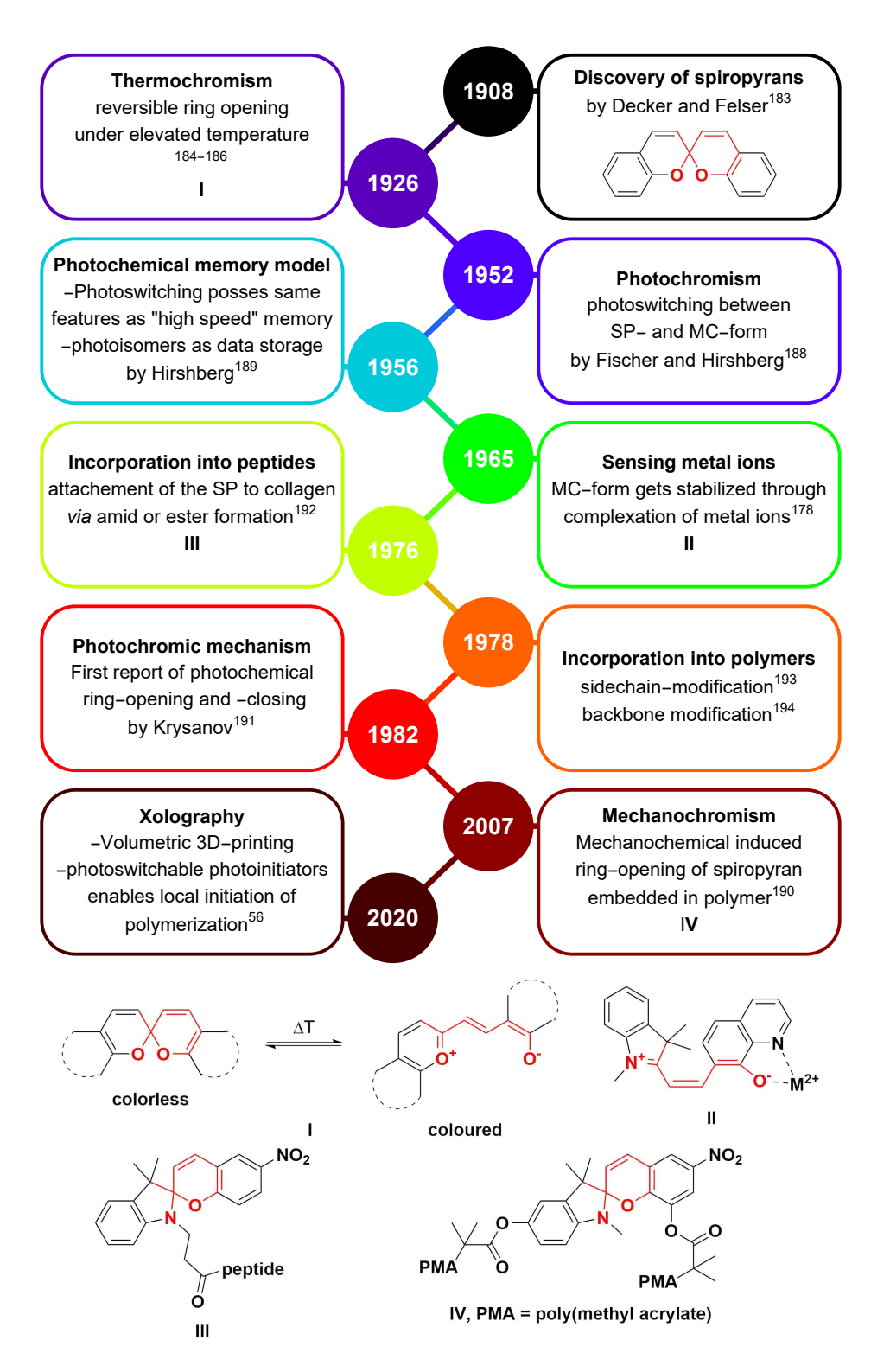


Figure 1.12: Milestones in the development of spiropyrans.

1.2. SPIROPYRANS 23

decades, the non-photochromic spiropyrans were further investigated and new properties were reported, e.g. their acidchromic behavior. 187 However, it was not until 1952, that E. Fischer and Y. Hirshberg reported the photochromic behavior of the nowadays with the term spiropyran associated structure (Figure 1.11), the condensation product of salicylaldehydes with a Fischer base. <sup>188</sup> Based on these insights Y. Hirshberg reported 1956 a reversible photochemical process, which possess the same features as computer memory, the first photochemical memory model. 189 In the following years, further findings were obtained about the switching behavior and the photoswitching process in detail. The metal ion sensitivity was reported 1965, 178 while the mechanochromic properties were not known until 2007. 190 The mechanism of the phototriggered isomerization process, however, was elucidated three decades after the discovery in 1982. 191 To use the property of photochromic molecules in materials, the photoswitch has to be brought into spatial proximity of the respective material. The first application on proteins was reported 1976, when a spiropyran was attached to the sidechains of a collagen membrane and enabled the control of the activity of urease. 192 The first introduction in the side-chain of synthetic polymers was two years later. 193 A spiropyran modified methacrylate was copolymerized with methylmethacrylate allowing the photoreversible change of the polymer viscosity. The introduction in the backbone of macromolecules did not take place until 2013, when spiropyran backbone modified polymers were synthesised via Suzuki-polycondensation. 194

#### 1.2.2 Synthesis

Compared to the variety of synthetic methods towards azobenzenes, the synthetic approaches towards spiropyrans can be reduced to one standard method: The condensation of *ortho*-hydroxy aromatic aldehydes, with methylene bases, in our case indole derivates, or their precursors (Figure 1.13). The proton, which interacts in the reaction is derived from the solvent molecules, most often alcohols.<sup>195</sup>

$$H^{+}$$
 $H^{+}$ 
 $H^{+$ 

Figure 1.13: General reaction mechanism for condensation of indolene species with *ortho*-hydroxy aromatic aldehydes towards spiropyrans.

Despite the single synthetic method, a variety of different structural features are possible due to simple access to the precursors. However, especially alterations in the pyran ring require a slighlty different reaction management (Figure 1.14). Two example are, on the one hand, the introduction of a

Figure 1.14: Modification of the reaction procedure to obtain pyran-ring modified spiropyrans. (A) Reaction procedure towars 4'-subtitution of the pyran ring. (B) Reaction procedure towards spiropyrans containing instead of the pyran ring a oxepin-2(3*H*)-one ring.

substituent in the 4'-position, which is obtained by replacing the indole(-precursor) with an acyl derivate thereof (Figure 1.14A) and adding phosphoroxychloride as an agent. On the other hand, replacing the *ortho*-hydroxy group by a carboxy group of the aromatic aldehyde led to spirooxyepinones with a seven-membered ring instead of the six-membered pyran ring (Figure 1.14B).

Spiropyran isomers differ vastly in their physicochemical properties and show significant differences in their structures. The SP-form, with the tetrahedrical C<sub>spiro</sub>, occupies less volume than the planar structure of the MC-isomer. 196 The alteration in the electronic structure results further in a large charge separation of the MC-form and therefore, gives a large rise in the electric dipole moment, ~14 D, compared to the SP-form, ~6 D. 197,198 Additionally, the changes in the electronic structures strongly alter the spectroscopic properties. The colourless SP-isomer, with the closed pyran-ring, possesses two transition bands. The  $\pi\pi^*$  transition of the indole moiety is located around ~285 nm and the  $\pi\pi^*$ transition of the chromene part is red-shifted towards ~340 nm. <sup>199</sup> The MC-isomer, however, appears with a deep blue colour and exhibits a new absorption maxima in the range of 550-600 nm. 174 In addition, they differ not only in their absorption behaviour, but also in their emission behaviour. While the SP-form does not show any strong emission, the extended  $\pi$ -conjugated system of the MC-form exhibits a strong emission of red light centered ~650 nm. <sup>200</sup> The MC-form possesses further special properties compared to the SP-form: It has a significantly increased basicity. The protonation leads to the protonated MCH<sup>+</sup>-isomer, which exhibits a characteristic band in absorption spectrum ~420 nm. <sup>201</sup> The MC-form also tends to aggregation, mainly driven by dipol-dipol interaction and promoted by  $\pi\pi$  stacking, whereby the aggregation takes place readily in non-polar solvents. <sup>202,203</sup> To understand the isomerization process, we must be aware that the MC-form adopts, additionally to its two resonance structures, eight isomers (Figures 1.15A). These isomers, firstly reported 1953, <sup>204</sup> result through rotation around three bonds (indicated through  $\alpha, \beta, \gamma$ ), and are energetically distinct. At any given temperature a weighted average of all states is obtained. The nomenclature consisting of three letters follows an cis/trans-orientation over the three adjoining bonds. <sup>175</sup> The isomers can be divided into two forms dependent on the configuration of the double bond (indicated with  $\beta$ , Figure 1.15A): The cisoid-MCs (cis-configuration) and the transoid-MCs (trans-configuration).

1.2. SPIROPYRANS 25

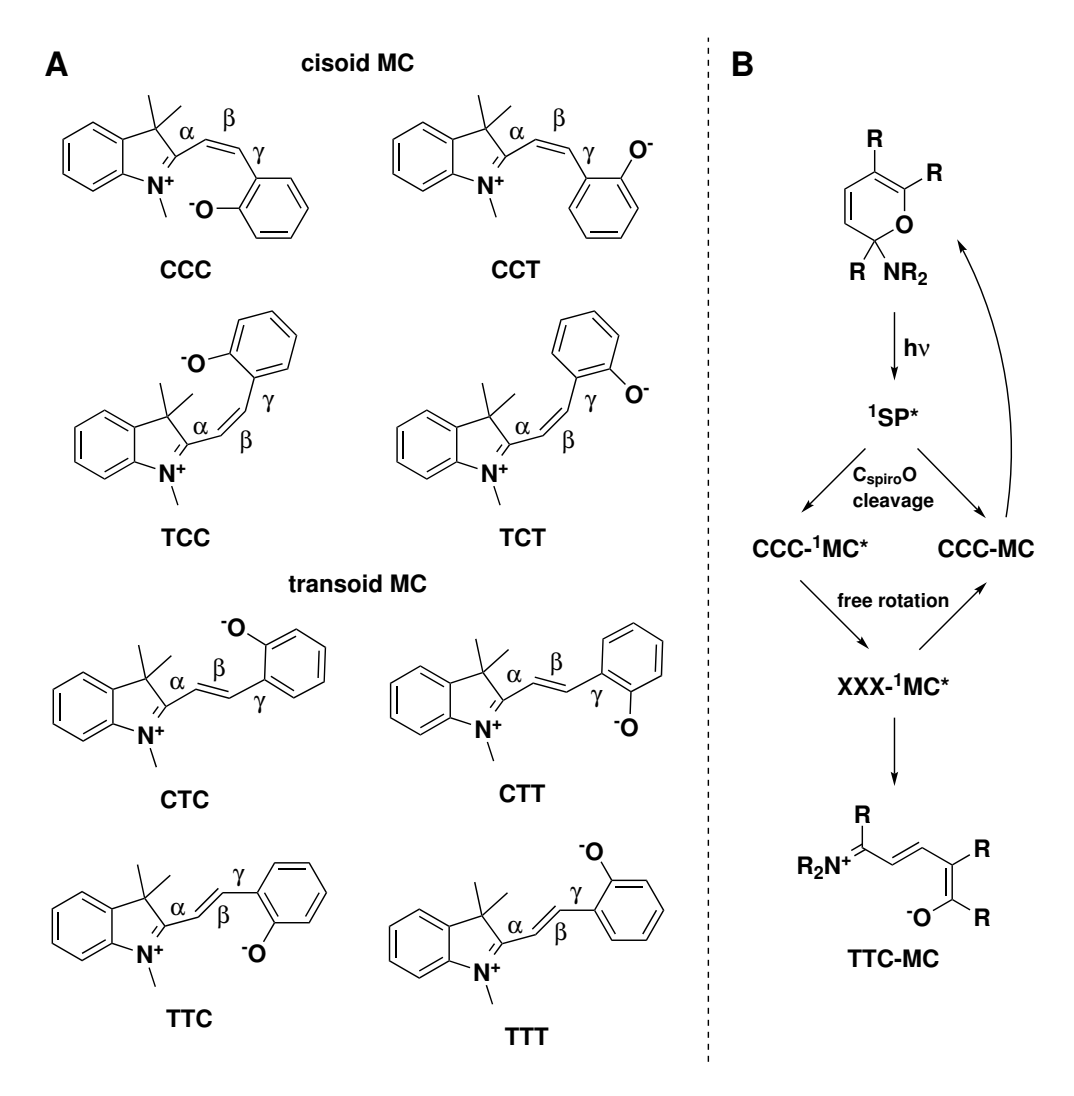


Figure 1.15: (A) The distinct isomers of the MC-form. The nomenclature refers to the spatial orientation (C - Z, T - E) of the three bonds (indicated as  $\alpha$ ,  $\beta$ , and  $\gamma$ ) between the  $C_{spiro}$  and the phenolate ring. The isomers are divided into two groups, cisoid and transoid, depending on the configuration of the double bond ( $\beta$ ). (B) The general mechanism of SP $\rightarrow$ MC-photoisomerization. XXX- $^1$ MC\* refers to species with unknown geometry, X can be either C or T. Reprinted and adapted with permission from the Royal Society of Chemistry, copyright ©2019 (open access).  $^{175}$ 

The first step in the UV triggered SP $\rightarrow$ MC-isomerization is electronic excitation of the SP-isomer, which undergoes subsequently cleavage of the  $C_{spiro}$ O-bond, thus, resulting in the CCC-MC\* (Figure 1.15B). The exact mechanism depends on the substitution pattern of the spiropyran. Spiropyrans without additional substituents access a singlet state  ${}^{1}$ SP\*, where it loses its double bond character through a  $\pi\pi*$  transition. As electronic processes are faster than nuclear motions, the cleavage of the  $C_{spiro}$ O bond reduces the energy before rotation processes take place. Through rotation processes of the three bonds ( $\alpha$ ,  $\beta$ ,  $\gamma$ ) a metastable species XXX- ${}^{1}$ MC\* is obtained, whereby X can be either C or T. This species can either undergo pericyclic rearrangement towards the SP-form or relaxate into the ground state. This ground state leads to thermally unstable cisoid MCs or thermally stable transoid MCs.  ${}^{175}$ In contrast, 6'-nitro substitution faciliates the access to triplet state via intersystem crossing from the

singulet  $^1SP^*$  to  $^3SP^*$  state, $^{205}$  which is similar to the  $S_1$ - $T_1$  intersystem crossing of nitro substituted stilbenes. $^{175}$  Furthermore, the  $SP \rightarrow MC$ -isomerization is also accessible through two-photon excitation in the near IR range. $^{206}$  The inverse photoreaction of the  $MC \rightarrow SP$  is more complex, as the MC-form not only exist in an equilibrium of the zwitterionic and the quinodial form, but also in a mixture of the most stable MC-isomer TTC and a minor amount of TTT. $^{207}$  A possible mechanism starts with the excitation of the MC ground state in a excited  $S_1$  state with a destabilized double bond  $(\beta)$ , which lowers the activation energy to adopt a twisted form. The twisted or cis-intermediate undergoes either ring closure towards the SP-form or re-forms the excited trans-MC  $S_1$ , which relaxes in the ground state MC  $S_0$ . $^{208}$ 

Despite the irradiation with light, the equilibrium of the MC-form and the SP-form is dependent of a variety of other environmental factors. The influence known for the longest time is the temperature, as mentioned in the history section (1.2.1). <sup>184–186</sup> The thermochromism of spiropyrans was even in the early 1960s one of best sudied. <sup>209</sup> Interestingly, the reversible colour change was not reported for the first spiropyran, the dibenzospiropyran. The insight, that the polarization of the spiro-centre is accessible through introduction of a indolino group, <sup>210</sup> was a breakthrough. While in non-polar solvents SP is the dominant form, elevated temperatures lead to a reversible shift in the equilibrium towards the MC-form. While the photoisomerization mechanism ends with the formation of the zwitterionic resonance structure, the thermal isomerization leads through an electrocyclic reaction path to the quinodial resonance structure (Figure 1.16). <sup>174</sup>

thermal photochemical

$$R \longrightarrow R$$
 $R_2 N \bigcirc R$ 
 $R_3 N \bigcirc R$ 
 $R_4 N \bigcirc R$ 
 $R_5 N \bigcirc R$ 

Figure 1.16: Simplified mechanism of the thermal and the photochemical isomerization of spiropyrans.

Another factor to alter the equilibrium is the solvent polarity. The solvatochromism of spiropyrans is known since the end of the first half of the twentieth century.<sup>211</sup> In non-polar solvents the SP is the dominant form and therefore positive photochromism occurs. Interactions with polar solvents, however, stabilizes and lowers the energy level of the MC-isomer,<sup>212</sup> which is why the MC is the dominant form and negative photochromism occurs. A phenomenom we could already observe in the solvatochromism of the spiropyrans is the charge-induced ionization, which leads to the coloured MC-form. This effect is further enhanced by the presence of protons, referred to as acidochromism, or the presence of metal

1.2. SPIROPYRANS 27

ions, referred to as metalochromism.  $^{175}$  The formation of coloured species through addition of acids is a general phenomenom of spiropyrans and was already known before the photochromism.  $^{210}$  Important for the protonation driven ring-opening is the strength of the acid. In 1929 it was demonstrated, that acetic acid is not able to induce acidochromism, whereas the replacement of the hydrogen atoms with chlorines in trichloroacetic acid enabled the acidochromic behavior of dinaphtospiropyrans.  $^{187}$  For indolino spiropyrans this effect was reported nearly seven decades later in 1995.  $^{213}$  Interestingly, the acidochromism enables an access to the actually non-available cisoid-MCs. Both, the transoid and cisoid forms, differ in their pK $_a$ .  $^{175}$  The use of acids, like hydrochloric acid or trifluoroacetic acid promotes the formation of transoid-MCs. Use of stronger acids, e.g. promotes the formation of a relative stable cis-MC form undergoing slow thermal isomerization towards the trans-form. This enables a further photochromic behavior, as the cis-MCH $^+$  is generated from the trans-MCH $^+$  by irradiation of light of 455 nm and  $vice\ versa$  with irradiation of 365 nm.  $^{214}$ 

The equilibrium of the MC-form and the SP-form can be adjusted by using different environment conditions. Similarly, applying mechanical force can cause a change of the molecular shape and therefore induce the ring-opening of the spiropyran. <sup>190,215</sup> It is necessary that the stress acts on both sides, the indolene and the chromene unit, of the spiro moiety (Figure 1.17). The pulling apart causes a breakage of the  $C_{spiro}$ -O bond and therefore a formation of the MC-form. Furthermore, grinding or ultrasound can induce strain that cause also a mechanochromic response. <sup>190,216</sup>

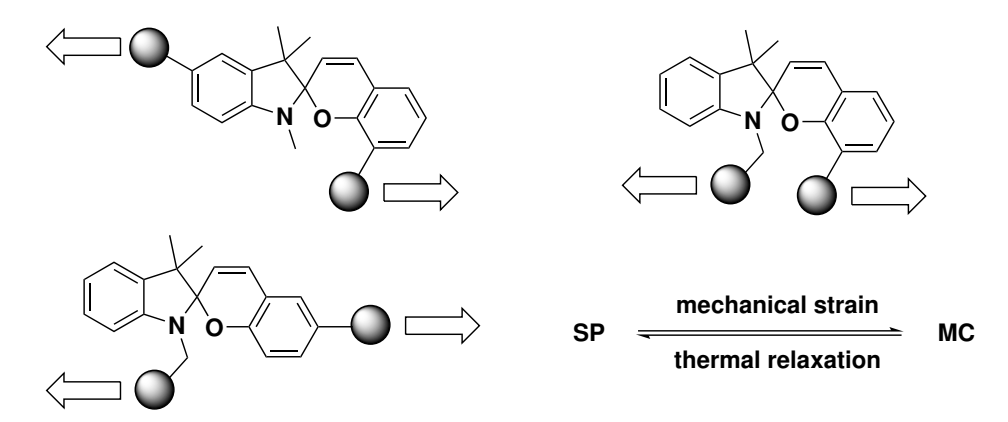


Figure 1.17: Types of mechano-activated spiropyrans. The types are based on the position of the attachements (direction of the force is indicated by the arrows). Reprinted and adapted with permission from the Royal Society of Chemistry, copyright ©2019 (open access). <sup>175</sup>

### 1.2.3 Structure-activity relationship

As we could already observe, the thermochromism of spiropyrans is dependent on the structural modification. Dibenzospiropyran is not able to undergo reversible thermochromism, but dinaphto- or indolinospiropyrans, which can be easier polarized, exhibit this property.<sup>209</sup> Similarly, changes in the substitution pattern of indolinospiropyrans offer an access to modify the equilibrium between the SP- and the MC-form, as well as between the zwitterionic and the quinoidal MC. An important factor are substituents on the pyran ring, which can stabilize or destabilize the phenolate formed upon the ring-opening. Electron withdrawing substituents, *e.g.* a nitro group, in the 6'- and 8'-position stabilize

the phenolate. Therefore, they enable instead of the singlet a triplet pathway for the photoinduced SP  $\rightarrow$  MC-isomerization and shift the thermal equilibrium in polar solvents to the zwitterionic MC-form, as the ring-opening reaction is promoted. <sup>175,205</sup> However, the electron withdrawing substituents reinforce as well photobleaching processes. In contrast, electron donating substituents, which lower stability of the phenolate, reduce the formation of the MC-form, respective its thermal stability. <sup>217</sup> This observation is supported by comparison of the p $K_a$  value of the corresponding MCH $^+$ . The less stable phenolate anion of MCs with electron donating substituents possesses a higher p $K_a$  value than the phenolate anion of MCs with electron withdrawing substituents. While the *vide supra* described sustituent effects on the 6'- and 8'-position favour the zwitterionic resonance structure, electron donating substituents, *e.g* in the 5'- or 7'-position enhance the amount of the quinoidal resonance structure of the MC-form without charge separation. <sup>175,218</sup>

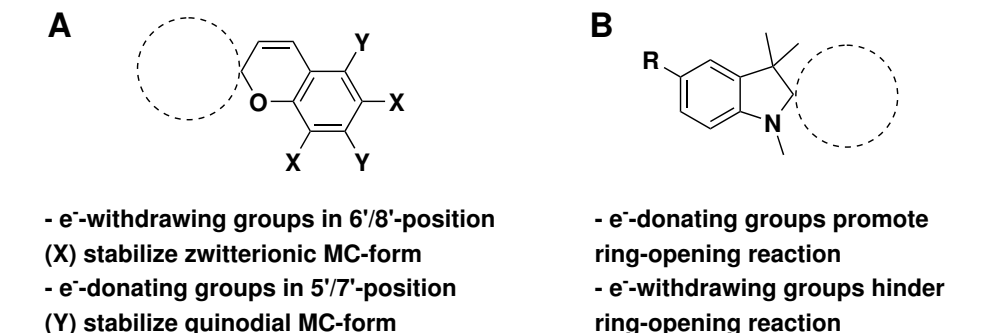


Figure 1.18: Influence of the substituents on the SP-MC-equilibrium. (A) Substituent influence of the chromene unit. (B) Substituent influence on the indolene unit. Reprinted and adapted with permission from the Royal Society of Chemistry, copyright ©2019 (open access).<sup>175</sup>

Substituents on the chromene unit mainly (de)stabilize the phenolate anion, whereas substituents at the indolene unit affect the stability of the N<sup>+</sup>-cation of the indolene ring. It was shown, that the introduction of electron donating substituents can shift the equilibrium also to the MC-form and *vice versa*. Electron withdrawing groups at the 5-position of the indolene destabilize the cation and therefore, decrease the rate of ring opening.<sup>217,219</sup>

#### 1.2.4 Photoswitching of materials

Spiropyrans are not as widely distributed as azobenzenes. Nevertheless, the Web of Science<sup>TM</sup>-database counts still more than 3.000 entries for the keyword "spiropyran" (effective 26.02.2025) and they are used in material science, due to their multiple possibilities to trigger isomerization and their facile synthesis. <sup>174,175,220,221</sup> For polymers, methods are known to incorporate them in the side chain <sup>193</sup> and the backbone. <sup>194</sup> However for peptides, only methods are known to introduce spiropyrans in the side chain of amino acids and not use them as backbone modifications. <sup>192</sup>

In general, the spiropyran structure offers four easy accessible positions, where linker units/functional groups can be introduced to attach the spiropyran to materials (Figure 1.19, Table 1.5). These are at the indolene subunit the 5-position and on the chromene side the 6'- and the 8' position, whereby the attachement occurs *via* amide, esters, or alkyl linkers. A special case is the 1-position at the

1.2. SPIROPYRANS 29

Figure 1.19: Positions used to incorporate/attach spiropyran moieties to polymers and peptides.

nitrogen-atom, where only alkyl linkers are available.

The first report of a spiropyran attached to a polymer was in 1978 (Table 1.5, #1). <sup>193</sup> Two spiropyran units containing an alkylester linker to polyethylacrylate at the 8'-position were connected *via* a xylylene linker at each 1-position. The aim of the study was to investigate the photocontractile behavior of the obtained photochromic rubbers and they could show, that the SP-MC equilibrium is able to mediate shrinking/recovery behaviour of the surrounding media *via* photoisomerization and thermal relaxation.

Table 1.5: Selected examples of spiropyran modified materials

#	Structure	Target/construct	Ref.
1	PEA PEA O O O O O O O O O O O O O O O O O O O	polyethylacrylate (PEA)	[193]
2	NO <sub>2</sub> O-hyperbranched polygylcerol	self-assembled micelles	[222]

#	structure	target/construct	Ref.
3	O NH O NH O NH	single-walled nanotubes	[223]
4	C <sub>8</sub> H <sub>17</sub> C <sub>8</sub> H <sub>17</sub>	alternating copolymer	[194]
5	O (CH <sub>2</sub> ) <sub>10</sub>	alternating copolymer	[182]
6	NO <sub>2</sub> NO <sub>2</sub> NO <sub>2</sub> NO <sub>2</sub> HN HN O (CH <sub>2</sub> ) <sub>4</sub> (CH <sub>2</sub> ) <sub>4</sub> ACHN-KADAAHAKAEAAE	helix forming peptide	[224]
7	AA-NHOONO2	peptide hydrogel	[225]
8	MeO O O O O O O O O O O O O O O O O O O	membrane active peptide	[226]

Table 1.5 #2 shows a spiropyran, bearing at the 1-position an 2-hydroxy ethyl group, that was used to initiate ring-opening multibranching polymerization of glycidol. 222 The so formed spiropyran-

1.2. SPIROPYRANS 31

hyperbranched gylcerol-conjugates comprise of an hydrophobic head, the spiropyran moiety, and an hydrophilic tail, the hyperbranched glycol. This enables reversible self-assembly of polymeric micelles in the SP-form, while photoswitching transform the hydrophobic head to the hydrophilic MC-form and therefore the micelles disassemble. This assembly/disassembly process was especially interesting as it shows potential for smart drug delivery systems of hydrophobic therapeutics. The next example (Table 1.5, #3) shows a spiropyran bearing a propionic acid group at the 1-position. This was anchored to a single-walled carbon nanotube scaffold, modified by Tour reaction, <sup>227</sup> via a bifunctional amide linker.<sup>223</sup> It was demonstrated that the spiropyran was able to reversibly complexate Zn<sup>2+</sup> ions in the MC-form and release them upon photoisomerization to the SP-form. Furthermore, the effect could be extended to potential drug delivery system, as the MC-Zn<sup>2+</sup>-complex can bind an additional molecule, e.g. salicylic acid, which is released as well upon photoswitching. <sup>228</sup> Completely different approaches are listed in Table 1.5 #4 and #5, where the spiropyran is part of the polymer backbone. #4 shows the first reported example for alternating copolymers with a spiropyran as one monomer. 194 The synthesis followed a Suzuki polycondensation, with a spiropyran bearing two bromine substituents in the 5and 6'-position and the fluorene monomer bearing two pinacolborane substituents. It was furthermore demonstrated, that the SP 

MC-isomerization can be accessed via mechanical strain induced through ultrasonication. In #5 polymers where obtained in a similar manner, except that another monomer was used. 182 The C<sub>10</sub>-alkyl chain made the polymer more flexible and enabled to create nanofibers through electrospinning from dimethylformamide (DMF)/ tetrahydrofuran (THF). The obtained fibers were further embedded in an polydimethylsiloxane matrix and the composites showed reversible mechanoresponsivness upon stretching. Remarkably, the use of fibers caused an anisotropic behaviour of the mechanochromism, depending if the material is stretched perpendicular or parallel to the fiber direction. The mechanochemical properties of such spiropyran mainchain polymers can be further tuned through variation in the substitution pattern of the spiropyran.<sup>229</sup>

In peptides, the use of spiropyrans is limited to modifications of the side chain and of the N-/Ctermini. To date, no use as a modification of the peptide backbone is known. A disadvantageous factor might be, that spiropyrans in the MC-form suffer hydrolysis in aqueous media at neutral pH<sup>230</sup> and therefore, their use is often limited to non-aqueous media, aqueous media with acidic pH, or targets with locally modified pH. Table 1.5 #6 shows a peptide cross linking agent composed of a spiropyran with two propionic acid linkers in the 1- and the 8'-position.<sup>224</sup> The carboxy groups were attached to the lysine side-chains via amide formation to a short peptide sequence known to form helical structures. With circular dichroism (CD) spectroscopy it was demonstrated that the spiropyran form, obtained with indoor lighting, stabilizes the helical structure, while the MC-form, obtained in the dark through thermal equilibration, destabilizes the helical structure. The hydrogel forming dipeptide conjugate in Table 1.5 #7 is composed of two D-alanine aminoacids linked at the N-terminal end to a spiropyran bearing an amino group at the 6'-position with a succinic acid. 225 The MC-form, which is known to form aggregates through  $\pi\pi$ -stacking interactions of the conjugate. <sup>231</sup> tends to form self-assembled hydrogels at low pH in aqueous solution. Photoisomerization to the SP-form, which prevents the  $\pi\pi$ -stacking, causes a disassembly of the hydrogel. Furthermore, the use of the two D-alanine moieties enable specific ligand-interaction with vancomycin. <sup>232</sup> This adds a second response mechanism MC-hydrogel, as the addition of vancomycin causes as well a disassembly of the peptide hydrogel. While usually the photoswitchable moiety is attached *via* a linker unit to the respective peptide, the approach in Table 1.5 #8 shows a spiropyran-derived amino acid. In the 6'-position of the chromene ring an L-alanyl is directly affixed.<sup>226</sup> The amino acid was introduced with SPPS to generate analogues of BP100, a membrane active pepitde. BP100 is known to form amphiphilic helices. In the analogues the polar MC-form is destroying this amphilicity, while the less polar SP-form maintains it. Furthermore, it was demonstrated, that the SP-form interacts with membranes in a similar manner than the original peptide, whereby the MC-form with destroyed amphilicity does not exhibit an interaction.

Figure 1.20: Other modes of actions of spiropyrans. (A) Ibuprofene prodrug for micellular release.<sup>233</sup> (B) Dual colour photoinitiator for xolography.<sup>56</sup>

Another approach to use spiropyrans with a potential medical application is shown in Figure 1.20A. The smart prodrug is a conjugate of a spiropyran and ibuprofene, which are connected *via* a hemiaminal.<sup>233</sup> The study uses different hydrophilic/hydrophobic behaviours of the SP- and the MC-form in a photoactivated drug delivery system. The nonpolar SP-form of the conjugate can be encapsulated in micelles with hydrophobic cores. Photoisomerization generates the polar MC-form, which is subsequently released from the micelles into the surrounding environment. The released pro-drug can be activated through esterases, which releases the ibuprofen moiety. A last example of spiropyrans in material science is the use in a volumetric 3D-printing method termed as xolography (Figure 1.20B).<sup>56</sup> The shown spiropyran contains a benzophenone type II photoinitiator. A first light sheet in this technique excites the dormant photointiator molecules, SP-form, in a latent state, which is regenerated through thermal isomerization after a specific lifetime. A projector orthogonal to this light sheet uses a second wavelength and focus sectional images of a 3D-model in the light sheet, whereby only initiators in the latent form absorb the light of the projector and therefore cause polymerization in the current layer.

### 1.3 Amyloidogenic proteins and peptides

Self-organization of molecules without guidance from the outside is referred to as molecular selfassembly. It is one of the key concepts in supramolecular chemistry<sup>234</sup> and provides an alternative way to creating (functional) nano structures using a bottom-up approach. <sup>235</sup> Furthermore, it is one of the fundamental principles of life: lipids and biopolymers (e.g. polysaccharides, polypeptides and polynucleotides) are able to arrange into nano- and microscale architectures.<sup>237</sup> These architecture are able to perform a variety of functions, e.g separation of cells and cell compartements, 238 acting as recognition elements, <sup>239</sup> store and transmit informations, <sup>240</sup> record and react to changing external influences. <sup>241</sup> In particular, proteins and peptides are of great interest<sup>237,242</sup> due to their compositional complexity, their simple synthesis, <sup>243</sup> and as well their inspiration from natural systems. <sup>244</sup> The first discovery of self-assembling proteins was in 1990.<sup>245</sup> In the following the term proteins is used representatively as well for peptides. A class of self-assembling proteins are the so called amyloidogenic proteins. The term "amyloid" arises from the protein aggregates (Figure 1.21A), formed by a representative of these proteins, in human brain tissue and underlies a mistaken identification of Rudolf Virchow in 1854.<sup>246</sup> He implied from a positive iodine staining test, that the substance has to be starch (amylum in Latin). Despite their differences in size, primary structure and natural functionality, all amyloidogenic proteins have one ability in common: They form so called amyloid fibrils, the protein aggregates mentioned before, that are unbranched, have a diameter usually between 70 and 120 Å, and if they are stained with Congo Red they exhibit a birefringence in polarized light (Figure 1.21B).<sup>247</sup>

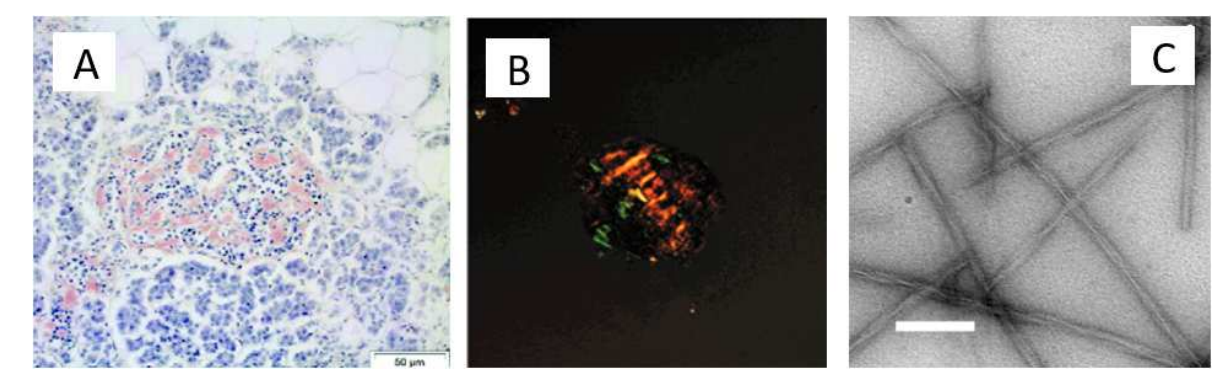


Figure 1.21: (A) Human pancratic islet with extracellular amyloid deposits (red). Stained with Congo red. Scale bar =  $50 \,\mu m$ . Reprinted and adapted with permission from American Physiological Society, copyright ©2011(open access). (B) *In vitro* A $\beta$ 40 amyloid fibrils stained with Congo Red using polarized filter. Reprinted and adapted with permission from the American Chemical Society, copyright ©2000 (open access). (C) Negativly stained transmission electron microscopy (TEM) image of recombinant PrP fibrils *in vitro*. Scale bar = 200 nm. Reprinted and adapted with permission from the American Chemical Society, copyright ©2013. (2013)

#### 1.3.1 Amyloids in nature

The first report of amyloid plaques, or at least tissue with a similar macroscopic appearance to that described by Virchow, occurred four centuries ago in 1639 as lardaceous or waxy liver and spongy and "white stone" containing spleens.<sup>251</sup> Just five years after Virchows misidentification as a polysaccharid, Friedreich and Kekulé were able to correct the error. They demonstrated the presence of proteins in the

mass and the absence of carbohydrates by identification of a high nitrogen content.<sup>251</sup> While it was initially assumed that the amyloids are structurally unordered, improvements in hystological dyes and microscopy revealed further structural information. In 1927 the finding of the birefringence mentioned *vide supra* suggested that amyloids consist of highly ordered organized proteins.<sup>252</sup> This achievement motivated in 1959 Cohen and Calkins to undertake electron microscopy (EM) studies, which revealed a general fibrillar ultrastructure of amyloids from patients and animals with amyloidosis.<sup>253</sup> For a long time these amyloid fibrils were only associated with diseases. Today we know more than fifty disease related amyloidogenic peptides, among them serious diseases (Table 1.6), *e.g.* Alzheimer disease, which was linked to amyloid fibrils by Alois Alzheimer at the beginning of the nineteenth century,<sup>254</sup> Parkinson disease,<sup>255</sup> Creutzfeld-Jacob disease,<sup>256</sup> or diabetes mellitus.<sup>248</sup>

Table 1	<ol><li>Selected</li></ol>	examples of	disease	with appearance	of amy	yloidogenic peptides

Clinical appearance	Affected organs (causation)	Protein	Structure (number of residues)
Alzheimer disease	$CNS(s, h)^a$	Amyloid- $\beta$ peptide (A $\beta$ )	disordered $(40 \text{ or } 42)^b$
Parkinson disease	$CNS(s, h)^a$	lpha-Synuclein	disordered (140)
Creutzfeld-Jakob disease	CNS (s, h, ia, in)	Prion protein (PrP)	disordered (1-102),
			$\alpha$ -helical (103-208)
Huntington disease	CNS (h)	Huntington exon I	disordered (03-187 <sup>b</sup> )
Familial Danish dementia	CNS (h)	ADan peptide	disordered (34)
Type II diabetes	pankreas (s)	Islet amyloid polypeptide	disordered (37)
Light-chain amyloidosis	systemic (s, h) <sup>a</sup>	Ig light chain or fragments	all- $\beta$ , Ig-like ( $\sim 100$ ) <sup>b</sup>
Heavy-chain amyloidosis	systemic (s, h) <sup>a</sup>	Ig heavy chain or	all- $\beta$ , Ig-like ( $\sim$ 190) <sup>b</sup>
		fragments	
Injection localized	skin (ia)	Insulin	all- $\alpha$ , insulin-like
amyloidosis			(30+21)
Aortic medial amyloidosis	cardiovascular	Medin	disordered (50)
	(s)		
C-Cell thyroid tumors	thyroid glands (s)	Calcitonin	disordered (32)
Familial amyloidosis,	PNS, cornea (h)	Gelsolin	disordered (53 or $71)^b$
Finnish-type			
Dialysis-related amyloidosis	HMS (ia)	$\beta_2$ microglobulin (h $\beta_2$ m)	all- $\beta$ , Ig-like (99) <sup>b</sup>

CNS - central nervous system, HMS - human musculosskeletal system, Ig - immunoglobuline, PNS - peripheric nervous system, s - sporadic, h - hereditary, ia - iatrogenic, in - infectious. <sup>a</sup> Predominantly sporadic, although hereditary forms are documented. <sup>b</sup> Fragments of various length were reported. Data were taken from Ref.[257–259]

In all cases, aggregation occurs on the basis of misfolding of the respective proteins.<sup>260</sup> What initiates the fibril formation remains unclear, however, many of the diseases are related with ageing and involve the spontaneous aggregation of wild-type protein (Table 1.6), which suggests that the phenomenon of protein aggregation originates from loss in regulatory control with ageing.<sup>261</sup> Inherited mutations in the precursor proteins can cause diseases to have an earlier onset.<sup>262,263</sup> Further factors can be medical treatment<sup>264</sup> or, like forms of the PrP, are even transmissible through contact with infected tissue.<sup>265</sup>

For more than a century amyloids were solely associated with these diseases. It was therefore surprising that several amyloid structures with different physiological functions were discovered at the turn of the millennium (Table 1.7). The first reports were about functional amyloids in bacteria, *e.g. E. coli*<sup>266</sup> or *Streptomyces*, <sup>267</sup> fungi<sup>268,269</sup> and even higher organisms like insects<sup>270</sup> or spiders. <sup>271</sup> The first functional amyloid in mammals was discovered in 2006<sup>272</sup> and to date more than 35 functional amyloid-forming proteins or protein families are known, suggesting that functional amyloids may rather be the rule than the exception. <sup>260,273,274</sup> In their functionality they can be divided into several classes. Especially in microorganisms they have six main purposes: Biofilm formation & stabilization, cell-to-cell adhesion & flocculation, surface tension modulation, cell cycle & gametogenesis, antimicrobials & toxins, symbiosis & host-pathogen interaction. <sup>274</sup> In higher organisms we have additional functions, *e.g.* controlled cell death, templating of melanin biosynthesis and the storage form of various peptide hormons. <sup>260</sup> Especially, the amyloid formation of peptide hormones is of interest. Several endocrine hormones, *e.g.* amylin, calcitocin, or atrial natriuretic factor, may be stored as functional amyloids in secretory granules in amyloid state and are also present as amyloids in amyloid diseases. <sup>275</sup>

Table 1.7: Selected examples of functional amyloid forming peptides

Protein Organism (number of residues) (year) <sup>a</sup>		Function Soluble form	Function Amyloid form			
	Bacteriae & Archaea					
Curli protein CsgA (~112) <sup>b</sup>	Enterobacteriacae (2002) <sup>266</sup>	None known	Biofilm formation			
Microcin E492 (84)	K. pneumoniae (2005) <sup>276</sup>	Bacteriocin, membrane pore-formation	inactive/storage			
Chaplins (63-225) <sup>b</sup>	S. coelicolor (2003) <sup>267</sup>	None known	Aerial hyphae forma- tion, modulates surface tension			
FapC (225)	P. fluorescence (2010) <sup>277</sup>	None known	Biofilm stabiliza- tion, cell-to-surface adhesion, host invasion			
	Fu	ngi				
Het-s (289)	P. anserina (1997) <sup>268</sup>		Prion form is active: involved in heterokaryon incompatibility			
Sup35 (685)	S. cerevisiae (2000) <sup>278</sup>	Translation regulator	Prion form is inactive			
Rim4 (718)	S. cerevisiae (2015) <sup>279</sup>	Sporulation-specific RNA-binding protein	Translation suppressor, regulates meiosis			
Hydrophobins (~100) <sup>b</sup>	Filamentous fungi (2000) <sup>280</sup>	None known	Surface attachement, aerial hyphae formation			

Protein (number of residues)	Organism (year) <sup>a</sup>	Function Soluble form	Function Amyloid form
	Pla	ints	
Rubber elongation factor (137)	H. brasiliensis (2012) <sup>281</sup>	Latex bio	osynthesis <sup>c</sup>
Vicilin (394)	P. $sativum (2019)^{282}$	Mediate protein storage in seeds <sup>c</sup>	
	Anii	mals	
Chorion $(\sim 100)^b$	B. mori (2000) <sup>270</sup>	None known	Protects moth oocyte and embryo
Pmel17 (661)	H. sapiens (2006) <sup>272</sup>	None known	Templates melanin synthesis in melanosomes
RIPK1 (671), RIPK3 (518)	H. sapiens (2012) <sup>283</sup>	None known	Signaling and cell death of necroptosis
Bombesin (14)	B.bombina (2009) <sup>275</sup>	Involved in hormone signaling	Sorting, storage, and release of hormone

<sup>&</sup>lt;sup>a</sup> Year of first report of functional amyloids. <sup>b</sup> Proteins of various length were reported. <sup>c</sup> Functionality could not be clearly assigned to the soluble protein or the amyloid form. Data were taken from Ref.[260, 273, 274, 284]

### 1.3.2 Structure, mechanism of aggregation and how to analyse

Despite, that amyloid fibrils are composed of proteins with little or no sequence homology, they share a common underlying architecture: a translational symmetry element that lies parallel to the fibril axis. In the repeating substructure, the cross- $\beta$ -sheet motif, <sup>285,286</sup> the protein chains are organized in  $\beta$ -sheets with the  $\beta$ -strands perpendicular to the fibril axis (Figure 1.22A). <sup>247</sup> X-ray diffraction studies <sup>287,288</sup> revealed characteristic patterns with a meridional reflection at ~4.8 Å corresponding to the interstrand spacing and an equatorial more diffuse reflection at ~10 Å arising from the distance between adjacent  $\beta$ -sheets (Figure 1.22B). <sup>289</sup>

The self-assembling process of the amyloid formation consists of multiple stages (Figure 1.23). In general the amyloid formation possesses a typical sigmoidal reaction time course. Herein, a lag phase is initially observed, followed by a rapid growth/elongation phase. If the total quantity of protein is limited, it reaches a stationary or plateau phase. <sup>290</sup> This behaviour is a feature of nucleated polymerization. <sup>291</sup> The triggering event is usually the complete or partial unfolding of monomeric precursor proteins, which generates aggregation-prone intermediates. <sup>292</sup> Alternatively, the assembly starts from intrinsically disordered proteins, <sup>293</sup> and in rare cases the aggregation is initiated by the folded protein itself. <sup>294</sup> In the nucleation phase the first step is the formation of oligomeric species by the precursor proteins. These oligomers can further associate to higher-ordered species, which either serve as critical nucleus for the fibril formation or are dead-end assemblies, which are not able to undergo fibrillization. <sup>295</sup> The probability of the formation of the critical nucleii is partially decisive for the length of lag phase as the rapid assembly/polymerization into amyloid fibrils takes place starting from them. <sup>258</sup> At a later point in the self-assembly a second structural transformation causes the assembling peptides to adopt the typical cross- $\beta$ -sheet structure, irrespective of their initial fold. <sup>296</sup>

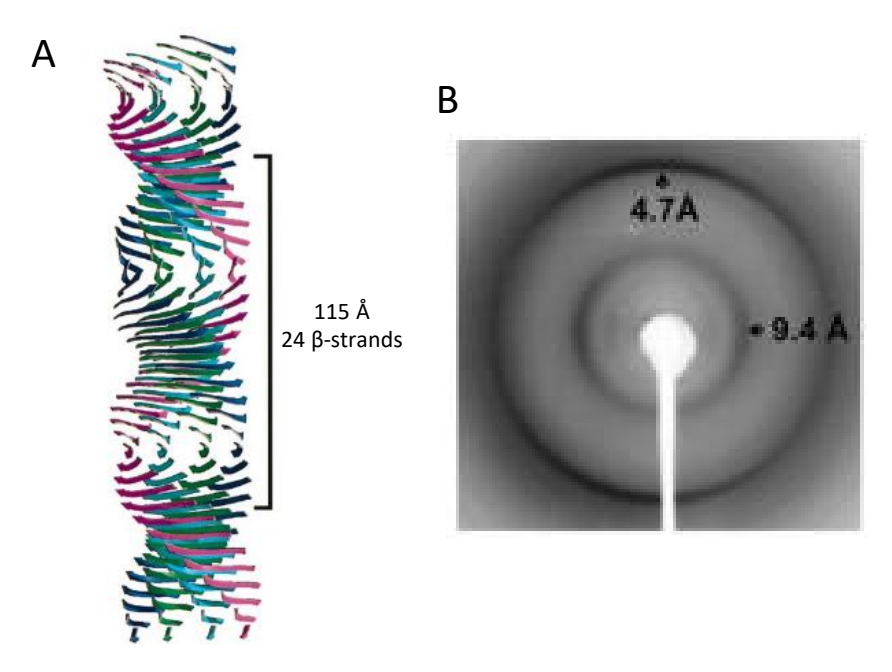


Figure 1.22: (A) Molecular model of the common core protofilament structure in amyloid fibrils. Exemplary four  $\beta$ -sheets make up the protofilament structure. The sheets run parallel to the axis of the protofilament, with their component  $\beta$  strands perdpendicular to the fibril axis. Twisting of  $\beta$ -sheets gives helical repeat of 115.5 Å containing 24  $\beta$ -strands (depicted by the box). Reprinted with permission from Elsevier, copyright ©1997. (B) X-ray diffraction of partially aligned RIP1/RIP3 fibrils. Arrows indicating the meridional (4.7Å) and the equatorial reflection (9.4 Å). Reprinted with permission from Elsevier, copyright ©2012. (283)

While the just described can be grouped under the term primary mechanisms, secondary mechanisms describe processes occurring starting from fibrils with the cross- $\beta$  form. These include fragmentation, which forms new fibril ends for further assembly, reduces the length of the lag-time, and result in exponential growth.<sup>297</sup> Another one is the secondary nucleation on the surface of preformed fibrils. The surface thereby, catalyses oligomer formation, which also enhances the rate of fibril formation.<sup>298</sup>

The ability of the amyloid fibrils to seed its own assembly is a characteristic of prion diseases, e.g. transmissible spongiform encephalopathies in mammals,  $^{256}$  as it allows to spread between cells and in some cases between organisms.  $^{258}$  However, in yeast prion-like spreading of functional amyloids is beneficial. It stimulates metabolic responses of daughter cells under certain selective pressures.  $^{299}$ 

To analyse the amyloidogenic proteins, with regard of fibril formation and structure, a variety of methodologies is available. The main tool used to monitor the fibrillization kinetic *in vivo* is the thioflavin T-monitored fluorescence assay (TMFA).<sup>300</sup> It is based on the histological used dye Thioflavin T (Figure 1.24A), which shows an increased fluorescence quantum yield and a bathochromic shift of its fluorescence excitation upon binding to the cross- $\beta$ -sheet motif of the amyloid fibrils.<sup>301,302</sup> Other *in situ* techniques that can be used are nuclear magnetic resonance (NMR),<sup>296</sup> CD,<sup>303</sup> or IR spectroscopy,<sup>304</sup> whereby these offer additional information about the secondary structure.<sup>305</sup> Microscopic approaches, *e.g.* thermophoretic trapping combined with fluorescence microscopy<sup>306</sup> or two-colour super resolution microscopy,<sup>307</sup> allow to investigate the fibrillization of single fibrils. Congo Red (Figure 1.24A) has a long history of identifying amyloid fibrils<sup>308</sup> and the appearence of birefringence is one of the three criteria for the presence of amyloids.<sup>309</sup> The other two criteria are a fibrillar morphology, which can

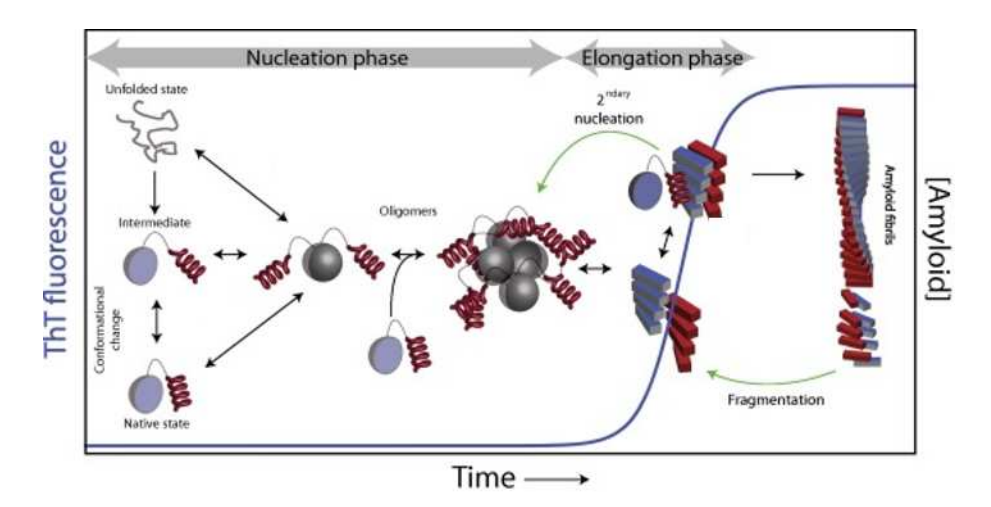


Figure 1.23: Mechanisms of amyloid self-assembly. The scheme shows primary (black arrows) and secondary (green arrows) pathways in the process of amyloid self-assembly, which starts from the unfolded state. Reprinted and adapted with permission from Elsevier, copyright ©2015 (open access).<sup>296</sup>

be proven by EM (Figure 1.24B)<sup>251</sup> and atomic force microscopy (AFM, Figure 1.24C),<sup>310</sup> and a cross- $\beta$ -structure, which is usually analyzed by X-ray fibre diffraction.<sup>286</sup> During the last decades, other methods have become particularly important to gain insights at a near atomic level. Especially breakthroughs in cryo-EM<sup>311,312</sup> and ssNMR<sup>313,314</sup> brought first impressions how individual protein subunits are able to form cross- $\beta$ -sheets (Figure 1.24D).<sup>258</sup>

### 1.3.3 Parathyroid hormone

Functional amyloids are widely distributed in nature. Among other things, they serve as the storage form of several peptide or protein hormones. In the cell they are synthesised as monomers and subsequently stored in secretory granules in the amyloid form.<sup>275</sup> When they are released into the blood, the fibrils dissociate from the end to release the active monomers.<sup>318</sup> In several studies it was proven that functional amyloids could release their constituents by being exposed to a different pH or by simply diluting.<sup>319–322</sup> The reason for this is that the fibrils have a much lower thermodynamic stability than, for example, amyloids of disease-related proteins. The Gibbs free energy  $\Delta G^0$  for the entire fibrillization process is for  $\Delta \beta$ , from Alzheimer disease, and for  $\Delta \beta$ , from dialysis-related amyloidosis, -36.0 kJ mol<sup>-1,323</sup> and -33.0 kJ mol<sup>-1</sup>,<sup>324</sup> respective, while for parathyroid hormone (PTH)  $\Delta G^0$  it is reported to be only -23.8 kJ mol<sup>-1</sup>.<sup>325</sup>

PTH is ubiquitously distributed in vertebrates.<sup>326–328</sup> In mammalians and birds it is the major secretory product of the chief cells of the parathyorid glands and was isolated 1959,<sup>329,330</sup> even though its physiological role was already investigated since 1925, when it was possible to produce an active extract of the glands.<sup>331</sup> As a hormone it plays a central role in maintaining the Ca<sup>2+</sup> and phosphate homeostasis of extracellular fluid.<sup>330</sup> Diseases associated to PTH can generally be attributed to an insufficient or an excess availability of PTH.<sup>331</sup> An excess of PTH (hyperparathyroidism) arises from hormone overproduction, *e.g.* in case of tumors. In this case the typical symptoms are hypercalcaemia, bone disease,

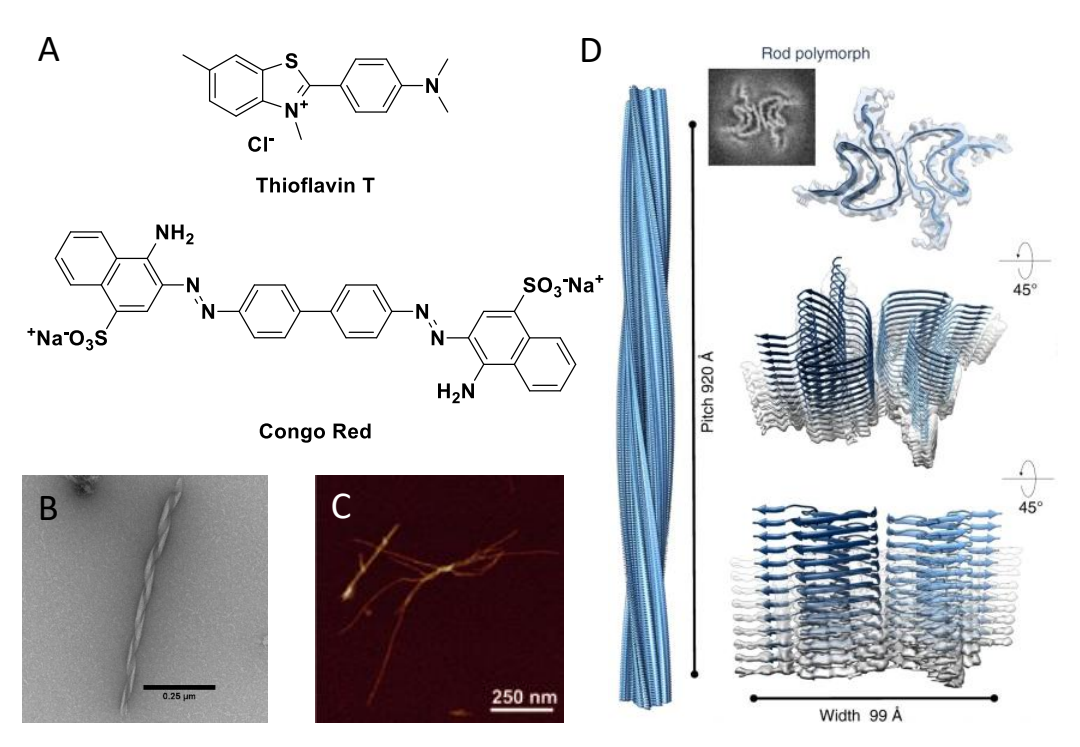


Figure 1.24: Methods to analyse amyloidogenic proteins. (A) Structure formulas of histological dyes thioflavin T and Congo Red used in assays to identify amyloid fibrils and analyse the fibrillization kinetic. (B) TEM image of fibril from azobenzene modified PTH-fragment. Reprinted and adapted with permission from American Chemical Society, copyright ©2024(open access). (C) AFM image of fibrils from endcapped heptapeptide CH<sub>3</sub>CONH- $\beta$ A $\beta$ AKLVFF-CONH<sub>2</sub> after 10 h at 25°C. Reprinted and adapted with permission from Wiley, copyright ©2011. (D) Cryo-EM structures and atomic model of  $\alpha$ -Synuclein rod (left), as density slice (top inlet), viewed from two different angles (lower panels). Reprinted and adapted with Permission from Springer Nature, copyright ©2018 (open access).

and kidney stones. The contrary, an insufficient parathyroid action, arises from either deficient hormone production (hypoparathyroidism) or hormone resistance (pseudohypoparathyroidism). Typical symptoms are hypocalcemia, hypophosphatemia (low blood level of  $Ca^{2+}$ , respective phosphate), and tetany. In the case of hypoparathyroidism recombinant PTH (Natpara<sup>TM</sup>) or the N-terminal PTH fragment PTH<sub>1-34</sub> (Forteo<sup>TM</sup>) are approved drugs.

The human PTH is 84 amino acids in length (Figure 1.25A). The cellular formation occurs *via* two precursor peptides. Initially, *prepro*-PTH (115 amino acids) is the product of translation of the respective mRNA (Figure 1.25B).<sup>334</sup> The *pre*-region is a signal sequence, that comprises the first 25 amino acids and directs the protein into the cell secretory pathway (Figure 1.25B).<sup>335</sup> In the endoplasmatic reticulum the proteolytical cleavage of the signal sequence takes place.<sup>336</sup> The formed *pro*-PTH (90 amino acids) is transferred to the Golgi apparatus, where the *pro*-region is removed proteolytically. The function of this region is not completely understood, however, it seems to prevent premature fibrillization of *pro*-PTH.<sup>322</sup> The mature PTH is packed and stored as functional amyloid fibrils in secretory granules.<sup>321</sup> After the release to the blood, PTH activates G-protein coupled receptors presented on the plasma membrane of kidney and bone cells.<sup>337</sup> It is known that the N-terminal first 34 amino acids are responsible for the activation of the receptor (Figure 1.25A).<sup>337</sup> In addition, the

# A 1SVSEIQLMHN11LGKHLNSMER21VEWLRKKLQD31VHNFVALGAP41LAPR DAGSQR51PRKKEDNVLV61ESHEKSLGEA71DKADVNVLTK81AKSQ

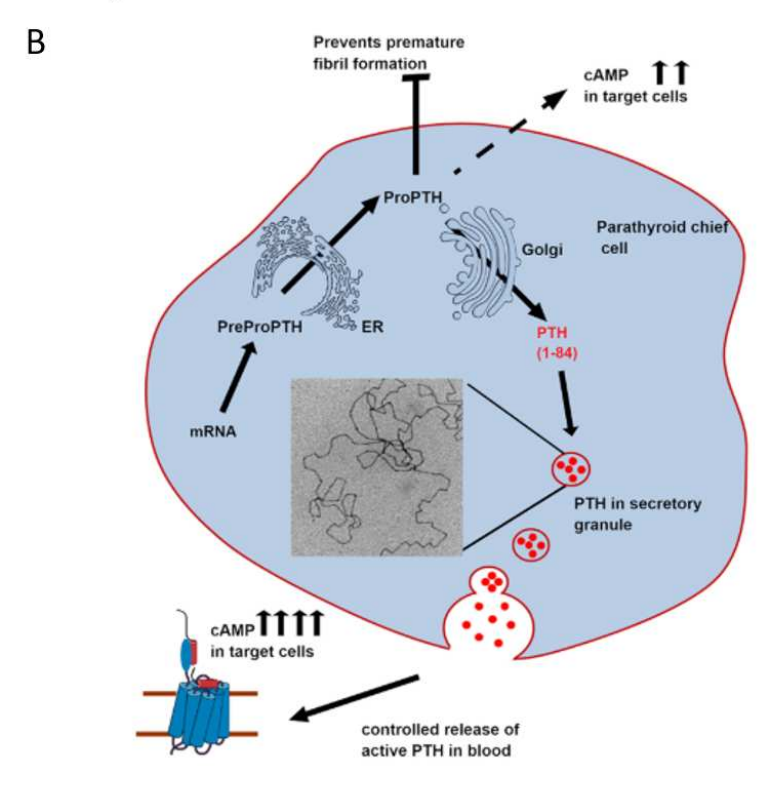


Figure 1.25: A PTH overview. (A) Primary structure of full-length  $PTH_{1-84}$ . PTH fragments are higlighted: N-terminal  $PTH_{1-34}$  is highlighted in blue & fibril forming core  $PTH_{25-37}$  is underlined. (B) Overview of the cell maturation and release of PTH. Reprinted and adapted with Permission from John Wiley & Sons Inc., copyright ©2023 (open access).<sup>322</sup>

amino acid sequence R25–L37, which is responsible for fibril formation, was identified by *in silico* predictions and proteolysis with chymotrypsin of preformed fibrils.<sup>321</sup> However, fibril formation and in particular its reversibility have hardly been investigated and are therefore the subject of current research.<sup>321,322,325,338,339,346</sup>

Amyloid fibrils play key roles in biological systems, both in connection with diseases and to maintain normal physiological functionalities. <sup>259,260</sup> In case of the first one, *e.g.* Alzheimer disease, diabetes type II, or AL amyloidosis, studies support, that cell death and resulting diseases are linked directly to the aggregation of peptides and formation of oligomeric peptide structures. <sup>340–342</sup> In this context it is of major interest to understand and control amyloid aggregation, as it can be crucial for the development of potential therapies. However, due to that amyloid formation comprises complex processes, *e.g.* extensive conformational changes at the level of secondary structure and inter- and intrapeptide interactions, it is a significant challenge to obtain control. Light seems to be therefore a powerful external trigger, as it is generally noninvasive and offers a high spatiotemporal resolution. While for

41

proteins in general a large number of examples are already known where the functionality is influenced by photoswitches,  $^{85,155,343}$  there are only a few reports about photoswitching of amyloidogenic peptides, mainly focusing on synthetic sequences  $^{344,345}$  or investigating the presence of  $\beta$ -turns (see Table 1.4 #9).  $^{163}$  The low thermodynamic stability of PTH therefore makes it a potential candidate to study light-switchable fibrillation. To the best of our knowledge, to date no reversibly switchable system of a natural amyloidogenic protein is known.

### Aim of the thesis

The aim of this thesis is to establish a model system to control the fibrillization of amyloidogenic peptides with irradiation of light. It comprises the design and synthesis of peptides, derived from a peptide hormone and including a photoswitchable moiety incorporated into the peptide backbone (Figure 2.1, left), which are able to form amyloid fibrils *in vitro* under physiological conditions. Furthermore, the modified peptides shall be switchable between two photostationary states, whereby one is able to form fibrils and the other one not, to enable photocontrol over the fibrillization process (Figure 2.1, right).

Thus, this thesis covers the following scientific issues represented in Figure 2.1: What is the most beneficial class of photoswitches to enable sufficient stability in relation to the fibrillization time? What is the influence of the position of the photoswitch? Does one isomer fibrillize and the other one not? And finally, is the system able to undergo multiple fibrillization/disaggregation cycles?

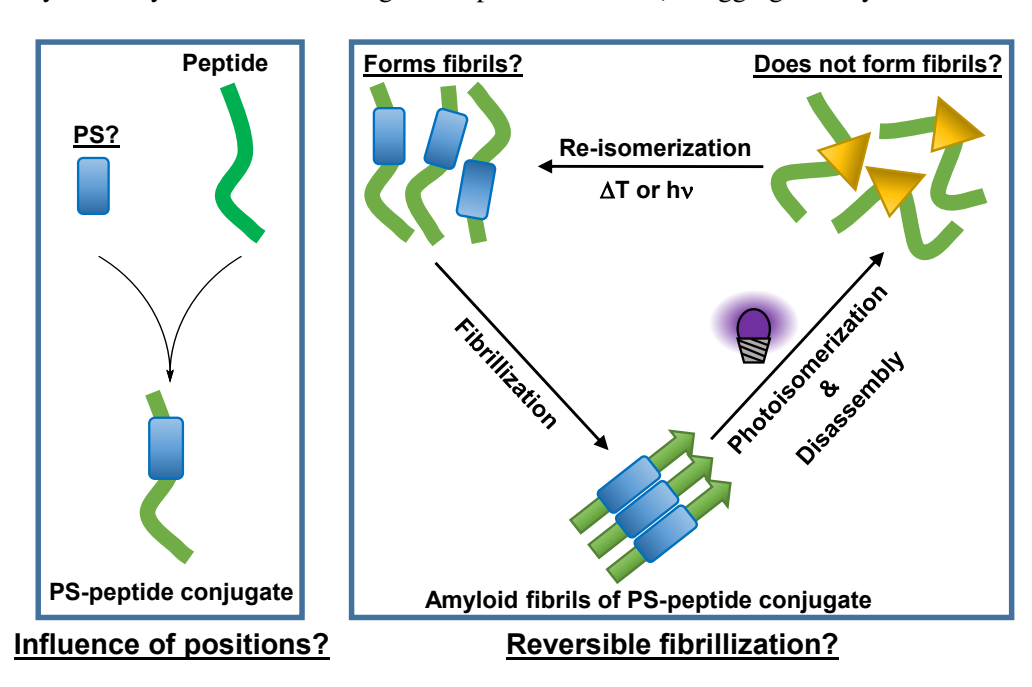


Figure 2.1: (left) Schematic interpretation of the incorporation of a photoswitchable moiety (PS) into an amyloidogenic peptide. (right) Concept for a light driven (de)-fibrillization process of a photoswitch (PS) peptide conjugate.

## Scientific concept

The first step involved identifying suitable model peptides and photoswitches. Among other peptide hormones,<sup>275</sup> the fibril forming core sequence of PTH, PTH<sub>25-37</sub> (Figure 1.25), is a potential candidate. Based on the current state of research it is assumed that the thermodynamic stability of fibrils formed by PTH is low enough to allow disaggregation under physiological conditions in contrast to disease-related amyloids, *e.g.* A $\beta$ . Furthermore, as the sequence in PTH participating in the fibril formation is only 13 amino acids in length,<sup>321</sup> the synthesis is less complex.

As potential candidates for the photoswitches the focus was on two classes: azobenzenes and spiropyrans. Both classes offer a facile synthesis and functionalization. While azobenzenes induce upon cis/trans-isomerization a huge spatial strain in the peptide (their end-to-end distance changes by  $\sim$  3.5 Å, see section 1.1.3), spiropyrans undergo a major change in their dipole-moment, thus, changing local polarity.

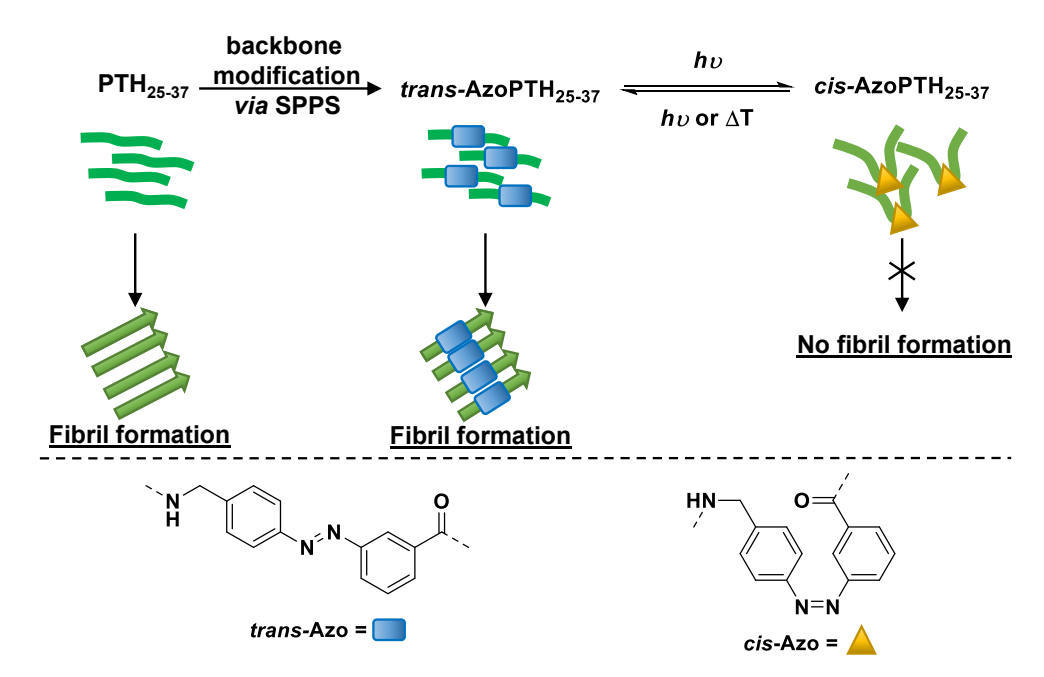


Figure 3.1: Schematic representation of the proof-of-principle. Azo-modified PTH<sub>25-37</sub>, bearing a 3,4'-AMPB moiety in the backbone, is able to undergo fibrillization in the *trans*-configuration of the photoswitch, while the *cis*-configuration is not able to.

In case of PTH previous research on the fibrillization mainly focused on the influence of the *pro*-sequence<sup>322</sup> and on the impact of environmental parameters on the fibril formation. However, there is only minor knowledge of the structural parameters of fibrils and the fibrillization of  $PTH_{25-37}$  has not been studied at all. Thus in the initial study, the proof-of-principle shows that both isomers

of the switch alter the propensity to form fibrils in opposite manners (Figure 3.1). An azobenzene photoswitch is introduced in the backbone of PTH<sub>25-37</sub> at various positions, replacing amino acids or being inserted between two adjacent amino acids. SPPS with fluorenylmethyloxycarbonyl (Fmoc) chemistry is the method of choice, as it has milder deprotection conditions than *tert*-butyloxycarbonyl (Boc) chemistry. The chosen 3,4'-AMPB building block possesses an elaborated synthesis and a sufficient thermodynamical stability. <sup>167</sup> The photoswitchable peptides will be investigated regarding their photophysical properties, such as half-life time of the *cis*-isomer and PSSs after photoisomerization, using UV/Vis spectroscopy and high-performance liquid chromatography (HPLC). Subsequently, the fibrillization process of both isomers is analyzed with TMFA and TEM.

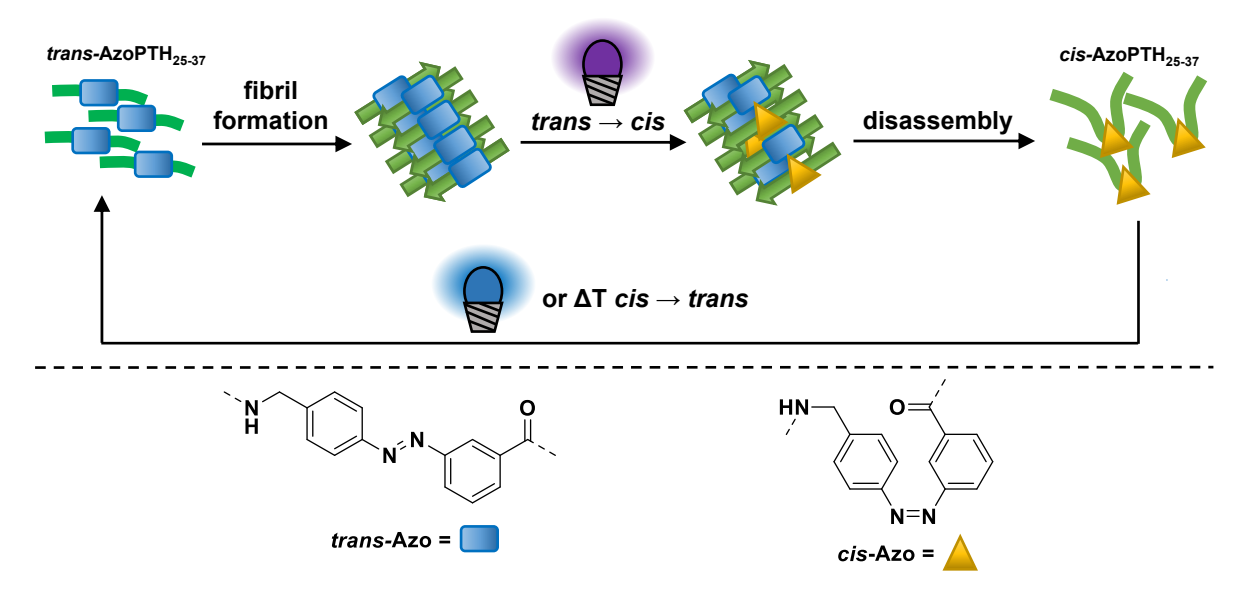


Figure 3.2: Concept of the light-controlled (de)-assembly of Azo-modified  $PTH_{25-37}$ . Reprinted and adapted with permission from the American Chemical Society, ©2024 (open access). 315.

The second concept comprises the determination of structural information of the fibrils from  $PTH_{25-37}$  and modified peptides with wide-angle X-ray scattering (WAXS), ssNMR and MD simulations and determination of fibrillization parameters of the modified peptides with TMFA. The aim thereof is to gain information about the influence of the position regarding the control of the fibrillization process. The most promising candidate, with the largest difference in fibrillization for the *trans*- and the *cis*-isomer, is then used to test whether amyloid formation can be toggled on and off *via* light (Figure 5.4). The fibril formation is in each cycle tracked by TMFA, while the fibrils/degradated fibrils are investigated by CD spectroscopy and transmission measurements.

The last part covers the impact of spiropyran moieties in  $PTH_{25-37}$ . As already described in section 1.2.4, there is still no reported spiropyran suitable for the incorporation into peptide backbone (Figure 3.3A). Thus, the first challenge is to design spiropyran building blocks suitable for SPPS. Two target structures (Figure 3.3B) were selected, the FASC switch bearing an amino group at the 5-position of the indolene unit and a carboxy group at the 6'-position and the SAFC switch bearing the amino group at the 6'-position and the carboxy group at the 5-position. The respective Fmoc-protected building

blocks are used in SPPS to incorporate the switches in the primary structure of  $PTH_{25-37}$  at similar positions as the 3,4'-AMPB switch. Subsequently, the photophysical properties are characterized with UV/Vis-spectroscopy and the fibrillization behaviour will be investigated with TMFA and TEM.

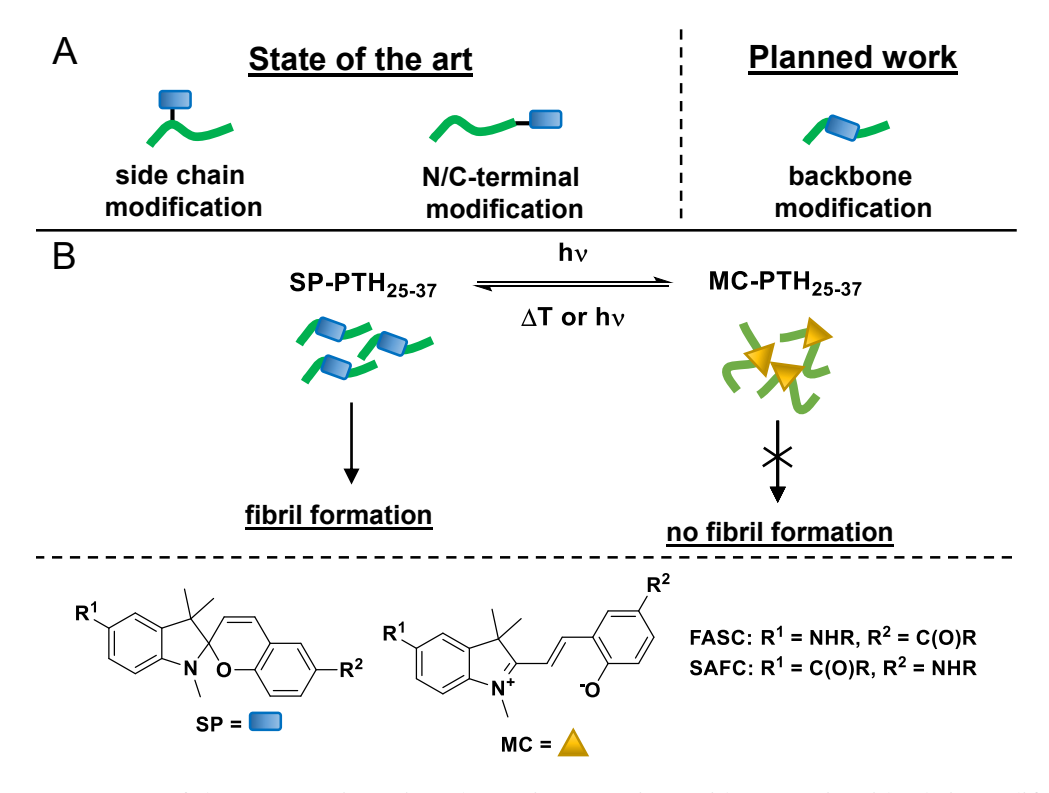


Figure 3.3: (A) State-of-the-art strategies to introduce spiropyrans in peptides comprise side-chain modifications and N-/C-terminal modifications. In this thesis it is planned to incorporate the spiropyrans in the peptide backbone via SPPS. (B) Spiropyran-modified PTH<sub>25-37</sub> is able to undergo fibrillization in the SP-form, while the MC-form is not able to fibrillize.

## List of publications

The results of this thesis are published in the following four publications. The three first-author publications [P1] - [P3] are reprinted as part of this cumulative thesis with the permissions from MDPI<sup>348</sup> and the American Chemical Society. 315,347

# [P1] Modulating the Fibrillization of Parathyroid-Hormone (PTH) Peptides: Azo-Switches as Reversible and Catalytic Entities.

**André Paschold**, Bruno Voigt, Gerd Hause, Tim Kohlmann, Sven Rothemund, Wolfgang H. Binder\* *Biomedicines* **2022**, 10 (7), 1512, DOI: https://doi.org/10.3390/biomedicines10071512.

The conceptualization and writing of this publication were performed by myself. Furthermore, I was responsible for the syntheses as well as chemical and structural characterization of all synthetic products. Together with B. Voigt I investigated the fibrillization behaviour and together with T. Kohlmann I conducted the photophysical analysis. G. Hause conducted the TEM recordings and evaluated the data. S. Rothemund was responsible for the peptide synthesis and characterization thereof. All steps of this project were supervised by W. H. Binder. All authors were involved in the reviewing process of this publication.

# [P2] Photocontrolled Reversible Amyloid Fibril Formation of Parathyroid Hormone-Derived Peptides.

**André Paschold**, Moritz Schäffler, Xincheng Miao, Luis Gardon, Stephanie Krüger, Henrike Heise, Merle I. S. Röhr, Maria Ott, Birgit Strodel\*, Wolfgang H. Binder\*

Biocon jugate Chemistry 2024, 35 (7), 981–995, DOI: https://doi.org/10.1021/acs.bioconjchem.4c00188. The conceptualization and writing of this publication were performed by myself. Furthermore, I was responsible for the syntheses as well as chemical and structural characterization of all products, the analysis of the fibrillization behaviour and together with S. Krüger I conducted the TEM recordings and evaluated this data. M. Schäffler conducted together with X. Miao, M. I. S. Röhr, and B. Strodel the computational analysis. L. Gardon and H. Heise were responsible for the NMR-experiments and evaluated th data. M. Ott conducted the WAXS measurements and evaluated the data. All steps of this project were supervised by W. H. Binder. All authors were involved in the reviewing process of this publication.

# [P3] Spiropyran as building block in peptide synthesis and modulation of photochromic properties.

**André Paschold**, Niclas Starke, Sven Rothemund, Wolfgang H. Binder\* *Organic Letters* **2024**, 26 (49), 10542–10547, DOI: https://doi.org/10.1021/acs.orglett.4c03929.

The conceptualization and writing of this publication were performed by myself. Furthermore, I investigated the photophysical behaviour of the peptides and together with N. Starke, I was responsible for the syntheses as well as chemical and structural characterization of all synthetic products. S. Rothemund conducted the peptide synthesis and analysis. All steps of this project were supervised by W. H. Binder. All authors were involved in the reviewing process of this publication.





Article

# Modulating the Fibrillization of Parathyroid-Hormone (PTH) Peptides: Azo-Switches as Reversible and Catalytic Entities

André Paschold <sup>1</sup>, Bruno Voigt <sup>2</sup>, Gerd Hause <sup>3</sup>, Tim Kohlmann <sup>1</sup>, Sven Rothemund <sup>4</sup> and Wolfgang H. Binder <sup>1,\*</sup>

- Department of Chemistry, Faculty of Natural Sciences II, Martin-Luther University Halle-Wittenberg, 06120 Halle (Saale), Germany; andre.paschold@chemie.uni-halle.de (A.P.); tim\_kohlmann@web.de (T.K.)
- Department of Physics, Faculty of Natural Sciences II, Martin-Luther University Halle-Wittenberg, 06120 Halle (Saale), Germany; bruno.voigt@physik.uni-halle.de
- <sup>3</sup> Biozentrum, Martin-Luther University Halle-Wittenberg, 06120 Halle (Saale), Germany; gerd.hause@biozentrum.uni-halle.de
- Core Unit Peptide—Technologies, University Leipzig, 04103 Leipzig, Germany; sven.rothemund@medizin.uni-leipzig.de
- Correspondence: wolfgang.binder@chemie.uni-halle.de

Abstract: We here report a novel strategy to control the bioavailability of the fibrillizing parathyroid hormone (PTH)-derived peptides, where the concentration of the bioactive form is controlled by an reversible, photoswitchable peptide. PTH<sub>1-84</sub>, a human hormone secreted by the parathyroid glands, is important for the maintenance of extracellular fluid calcium and phosphorus homeostasis. Controlling fibrillization of PTH<sub>1-84</sub> represents an important approach for in vivo applications, in view of the pharmaceutical applications for this protein. We embed the azobenzene derivate 3-{[(4-aminomethyl)phenyl]diazenyl}benzoic acid (3,4'-AMPB) into the PTH-derived peptide PTH<sub>25-37</sub> to generate the artificial peptide AzoPTH<sub>25-37</sub> via solid-phase synthesis. AzoPTH<sub>25-37</sub> shows excellent photostability (more than 20 h in the dark) and can be reversibly photoswitched between its *cis/trans* forms. As investigated by ThT-monitored fibrillization assays, the *trans*-form of AzoPTH<sub>25-37</sub> fibrillizes similar to PTH<sub>25-37</sub>, while the *cis*-form of AzoPTH<sub>25-37</sub> generates only amorphous aggregates. Additionally, *cis*-AzoPTH<sub>25-37</sub> catalytically inhibits the fibrillization of PTH<sub>25-37</sub> in ratios of up to one-fifth. The approach reported here is designed to control the concentration of PTH-peptides, where the bioactive form can be catalytically controlled by an added photoswitchable peptide.

Keywords: azobenzene; photoswitchable peptides; fibrillization; parathyroid hormone; aggregation



Citation: Paschold, A.; Voigt, B.; Hause, G.; Kohlmann, T.; Rothemund, S.; Binder, W.H. Modulating the Fibrillization of Parathyroid-Hormone (PTH) Peptides: Azo-Switches as Reversible and Catalytic Entities. *Biomedicines* 2022, 10, 1512. https://doi.org/ 10.3390/biomedicines10071512

Academic Editors: Anne Skaja Robinson and Christopher J. Roberts

Received: 23 May 2022 Accepted: 23 June 2022 Published: 26 June 2022

Publisher's Note: MDPI stays neutral with regard to jurisdictional claims in published maps and institutional affiliations.



Copyright: © 2022 by the authors. Licensee MDPI, Basel, Switzerland. This article is an open access article distributed under the terms and conditions of the Creative Commons Attribution (CC BY) license (https://creativecommons.org/licenses/by/4.0/).

### 1. Introduction

Fibrillization of proteins and peptides is a supramolecular process [1,2] that leads to the formation of peptide aggregates, containing a cross-β-sheet motif [3]. It involves multiple steps [4] and is associated with many diseases such as Alzheimer's disease, Parkinson's disease or diabetes type II [5–7]. However, in the past decades, it has also been associated with amyloids with distinct physiological functions, so-called functional amyloids, which are found in lower organisms [8–11]. Subsequently, functional amyloids were also discovered in humans, whereby the amyloid can be the active physiological form [12,13] or the storage form of peptide hormones [14].

The parathyroid hormone, abbreviated PTH, is a human hormone secreted by the parathyroid glands [15], with PTH-like peptides also known from other animals [16,17]. It is expressed as a 115 residue pre-pro-protein, whereby the first 25 amino acids at the N-terminus (referred to  $PTH_{-31--7}$ ) serve as a signaling peptide for the transport to the endoplasmic reticulum and are removed by a signal peptidase [18]. The formed pro-peptide is subsequently transferred to the Golgi apparatus and the N-terminal six amino acids (referred to  $PTH_{-6--1}$ ) are proteolytically removed [19]. Before mature  $PTH_{1-84}$  is released into the blood, it is stored in secretory granules as amyloid fibrils [20]. The physiological role

Biomedicines 2022, 10, 1512 2 of 13

is well studied [21,22], being important in the maintenance of extracellular fluid calcium and phosphorus homeostasis. The receptor is mainly activated through the first 34 N-terminal amino acids [23], wherefore recombinant  $PTH_{1-84}$  and recombinant  $PTH_{1-34}$  are approved drugs against osteoporosis, Natpara® and Forteo®, respectively. However, its fibrillization has barely been investigated. Thus far, it is known that the amyloid fibrils of  $PTH_{1-84}$  are formed by the amino acid residues R25-L37, and the thermodynamic stability of the fibrils is sufficiently low to dissociate after dilution [20]. Thus, control over the fibrillization of amyloids and PTH specifically represents an important approach for controlling its factual concentration for in vivo applications, placing modulators of fibrillization and thus reversible fibrillization into the focus of pharmaceutically applicable proteins [24–27].

In the past decades, the photoinduced switching of protein functionalities has emerged as an important concept to modulate protein function, often by modulations in binding specificity between proteins and ligands. Thus, not only enzymes have been equipped with photosensitive switches, but also larger protein complexes, involved in many physiological or neurological functions [28]. To this end, artificial photoswitches are embedded into either the main chain or side chains of polypeptides, in order to change their secondary structures by photoinduced conformational changes of the photoswitches. Thereby, a plethora of different photoswitches, such as those based on cis-trans-isomerization of azo-dyes [29,30] stilbenes [31] and hemithioindigos [32,33], have been developed. Important for the proper use of a specific photoswitch inside a polypeptide chain is not only the quest to retain the initial (functional) secondary structure of the protein, but also to achieve a reasonably stable conformation after photoswitching, so as to allow for sufficient time to exert the desired effect. Many examples of such sufficiently stable and also reversible photoswitches have been reported, allowing one to modulate several expects of protein function [34–39]. Here, we report on an approach to modulate the fibrillization of PTH, equipped with a photoswitch at a specific position in the peptide sequence, in order to reversibly trigger its aggregation/disaggregation (see Figure 1).

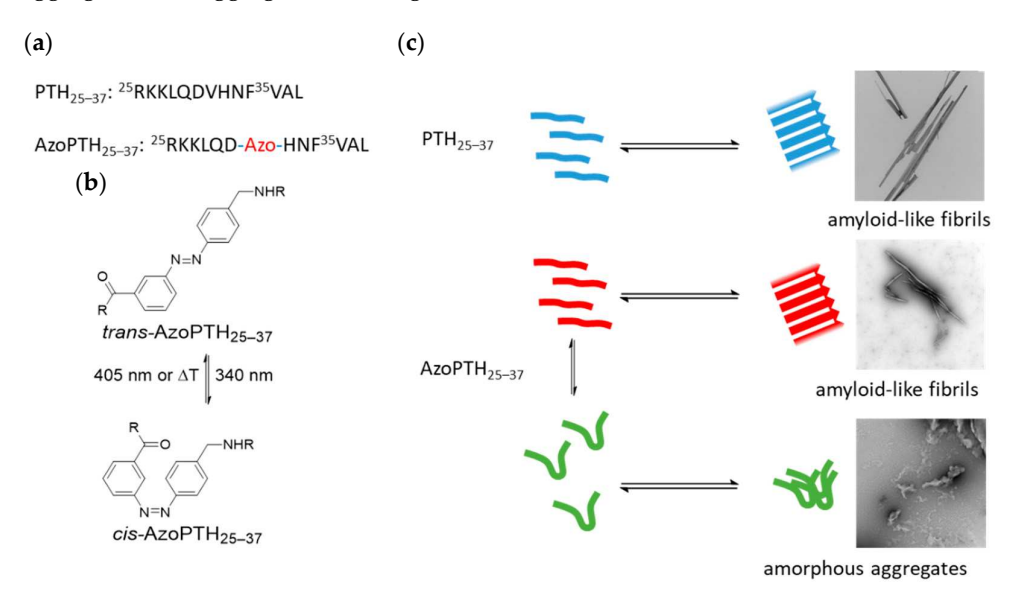


**Figure 1.** (a) Primary sequence of  $PTH_{25-37}$  and the azobenzene-modified  $PTH_{25-37}$  (AzoPTH<sub>25-37</sub>, azobenzene-moiety highlighted in red). (b) *Cis-trans*-isomerization of the incorporated 3,4'-AMPB switch. (c) Equilibrium of the monomeric peptides  $PTH_{25-37}$  and AzoPTH<sub>25-37</sub> in both forms and their aggregates.

In view of the functional design of the modified PTH<sub>25–37</sub>, we sought to embed the photoswitch into a region of the protein where aggregation is still possible, but only in a specific (untriggered) conformation of the photoswitch, whereby fibrillization should be inhibited after the conformational change. As a model system, we chose peptides derived

Biomedicines 2022, 10, 1512 3 of 13

from the PTH fibril core structure, including the amino acids 25R-37L (Figure 1a) [20], which is able to form fibrils itself. In addition, we investigated the influence of both conformations on the fibrillization of the unmodified peptide. As the photoswitch we chose a structural motif from the class of azobenzenes, as they are well known for enabling reversible control of peptide conformation [29,34,39–41]. Specifically we chose the azobenzene derivate 3-{[(4-aminomethyl)phenyl]diazenyl}benzoic acid (3,4'-AMPB; Figure 1b) [42], which is known to introduce a significant geometric change. 3,4'-AMPB displays both: a high photoisomerization yield and a sufficient thermodynamically stability of the *cis*-isomer [41]. If desired, the photoswitch can be reversed via irradiation at 405 nm, or thermally, with a half-life time of more than 20 h in the dark. We hypothesized that the incorporation of the azobenzene into the backbone would allow us to switch between the *cis*- and the *trans*-conformation, whereby one of them is able to fibrillize and the other one is not. Furthermore, azobenzenes in their *cis*-conformation are known to mimic  $\beta$ -hairpins, which allowed us to investigate the hypothesis if the PTH fibrils possess a turn region like amyloid fibrils from other peptides [43–45].

#### 2. Materials and Methods

#### 2.1. General

All technical solvents were distilled prior to use. Air- and moisture-sensitive reactions were carried out in flame-dried glassware under atmospheric pressure of nitrogen. 2-(6-Chloro-1-H-benzotriazole-1-yl)-1,1,3,3-tetramethylaminium hexafluorophosphate (HCTU), *N*-methyl-morpholine (NMM), *N*,*N*-dicyclohexylcarbodiimide (DIC), *N*-Hydroxybenzotriazole (HOBT), trifluoroacetic acid, 4-aminobenzylamine, and oxone<sup>®</sup> were purchased from Sigma Aldrich (Taufkirchen, Germany). 9-Fluorenylmethyl-*N*-succinimidylcarbonat (Fmoc-OSu) was received from Fluorochem. 3-Aminobenzoic acid was purchased from Merck (Darmstadt, Germany). All these chemicals were used without further purification.

NMR spectra were recorded on a Varian Gemini 400 or 500 spectrometer (400 MHz or 500 MHz; Agilent Technologies, Waldbronn, Germany) at 27 °C in DMSO– $d_6$  (99.8 Atom%D; Chemotrade, Düsseldorf, Germany) or D<sub>2</sub>O (99.8 Atom%D; Sigma-Aldrich, Taufkirchen, Germany). Chemical shifts are given in ppm and referred to the solvent residual signal (DMSO– $d_6$ :  $\delta$  = 2.50 ppm and  $\delta$  = 39.5 ppm; D<sub>2</sub>O:  $\delta$  = 4.79 ppm). The following abbreviations were used for  $^1$ H- and  $^{13}$ C-NMR peaks' assignment: s = singlet, d = doublet, t = triplet, td = triplet of doublet, and m = multiplet. MestReNova (version 6.0.2–5475, Mestrelab Research S.L., Santiago de Compostela, Spain) was used for data interpretation.

ESI-ToF mass spectrometry was performed on a Bruker Daltonics microTOF (Bruker Corporation, Billerica, MA, USA). Samples were dissolved in HPLC-grade solvents (MeOH, THF, or mixtures; Sigma Aldrich, Taufkirchen, Germany) at concentrations of 0.1 mg/mL and measured via direct injection with a flow rate of 180  $\mu$ L/h using the positive mode with a capillary voltage of 4.5 kV. The spectra were analyzed with otofControl (version 3.4, Bruker Daltonik, Bremen, Germany).

#### 2.2. *Organic Synthesis*

Fmoc-protected 3,4′-AMPB was synthesized in two steps according to literature procedures [42,46].

#### 2.3. Peptide Synthesis and Purification

Solid-phase peptide synthesis was utilized on an automated peptide synthesizer MultiPep RS (Intavis AG, Koeln, Germany) using standard Fmoc-chemistry and preloaded resins. Standard coupling of all protected natural amino acids was performed as single couplings in dimethylformamid (DMF) using 5 equivalents of amino acids, HCTU as coupling reagents, and 10 equivalents of NMM as base for 1 h at room temperature. Special building groups, such as Fmoc-3,4'-AMPB, were coupled with 3 equivalents using DIC and HOBT in DMF/N-methyl-2-pyrrolidone (NMP) at room temperature and with gentle shaking in the dark overnight.

Biomedicines 2022, 10, 1512 4 of 13

The *N*-terminal Fmoc-protecting group was removed by washing the resin with 20% piperidine for 20 min. The final side chain deprotection and cleavage from the resin employed a mixture of trifluoroacetic acid and water (90:10 Vol%) with gentle agitation for 2 h at room temperature.

The crude peptides were purified to >95% purity using preparative RP-HPLC (Gilson, Limburg, Germany). For both analytical and preparative use, the mobile phase was a mixture of water (eluent A) and acetonitrile (eluent B), respectively, each containing 0.1% trifluoroacetic acid. Samples were eluted with a linear gradient from 5% B to 95% B in 15 min for analytical runs and in 90 min for preparative runs on a semipreparative PLRP-S column (300  $\times$  25 mm, 8  $\mu$ m; Agilent Technologies, Waldbronn, Germany). Finally, all peptides were characterized by analytical HPLC Dionex Ultimate 3000 (Thermo Fisher Scientific, Dreieich, Germany) using a PLRP-S column (150  $\times$  4.6 mm, 3  $\mu$ m; Agilent Technologies, Waldbronn, Germany) and MALDI-MS (Bruker Microflex LT, Bremen, Germany), which gave the expected [M+H] $^+$  mass peaks.

#### 2.4. Azobenzene Peptide Photoisomerization

 $Trans \rightarrow cis$  isomerization was performed by irradiating the dissolved peptide in a 1 cm quartz cuvette for 30 min with light of 340 nm wavelength using a 50 W mercury lamp (VEB) and a 340 nm band pass filter (FB340-10, Thorlabs, Bergkirchen, Germany) under stirring. For  $cis \rightarrow trans$  isomerization, the dissolved peptide was irradiated with light of 405 nm wavelength using a 1.4 W LED (M405L4, Thorlabs, Bergkirchen, Germany) for 30 min under stirring.

#### 2.5. Aggregation Kinetics

ThT-monitored fibrillization assays of artificial peptides and mixtures with PTH<sub>25-37</sub> were investigated by fluorescence intensity measurements using thioflavin T (ThT) as fluorescent dye. Lyophilized peptides were dissolved in 50 mM Na<sub>2</sub>HPO<sub>4</sub> buffer solution with a pH value of 7.4 in a concentration of 2 mg/mL and kept on ice for the next steps. The samples were centrifuged at  $13,000 \times g$  rpm for 10 s and the concentrations were determined with a JASCO V-660 absorbance spectrometer (JASCO, Pfungstadt, Germany; PTH<sub>25-37</sub> by absorbance at 205 nm and the molar extinction coefficient of 49,310 cm<sup>-1</sup>M<sup>-1</sup>; trans-AzoPTH<sub>25-37</sub> by absorbance at 327 nm and the molar extinction coefficient of 13,000 cm $^{-1}$ M $^{-1}$ ). Cis-AzoPTH<sub>25–37</sub> was produced as described before. The solutions were centrifuged at 10,000 rpm for 1 h at 4  $^{\circ}\text{C}$  , the supernatant was transferred to another tube. The protein solutions were mixed in the desired ration and diluted with 50 mM Na<sub>2</sub>HPO<sub>4</sub> buffer (pH 7.4) to obtain final concentrations of 0/100 μM PTH<sub>25-37</sub>,  $50 \mu M$  ThT, and  $0/10/20/50/100 \mu M$  AzoPTH<sub>25-37</sub>. For each sample, a total volume of 480  $\mu$ L was prepared and 3  $\times$  150  $\mu$ L were transferred to a medium binding 96-well plate (Greiner Bio-One, Kremsmünster, Austria). The plate was sealed with a microplate cover. The fluorescence intensity was monitored at 37 °C using a BMG FLUOStar Omega multimode plate reader (BMG LABTECH, Ortenberg, Germany) using fluorescence excitation and emission wavelengths at 460 nm and 485 nm, respectively. One measurement cycle of 5 min consisted of double-orbital shaking for 150 s and incubating for 150 s.

#### 2.6. Transmission Electron Microscopy (TEM)

TEM images were taken with an electron microscope (EM 900; Zeiss, Oberkochen, Germany) at 80 kV acceleration voltage. For preparation, 5  $\mu$ L of the peptide solution were added on Formvar/Cu grids (mesh 200). After 3 min of incubation, the grids were gently cleaned with water for o1 min and then negatively stained using uranyl acetate (1%, w/v) for 1 min.

#### 2.7. Seeding Assay

The seeding assay follows the same procedure as the ThT-monitored fibrillization assay for the determination of the aggregation kinetics. In addition, the final samples

Biomedicines 2022, 10, 1512 5 of 13

contained 20  $\mu$ M of seeds from trans-AzoPTH<sub>25–37</sub> fibrils. The seeds were prepared via ultrasonification of a 100  $\mu$ M mature trans-AzoPTH<sub>25–37</sub> fibrils solution (Sonifier W-250 D, Branson Ultraschall, Dietzenbach, Germany; 15 times, 1 s 10% amplitude, 1 s pause).

#### 3. Results & Discussion

#### 3.1. Chemistry

To investigate the fibrillization behavior of PTH $_{25-37}$ , the azobenzene switch was incorporated directly into the peptide backbone. We selected the 3,4'-azobenzene motif (Figure 1b) [42]. As it possesses suitable photochemical properties, e.g., an excellent half-life time with a stability larger than 20 h and switching wavelengths >300 nm. These are easily addressable by our photophysical equipment and also avoid eventual photodegradation. The synthesis was conducted in two steps (Figure 2a): in the first step, we conducted the Fmoc-protection of 2 [46], which in the second step reacts in a Mills reaction with an in situ-generated nitroso compound 3 to obtain the Fmoc-protected 3,4'-AMPB 5 in an overall yield of 68%.

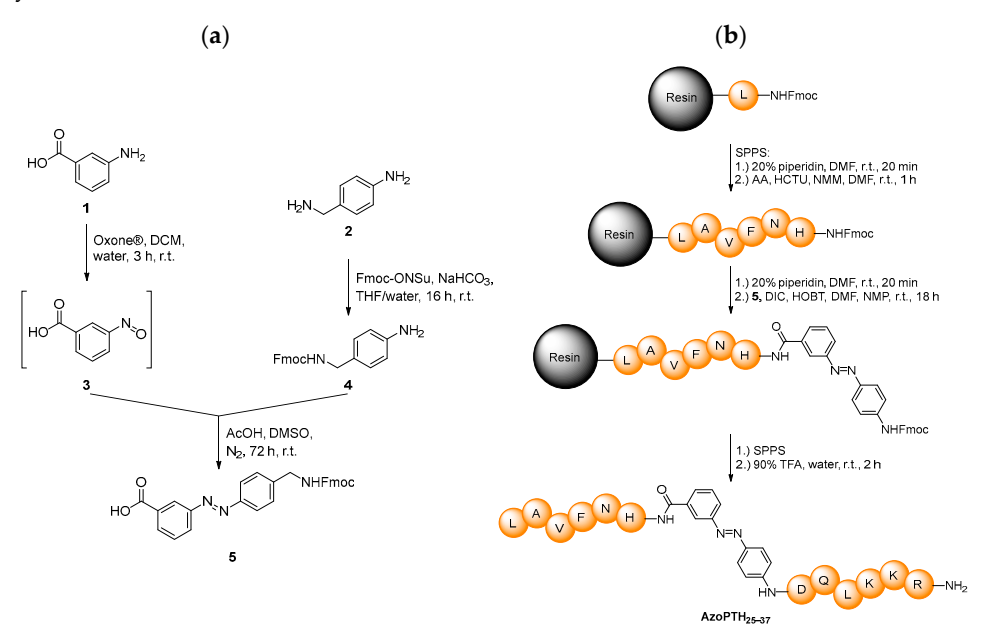


**Figure 2.** (a) Synthesis of Fmoc-protected *trans*-3,4'-AMPB 5. (b) Solid-phase peptide synthesis strategy towards the peptide AzoPTH<sub>25–37</sub>.

The modified azobenzene switch 5, bearing the proper functionalities for Fmocchemistry, was incorporated into the peptide backbone of  $PTH_{25-37}$  via solid-phase peptide synthesis (Figure 2b). It replaces V31 in the artificial peptide AzoPTH<sub>25-37</sub>, due to its central position along the peptide, expecting the largest impact on fibrillization after photoswitching. Furthermore, we probed the replacement of D30 or the insertion between D30 and V31, which led to a greater loss of solubility in the fibrillization buffer (240  $\mu$ M vs. 25  $\mu$ M vs. 60  $\mu$ M; Table S1). Thus, several of the generated peptides displayed strongly reduced solubility—an effect that is important for the subsequent investigations. All peptides were obtained in yields of 10–19%, and high purities as proven by both HPLC and MALDI-ToF measurements, in addition to 500 MHz NMR spectroscopy (Figures S1–S5 and S13–S15).

#### 3.2. Photophysical Properties

We first studied the photophysical properties of the *cis-trans*-isomerization of AzoPTH $_{25-37}$  (Figure 1b) by UV/Vis spectroscopy and HPLC analysis in pure water in order to minimize effects of a potential self-assembly and to quantify the generated amounts of the respective *cis/trans*-modified peptides before and after photoswitching. The UV/Vis spectra for the

Biomedicines 2022, 10, 1512 6 of 13

pure isomers (Figure S6) were separated from the spectra of trans-enriched AzoPTH<sub>25-37</sub> in the thermodynamically stable state after synthesis and in the cis-enriched photostationary state (PSS, Figure 3) with Wolfram Mathematica 12.2. The trans-isomer displays an absorption maximum at 327 nm ( $\varepsilon$  = 13,000 cm<sup>-1</sup>M<sup>-1</sup>) and a second maximum at 427 nm, while the cis-isomer possesses maxima at 288 nm and 433 nm. Both isomers display two isobestic points at 278 nm and 388 nm. They represent in the thermodynamically stable state a cis-trans ratio of 3:97. Under irradiation with UV light (340 nm), the cis-content could be increased of up to 82% in the cis-enriched PSS. Visible light (405 nm) yields 76% of the transisomer in the trans-enriched PSS via the back reaction. The difference of the trans-content between the trans-enriched PSS at 405 nm and the thermodynamically stable state arises from the overlapping of the n  $\rightarrow \pi^*$  transitions of both isomers at this wavelength [47]. The rate of thermal cis-to-trans isomerization of AzoPTH<sub>25–37</sub> follows first-order kinetics, and was determined by monitoring the increase of the  $\pi \to \pi^*$  absorption band at 327 nm (Figure S7) via time-dependent UV measurements. In the absence of light at 37 °C, cis-AzoPTH<sub>25-37</sub> isomerizes thermally with a rate constant of  $3.53 \times 10^{-6} \text{ s}^{-1}$ , corresponding to a half-life time of 79 h.

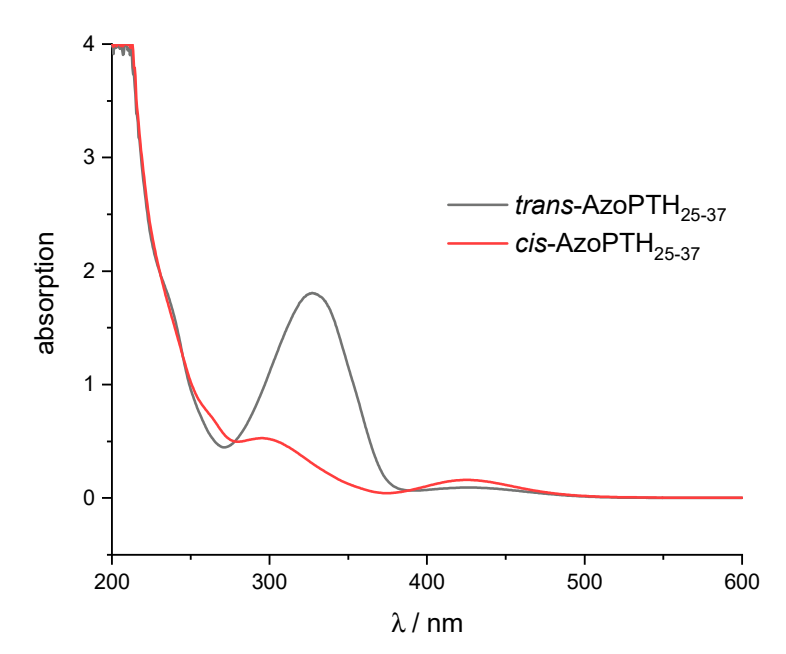


**Figure 3.** UV/Vis absorption spectra for *trans*-AzoPTH $_{25-37}$  after synthesis and for the *cis*-enriched photo-stationary state after irradiation at 340 nm, which almost corresponds to *cis*-AzoPTH $_{25-37}$ .

#### 3.3. Aggregation Kinetics and TEM-Recordings

In order to determine the kinetics of fibril formation of both modified AzoPTH $_{25-37}$  isomers a thioflavin T (ThT)-monitored fibrillization assay was conducted and compared to PTH $_{25-37}$ . ThT is a benzothiazole compound that binds to the cross- $\beta$ -sheet structure of amyloid fibrils [48]. Causing a large red shift of fluorescence excitation of ThT, which in turn enables the selective excitation of amyloid fibril-bound ThT and therefore the in situ observation of fibril formation.

In a first attempt, the fibrillization kinetics for pure trans-AzoPTH<sub>25-37</sub>, cis-AzoPTH<sub>25-37</sub>, and the PTH-derived peptide PTH<sub>25-37</sub> were measured at 37 °C and the results are shown in Figure 4. Two characteristic times were used to characterize the fibrillization (Figure 4, Table 1): the lag time  $t_{\rm lag}$  corresponds to the time before an increase in the fluorescence signal occurs; the characteristic time  $t_{\rm char}$  indicates at which time 50% of the maximum fluorescence was reached.

Biomedicines 2022, 10, 1512 7 of 13

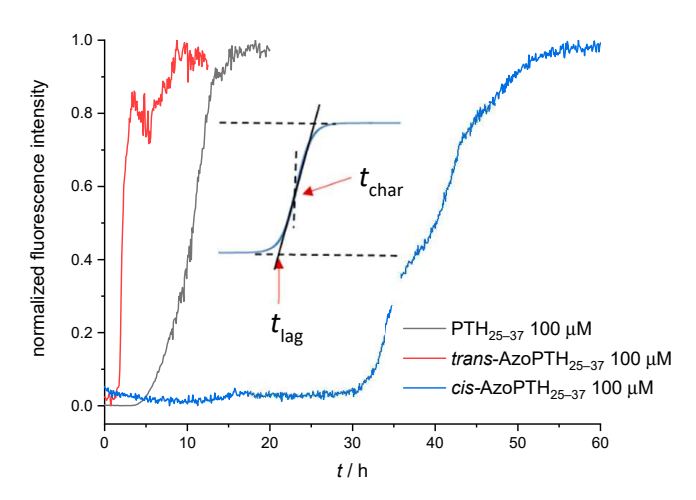


**Figure 4.** ThT-monitored fibrillization assay of PTH<sub>25–37</sub>, *cis*-AzoPTH<sub>25–37</sub>, and *trans*-AzoPTH<sub>25–37</sub> (average of triplets; T = 37 °C, buffer = 50 mM Na<sub>2</sub>HPO<sub>4</sub>, pH = 7.4): (black) PTH<sub>25–37</sub> (100  $\mu$ M), (red) *trans*-AzoPTH<sub>25–37</sub> (100  $\mu$ M), and (blue) *cis*-AzoPTH<sub>25–37</sub> (100  $\mu$ M).

**Table 1.** Fibrillization parameters ( $t_{\text{lag}}$ ,  $t_{\text{char}}$ ) of PTH<sub>25–37</sub>, cis-AzoPTH<sub>25–37</sub>, trans-AzoPTH<sub>25–37</sub>, and mixtures thereof ( $T = 37 \,^{\circ}\text{C}$ , buffer = 50 mM Na<sub>2</sub>HPO<sub>4</sub>, pH = 7.4).

Sample	$t_{ m lag}$ [h]	$t_{ m char}$ [h]
PTH <sub>25-37</sub> (100 μM)	7.2	10.9
$cis$ -AzoPTH <sub>25–37</sub> (100 $\mu$ M)	34.4	42.4
cis-AzoPTH <sub>25-37</sub> :PTH <sub>25-37</sub> (100 μM:100 μM)	27.9	35.7
cis-AzoPTH <sub>25-37</sub> :PTH <sub>25-37</sub> (50 μM:100 μM)	16.3	21.2
cis-AzoPTH <sub>25-37</sub> :PTH <sub>25-37</sub> (20 μM:100 μM)	10.1	14.5
cis-AzoPTH <sub>25-37</sub> :PTH <sub>25-37</sub> (10 μM:100 μM)	6.9	7.9
$trans$ -AzoPTH <sub>25-37</sub> (100 $\mu$ M)	1.6	2.1
trans-AzoPTH <sub>25-37</sub> :PTH <sub>25-37</sub> (100 μM:100 μM)	3.0	4.8
trans-AzoPTH <sub>25-37</sub> :PTH <sub>25-37</sub> (50 μM:100 μM)	8.0	8.6
trans-AzoPTH <sub>25-37</sub> :PTH <sub>25-37</sub> (20 μM:100 μM)	8.7	9.7
trans-AzoPTH <sub>25-37</sub> :PTH <sub>25-37</sub> (10 μM:100 μM)	7.5	8.9

The self-assembly of the trans-AzoPTH<sub>25–37</sub> was accelerated compared to PTH<sub>25–37</sub>, while cis-AzoPTH<sub>25–37</sub> exhibited the opposite effect (Figure 4). The first increase of ThT fluorescence was observable after >30 h. Furthermore, cis-AzoPTH<sub>25–37</sub> shows a biphasic fibrillization behavior, while trans-AzoPTH<sub>25–37</sub> and PTH<sub>25–37</sub> show monophasic fibrillization. Compared to PTH<sub>25–37</sub>, the magnitude of the ThT fluorescence of both AzoPTH<sub>25–37</sub> isomers was significant lower (Figure S9). This effect might arise from fluorescence quenching via the azobenzene moiety. To test this hypothesis, the fluorescence lifetime of ThT was measured either alone, in the presence of PTH<sub>25–37</sub> fibrils, or in the presence of trans-AzoPTH<sub>25–37</sub> fibrils (Figure S8). As expected the lifetime is increased in the presence of PTH<sub>25–37</sub> fibrils compared to the control experiment, while it is decreased significantly in the presence of trans-AzoPTH<sub>25–37</sub>, which further supports our concept. In addition, this effect could be enhanced from a reduced binding affinity of ThT through a different peptide conformation of the fibril.

The observations of the ThT-monitored fibrillization assay were supported by negative stain transmission electron microscopy (TEM) after different time points (Figure 5). After 20 h, amyloid fibrils were only observable for PTH $_{25-37}$  and trans-AzoPTH $_{25-37}$  (Figure 5a,b), while cis-AzoPTH $_{25-37}$  formed amorphous aggregates (Figure 5e). Both peptides produced straight fibrils, whereby the single fibrils of PTH $_{25-37}$  were larger (>6  $\mu$ m vs. <1.5  $\mu$ m) and tend to aggregate further. Interestingly, we found fibrils after 60 h for cis-AzoPTH $_{25-37}$  (Figure 5g), which matched in the morphology those of trans-AzoPTH $_{25-37}$  even if they were

Biomedicines 2022, 10, 1512 8 of 13

significantly shorter (<300 nm). This may result from the thermal *cis-trans*-isomerization, as the *cis*-content decreases and is reduced to 48% after 60 h.

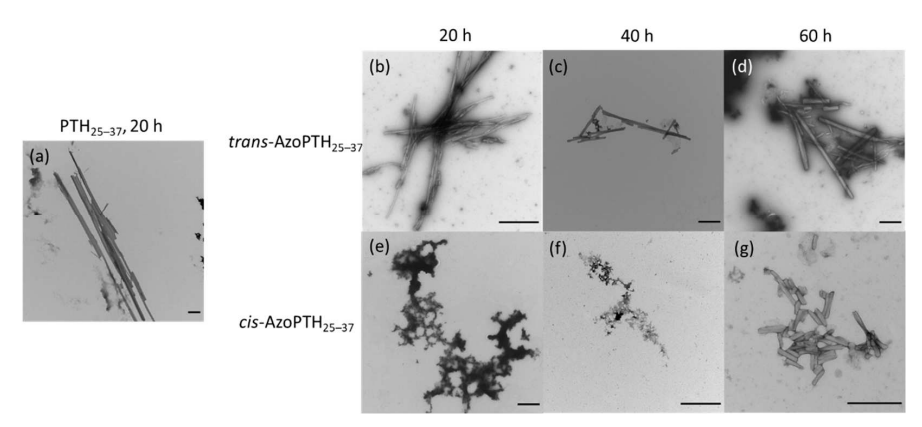


**Figure 5.** TEM recordings of fibrils obtained from PTH<sub>25–37</sub>, *cis*-AzoPTH<sub>25–37</sub>, and *trans*-AzoPTH<sub>25–37</sub> at (T = 37 °C, buffer = 50 mM Na<sub>2</sub>HPO<sub>4</sub>, pH = 7.4) after different time points (all scale bars corresponds to 500 nm). (**a**). PTH<sub>25–37</sub> after 20 h, (**b**) *trans*-AzoPTH<sub>25–37</sub> after 20 h (100 μM), (**c**) *trans*-AzoPTH<sub>25–37</sub> after 40 h (100 μM), (**d**) *trans*-AzoPTH<sub>25–37</sub> after 60 h (100 μM), (**e**) *cis*-AzoPTH<sub>25–37</sub> after 20 h (100 μM), (**f**) *cis*-AzoPTH<sub>25–37</sub> after 40 h (100 μM), and (**g**) *cis*-AzoPTH<sub>25–37</sub> after 60 h (100 μM).

In further experiments, we investigated the (catalytic) influence of the AzoPTH $_{25-37}$  isomers on the fibrillization of PTH $_{25-37}$  (Figure 6). We previously observed such catalytic effects of  $\beta$ -turn modified amyloids (A $\beta$ ) on the fibrillization of the Alzheimer peptide A $\beta_{1-40}$  [49]. Thus 100  $\mu$ M of PTH $_{25-37}$  were fibrillized in the presence of various concentrations of the respective AzoPTH $_{25-37}$  isomer (10/20/50/100  $\mu$ M). Kinetic measurements revealed that the fibrillization behavior of PTH $_{25-37}$  was affected in the same way as the pure AzoPTH $_{25-37}$  isomers.

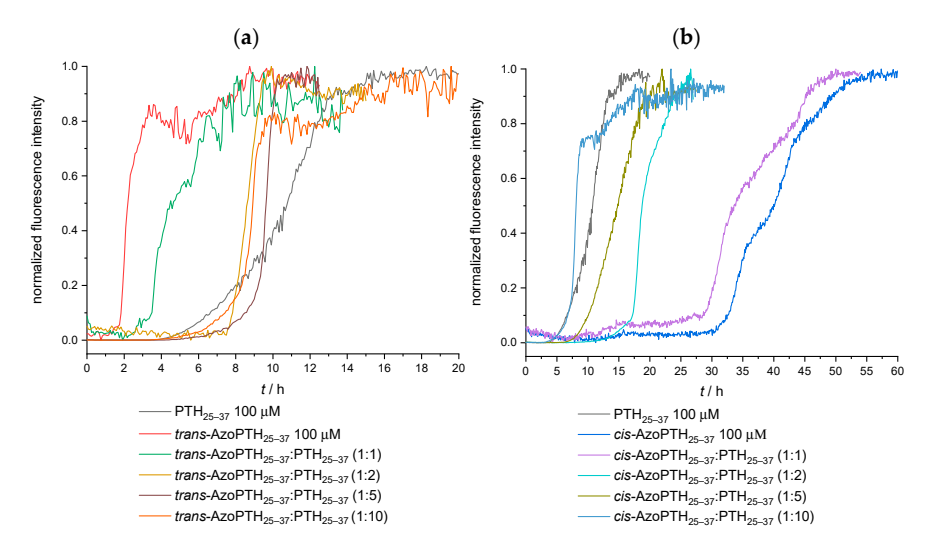


**Figure 6.** (a) ThT-monitored fibrillization assay of PTH<sub>25–37</sub> and mixtures with *trans*-AzoPTH<sub>25–37</sub> (average of triplets; T = 37 °C, buffer = 50 mM Na<sub>2</sub>HPO<sub>4</sub>, pH = 7.4): (black) PTH<sub>25–37</sub> (100 μM), (red) *trans*-AzoPTH<sub>25–37</sub>: (100 μM), (green) *trans*-AzoPTH<sub>25–37</sub>: PTH<sub>25–37</sub>: (100 μM:100 μM), (dark yellow) *trans*-AzoPTH<sub>25–37</sub>: PTH<sub>25–37</sub>: (50 μM:100 μM), (brown) *trans*-AzoPTH<sub>25–37</sub>: PTH<sub>25–37</sub> (20 μM:100 μM), and (orange) *trans*-AzoPTH<sub>25–37</sub>: PTH<sub>25–37</sub> (10 μM:100 μM) (b) ThT-monitored fibrillization assay of PTH<sub>25–37</sub> and mixtures with *cis*-AzoPTH<sub>25–37</sub> at 37 °C: (black) PTH<sub>25–37</sub> (100 μM), (blue) *cis*-AzoPTH<sub>25–37</sub>: PTH<sub>25–37</sub> (100 μM), (cyan) *cis*-AzoPTH<sub>25–37</sub>: PTH<sub>25–37</sub> (50 μM:100 μM), (olive) *cis*-AzoPTH<sub>25–37</sub>: PTH<sub>25–37</sub> (20 μM:100 μM), and (light blue) *cis*-AzoPTH<sub>25–37</sub>: PTH<sub>25–37</sub> (10 μM:100 μM).

Biomedicines 2022, 10, 1512 9 of 13

While trans-AzoPTH<sub>25-37</sub> accelerated the fibrillization and therefore reduced  $t_{\rm lag}$  and  $t_{\rm char}$  of the mixtures (Figure 6a), cis-AzoPTH<sub>25-37</sub> inhibited the fibrillization and extended  $t_{\rm lag}$  and  $t_{\rm char}$  (Figure 6b). Interestingly, the biphasic fibrillization behavior of cis-AzoPTH<sub>25-37</sub> was also observable for the cis-AzoPTH<sub>25-37</sub>:PTH<sub>25-37</sub> (100  $\mu$ M:100  $\mu$ M) mixture. These effects are reduced with decreasing concentration of the respective AzoPTH<sub>25-37</sub> isomer. While the mixtures with trans-AzoPTH<sub>25-37</sub> exhibited a concentration below 50  $\mu$ M, trans-AzoPTH<sub>25-37</sub> had a higher  $t_{\rm lag}$  than pure PTH<sub>25-37</sub>. However,  $t_{\rm char}$  was still shorter, and the stationary phase of the fibrillization was reached earlier.

TEM images were recorded for the peptide mixtures after 20 h (Figure 7). In contrast to the pure peptides, we could observe fibrils for all investigated ratios. Interestingly, the fibrils formed by the mixtures exhibit a similar twisted morphology regardless of the used AzoPTH $_{25-37}$  isomer. Furthermore, the formation of larger aggregates like for the pure PTH $_{25-37}$  (Figure 5) were only observed for a ratio of 1:10, indicating that the AzoPTH $_{25-37}$  inhibits the formation of larger fibril aggregates.

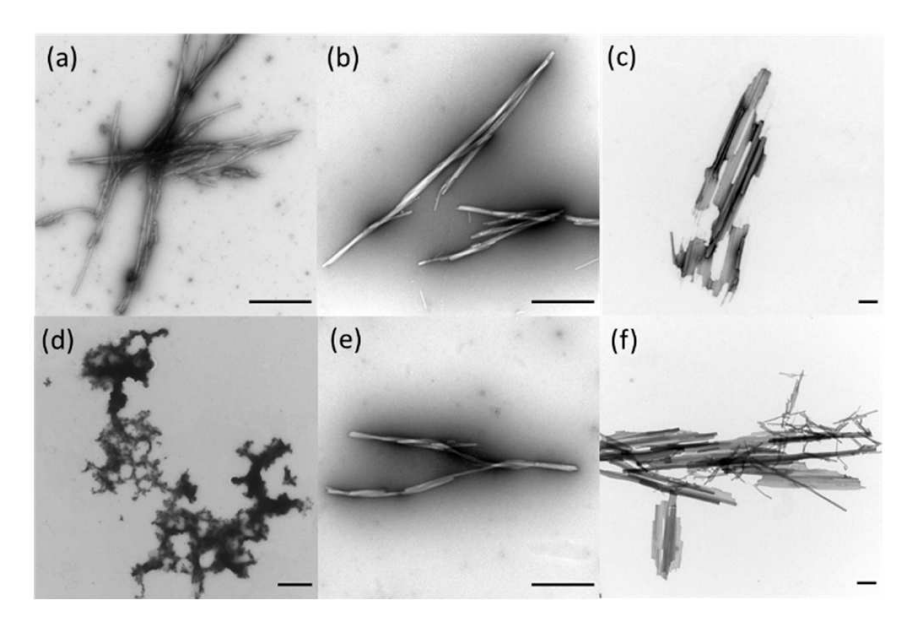


**Figure 7.** TEM recordings of fibrils obtained from PTH<sub>25–37</sub>, *cis*-AzoPTH<sub>25–37</sub>, and *trans*-AzoPTH<sub>25–37</sub> at 37 °C after 20 h (scale bar = 500 nm): (a) *trans*-AzoPTH<sub>25–37</sub> (100 μM), (b) *trans*-AzoPTH<sub>25–37</sub>:PTH<sub>25–37</sub> (100 μM:100 μM), (c) *trans*-AzoPTH<sub>25–37</sub>:PTH<sub>25–37</sub> (10 μM:100 μM), (d) *cis*-AzoPTH<sub>25–37</sub> (100 μM), (e) *cis*-AzoPTH<sub>25–37</sub>:PTH<sub>25–37</sub> (100 μM:100 μM), and (f) *cis*-AzoPTH<sub>25–37</sub>:PTH<sub>25–37</sub> (10 μM:100 μM).

#### 3.4. Seeding Experiments

To determine whether both isomers of AzoPTH $_{25-37}$  are able to form fibrils or only the *trans*-isomer, we investigated, if *trans*-AzoPTH $_{25-37}$  fibrils were able to induce seeding [50]. A 100  $\mu$ M solution of each isomer was treated with 20  $\mu$ M of mature *trans*-AzoPTH $_{25-37}$  fibrils, and the kinetics of the fibril formation were investigated via a ThT-monitored fibrillization assay (Figure 8). While the fibrillization of the *trans*-isomer was accelerated compared to the unseeded monomer, we were not able to observe fibrillization for the *cis*-isomer. This indicates that the *cis*-isomer is unable to nucleate amyloid formation as well as elongate preformed fibrils. The observed fibrils after 60 h for the *cis*-isomer are presumably formed by the thermally isomerized *trans*-isomer.

Biomedicines 2022, 10, 1512 10 of 13

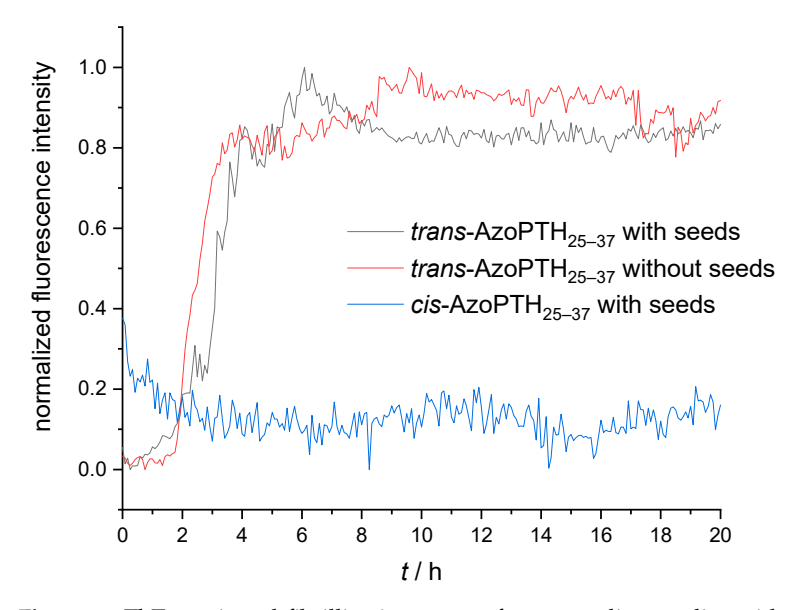


**Figure 8.** ThT-monitored fibrillization assay of cross-seeding studies with cis-AzoPTH<sub>25-37</sub> and trans-AzoPTH<sub>25-37</sub> monomeric peptides and mature trans-AzoPTH<sub>25-37</sub> fibrils as seeds (average of triplets;  $c_{monomer} = 100 \mu M$ ,  $c_{seed} = 20 \mu M$ ,  $T = 37 \, ^{\circ}C$ , buffer 50 mM Na<sub>2</sub>HPO<sub>4</sub>, pH = 7.4): (black) trans-AzoPTH<sub>25-37</sub> with seeds, (red) trans-AzoPTH<sub>25-37</sub> without seeds, and (blue) cis-AzoPTH<sub>25-37</sub> with seeds.

#### 4. Conclusions

We here report for the first time a photoswitchable fibrillizing PTH-derived peptide, which is able to modulate its fibrillization by embedding an azobenzene photoswitch in the middle of PTH<sub>25-37</sub>. PTH<sub>1-84</sub> is a peptide hormone, which is stored as functional amyloids in secretory granules. Its physiological role is well studied, but it still lacks detailed information about its exact fibril structure. We used the 3,4'-AMPB photoswitch to investigate the fibril formation of the fibril core fragment of PTH<sub>1-84</sub> by incorporating the azobenzene into the peptide backbone, yielding the modified PTH-derived peptide AzoPTH<sub>25-37</sub>. We could show that the *trans*-isomer is able to form fibrils, while the *cis*isomer induces a conformational change that inhibits fibril formation. Hypothetically, we can also conclude that there might not be a  $\beta$ -turn in the fibril structure of PTH<sub>1–84</sub>, as the cis-conformer would be reminiscent of such a structure, whereas the trans-conformer would not. Most importantly, we were able to show that the modified peptides can catalytically inhibit fibrillization of the PTH<sub>25-37</sub>, underscoring the importance of seeding during this fibrillization process, which in the future allows for a reversible triggering of the fibrillization by light as an external stimulus. Studies are in progress to investigate if the photocontrol is also possible with the photoswitch at other positions of the backbone and if we can also control the fibrillization of full-length PTH<sub>1-84</sub> with ours or other modified peptides. This represents a novel strategy to control bioavailability of proteins, specifically of PTH peptides and other fibrillating peptides, where not only the concentration of the bioactive form can be controlled by an added photoswitchable peptide, but also the fibrillization as such, important to guide nerve cell regeneration and other directed growth processes in euraryotic cells. For a potential clinical perspective, we want to investigate the cytotoxicity of our peptides as well as the ability to influence the fibrillization of larger PTH-derived peptides (e.g.,  $PTH_{1-34}$  and  $PTH_{1-84}$ ) in vitro and in vivo. As known from other azobenzene containing drugs/prodrugs (e.g., Prontosil), the azobenzene moiety is metabolized in liver tissue via azoreductases, yielding two aniline moieties or through intestinal microbes [51,52]. This is potentially important for the photoswitching inside cells by light, allowing them to tune the reversible fibrillization of other amyloidogenic peptides, which important for regeneration of nerve cells, as reported earlier. Thus, peptide fibrils

Biomedicines 2022, 10, 1512 11 of 13

can seed potential harmful amyloidogenic peptides, which is known from recent work quite prominently [53]. This is a strategy to trigger fiber-formation from the outside via photochemical triggering—thus avoiding the toxic effects of the fibers outside the cells but enabling triggered fibrillization inside the cell to exert the desired effects, allowing them to promote the recovery of spinal cord injuries.

Supplementary Materials: The following supporting information can be downloaded at: https:// www.mdpi.com/article/10.3390/biomedicines10071512/s1, Figure S1: (A) HPLC-trace of AzoPTH<sub>25-37</sub> (cis-isomer at 5.353, trans-isomer at 5.530). (B) MALDI-spectrum of AzoPTH<sub>25-37</sub>; Figure S2: (A) HPLC-trace of SP1 (cis-isomer at 5.557, trans-isomer at 5.790). (B) MALDI-spectrum of SP1; Figure S3: (A) HPLC-trace of SP2 (cis-isomer at 5.223, trans-isomer at 5.460). (B) MALDI-spectrum of SP2; Figure S4: (A) HPLC-trace of SP3 (cis-isomer at 5.560, trans-isomer at 5.807). (B) MALDIspectrum of SP3; Figure S5: (A) HPLC-trace of SP4 (cis-isomer at 5.363, trans-isomer at 5.547). (B) MALDI-spectrum of SP4; Figure S6: Separated UV/Vis-spectra of the pure isomers of AzoPTH<sub>25–37</sub>; spectra were seperated with Wolfram Mathematica 12.2; Figure S7: (A) UV/Vis-spectra of trans-isomer, cis-enriched PSS, and cis-enriched PSS sample after distinct time points in the dark. (B) logarithmic application of the absorption change over time to determine rate constant k and half-life time  $t_{1/2}$ ; Figure S8: Time-resolved fluorescence measurement (excitation wavelength = 460 nm, emission wavelength = 480 nm) of unbound ThT (black), ThT bound to PTH<sub>25-37</sub> fibrils (dark green), ThT bound to trans-AzoPTH<sub>25-37</sub> fibrils (light green); Figure S9: ThT monitored fibrillation assays (c = 100  $\mu$ M, 37 °C, 50 mM Na<sub>2</sub>HPO<sub>4</sub>, pH 7.4). (A) PTH<sub>25-37</sub>, (B) trans-AzoPTH<sub>25-37</sub>, (C) cis-AzoPTH<sub>25-37</sub>; Figure S10: ThT monitored fibrillization assays of mixtures of PTH<sub>25-37</sub>, trans-AzoPTH<sub>25-37</sub>, and cis-AzoPTH<sub>25-37</sub> (37 °C, 50 mM Na<sub>2</sub>HPO<sub>4</sub>, pH 7.4). (A) trans-AzoPTH<sub>25-37</sub>:PTH<sub>25-37</sub> (100 μM:100 μM), (B) cis-AzoPTH<sub>25-37</sub>:PTH<sub>25-37</sub> (100 μM:100 μM), (C) trans-AzoPTH<sub>25-37</sub>:PTH<sub>25-37</sub> (50 μM:100 μM), (D) cis-AzoPTH<sub>25-37</sub>:PTH<sub>25-37</sub> (50 μM:100 μM), (E) trans-AzoPTH<sub>25-37</sub>:PTH<sub>25-37</sub> (20 μM:100 μM), (F) cis-AzoPTH<sub>25-37</sub>:PTH<sub>25-37</sub> (20 μM:100 μM), (G) trans-AzoPTH<sub>25-37</sub>:PTH<sub>25-37</sub> (10 μM:100 μM), (H) cis-AzoPTH<sub>25-37</sub>:PTH<sub>25-37</sub> (10 μM:100 μM); Figure S11: <sup>1</sup>H-NMR spectrum (top; 400 MHz, DMSO-d<sub>6</sub>) and <sup>13</sup>C-NMR spectrum (bottom; 100 MHz, DMSO-d<sub>6</sub>) of (9H-Fluoren-9-yl)methyl (4aminobenzyl)carbamate; Figure S12: <sup>1</sup>H-NMR spectrum (top; 400 MHz, DMSO-d<sub>6</sub>) and <sup>13</sup>C-NMR spectrum (bottom; 100 MHz, DMSO-d<sub>6</sub>) of Fmoc-3,4'-AMPB (mixture of isomers); Figure S13: <sup>1</sup>H-NMR spectra (500 MHz, D<sub>2</sub>O) of AzoPTH<sub>25-37</sub> (top, trans-isomer) and SP1 (bottom, trans-isomer); Figure S14: <sup>1</sup>H-NMR spectra (500 MHz, D<sub>2</sub>O) of SP2 (top, trans-isomer) and SP3 (bottom, transisomer); Figure S15: <sup>1</sup>H-NMR spectrum (500 MHz, D<sub>2</sub>O) of SP4 (*trans*-isomer); Scheme S1: Synthesis of Fmoc-protected 3,4'-AMPB 7. (a) Fmoc-ONSu, triethylamin, DMF/MeCN, 16 h, room temperature. (b) Oxone<sup>®</sup>, DCM, water, 3 h, room temperature. (c) AcOH, DMSO, N2, 72 h, room temperature; Table S1: Primary sequence and solubility in 50 mM Na<sub>2</sub>HPO<sub>4</sub> buffer (pH 7.4) of peptides AzoPTH<sub>25-37</sub> and SP1-SP4.

**Author Contributions:** Conceptualization, A.P. and W.H.B.; methodology, A.P., B.V., G.H., T.K. and S.R.; validation, A.P. and B.V.; investigation, A.P.; writing—original draft preparation, A.P.; writing—review and editing, A.P. and W.H.B.; supervision, W.H.B.; project administration, W.H.B.; funding acquisition, W.H.B. All authors have read and agreed to the published version of the manuscript.

**Funding:** This research was funded by DFG—Deutsche Forschungsgemeinschaft, Project ID 189853844—TRR 102, TP A12.

Institutional Review Board Statement: Not applicable.

Informed Consent Statement: Not applicable.

Data Availability Statement: Data are contained within the article.

**Acknowledgments:** The authors thank Jochen Balbach (Martin Luther University Halle-Wittenberg, Department of Physics) and Maria Ott (Martin Luther University Halle-Wittenberg, Department of Biochemistry and Biotechnology) for the use of equipment, their advice, and for discussions.

**Conflicts of Interest:** The authors declare no conflict of interest. The funders had no role in the design of the study; in the collection, analyses, or interpretation of data; in the writing of the manuscript, or in the decision to publish the results.

Biomedicines 2022, 10, 1512 12 of 13

#### References

- 1. Hamley, I.W. Peptide fibrillization. Angew. Chem. Int. Ed. 2007, 46, 8128–8147. [CrossRef] [PubMed]
- 2. Binder, W.H.; Smrzka, O.W. Self-Assembly of Fibers and Fibrils. Angew. Chem. Int. Ed. 2006, 45, 7324–7328. [CrossRef] [PubMed]
- 3. Sunde, M.; Serpell, L.C.; Bartlam, M.; Fraser, P.E.; Pepys, M.B.; Blake, C.C. Common core structure of amyloid fibrils by synchrotron X-ray diffraction. *J. Mol. Biol.* **1997**, 273, 729–739. [CrossRef]
- 4. Karamanos, T.K.; Kalverda, A.P.; Thompson, G.S.; Radford, S.E. Mechanisms of amyloid formation revealed by solution NMR. *Prog. Nucl. Magn. Reson. Spectrosc.* **2015**, *88*, 86–104. [CrossRef]
- 5. Ferreira, S.T.; Vieira, M.N.; De Felice, F.G. Soluble protein oligomers as emerging toxins in Alzheimer's and other amyloid diseases. *IUBMB Life* **2007**, *59*, 332–345. [CrossRef] [PubMed]
- Irvine, G.B.; El-Agnaf, O.M.; Shankar, G.M.; Walsh, D.M. Protein aggregation in the brain: The molecular basis for Alzheimer's and Parkinson's diseases. Mol. Med. 2008, 14, 451–464. [CrossRef] [PubMed]
- 7. Haataja, L.; Gurlo, T.; Huang, C.J.; Butler, P.C. Islet amyloid in type 2 diabetes, and the toxic oligomer hypothesis. *Endocr. Rev.* **2008**, 29, 303–316. [CrossRef]
- 8. Chapman, M.R.; Robinson, L.S.; Pinkner, J.S.; Roth, R.; Heuser, J.; Hammar, M.; Normark, S.; Hultgren, S.J. Role of Escherichia coli curli operons in directing amyloid fiber formation. *Science* **2002**, *295*, 851–855. [CrossRef]
- 9. Bayro, M.J.; Daviso, E.; Belenky, M.; Griffin, R.G.; Herzfeld, J. An amyloid organelle, solid-state NMR evidence for cross-β assembly of gas vesicles. *J. Biol. Chem.* **2012**, *287*, 3479–3484. [CrossRef]
- 10. Mackay, J.P.; Matthews, J.M.; Winefield, R.D.; Mackay, L.G.; Haverkamp, R.G.; Templeton, M.D. The hydrophobin EAS is largely unstructured in solution and functions by forming amyloid-like structures. *Structure* **2001**, *9*, 83–91. [CrossRef]
- 11. Kenney, J.M.; Knight, D.; Wise, M.J.; Vollrath, F. Amyloidogenic nature of spider silk. *Eur. J. Biochem.* **2002**, 269, 4159–4163. [CrossRef] [PubMed]
- 12. Fowler, D.M.; Koulov, A.V.; Alory-Jost, C.; Marks, M.S.; Balch, W.E.; Kelly, J.W. Functional amyloid formation within mammalian tissue. *PLoS Biol.* **2006**, *4*, e6. [CrossRef]
- 13. Li, J.; McQuade, T.; Siemer, A.B.; Napetschnig, J.; Moriwaki, K.; Hsiao, Y.-S.; Damko, E.; Moquin, D.; Walz, T.; McDermott, A. The RIP1/RIP3 necrosome forms a functional amyloid signaling complex required for programmed necrosis. *Cell* **2012**, *150*, 339–350. [CrossRef] [PubMed]
- 14. Maji, S.K.; Perrin, M.H.; Sawaya, M.R.; Jessberger, S.; Vadodaria, K.; Rissman, R.A.; Singru, P.S.; Nilsson, K.R.; Simon, R.; Schubert, D.; et al. Functional Amyloids As Natural Storage of Peptide Hormones in Pituitary Secretory Granules. *Science* **2009**, *325*, 328–332. [CrossRef]
- 15. Cohn, D.V.; Elting, J. Biosynthesis, processing, and secretion of parathormone and secretory protein-I. *Recent Prog. Horm. Res.* 1983, 39, 181–209.
- 16. Usdin, T.B. The PTH2 receptor and TIP39: A new peptide-receptor system. Trends Pharmacol. Sci. 2000, 21, 128-130. [CrossRef]
- 17. Guerreiro, P.M.; Renfro, J.L.; Power, D.M.; Canario, A.V. The parathyroid hormone family of peptides: Structure, tissue distribution, regulation, and potential functional roles in calcium and phosphate balance in fish. *Am. J. Physiol. Regul. Integr. Comp. Physiol.* **2007**, 292, R679–R696. [CrossRef] [PubMed]
- 18. Freeman, M.W.; Wiren, K.M.; Rapoport, A.; Lazar, M.; Potts, J.T., Jr.; Kronenberg, H.M. Consequences of Amino-Terminal Deletions of Preproparathyroid Hormone Signal Sequence. *Mol. Endocrinol.* **1987**, *1*, 628–638. [CrossRef] [PubMed]
- 19. Wiren, K.M.; Potts, J.T., Jr.; Kronenberg, H.M. Importance of the propeptide sequence of human preproparathyroid hormone for signal sequence function. *J. Biol. Chem.* **1988**, *263*, 19771–19777. [CrossRef]
- 20. Gopalswamy, M.; Kumar, A.; Adler, J.; Baumann, M.; Henze, M.; Kumar, S.T.; Fändrich, M.; Scheidt, H.A.; Huster, D.; Balbach, J. Structural characterization of amyloid fibrils from the human parathyroid hormone. *Biochim. Biophys. Acta (BBA)-Proteins Proteom.* **2015**, 1854, 249–257. [CrossRef]
- 21. Friedlander, G.; Amiel, C. Cellular mode of action of parathyroid hormone. *Adv. Nephrol. Necker Hosp.* **1994**, 23, 265–279. [PubMed]
- 22. Martin, T.J.; Sims, N.A.; Seeman, E. Physiological and Pharmacological Roles of PTH and PTHrP in Bone using their Shared Receptor, PTH1R. *Endocr. Rev.* **2021**, *42*, 383–406. [CrossRef] [PubMed]
- 23. Mosekilde, L.; Søgaard, C.; Danielsen, C.; Tørring, O.; Nilsson, M. The anabolic effects of human parathyroid hormone (hPTH) on rat vertebral body mass are also reflected in the quality of bone, assessed by biomechanical testing: A comparison study between hPTH-(1–34) and hPTH-(1–84). *Endocrinology* **1991**, *129*, 421–428. [CrossRef]
- 24. Evgrafova, Z.; Voigt, B.; Roos, A.H.; Hause, G.; Hinderberger, D.; Balbach, J.; Binder, W.H. Modulation of amyloid β peptide aggregation by hydrophilic polymers. *Phys. Chem. Chem. Phys.* **2019**, *21*, 20999–21006. [CrossRef] [PubMed]
- 25. Evgrafova, Z.; Voigt, B.; Baumann, M.; Stephani, M.; Binder, W.H.; Balbach, J. Probing Polymer Chain Conformation and Fibril Formation of Peptide Conjugates. *ChemPhysChem* **2019**, 20, 236–240. [CrossRef] [PubMed]
- 26. Evgrafova, Z.; Rothemund, Ś.; Voigt, B.; Hause, G.; Balbach, J.; Binder, W.H. Synthesis and Aggregation of Polymer-Amyloid β Conjugates. *Macromol. Rapid Commun.* **2020**, *41*, 1900378. [CrossRef] [PubMed]
- 27. Funtan, S.; Evgrafova, Z.; Adler, J.; Huster, D.; Binder, W.H. Amyloid Beta Aggregation in the Presence of Temperature-Sensitive Polymers. *Polymers* 2016, 8, 178. [CrossRef]
- 28. Hull, K.; Morstein, J.; Trauner, D. In Vivo Photopharmacology. Chem. Rev. 2018, 118, 10710–10747. [CrossRef]

Biomedicines 2022, 10, 1512 13 of 13

29. Volgraf, M.; Gorostiza, P.; Numano, R.; Kramer, R.H.; Isacoff, E.Y.; Trauner, D. Allosteric control of an ionotropic glutamate receptor with an optical switch. *Nat. Chem. Biol.* **2006**, *2*, 47–52. [CrossRef]

- 30. Samanta, S.; Qin, C.; Lough, A.J.; Woolley, G.A. Bidirectional photocontrol of peptide conformation with a bridged azobenzene derivative. *Angew. Chem. Int. Ed.* **2012**, *51*, 6452–6455. [CrossRef]
- 31. Lindgren, N.J.V.; Varedian, M.; Gogoll, A. Photochemical Regulation of an Artificial Hydrolase by a Backbone Incorporated Tertiary Structure Switch. *Chem. Eur. J.* **2009**, *15*, 501–505. [CrossRef] [PubMed]
- 32. Schadendorf, T.; Hoppmann, C.; Rück-Braun, K. Synthesis of rigid photoswitchable hemithioindigo ω-amino acids. *Tetrahedron Lett.* **2007**, *48*, 9044–9047. [CrossRef]
- Lougheed, T.; Borisenko, V.; Hennig, T.; Ruck-Braun, K.; Woolley, G.A. Photomodulation of ionic current through hemithioindigo-modified gramicidin channels. Org. Biomol. Chem. 2004, 2, 2798–2801. [CrossRef] [PubMed]
- 34. Albert, L.; Peñalver, A.; Djokovic, N.; Werel, L.; Hoffarth, M.; Ruzic, D.; Xu, J.; Essen, L.O.; Nikolic, K.; Dou, Y. Modulating Protein–Protein Interactions with Visible-Light-Responsive Peptide Backbone Photoswitches. *ChemBioChem* **2019**, *20*, 1417–1429. [CrossRef]
- 35. Pozhidaeva, N.; Cormier, M.-E.; Chaudhari, A.; Woolley, G.A. Reversible photocontrol of peptide helix content: Adjusting thermal stability of the cis state. *Bioconjug. Chem.* **2004**, *15*, 1297–1303. [CrossRef]
- 36. Broichhagen, J.; Podewin, T.; Meyer-Berg, H.; Von Ohlen, Y.; Johnston, N.R.; Jones, B.J.; Bloom, S.R.; Rutter, G.A.; Hoffmann-Röder, A.; Hodson, D.J. Optical control of insulin secretion using an incretin switch. *Angew. Chem. Int. Ed.* **2015**, *54*, 15565–15569. [CrossRef]
- 37. Zhang, Y.; Erdmann, F.; Fischer, G. Augmented photoswitching modulates immune signaling. *Nat. Chem. Biol.* **2009**, *5*, 724–726. [CrossRef]
- 38. Hoppmann, C.; Schmieder, P.; Domaing, P.; Vogelreiter, G.; Eichhorst, J.; Wiesner, B.; Morano, I.; Rück-Braun, K.; Beyermann, M. Photocontrol of contracting muscle fibers. *Angew. Chem. Int. Ed.* **2011**, *50*, 7699–7702. [CrossRef]
- 39. Zhang, F.; Timm, K.A.; Arndt, K.M.; Woolley, G.A. Photocontrol of coiled-coil proteins in living cells. *Angew. Chem. Int. Ed.* **2010**, 49, 3943–3946. [CrossRef]
- 40. Aemissegger, A.; Kräutler, V.; van Gunsteren, W.F.; Hilvert, D. A photoinducible β-hairpin. *J. Am. Chem. Soc.* **2005**, 127, 2929–2936. [CrossRef]
- 41. Yeoh, Y.Q.; Yu, J.; Polyak, S.W.; Horsley, J.R.; Abell, A.D. Photopharmacological Control of Cyclic Antimicrobial Peptides. *ChemBioChem* **2018**, *19*, 2591–2597. [CrossRef]
- 42. Rück-Braun, K.; Kempa, S.; Priewisch, B.; Richter, A.; Seedorff, S.; Wallach, L. Azobenzene-Based ω-Amino Acids and Related Building Blocks: Synthesis, Properties, and Application in Peptide Chemistry. *Synthesis* **2009**, 24, 4256–4267. [CrossRef]
- 43. Ahmed, M.; Davis, J.; Aucoin, D.; Sato, T.; Ahuja, S.; Aimoto, S.; Elliott, J.I.; Van Nostrand, W.E.; Smith, S.O. Structural conversion of neurotoxic amyloid-β 1–42 oligomers to fibrils. *Nat. Struct. Mol. Biol.* **2010**, *17*, 561–567. [CrossRef] [PubMed]
- 44. Der-Sarkissian, A.; Jao, C.C.; Chen, J.; Langen, R. Structural organization of α-synuclein fibrils studied by site-directed spin labeling. *J. Biol. Chem.* **2003**, 278, 37530–37535. [CrossRef] [PubMed]
- 45. Makin, O.S.; Serpell, L.C. Structural characterisation of islet amyloid polypeptide fibrils. *J. Mol. Biol.* **2004**, *335*, 1279–1288. [CrossRef]
- 46. Murawska, G.M.; Poloni, C.; Simeth, N.A.; Szymanski, W.; Feringa, B.L. Comparative Study of Photoswitchable Zinc-Finger Domain and AT-Hook Motif for Light-Controlled Peptide–DNA Binding. *Chem. Eur. J.* **2019**, 25, 4965–4973. [CrossRef]
- 47. Bandara, H.M.D.; Burdette, S.C. Photoisomerization in different classes of azobenzene. *Chem. Soc. Rev.* **2012**, *41*, 1809–1825. [CrossRef]
- 48. LeVine, H., III. [18] Quantification of β-sheet amyloid fibril structures with thioflavin T. In *Methods in Enzymology*; Elsevier: Amsterdam, The Netherlands, 1999; Volume 309, pp. 274–284.
- 49. Deike, S.; Rothemund, S.; Voigt, B.; Samantray, S.; Strodel, B.; Binder, W.H. β-Turn mimetic synthetic peptides as amyloid-β aggregation inhibitors. *Bioorg. Chem.* **2020**, *101*, 104012. [CrossRef]
- 50. Ren, B.; Zhang, Y.; Zhang, M.; Liu, Y.; Zhang, D.; Gong, X.; Feng, Z.; Tang, J.; Chang, Y.; Zheng, J. Fundamentals of cross-seeding of amyloid proteins: An introduction. *J. Mater. Chem. B* **2019**, 7, 7267–7282. [CrossRef]
- 51. Mulatihan, D.; Guo, T.; Zhao, Y. Azobenzene photoswitch for isomerization-dependent cancer therapy via azo-combretastatin A4 and phototrexate. *Photochem. Photobiol.* **2020**, *96*, 1163–1168. [CrossRef]
- 52. Williams, R. Hepatic metabolism of drugs. *Gut* 1972, 13, 579. [CrossRef] [PubMed]
- 53. Álvarez, Z.; Kolberg-Edelbrock, A.N.; Sasselli, I.R.; Ortega, J.A.; Qiu, R.; Syrgiannis, Z.; Mirau, P.A.; Chen, F.; Chin, S.M.; Weigand, S.; et al. Bioactive scaffolds with enhanced supramolecular motion promote recovery from spinal cord injury. *Science* **2021**, *374*, 848–856. [CrossRef] [PubMed]



pubs.acs.org/bc Article

# Photocontrolled Reversible Amyloid Fibril Formation of Parathyroid **Hormone-Derived Peptides**

André Paschold, Moritz Schäffler, Xincheng Miao, Luis Gardon, Stephanie Krüger, Henrike Heise, Merle I. S. Röhr, Maria Ott, Birgit Strodel,\* and Wolfgang H. Binder\*



Cite This: Bioconjugate Chem. 2024, 35, 981–995



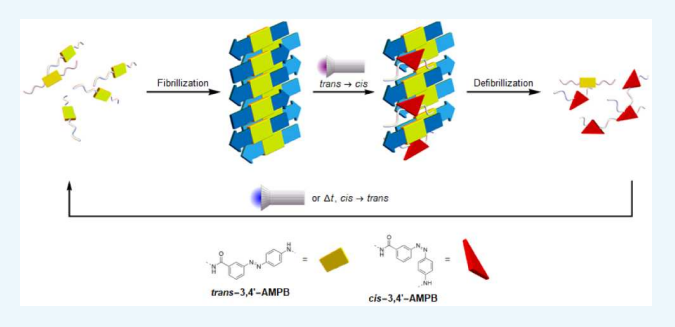
**ACCESS** I

III Metrics & More

Article Recommendations

Supporting Information

ABSTRACT: Peptide fibrillization is crucial in biological processes such as amyloid-related diseases and hormone storage, involving complex transitions between folded, unfolded, and aggregated states. We here employ light to induce reversible transitions between aggregated and nonaggregated states of a peptide, linked to the parathyroid hormone (PTH). The artificial light-switch 3-{[(4-aminomethyl)phenyl]diazenyl}benzoic acid (AMPB) is embedded into a segment of PTH, the peptide PTH<sub>25-37</sub>, to control aggregation, revealing position-dependent effects. Through in silico design, synthesis, and experimental validation of 11 novel PTH<sub>25-37</sub>-derived peptides, we predict and



confirm the amyloid-forming capabilities of the AMPB-containing peptides. Quantum-chemical studies shed light on the photoswitching mechanism. Solid-state NMR studies suggest that  $\beta$ -strands are aligned parallel in fibrils of PTH<sub>25-37</sub>, while in one of the AMPB-containing peptides,  $\beta$ -strands are antiparallel. Simulations further highlight the significance of  $\pi-\pi$  interactions in the latter. This multifaceted approach enabled the identification of a peptide that can undergo repeated phototriggered transitions between fibrillated and defibrillated states, as demonstrated by different spectroscopic techniques. With this strategy, we unlock the potential to manipulate PTH to reversibly switch between active and inactive aggregated states, representing the first observation of a photostimulus-responsive hormone.

#### INTRODUCTION

Modulating a protein's secondary structure stands as a pivotal strategy to define and harness its functionality. While numerous protein structures are identified, predicted, and engineered, the concept of inducing conformational changes by external triggers to alter their biological activities remains rare. Temperature, pH, polarity, or light offer avenues for such a dynamic control, in particular when applied to sensitive functional groups inserted inside the protein. Among these, light emerges as a particularly advantageous stimulus, providing precise temporal control across vast time scales, noninvasiveness, and compatibility with intricate matrices like living tissues.<sup>5</sup> Leveraging light-induced conformational changes has demonstrated success in various proteins, from transporter-proteins like rhodopsins to enzymes, showcasing potential applications in photopharmacology and diverse enzymatic processes. 5,6 Moreover, external photoswitches have successfully enabled photomodulation in a diverse array of enzymes, modifying binding affinities, facilitating peptide purification through photoaffinity,9 and controlling secondary structure alterations. 10 Beyond the structure of individual peptides or proteins, there is a strong interplay between secondary structure and aggregation of peptides. This process is particularly pronounced in the context of amyloid

aggregation, where proteins form  $\beta$ -sheet-rich structures, leading to the formation of highly ordered fibrillar aggregates.<sup>11</sup> Such fibrils are a hallmark of several neurodegenerative diseases, including Alzheimer's and Parkinson's. Understanding and controlling amyloid aggregation can thus be crucial for developing therapies for diseases associated with these pathological protein assemblies. However, controlling peptide aggregation proves to be a significant challenge, given the complex processes involved. This challenge arises from intricate intrapeptide and interpeptide interactions, coupled with extensive conformational changes on a large scale, particularly when considering the regulation of primary and secondary nucleation preceding fibrillization. Therefore, the utilization of light to control amyloid assembly processes represents a groundbreaking advancement, enabling control over the bioavailability of hormones, such as the parathyroid hormone (PTH). PTH is reversibly stored in functional

Received: April 22, 2024 May 21, 2024 Revised: Accepted: May 24, 2024 Published: June 12, 2024





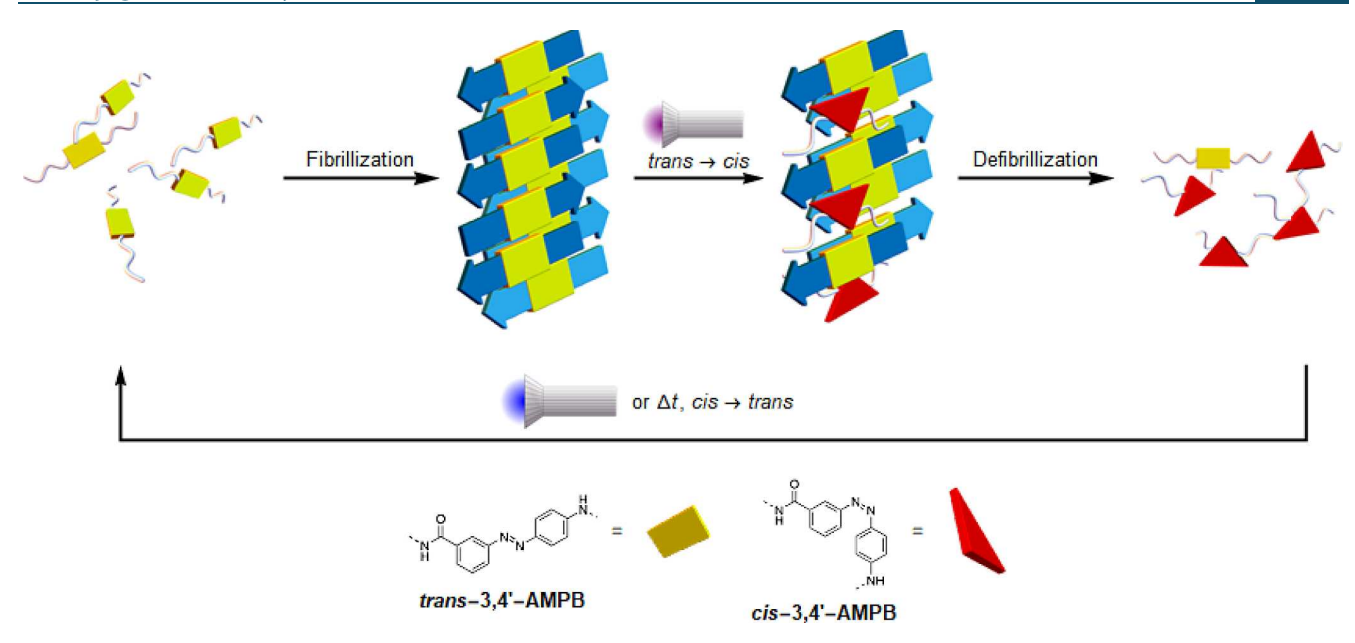


**Figure 1.** Concept for a light-driven (de)-aggregation of the parathyroid-hormone (PTH). The artificial light-switch, 3-{[(4-aminomethyl)-phenyl]diazenyl}benzoic acid (*cis/trans*-3,4'-AMPB) is embedded at various positions of a peptide-fragment of PTH, switching between the *cis/trans*-form, in this mode regulating the reversible assembly of the peptide into fibrils.

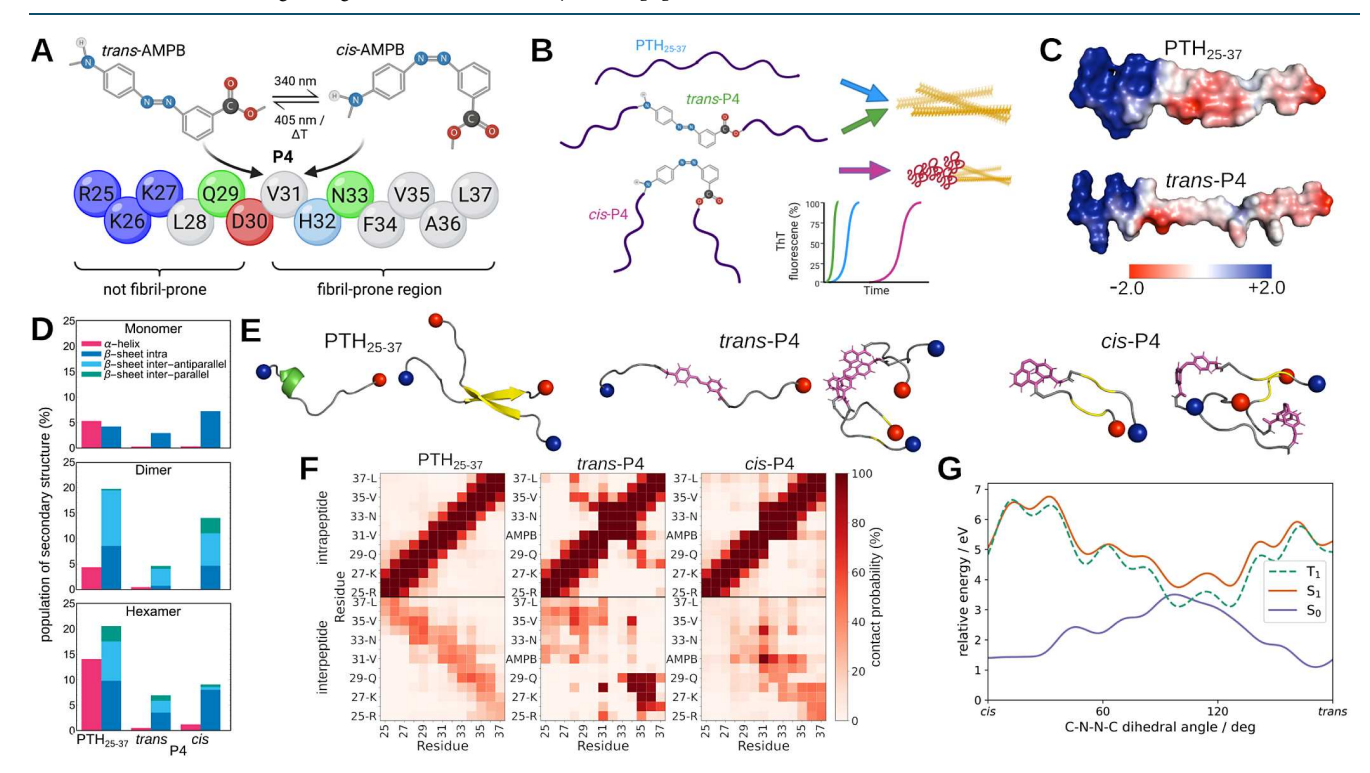


Figure 2. (A) Sequence of PTH<sub>25-37</sub>, where the fibril-forming region identified by bioinformatic analysis is labeled, and the chemical structure of AMPB, which replaces V31 in P4, is shown. The side chains of the amino acids, shown in blue and red, are positively and negatively charged at pH 7.4, respectively, with H32 shown in light blue as a borderline case, while green and gray indicate polar and hydrophobic amino acids, respectively. (B) PTH<sub>25-37</sub> and *trans*-P4 form fibrils, as shown in the ThT fluorescence cartoon below (blue and green line), while *cis*-P4 initially forms amorphous aggregates, which then transform into fibrils (red line in ThT cartoon). (C) Electrostatic potentials surface (values in kTe<sup>-1</sup> according to the color scale at the bottom) of PTH<sub>25-37</sub> and *trans*-P4. (D) Average simulated secondary structure population, divided into α-helical, intrapeptide β-sheets, interpeptide parallel, and antiparallel β-sheets as indicated by the color code. Results are shown for simulations of monomers, dimers, and hexamers of PTH<sub>25-37</sub>, *trans*-P4, and *cis*-P4. (E) Representative snapshots of the monomer and dimer simulations, with the α-helix shown in green, the β-sheets in yellow, the random coil in gray, the N- and C-termini as blue and red spheres, respectively, and AMPB in purple. (F) Contact matrix of dimer simulations for PTH<sub>25-37</sub>, *trans*-P4, and *cis*-P4. (G) Quantum chemical potential energy scan of the *trans* → *cis* isomerization of the AMPB photoswitch in P4.

pubs.acs.org/bc

amyloid fibrils, as these fibrils, unlike, e.g., amyloid-A $\beta$  fibrils, can disintegrate again after aggregation. In this study, we pioneer the utilization of light to achieve a reversible transition between the aggregated and nonaggregated states of PTH (Figure 1), allowing the regeneration of PTH fibrils through precise light control, presenting a transformative advancement in the field.

PTH, a reversibly fibrillating 84-amino acid hormone, is ubiquitously distributed in animals. 13 Responsible for regulating calcium and phosphate homeostasis, <sup>14</sup> mature PTH<sub>1-84</sub> is stored in functional amyloids before secretion, 15 wherein its Nterminal pro-sequence potentially prevents premature aggregation.<sup>16</sup> PTH-related diseases prompt the use of approved drugs, Natpara ( $PTH_{1-84}$ ) and Forteo ( $PTH_{1-34}$ ), addressing hormone imbalances.<sup>17</sup> While the physiological role of the Nterminal 34 amino acids of PTH<sub>1-84</sub> is well investigated, being crucial for the activation of G-protein coupled receptors of bone and kidney cells<sup>18</sup> and in the nervous system for calcium and phosphate homeostasis, 19 there remains a knowledge gap regarding the fibrillization process and the resulting fibrils. Current knowledge indicates that under physiological conditions, the thermodynamic stability of  $PTH_{1-84}$  fibrils is low enough to allow dissociation upon dilution, with the fibrilforming sequence encompassing amino acids R25-L37.15 Previous research explored the impact of the pro-sequence 16 and environmental factors on the fibrillization process<sup>20,21</sup> of PTH, however, with an only limited insight into the precise structural parameters controlling assembly and disassembly of the fibrils.<sup>22</sup> The aim of the current work is to gain deeper insights into the fibrillization of PTH<sub>25-37</sub>, coupled with the ability to reversibly control this process and understand the structural principles of the assembly process. We employ a synthetic approach for synthesizing PTH<sub>25-37</sub> peptides bearing the azobenzene photoswitch, 3-{[(4-aminomethyl)phenyl]diazenyl}benzoic acid (AMPB), guided by bioinformatics to strategically place AMPB for optimal photocontrol, with biophysical techniques such as thioflavin T (ThT) fluorescence, CD spectroscopy, and transmission electron microscopy (TEM) to assess the peptide aggregation dynamics and aggregate morphology. This is further combined with molecular dynamics (MD) simulations to elucidate the impact of AMPB on the structure and dynamics of the designed peptides and their small oligomers (amounting to a total of 285  $\mu$ s simulation time), while wide-angle X-ray scattering (WAXS) and solid-state nuclear magnetic resonance (ssNMR) spectroscopy in conjunction with MD are employed to provide structure models for selected amyloid fibrils. Finally, quantumchemical potential energy scans of both the ground  $(S_0)$  and excited states  $(S_1 \text{ and } T_1)$  reveal insights into the photoswitching mechanism of the AMPB group and its electronic interaction when integrated into PTH<sub>25-37</sub>, considering both the monomeric and dimeric peptide state. Providing a thorough understanding of the aggregation behavior of PTH<sub>25-37</sub> and its derivatives, we have engineered a peptide analogue with the unique capability of reversible light-induced switching of its aggregation state.

#### RESULTS AND DISCUSSION

Aggregation Characteristics of Unmodified PTH<sub>25-37</sub> and Engineered Peptide. To understand the aggregation of PTH<sub>25-37</sub> and make informed design decisions, we began our analysis with a detailed examination of the original peptide  $PTH_{25-37}$  and one engineered peptide (P4),<sup>22</sup> bearing the

photoswitch in the central part of the peptide (Figure 2A). Unmodified PTH<sub>25-37</sub> and *trans*-P4 form amyloid fibrils within 15 and 10 h, respectively, whereas cis-P4 initially forms amorphous aggregates and only forms amyloid fibrils after about 50 h (Figure 2B).<sup>22</sup> The increased rate of aggregation of trans-P4 compared to PTH<sub>25-37</sub> is assigned to the physicochemical properties of the amino acids and the phototrigger, AMPB, that make up the peptide (Figure 2A). PTH<sub>25-37</sub> has three positive charges (RKK) at the N-terminus, followed by a mixture of hydrophobic, polar and one negatively charged residue (D30) in the middle, while the C-terminal residues are mainly hydrophobic. This uneven distribution of physicochemical properties across the sequence is also reflected in the electrostatic potential surface, which shows a strongly positively charged N-terminus and a more hydrophobic C-terminal half with some negative charge accumulation beyond the first three residues (Figure 2C). The assumption therefore is that amyloid aggregation of PTH<sub>25-37</sub> is driven by the residues after the initial RKK sequence. To test this assumption, we used four aggregation predictors: PASTA,<sup>23</sup> AGGRESCAN,<sup>24</sup> AmyloGRAM,<sup>25</sup> and FoldAmyloid, 26 which show that the sequence 32HNFVA37L is an aggregation hotspot and that the first five amino acids <sup>25</sup>RKKL<sup>29</sup>Q should not contribute to fibrillization. For <sup>30</sup>DV, a low tendency to aggregation was observed. In P4, one of the residues of the later sequence, V31, is replaced by AMPB. This increases the overall hydrophobicity of the peptide, while the azo group itself adds some positive charge to the electrostatic potential, which compensates for the predominant negative charge in the C-terminal part of the peptide. These two effects, therefore, explain the faster aggregation kinetics of trans-P4 compared to  $PTH_{25-37}$ .

To understand the aggregation mechanisms and elucidate the structures that form during aggregation, namely first oligomers and finally fibrils, we performed MD simulations and ssNMR spectroscopy of both PTH<sub>25-37</sub> and P4, the latter simulated in the trans- and cis-states (see Table S1 for an overview of simulations performed). In this way, we can also develop a structural understanding of why the fibrillization of cis-P4 is slowed down and generally reduced. The monomers of either PTH<sub>25-37</sub>, trans-P4, and cis-P4 are mainly in a random coil state (Figure 2D). Nevertheless, small differences between the monomeric peptides can be observed. One of them is that PTH<sub>25-37</sub> shows a certain tendency to form an  $\alpha$ -helix in the N-terminal residues up to D30, which is lost when V31 is replaced by AMPB (Figure 2E). When the azo group is in the cis-state, this allows more intrapeptide contacts, including the formation of a  $\beta$ -hairpin, whereas in the *trans*-state, P4 is mostly in a fully elongated state. The dimer simulations showed an increase in  $\beta$ -sheets for all three peptides, but most for PTH<sub>25-37</sub>. This is a result of peptide aggregation, as there is a particular increase in  $\beta$ -sheets between the peptides (Figure 2D), which are mainly arranged antiparallel, as shown by the contact matrix (Figure 2F). In an antiparallel arrangement, the three positively charged N-terminal residues RKK can interact with the negative charge at the C-terminus of the neighboring peptide. Interestingly, the trans-P4 peptide, which we expected to aggregate the fastest based on the fibrillization data, forms fewer  $\beta$ -sheets at the oligomer level. Instead, the interpeptide interactions are dominated by contacts between the two AMPB groups, while the peptides are aligned antiparallel to each other. In contrast, although the *cis*-P4 peptide adopts  $\beta$ sheet structures to some extent due to intrapeptide hairpins, it

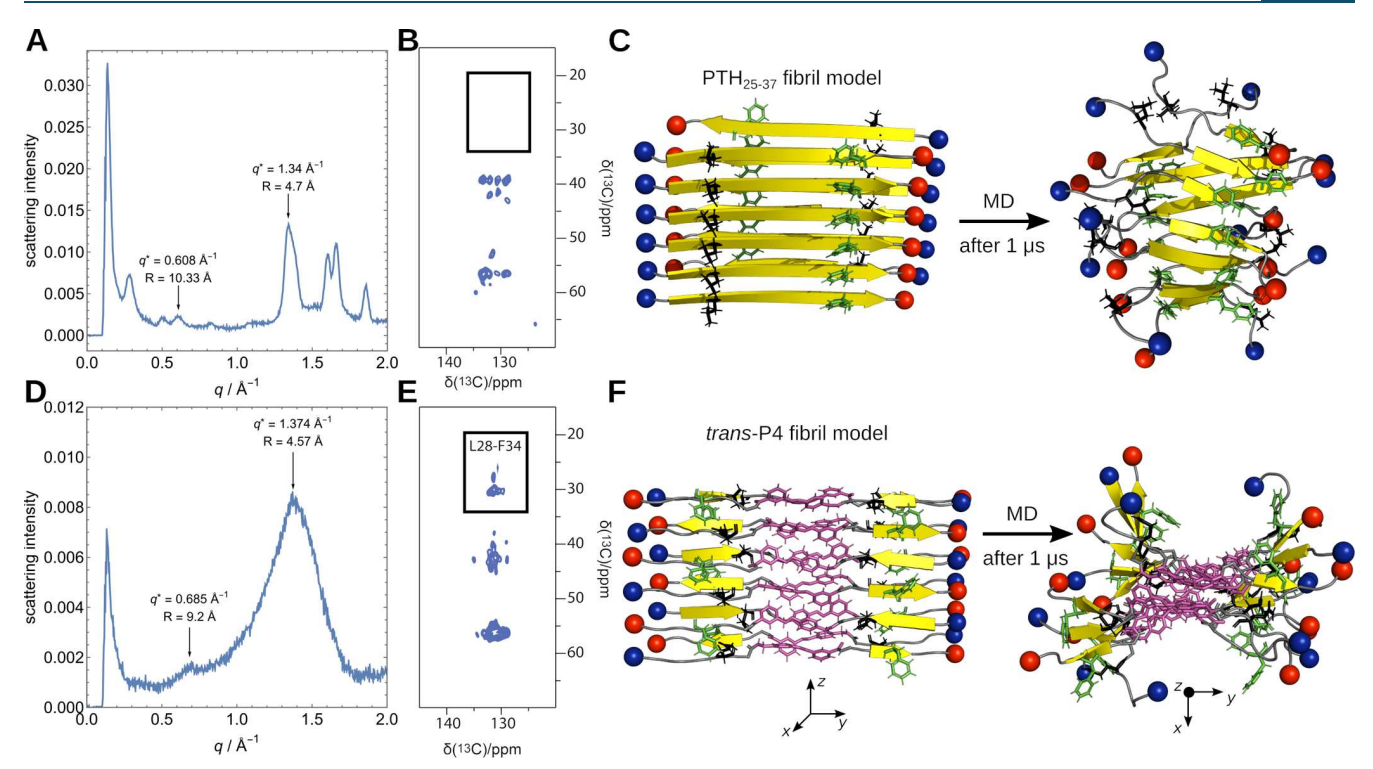


Figure 3. (A, D) WAXS results for PTH<sub>25-37</sub> and the AMPB-modified PTH<sub>25-37</sub> peptide *trans*-P4. (B, E) Solid-state NMR (ssNMR) 2D  $^{13}$ C- $^{13}$ C proton driven spin diffusion spectra close to rotational resonance (mixing time 1s) of fibrils of the PTH<sub>25-37</sub> and *trans*-P4 peptide with uniformly  $^{13}$ C-labeled L28 and F34. (C, F) Fibril models of PTH<sub>25-37</sub> and *trans*-P4 constructed based on the ssNMR (left) and at the end of MD simulations (right), where β-sheets are shown in yellow, random coil in gray, the N- and C-termini as blue and red spheres, respectively, AMPB in purple, and the side chains of L28 and F34 are highlighted as black and green sticks, respectively. Note that in panel F, the structure on the right-hand side is rotated by 90° to better represent the fibrillar arrangement.

aggregates mainly randomly, as confirmed by the many interpeptide contacts, which is consistent with the amorphous aggregates observed *in vitro*. The distinct differences between peptide aggregation involving *cis-* and *trans-AMPB* allow fibril formation to be controlled at the molecular level by isomerization, providing a solid basis for photocontrol of amyloid formation.

In an effort to identify the nucleus of fibril formation, we also simulated the hexamer formation of PTH<sub>25-37</sub>, trans-P4, and cis-P4. However, this system size is still too small (or the simulation time too short) to observe the emergence of fibrillar structures. On the contrary, the hexamers of these peptides are less ordered than the dimers. This confirms the experimental observation that the propensity of PTH<sub>25-37</sub> to form amyloid is much lower than that of other peptides, such as that of  $A\beta_{16-22}$ . For the latter, we observe the formation of ordered hexamers when simulated under the same conditions as here,<sup>27</sup> while ThT experiments for this peptide show that fibrils are already present at the beginning of the measurements.<sup>28</sup> For both PTH<sub>25-37</sub> and P4, we even see a decrease in interpeptide  $\beta$ sheets when we increase the system size to the hexamer, which can be explained by the increase in dimensionality of the conformational space, which allows for more interpeptide interactions and makes it less likely to see ordered aggregates on short time scales. Another interesting observation is that the amount of helix formed increased in the hexamer system of the PTH<sub>25-37</sub> compared to its monomer and dimer. This again reflects the helical propensity of this peptide, which can be stabilized by interpeptide interactions, a common observation in intrinsically disordered peptides that can fold after binding to interaction partners.  $^{29}$ 

We further investigated the electronic interactions and the photoswitching mechanism of AMPB integrated into PTH<sub>25-37</sub>, both in the monomer and dimer states. To this end, we generated 34 switching trajectories using MD simulations to model the  $trans \rightarrow cis$  isomerization of the AMPB photoswitch along the CNNC dihedral angle. The resulting ensemble of pathways was individually analyzed using ONIOM-based QM/QM2<sup>30</sup> (NEVPT2<sup>31</sup>/xTB<sup>32</sup>) calculations, yielding potential energy scans for the ground and first excited triplet and singlet states (Figures 2G and S1). While the calculations clearly indicate that photoswitching is feasible, we also found that several scans exhibit structural barriers, that may impact the fluorescence wavelength and lifetime compared to the pure photoswitch (Figure S2).33 Further elucidation through principal component analysis of the distance matrices between peptide residues (Figures S3 and S4) revealed critical structural motifs potentially responsible for the observed  $S_1$  barrier in *trans*  $\rightarrow$  *cis* isomerization paths. These motifs particularly involve configurations of R25 interacting with A36/L37 and H32/Q33, in both monomeric and dimeric forms (Figure S5).

**Structures of PTH**<sub>25-37</sub> **and P4 Fibrils.** The final state of aggregation, the amyloid fibrils, was characterized by wide-angle X-ray scattering (WAXS) and ssNMR, and the resulting data were used to generate structural models whose stability was evaluated in MD simulations. The WAXS measurement was performed with preformed fibrils of either PTH<sub>25-37</sub> or *trans*-P4. Due to the isotropic orientations of the fibrils and the

Table 1. Designed PTH<sub>25-37</sub> Peptides Containing the AMPB Photoswitch (Azo) Inserted between Two Amino Acids (i) or an Amino Acid Exchanged by AMPB (e)<sup>a</sup>

	peptide	primary sequence	modification	$t_{1/2}(cis)$ [h]
	PTH <sub>25-37</sub>	<sup>25</sup> RKKLQ <sup>30</sup> DVHNF <sup>35</sup> VAL	-	-
	P1 (i)	<sup>25</sup> RKKLQ <sup>30</sup> D-Azo-VHNF <sup>35</sup> VAL	D30-Azo-V31	90
	P2 (i)	<sup>25</sup> RKKLQ <sup>30</sup> DV-Azo-HNF <sup>35</sup> VAL	V31-Azo-H32	90
central	P3 (e)	<sup>25</sup> RKKLQ-Azo-VHNF <sup>35</sup> VAL	$D30 \rightarrow Azo$	-
	P4 (e)	<sup>25</sup> RKKLQ <sup>30</sup> D-Azo-HNF <sup>35</sup> VAL	$V31 \rightarrow Azo$	97
	P5 (e)	<sup>25</sup> RKKLQ-Azo-HNF <sup>35</sup> VAL	D30,V31 → Azo	-
	P6 (i)	<sup>25</sup> RKKLQ-Azo- <sup>30</sup> DVHNF <sup>35</sup> VAL	Q29-Azo-D30	-
	P7 (i)	<sup>25</sup> RKKL-Azo-Q <sup>30</sup> DVHNF <sup>35</sup> VAL	L28-Azo-Q29	72
N-terminal	P8 (i)	<sup>25</sup> RK-Azo-KLQ <sup>30</sup> DVHNF <sup>35</sup> VAL	K26-Azo-K27	89
	P9 (e)	<sup>25</sup> R-Azo-KLQ <sup>30</sup> DVHNF <sup>35</sup> VAL	$K26 \rightarrow Azo$	86
	P10 (i)	<sup>25</sup> RKKLQ <sup>30</sup> DVHN-Azo-F <sup>35</sup> VAL	N33-Azo-F34	-
C-terminal	P11 (i)	<sup>25</sup> RKKLQ <sup>30</sup> DVHNF <sup>35</sup> V-Azo-AL	V35-Azo-A36	-
	P12 (e)	<sup>25</sup> RKKLQ <sup>30</sup> DVHNF-Azo-AL	V35 → Azo	63

"The corresponding peptides were prepared by on-resin synthesis (Merrifield-synthesis) using Fmoc-based building blocks. The synthesis of the AMPB photoswitch follows previously published methods. The half-life time  $t_{1/2}$  (hours) of the cis-form of the peptides was investigated via UV/ vis spectroscopy (see the experimental section for further experimental details).

resulting isotropic scattering pattern (see Figure S6), the scattering intensities were angular averaged and are displayed in Figure 3 A, D. For PTH<sub>25-37</sub>, we observed a diffraction pattern typical for  $\beta$ -sheet-containing amyloid fibrils.<sup>34</sup> The reflection at 4.7 Å indicates a structural repeat corresponding to the distance between two  $\beta$ -strands within a sheet, whereas the reflection at 10.3 Å corresponds to the distance between two  $\beta$ -sheets in a fibril. A reflection at 9.4 Å, which would correspond to the repeating unit of two antiparallel  $\beta$ -strands within a  $\beta$ -sheet (i.e., 2 × 4.7 Å), is not observed, suggesting a parallel alignment of the strands within the  $\beta$ -sheets, which allows the hydrophobic, aggregation-prone residues on the Cterminal side of the peptide to lie adjacent to each other. To test this conclusion, we performed ssNMR measurements of synthesized  $PTH_{25-37}$  with uniformly  $^{13}C$ -labeled L28 and F34. In the 2D <sup>13</sup>C-<sup>13</sup>C spin diffusion measurements with longitudinal mixing times of 500 ms to 1 s, we did not observe any cross-peaks between these residues (Figures 3B, S7). This finding is indicative of a distance of >6 Å between these residues<sup>35</sup> and thus supports parallel  $\beta$ -sheets in PTH<sub>25-37</sub> fibrils. To answer the question of how two sheets of parallel stacked peptides could be arranged in the fibril, <sup>30</sup> we constructed four possible fibril models (with 6 peptides per sheet) consistent with the NMR distance data and tested their stability in MD simulations. Only one of these arrangements proved to be stable, even after 1  $\mu$ s MD. In this model, the  $\beta$ sheets, which consist of parallel and in-register strands, are oriented antiparallel and their R25 side chains point inward (Figure 3C). This also agrees with our findings from the oligomer simulations, which revealed a preferred antiparallel arrangement between the PTH<sub>25-37</sub> peptides, as this allows the positive charges at the N-terminus to interact with the negatively charged C-terminus. In the fibril, this is realized via intersheet interactions, while within the sheets, the hydrophobic residues are adjacent to each other for optimal  $\beta$ -sheet stability. The fibril model at the end of the simulation confirms that the  $\beta$ -sheets are stable. The  $\beta$ -conformation is partially lost only at the terminal residues, which is due to the electrostatic repulsion between the three positive charges on the RKK residues, which also cause twisting of the fibril. The simulation-averaged distance between  $\beta$ -strands is 4.8 Å, and

between two sheets, it is 10.3 Å, in agreement with the WAXS data.

The WAXS signals for trans-P4 (Figure 3D) are much broader than for PTH<sub>25-37</sub>, indicating less structured fibrils for P4. Nevertheless, the peak for strand spacing at 4.6 Å dominates the signal, clearly indicating  $\beta$ -sheet formation. The next peak is at 9.2 Å, which corresponds to twice the interstrand distance. This indicates an antiparallel arrangement of the trans-P4 peptides within a sheet, as here the antiparallel unit consisting of two peptides is another repeat unit leading to a scattering signal. A signal for the intersheet distance is not visible, but could be hidden under the 9.2 Å signal, considering that the signal at 10.3 Å for the PTH<sub>25-37</sub> fibrils is also not strong. The conclusion that the trans-P4 peptides are antiparallel in the fibrils is supported by the ssNMR measurements showing an L28-F34 cross-peak in 2D <sup>13</sup>C-<sup>13</sup>C spin diffusion spectra, which is indicative of an inter-residual distance <6 Å (Figures 3E and S8). Based on this information and in addition to the results of our dimer and hexamer simulations of trans-P4, which revealed a strong interaction between the AMPB groups, we created several possible fibril structures and tested their stability in MD simulations. The structure that met all our experimental specifications and was also stable during the 1  $\mu$ s simulation is the one shown in Figure 3F. The structure at the end of the simulation shows a larger deviation from the idealized fibril model and with shorter  $\beta$ -sheets than observed for PTH<sub>25-37</sub>, which explains the broader WAXS signal. Stabilizing aspects are that the oppositely charged N- and C-terminal ends are directly adjacent within and between the  $\beta$ -sheets and that the central AMPB groups are aligned parallel to each other for  $\pi$ – $\pi$  stacking interactions. The antiparallel  $\beta$ -sheets themselves are less stable, however, as they are formed between the hydrophobic C-terminal half and the nonamyloid-prone Nterminal half on both sides of the AMBP group. Moreover, the AMPB group in the center of the peptide breaks the  $\beta$ -sheet structure, which explains that the P4 fibrils are shorter than those of PTH<sub>25-37</sub>. In addition, the  $\pi$ - $\pi$  stacking and  $\beta$ -sheet stacking have opposite spacing requirements with  $\approx$ 3.8 Å and  $\approx$ 10 Å, respectively, which can be clearly seen in the MD

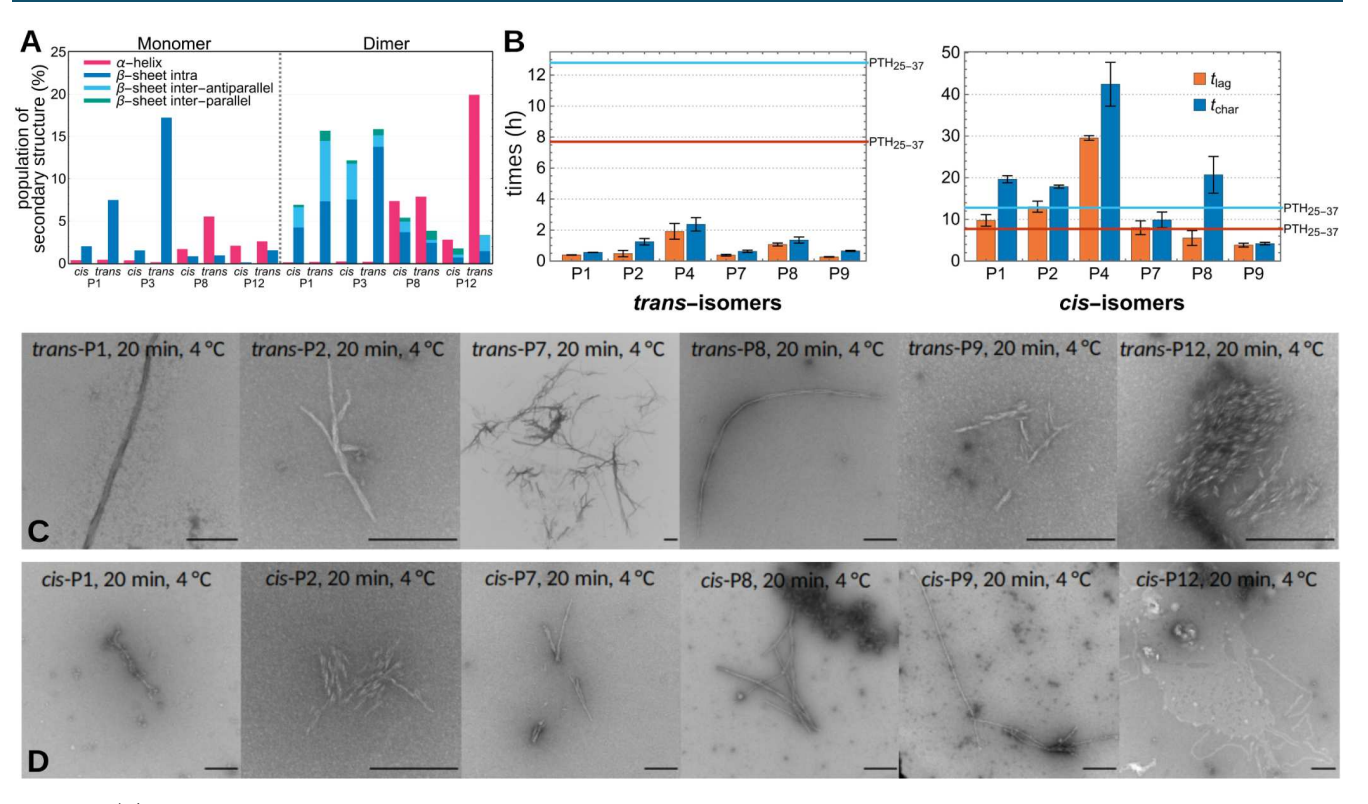


Figure 4. (A) Simulated average secondary structure population, divided into α-helical, intrapeptide  $\beta$ -sheets, and interpeptide parallel and antiparallel  $\beta$ -sheets as indicated by the color code. Results are shown for simulations of monomers and dimers of the *trans*- and *cis*-forms of P1, P3, P8, and P12. (B) Lag time  $t_{lag}$  (orange) and characteristic time  $t_{char}$  (blue) of the *trans*-forms (left) and *cis*-forms (right) of the peptides P1, P2, P4, P7, P8, and P9. The corresponding values of PTH<sub>25-37</sub> are indicated as orange ( $t_{lag}$ ) and blue line ( $t_{char}$ ). (C) TEM images of the *trans*-isomers of P1, P2, P7, P8, P9, and P12 after 20 min at 4 °C. Scale bar = 250 nm. (D) TEM images if the *cis*-isomers of P1, P2, P7, P8, P9, and P12 after 20 min at 4 °C. Scale bar = 250 nm. TEM data for the photoswitching of P4 are presented in Figure S23.

snapshot shown in Figure 3F and further explains the broadness of the corresponding WAXS signal.

**Peptide Design.** Based on all simulations and structural investigations made for  $PTH_{25-37}$  and the P4 variant, we designed 11 novel  $PTH_{25-37}$ -derived peptides, wherein the amyloid-forming capabilities of the AMPB group in view of fibrillization were probed by placing the photoswitch at positions in the center of the peptide (P1–P6), at the N-terminal (P7–P9) or at the C-terminal part (P10–P12), with an amino acid either being exchanged by AMPB or AMPB being inserted between two amino acids (Table 1).

Our design strategy is based on the assumption that moving the AMPB group to the N-terminal side will enhance fibrillization by introducing the hydrophobic AMPB into the polar and charged N-terminal region, whereas moving it to the C-terminal side should impair amyloid formation by disrupting the amyloid-prone peptide region. In addition, we expect that the difference between the cis- and trans-forms of AMPB will become less important as it is shifted toward the termini, since hairpinning should no longer be possible in the cis-form. To refine these predictions, we performed MD simulations of the P1, P3, P8, and P12 variants, considering both the cis- and trans-configurations of each peptide as monomer and dimer (Figure 4A; P1 was also simulated as hexamer, see Figure S9). The simulations of P1 revealed a similar tendency for  $\beta$ -sheet formation as seen for P4 (Figure 2D), which makes sense given that AMPB is at the same position in both peptides, but instead of replacing V31 as in P4 it is added between D30 and V31, thereby extending the hydrophobic stretch on the Cterminal side of the peptide (Figure S10), which might lead to

a faster aggregation kinetics in the experiments. In P3, the AMPB group is shifted by one position toward the N-terminus compared to P4, replacing D30. This increases the hydrophobicity of the peptide in support of aggregation, while the removal of the negative charge increases the overall positive peptide charge, which could discourage aggregation. The simulations revealed that the increase in hydrophobicity prevails, as random dimerization with mainly intrapeptide instead of interpeptide  $\beta$ -sheets dominated in the simulations of trans-P3. P8 was simulated as a representative peptide in which AMPB is significantly shifted toward the N-terminus and inserted between K26 and K27. The electrostatic potential surface (Figure S10) shows that the insertion of the hydrophobic AMPB into the positively charged N-terminal region indeed significantly increases its hydrophobicity, promoting fibrillization. However, the secondary structure preferences are somewhat shifted away from  $\beta$ -sheet toward the formation of  $\alpha$ -helices in both *cis*- and *trans*-configurations and both as monomers and dimers, which was not seen for the P3 and P4 variants and may counteract amyloid fibrillization. Finally, we examined the P12 mutant in which the AMPB photoswitch is introduced into the aggregation-prone Cterminal region in the form of an exchange of V35. As predicted, the simulations confirm a drastic decrease in  $\beta$ -sheet formation compared to PTH<sub>25-37</sub> and the other simulated peptide designs. As with P8, where AMPB is placed at the Nterminal side, its C-terminal position in P12 also leads to the formation of  $\alpha$ -helices, which could also counteract amyloid aggregation.

Next, we investigated the influence of the AMPB site experimentally. The designed peptides displayed varying solubility in a buffered aqueous solution (50 mM Na<sub>2</sub>HPO<sub>4</sub>, pH 7.4), ranging from 370  $\mu$ M for P4 to 7  $\mu$ M for P10 (Table S2), thus limiting the assay-copnditions to those wherein sufficient critical concentrations could be reached. The critical concentration ( $c_{cr}$ ) of monomers in a fibril-forming system is the minimum concentration required to form fibrils in the dynamic equilibrium between the fibrils and the monomeric peptide form, which can be converted to a standard free energy of the fibril elongation reaction ( $\Delta G^0$ ). Since the  $c_{cr}$  of  $PTH_{25-37}$  is 42  $\mu M$  at the chosen conditions, we decided to exclude the peptides with lower solubility, also motivated by the observation that no fibrillization was observed in P3 and P5, due to their low solubility. The peptides with small  $c_{cr}$  are the ones in which the hydrophobicity in the otherwise rather polar and positively charged peptide region was increased (P3, P5, P6), or in which the already hydrophobic C-terminal region was made more hydrophobic by placing the AMPB there (P10, P11). The reduced solubility of P3 is consistent with our MD simulation prediction of random aggregation. For the remaining peptides (P1, P2, P7, P8, P9, and P12, in addition to P4), we determined the photophysical characteristics of the isomerization reaction, such as the half-life time  $t_{1/2}$  of the thermodynamically less favorable *cis*-isomer, which is influenced by the position of the azobenzene switch (Table 1). To ensure probing of the fibrillization kinetics, it is important that the stability of the cis-isomer is significantly larger than the lag time of the fibrillization process. As both process are competing we strived to minimize the rate of  $cis \rightarrow trans$ isomerization to primarily investigate the behavior of the cisisomer in the relevant time range. These half-life times range from 63 to 97 h, with the longest time observed for P4, where the central V31 was replaced by AMPB, and the shortest time, when the azo switch was shifted toward the C-terminus, replacing V35. The increased half-life time can be explained by the energy barrier for the  $cis \rightarrow trans$  isomerization in the ground state due to interaction between the residues at either side of the AMPB group (Figure 2G), which is also reflected in the cis:trans ratio. After synthesis, this ratio is between 3:97 and 6:94 for the freshly prepared peptides, subsequently increasing during the photo-induced trans  $\rightarrow$  cis isomerization to the photostationary state (PSS), reaching values of 90:10 to 82:18. Isomerization back under dark conditions reduces this ratio to 19:81 and 24:76 in the PSS of  $cis \rightarrow trans$  isomerization (Table S3). To exclude a photobleaching effect of the AMPB photoswitch, we repetitively conducted alternating  $trans \rightarrow$ cis and cis  $\rightarrow$  trans isomerizations over 5 cycles (Figure S11). When monitoring the absorption at two wavelengths (absorption maxima of trans- and cis-isomer, respectively) we did not observe a decline in the overall absorption, except for the first cycle, which can be explained by the fact that the initial peptides directly after synthesis possess an increased transcontent compared to the subsequent photostationary state. To assess the toxicity of the peptides with the incorporated photoswitch, we conducted cytotoxicity assays with the Nterminally modified P8, the centrally modified P4, and the Cterminally modified P12 (Figure S12), and we did not observe any toxicity toward 3T3 and NHDF cells.

We then examined the fibrillization process of the peptides using the ThT fluorescence assay after an established protocol for  $PTH_{1-84}^{20}$  (Figures S13–S20) and followed the formation of fibrils with TEM images after 20 min at 4 °C and after 1, 3,

24, and 96 h at 37 °C (Figures S21-27, original data for the photoswitching (TEM) for P4 are presented in Figure S23). The ThT fluorescence curves were fitted using eq. 1 and yielded the lag time  $t_{lag}$ , which corresponds to the onset of the fibril growth phase, and the characteristic time  $t_{char}$ , the point at which the fluorescence intensity reaches 50% of its maximum (Figures 4B, S13-20). Compared to  $PTH_{25-37}$ , the fluorescence intensity was significantly lower, resulting in a poorer signal-to-noise ratio. We attribute this to fluorescence quenching by the azobenzene moiety, which is an already known property of this molecular building block. 10 g,22 Nevertheless, a sigmoidal fibrillization curve is clearly visible for the three replicate measurements of each peptide. Peptides P1, P2, P4, P7, P8 and P9 show typical fibrillization behavior with lag phase, growth phase, and stationary phase (Table S4). This observation is consistent with our prediction that the placement of AMPB in the middle or at the N-terminus of PTH<sub>25-37</sub> should not prevent the amyloid aggregation ability of the peptide. All trans-peptides exhibited, irrespective of the positioning of the photoswitch, a faster fibrillization process than PTH<sub>25-37</sub> with significantly shortened lag phases ( $t_{lag}$  of 8 h for  $PTH_{25-37}$  vs 0-2 h for the peptide designs) and reduced  $t_{\rm char}$  (Figure 4B). We assume that the increased hydrophobicity and the organizing effect of the AMPB group are the driving forces for the increased tendency of amyloid aggregation. TEM images of the fibrils were obtained for all peptides after only 20 min at 4 °C (Figure 4C). The cis-forms of peptides P1, P2, and P4, in which AMPB was inserted at the central position next to the aggregation hot-spot sequence H32-L37, showed slower fibrillization compared to PTH<sub>25-37</sub>, whereby for cis-P1 and cis-P2 the fibrillization occurred in a similar time range, while the fibrillization of cis-P4 was strongly delayed. In agreement with our predictions, the incorporation of the photoswitch in its cisform at the N-terminal part had almost no influence on the fibrillization kinetics: cis-P7 and cis-P8 aggregated at a similar rate as PTH<sub>25-37</sub>, while the fibrillization of cis-P9 was even faster (due to the increased hydrophobicity of the peptide). The TEM images (Figures 4D, S21-27) confirm these observations. For the cis-isomers of P1 and P2, we mainly observed amorphous aggregates in the early images (after 20 min); the first objects, which could be clearly assigned to fibrillar aggregates, as with the trans-forms, were only detected after 24 h. For P4 (Figure S20) the difference was even more significant: in the cis-form, the first fibrillar aggregates were visible in the image only after 60 h. For the N-terminally modified peptides cis-P7, cis-P8, and cis-P9, however, fibrils were already visible after 20 min.

For the fibrillization behavior of the C-terminally modified P12, where V35 was replaced by AMPB, we found that it is entirely different. Unlike other peptides, ThT fluorescence curves for both *trans-* and *cis-*P12 show a linear increase after a lag phase of approximately 20 h, with no saturation observed even after 140 h, indicating reduced fibrillization. This also holds true for fibril morphologies, as both P12 isomers exhibit similar shorter fibrils in the TEM images, with *trans-*P12 forming fibril-like structures after 1 h and *cis-*P12 after 3 h.

In summary, our study revealed that the impact of the photoswitch varies depending on its placement: when positioned within the fibril-forming segment, such as in P12, fibril formation is significantly hindered, whereas outside this crucial region, the *trans*-isomers demonstrate faster fibril formation compared to  $PTH_{25-37}$ . Notably, *cis*-isomers display a strongly hindered fibril formation or the formation of

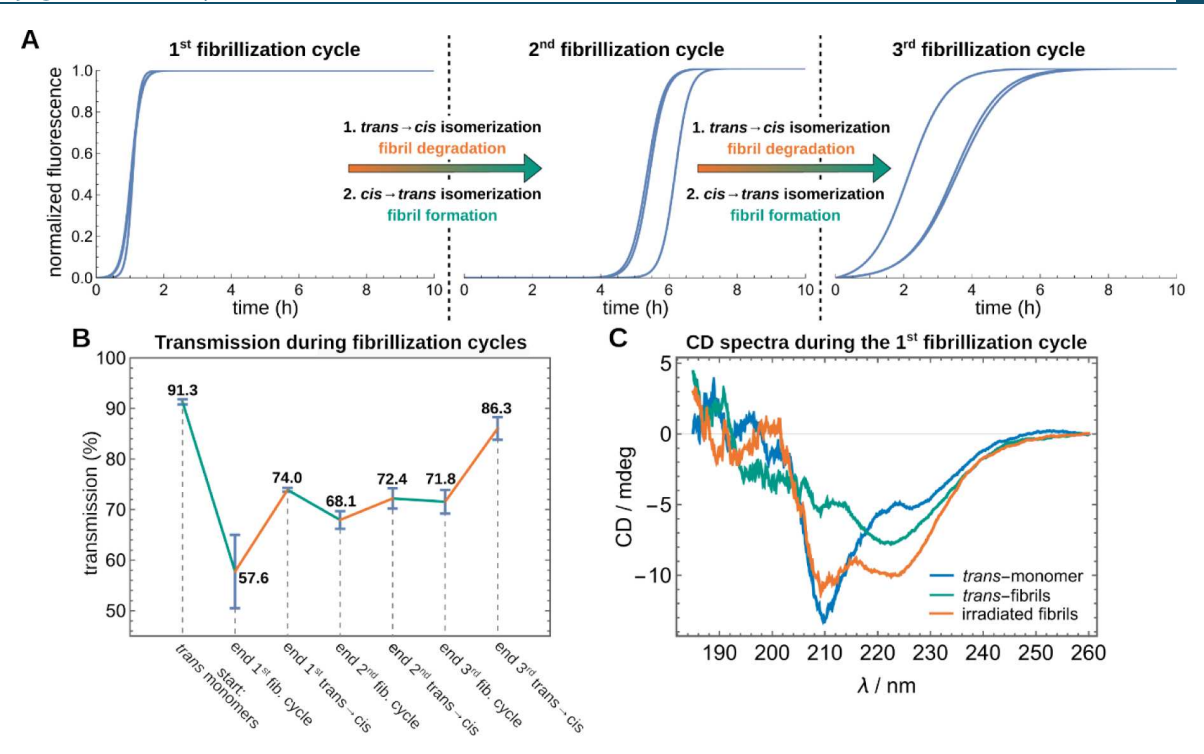


Figure 5. Multiple fibrillization and degradation cycles of *trans*-P4 fibrils through photoisomerization. (A) Fitted ThT signal monitored by the fluorescence assay of three fibrillization cycles of *trans*-P4 comprising degradation of fibrils by photoinduced  $trans \rightarrow cis$  isomerization and subsequent photoinduced  $cis \rightarrow trans$  isomerization leading to renewed fibrillization. (B) Change in the transmission of a P4 sample over several switching cycles (cyan for fibrillization periods and orange during  $trans \rightarrow cis$  isomerization). (C) CD spectra of monomeric trans-P4 (blue), trans-P4 fibrils (green), and the fibrils after  $trans \rightarrow cis$  isomerization via irradiation with 340 nm for 5 h (orange).

amorphous aggregates, with the inhibition decreasing as the distance from the fibril-forming C-terminal region increases.

Photocontrolled Multiple Switching of Fibril Formation. By computationally analyzing the primary structure, modeling the peptide structures in their monomeric and aggregated forms, and studying the fibrillation process of  $PTH_{25-37}$  and the designed peptides, we aimed to determine the most suitable position for the incorporation of the photoswitch into the peptide sequence to control fibril formation. Based on the results obtained, we applied several criteria to select the most promising candidate from the designed peptides (Table 1) to test whether amyloid formation can be reversibly switched on and off by light. After excluding peptides with insufficient solubility (P10 and P11) as well as the poorly aggregating P12, the focus was placed on the peptides P1, P2, and P4, which show accelerated fibrillization due to the central placement of the photoswitch in the transconformation, while the cis-form slows down fibrillization. Of these peptides, P4 exhibited both the best solubility and the largest difference in fibrillization for trans- and cis-P4. Therefore, we selected this peptide P4 to further test whether we could achieve reversible fibril formation (Figures 5, S19, \$28). It should be noted that during the following sequence of experiments, the cuvettes were not changed; moreover, also no new peptides were added to the solution. Starting from the trans-isomer of P4, fibrils were formed in the first cycle at 37 °C in phosphate buffered aqueous solution and the aggregation kinetics followed via ThT fluorescence (Figure 5A, left). After the fibrillization passed over to the stationary phase, the solution was shaken another 20 h to affirm that the equilibrium has been established. Subsequently, the suspension was irradiated at a wavelength of 340 nm for 5 h under stirring,

after which UV/vis spectroscopy was used to verify that the cisphotostationary state of P4 was reached. Now, the solution was irradiated for 20 min with light of 405 nm wavelength to switch the cis-PSS to the trans-PSS to produce monomeric transpeptides, which underwent another fibrillization cycle (Figure 5A, middle). The newly formed fibrils were again exposed to the photoisomerization treatment involving  $trans \rightarrow cis$ isomerization to degradate the fibrils. The ThT-monitored fibrillization assay was repeated with a portion of the solution, and fibril formation was observed for a third time (Figure 5A, right). For the second and the third fibrillization cycle, a decreased starting concentration of the trans-isomer was observed (UV/vis spectra, Figure S29). As we could already exclude photobleaching, we suppose that aggregates adhere to the wall of the 96-well plates and are, therefore, not available for further fibrillization cycles. The fibrils formed during the fibrillization process can precipitate and thus disturb the measurement via scattering effects, causing noise in the signal after the first stationary phase. Because the trans  $\rightarrow$  cis isomerization of the AMPB-switch is not reaching 100% due to the photostationary state, there certainly are fibrillar aggregates present in the solution, which, however, may interfere in the subsequent fibrillization processes and thus change the following fibrillation kinetics. Nonetheless, for each new fibrillization process monitored here, a lag phase, growth phase, and stationary phase were observed.

While monomers remain soluble, fibrils tend to precipitate, causing the solution to become turbid during the fibrillization assay and leading to a decrease in transmission. Observing the transmission across three switching cycles, it was evident that transmission decreases during the fibrillization process (Figure 5B, cyan lines). Degradation of the fibrils via  $trans \rightarrow cis$ 

isomerization, however, led to an increase in transmission, as released monomers dissolve back into the solution (Figure 5 B. orange lines). The incomplete recovery of the transmission during degradation results from the aforementioned observation that the  $trans \rightarrow cis$  isomerization only leads to a maximum trans:cis ratio of 18:82. Therefore, the degradation process of the fibrils is an only partial one, presumably as a full isomerization cannot be reached. The changes in secondary structure during fibrillization were probed by CD spectroscopy (Figures 5C, S28). In its monomeric form, trans-P4 displays a shoulder around 220-230 nm and a minimum around 210 nm. In the CD spectrum of the trans-P4 fibrils, a minimum is observable between 220 and 230 nm, while the minimum around 210 nm is nearly completely absent. Degradation of the fibrils by the *trans*  $\rightarrow$  *cis* isomerization leads to a CD spectrum where the minimum around 210 nm reappeared and the other minimum between 220 and 230 nm still exists. The minimum at 210 nm arises from the monomeric peptides, while the minimum between 220 and 230 nm is indicative for the fibril form. The observed CD spectrum is thus a superposition of both forms, the monomeric and the fibrillated form. From the CD spectra, we can, therefore, conclude that fibrillization from the trans-form and incomplete fibril degradation during trans → *cis* isomerization can be observed.

Fibrillization of proteins are complex, often irreversible processes, which are characterized by a strong thermodynamic negative free energy, as e.g., in  ${\rm A}\beta$  fibrillization, and thus conventionally termed as "irreversible." This is often connected with a high kinetic barrier, usually preceding the fibrillization process, wherein nucleation is central to initiate that nucleation process. The PTH peptides studied here are "more reversibly" fibrillating peptides, wherein the thermodynamic stabilization of the amyloid state is less and, therefore, also the kinetic barriers. 15,59 Nonetheless, until now, it has not been possible to control the reversibility of this process, as accomplished here via the introduction of a photoswitch. However, in contrast to other reversibly (photo)-switchable systems, such as reported for small molecule assemblies,<sup>6</sup> adhesives, 61 or photoswitchable enzymes, 62 a full reversion of the aggregation of the current system is not reached, as expected, as the fibrillization and defibrillization processes depend on many factors, such as the kinetic barriers in either direction, the kind and number of nuclei present during the different switching cycles, or also the precipitation of fibrils.

#### CONCLUSION

In this study, we have demonstrated precise control over reversible peptide fibrillization by strategically positioning a photoswitch within the central region of a fibril-forming peptide. Utilizing the artificial light switch 3-{[(4aminomethyl)phenyl]diazenyl}benzoic acid (AMPB) embedded in a peptide containing residues 25-37 of the parathyroid hormone (PTH), we investigated the impact of position on peptide aggregation. Through a comprehensive approach involving computational modeling, peptide synthesis, aggregation assays, and structural analyses, we elucidated key features governing the fibrillization of both unmodified and modified PTH<sub>25-37</sub> peptides. Notably, the trans-peptides with the modification positioned adjacent to the fibril-forming region in the center of the peptide (P1, P2, and P4) displayed enhanced fibrillization compared to unmodified PTH<sub>25-37</sub>, while the aggregation is slowed down for their cis-isomers. Peptides featuring the photoswitch in the nonamyloidogenic

N-terminal region behaved similarly to unmodified PTH<sub>25-37</sub> (P7, P8, and P9), whereas peptide P12, where the azobenzene unit replaced V35 in the amyloid-prone region, showed decreased fibrillization, largely unaffected by the photoswitch's isomer state. Our bioinformatics and simulation analysis uncovered that modification with AMPB typically boosts the peptides' hydrophobicity, thereby augmenting their tendency to aggregate. Furthermore, AMPB facilitates self-interaction among peptides through  $\pi - \pi$  interactions, further enhancing their aggregation propensity. Structural investigations of P4 employing WAXS and ssNMR suggest that  $\beta$ -strands in amyloid fibrils of P4 are—in contrast to fibrils of unmodified PTH<sub>25-37</sub>— aligned antiparallel. Simulations suggest that AMPB might not fully adhere to the amyloid fold, owing to the distinct demands for interpeptide distances in  $\pi - \pi$ interactions and fibril formation. This elucidates the diminished fibrillization observed when the photoswitch is positioned within the amyloid-forming segment of the peptide, as seen in P12. Importantly, our results showcase the potential of strategically placing the azo photoswitch, particularly exemplified by peptide P4, to control reversible amyloid aggregation. The phototriggered degradation of fibrils formed in the trans-state of AMPB enables repeated fibril formation, which in fact may allow to reversibly modulate the fibrillization of the PTH hormone, with the monomeric peptides released upon fibril degradation serving as the active form and the fibrillar structures acting as an inert peptide reservoir. Given the peptides' nontoxic nature (Figure S12), this light-triggered approach, therefore, presents a promising method for controlled drug delivery and release of such reversibly fibrillating peptides. We regard our system here as a switchable fibrillization system, where a phototrigger from the outside is able to induce fibrillization, as e.g., needed in many modern neuro-cellbiology systems.6

#### ■ EXPERIMENTAL SECTION

**Materials.** All technical solvents were distilled prior use; air- and moisture-sensitive reactions were carried out in flamedried glassware under atmospheric pressure of nitrogen. 2-(6-Chloro-1-H-benzotriazole-1-yl)-1,1,3,3-tetramethylaminium hexafluorophosphate (HCTU), N-methyl-morpholine (NMM), N,N-dicyclohexylcarbodiimide (DIC), N-Hydroxybenzotriazole (HOBT), trifluoroacetic acid, 4-amino-benzylamine, and oxone were purchased from Sigma-Aldrich. 9-Fluorenylmethyl-N-succinimidylcarbonat (Fmoc-OSu) was received from Fluorochem. 3-Aminobenzoic acid was purchased from Merck and was used without further purification.

UV/Vis, CD, and Transmission Spectroscopy Measurements. UV/vis-absorbance spectroscopy was measured on a JASCO V-660 absorbance spectrometer in a 1 cm quartz glass cuvette. For  $PTH_{25-37}$ , the absorbance was measured at 205 nm with a molar extinction coefficient of 49.310 cm<sup>-1</sup>  $M^{-1}$ ; trans-azobenzene containing peptides were measured at 327 nm with a molar extinction coefficient of 13.000 cm<sup>-1</sup>  $M^{-1}$ . CD spectroscopy was measured with a JASCO J-1500 CD Spectrometer in either a 1 mm. As buffered solution, a 50 mM aqueous  $Na_2HPO_4$  buffer solution was used with a pH value adjusted to 7.4. Transmission was measured with a Litesizer DLS 500 from Anton Paar using a 3 mm  $\times$  3 mm quartz glass cuvette. The irradiation wavelength was 658 nm. The equilibration time was 1 min, and the measurement time was 10 s. The temperature was maintained at 25 °C.

Peptide Synthesis. The 3,4'-AMPB photoswitch was synthesized in two steps according to our published procedure.<sup>22</sup> Solid-phase peptide synthesis was utilized on an automated peptide synthesizer MultiPep RS (Intavis AG, Koeln, Germany) using standard Fmoc-chemistry and preloaded resins. Standard coupling of all protected natural amino acids was performed as single couplings in dimethylformamid (DMF) using 5 equiv of amino acids, HCTU as coupling reagents, and 10 equiv of NMM as base for 1 h at room temperature. Special building groups, such as Fmoc-3,4'-AMPB, were coupled with 3 equiv using DIC and HOBT in DMF/ N-methyl-2-pyrrolidone (NMP) at room temperature and with gentle shaking in the dark overnight. The N-terminal Fmoc protecting group was removed by washing the resin with 20% piperidine for 20 min. The final side chain deprotection and cleavage from the resin employed a mixture of trifluoroacetic acid and water (90:10 Vol%) with gentle agitation for 2 h at room temperature. The crude peptides were purified to >95% purity using preparative RP-HPLC (Gilson, Limburg, Germany). For both analytical and preparative use, the mobile phase was a mixture of water (eluent A) and acetonitrile (eluent B), respectively, each containing 0.1% trifluoroacetic acid. Samples were eluted with a linear gradient from 5% B to 95% B in 15 min for analytical runs and in 90 min for preparative runs on a semipreparative PLRP-S column (Agilent Technologies, 300 × 25 mm, 8 um). Finally, all peptides were characterized by analytical HPLC Dionex Ultimate 3000 (Thermo Scientific, Germany) using a PLRP-S column (Agilent Technologies, 150 × 4.6 mm, 3 um) and MALDI-MS (Bruker Microflex LT, Bremen, Germany), which gave the expected [M + H]<sup>+</sup> mass peaks. The full molecular characterizations are shown for all peptides in Figures S30-

Aggregation Kinetics. The fibrillization process was investigated using a thioflavin T (ThT) monitored fluorescence assay following the established process for PTH<sub>1-84</sub>.<sup>20</sup> Therefore, the fluorescence intensity of ThT was measured. Lyophilized peptides were dissolved in buffered solution and kept on ice for the next steps. The sample solutions were centrifuged at 13 000 rpm for 10 s, and the concentration of the respective peptide was determined using UV/visabsorbance spectroscopy. If required, the cis-isomer of the azobenzene containing peptides was produced as described below. The sample solutions were centrifuged at 10 000 rpm for 1 h at 4 °C, and the supernatant was transferred to another tube. The solutions were diluted with buffer, and ThT was added as a 1 mM stock solution to obtain a final concentration of 100  $\mu$ M for the peptides, with a solubility above 100  $\mu$ M, and 50  $\mu$ M for ThT. For the other peptides, the solutions were solely diluted with the ThT stock solution, to achieve the highest possible concentration. For each sample, a total volume of 480  $\mu$ L was prepared, and three aliquots with 150  $\mu$ L were transferred to a medium binding 96-well plate (GREINER Bio-One 675 076). The plate was sealed with a microplate cover, and the fluorescence intensity was monitored at 37 °C using a BMG FLUOStar Omega multimode plate reader using fluorescence excitation and emission wavelengths at 460 and 485 nm, respectively. One measurement cycle lasted 5 min, consisting of double-orbital shaking for 150 s and incubating for 150 s. To describe the fibrillization process, the source data were fitted. As the description of fibrillar growth in terms of the molecular rate, kinetic can be considered as two main fibrillation processes.<sup>37</sup> Their contributions to the increase in

fluorescence  $\Delta F(t)$  can be analyzed by a function, which was derived by Dear et al.<sup>38</sup> and has been used to characterize the fibrillation kinetics of full-length PTH.<sup>20</sup>

$$\Delta F(t) = \left(1 - \frac{1}{\frac{\kappa^3}{\lambda^3} (e^{\kappa t} - 1) + 1}\right) \Delta F_{\text{pl}}$$
(1)

 $\Delta F_{\rm pl}$  corresponds to the plateau value of the fluorescence in the stationary phase, while  $\lambda$  and  $\kappa$  are the rate constants of the primary and secondary nucleation processes.

Determination of the Solubility Parameters. To determine the maximal solubility of a peptide, small amounts (0.5 mg) of the respective peptide were added to 1 mL of buffered solution and shacked for 10 s until an insoluble precipitate was visible. The suspensions were centrifuged at 10 000 rpm for 1 h at 4 °C, and the supernatant was transferred to another tube. The remaining monomer concentration was determined using UV/vis-absorbance spectroscopy. To determine the critical concentration  $c_{cr}$ , two samples were prepared for each peptide according to the procedure for the ThT monitored fibrillization assay, one with ThT as a reference sample and the other one without ThT. Twenty hours after the reference sample reached the stationary phase, the fibril containing solutions from the sample without ThT were transferred to a tube and centrifuged at 10 000 rpm for 1 h at room temperature. The supernatant was transferred to another tube, and the concentration of the remaining monomers was determined using UV/vis-absorbance spectroscopy at 278 nm with a molar extinction coefficient of 3750 cm<sup>-1</sup> M<sup>-1</sup> for the azobenzene containing peptides and at 205 nm with a molar extinction coefficient of 49 310 cm<sup>-1</sup> M<sup>-1</sup> for

**Photosiomerization.** The photoisomerization of the *trans*-azobenzene moiety in the peptides was performed by irradiating the dissolved peptides in a 1 cm quartz cuvette for 30 min with light of 340 nm wavelength using a 69.2 mW LED (Thorlabs, M340L5) equipped with a controller (Thorlabs, LEDD1B). The photoisomerization of the *cis*-azobenzene moiety in the peptides was performed by irradiating the dissolved peptides in a 1 cm quartz cuvette for 30 min with light of 405 nm wavelength using a 1.4 W LED (Thorlabs, M405L4) equipped with a controller (Thorlabs, LEDD1B).

**Photobleaching.** To test whether photobleaching occurs during the photoisomerization, a solution of 50  $\mu$ M P4 was irradiated alternatingly for 30 min with light of 340 nm wavelength ( $trans \rightarrow cis$  isomerization) and light of 405 nm wavelength ( $cis \rightarrow trans$  isomerization). The absorption was measured after each isomerization step at two wavelengths: 295 nm (absorption maximum of the cis-isomer) and 327 nm (absorption maximum of the trans-isomer).

**Transmission Electron Microscopy.** TEM images were taken with an electron microscope (EM 900; Zeiss) at 80 kV acceleration voltage. For preparation, 5  $\mu$ L of the peptide solution were added on Formvar/Cu grids (mesh 200). After 3 min of incubation, the grids were gently rinsed two times with water and then negatively stained using uranyl acetate (1%, w/ v) for one minute.

**Fibril Degradation.** To investigate the fibril degradation through photoisomerization, 3 mL of a 100  $\mu$ M trans-P4 in buffer was prepared according to the procedure for the ThT monitored fibrillization assay, except that ThT was excluded,

and aliquots of 150  $\mu$ L were transferred to a medium binding 96-well plate. As a reference sample, 480  $\mu$ L of a 100  $\mu$ M trans-P4 in buffer was prepared with ThT, and both approaches were incubated as described for the ThT monitored fibrillization assay. Twenty hours after the reference sample reached the stationary, the fibril containing solutions of the sample without ThT were collected in one tube. UV/vis-absorbance and CD were measured, and the fibril solution was transferred in a 1 cm quartz glass cuvette and treated according to the procedure for the *trans*  $\rightarrow$  *cis* isomerization, except that the irradiation time was prolonged to 5 h. Again UV/vis-absorbance and CD were measured. Subsequently, the cis-isomer was photoisomerized back to the trans-form. 456  $\mu$ L of the solution was mixed with 24 µL of a 1 mM ThT stock solution and transferred as 150  $\mu$ M aliquots to a medium binding 96-well plate for a ThT monitored fibrillization assay. The remaining solution was transferred as well in 150  $\mu$ L aliquots to the 96-well plate and incubated under the same conditions. This procedure was repeated for every degradation cycle.

Solid-State NMR Spectroscopy. For the solid-state NMR spectroscopy, 6 mL of a 100  $\mu$ M solution of the respective peptides (PTH<sub>25-37</sub> and P4 with uniformly <sup>15</sup>N/<sup>13</sup>C labeled residues L28 and F34) was prepared according to the procedure for the ThT monitored fibrillization assay and transferred in 150 µL aliquots to a medium binding 96-well plate. Twenty hours after the stationary phase was reached, the fibril containing solutions were collected in a tube and centrifuged at 60 000 rpm for 15 min at 10 °C. The supernatant was discarded, the remaining fibril pellet was frozen with liquid nitrogen, and the residual water was removed using lyophilization. The lyophilized peptides were packed into Bruker MAS rotors with outer diameters of 3.2 mm (PTH $_{25-37}$ ) and 1.9 mm (P4), respectively. Solid-state NMR experiments were conducted on an 18.8 T (800 MHz <sup>1</sup>H frequency) Bruker Avance III spectrometer equipped with a triple resonance HCN 3.2 mm MAS Efree probe and a 1.9 mm triple resonance probe. For determination of intermolecular long-range contacts between L28 and F34 resonances, protondriven spin diffusion (PDSD) experiments with an MAS frequency of 20 kHz close to the rotational resonance condition between aromatic 13C resonances of F34 and aliphatic  $C_{\nu}$  / $C_{\delta}$  resonances of L28 were recorded with mixing times ranging from 50 ms to 1 s. For PTH<sub>25-37</sub>, additional PDSD and DQSQ spectra were recorded on a 14.1 T (600 MHz <sup>1</sup>H frequency) Bruker Avance wide bore spectrometer equipped with a with a 3.2 mm MAS triple resonance <sup>1</sup>H, <sup>13</sup>C, <sup>15</sup>N probe. Typical radiofrequency field strengths were 91–100 kHz for <sup>1</sup>H, and 55.6 kHz for <sup>13</sup>C Spinal64 <sup>1</sup>H decoupling <sup>39</sup> (rf field of 85 kHz) was applied during 13C evolution and acquisition. The VT gas temperature was set to 263 K (thermocouple reported temperature); the sample temperature was estimated to be around 10-20 K higher due to frictional heating under MAS.

**WAXS Measurements.** The WAXS measurements were performed in transmission mode with a SAXSLAB laboratory setup (Retro-F) equipped with an AXO microfocus X-ray source. As a monochromator, the AXO multilayer X-ray optic (AXO Dresden GmBH, Dresden, Germany) was used for Cu–K $\alpha$  ( $\lambda$  = 0.154 nm). The two-dimensional scattering patterns were recorded with a two-dimensional detector (PILATUS3 R 300 K, DECTRIS, Baden, Switzerland). The preformed fibrils were prepared as described for the measurement of the aggregation kinetics in a total volume of 1 mL. Twenty hours

after the fibrillization reached the stationary phase, the fibril suspension was ultracentrifugated at 60.000 g for 15 min, and the obtained pellet was transferred into a glass capillary and dried overnight. The scattering measurements were performed at room temperature in vacuum and corrected for background.

**Cytotoxicity Tests.** Cell viability was determined for *trans*-P4, trans-P8, and trans-P12 on NHDF as well as 3T3 fibroblasts with a resazurin reduction assay. Briefly, cells were seeded at desired cell densities in corresponding culture media supplemented with 10% FCS and penicillin/streptomycin in 96-well plates on day 0 and incubated overnight under standard cell culture conditions. On day 1, serial dilutions of the peptides in cell culture media were prepared. Then, medium (background and negative control-100% viability), TritonX in medium f.c. 0.025% (postive control-0% viability), and the peptide dilutions were added with one treatment per column (n = 8). Incubation for 24 h or 96 h under standard cell culture conditions followed. On day of measurement, resazurin stock solution was added to a final concentration of 44 µM into each well. After 2 h incubation, the resorufin fluorescence was measured with a Cytation 5 plate reader system. Means and standard deviation of each column were calculated. Experiments were repeated independently 3 times, and average values were evaluated (see Figure S12).

MD Simulations. For all MD simulations of the  $PTH_{25-37}$ peptide, as well as the mutants P1, P3, P4, P8, and P12, we used the GROMACS simulation package. 40 Since the PTH<sub>25-37</sub> sequence classifies as an intrinsically disordered protein (IDP), we have used the CHARMM36m force field<sup>41</sup> to model protein interaction, which has previously been shown to be a suitable choice for IDPs. 42 For the azobenzene photoswitch (denoted AZO in our force field implementation), we parametrized the interactions following the cgenff standard protocol<sup>43</sup> and refined the parametrization using data from QM/MM simulations, 44 by fitting our parameters to reproduce the bond, angle, and dihedral angle distributions of the cis- and trans-state as obtained from QM/MM. The resulting force field parameters are available at https://github. com/strodel-group/Charmm36m\_Azobenzene-FF. During the MD simulations of the modified PTH<sub>25-37</sub> peptides, the ∠CNNC dihedral angle was restricted to either the cis- or trans-states; thus, transitions between the two states of the AMPB photoswitch were not modeled. The MD simulations of all systems were prepared following the same protocol: first, the peptide(s) were placed in the simulation box, where in case of the dimer and hexamer simulations, the box size was always chosen to achieve a peptide concentration of 10 mM. Then, the box was filled with TIP3P water molecules, 45 as well as Na+ and Cl ions to neutralize the system and achieve a physiological salt concentration of 150 mM. After equilibration of the systems, a production run of 10  $\mu$ s per system (1  $\mu$ s for the fibril models) was carried out under NpT conditions at constant number of particles N, pressure p = 1, bar and temperature T = 300 K. The pressure and temperature were regulated using the Parrinello-Rahman pressure coupling scheme<sup>46</sup> and Nosé-Hoover thermostat,<sup>47</sup> respectively. To exclude edge effects, periodic boundary conditions in all directions were applied, and the particle-mesh Ewald method<sup>48</sup> was used to calculate electrostatic interactions. For the calculation of van der Waals and Coulomb interaction in real space, a cutoff of 12 Å was applied. An overview over all simulations performed is given in Table S1, yielding 285  $\mu$ s of total simulation time across all systems. All MD simulations

were run on the high-performance cluster JURECA-DC.<sup>49</sup> Analysis of the MD data was performed with python using the MDAnalysis<sup>50</sup> package for reading of the MD trajectory and the calculation of distances between groups of atoms, while the MDTraj<sup>51</sup> package was used for secondary structure analysis. For visualization of the MD structures, the PyMOL<sup>52</sup> software was used. Additionally, PyMOL in combination with the APBS<sup>53</sup> plugin was used for the calculation and visualization of electrostatic potential surfaces.

QM Calculations. The photoswitching mechanism of AMPB integrated into PTH<sub>25-37</sub> was monitored in the ground and excited states along the ∠CNNC dihedral angle for the cis ↔ trans-transition of the azobenzene photoswitch. As a starting point for the QM calculations, we constructed pathways from cis to trans and vice versa, using MD simulations. To consider the structural ensemble along the pathway, we simulated 40 cis  $\leftrightarrow$  trans switching trajectories. We started the switching from equilibrated cis- and trans-P4 structures obtained from equidistant time steps of 250 ns from the 10  $\mu$ s MD simulations. The switching in the MD simulations was achieved by imposing a restraining potential on the ∠CNNC dihedral angle and changing it every 2 ns in increments of  $10^{\circ}$  between  $0^{\circ}$  and  $180^{\circ}$ . All other MD simulation parameters were the same as described above. The resulting trajectories were used as input for the subsequent QM calculations. The QM calculations were conducted using the ONIOM-based QM/QM2 method, 30 with NEVPT2(2,2)/ def2-TZVP31,54 for QM and xTB232 for QM2, as implemented in the ORCA program package.<sup>55</sup> The QM region was focused on the azobenzene core, including the peptide in  $\pi$ -conjugation with it. The solvent was implicitly modeled using the ALPB method.<sup>56</sup> Due to convergence issues, analysis was limited to 34 of the original 40 trajectories. For these paths, the energies of electronic states  $S_0$ ,  $S_1$ , and  $T_1$  were interpolated to obtain potential energy curves using Gaussian process regression from the scikit-learn package.<sup>57</sup> Some of the paths that have an energy barrier at dihedral angles around 170° were analyzed at the structural level. To this end, the inter-residue distances based on the centers of mass of the residues were calculated for all structures exhibiting a dihedral angle near 170° and then analyzed through dimensionality reduction via principal component analysis (PCA). The first three principal components were transferred back into the original distance matrix format and illustrated with three representative distance matrices from the corresponding cluster of structures. Representative structures for the distance matrices were also extracted and visualized.

#### ASSOCIATED CONTENT

#### Supporting Information

The Supporting Information is available free of charge at https://pubs.acs.org/doi/10.1021/acs.bioconjchem.4c00188.

**Supplementary figures** S1, QM potential energy curves for 34 *cis*  $\leftrightarrow$  *trans* isomerization paths; S2, fluorescence lifetime measurements; S3, PCA analysis of selected P4 structures; S4, principal components projected onto inter-residue distance space; S5, selected P4 snapshots; S6, WAXS data of P4 and PTH<sub>25−37</sub>, S7 ssNMR data for PTH<sub>25−37</sub> fibrils; S8, ssNMR data for *trans*-P4 fibrils; S9, summary of all MD simulation results; S10, electrostatic potential surface of PTH<sub>25−37</sub> and selected peptides; S11, absorption data to exclude photobleaching; S12,

cell viability assay of *trans*-P4, *trans*-P8, and *trans*-P12; S13–S20, ThT fluorescence data; S21–S27, TEM images of fibrils; S28, CD spectra during reversible fibrillization of P4; S29, UV–vis spectra of *trans*-P4 before each fibrillization cycle; S30–S47, <sup>1</sup>H NMR, HPLC traces, and MALDI data of the peptides P1–P12. **Supplementary tables** S1, list of all MD simulations performed; S2, sequence of PTH<sub>25–37</sub> and P1–P12 and their respective solubility; S3, photophysical properties of peptides; S4: fibrillization parameters of peptides (PDF)

#### AUTHOR INFORMATION

#### **Corresponding Authors**

Birgit Strodel — Institute of Theoretical and Computational Chemistry, Heinrich Heine University Düsseldorf, Düsseldorf 40225, Germany; Institute of Biological Information Processing, Structural Biochemistry (IBI-7), Forschungszentrum Jülich, Jülich 52425, Germany; orcid.org/0000-0002-8734-7765; Email: b.strodel@fz-juelich.de

Wolfgang H. Binder – Macromolecular Chemistry, Institute of Chemistry, Faculty of Natural Science II, Martin Luther University Halle Wittenberg, Halle 06120, Germany;
ocid.org/0000-0003-3834-5445;

Email: wolfgang.binder@chemie.uni-halle.de

#### **Authors**

André Paschold – Macromolecular Chemistry, Institute of Chemistry, Faculty of Natural Science II, Martin Luther University Halle Wittenberg, Halle 06120, Germany

Moritz Schäffler – Institute of Theoretical and Computational Chemistry, Heinrich Heine University Düsseldorf, Düsseldorf 40225, Germany; Institute of Biological Information Processing, Structural Biochemistry (IBI-7), Forschungszentrum Jülich, Jülich 52425, Germany

Xincheng Miao – Center for Nanosystems Chemistry (CNC), Theodor-Boveri Weg, Universität Würzburg, Würzburg 97074, Germany

Luis Gardon – Institute of Biological Information Processing, Structural Biochemistry (IBI-7), Forschungszentrum Jülich, Jülich 52425, Germany; Institut für Physikalische Biologie, Heinrich-Heine-Universität Düsseldorf, 40225 Düsseldorf, Germany

Stephanie Krüger – Biozentrum, Martin Luther University Halle-Wittenberg, Halle 06120, Germany

Henrike Heise – Institute of Biological Information Processing, Structural Biochemistry (IBI-7), Forschungszentrum Jülich, Jülich 52425, Germany; Institut für Physikalische Biologie, Heinrich-Heine-Universität Düsseldorf, 40225 Düsseldorf, Germany; orcid.org/0000-0002-9081-3894

Merle I. S. Röhr — Center for Nanosystems Chemistry (CNC), Theodor-Boveri Weg, Universität Würzburg, Würzburg 97074, Germany; © orcid.org/0000-0002-2128-3498

Maria Ott — Institute of Biophysics, Faculty of Natural Science I, Martin Luther University Halle-Wittenberg, Halle 06120, Germany; orcid.org/0000-0002-4686-9516

Complete contact information is available at: https://pubs.acs.org/10.1021/acs.bioconjchem.4c00188

### **Author Contributions**

OA.P. and M.S. contributed equally

#### Notes

The authors declare no competing financial interest.

#### ACKNOWLEDGMENTS

WHB thanks the DFG project INST 271/444-1 FUGG for financial support; the DFG-Project BI1337/16-1; BI 1337/14-1 and the GRK 2670, W69000789, ProjectNr 436494874. MISR acknowledges funding by the Bavarian State Initiative "Solar Technologies Go Hybrid." MS and BS gratefully acknowledge computing time on the supercomputer JURECA at Forschungszentrum Jülich under grant no. IDP. H.H. and L.G. thank the DFG (INST 208/771-1 FUGG) for financial support. Access to the Jülich-Düsseldorf Biomolecular NMR Center jointly run by Forschungszentrum Jülich and HHU is acknowledged. We thank Dr. Sven Rothemund, from the Core Unit Peptide-Technologies of University Leipzig, for synthesizing the peptides and Julia Kollan and Dr. Henrike Lucas from the AG Mäder, Department of Pharmaceutical Technology at the Martin Luther University Halle-Wittenberg, for conducting the toxicological studies.

#### ABBREVIATIONS

AMPB, 3-{[(4-aminomethyl)phenyl]diazenyl}benzoic acid; CD, circular dichroism; MD, molecular dynamics; NMR, nuclear magnetic resonance; PSS, photostationary state; PTH, parathyroid hormone; ssNMR, solid state nuclear magnetic resonance; TEM, transmission electron microscopy; ThT, thioflavin T; UV/vis, ultraviolet/visible; WAXS, wide-angle X-ray scattering

#### REFERENCES

- (1) Li, D.; Liu, C. Conformational strains of pathogenic amyloid proteins in neurodegenerative diseases. Nat. Rev. Neurosci. 2022, 23 (9), 523-534. (b) Alberstein, R. G.; Guo, A. B.; Kortemme, T. Design principles of protein switches. Curr. Opin. Struct. Biol. 2022, 72, 71-78. (c) Adamson, H.; Jeuken, L. J. Engineering protein switches for rapid diagnostic tests. ACS Sens. 2020, 5 (10), 3001-3012. (d) Wang, H.; Feng, Z.; Xu, B. Assemblies of peptides in a complex environment and their applications. Angew. Chem., Int. Ed. 2019, 131 (31), 10532-10541. (e) Bierlmeier, J.; Álvaro-Benito, M.; Scheffler, M.; Sturm, K.; Rehkopf, L.; Freund, C.; Schwarzer, D. Sortase-Mediated Multi-Fragment Assemblies by Ligation Site Switching. Angew. Chem., Int. Ed. 2022, 61 (5), No. e202109032. (f) Shen, Y.; Wang, Y.; Hamley, I. W.; Qi, W.; Su, R.; He, Z. Chiral self-assembly of peptides: Toward the design of supramolecular polymers with enhanced chemical and biological functions. Prog. Polym. Sci. 2021, 123, 101469.
- (2) Li, Q.; Zhang, G.; Wu, Y.; Wang, Y.; Liang, Y.; Yang, X.; Qi, W.; Su, R.; He, Z. Control of peptide hydrogel formation and stability via heating treatment. *J. Colloid Interface Sci.* **2021**, *583*, 234–242. (b) Trzebicka, B.; Szweda, R.; Kosowski, D.; Szweda, D.; Otulakowski, Ł.; Haladjova, E.; Dworak, A. Thermoresponsive polymer-peptide/protein conjugates. *Prog. Polym. Sci.* **2017**, *68*, 35–76. (c) Hamley, I. W.; Dehsorkhi, A.; Castelletto, V.; Furzeland, S.; Atkins, D.; Seitsonen, J.; Ruokolainen, J. Reversible helical unwinding transition of a self-assembling peptide amphiphile. *Soft Mater.* **2013**, 9 (39), 9290–9293.
- (3) Gontsarik, M.; Yaghmur, A.; Ren, Q.; Maniura-Weber, K.; Salentinig, S. From structure to function: pH-switchable antimicrobial nano-self-assemblies. ACS Appl. Mater. Interfaces 2019, 11 (3), 2821–2829. (b) Chen, H.; Cheng, J.; Cai, X.; Han, J.; Chen, X.; You, L.; Xiong, C.; Wang, S. pH-switchable antimicrobial supramolecular hydrogels for synergistically eliminating biofilm and promoting wound healing. ACS Appl. Mater. Interfaces 2022, 14 (16), 18120–18132.
- (4) Fu, Y.; Xiao, K.; Zhang, X.; Du, C.; Chen, J. Peptide cleavage-mediated and environmentally friendly photocurrent polarity switch-

- ing system for prostate-specific antigen assay. Anal. Chem. 2021, 93 (2), 1076-1083.
- (5) Szymański, W.; Beierle, J. M.; Kistemaker, H. A.; Velema, W. A.; Feringa, B. L. Reversible photocontrol of biological systems by the incorporation of molecular photoswitches. *Chem. Rev.* **2013**, *113* (8), 6114–6178.
- (6) Liu, X.; Ramirez, S.; Pang, P. T.; Puryear, C. B.; Govindarajan, A.; Deisseroth, K.; Tonegawa, S. Optogenetic stimulation of a hippocampal engram activates fear memory recall. *Nature* **2012**, 484 (7394), 381–385. (b) Banghart, M.; Borges, K.; Isacoff, E.; Trauner, D.; Kramer, R. H. Light-activated ion channels for remote control of neuronal firing. *Nat. Neurosci.* **2004**, 7 (12), 1381–1386. (c) Hull, K.; Morstein, J.; Trauner, D. In Vivo Photopharmacology. *Chem. Rev.* **2018**, *118* (21), 10710–10747. (d) Peddie, V.; Abell, A. D. Photocontrol of Peptide Secondary Structure through Non-Azobenzene Photoswitches. *J. Photochem. Photobiol.*, *C* **2019**, 40, 1–20.
- (7) DuBay, K. H.; Iwan, K.; Osorio-Planes, L.; Geissler, P. L.; Groll, M.; Trauner, D.; Broichhagen, J. A predictive approach for the optical control of carbonic anhydrase II activity. *ACS Chem. Biol.* **2018**, *13* (3), 793–800. (b) Volgraf, M.; Gorostiza, P.; Numano, R.; Kramer, R. H.; Isacoff, E. Y.; Trauner, D. Allosteric control of an ionotropic glutamate receptor with an optical switch. *Nat. Chem. Biol.* **2006**, *2* (1), 47–52.
- (8) Jankovic, B.; Bozovic, O.; Hamm, P. Intrinsic dynamics of protein—peptide unbinding. *Biochemistry* **2021**, *60* (22), 1755–1763. (b) Yeoh, Y. Q.; Yu, J.; Polyak, S. W.; Horsley, J. R.; Abell, A. D. Photopharmacological Control of Cyclic Antimicrobial Peptides. *ChemBioChem* **2018**, *19* (24), 2591–2597. (c) Ventura, C. R.; Wiedman, G. R. Substituting azobenzene for proline in melittin to create photomelittin: A light-controlled membrane active peptide. *Biochim. Biophys. Acta, Biomembr.* **2021**, *1863* (12), 183759.
- (9) Prodromou, R.; Moore, B. D.; Chu, W.; Deal, H.; San Miguel, A.; Brown, A. C.; Daniele, M. A. A.; Pozdin, V. A.; Menegatti, S. Molecular Engineering of Cyclic Azobenzene-Peptide Hybrid Ligands for the Purification of Human Blood Factor VIII via Photo-Affinity Chromatography. *Adv. Funct. Mater.* 2023, 33 (14), 2213881.
- (10) Dong, S. L.; Löweneck, M.; Schrader, T. E.; Schreier, W. J.; Zinth, W.; Moroder, L.; Renner, C. A Photocontrolled  $\beta$ -Hairpin Peptide. Chem. Eur. J. 2006, 12 (4), 1114-1120. (b) Kumita, J. R.; Flint, D. G.; Smart, O. S.; Woolley, G. A. Photo-control of peptide helix content by an azobenzene cross-linker: steric interactions with underlying residues are not critical. Protein Eng. 2002, 15 (7), 561-569. (c) Nuti, F.; Gellini, C.; Larregola, M.; Squillantini, L.; Chelli, R.; Salvi, P. R.; Lequin, O.; Pietraperzia, G.; Papini, A. M. A photochromic azobenzene peptidomimetic of a  $\beta$ -turn model peptide structure as a conformational switch. Front. Chem. 2019, 7, 180. (d) Ulysse, L.; Cubillos, J.; Chmielewski, J. Photoregulation of cyclic peptide conformation. J. Am. Chem. Soc. 1995, 117 (32), 8466-8467. (e) Cataldi, E.; Raschig, M.; Gutmann, M.; Geppert, P. T.; Ruopp, M.; Schock, M.; Gerwe, H.; Bertermann, R.; Meinel, L.; Finze, M. Amber light control of peptide secondary structure by a perfluoroaromatic azobenzene photoswitch. ChemBioChem 2023, 24 (5), No. e202200570. (f) Parlato, R.; Volarić, J.; Lasorsa, A.; Kobauri, P.; Jain, G.; Miettinen, M. S.; Feringa, B. L.; Szymanski, W.; van der Wel, P. C. Photocontrol of the  $\beta$ -Hairpin Polypeptide Structure through an Optimized Azobenzene-Based Amino Acid Analogue. J. Am. Chem. Soc. 2024, 146 (3), 2062-2071. (g) Doran, T. M.; Anderson, E. A.; Latchney, S. E.; Opanashuk, L. A.; Nilsson, B. L. An azobenzene photoswitch sheds light on turn nucleation in amyloidbeta self-assembly. ACS Chem. Neurosci. 2012, 3 (3), 211-220.
- (11) Binder, W. H.; Smrzka, O. W. Self-Assembly of Fibers and Fibrils. *Angew. Chem., Int. Ed.* **2006**, 45 (44), 7324–7328.
- (12) Evgrafova, Z.; Rothemund, S.; Voigt, B.; Hause, G.; Balbach, J.; Binder, W. H. Synthesis and Aggregation of Polymer-Amyloid  $\beta$  Conjugates. *Macromol. Rapid Commun.* **2020**, 41 (1), 1900378. (b) Evgrafova, Z.; Voigt, B.; Roos, A. H.; Hause, G.; Hinderberger, D.; Balbach, J.; Binder, W. H. Modulation of amyloid  $\beta$  peptide aggregation by hydrophilic polymers. *Phys. Chem. Chem. Phys.* **2019**,

- 21 (37), 20999–21006. (c) Deike, S.; Rothemund, S.; Voigt, B.; Samantray, S.; Strodel, B.; Binder, W. H.  $\beta$ -Turn mimetic synthetic peptides as amyloid- $\beta$  aggregation inhibitors. *Bioorg. Chem.* 2020, p 104012. (d) Funtan, S.; Evgrafova, Z.; Adler, J.; Huster, D.; Binder, W. H. Amyloid Beta Aggregation in the Presence of Temperature-Sensitive Polymers. *Polymers* 2016, 8 (5), 178. (e) Sen, N.; Hause, G.; Binder, W. H. Membrane Anchored Polymers Modulate Amyloid Fibrillation. *Macromol. Rapid Commun.* 2021, p 2100120.
- (13) Zweifler, L. E.; Koh, A. J.; Daignault-Newton, S.; McCauley, L. K. Anabolic actions of PTH in murine models: two decades of insights. J. Bone Miner. Res. 2020, 36 (10), 1979–1998. (b) Pinheiro, P. L.; Cardoso, J. C.; Power, D. M.; Canário, A. V. Functional characterization and evolution of PTH/PTHrP receptors: Insights from the chicken. BMC Evol. Biol. 2012, 12 (1), 1–15. (c) Guerreiro, P. M.; Renfro, J. L.; Power, D. M.; Canario, A. V. The parathyroid hormone family of peptides: structure, tissue distribution, regulation, and potential functional roles in calcium and phosphate balance in fish. Am. J. Physiol. Regul. Integr. Comp. Physiol. 2007, 292 (2), R679–R696. (d) Xie, J.; Sang, M.; Song, X.; Zhang, S.; Kim, D.; Veenstra, J. A.; Park, Y.; Li, B. A new neuropeptide insect parathyroid hormone iPTH in the red flour beetle Tribolium castaneum. PLoS Genet. 2020, 16 (5), No. e1008772.
- (14) Martin, T. J.; Sims, N. A.; Seeman, E. Physiological and Pharmacological Roles of PTH and PTHrP in Bone using their Shared Receptor, PTH1R. *Endocr. Rev.* **2021**, 42 (4), 383–406. (b) Friedlander, G.; Amiel, C. Cellular mode of action of parathyroid hormone. *Adv. Nephrol. Necker Hosp.* **1994**, 23, 265–279.
- (15) Gopalswamy, M.; Kumar, A.; Adler, J.; Baumann, M.; Henze, M.; Kumar, S. T.; Fändrich, M.; Scheidt, H. A.; Huster, D.; Balbach, J. Structural characterization of amyloid fibrils from the human parathyroid hormone. *Biochim. BIOPhys. Acta Proteins Proteom.* **2015**, *1854* (4), 249–257.
- (16) Sachan, S.; Moya, C. G.; Voigt, B.; Köhn, M.; Balbach, J. The pro-sequence of parathyroid hormone prevents premature amyloid fibril formation. *FEBS Lett.* **2023**, *597*, 995–1006.
- (17) Potts, J. T. Parathyroid hormone: past and present. J. Endocrinol. 2005, 187 (3), 311-325.
- (18) Rendina-Ruedy, E.; Rosen, C. J. Parathyroid hormone (PTH) regulation of metabolic homeostasis: An old dog teaches us new tricks. *Mol. Metab.* **2022**, *60*, 101480.
- (19) Wang, X.; Cheng, X.; Zhao, L.; Wang, Y.; Ye, C.; Zou, X.; Dai, A.; Cong, Z.; Chen, J.; Zhou, Q. Molecular insights into differentiated ligand recognition of the human parathyroid hormone receptor 2. *Proc. Natl. Acad. Sci. U. S. A.* **2021**, *118* (32), No. e2101279118.
- (20) Lauth, L. M.; Voigt, B.; Bhatia, T.; Machner, L.; Balbach, J.; Ott, M. Heparin promotes rapid fibrillation of the basic parathyroid hormone at physiological pH. *FEBS Lett.* **2022**, *596* (22), *2928*–2939.
- (21) Evgrafova, Z.; Voigt, B.; Baumann, M.; Stephani, M.; Binder, W. H.; Balbach, J. Probing Polymer Chain Conformation and Fibril Formation of Peptide Conjugates. *ChemPhyschem* **2019**, *20* (2), 236–240.
- (22) Paschold, A.; Voigt, B.; Hause, G.; Kohlmann, T.; Rothemund, S.; Binder, W. H. Modulating the Fibrillization of Parathyroid-Hormone (PTH) Peptides: Azo-Switches as Reversible and Catalytic Entities. *Biomedicines* **2022**, *10* (7), 1512.
- (23) Walsh, I.; Seno, F.; Tosatto, S. C. E.; Trovato, A. PASTA 2.0: an improved server for protein aggregation prediction. *Nucleic Acids Res.* **2014**, *42* (W1), W301–W307.
- (24) Conchillo-Solé, O.; de Groot, N. S.; Avilés, F. X.; Vendrell, J.; Daura, X.; Ventura, S. AGGRESCAN: a server for the prediction and evaluation of "hot spots" of aggregation in polypeptides. *BMC Bioinform.* **2007**, *8* (1), 65.
- (25) Burdukiewicz, M.; Sobczyk, P.; Rödiger, S.; Duda-Madej, A.; Mackiewicz, P.; Kotulska, M. Amyloidogenic motifs revealed by n-gram analysis. *Sci. Rep.* **2017**, *7* (1), 12961.
- (26) Garbuzynskiy, S. O.; Lobanov, M. Y.; Galzitskaya, O. V. FoldAmyloid: a method of prediction of amyloidogenic regions from protein sequence. *Bioinformatics* **2010**, *26* (3), 326–332.

- (27) Illig, A.-M.; Strodel, B. Performance of Markov State Models and Transition Networks on Characterizing Amyloid Aggregation Pathways from MD Data. *J. Chem. Theory Comput.* **2020**, *16* (12), 7825–7839. (b) Smorodina, E.; Kav, B.; Fatafta, H.; Strodel, B. Effects of ion type and concentration on the structure and aggregation of the amyloid peptide  $A\beta16-22$ . *Proteins: struct., Funct., Bioinf.* 2023, Vol. 91 (1–14).
- (28) Bera, S.; Arad, E.; Schnaider, L.; Shaham-Niv, S.; Castelletto, V.; Peretz, Y.; Zaguri, D.; Jelinek, R.; Gazit, E.; Hamley, I. W. Unravelling the role of amino acid sequence order in the assembly and function of the amyloid- $\beta$  core. *Chem. Commun.* **2019**, 55 (59), 8595–8598.
- (29) Dyson, H. J.; Wright, P. E. Coupling of folding and binding for unstructured proteins. *Curr. Opin. Struct. Biol.* **2002**, *12* (1), 54–60.
- (30) Mayhall, N. J.; Raghavachari, K.; Hratchian, H. P. ONIOMbased QM: QM electronic embedding method using Löwdin atomic charges: Energies and analytic gradients. *J. Chem. Phys.* **2010**, *132* (11), 114107.
- (31) Angeli, C.; Cimiraglia, R.; Malrieu, J.-P. N-electron valence state perturbation theory: a fast implementation of the strongly contracted variant. *Chem. Phys. Lett.* **2001**, 350 (3–4), 297–305.
- (32) Bannwarth, C.; Ehlert, S.; Grimme, S. GFN2-xTB—An accurate and broadly parametrized self-consistent tight-binding quantum chemical method with multipole electrostatics and density-dependent dispersion contributions. *J. Chem. Theory Comput.* **2019**, *15* (3), 1652–1671.
- (33) Shimomura, M.; Kunitake, T. Fluorescence and photo-isomerization of azobenzene-containing bilayer membranes. *J. Am. Chem. Soc.* **1987**, *109* (17), 5175–5183.
- (34) Serpell, L. C.; Fraser, P. E.; Sunde, M. [34] X-Ray fiber diffraction of amyloid fibrils. In *Methods in Enzymology*; Elsevier, 1999; Vol. 309, pp. 526536.
- (35) Petkova, A. T.; Yau, W.-M.; Tycko, R. Experimental constraints on quaternary structure in Alzheimer's  $\beta$ -amyloid fibrils. *Biochemistry* **2006**, 45 (2), 498–512.
- (36) Sawaya, M. R.; Sambashivan, S.; Nelson, R.; Ivanova, M. I.; Sievers, S. A.; Apostol, M. I.; Thompson, M. J.; Balbirnie, M.; Wiltzius, J. J. W.; McFarlane, H. T.; et al. Atomic structures of amyloid cross- $\beta$  spines reveal varied steric zippers. *Nature* **2007**, 447 (7143), 453–457. Riek, R. The three-dimensional structures of amyloids. *Cold Spring Harb Perspect. Biol.* **2017**, 9 (2), a023572.
- (37) Meisl, G.; Rajah, L.; Cohen, S. A.; Pfammatter, M.; Šarić, A.; Hellstrand, E.; Buell, A. K.; Aguzzi, A.; Linse, S.; Vendruscolo, M.; Dobson, C. M. Scaling behaviour and rate-determining steps in filamentous self-assembly. *Chem. Sci.* **2017**, 8 (10), 7087–7097.
- (38) Dear, A. J.; Michaels, T. C.; Meisl, G.; Klenerman, D.; Wu, S.; Perrett, S.; Linse, S.; Dobson, C. M.; Knowles, T. P. Kinetic diversity of amyloid oligomers. *Proc. Natl. Acad. Sci. U. S. A.* **2020**, *117* (22), 12087–12094.
- (39) Fung, B.; Khitrin, A.; Ermolaev, K. An improved broadband decoupling sequence for liquid crystals and solids. *J. Magn. Reson.* **2000**, *142* (1), 97–101.
- (40) Abraham, M. J.; Murtola, T.; Schulz, R.; Páll, S.; Smith, J. C.; Hess, B.; Lindahl, E. GROMACS: High performance molecular simulations through multi-level parallelism from laptops to supercomputers. *SoftwareX* **2015**, *1*, 19–25.
- (41) Huang, J.; Rauscher, S.; Nawrocki, G.; Ran, T.; Feig, M.; De Groot, B. L.; Grubmüller, H.; MacKerell Jr, A. D. CHARMM36m: an improved force field for folded and intrinsically disordered proteins. *Nat. Methods* **2017**, *14* (1), 71–73.
- (42) Samantray, S.; Yin, F.; Kav, B.; Strodel, B. Different force fields give rise to different amyloid aggregation pathways in molecular dynamics simulations. *J. Chem. Inf. Model.* **2020**, *60* (12), 6462–6475.
- (43) Vanommeslaeghe, K.; Hatcher, E.; Acharya, C.; Kundu, S.; Zhong, S.; Shim, J.; Darian, E.; Guvench, O.; Lopes, P.; Vorobyov, I.; Mackerell, A. D. CHARMM general force field: A force field for druglike molecules compatible with the CHARMM all-atom additive biological force fields. *J. Comput. Chem.* **2010**, *31* (4), 671–690.

- (44) Böckmann, M.; Peter, C.; Site, L. D.; Doltsinis, N. L.; Kremer, K.; Marx, D. Atomistic force field for azobenzene compounds adapted for QM/MM simulations with applications to liquids and liquid crystals. *J. Chem. Theory Comput.* **2007**, 3 (5), 1789–1802.
- (45) Jorgensen, W. L.; Chandrasekhar, J.; Madura, J. D.; Impey, R. W.; Klein, M. L. Comparison of simple potential functions for simulating liquid water. *J. Chem. Phys.* **1983**, 79 (2), 926–935.
- (46) Parrinello, M.; Rahman, A. Polymorphic transitions in single crystals: A new molecular dynamics method. *J. Appl. Phys.* **1981**, 52 (12), 7182–7190.
- (47) Nosé, S. A molecular dynamics method for simulations in the canonical ensemble. *Mol. Phys.* **1984**, *52* (2), 255–268. Hoover, W. G. Canonical dynamics: Equilibrium phase-space distributions. *Phys. Rev. A* **1985**, *31* (3), 1695.
- (48) Darden, T.; York, D.; Pedersen, L. Particle mesh Ewald: An N  $\cdot$  log(N) method for Ewald sums in large systems. *J. Chem. Phys.* **1993**, 98 (12), 10089–10092.
- (49) Krause, D.; Thörnig, P. JURECA: modular supercomputer at Jülich supercomputing centre. *JLSRF* **2018**, *4*, A132–A132.
- (50) Gowers, R. J.; Linke, M.; Barnoud, J.; Reddy, T. J.; Melo, M. N.; Seyler, S. L.; Domanski, J.; Dotson, D. L.; Buchoux, S.; Kenney, I. M. MDAnalysis: a Python package for the rapid analysis of molecular dynamics simulations. *Proceedings of the 15th python in science conference* Los Alamos National Laboratory 2016, 98, 105.
- (51) McGibbon, R. T.; Beauchamp, K. A.; Harrigan, M. P.; Klein, C.; Swails, J. M.; Hernández, C. X.; Schwantes, C. R.; Wang, L.-P.; Lane, T. J.; Pande, V. S. MDTraj: a modern open library for the analysis of molecular dynamics trajectories. *Biophys. J.* **2015**, *109* (8), 1528–1532.
- (52) Schrödinger, L. The PyMOL Molecular Graphics System, Version 1.8; CiNii, 2015.
- (53) Jurrus, E.; Engel, D.; Star, K.; Monson, K.; Brandi, J.; Felberg, L. E.; Brookes, D. H.; Wilson, L.; Chen, J.; Liles, K.; Chun, M. Improvements to the APBS biomolecular solvation software suite. *Protein Sci.* **2018**, 27 (1), 112–128.
- (54) Weigend, F.; Ahlrichs, R. Balanced basis sets of split valence, triple zeta valence and quadruple zeta valence quality for H to Rn: Design and assessment of accuracy. *Phys. Chem. Chem. Phys.* **2005**, 7 (18), 3297–3305. Stoychev, G. L.; Auer, A. A.; Neese, F. Automatic generation of auxiliary basis sets. *J. Chem. Theory Comput.* **2017**, 13 (2), 554–562.
- (55) Neese, F. Software update: The ORCA program system Version 5.0. WIREs Comput. Mol. Sci. 2022, 12 (5), No. e1606.
- (56) Sigalov, G.; Fenley, A.; Onufriev, A. Analytical electrostatics for biomolecules: Beyond the generalized Born approximation. *J. Chem. Phys.* **2006**, *124* (12), *124*902.
- (57) Pedregosa, F.; Varoquaux, G.; Gramfort, A.; Michel, V.; Thirion, B.; Grisel, O.; Blondel, M.; Prettenhofer, P.; Weiss, R.; Dubourg, V. Scikit-learn: Machine learning in Python. *J. Mach. Learn. Resd.* **2011**, *12*, 2825–2830.
- (58) Meisl, G.; Kirkegaard, J. B.; Arosio, P.; Michaels, T. C.; Vendruscolo, M.; Dobson, C. M.; Linse, S.; Knowles, T. P. Molecular mechanisms of protein aggregation from global fitting of kinetic models. *Nat. Prot.* **2016**, *11* (2), 252–272.
- (59) Voigt, B.; Bhatia, T.; Hesselbarth, J.; Baumann, M.; Schmidt, C.; Ott, M.; Balbach, J. The Prenucleation Equilibrium of the Parathyroid Hormone Determines the Critical Aggregation Concentration and Amyloid Fibril Nucleationation Concentration and Amyloid Fibril Nucleation. *ChemPhysChem* **2023**, 24 (19), No. e202300439. Voigt, B.; Ott, M.; Balbach, J. A Competition of Secondary and Primary Nucleation Controls Amyloid Fibril Formation of the Parathyroid Hormone. *Macromol. Biosci.* **2023**, 23 (4), 2200525.
- (60) Maity, C.; Hendriksen, W. E.; van Esch, J. H.; Eelkema, R. Spatial structuring of a supramolecular hydrogel by using a visible-light triggered catalyst. *Angew. Chem., Int. Ed.* **2015**, *54* (3), 998–1001.
- (61) Li, J.; Wang, H.; Liu, B.; Chen, J.; Gu, J.; Lin, S. Photoinduced Contraction Fibers and Photoswitchable Adhesives Generated by

- Stretchable Supramolecular Gel. Adv. Funct. Mater. 2022, 32 (30), 2201851
- (62) Trauner, D.; Fialho, D. M. A Modular Platform for Covalent, Photoswitchable Control over Enzyme Activity. *Synfacts* **2023**, *19* (8), 0831
- (63) Alvarez, Z.; Kolberg-Edelbrock, A. N.; Sasselli, I. R.; Ortega, J. A.; Qiu, R.; Syrgiannis, Z.; Mirau, P. A.; Chen, F.; Chin, S. M.; Weigand, S.; et al. Bioactive scaffolds with enhanced supramolecular motion promote recovery from spinal cord injury. *Sciences* **2021**, 374 (6569), 848–856.

# Spiropyran as Building Block in Peptide Synthesis and Modulation of Photochromic Properties

André Paschold, Niclas Starke, Sven Rothemund, and Wolfgang H. Binder\*



Cite This: Org. Lett. 2024, 26, 10542-10547



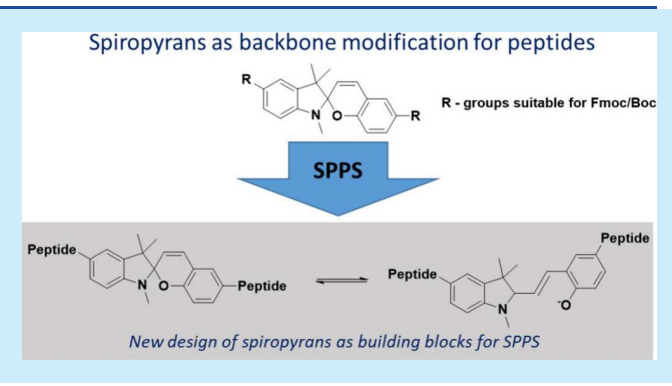
**ACCESS** 

III Metrics & More

Article Recommendations

Supporting Information

ABSTRACT: Light-controlled triggering of materials requires efficient embedding of molecular photoswitches into larger molecules. We herein present the synthesis of two new building blocks for the synthesis of photoswitchable peptides, embedding spiropyranes as a central unit into peptide-backbones via a novel, yet unreported approach. The synthesis presented here allows us to embed spiropyranes directly into solid-phase peptide synthesis (SPPS), further describing the resulting photophysical properties of the as-prepared photoswitchable peptides.



he incorporation of photoswitchable moieties into functional materials allows to address molecular conformation<sup>2</sup> and dynamics<sup>3</sup> by light as external trigger.<sup>4</sup> Besides azobenzenes, diarylethenes, and thioindigos, spiropyrans are important photoswitches.<sup>8</sup> Spiropyrans exist in two forms (Figure 1A): a colorless, closed form of the cyclic spiropyran (SP) and the colored merocyanin (MC) form, the latter displaying an extended molecular shape. Irradiation by UV-light causes cleavage of the C-O bond at the spiro-carbon and its isomerization to the MC-form, reversing isomerization by visible light.9 There is a strong change in the dipolemoment upon isomerization: 10 while the dipole moment of the SP-form is  $\sim$ 4–6 D, it is increased in the MC-form to  $\sim$ 14–18 D. Spiropyranes are not only sensitive to light<sup>11</sup> but can also also be modulated by temperature,<sup>12</sup> pH,<sup>13</sup> the redox potential,<sup>14</sup> solvent polarity,<sup>15</sup> ions,<sup>16</sup> and even by mechanical force.<sup>17</sup> Thus, they are of great interest in the generation of smart materials, where multiple stimuli can be transferred to the shape, strength, and dynamic properties of a material they are embedded into. 10,18 Their incorporation into biological and synthetic macromolecules was first reported in 1976 for peptides<sup>19</sup> and in 1978 for synthetic polymers<sup>20</sup> but only in the side-chain of the respective monomer unit. Thus, for decades, side-chain or end-group modification of peptides and polymers<sup>21</sup> (Figure 1B) remained the only method to incorporate spiropyrans into (biological) macromolecules to transfer their adaptive and stimuli-responsive properties therein. In 2013 the spiropyran unit was embedded directly into a polymer-backbone, revealing significant property changes upon their photoswitching.<sup>22</sup> While spiropyrans play an important role in the control of peptide properties, 8b,23 a general methodology to embed spiropyrans into the main

backbone of a peptide is still missing. We herein report new spiropyran building blocks (Figure 1C) and their incorporation into peptides via SPPS (solid-phase peptide synthesis): two blocks via a Fmoc-synthesis strategy and two blocks via a Bocstrategy. Based on suitable indole and salicylaldehyde precursors, equipped with either a protected amine- or a carboxy functionality, the desired spiropyran can be formed subsequently be embedded into peptides via Fmoc-SPPS at different positions of a fibrillating peptide (see Table 1), and further investigated for their photophysical properties.

As non-natural amino acid building blocks for SPPS, we synthesized the four spiropyrans 1a, 1b, 2a, and 2b (Scheme 1). Spiropyrans 1a and 1b are designed for introducing the FASC building block containing the N-terminal protected amino group at the indolinium entity and the C-terminal carboxy function at the chromene unit. The synthetic strategy was reversed for spiropyrans 2a and 2b, introducing the SAFC building block.

#### Synthesis of the Photoswitch

We designed the building blocks 1a and 2a bearing a Fmocprotection group, and 1b and 2b with a Boc-protection group.<sup>24</sup> The key step in both strategies was a condensation reaction of an indoline compound with an o-hydroxy-aromatic aldehyde. The synthesis of the spiropyrans 1a and 1b (Scheme

Received: October 19, 2024 November 22, 2024 Revised: Accepted: November 26, 2024 Published: December 2, 2024





Organic Letters pubs.acs.org/OrgLett Letter

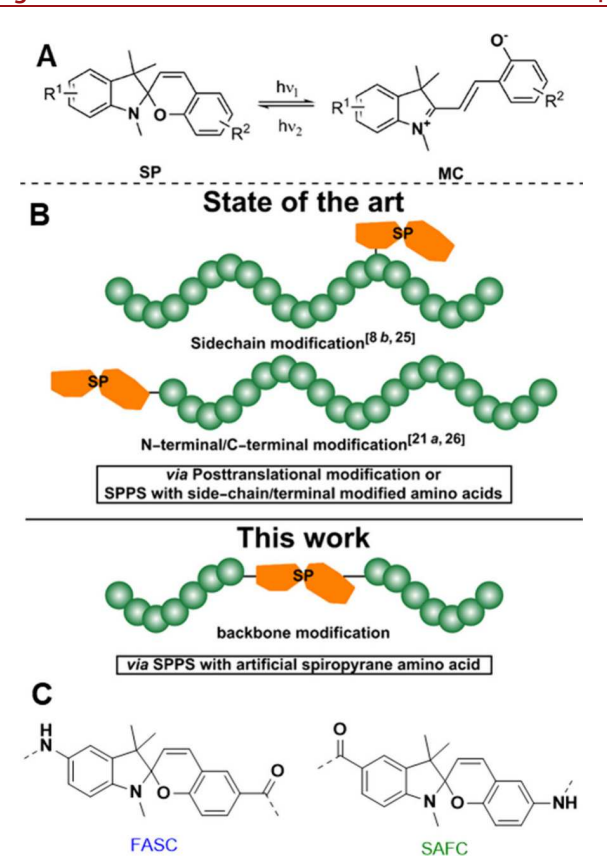


Figure 1. (A) Isomerization of spiropyrans between their closed form (SP) and their ring-opened merocyanine form (MC). (B) State-of-the-art strategies to modify peptides with spiropyrans consists of post-translational modifications of the synthesized peptide at the side chain <sup>8b,25</sup> and at the N-/C-terminal end of the peptide chain (above). <sup>21a,26</sup> This work: solid-phase peptide synthesis (SPPS) to incorporate a spiropyran building block into the peptide backbone (below). (C) Structures of the spiropyran two different building blocks, FASC and SAFC.

Table 1. Peptides Containing the Photoswitchable Spiropyran Moiety (SAFC, FASC) Synthesized *via* Fmoc Solid-Phase Peptide Synthesis

peptide	primary sequence	embedded spiropyran
P1	<sup>25</sup> RKKLQ <sup>30</sup> D-FASC-VHNF <sup>35</sup> VAL	1a
P2	<sup>25</sup> RK-FASC-KLQ <sup>30</sup> DVHNF <sup>35</sup> VAL	1a
P3	GSGSGS-FASC-GSGSGS	1a
P4	<sup>25</sup> RKKLQ <sup>30</sup> D-SAFC-HNF <sup>35</sup> VAL	2a

1) started with commercially available 5, where a nitro group was introduced at position 5.<sup>27</sup> Subsequently, the nitro group was reduced to the amine<sup>27</sup> and protected with a Boc- or Fmoc-group. Finally a condensation reaction with commercially available carboxylic acid 5 leads to the desired product 1a with an overall yield of 5% over 4 steps and the spiropyran 1b in a yield of 18%. The convergent synthesis toward spiropyrans 2a and 2b (Scheme 1) started with the indole precursor. 4-Hydrazinobenzoic acid 6 was converted in a Fischer indole like reaction<sup>28</sup> followed by a methylation to yield the indolinium iodide 7.<sup>28</sup> In contrast to the spiropyrans 1a and 1b we additionally prepared o-hydroxy benzaldehydes 10a and 10b. First step was to protect the hydroxy- and the aldehyde-functionality of nitro salicyl aldehyde 8 with acetoxy groups, followed by reduction of the nitro group and attaching the

Scheme 1. Synthesis of the Spiropyrans 1a/1b and 2a/2b

group (Boc or Fmoc).<sup>29</sup> To remove the acetoxy protecting groups, we probed de-esterification under different conditions. The Boc-protected **9a** was treated under basic conditions, while the Fmoc-protected **9b** was treated under acidic conditions. To obtain the final compounds, the indolinium iodide and the respective protected *o*-hydroxybenzaldehyde were converted in a condensation reaction. Spiropyran **2a** was obtained in an overall yield of 4% and spiropyran **2b** in 3%, both in 6 steps.

#### **Peptide Synthesis and Photophysical Properties**

To test if the Fmoc-protected spiropyrans 1a and 2a are compatible with standard SPPS conditions and to investigate the photophysical properties we synthesized four different peptides (Table 1). We chose the fibril core sequence of the parathyroid hormone (PTH<sub>25-37</sub>) as a model peptide<sup>30</sup> to probe a modulation of the fibrillization of the peptide, in addition to the GlySer-sequence at the N-terminus and the C-terminus. The peptides were synthesized using standard SPPS conditions and characterized with ESI-Tof, MALDI-ToF, and  $^1$ H NMR (see the Supporting Information). The isomerization between the MC and the SP-form was probed via UV/vis-spectroscopy and HPLC. As spiropyrans display an acid-

Organic Letters pubs.acs.org/OrgLett Letter

Scheme 2. Photophysical Isomerization Process of the FASC (top) and SAFC (bottom) Building Blocks

Table 2. Photochromic Properties of Peptides P1-P4 in Aqueous Media

peptide	$\lambda_{\text{max, SP}}$ [nm]	$\lambda_{ ext{max, MC}}$ [nm]	$\lambda_{\mathrm{iso}}$ [nm]	$\varepsilon^a  [\mathrm{mol^{-1}}\mathrm{cm^{-1}}]$	$ au_{1/2}$ at 37 °C (4°) [min]
P1 <sup>b</sup>	244, 511	244, 376, 518	292	_f	$3.74 \pm 0.06 \ (171.43 \pm 0.28)$
c	250	257, 321, 428	314	$6201 \pm 386 \ (314 \ nm)$	$10.74 \pm 0.02 \ (1155.2 \pm 0.4)$
$P2^b$	242	286, 376, 518	282	_f	$2.92 \pm 0.04 \ (321.44 \pm 0.30)$
c	n.d.	257, 321, 427	314	$5910 \pm 553 (314 \text{ nm})$	$11.31 \pm 0.02 \ (1151.1 \pm 0.2)$
Р3	240	244, 375, 515	283	_f	$5.95 \pm 0.10 \ (358.88 \pm 0.18)$
c	n.d.	257, 323, 426	313	$5644 \pm 66 (313 \text{ nm})$	$15.78 \pm 0.03$
$P4^c$	247, 305	253, 379, 442	265, 326	_f	$1.65 \pm 0.04$
d	305,357,450	253, 379, 442	329	$6153 \pm 90 (329 \text{ nm})$	$10.04 \pm 0.21 \ (384.88 \pm 0.86)$

<sup>a</sup>At the isosbestic point. <sup>b</sup>50  $\mu$ M NaH<sub>2</sub>PO<sub>4</sub>, 0,01% NaN<sub>3</sub>, pH 7.4. <sup>c</sup>100  $\mu$ M citric acid/sodium citrate, pH 2.5. <sup>d</sup>1 M HCl, pH 1. <sup>f</sup>Not determined as MC-form is hydrolyzed. n.d.: not determined.

ochromic behavior, we investigated the behavior at physiological pH (FASC; buffered aqueous solution, pH 7.4), in a citrate buffered solution (FASC and SAFC; pH 2.5), and in 0.1 M HCl (SAFC; pH 1). For both spiropyran-building blocks (peptides P1-P4, Figures S1-S4) the colored MC-form showed absorption in the UV and visible range, while the colorless SP-isomer usually showed absorption only in the UV range. Furthermore, the MC-isomer was the thermodynamically favored form in aqueous solution (Scheme 2, Figures S5-S14), which is well-known for this class of spiropyrans in the presence of water.<sup>31</sup> Irradiation with green light (525 nm) of P1-P4 led to the SP-isomer, determined by UV/visspectroscopy. The thermal (dark) relaxation toward the MC-form follows a first-order kinetic 15b,32 and occurred fast at 37 °C. At all tested conditions, a half-life time of less than 20 min was observed which increased to up to 1155 min if the temperature was decreased to 4 °C (Table 2, Figures S5-S16). A competitive reaction is the degradation process of the MCform via hydrolysis of the bridging double bond, which was first described by Stafforst et al.<sup>33</sup> Decomposition led to a peptide with the Fischer's base moiety and a peptide bearing a salicyl aldehyde moiety, both detected via MALID-ToF measurements (Figure S17-S19). The hydrolysis rate compared to the thermal isomerization of the MC-FASC unit is slower, whereby the rate constant of the hydrolysis is 13  $(0.116 \text{ min}^{-1} \text{ vs } 0.00921 \text{ min}^{-1} \text{ for } P3) \text{ to } 150\text{-times lower}$  $(0.237 \text{ min}^{-1} \text{ vs } 0.00162 \text{ min}^{-1} \text{ for } P2, \text{ Table } S1)$ . In contrast, the SAFC building block could not be handled at a physiological pH value, as the hydrolysis occurs within several minutes.

If FASC is kept in the SP-form through continuous irradiation with green light, it remains stable until the light source is switched off, and the isomerization and degradation kinetics can be followed via UV/vis-spectroscopy (irradiation time of 5 h). Spiropyrans are known to act as photoacids; therefore, we further investigated the behavior at pH values,

where the MC-form should mainly exist in its protonated form. As the p $K_a$  value of the MC-form was determined to be  $\sim 7.2$ for several spiropyrans,<sup>34</sup> strong acidic conditions (pH 2.5 or pH 1) were used. The FASC-containing peptides are stable  $(\tau_{1/2})$  of hydrolysis >15,000 min) at a pH value of 2.5. The SPto-MC isomerization reaches thermal equilibrium usually after 2 h, while the SP-PSS (photostationary state) was obtained through irradiation with green light after 10 min. Analysis with HPLC revealed that the thermal equilibrium consists of nearly 100% of the MC-form, while the photoconversion was almost quantitative (Table S2 and Figures S23 and 24). The SAFCswitch was not stable at pH 2.5, but the decomposition was strongly inhibited (the rate constant was ~1300 fold smaller than the thermal isomerization, Table S1), so that photophysical parameters could be determined (Table 2). Irradiation at 405 nm leads to a conversion of at least ~75% to the SPform, whereby the thermal back-isomerization at 37 °C exhibits a half-life time of 1.65 min, completely stable at pH 1. The photoisomerization at pH 1 could be achieved with irradiation of light of two different wavelengths, where 405 nm led to an SP content of 51% at the PSS, while green light generated 62% (Figure S21).

The thermal back-isomerization exhibits a half-life time of 10 min at 37 °C and 385 min at 4 °C, respectively (Figures S17–19).

We observed that the stability of the spiropyrans in our peptides against hydrolysis was strongly pH-dependent. Thus, the peptide P2 at pH 7.4 and 37 °C is almost six times more stable than the peptide P1. Furthermore, the substituents at the spiropyrane rings also have a significant impact, as the FASC building block could at least be investigated at pH 7.4, while the SAFC building block was hydrolyzed already within a few minutes. Increasing the stability of the spiropyrans against hydrolysis at higher pH values by different substituents is currently a subject of intensive research strategies. Thus, substituents can influence the SP-MC ratio in thermal

**Organic Letters** pubs.acs.org/OrgLett Letter

equilibrium,<sup>35</sup> wherein the SP-form does not undergo hydrolysis but the hydrolytic rate of the MC-form remains almost unchanged. Another approach is to modulate the stability of the bridging double bond against hydrolysis.<sup>36</sup> Introducing an electron-donating methoxy group in the paraposition conjugated with the double bond improved stability. Recently a spiropyran was reported bearing a napthalimide moiety, which was stable at pH 7.37

#### Conclusion

Herein, we for the first time presented an approach to use Bocand Fmoc-protected spiropyran photoswitches directly as a backbone modification, applicable via solid phase peptide synthesis (SPPS). We have developed an easy synthetic route and demonstrated the incorporation with standard Fmocchemistry as well as the photophysical behavior of the generated, fibrillating peptides under acidic conditions. Our future efforts will focus on the design of new photoswitches to increase the stability at higher pH values and to further modulate aggregation of peptides and proteins.

#### ASSOCIATED CONTENT

#### **Data Availability Statement**

Some data underlying this study are not publicly available due to patent issues. Most data of this study however are available within this article and its Supporting Information. The raw data that support the findings of this study are stored electronically according to the requirements of the DFG and are available from the corresponding author upon reasonable request by email (please contact the corresponding author, WHB, via Email (Wolfgang-binder@chemie.uni-halle.de).

#### Supporting Information

The Supporting Information is available free of charge at https://pubs.acs.org/doi/10.1021/acs.orglett.4c03929.

General information, experimental procedures, characterization data, and copies of <sup>1</sup>H, <sup>13</sup>C NMR spectra; HPLC data; spectroscopic investigations; Supplementary Tables: (S1) Kinetic parameters of thermal isomerization and decomposition of peptides P1-P4; (S2) isomeric ratio in the thermal equilibrium and at the respective PSS of P1-P4; Supplementary Figures: (S1-S4) UV/vis-spectra of P1-P4 at different pH values; (S5-S19) UV/vis kinetic measurements of thermal isomerization and decomposition of P1-P4; (S20-S22) MALDI-ToF measurements of P1, P2, and P4 at different pH values; (S23-S24) UV/vis spectra, measured (thermal equilibrium and PSS) and calculated (pure isomers) of P1-P4; (S25-S42) NMR data of compounds and peptides; (S43-S46) HPLC and MS data of peptides (PDF)

#### AUTHOR INFORMATION

#### **Corresponding Author**

Wolfgang H. Binder - Macromolecular Chemistry, Institute of Chemistry, Faculty of Natural Science II, Martin Luther University Halle Wittenberg, 06120 Halle, Germany; © orcid.org/0000-0003-3834-5445;

Email: wolfgang.binder@chemie.uni-halle.de

#### **Authors**

André Paschold - Macromolecular Chemistry, Institute of Chemistry, Faculty of Natural Science II, Martin Luther University Halle Wittenberg, 06120 Halle, Germany Niclas Starke - Macromolecular Chemistry, Institute of Chemistry, Faculty of Natural Science II, Martin Luther University Halle Wittenberg, 06120 Halle, Germany Sven Rothemund - Core Unit Peptide-Technologies, University of Leipzig Medical Center, 04103 Leipzig,

Complete contact information is available at: https://pubs.acs.org/10.1021/acs.orglett.4c03929

#### **Author Contributions**

The manuscript was written through contributions of all authors. All authors have given approval to the final version of the manuscript.

#### **Notes**

The authors declare no competing financial interest.

#### ACKNOWLEDGMENTS

We thank the following projects for financial support: the DFG project INST 271/444-1 FUGG; the DFG-Project BI1337/16-1; BI1337/17-1, BI1337/18-1, and BI 1337/14-1; and the GRK 2670, W69000789, ProjectNr 436494874, TP B02. W.H.B. thanks the European Center of Just Transition Research and Impact-Driven Transfer (JTC) and the PoliFaces Initiative.

#### **REFERENCES**

- (1) (a) Goulet-Hanssens, A.; Eisenreich, F.; Hecht, S. Enlightening materials with photoswitches. Adv. Mater. 2020, 32 (20), 1905966. (b) Albert, L.; Vázquez, O. Photoswitchable peptides for spatiotemporal control of biological functions. Chem. Commun. 2019, 55 (69), 10192-10213. (c) Boelke, J.; Hecht, S. Designing molecular photoswitches for soft materials applications. Adv. Opt. Mater. 2019, 7 (16), 1900404.
- (2) (a) Cataldi, E.; Raschig, M.; Gutmann, M.; Geppert, P. T.; Ruopp, M.; Schock, M.; Gerwe, H.; Bertermann, R.; Meinel, L.; Finze, M.; et al. Amber light control of peptide secondary structure by a perfluoroaromatic azobenzene photoswitch. ChemBioChem. 2023, 24 (5), No. e202200570. (b) Parlato, R.; Volarić, J.; Lasorsa, A.; Bagherpoor Helabad, M.; Kobauri, P.; Jain, G.; Miettinen, M. S.; Feringa, B. L.; Szymanski, W.; van der Wel, P. C. Photocontrol of the  $\beta$ -Hairpin Polypeptide Structure through an Optimized Azobenzene-Based Amino Acid Analogue. J. Am. Chem. Soc. 2024, 146 (3), 2062-
- (3) (a) Jankovic, B.; Bozovic, O.; Hamm, P. Intrinsic dynamics of protein-peptide unbinding. Biochemistry 2021, 60 (22), 1755-1763. (b) Bozovic, O.; Jankovic, B.; Hamm, P. Using azobenzene photocontrol to set proteins in motion. Nat. Rev. Chem. 2022, 6 (2), 112-124.
- (4) Peddie, V.; Abell, A. D. Photocontrol of Peptide Secondary Structure through Non-Azobenzene Photoswitches. J. Photochem. Photobiol. C 2019, 40, 1-20.
- (5) (a) Vybornyi, O.; Liu, S. X.; Häner, R. Stimuli-responsive supramolecular polymers from amphiphilic phosphodiester-linked azobenzene trimers. Angew. Chem., Int. Ed. 2021, 133 (49), 26076-26081. (b) Fuentes, E.; Gerth, M.; Berrocal, J. A.; Matera, C.; Gorostiza, P.; Voets, I. K.; Pujals, S.; Albertazzi, L. An azobenzenebased single-component supramolecular polymer responsive to multiple stimuli in water. J. Am. Chem. Soc. 2020, 142 (22), 10069-10078. (c) Yang, J.; Ye, H. J.; Xiang, H. M.; Zhou, X.; Wang, P. Y.; Liu, S. S.; Yang, B. X.; Yang, H. B.; Liu, L. W.; Yang, S. Photo-

Organic Letters pubs.acs.org/OrgLett Letter

- Stimuli Smart Supramolecular Self-Assembly of Azobenzene/β-Cyclodextrin Inclusion Complex for Controlling Plant Bacterial Diseases. *Adv. Funct. Mater.* **2023**, 33 (42), 2303206. (d) Crone, N. S.; van Hilten, N.; van der Ham, A.; Risselada, H. J.; Kros, A.; Boyle, A. L. Azobenzene-Based Amino Acids for the Photocontrol of Coiled-Coil Peptides. *Bioconjugate Chem.* **2023**, 34 (2), 345–357.
- (6) (a) Nevskyi, O.; Sysoiev, D.; Dreier, J.; Stein, S. C.; Oppermann, A.; Lemken, F.; Janke, T.; Enderlein, J.; Testa, I.; Huhn, T.; et al. Fluorescent Diarylethene Photoswitches—A Universal Tool for Super-Resolution Microscopy in Nanostructured Materials. *Small* **2018**, *14* (10), 1703333. (b) Pu, S.-Z.; Sun, Q.; Fan, C.-B.; Wang, R.-J.; Liu, G. Recent advances in diarylethene-based multi-responsive molecular switches. *J. Mater. Chem. C* **2016**, *4* (15), 3075–3093.
- (7) Walden, S. L.; Nguyen, P. H.; Li, H.-K.; Liu, X.; Le, M. T.; Xian Jun, L.; Barner-Kowollik, C.; Truong, V. X. Visible light-induced switching of soft matter materials properties based on thioindigo photoswitches. *Nat. Commun.* **2023**, *14* (1), 8298.
- (8) (a) Keyvan Rad, J.; Balzade, Z.; Mahdavian, A. R. Spiropyran-based advanced photoswitchable materials: A fascinating pathway to the future stimuli-responsive devices. *J. Photochem. Photobiol. C* 2022, 51, No. 100487. (b) Inaba, H.; Sakaguchi, M.; Watari, S.; Ogawa, S.; Kabir, A. M. R.; Kakugo, A.; Sada, K.; Matsuura, K. Reversible Photocontrol of Microtubule Stability by Spiropyran-Conjugated Tau-Derived Peptides. *ChemBioChem.* 2023, 24 (8), No. e202200782.
- (9) Fagan, A.; Bartkowski, M.; Giordani, S. Spiropyran-based drug delivery systems. *Front. Chem.* **2021**, *9*, No. 720087.
- (10) Klajn, R. Spiropyran-based dynamic materials. *Chem. Soc. Rev.* **2014**, 43 (1), 148–184.
- (11) (a) Ali, A. A.; Kharbash, R.; Kim, Y. Chemo-and biosensing applications of spiropyran and its derivatives-A review. *Anal. Chim. Acta* **2020**, *1110*, 199–223. (b) Kortekaas, L.; Browne, W. R. The evolution of spiropyran: fundamentals and progress of an extraordinarily versatile photochrome. *Chem. Soc. Rev.* **2019**, *48* (12), 3406–3424.
- (12) Hirshberg, Y.; Fischer, E. Multiple reversible color changes initiated by irradiation at low temperature. *J. Chem. Phys.* **1953**, *21* (9), 1619–1620.
- (13) (a) Satoh, T.; Sumaru, K.; Takagi, T.; Takai, K.; Kanamori, T. Isomerization of spirobenzopyrans bearing electron-donating and electron-withdrawing groups in acidic aqueous solutions. *Phys. Chem. Chem. Phys.* **2011**, *13* (16), 7322–7329. (b) Kortekaas, L.; Chen, J.; Jacquemin, D.; Browne, W. Proton-stabilized photochemically reversible E/Z isomerization of spiropyrans. *J. Phys. Chem. B* **2018**, *122* (24), 6423–6430.
- (14) Wagner, K.; Byrne, R.; Zanoni, M.; Gambhir, S.; Dennany, L.; Breukers, R.; Higgins, M.; Wagner, P.; Diamond, D.; Wallace, G. G.; et al. A multiswitchable poly (terthiophene) bearing a spiropyran functionality: understanding photo-and electrochemical control. *J. Am. Chem. Soc.* **2011**, *133* (14), 5453–5462.
- (15) (a) Zhou, J.; Li, Y.; Tang, Y.; Zhao, F.; Song, X.; Li, E. Detailed investigation on a negative photochromic spiropyran. *J. Photochem. Photobiol., A* **1995**, *90* (2–3), 117–123. (b) Piard, J. Influence of the solvent on the thermal back reaction of one spiropyran. *J. Chem. Educ.* **2014**, *91* (12), 2105–2111.
- (16) (a) Kang, J.; Li, E.; Cui, L.; Shao, Q.; Yin, C.; Cheng, F. Lithium ion specific fluorescent reversible extraction-release based on spiropyran isomerization combining crown ether coordination and its bioimaging. Sens. Actuators B: Chem. 2021, 327, No. 128941. (b) Prakash, K.; Sahoo, P. R.; Kumar, S. A substituted spiropyran for highly sensitive and selective colorimetric detection of cyanide ions. Sens. Actuators B: Chem. 2016, 237, 856–864.
- (17) (a) Kim, T. A.; Robb, M. J.; Moore, J. S.; White, S. R.; Sottos, N. R. Mechanical reactivity of two different spiropyran mechanophores in polydimethylsiloxane. *Macromolecules* **2018**, *51* (22), 9177–9183. (b) Gossweiler, G. R.; Kouznetsova, T. B.; Craig, S. L. Forcerate characterization of two spiropyran-based molecular force probes. *J. Am. Chem. Soc.* **2015**, *137* (19), 6148–6151. (c) Raisch, M.; Genovese, D.; Zaccheroni, N.; Schmidt, S. B.; Focarete, M. L.; Sommer, M.; Gualandi, C. Highly sensitive, anisotropic, and reversible

- stress/strain-sensors from mechanochromic nanofiber composites. *Adv. Mater.* **2018**, *30* (39), 1802813.
- (18) (a) Wang, W.; Hu, J.; Zheng, M.; Zheng, L.; Wang, H.; Zhang, Y. Multi-responsive supramolecular hydrogels based on merocyanine—peptide conjugates. *Org. Biomol. Chem.* **2015**, *13* (47), 11492—11498. (b) Beyer, C.; Wagenknecht, H.-A. Synthesis of spiropyrans as building blocks for molecular switches and dyads. *J. Org. Chem.* **2010**, *75* (8), 2752—2755.
- (19) Karube, I.; Nakamoto, Y.; Suzuki, S. Photocontrol of urease activity in spiropyran collagen membrane. *Biochim. Biophys. Acta* **1976**, 445 (3), 774–779.
- (20) Smets, G.; Braeken, J.; Irie, M. Photomechanical effects in photochromic systems. *Pure Appl. Chem.* 1978, 50, 845–856.
- (21) (a) Tomizaki, K.-y.; Mihara, H. Phosphate-mediated molecular memory driven by two different protein kinases as information input elements. *J. Am. Chem. Soc.* **2007**, 129 (26), 8345–8352. (b) Ventura, C.; Byrne, R.; Audouin, F.; Heise, A. Atom transfer radical polymerization synthesis and photoresponsive solution behavior of spiropyran end-functionalized polymers as simplistic molecular probes. *J. Polym. Sci., Part A: Polym. Chem.* **2011**, 49 (16), 3455–3463.
- (22) Sommer, M.; Komber, H. Spiropyran Main-Chain Conjugated Polymers. *Macromol. Rapid Commun.* **2013**, 34 (1), 57–62.
- (23) (a) Chen, L.; Zhu, Y.; Yang, D.; Zou, R.; Wu, J.; Tian, H. Synthesis and antibacterial activities of antibacterial peptides with a spiropyran fluorescence probe. *Sci. Rep.* **2014**, *4* (1), 6860. (b) Hrebonkin, A.; Afonin, S.; Nikitjuka, A.; Borysov, O. V.; Leitis, G.; Babii, O.; Koniev, S.; Lorig, T.; Grage, S. L.; Nick, P.; et al. Spiropyran-Based Photoisomerizable  $\alpha$ -Amino Acid for Membrane-Active Peptide Modification. *Chem.—Eur. J.* **2024**, 30 (22), No. e202400066.
- (24) Stawikowski, M.; Fields, G. B. Introduction to peptide synthesis. *Curr. Protoc. Protein Sci.* **2012**, 69 (1), 18.11.11–18.11.13.
- (25) (a) Fujimoto, K.; Amano, M.; Horibe, Y.; Inouye, M. Reversible photoregulation of helical structures in short peptides under indoor lighting/dark conditions. *Org. Lett.* **2006**, 8 (2), 285–287. (b) Liu, M.; Creemer, C. N.; Reardon, T. J.; Parquette, J. R. Light-driven dissipative self-assembly of a peptide hydrogel. *Chem. Commun.* **2021**, 57 (100), 13776–13779.
- (26) Qiu, Z.; Yu, H.; Li, J.; Wang, Y.; Zhang, Y. Spiropyran-linked dipeptide forms supramolecular hydrogel with dual responses to light and to ligand—receptor interaction. *Chem. Commun.* **2009**, 23, 3342—2244
- (27) Shvartsman, F. P.; Krongauz, V. A. Quasi-liquid crystals of thermochromic spiropyrans. A material intermediate between supercooled liquids and mesophases. *J. Phys. Chem.* **1984**, *88* (25), 6448–6453
- (28) Tomasulo, M.; Kaanumal, S. L.; Sortino, S.; Raymo, F. M. Synthesis and properties of benzophenone–spiropyran and naphthalene–spiropyran conjugates. *J. Org. Chem.* **2007**, 72 (2), 595–605.
- (29) Di Bella, S.; Consiglio, G.; Leonardi, N.; Failla, S.; Finocchiaro, P.; Fragalà, I. Film polymerization—a new route to the synthesis of insoluble polyimides containing functional nickel (II) schiff base units in the main chain. *Eur. J. Inorg. Chem.* **2004**, 2004 (13), 2701—2705.
- (30) (a) Paschold, A.; Voigt, B.; Hause, G.; Kohlmann, T.; Rothemund, S.; Binder, W. H. Modulating the Fibrillization of Parathyroid-Hormone (PTH) Peptides: Azo-Switches as Reversible and Catalytic Entities. *Biomedicines* 2022, 10 (7), 1512. (b) Paschold, A.; Schaffler, M.; Miao, X.; Gardon, L.; Krüger, S.; Heise, H.; Röhr, M. I. S.; Ott, M.; Strodel, B.; Binder, W. H. Photocontrolled Reversible Amyloid Fibril Formation of Parathyroid Hormone-Derived Peptides. *Bioconjugate Chem.* 2024, 35 (7), 981–995.
- (31) Tian, W.; Tian, J. An insight into the solvent effect on photo-solvato-chromism of spiropyran through the perspective of intermolecular interactions. *Dyes Pigm.* **2014**, *105*, 66–74.
- (32) Shiraishi, Y.; Itoh, M.; Hirai, T. Thermal isomerization of spiropyran to merocyanine in aqueous media and its application to colorimetric temperature indication. *Phys. Chem. Chem. Phys.* **2010**, 12 (41), 13737–13745.

Organic Letters pubs.acs.org/OrgLett Letter

- (33) Stafforst, T.; Hilvert, D. Kinetic characterization of spiropyrans in aqueous media. *Chem. Commun.* **2009**, *3*, 287–288.
- (34) Berton, C.; Busiello, D. M.; Zamuner, S.; Solari, E.; Scopelliti, R.; Fadaei-Tirani, F.; Severin, K.; Pezzato, C. Thermodynamics and kinetics of protonated merocyanine photoacids in water. *Chem. Sci.* **2020**, *11* (32), 8457–8468.
- (35) Hammarson, M.; Nilsson, J. R.; Li, S.; Beke-Somfai, T. s.; Andréasson, J. Characterization of the thermal and photoinduced reactions of photochromic spiropyrans in aqueous solution. *J. Phys. Chem. B* **2013**, *117* (43), 13561–13571.
- (36) Abeyrathna, N.; Liao, Y. Stability of merocyanine-type photoacids in aqueous solutions. *J. Phys. Org. Chem.* **2017**, 30 (8), No. e3664.
- (37) Shiraishi, Y.; Oshima, T.; Hirai, T. Isomerization, Protonation, and Hydrolysis Properties of Naphthalimide-Containing Spiropyran in Aqueous Media. *J. Phys. Chem. B* **2024**, *128* (36), 8797–8806.

# **Conclusion**

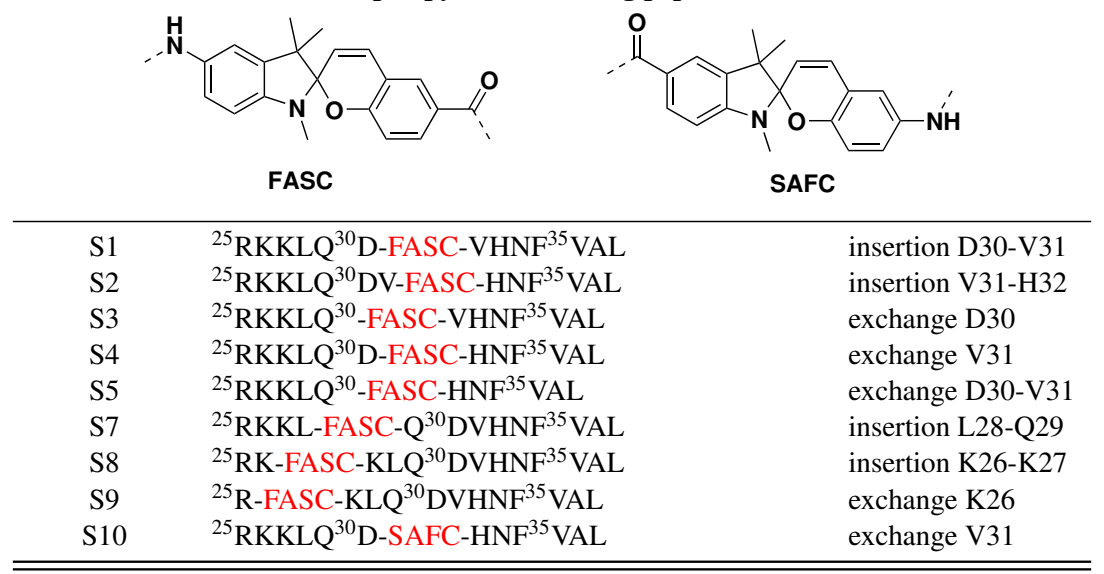
According to the scope of this thesis, the three photoswitchable building blocks 3,4'-AMPB, FASC and FASC were successfully synthesised as their Fmoc-protected forms. The respective photoswitches were incorporated into the backbone of PTH<sub>25-37</sub> at various positions using SPPS with Fmoc-chemistry (see Table 5.1). In total 22 variants of the modified sequence were generated, whereby twelve peptides contained the 3,4'-AMPB moiety, nine containing the FASC moiety and one peptide bears the SAFC moiety. The photophysical properties of the peptides were characterized with UV/Vis spectroscopy, in particular the optimal switching wavelengths, the composition in the PSS, and the half-life time of the metastable state (for azobenzenes the *cis*-form and for spiropyrans the SP-form). The investigation of the fibrillization behaviour was mainly conducted with the azobenzene containing peptides (see section 5.1 and 5.2). The spiropyran containing peptides were not able to fibrillize under physiological conditions and therefore their switching behaviour was investigated at different pH values, which is described in section 5.3. Additionally, two peptides with uniformly <sup>15</sup>N/<sup>13</sup>C labeled L28 and F34 were used in the ssNMR studies (see section 5.2).

Table 5.1: Primary sequences of the PTH-fragments, and the  $PTH_{25-37}$  derived azobenzene and spiropyran containing peptides. Position of the azobenzene moiety is highlighted in violet. Position of the spiropyran moieties is highlighted in red.

peptide	primary sequence	modification		
PTH fragments				
DTH	<sup>1</sup> SVSEIQLMHN <sup>11</sup> LGKHLNSMER <sup>21</sup> VEWLRK <sup>31</sup> VHNFVALGAP <sup>41</sup> LAPRDAGSQR <sup>51</sup> PRKKED	~		
$PTH_{1-84}$	61ESHEKSLGEA <sup>71</sup> DKADVNVLTK <sup>81</sup> AKSQ			
PTH <sub>25-37</sub>	<sup>25</sup> RKKLQ <sup>30</sup> DVHNF <sup>35</sup> VAL -			
Azobenzene containing peptides				
N N N				
3,4'-AMPB				
A1	<sup>25</sup> RKKLQ <sup>30</sup> D-3,4'-AMPB-VHNF <sup>35</sup> VAL	insertion D30-V31		
A2	<sup>25</sup> RKKLQ <sup>30</sup> DV-3,4'-AMPB-HNF <sup>35</sup> VAL	insertion V31-H32		
A3	<sup>25</sup> RKKLQ <sup>30</sup> -3,4'-AMPB-VHNF <sup>35</sup> VAL	exchange D30		
A4	<sup>25</sup> RKKLQ <sup>30</sup> D-3,4'-AMPB-HNF <sup>35</sup> VAL	exchange V31		
A5	<sup>25</sup> RKKLQ <sup>30</sup> -3,4'-AMPB-HNF <sup>35</sup> VAL	exchange D30-V31		

peptide	primary sequence	modification
A6	<sup>25</sup> RKKLQ-3,4'-AMPB- <sup>30</sup> DVHNF <sup>35</sup> VAL	insertion Q29-D30
A7	<sup>25</sup> RKKL-3,4'-AMPB-Q <sup>30</sup> DVHNF <sup>35</sup> VAL	insertion L28-Q29
A8	<sup>25</sup> RK-3,4'-AMPB-KLQ <sup>30</sup> DVHNF <sup>35</sup> VAL	insertion K26-K27
A9	<sup>25</sup> R-3,4'-AMPB-KLQ <sup>30</sup> DVHNF <sup>35</sup> VAL	exchange K26
A10	<sup>25</sup> RKKLQ <sup>30</sup> DVHN-3,4'-AMPB-F <sup>35</sup> VAL	insertion N33-F34
A11	<sup>25</sup> RKKLQ <sup>30</sup> DVHNF <sup>35</sup> V-3,4'-AMPB-AL	insertion V35-A36
A12	<sup>25</sup> RKKLQ <sup>30</sup> DVHNF-3,4'-AMPB-AL	exchange V35

### Spiropyran containing peptides



# 5.1 Photocontrol of azo-modified PTH<sub>25-37</sub>-derived peptides

The aim of the initial study was to test the hypothesis, wether it is possible to control the fibrillization behaviour of the model peptide  $PTH_{25-37}$  with the 3-4'-AMPB switch, *i.e.* one isomer is able to form amyloid fibrils and the other is not. Therefore, the Fmoc-protected 3,4'-AMPB building block 4 was synthesized according to literature (Figure 5.1)<sup>167</sup> and introduced into the  $PTH_{25-37}$  backbone *via* SPPS. Peptide A4 (primary structure in Table 5.1) had the highest solubility and was therefore chosen

$$H_2N$$
 $H_2N$ 
 $NH_2$ 
 $NH_2$ 

Figure 5.1: Synthesis scheme of Fmoc-protected 3,4'-AMPB building block. 167

to be investigated in accordance to the fibrillization behaviour of both isomers (Figure 5.2). While the fibrillization kinetic was characterized by the lag time  $t_{lag}$ , which corresponds to the onset of the process, and the characteristic time  $t_{char}$ , displaying the point fluorescence reaches 50% of the stationary phase, the presence of fibrils was verified with TEM-recordings taken after distinct time points. In Figure 5.2A it is visible that fibrillization of trans-A4 is accelerated compared to the unmodified PTH<sub>25-37</sub>, while the fibrillization of the cis-isomer is inhibited. Similar conclusions can be drawn from the TEM images (Figure 5.2B), where fibrils are observed in all recordings with the exception of cis-A4, where fibrils are firstly present in the recording after 60 h.

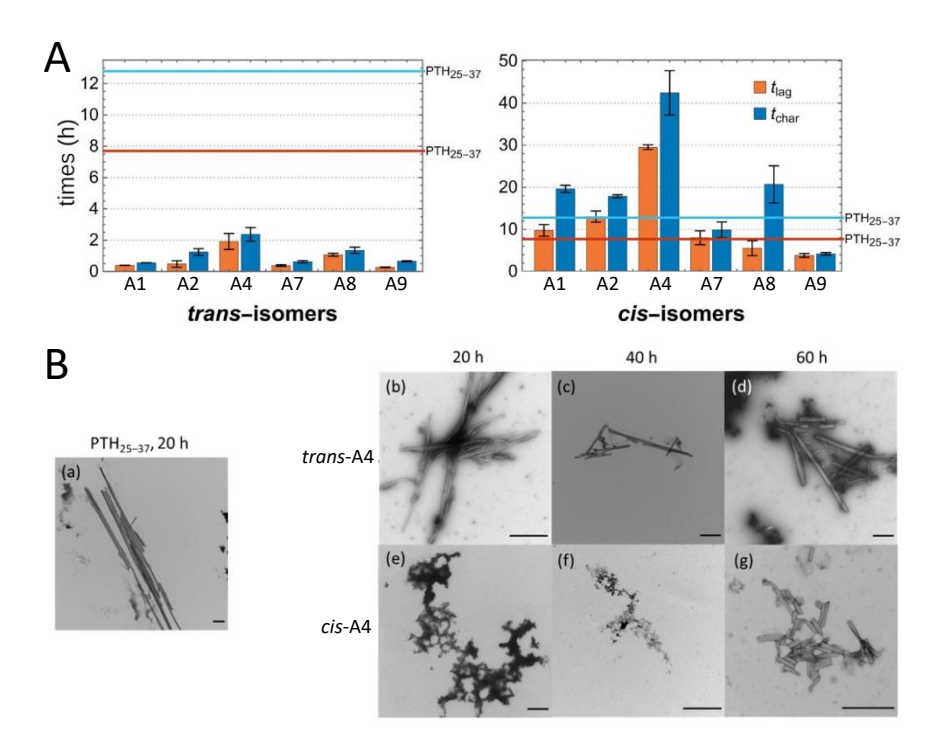


Figure 5.2: (A) Kinetic parameters  $t_{lag}$  (orange) and  $t_{char}$  (blue) of unmodified and modified PTH<sub>25-37</sub>-derived peptides. Reprinted and adapted with permission from American Chemical Society, copyright ©2024 (open access).<sup>315</sup> (B) TEM-recordings of unmodified PTH<sub>25-37</sub>, trans-A4, and cis-A4. (a), (b), and (e) were taken after 20 h. (c) and (f) after 40 h. (d) and(g) after 60 h. Scale bar = 500 nm. Reprinted and adapted with permission from MDPI, copyright ©2022 (open access).<sup>348</sup>

Based on these findings, the structural nature of fibrils formed by trans-A4 and PTH<sub>25-37</sub> was investigated using WAXS, ssNMR with <sup>13</sup>C-labeled peptides, and, combined with these data, MD simulations. While WAXS measurements could verify the fibrillar structure (Figure 5.3A,D) and allows an assumption towards the arrangement of the  $\beta$ -sheets, ssNMR measurements could prove that PTH<sub>25-37</sub>  $\beta$ -strands are arranged in a parallel manner (Figure 5.3B), while  $\beta$ -strands of trans-A4 adopt an antiparallel order (Figure 5.3E). According to the MD simulations, it is anticipated that in PTH<sub>25-37</sub> mainly the C-terminal amino acids form the  $\beta$ -sheet (Figure 5.3C). In the MD simulations of trans-A4, however, the photoswitch breaks partially the  $\beta$ -sheet, which is formed by the C- and N-terminal regions (Figure 5.3F). The antiparallel arrangement is herein favoured, as electrostatic interactions, between positively charged N-termini and negatively charged C-termini, and the  $\pi$ - $\pi$ -interactions of the azobenzene switch are stabilizing.

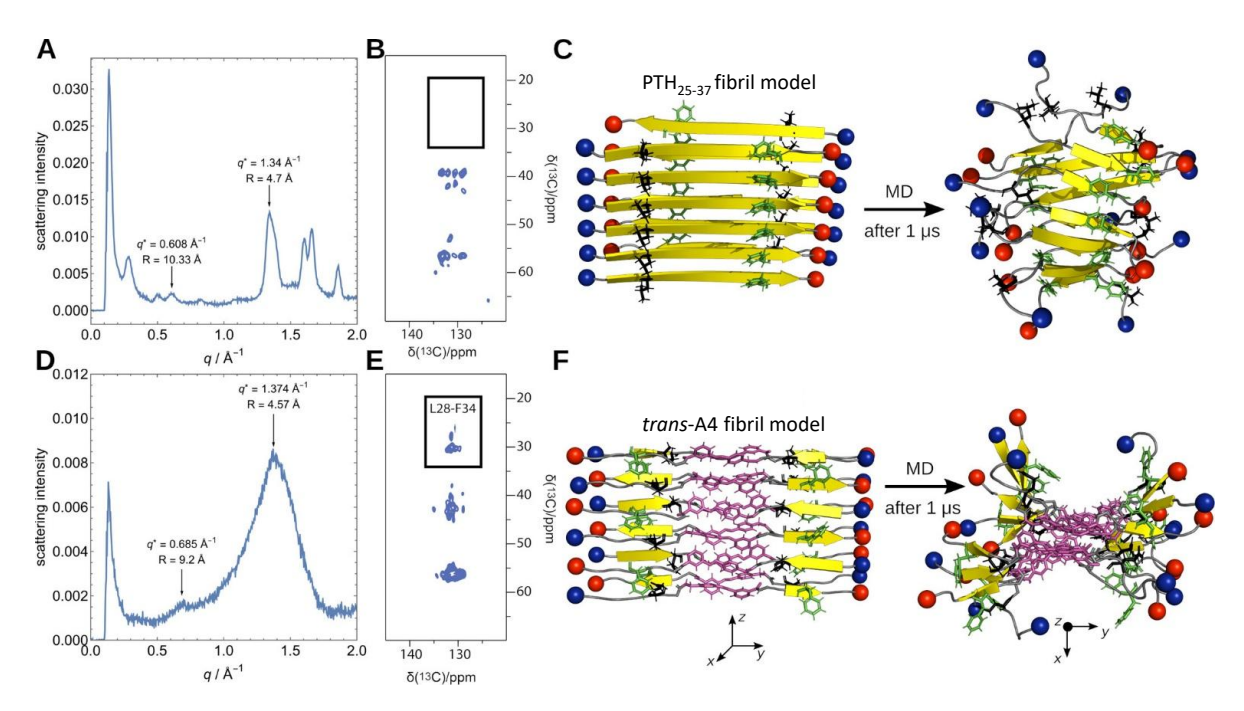


Figure 5.3: Structural investigations of fibrils of PTH<sub>25-37</sub> and *trans*-A4. (A, D) WAXS results. (B, E) ssNMR 2D  $^{13}$ C- $^{13}$ C proton driven spin diffusion spectra close to rotational resonance (mixing time 1s) of fibrils of the PTH<sub>25-37</sub> and *trans*-A4 peptide with uniformly  $^{13}$ C-labeled L28 and F34. (C, F) Fibril models of PTH<sub>25-37</sub> and *trans*-A4 constructed based on the ssNMR (left) and at the end of MD simulations (right), where  $\beta$ -sheets are shown in yellow, random coil in gray, the N- and C-termini as blue and red spheres, respectively, 3,4'-AMPB in purple, and the side chains of L28 and F34 are highlighted as black and green sticks, respectively. Note that in panel F, the structure on the right-hand side is rotated by 90° to better represent the fibrillar arrangement. Reprinted with permission from American Chemical Society, copyright ©2024 (open access).

In total twelve peptides were synthesised containing the 3,4'-AMPB switch at various positions, three bearing the switch at the N-terminal end, six in the central region and three at the C-terminus. The determination of the fibrillization parameters  $t_{lag}$  and  $t_{char}$  of both isomers (Figure 5.2) of all peptides was in accordance with the prediction drawn from the MD simulations: the *trans*-configuration does not prevent the ability to form fibrils, if placed in the N-terminal and central region, moreover, the fibrillization was significantly faster compared to the unmodified peptide due to the increased hydrophobicity and the organizing effect of the 3,4'-AMPB. The *cis*-configuration caused a delay of fibrillization, whereby the effect decreases with increasing distance to the aggregation-prone region at the C-terminus. However, if the switch is positioned in the fibril forming region, *e.g.* A12, the fibrillization is hindered for both isomers.

The reversible fibrillization was conducted with A4, as it had the highest solubility and largest difference in fibrillization between the two isomers. In Figure 5.4 the TMFAs are shown, subsequently followed by a degradation process. The presence of a new fibrillization process, comprising of lag phase, growth phase and stationary phase for each cycle indicates that monomers in a sufficient amount were released during each fibril degradation by  $trans \rightarrow cis$ -photoisomerization.

Thus, the herein described system is the first report of an amyloidogenic peptide model, which is able to undergo reversibly fibril formation/fibril degradation cycles *via* light. Furthermore, the results showcased the importance of the strategical placement of the photoswitchable entity in the peptide.

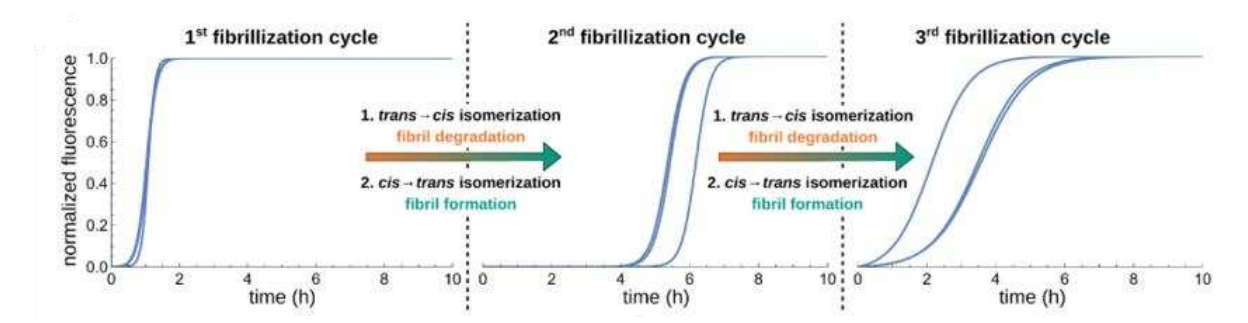


Figure 5.4: Three (de)-aggregation cycles via photoisomerization of A4. Fitted signals of TMFAs of each fibrillization of trans-A4 followed by fibril degradation through  $trans \rightarrow cis$ -isomerization and reisomerization towards the trans-form. Reprinted with permission from American Chemical Society, copyright ©2024 (open access).

# **5.2** Co-fibrillization of azo-modified $PTH_{25-37}$ and PTH(-derived peptides)

From previous studies it is known that heterologous sequences are known to undergo cross-amyloid aggregation<sup>349</sup> and that as well synthetic  $\beta$ -turn modified  $A\beta$ -derivatives are able to catalytically effect the fibrillization of the Alzheimer peptide  $A\beta_{1-40}$ .<sup>350</sup> This raises the question, whether it is possible to modulate fibrillization of the full-length PTH with the azobenzene modified peptides as well. As the fibrils of PTH serve as an inactive peptide storage, the monomers released upon degradation represents the active form. Thus, controlled (de)-fibrillization would be a promising method for regulating the bioavailability of the hormone or triggering drug release.

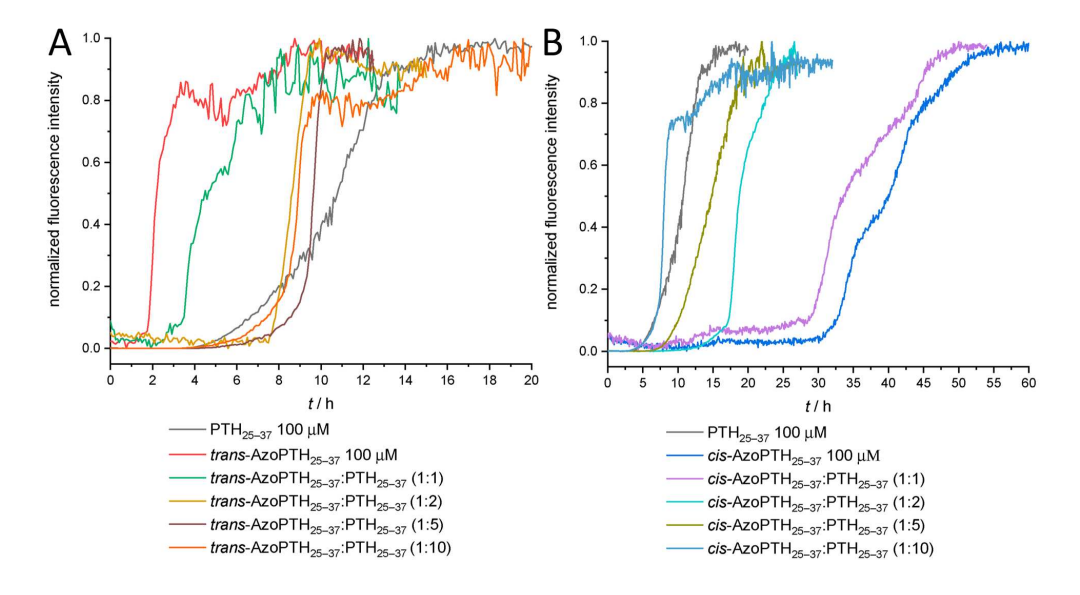


Figure 5.5: TMFA of mixtures of A4 and unmodified PTH<sub>25-37</sub>. (A) *trans*-A4. (B) *cis*-A4. Reprinted and adapted with permission from MDPI, copyright ©2022 (open access).  $^{348}$ 

A4 has proven to be suitable to catalytically modulate the fibrillization process of PTH and PTH-derived peptides. In case of  $PTH_{25-37}$  mixtures (Figure 5.5) the fibrillization process was affected in the same

manner as for the modified peptide: trans-A4 accelerated the fibrillizaiton, while cis-A4 hindered the process. Even the full-length peptide is affected by the A4-isomers (Figure 5.6). Unfortunately,  $t_{lag}$  of PTH<sub>1-84</sub> is significantly larger than the half-life time of cis-A4. Nevertheless, it is observable that the cis-isomer hinders the fibrillization compared to the trans-isomer, however, both isomers still accelerate the aggregation compared to the native peptide. Interestingly, the morphology of the fibrils is altered in presence of A4. While the native peptide produces curly fibrils, only straight fibrils were observable in the case of the mixture.

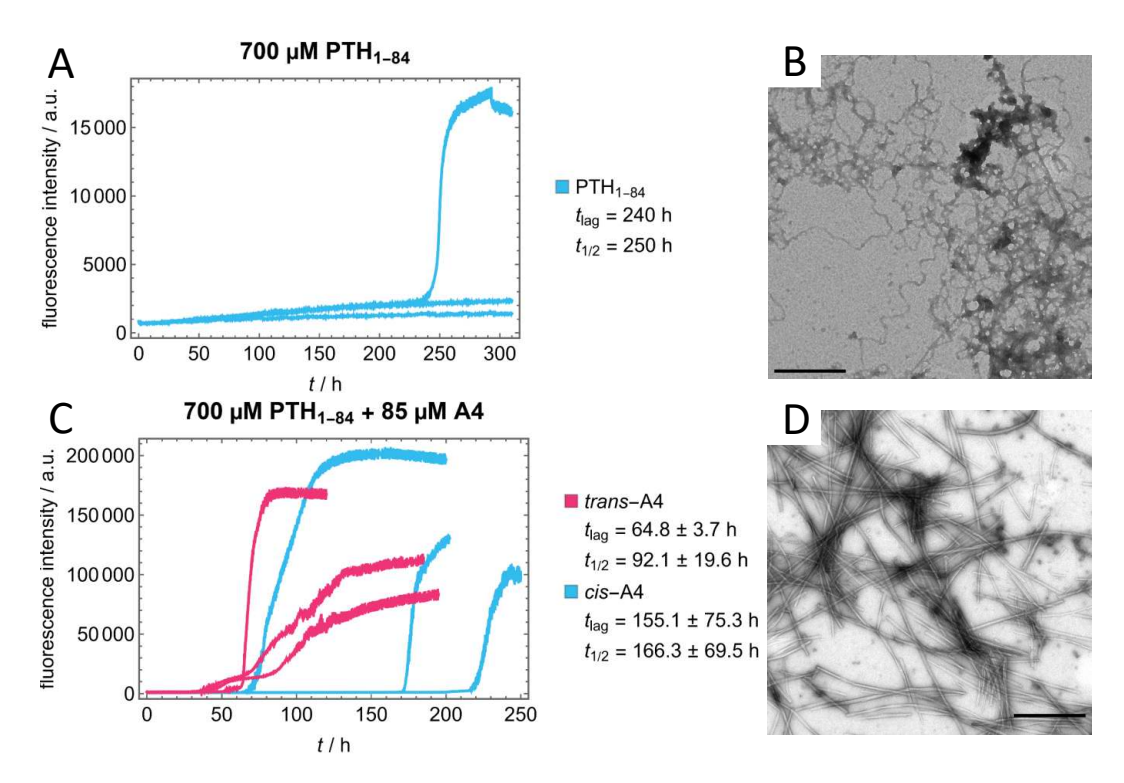


Figure 5.6: (A) TMFA and kinetic parameters of  $PTH_{1-84}$ . (B) TEM recording of  $PTH_{1-84}$  fibrils. (A) TMFA and kinetic parameters of  $PTH_{1-84}$ -A4-mixture. (B) TEM recording of heterologous fibrils from  $PTH_{1-84}$  and *trans*-A4. Scale bar = 500 nm.

Even if the half-life time of *cis*-A4 was too short, this light-triggered approach is a promising method regarding the controlled drug delivery of PTH. It is clearly visible that the A4 isomers had a different influence on the fibrillization of native PTH. In further studies the use of another azobenzene moiety with a higher stability of the *cis*-form, *e.g. ortho*-fluoro azobenzenes<sup>88</sup> or *ortho*-methoxy azobenzenes, <sup>87</sup> could enable full control of the fibrillization of PTH.

# 5.3 Novel spiropyran building blocks for SPPS

While for the azobenzene class several suitable building blocks for SPPS exist, <sup>161,167,351</sup> there is no known example of a spiropyran backbone modification suitable for SPPS using either Boc-chemistry or Fmoc-chemistry. Thus, during this thesis spiropyran backbone modifications, FASC and the SAFC (Figure 5.7), were designed. FASC contains the N-terminus at the indolene unit and the C-terminus

at the chromene, while SAFC bears the N-terminus at the chromene unit and the C-terminus at the indolene unit. A facile synthetic route was elaborated to obtain both switches as ready-to-use building blocks for SPPS, either Boc- (9, 18) or Fmoc-protected (10, 19). To investigate their behaviour in the peptide backbone, the photoswitches were introduced using SPPS with Fmoc chemistry at similar positions as the 3,4'-AMPB photoswitch in 5.1 and 5.2 (see Table 5.1, S1-10). Unfortunately, it was not possible to investigate the fibrillization behaviour of the SP- and MC- isomer of the modified peptides, as the spiropyrans are unstable at neutral pH. Nevertheless, it was proven that the FASC and SAFC switch are stable at acidic pH and the photophysical properties were charaterized for different pH values. The herein presented photoswitchable entities are the first reported spiropyran building blocks for SPPS and extend the possible modification options in peptide chemistry by a powerful tool even if future research has taken improvements in pH stability in account.

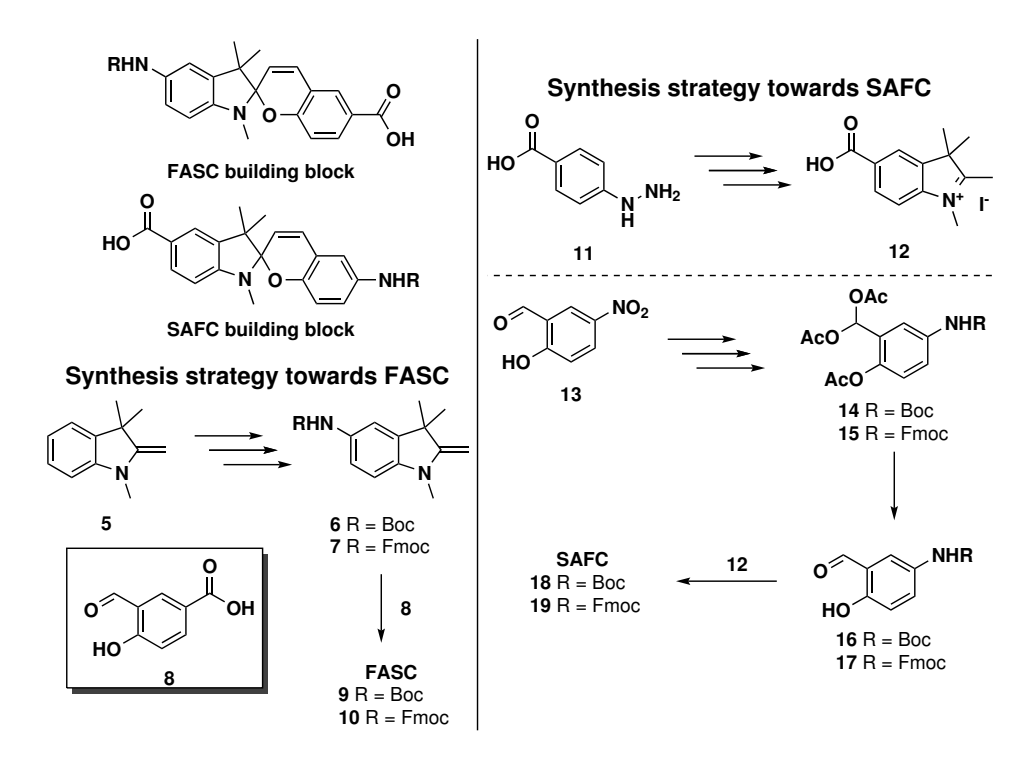


Figure 5.7: Synthesis schemes of Boc- and Fmoc-protected FASC and SAFC building blocks.

In this thesis photoswitchable PTH-derived peptides were successfully generated. It was demonstrated that the azobenzene moiety is able to influence the fibrillization process in different ways, depending on the configuration of the azo bond. This made it possible to control the fibrillization in a reversible and switchable manner. In addition, the structural understanding of the fibrillization of  $PTH_{25-37}$  was improved and it was shown that azobenzene-modified peptides have a catalytic effect on the fibrillization of  $PTH_{25-37}$  and PTH. It could therefore be a potential method for modulating the bioavailability of hormones.

# **Syntheses**

The following compounds were synthesized and characterized together with Niclas Starke during his master thesis.

NHFmoc HOOC N, N HFmoc 
$$O_2N$$
  $O_2N$   $O_2N$ 

# 6.1 Azobenzenes

# (9H-Fluoren-9-yl)methyl (4-aminobenzyl)carbamate (2)

4-Aminobenzylamine 1 (2.5 g, 20.5 mmol, 1 eq.) was dissolved in a mixture of 24 mL MeCN and 2 mL DMF and triethylamine (TEA) (3 mL, 22.5 mmol, 1.1 eq.) was added. Fmoc-OSu (7.6 g, 22.5 mmol, 1.1 eq.) was dissolved in 50 mL MeCN and slowly added over a duration of 90 min to the reaction solution at ambient temperature. The formed precipitate was filtrated and washed with  $EtO_2$  and water. Compound 2 was obtained as a white powder (6.6 g, 19.2 mmol, 84%).

Analytical data match reported literature values.<sup>352</sup>

 $\mathbf{R}_f = 0.2 \text{ (hexane:EE / 3:2)}.$ 

6.1. AZOBENZENES 91

<sup>1</sup>**H-NMR** (500 MHz, CDCl<sub>3</sub>):  $\delta$  = 7.76 (dt, J = 7.6, 1.0 Hz, 2H), 7.59 (d, J = 7.5 Hz, 2H), 7.40 (tt, J = 7.5, 0.9 Hz, 2H), 7.31 (td, J = 7.5, 1.2 Hz, 2H), 7.07 (d, J = 7.9 Hz, 2H), 6.64 (d, J = 8.4 Hz, 2H), 4.98 (s, 1H), 4.44 (d, J = 6.9 Hz, 2H), 4.31–4.16 (m, 3H), 3.65 (s, 2H).

<sup>13</sup>**C-NMR** (125 MHz, CDCl<sub>3</sub>):  $\delta$  = 156.3, 145.9, 144.0, 141.3, 129.0, 128.2, 127.6, 127.0, 125.1, 120.0, 115.2, 66.6, 47.3, 44.8.

**MS** (ESI+, MeCN/MeOH):  $m/z = 383.11 \text{ [M+K]}^+$ .

# (trans)-3-((4-(((((9H-Fluoren-9-yl)methoxy)carbonyl)amino)-methyl)phenyl)diazenyl)benzoic acid (4)

3-Aminobenzoic acid (2 g, 14.6 mmol) were suspended in 36 mL dichloromethane (DCM) and Oxone (17.9 g, 29 mmol) dissolved in 160 mL water was added dropwise. The reaction mixture is stirred at ambient temperature for 3.5 h. The formed precipitate is seperated through filtration, washed with water and dried *in vacuo*. 3-Nitrosobenzoic acid 3 (1.8 g, 13.2 mmol) were obtained as a greenish solid and used without further purification. Compound 3 (1.8 g, 13.2 mmol, 2 eq.) was dissolved in 150 mL DMSO and 150 mL acetic acid were added. The solution was degassed for 30 min with nitrogen and compound 2 (2.28 g, 6.6 mmol, 1 eq.) was added. The reaction solution was stirred for 3 d at ambient temperature and 300 mL water were added. The solution was extracted three times with ethyl acetate (EE). The combined organic phases were dried over  $Na_2SO_4$  and the solvent was removed *in vacuo*. The residue was purified by flash chromatography on normal phase silica gel (solvent A: DCM + 0.1% FA, solvent B: MeOH + 0.1% FA, 9% A) and compound 4 was obtained as an orange solid (1.5 g, 3.2 mmol, 47%).

Analytical data match reported literature values. 167

 $\mathbf{R}_f = 0.7 \text{ (hexane:EE} + 0.1\% \text{ FA} / 1:4).$ 

<sup>1</sup>**H-NMR** (500 MHz, DMSO- $d_6$ ):  $\delta$  = 8.38 (t, J = 1.8 Hz, 1H), 8.13 (ddt, J = 10.5, 7.7, 1.4 Hz, 2H), 7.90 (dd, J = 7.8, 5.1 Hz, 4H), 7.76–7.68 (m, 3H), 7.47–7.39 (m, 4H), 7.34 (td, J = 7.4, 1.1 Hz, 2H), 4.40 (d, J = 6.7 Hz, 2H), 4.30 (d, J = 6.1 Hz, 2H), 4.25 (t, J = 6.8 Hz, 1H).

<sup>13</sup>**C-NMR** (125 MHz, DMSO- $d_6$ ): δ = 167.1, 156.9, 152.3, 151.2, 144.5, 144.3, 141.2, 132.6, 132.2, 130.4, 128.4, 128.1, 127.8, 127.5, 125.6, 123.3, 122.6, 120.6, 65.8, 47.3, 43.9.

**MS** (ESI+, MeCN/MeOH):  $m/z = 516.13 \text{ [M+K]}^+$ .

# **6.2** Spiropyrans

## 1,3,3-Trimethyl-2-methylene-5-nitroindoline (20)

1,3,3-Trimethyl-2-methylenindolin **5** (10 g, 57.7 mmol, 1 eq.) was slowly added to 60 mL concentrated  $H_2SO_4$  and cooled down to 0°C. NaNO<sub>3</sub> (7.9 g, 63.5 mmol, 1.1 eq.) was added in small portions and the reaction mixture is stirred for 1 h. The solution was poured onto 100 g ice and neutralized with solid  $Na_2CO_3$ . The formed precipitate was filtrated and recrystallized in a mixture of acetone/water (1:1). Compound **20** was obtained as a red solid. (7.3 g, 33.2 mmol, 58%).

Analytical data match reported literature values.<sup>353</sup>

 $\mathbf{R}_f = 0.7$  (hexane:EE / 3:2).

<sup>1</sup>**H-NMR** (500 MHz, CDCl<sub>3</sub>):  $\delta$  = 8.12 (dd, J = 8.8, 2.3 Hz, 1H), 7.92 (d, J = 2.3 Hz, 1H), 6.51 (d, J = 8.8 Hz, 1H), 4.16–4.06 (m, 2H), 3.12 (s, 3H), 1.36 (s, 6H).

<sup>13</sup>**C-NMR** (125 MHz, CDCl<sub>3</sub>): δ = 161.2, 151.5, 140.0, 138.2, 126.2, 118.1, 103.9, 78.9, 43.4, 29.7, 29.1.

**MS** (ESI+, MeCN/MeOH):  $m/z = 225.122 \text{ [M+Li]}^+$ .

### 1,3,3-Trimethyl-2-methyleneindolin-5-amine (21)

Compound **20** (2 g, 9.1 mmol, 1 eq.) and dried tin(II) chloride (10.4 g, 55 mmol, 6 eq.) were dissolved in 60 mL concentrated aqueous hydrogen chloride solution and refluxed for 2 h. The reaction solution was alkalinized and extracted three times with 60 mL Et<sub>2</sub>O. The organic phases were combined and the solvent removed *in vacuo*. The residue was recristallized in hexane and compound **21** was obtained as a green solid (1 g, 5.3 mmol, 58%).

Analytical data match reported literature values.<sup>354</sup>

 $\mathbf{R}_f = 0.1 \text{ (DCM:MeOH} + 0.1\% \text{ FA} / 9:1).$ 

6.2. SPIROPYRANS 93

<sup>1</sup>**H-NMR** (500 MHz, CDCl<sub>3</sub>):  $\delta$  = 6.56 (d, J = 2.3 Hz, 1H), 6.51 (dd, J = 8.1, 2.3 Hz, 1H), 6.35 (d, J = 8.0 Hz, 1H), 3.79–3.72 (m, 2H), 3.35 (s, 2H), 2.99 (s, 3H), 1.33 (s, 6H).

<sup>13</sup>**C-NMR** (125 MHz, CDCl<sub>3</sub>): δ = 163.4, 139.7, 138.9, 138.5, 114.1, 111.3, 105.1, 71.5, 44.4, 29.9, 29.0.

**MS** (ESI+, MeCN/MeOH):  $m/z = 189.14 \text{ [M+H]}^+$ .

## tert-Butyl (1,3,3-trimethyl-2-methyleneindolin-5-yl)carbamate (6)

Compound **21** (585 mg, 3.1, mmol, 1 eq.) was dissolved in 40 mL THF. Boc<sub>2</sub>O (680 mg, 3.1 mmol, 1 eq.) and TEA (440  $\mu$ L, 3.1 mmol, 1 eq.) were added under a nitrogen atmosphere and the reaction mixture was stirred at ambient temperature for 18 h. The solvent was removed *in vacuo* and the residue was dissolved in 50 mL DCM. The solution was extracted three times with 50 mL of an aqueous solution with 5% acetic acid. The combined aqueous phases were washed two times with 50 mL Et<sub>2</sub>O and the solution was made alkaline (pH 9–10) with NaHCO<sub>3</sub>. The aqueous solution was extracted three times with 50 mL DCM. The combined organic phases were dried over Na<sub>2</sub>SO<sub>4</sub> and the solvent was removed *in vacuo*. The residue of compound **6** (yellowish oil, 760 mg) was used without further purification.

 $\mathbf{R}_f = 0.4 \text{ (DCM:MeOH / 19:1)}.$ 

<sup>1</sup>**H-NMR** (400 MHz, CDCl<sub>3</sub>)  $\delta$  = 7.17 (s, 1H), 7.02–6.90 (m, 1H), 6.41 (d, J = 8.3 Hz, 1H), 6.26 (s, 1H), 3.79 (q, J = 2.0 Hz, 2H), 2.99 (s, 3H), 1.49 (s, 9H), 1.31 (s, 6H).

<sup>13</sup>**C-NMR** (100 MHz, CDCl<sub>3</sub>)  $\delta$  = 163.0, 155.0, 142.7, 138.2, 129.7, 118.7, 114.7, 104.5, 79.6, 72.7, 44.3, 29.9, 28.9, 28.4.

**MS** (ESI+, MeCN/MeOH):  $m/z = 289.19 \text{ [M+H]}^+$ .

### (9H-Fluoren-9-yl)methyl (1,3,3-trimethyl-2-methyleneindolin-5-yl)carbamate (7)

To a mixture of compound 21 (0.5 g, 2.7 mmol, 1 eq.) and Fmoc-Cl (0.82 g, 3.2 mmol, 1.2 eq.) were added 4 mL water and the suspension was stirred at  $60^{\circ}$ C for 2 h. The reaction suspension was neutralized with saturated aqueous NaHCO<sub>3</sub> solution and extracted three times with 60 mL DCM. The

organic phases were combined and the solvent removed *in vacuo*. The residue was purified by flash chromatography on normal phase silica gel (solvent A: DCM + 0.1% FA, solvent B: MeOH + 0.1% FA, 95% A) and compound **7** was obtained as a lightpurple solid. (0.38 g, 0.93 mmol, 35%).

 $\mathbf{R}_f = 0.2 \text{ (DCM:MeOH} + 0.1\% \text{ FA} / 9:1).$ 

<sup>1</sup>**H-NMR** (500 MHz, CDCl<sub>3</sub>):  $\delta$  = 7.78 (d, J = 7.5 Hz, 2H), 7.69–7.52 (m, 2H), 7.41 (t, J = 7.4 Hz, 2H), 7.37–7.29 (m, 2H), 7.24–7.15 (m, 1H), 7.05 (s, 1H), 6.52 (s, 1H), 6.45 (d, J = 8.3 Hz, 1H), 4.50 (d, J = 6.8 Hz, 2H), 4.28 (t, J = 6.9 Hz, 1H), 3.84 (q, J = 2.0 Hz, 2H), 3.02 (s, 3H), 1.34 (s, 6H).

<sup>13</sup>**C-NMR** (125 MHz, CDCl<sub>3</sub>):  $\delta$  = 162.8, 154.1, 143.9, 143.2, 141.3, 138.3, 129.2, 127.7, 127.1, 125.0, 120.0, 119.2, 114.9, 104.6, 73.1, 66.7, 47.2, 44.3, 29.9, 28.9.

**IR** (ATR): v = 3303w, 2959w, 1697s, 1499s, 1208s cm<sup>-1</sup>.

**UV/Vis** (c = 0.06  $\mu$ mol mL<sup>-1</sup> in MeOH):  $\lambda_{max,1} = 289.2$ ,  $\lambda_{max,2} = 277.3$ ,  $\lambda_{max,3} = 265.3$  nm.

**HR-MS** (ESI+, MeCN/MeOH): calcd. for  $[C_{27}H_{26}N_2O_2+H]^+ = 411.210$  found: 411.210.

# 5'-((*tert*-Butoxycarbonyl)amino)-1',3',3'-trimethylspiro[chromene-2,2'-indoline]-6-carboxylic acid (9)

The unpurified residue of compound 6 (700 mg, ~2.4 mmol, 1 eq.) and 3-formyl-4-hydroxybenzoic acid 8 (400 mg, 2.43 mmol, 1 eq.) were dissolved in 50 mL MeCN and the solution was refluxed (heated with an oil bath) for 4.5 h under a nitrogen atmosphere. The solvent was removed *in vacuo* and the residue was purified by flash chromatography in normal phase silica (solvent A: hexane + 0.1% FA, solvent B: EE + 0.1% FA, 60% A). Compound 9 was obtained as a redish solid (0.680 mg, 1.56 mmol, 64%).

 $\mathbf{R}_f = 0.4 \text{ (hexane:EE} + 0.1\% \text{ FA} / 3:2).$ 

<sup>1</sup>**H-NMR** (500 MHz, DMSO- $d_6$ ):  $\delta$  = 12.65 (s, 1H), 8.97 (s, 1H), 7.80 (d, J = 2.3 Hz, 1H), 7.68 (dd, J = 8.5, 2.3 Hz, 1H), 7.25 (s, 1H), 7.18–6.99 (m, 2H), 6.74 (d, J = 8.6 Hz, 1H), 6.48 (d, J = 8.3 Hz, 1H), 5.83 (d, J = 10.3 Hz, 1H), 2.61 (s, 3H), 1.46 (s, 9H), 1.17 (s, 3H), 1.10 (s, 3H).

<sup>13</sup>**C-NMR** (125 MHz, DMSO- $d_6$ ): δ = 166.7, 157.7, 153.1, 143.2, 136.3, 131.3, 129.0, 128.5, 122.7, 122.0, 119.8, 118.4, 117.5, 114.4, 113.6, 106.7, 105.3, 78.4, 51.6, 28.7, 28.2, 25.6, 19.7.

**IR** (ATR): v = 3319w, 3069w, 2973br, 1683s, 1158s cm<sup>-1</sup>.

**HR-MS** (ESI+, MeCN/MeOH): calcd. for  $[C_{25}H_{28}N_2O_5Na]^+ = 459.1890$  found 459.1909.

6.2. SPIROPYRANS 95

5'-(((9H-Fluoren-9-yl)methoxy)carbonyl)amino)-1',3',3'-tri-methylspiro[chromene-2,2'-indoline]-6-carboxylic acid (10)

Compound **7** (0.3 g, 0.73 mmol, 1 eq.) and 3-formyl-4-hydroxybenzoic acid **8** (0.16 g, 0.95 mmol, 1.3 eq.) were dissolved in 25 mL MeCN for 6 h and refluxed under a nitrogen atmosphere. The solvent was removed *in vacuo* and the residue was purified by flash chromatography on normal phase silica gel (solvent A: hexane + 0.1% FA, solvent B: EE + 0.1% FA, 60% A). compound **10** was obtained as a redish solid (0.17 g, 0.3 mmol, 42%).

 $\mathbf{R}_f = 0.5 \text{ (hexane:EE} + 0.1\% \text{ FA} / 3:2).$ 

<sup>1</sup>**H-NMR** (500 MHz, DMSO- $d_6$ ):  $\delta$  = 12.60 (s, 1H), 9.40 (s, 1H), 7.89 (d, J = 7.0 Hz, 2H), 7.79 (d, J = 2.2 Hz, 1H), 7.77–7.69 (m, 2H), 7.67 (dd, J = 8.5, 2.2 Hz, 1H), 7.41 (t, J = 7.4 Hz, 2H), 7.34 (t, J = 7.4 Hz, 2H), 7.23 (s, 1H), 7.15 (s, 1H), 7.10 (d, J = 10.5 Hz, 1H), 6.73 (d, J = 8.5 Hz, 1H), 6.49 (d, J = 8.3 Hz, 1H), 5.82 (d, J = 10.2 Hz, 1H), 4.41 (d, J = 6.9 Hz, 2H), 4.28 (t, J = 6.9 Hz, 1H), 2.60 (s, 3H), 1.17–1.07 (m, 6H).

<sup>13</sup>C-NMR (125 MHz, DMSO- $d_6$ ): δ = 167.2, 158.1, 154.2, 144.3, 141.2, 137.3, 136.9, 131.8, 131.2, 129.5, 129.0, 128.1, 127.6, 125.6, 123.2, 120.6, 120.2, 118.9, 118.0, 114.9, 107.3, 105.7, 65.9, 52.1, 47.2, 40.6, 40.4, 40.3, 40.1, 39.9, 39.8, 39.6, 29.2, 26.1, 20.1.

**IR** (ATR):  $\nu = 3338$ w, 2968br, 1693s, 1234m, 1208s cm<sup>-1</sup>.

**UV/Vis** (c = 0.46  $\mu$ mol mL<sup>-1</sup> in MeOH):  $\lambda_{max,1} = 443.7$  nm.

**HR-MS** (ESI+, MeCN/MeOH): calcd. for  $[C_{35}H_{30}N_2O_5]^+ = 558.220$  found 558.214.

Ethyl 5'-((((9*H*-fluoren-9-yl)methoxy)carbonyl)amino)-1',3',3'-trimethylspiro[chromene-2,2'-indoline]-6-carboxylate (22)

Compound 10 (0.15 g, 0.27 mmol, 1 eq.) was dissolved in a mixture of 30 mL ethanol and 3 mL concentrated  $H_2SO_4$  and the solution was refluxed for 2 h. Subsequently, the reaction solution was neutralized with saturated aqueous NaHCO<sub>3</sub> solution and extracted 3 time s with 50 mL EE. The combined organic phases were dried over Na<sub>2</sub>SO<sub>4</sub> and the solvent was removed *in vacuo*. The residue

was purified by flash chromatography on normal phase silica gel (solvent A: hexane + 0.1% FA, solvent B: EE + 0.1% FA, 90% A) and compound **22** was obtained as a purple solid (0.09 g, 0.15 mmol, 57%).

 $\mathbf{R}_f = 0.5 \text{ (hexane:EE} + 0.1\% \text{ FA} / 4:1).$ 

<sup>1</sup>**H-NMR** (500 MHz, CDCl<sub>3</sub>):  $\delta$  = 9.42 (s, 1H), 7.91 (d, J = 7.5 Hz, 2H), 7.83 (d, J = 2.2 Hz, 1H), 7.74 (s, 2H), 7.71 (dd, J = 8.6, 2.2 Hz, 1H), 7.43 (t, J = 7.4 Hz, 2H), 7.35 (t, J = 7.4 Hz, 2H), 7.24 (s, 1H), 7.20–7.09 (m, 2H), 6.78 (d, J = 8.6 Hz, 1H), 6.51 (d, J = 8.3 Hz, 1H), 5.85 (d, J = 10.3 Hz, 1H), 4.43 (d, J = 6.8 Hz, 1H), 4.33–4.21 (m, 3H), 1.29 (t, J = 7.1 Hz, 3H), 1.17 (s, 3H), 1.10 (s, 1H).

<sup>13</sup>**C-NMR** (125 MHz, CDCl<sub>3</sub>):  $\delta$  = 165.7, 158.4, 154.2, 144.3, 141.2, 136.9, 131.6, 129.4, 128.8, 128.1, 127.6, 125.6, 122.3, 120.6, 120.4, 119.1, 118.9, 115.1, 115.2, 107.3, 105.8, 65.9, 60.8, 52.1, 47.2, 29.1, 26.1, 20.1, 14.7.

**IR** (ATR):  $\nu = 3320$ br, 2959w, 1711s, 1486m, 1203s cm<sup>-1</sup>.

UV/Vis (c = 0.13  $\mu$ mol mL<sup>-1</sup> in MeOH):  $\lambda_{max,1} = 288.4$ ,  $\lambda_{max,1} = 277.6$  nm.

**HR-MS** (ESI+, MeCN/MeOH): calcd. for  $[C_{35}H_{34}N_2O_5+Li]^+ = 593.261$  found: 593.262.

## 2,3,3-Trimethyl-3*H*-indole-5-carboxylic acid (23)

4-Hydrazinobenzoic acid **11** (5 g, 33 mmol, 1 eq.) and 3-methyl-2-butanone (5 ml, 59 mmol, 1.8 eq.) were added to 50 mL acetic acid and refluxed for 16 h. The solvent was removed *in vacuo*, the residue redissolved in 50 mL DCM and neutralized with saturated aqueous NaHCO<sub>3</sub>-solution. The combined organic phases were dried over Na<sub>2</sub>SO<sub>4</sub> and the solvent was removed *in vacuo* to obtain compound **23** as an orange solid (1.3 g, 6.4 mmol, 19%).

Analytical data match reported literature values.<sup>355</sup>

 $\mathbf{R}_f = 0.7 \text{ (DCM:MeOH} + 0.1\% \text{ FA} / 9:1).$ 

<sup>1</sup>**H-NMR** (500 MHz, CDCl<sub>3</sub>):  $\delta$  = 12.76 (s, 1H), 7.97 (d, J = 1.6 Hz, 1H), 7.90 (dd, J = 8.1, 1.5 Hz, 1H), 7.49 (dd, J = 8.0, 1.2 Hz, 1H), 2.23 (s, 3H), 1.25 (s, 6H).

<sup>13</sup>**C-NMR** (125 MHz, CDCl<sub>3</sub>): δ = 192.1, 167.9, 157.9, 146.6, 130.0, 127.7, 123.2, 119.6, 53.9, 22.7, 15.8.

**MS** (ESI+, MeCN/MeOH):  $m/z = 204.10 [M+H]^+$ .

#### 5-Carboxy-1,2,3,3-tetramethyl-3*H*-indol-1-ium iodide (12)

Compound **23** (5 g, 25 mmol, 1 eq.) was dissolved in 70 mL toluene and 35 mL MeCN under nitrogen atmosphere. Iodomethane (1.8 ml, 30 mmol, 1.2 eq.) was added and the reaction mixture was refluxed for 16 h. The formed precipitate was separated, washed with hexane and cold ethanol and dried. Compound **12** was obtained as an orange-pinkish solid (2.9 g, 8.4 mmol, 34%).

Analytical data match reported literature values.<sup>355</sup>

 $\mathbf{R}_f = 0.2 \text{ (DCM:MeOH} + 0.1\% \text{ FA} / 9:1).$ 

<sup>1</sup>**H-NMR** (400 MHz, DMSO- $d_6$ ):  $\delta$  = 8.35 (s, 1H), 8.17 (d, J = 8.4 Hz, 1H), 8.02 (d, J = 8.4 Hz, 1H), 3.98 (s, 3H), 2.80 (s, 3H), 1.55 (s, 6H).

<sup>13</sup>**C-NMR** (100 MHz, DMSO- $d_6$ ):  $\delta$  = 199.5, 166.9, 145.7, 142.4, 132.0, 130.8, 124.7, 115.8, 54.7, 35.5, 21.9, 15.0.

**MS** (ESI+, MeCN/MeOH):  $m/z = 218.12 \text{ [M]}^+$ .

#### (2-Acetoxy-5-nitrophenyl)methylene diacetate (24)

2-Hydroxy-5-nitrobenzaldehyd 13 (2.5 g, 15 mmol, 1 eq.) was dissolved in 50 mL acetic anhydride. Three drops of concentrated  $H_2SO_4$  were added and the solution was stirred for 1 h under nitrogen atmosphere at ambient temperature. The reaction mixture was poured in 500 mL water and stirred for 30 min. The formed precipitate was separated, washed with water and dried. Compound 24 was obtained as white crystals (3.57 g, 11.5 mmol, 76%).

Analytical data match reported literature values.<sup>356</sup>

 $\mathbf{R}_f = 0.2$  (hexane:EE/ 8:2).

<sup>1</sup>**H-NMR** (400 MHz, CDCl<sub>3</sub>):  $\delta$  = 8.53 (d, J = 2.8 Hz, 1H), 8.29 (dd, J = 8.9, 2.8 Hz, 1H), 7.93 (s, 1H), 7.35 (d, J = 8.9 Hz, 1H), 2.38 (s, 3H), 2.13 (s, 6H).

<sup>13</sup>**C-NMR** (100 MHz, CDCl<sub>3</sub>):  $\delta$  = 168.3, 168.2, 152.7, 145.6, 129.6, 125.8, 124.4, 123.8, 84.1, 20.8, 20.6.

**MS** (ESI+, MeCN/MeOH):  $m/z = 318.08 \text{ [M+Li]}^+$ .

#### (2-Acetoxy-5-aminophenyl)methylene diacetate (25)

Compound **24** (1.5 g, 4.8 mmol, 1 eq.) was dissolved in 40 mL ethanol and  $PtO_2$  (109 mg, 480  $\mu$ M, 0.1 eq.) was added. The reaction suspension was stirred for 12 h under a hydrogen atmosphere (5 bar) at ambient temperature. The suspension was filtrated over Celite®and the solvent of the filtrate was removed *in vacuo*. The residue was purified by flash chromatography on normal phase silica gel (solvent A: hexane, solvent B: EE, 60% A) and compound **25** was obtained as a yellowish solid (0.95 g, 3.4 mmol, 70%).

Analytical data match reported literature values.<sup>356</sup>

 $\mathbf{R}_f = 0.4 \text{ (hexane:EE / 1:1)}.$ 

<sup>1</sup>**H-NMR** (500 MHz, CDCl<sub>3</sub>):  $\delta$  = 7.79 (s, 1H), 6.95–6.83 (m, 2H), 6.69 (dd, J = 8.7, 2.8 Hz, 1H), 3.72 (s, 2H), 2.30 (s, 3H), 2.10 (s, 6H).

<sup>13</sup>**C-NMR** (125 MHz, CDCl<sub>3</sub>): δ = 170.1, 168.4, 144.6, 140.1, 128.1, 123.8, 117.0, 113.5, 85.4, 20.8, 20.7.

**MS** (ESI+, MeCN/MeOH):  $m/z = 288.11 \text{ [M+Li]}^+$ .

#### (2-Acetoxy-5-((tert-butoxycarbonyl)amino)phenyl)methylene diacetate (14)

Compound **25** (1 g, 3.6 mmol, 1 eq.) and Boc<sub>2</sub>O (1.55 g, 7 mmol, 2 eq.) were dissolved in 10 mL DCM and stirred at ambient temperature for 12 h under a nitrogen atmosphere. The solvent was removed *in vacuo* and the residue was purified by flash chromatography on normal phase silica gel (solvent A: hexane, solvent B: EE, 80% A) to obtain compound **14** as a transparent gel (0.57 g, 1.5 mmol, 42%).

Analytical data match reported literature values.<sup>356</sup>

 $\mathbf{R}_f = 0.6 \text{ (hexane:EE / 3:2)}.$ 

<sup>1</sup>**H-NMR** (400 MHz, CDCl<sub>3</sub>):  $\delta$  = 7.84 (s, 1H), 7.64 (d, J = 2.5 Hz, 1H), 7.41 (d, J = 8.8, 2.7 Hz, 1H), 7.03 (d, J = 8.8 Hz, 1H), 6.52 (s, 1H), 2.31 (s, 3H), 2.09 (s, 6H), 1.52 (s, 9H).

<sup>13</sup>**C-NMR** (100 MHz, CDCl<sub>3</sub>): δ = 169.6, 168.4, 152.5, 143.3, 136.5, 128.2, 123.7, 120.7, 117.6, 85.1, 80.9, 28.3, 20.8, 20.7.

IR (ATR): v = 3316m, 2985w, 1764s, 1689s, 1151s cm<sup>-1</sup>.

**UV/Vis** (c = 0.07  $\mu$ mol mL<sup>-1</sup> /MeOH):  $\lambda_{max,1} = 287$  nm,  $\lambda_{max,2} = 242$  nm.

**MS** (ESI+, MeCN/MeOH):  $m/z = 388.157 \text{ [M+Li]}^+$ .

#### tert-Butyl (3-formyl-4-hydroxyphenyl)carbamate (16)

Compound 14 (0.5 g, 1.3 mmol, 1 eq.) was dissolved in 10 mL methanol and 5 g NaOH dissolved in 5 mL water were added. The solution was refluxed for 3 h and neutralized with an aqueous 1 M HCl-solution. The solution was extracted three times with 20 mL EE and the combined organic phases were dried over Na<sub>2</sub>SO<sub>4</sub>. The solvent was removed *in vacuo* and the residue was purified by flash chromatography on normal phase silica gel (solvent A: hexane, solvent B: EE, 90% A) to obtain compound 16 as a yellow solid (0.21 g, 890 μmol, 45%).

Analytical data match reported literature values.<sup>356</sup>

 $\mathbf{R}_f = 0.5 \text{ (hexane:EE / 4:1)}.$ 

<sup>1</sup>**H-NMR** (400 MHz, CDCl<sub>3</sub>):  $\delta$  = 10.76 (s, 1H), 9.86 (d, J = 0.5 Hz, 1H), 7.83 (s, 1H), 7.29 (dd, J = 8.9, 2.7 Hz, 1H), 6.92 (d, J = 8.9 Hz, 1H), 6.45 (s, 1H), 1.52 (s, 6H).

<sup>13</sup>**C-NMR** (100 MHz, CDCl<sub>3</sub>):  $\delta$  = 196.5, 156.7, 153.0, 130.8, 128.4, 123.3, 120.2, 118.0, 80.9, 28.3.

**MS** (ESI+, MeCN/MeOH):  $m/z = 244.11 \text{ [M+Li]}^+$ .

# (5-(((9H-Fluoren-9-yl)methoxy)carbonyl)amino)-2-acetoxy-phenyl)methylene diacetate (15)

Compound **25** (2 g, 7.1 mmol, 1 eq.) and Fmoc-Cl (2.2 g, 8.5 mmol, 1.2 eq.) were suspended in 10 mL water and stirred for 2h at 60°C. The reaction mixture was extracted three times with 60 mL EE and the combined organic phases were dried over Na<sub>2</sub>SO<sub>4</sub>. The solvent was removed *in vacuo* and the residue was purified by flash chromatography on normal phase silica gel (solvent A: hexane, solvent B: EE, 80% A) to obtain compound **15** as transparent crystals (1.45 g, 2.9 mmol, 41%).

 $\mathbf{R}_f = 0.1 \text{ (hexane:EE / 4:1)}.$ 

<sup>1</sup>**H-NMR** (500 MHz, CDCl<sub>3</sub>):  $\delta$  = 7.85 (s, 1H), 7.79 (d, J = 7.6 Hz, 2H), 7.68 (s, 1H), 7.61 (d, J = 7.5 Hz, 2H), 7.44–7.40 (m, 3H), 7.33 (t, J = 7.4 Hz, 2H), 7.05 (d, J = 8.8 Hz, 1H), 6.74 (s, 1H), 4.56 (d, J = 6.6 Hz, 2H), 4.28 (t, J = 6.5 Hz, 1H), 2.32 (s, 3H), 2.09 (s, 6H).

<sup>13</sup>**C-NMR** (125 MHz, CDCl<sub>3</sub>):  $\delta$  = 169.5, 168.4, 153.2, 143.8, 143.6, 141.4, 135.8, 128.4, 127.8, 127.2, 124.9, 123.8, 120.8, 120.1, 117.8, 85.0, 67.0, 47.1, 20.8, 20.7.

**IR** (ATR):  $\nu = 3399$ m, 1749s, 1727s, 1543m, 1195s cm<sup>-1</sup>.

UV/Vis (c = 0.05  $\mu$ mol mL<sup>-1</sup>/MeOH):  $\lambda_{max,1} = 300$ ,  $\lambda_{max,2} = 289$ ,  $\lambda_{max,1} = 264$ ,  $\lambda_{max,1} = 244$  nm.

**HR-MS** (ESI+, MeCN/MeOH): calcd. for  $[C_{28}H_{25}NO_8+Li]^+ = 510.172$  found: 510.173.

#### (9*H*-Fluoren-9-vl)methyl (3-formyl-4-hydroxyphenyl)carbamate (17)

Compound **15** (0.1 g, 0.2 mmol, 1 eq.) was dissolved in 20 mL ethanol and 1 mL of concentrated  $H_2SO_4$  was added. The solution was refluxed for 2 h and neutralized with a saturated aqueous NaHCO<sub>3</sub>-solution. The solution was extracted three times with 50 mL  $Et_2O$  and the combined organic phases were dried over  $Na_2SO_4$ . The solvent is removed *in vacuo* and compound **17** was obtained as beige crystals (52 mg, 0.14 mmol, 73%).

 $\mathbf{R}_f = 0.3 \text{ (hexane:EE / 4:1)}.$ 

<sup>1</sup>**H-NMR** (400 MHz, THF- $d_8$ ):  $\delta$  = 10.58 (s, 1H), 9.91 (s, 1H), 8.82 (s, 1H), 7.88 (s, 1H), 7.79 (d, J = 7.5 Hz, 2H), 7.67 (d, J = 7.3 Hz, 2H), 7.51 (s, 1H), 7.36 (t, J = 7.5 Hz, 2H), 7.28 (t, J = 7.4 Hz, 2H), 6.85 (d, J = 8.9 Hz, 1H), 4.55 (d, J = 6.3 Hz, 2H), 4.26 (t, J = 6.2 Hz, 1H).

<sup>13</sup>**C-NMR** (100 MHz, THF- $d_8$ ):  $\delta$  = 196.8, 157.8, 154.3, 145.0, 142.2, 132.8, 128.2, 128.0, 127.6, 125.5, 122.6, 121.5, 120.5, 118.0, 66.6, 48.1.

IR (ATR): v = 3294m, 1693s, 1658s, 1243s, 732m cm<sup>-1</sup>.

UV/Vis (c = 0.07  $\mu$ mol mL<sup>-1</sup>/MeOH):  $\lambda_{max,1} = 356$ ,  $\lambda_{max,2} = 256$ ,  $\lambda_{max,3} = 235$  nm.

**HR-MS** (ESI+, MeCN/MeOH): calcd. for  $[C_{22}H_{17}NO_4+H]^+ = 360.123$  found: 360.123.

# 6-((*tert*-Butoxycarbonyl)amino)-1',3',3'-trimethylspiro-[chromene-2,2'-indoline]-5'-carboxylic acid (18)

Compound **16** (0.5 g, 2.1 mmol, 0.5 eq.) and compound **12** (1.45 g, 4.2 mmol, 2 eq.) were dissolved in 100 mL ethanol under a nitrogen atmosphere and TEA (1.2 mL, 8.4 mmol, 4 eq.) was added slowly. The solution was refluxed for 3 h and neutralized with an aqueous 1M HCl-solution. The solution was extracted three times with 60 mL EE and the combined organic phases were dried over Na<sub>2</sub>SO<sub>4</sub>. The solvent was removed *in vacuo* and the residue was purified by flash chromatography on normal phase silica gel (solvent A: hexane, solvent B: EE, 20% A) to obtain compound **18** as a pink solid (0.3 g, 0.7 mmol, 33%).

 $\mathbf{R}_f = 0.4 \text{ (DCM:MeOH / 19:1)}.$ 

<sup>1</sup>**H-NMR** (400 MHz, DMSO- $d_6$ ):  $\delta$  = 12.25 (s, 1H), 9.10 (s, 1H), 7.76 (dd, J = 8.2, 1.7 Hz, 1H), 7.61 (d, J = 1.6 Hz, 1H), 7.34 (s, 1H), 7.04 (dd, J = 8.8, 2.4 Hz, 1H), 6.98 (d, J = 10.2 Hz, 1H), 6.59 (dd, J = 8.4, 6.2 Hz, 2H), 5.75 (d, J = 10.2 Hz, 1H), 2.70 (s, 3H), 1.44 (s, 3H), 1.21 (s, 3H), 1.08 (s, 3H).

<sup>13</sup>**C-NMR** (100 MHz, DMSO- $d_6$ ): δ = 167.9, 153.4, 153.0, 149.3, 136.8, 132.9, 131.1, 130.2, 123.3, 121.4, 120.9, 119.5, 118.6, 117.4, 114.8, 106.3, 104.0, 79.2, 51.3, 28.9, 28.6, 26.0, 20.2.

IR (ATR): v = 3448w, 2980m, 1724s, 1667s, 1155s cm<sup>-1</sup>.

**UV/Vis** (c = 0.03  $\mu$ mol mL<sup>-1</sup> /MeOH):  $\lambda_{max,1} = 301$ ,  $\lambda_{max,2} = 233$  nm.

**HR-MS** (ESI+, MeCN/MeOH): calcd. for  $[C_{25}H_{28}N_2O_5+Li]^+ = 443.214$  found: 443.212.

6-((((9*H*-Fluoren-9-yl)methoxy)carbonyl)amino)-1',3',3'-tri-methylspiro[chromene-2,2'-indoline]-5'-carboxylic acid (19)

Compound **17** (0.3 g, 0.83 mmol, 1 eq.) and compound **12** (0.58 g, 1.7 mmol, 2 eq.) were dissolved in 100 mL ethanol under a nitrogen atmosphere and TEA (0.47 mL, 3.3 mmol, 4 eq.) was added slowly. The solution was refluxed for 3 h and neutralized with an aqueous 1M HCl-solution. The solution was extracted three times with 60 mL EE and the combined organic phases were dried over Na<sub>2</sub>SO<sub>4</sub>. The solvent was removed *in vacuo* and the residue was purified by flash chromatography on normal phase silica gel (solvent A: DCM, solvent B: MeOH, 98% A) to obtain compound **19** as a red solid (0.12 g, 0.21 mmol, 26%).

 $\mathbf{R}_f = 0.4 \, (\text{DCM:MeOH} / 19:1).$ 

<sup>1</sup>**H-NMR** (400 MHz, THF- $d_8$ ):  $\delta$  = 12.83 (s, 1H), 8.64 (s, 1H), 7.87 (dd, J = 8.2, 1.7 Hz, 1H), 7.80 (d, J = 7.6 Hz, 2H), 7.72 (d, J = 1.7 Hz, 1H), 7.68 (d, J = 7.4 Hz, 2H), 7.43 –7.34 (m, 3H), 7.29 (td, J = 7.4, 1.2 Hz, 2H), 7.10 (d, J = 8.7 Hz, 1H), 6.93 (d, J = 10.2 Hz, 1H), 6.58 (d, J = 8.7 Hz, 1H), 6.53 (d, J = 8.2 Hz, 1H), 5.76 (d, J = 10.2 Hz, 1H), 4.51 (d, J = 6.5 Hz, 2H), 4.27 (t, J = 6.4 Hz, 1H), 2.77 (s, 3H), 1.33 (s, 3H), 1.17 (s, 3H).

<sup>13</sup>**C-NMR** (100 MHz, THF- $d_8$ ): δ = 167.6, 154.2, 152.6, 150.5, 145.1, 142.2, 137.3, 133.3, 131.6, 130.6, 128.1, 127.6, 125.6, 123.8, 122.3, 120.5, 119.8, 119.4, 117.5, 115.3, 106.2, 104.8, 66.5, 51.8, 48.2, 28.7, 25.9, 20.3.

IR (ATR): v = 3303br, 3064br, 1671s, 1583s, 1199s cm<sup>-1</sup>.

UV/Vis (c = 0.09  $\mu$ mol mL<sup>-1</sup>/MeOH):  $\lambda_{max,1} = 474$ ,  $\lambda_{max,2} = 378$ ,  $\lambda_{max,3} = 299$ ,  $\lambda_{max,4} = 264$  nm.

**HR-MS** (ESI+, MeCN/MeOH): calcd. for  $[C_{35}H_{30}N_2O_5+H]^+ = 559.222$  found: 559.220.

#### 1',3',3'-Trimethyl-6-nitrospiro[chromene-2,2'-indoline]-5'-carboxylic acid (26)

Compound **12** (1 g, 2.9 mmol, 1 eq.), 2-hydroxy-5-nitrobenzaldehyde **13** (0.54 g, 3.2 mmol, 1 eq.), TEA (1.1 ml, 7.6 mmol, 1 eq.) were dissolved in 100 mL ethanol under a nitrogen atmosphere. The solution was refluxed for 3 h and quenched with 100 mL aqueous 0.1 M HCl-solution. The formed precipitate is

separated and solved in aqueous 10% KOH-solution. The solution is washed with DCM and the pH value is adjusted to 4. The formed precipitate is recrytallized in ethanol and compound **26** is obtained as a brownish solid (0.05 g, 0.14 mmol, 5%).

Analytical data match reported literature values.<sup>357</sup>

 $\mathbf{R}_f = 0.3 \text{ (hexane:EE} + 0.1\% \text{ FA} / 4:1).$ 

<sup>1</sup>**H-NMR** (500 MHz, CDCl<sub>3</sub>):  $\delta$  = 12.35 (s, 1H), 8.24 (d, J = 2.8 Hz, 1H), 8.02 (dd, J = 9.0, 2.8 Hz, 1H), 7.82 (dd, J = 8.2, 1.7 Hz, 1H), 7.68 (d, J = 1.7 Hz, 1H), 7.26 (d, J = 10.4 Hz, 1H), 6.92 (d, J = 9.0 Hz, 1H), 6.70 (d, J = 8.3 Hz, 1H), 6.02 (d, J = 10.4 Hz, 1H), 2.76 (s, 3H, ), 1.25 (s, 3H), 1.14 (s, 3H).

<sup>13</sup>**C-NMR** (125 MHz, CDCl<sub>3</sub>):  $\delta$  = 167.8, 159.4, 151.7, 141.2, 136.3, 131.3, 128.9, 126.3, 123.4, 123.3, 122.0, 121.3, 119.2, 115.9, 106.8, 106.4, 52.0, 28.8, 25.9, 20.0.

**MS** (ESI+, MeCN/MeOH):  $m/z = 373.136 \text{ [M+Li]}^+$ 

#### 6-Amino-1',3',3'-trimethylspiro[chromene-2,2'-indoline]-5'-carboxylic acid (27)

Compound **18** (0.2 g, 0.46 mmol, 1 eq.) was dissolved in 10 mL of a 1:1 mixture of trifluoroacetic acid and DCM and stirred ambient temperature for an hour. The solvent is removed **in vacuo** and the residue is purified by flash chromatography on normal phase silica gel (solvent A: DCM, solvent B: MeOH, 96% A) to obtain compound **27** as a red solid (0.14 g, 0.42 mmol, 91%).

Analytical data match reported literature values.<sup>358</sup>

 $\mathbf{R}_f = 0.3 \text{ (DCM:MeOH / 19:1)}.$ 

<sup>1</sup>**H-NMR** (500 MHz, CDCl<sub>3</sub>):  $\delta$  = 10.09 (s, 1H), 7.78 (dd, J = 8.2, 1.7 Hz, 1H), 7.62 (d, J = 1.7 Hz, 1H), 7.10–7.04 (m, 2H), 6.97 (dd, J = 8.6, 2.6 Hz, 1H), 6.74 (d, J = 8.6 Hz, 1H), 6.62 (d, J = 8.2 Hz, 1H), 5.85 (d, J = 10.3 Hz, 1H), 2.71 (s, 3H), 1.21 (s, 3H), 1.09 (s, 3H).

<sup>13</sup>**C-NMR** (125 MHz, CDCl<sub>3</sub>):  $\delta$  = 167.9, 152.2, 151.9, 136.6, 131.2, 129.4, 123.5, 123.3, 121.6, 120.6, 120.4, 119.6, 115.9, 106.5, 104.6, 51.6, 28.9, 25.9, 20.2.

IR (ATR): v = 2889m, 2641br, 1658s, 1605s, 1182s cm<sup>-1</sup>.

UV/Vis (c = 0.15  $\mu$ mol mL<sup>-1</sup> /MeOH):  $\lambda_{max,1} = 407$ ,  $\lambda_{max,2} = 300$  nm.

**HR-MS** (ESI+, MeCN/MeOH): calcd. for  $[C_{20}H_{21}N_2O_3+H]^+ = 337.154$  found: 337.153.

#### **6.3** Solid-phase peptide synthesis

The Fmoc-protected photoswitches 3,4'-AMPB **4**, FASC **10**, and SAFC **19** were incorporated into the PTH<sub>25-37</sub> sequence *via* SPPS. Therefore, an automated peptide synthesizer (MultiPep RS; Invatis AG, Cologne, Germany) was used together with standard Fmoc-chemistry and preloaded resins (210 μmol/g resin). Coupling of protected natural amino acids was performed as single couplings in DMF using 5 eq. of the respective amino acid, 5 eq. of HCTU as coupling reagent, and 10 eq. of *N*-methylmorpholine as base for 1 h at ambient temperature.

For the coupling of the special Fmoc-building blocks **4**, **10**, and **19**, 3 eq. of the respective building block, 3 eq. N,N'-diisopropylcarbodiimide, and 3 eq. hydroxybenzotriazole were used in a mixture of DMF and N-methyl-2-pyrrolidone (50:50 vol.-%) at ambient temperature gently shaked in the absence of light overnight.

The N-terminal Fmoc-protecting group was removed by washing the resin with 20% piperidine in DMF. The final side chain deprotection and cleavage from the resin occured in a mixture of trifluoroacetic acid and water (90:10 vol.-%) with gentle agitation for 2 h at ambient temperature.

The crude peptides were further processed to a purity of >95% using preparative RP-HPLC (Gilson, Limburg, Germany). For both, analytical and preparative purification, the mobile phase was a mixture of water (eluent A) and acetonitrile (eluent B), each containing 0.1% trifluoroacetic acid. The crude peptides were purified using a linear gradient from 95% A to 15% A in 15 min for analytical separation and 90 min for preparative runs. The column was a semi.preparative PLRP-S column (Agilent Technologies, 300x25 mm, 8 um).

All peptides were characterized by analytical HPLC (Dionex Ultimate 3000; Thermo Scientific, Germany) using a PLRP-S column (Agilent Technologies, 150x4.6mm, 3um), MALDI-Tof-MS (Bruker Microflex LT; Bruker, Bremen, Germany), and <sup>1</sup>H-NMR.

## References

- (1) Palczewski, K. J. Biol. Chem. **2012**, 287, 1612–1619, DOI: https://doi.org/10.1074/jbc.R111.301150.
- (2) Terakita, A. *Genome Biol.* **2005**, *6*, 1–9, DOI: https://doi.org/10.1186/gb-2005-6-3-213.
- (3) Liu, W.; Yang, S.; Li, J.; Su, G.; Ren, J. Wiley Interdiscip. Rev. Comput. Mol. Sci. 2021, 11, e1511, DOI: https://doi.org/10.1002/wcms.1511.
- (4) Ghaffarizadeh, A.; Flann, N. S.; Podgorski, G. J. *BMC Bioinform.* **2014**, *15*, 1–13, DOI: https://doi.org/10.1186/1471-2105-15-S7-S7.
- (5) Zhang, J. L.; Zhong, J. Q.; Lin, J. D.; Hu, W. P.; Wu, K.; Xu, G. Q.; Wee, A. T.; Chen, W. *Chem. Soc. Rev.* **2015**, *44*, 2998–3022, DOI: https://doi.org/10.1039/c4cs00377b.
- (6) Goulet-Hanssens, A.; Eisenreich, F.; Hecht, S. *Adv. Mater.* **2020**, *32*, 1905966, DOI: https://doi.org/10.1002/adma.201905966.
- (7) Russew, M.; Hecht, S. *Adv. Mater.* **2010**, *22*, 3348–3360, DOI: https://doi.org/10.1002/adma.200904102.
- (8) Trzebicka, B.; Szweda, R.; Kosowski, D.; Szweda, D.; Otulakowski, L.; Haladjova, E.; Dworak, A. *Prog. Polym. Sci.* **2017**, *68*, 35–76, DOI: https://doi.org/10.1016/j.progpolymsci. 2016.12.004.
- (9) Komori, H.; Inai, Y. J. Org. Chem. 2007, 72, 4012–4022. DOI: https://doi.org/10.1021/jo0625305.
- (10) Hush, N. S.; Wong, A. T.; Bacskay, G. B.; Reimers, J. R. J. Am. Chem. Soc. **1990**, 112, 4192–4197, DOI: https://doi.org/10.1021/ja00167a014.
- (11) Han, Y.; Nickle, C.; Zhang, Z.; Astier, H. P.; Duffin, T. J.; Qi, D.; Wang, Z.; Del Barco, E.; Thompson, D.; Nijhuis, C. A. *Nat. Mater.* **2020**, *19*, 843–848, DOI: https://doi.org/10.1038/s41563-020-0697-5.
- (12) Liljeroth, P.; Repp, J.; Meyer, G. Science 2007, 317, 1203–1206, DOI: https://doi.org/ 10.1126/science.1144366.
- (13) Henzl, J.; Morgenstern, K. *Phys. Chem. Chem. Phys.* **2010**, *12*, 6035–6044, DOI: https://doi.org/10.1039/b924488c.
- (14) Ambrosi, G.; Dapporto, P.; Formica, M.; Fusi, V.; Giorgi, L.; Guerri, A.; Micheloni, M.; Paoli, P.; Pontellini, R.; Rossi, P. Chem. Eur. J. 2003, 9, 800–810, DOI: https://doi.org/10.1002/chem.200390090.
- (15) Ahn, H.; Hong, J.; Kim, S. Y.; Choi, I.; Park, M. J. *ACS Appl. Mater. Interfaces.* **2015**, 7, 704–712, DOI: https://doi.org/10.1021/am5070188.
- (16) Bencic-Nagale, S.; Sternfeld, T.; Walt, D. R. *J. Am. Chem. Soc.* **2006**, *128*, 5041–5048, DOI: https://doi.org/10.1021/ja057057b.

- (17) Audi, H.; Viero, Y.; Alwhaibi, N; Chen, Z.; Iazykov, M.; Heynderickx, A.; Xiao, F.; Guérin, D.; Krzeminski, C.; Grace, I. M. *Nanoscale* 2020, 12, 10127–10139, DOI: https://doi.org/10.1039/d0nr02461a.
- (18) Nakamura, T.; Takashima, Y.; Hashidzume, A.; Yamaguchi, H.; Harada, A. *Nat. Commun.* **2014**, *5*, 4622, DOI: https://doi.org/10.1038/ncomms5622.
- (19) Funtan, S.; Evgrafova, Z.; Adler, J.; Huster, D.; Binder, W. H. *Polymers* **2016**, *8*, 178, DOI: https://doi.org/10.3390/polym8050178.
- (20) Alberstein, R. G.; Guo, A. B.; Kortemme, T. *Curr. Opin. Struct. Biol.* **2022**, *72*, 71–78, DOI: https://doi.org/10.1016/j.sbi.2021.08.004.
- (21) Ma, J.; Karplus, M. *Proc. Natl. Acad. Sci. U.S.A.* **1997**, *94*, 11905–11910, DOI: https://doi.org/10.1073/pnas.94.22.11905.
- (22) Gay, N. J.; Gangloff, M.; Weber, A. N. *Nat. Rev. Immunol.* **2006**, *6*, 693–698, DOI: https://doi.org/10.1038/nri1916.
- (23) Fishel, R. Genes Dev. 1998, 12, 2096–2101, DOI: https://doi.org/10.1101/gad.12.14. 2096.
- (24) Hörner, M.; Weber, W. *FEBS Lett.* **2012**, *586*, 2084–2096, DOI: https://doi.org/10.1016/j.febslet.2012.02.032.
- (25) Yang, W.; Li, Y.; Liu, H.; Chi, L.; Li, Y. *Small* **2012**, *8*, 504–516, DOI: https://doi.org/10.1002/smll.201101738.
- (26) Harris, J. D.; Moran, M. J.; Aprahamian, I. *Proc. Natl. Acad. Sci. U.S.A.* **2018**, *115*, 9414–9422, DOI: https://doi.org/10.1073/pnas.1714499115.
- (27) Ma, J.; Xuan, L. *Displays* **2013**, *34*, 293–300, DOI: https://doi.org/10.1016/j.displa. 2013.05.005.
- (28) Wang, Y.; Li, Q. Adv. Mater. **2012**, 24, 1926–1945, DOI: https://doi.org/10.1002/adma. 201200241.
- (29) Willner, I.; Basnar, B.; Willner, B. *Adv. Funct. Mater.* **2007**, *17*, 702–717, DOI: https://doi.org/10.1002/adfm.200601154.
- (30) Raymo, F. M. *Adv. Mater.* **2002**, *14*, 401–414, DOI: https://doi.org/10.1002/1521-4095(20020318)14:6<401::Aid-Adma401>3.0.Co;2-F.
- (31) Ward, M. D. J. Chem. Educ. **2001**, 78, 321, DOI: https://doi.org/10.1021/ed078p321.
- (32) Reed, M. A.; Tour, J. M. *Sci. Am.* **2000**, 282, 86–93, DOI: https://doi.org/10.1038/scientificamerican0600-86.
- (33) Waldrop, M. M. *Nature* **2016**, *530*, 144, DOI: https://doi.org/10.1038/530144a.
- (34) Van der Horst, M. A.; Hellingwerf, K. J. *Acc. Chem. Res.* **2004**, *37*, 13–20, DOI: https://doi.org/10.1021/ar020219d.
- (35) Oesterhelt, D.; Tittor, J. *Trends Biochem. Sci.* **1989**, *14*, 57–61, DOI: https://doi.org/10. 1016/0968-0004(89)90044-3.
- (36) Provencio, I.; Jiang, G.; De Grip, W. J.; Hayes, W. P.; Rollag, M. D. *Proc. Natl. Acad. Sci. U.S.A.* **1998**, *95*, 340–345, DOI: https://doi.org/10.1073/pnas.95.1.340.
- (37) Calligaro, H.; Dkhissi-Benyahya, O.; Panda, S. *Trends Neurosci.* **2022**, *45*, 200–211, DOI: https://doi.org/10.1016/j.tins.2021.11.008.

- (38) Nagel, G.; Ollig, D.; Fuhrmann, M.; Kateriya, S.; Musti, A. M.; Bamberg, E.; Hegemann, P. *Science* **2002**, *296*, 2395–2398, DOI: https://doi.org/10.1126/science.1072068.
- (39) Blanck, A.; Oesterhelt, D; Ferrando, E; Schegk, E.; Lottspeich, F. *EMBO J.* **1989**, *8*, 3963–3971, DOI: https://doi.org/10.1002/j.1460-2075.1989.tb08579.x.
- (40) Braslavsky, S.; Gärtner, W; Schaffner, K *Plant Cell Environ.* **1997**, *20*, 700–706, DOI: https://doi.org/10.1046/j.1365-3040.1997.d01-101.x.
- (41) Rockwell, N. C.; Lagarias, J. C. *Plant Cell* **2006**, *18*, 4–14, DOI: https://doi.org/10.1105/tpc.105.038513.
- (42) Ikeuchi, M.; Ishizuka, T. *Photochem. Photobiol. Sci.* **2008**, 7, 1159–1167, DOI: https://doi.org/10.1039/b802660m.
- (43) Perman, B.; Srajer, V.; Ren, Z.; Teng, T.-y.; Pradervand, C.; Ursby, T.; Bourgeois, D.; Schotte, F.; Wulff, M.; Kort, R. *Science* **1998**, *279*, 1946–1950, DOI: https://doi.org/10.1126/science.279.5358.1946.
- (44) Müller, P.; Bouly, J.-P.; Hitomi, K.; Balland, V.; Getzoff, E. D.; Ritz, T.; Brettel, K. *Sci. Rep.* **2014**, *4*, 5175, DOI: https://doi.org/10.1038/srep05175.
- (45) Ozturk, N.; Selby, C. P.; Annayev, Y.; Zhong, D.; Sancar, A. *Proc. Natl. Acad. Sci. U.S.A.* **2011**, *108*, 516–521, DOI: https://doi.org/10.1073/pnas.1017093108.
- (46) Łabuz, J.; Sztatelman, O.; Hermanowicz, P. *J. Exp. Bot.* **2022**, *73*, 6034–6051, DOI: https://doi.org/10.1093/jxb/erac271.
- (47) Christie, J. M.; Arvai, A. S.; Baxter, K. J.; Heilmann, M.; Pratt, A. J.; O'Hara, A.; Kelly, S. M.; Hothorn, M.; Smith, B. O.; Hitomi, K. *Science* **2012**, *335*, 1492–1496, DOI: https://doi.org/10.1126/science.1218091.
- (48) Roth, H. D. *Angew. Chem. Int. Ed.* **1989**, 28, 1193–1207, DOI: https://doi.org/10.1002/anie.198911931.
- (49) Dessauer, R.; Paris, J. P. In Advances in photochemistry, Noyes, J. W. A., Hammon, G. S., N., P. J. J., Eds.; John Wiley & Sons Inc.: 1963, 275–321, DOI: https://doi.org/10.1002/ 9780470133316.ch8.
- (50) Towns, A. *Phys. Sci. Rev.* **2021**, *6*, 477–511, DOI: https://doi.org/10.1515/psr-2020-0191.
- (51) Fritsche, J C. R. Acad. Sci. **1867**, 69, 1035.
- (52) Ter Meer, E. Justus Liebigs Ann. Chem. **1876**, 181, 1–22.
- (53) Phipson, T. L. Chem. News **1881**, 43, 283.
- (54) Hirshberg, Y. C. R. Hebd. Acad. Sci. **1950**, 231, 903–904.
- (55) Saßmannshausen, T.; Kunz, A.; Oberhof, N.; Schneider, F.; Slavov, C.; Dreuw, A.; Wachtveitl, J.; Wegner, H. A. *Angew. Chem. Int. Ed.* **2024**, *63*, e202314112, DOI: https://doi.org/10.1002/anie.202314112.
- (56) Regehly, M.; Garmshausen, Y.; Reuter, M.; König, N. F.; Israel, E.; Kelly, D. P.; Chou, C.-Y.; Koch, K.; Asfari, B.; Hecht, S. *Nature* 2020, 588, 620–624, DOI: https://doi.org/10.1038/s41586-020-3029-7.
- (57) Pianowski, Z. L. Chem. Eur. J. 2019, 25, 5128–5144, DOI: https://doi.org/10.1002/ chem.201805814.

- (58) Peddie, V.; Abell, A. D. *J. Photochem. Photobiol. C* **2019**, *40*, 1–20, DOI: https://doi.org/10.1016/j.jphotochemrev.2019.05.001.
- (59) Boelke, J.; Hecht, S. Adv. Opt. Mater. 2019, 7, 1900404, DOI: https://doi.org/10.1002/adom.201900404.
- (60) Waldeck, D. H. *Chem. Rev.* **1991**, *91*, 415–436, DOI: https://doi.org/10.1021/cr00003a007.
- (61) Turanský, R.; Konôpka, M.; Doltsinis, N. L.; Štich, I.; Marx, D. *Phys. Chem. Chem. Phys.* 2010, 12, 13922–13932, DOI: https://doi.org/10.1039/C0CP00588F.
- (62) Henzl, J.; Mehlhorn, M.; Gawronski, H.; Rieder, K.; Morgenstern, K. *Angew. Chem. Int. Ed.* **2006**, *45*, 603–606, DOI: https://doi.org/10.1002/anie.200502229.
- (63) Birla, H.; Mir, S. H.; Yadav, K.; Halbritter, T.; Heckel, A.; Singh, J. K.; Gopakumar, T. G. *J. Phys. Chem. C* **2023**, *127*, 17039–17050, DOI: https://doi.org/10.1021/acs.jpcc.3c02334.
- (64) Griffiths, J Chem. Soc. Rev. **1972**, 1, 481–493, DOI: https://doi.org/10.1039/CS9720100481.
- (65) Beharry, A. A.; Woolley, G. A. *Chem. Soc. Rev.* **2011**, *40*, 4422–4437, DOI: https://doi.org/10.1039/c1cs15023e.
- (66) Bandara, H. M. D.; Burdette, S. C. *Chem. Soc. Rev.* **2012**, *41*, 1809–1825, DOI: https://doi.org/10.1039/C1CS15179G.
- (67) Merino, E.; Ribagorda, M. *Beilstein J. Org. Chem.* **2012**, 8, 1071–1090, DOI: https://doi.org/10.3762/bjoc.8.119.
- (68) Mitscherlich, E *Ann. Phys. Chem.* **1834**, *12*, 305–311, DOI: https://doi.org/10.1002/andp.18341081502.
- (69) Nobel, A. Justus Liebigs Ann. Chem. **1856**, 98, 253–256.
- (70) Béchamp, A. Ann. Chim. Phys. **1854**, 42, 186–196.
- (71) Bopp, A.; v. Hofmann, A.; Fischer, E. Ber. Dtsch. Chem. Ges. 1891, 24, 1006–1078.
- (72) Gordon, P. F.; Gregory, P., *Organic chemistry in colour*; Springer Science & Business Media: 2012.
- (73) Benkhaya, S.; M'rabet, S.; El Harfi, A. *Heliyon* **2020**, *6*, e03271, DOI: https://doi.org/10.1016/j.heliyon.2020.e03271.
- (74) Berg, M.; Hudson, P. *The Economic History Review* **1992**, *45*, 24–50, DOI: https://doi.org/10.1111/j.1468-0289.1992.tb01290.x.
- (75) Franck, H.-G.; Stadelhofer, J. W. In *Industrielle Aromatenchemie*. Springer-Verlag Berlin Heidelberg: 1987, pp 1–7, DOI: https://doi.org/10.1007/978-3-662-07875-4\_1.
- (76) Mene, C In Wagner's Jahresberichte, 1861, p 496.
- (77) Glaser, C. *Justus Liebigs Ann. Chem.* **1867**, *142*, 364–369, DOI: https://doi.org/10.1002/jlac.18671420319.
- (78) Domagk, G. *Dtsch. Med. Wochenschr.* **1935**, *61*, 250–253, DOI: https://doi.org/10.1055/s-0028-1129486.
- (79) Hartley, G. S. Nature 1937, 140, 281–281, DOI: https://doi.org/10.1038/140281a0.

- (80) Bieth, J.; Vratsanos, S. M.; Wassermann, N.; Erlanger, B. F. *Proc. Natl. Acad. Sci. U.S.A.* **1969**, 64, 1103–1106, DOI: https://doi.org/10.1073/pnas.64.3.1103.
- (81) Sackmann, E J. Am. Chem. Soc. **1971**, 93, 7088-7090, DOI: https://doi.org/10.1021/ja00754a068.
- (82) Shinkai, S.; Ogawa, T.; Nakaji, T.; Kusano, Y.; Nanabe, O. *Tetrahedron Lett.* **1979**, *20*, 4569–4572, DOI: https://doi.org/10.1016/S0040-4039(01)86651-X.
- (83) Lerch, M. M.; Hansen, M. J.; van Dam, G. M.; Szymański, W.; Feringa, B. L. *Angew. Chem. Int. Ed.* **2016**, *55*, 10978–10999, DOI: https://doi.org/10.1002/anie.201601931.
- (84) Broichhagen, J.; Frank, J. A.; Trauner, D. *Acc. Chem. Res.* **2015**, *48*, 1947–1960, DOI: https://doi.org/10.1021/acs.accounts.5b00129.
- (85) Hull, K.; Morstein, J.; Trauner, D. *Chem. Rev.* **2018**, *118*, 10710–10747, DOI: https://doi.org/10.1021/acs.chemrev.8b00037.
- (86) Siewertsen, R.; Neumann, H.; Buchheim-Stehn, B.; Herges, R.; Nather, C.; Renth, F.; Temps, F. *J. Am. Chem. Soc.* **2009**, *131*, 15594–15595, DOI: https://doi.org/10.1021/ja906547d.
- (87) Beharry, A. A.; Sadovski, O.; Woolley, G. A. *J. Am. Chem. Soc.* **2011**, *133*, 19684–19687, DOI: https://doi.org/10.1021/ja209239m.
- (88) Bléger, D.; Schwarz, J.; Brouwer, A. M.; Hecht, S. *J. Am. Chem. Soc.* **2012**, *134*, 20597–20600, DOI: https://doi.org/10.1021/ja310323y.
- (89) Croissant, J.; Chaix, A.; Mongin, O.; Wang, M.; Clément, S.; Raehm, L.; Durand, J.; Hugues, V.; Blanchard-Desce, M.; Maynadier, M. Small 2014, 10, 1752–1755, DOI: https://doi.org/10.1002/smll.201400042.
- (90) Merino, E. Chem. Soc. Rev. 2011, 40, 3835-53, DOI: https://doi.org/10.1039/ c0cs00183j.
- (91) Hamon, F.; Djedaini-Pilard, F.; Barbot, F.; Len, C. *Tetrahedron* **2009**, *65*, 10105–10123, DOI: https://doi.org/10.1016/j.tet.2009.08.063.
- (92) Hegarty, A. F. In *The Chemistry of Diazonium and Diazo Groups: Part 2*, Patai, S., Ed.; Wiley: New York, 1978, pp 511–591.
- (93) Baeyer, A. *Ber. Dtsch. Chem. Ges.* **1874**, 7, 1638–1640, DOI: https://doi.org/10.1002/cber.187400702214.
- (94) Mills, C. J. Chem. Soc., Trans. **1895**, 67, 925–933, DOI: https://doi.org/10.1039/CT8956700925.
- (95) Wallach, O; Belli, L *Ber. Dtsch. Chem. Ges.* **1880**, *13*, 525–527, DOI: https://doi.org/10.1002/cber.188001301153.
- (96) Shimao, I.; Matsumura, S. *Bull. Chem. Soc. Jpn.* **1976**, *49*, 2294–2297, DOI: https://doi.org/10.1246/bcsj.49.2294.
- (97) Shimao, I.; Oae, S. *Bull. Chem. Soc. Jpn.* **1983**, *56*, 643–644, DOI: https://doi.org/10.1246/bcsj.56.643.
- (98) Pausacker, K. H. *J. Chem. Soc.* **1953**, 1989–1990, DOI: https://doi.org/10.1039/JR9530001989.
- (99) Wawzonek, S; McIntyre, T. J. Electrochem. Soc. 1972, 119, 1350, DOI: https://doi.org/ 10.1149/1.2403994.

- (100) Crecca, C. R.; Roitberg, A. E. *J. Phys. Chem. A* **2006**, *110*, 8188–8203, DOI: https://doi.org/10.1021/jp057413c.
- (101) Mostad, A.; Rømming, C. *Acta Chem. Scand.* **1971**, 25, 3561–3568, DOI: https://doi.org/10.3891/acta.chem.scand.25-3561.
- (102) Schulze, F.-W.; Petrick, H.-J.; Cammenga, H. K.; Klinge, H. Z. Phys. Chem. **1977**, 107, 1–19, DOI: https://doi.org/10.1524/zpch.1977.107.1.001.
- (103) Brown, E. V.; Granneman, G. R. *J. Am. Chem. Soc.* **1975**, *97*, 621–627, DOI: https://doi.org/10.1021/ja00836a025.
- (104) Talaty, E. R.; Fargo, J. C. *Chem. Commun.* **1967**, 65–66, DOI: https://doi.org/10.1039/C19670000065.
- (105) Hartley, G. S.; Le Fevre, R. J. W. *J. Chem. Soc.* **1939**, 531–535, DOI: https://doi.org/10. 1039/JR9390000531.
- (106) Kumar, G. S.; Neckers, D. C. Chem. Rev. 1989, 89, 1915–1925, DOI: https://doi.org/10.1021/cr00098a012.
- (107) Volker, A.; Steen, J. D.; Crespi, S. *Beilstein J. Org. Chem.* **2024**, *20*, 1684–1692, DOI: https://doi.org/10.3762/bjoc.20.150.
- (108) Cusati, T.; Granucci, G.; Persico, M.; Spighi, G. *J. Phys. Chem.* **2008**, *128*, 194312, DOI: https://doi.org/10.1063/1.2925678.
- (109) Kawaguchi, Y. J. Chem. Phys. 1994, 100, 8856–8868, DOI: https://doi.org/10.1063/1. 466688.
- (110) Bortolus, P.; Monti, S. *J. Phys. Chem.* **1979**, *83*, 648–652, DOI: https://doi.org/10.1021/j100469a002.
- (111) Gagliardi, L.; Orlandi, G.; Bernardi, F.; Cembran, A.; Garavelli, M. *Theor. Chem. Acc.* **2004**, *111*, 363–372, DOI: https://doi.org/10.1007/s00214-003-0528-1.
- (112) Lednev, I.; Ye, T.-Q.; Matousek, P; Towrie, M; Foggi, P.; Neuwahl, F.; Umapathy, S; Hester, R.; Moore, J. N. *Chem. Phys. Lett.* **1998**, *290*, 68–74, DOI: https://doi.org/10.1016/S0009-2614(98)00490-4.
- (113) Fujino, T.; Arzhantsev, S. Y.; Tahara, T. *Bull. Chem. Soc. Jpn.* **2002**, *75*, 1031–1040, DOI: https://doi.org/10.1246/bcsj.75.1031.
- (114) Ootani, Y.; Satoh, K.; Nakayama, A.; Noro, T.; Taketsugu, T. *J. Chem. Phys.* **2009**, *131*, DOI: https://doi.org/10.1063/1.3263918.
- (115) Conti, I.; Garavelli, M.; Orlandi, G. *J. Am. Chem. Soc.* **2008**, *130*, 5216–5230, DOI: https://doi.org/10.1021/ja710275e.
- (116) Cattaneo, P.; Persico, M. *Phys. Chem. Chem. Phys.* **1999**, *1*, 4739–4743, DOI: https://doi.org/10.1039/a905055h.
- (117) Cembran, A.; Bernardi, F.; Garavelli, M.; Gagliardi, L.; Orlandi, G. *J. Am. Chem. Soc.* **2004**, *126*, 3234–3243, DOI: https://doi.org/10.1021/ja038327y.
- (118) Leigh, W. J.; Frendo, D. T.; Klawunn, P. J. *Can. J. Chem.* **1985**, *63*, 2131–2138, DOI: https://doi.org/10.1139/v85-351.
- (119) Asano, T.; Okada, T.; Shinkai, S.; Shigematsu, K.; Kusano, Y.; Manabe, O. *J. Am. Chem. Soc.* **1981**, *103*, 5161–5165, DOI: https://doi.org/10.1021/ja00407a034.

- (120) Whitten, D. G.; Wildes, P. D.; Pacifici, J. G.; Irick Jr, G. J. Am. Chem. Soc. **1971**, 93, 2004–2008, DOI: https://doi.org/10.1021/ja00737a027.
- (121) Gegiou, D.; Muszkat, K. A.; Fischer, E. J. Am. Chem. Soc. **1968**, 90, 3907–3918.
- (122) Ciccone, S.; Halpern, J. *Can. J. Chem.* **1959**, *37*, 1903–1910, DOI: https://doi.org/10.1139/v59-278.
- (123) Fischer, E. J. Am. Chem. Soc. **1960**, 82, 3249–3252, DOI: https://doi.org/10.1021/ja01498a005.
- (124) Nishimura, N.; Sueyoshi, T.; Yamanaka, H.; Imai, E.; Yamamoto, S.; Hasegawa, S. *Bull. Chem. Soc. Jpn.* **1976**, *49*, 1381–1387, DOI: https://doi.org/10.1246/bcsj.49.1381.
- (125) Blevins, A. A.; Blanchard, G. J. *J. Phys. Chem. B* **2004**, *108*, 4962–4968, DOI: https://doi.org/10.1021/jp037436w.
- (126) García-Amorós, J.; Sanchez-Ferrer, A.; Massad, W. A.; Nonell, S.; Velasco, D. *Physical Chemistry Chemical Physics* **2010**, *12*, 13238–13242, DOI: https://doi.org/10.1039/c004340k.
- (127) García-Amorós, J.; Nonell, S.; Velasco, D. *Chem. Commun.* **2011**, *47*, 4022–4024, DOI: https://doi.org/10.1039/c1cc10302d.
- (128) De Melo, C. E.; Nandi, L. G.; Domínguez, M.; Rezende, M. C.; Machado, V. G. *J. Phys. Org. Chem.* **2015**, 28, 250–260, DOI: https://doi.org/10.1002/poc.3402.
- (129) Asano, T.; Okada, T. *J. Org. Chem.* **1984**, *49*, 4387–4391, DOI: https://doi.org/10.1021/jo00197a011.
- (130) Tamai, N.; Miyasaka, H. *Chem. Rev.* **2000**, *100*, 1875–1890, DOI: https://doi.org/10.1021/cr9800816.
- (131) Brode, W. R.; Gould, J. H.; Wyman, G. M. *J. Am. Chem. Soc.* **1952**, *74*, 4641–4646, DOI: https://doi.org/10.1021/ja01138a059.
- (132) Ohtani, O.; Furukawa, T.; Sasai, R.; Hayashi, E.; Shichi, T.; Yui, T.; Takagi, K. *J. Mater. Chem.* **2004**, *14*, 196–200, DOI: https://doi.org/10.1039/b302869k.
- (133) Lednev, I. K.; Ye, T.-Q.; Abbott, L. C.; Hester, R. E.; Moore, J. N. *J. Phys. Chem. A* **1998**, *102*, 9161–9166, DOI: https://doi.org/10.1021/jp982368c.
- (134) Zacharias, P. S.; Korupoju, S. R. *J. Chem. Soc., Perkin Trans.* 2 **1998**, 2055–2060, DOI: https://doi.org/10.1039/a706775e.
- (135) Tang, Z.; Johal, M. S.; Scudder, P.; Caculitan, N.; Magyar, R. J.; Tretiak, S.; Wang, H.-L. *Thin Solid Films* **2007**, *516*, 58–66, DOI: https://doi.org/10.1016/j.tsf.2007.04.149.
- (136) Ruslim, C.; Ichimura, K. J. Mater. Chem. 2000, 10, 2704–2707, DOI: https://doi.org/10. 1039/b003975f.
- (137) Asanuma, H.; Liang, X.; Komiyama, M. *Tetrahedron Lett.* **2000**, *41*, 1055–1058, DOI: https://doi.org/10.1016/S0040-4039(99)02233-9.
- (138) Dokic, J.; Gothe, M.; Wirth, J.; Peters, M. V.; Schwarz, J.; Hecht, S.; Saalfrank, P. *J. Phys. Chem. A* **2009**, *113*, 6763–6773, DOI: https://doi.org/10.1021/jp9021344.
- (139) García-Amorós, J.; Velasco, D. *Beilstein J. Org. Chem.* **2012**, *8*, 1003–1017, DOI: https://doi.org/10.3762/bjoc.8.113.

- (140) Serra, F.; Terentjev, E. M. *Macromolecules* **2008**, *41*, 981–986, DOI: https://doi.org/10.1021/ma702033e.
- (141) Chi, L.; Sadovski, O.; Woolley, G. A. *Bioconjug. Chem.* **2006**, *17*, 670–676, DOI: https://doi.org/10.1021/bc050363u.
- (142) Forber, C. L.; Kelusky, E. C.; Bunce, N. J.; Zerner, M. C. *J. Am. Chem. Soc.* **1985**, *107*, 5884–5890, DOI: https://doi.org/10.1021/ja00307a009.
- (143) Tauer, E.; Machinek, R. *Liebigs Ann.* **1996**, *1996*, 1213–1216, DOI: https://doi.org/10.1002/jlac.199619960723.
- (144) Konrad, D. B.; Savasci, G.; Allmendinger, L.; Trauner, D.; Ochsenfeld, C.; Ali, A. M. *J. Am. Chem. Soc.* **2020**, *142*, 6538–6547, DOI: https://doi.org/10.1021/jacs.9b10430.
- (145) Knie, C.; Utecht, M.; Zhao, F.; Kulla, H.; Kovalenko, S.; Brouwer, A. M.; Saalfrank, P.; Hecht, S.; Bléger, D. Chem. Eur. J. 2014, 20, 16492–16501, DOI: https://doi.org/10.1002/chem.201404649.
- (146) Yang, Y.; Hughes, R. P.; Aprahamian, I. *J. Am. Chem. Soc.* **2012**, *134*, 15221–15224, DOI: https://doi.org/10.1021/ja306030d.
- (147) Moreno, J.; Gerecke, M.; Grubert, L.; Kovalenko, S. A.; Hecht, S. *Angew. Chem. Int. Ed.* **2016**, 55, 1544–1547, DOI: https://doi.org/10.1002/anie.201509111.
- (148) Gemen, J.; Church, J. R.; Ruoko, T.-P.; Durandin, N.; Białek, M. J.; Weißenfels, M.; Feller, M.; Kazes, M.; Odaybat, M.; Borin, V. A. *Science* **2023**, *381*, 1357–1363, DOI: https://doi.org/10.1126/science.adh9059.
- (149) Mahimwalla, Z.; Yager, K. G.; Mamiya, J.-i.; Shishido, A.; Priimagi, A.; Barrett, C. J. *Polym. Bull.* **2012**, *69*, 967–1006, DOI: https://doi.org/10.1007/s00289-012-0792-0.
- (150) Yesodha, S. K.; Pillai, C. K. S.; Tsutsumi, N. *Prog. Polym. Sci.* **2004**, *29*, 45–74, DOI: https://doi.org/10.1016/j.progpolymsci.2003.07.002.
- (151) Pang, X.; Lv, J.; Zhu, C.; Qin, L.; Yu, Y. Adv. Mater. **2019**, 31, 1904224, DOI: https://doi.org/10.1002/adma.201904224.
- (152) Dong, L.; Feng, Y.; Wang, L.; Feng, W. *Chem. Soc. Rev.* **2018**, *47*, 7339–7368, DOI: https://doi.org/10.1039/c8cs00470f.
- (153) Fedele, C; Netti, P.; Cavalli, S *Biomater. Sci.* **2018**, *6*, 990–995, DOI: https://doi.org/10.1039/c8bm00019k.
- (154) Mart, R. J.; Allemann, R. K. *Chem. Commun.* **2016**, *52*, 12262–12277, DOI: https://doi.org/10.1039/c6cc04004g.
- (155) Szymański, W.; Beierle, J. M.; Kistemaker, H. A.; Velema, W. A.; Feringa, B. L. *Chem. Rev.* **2013**, *113*, 6114–6178, DOI: https://doi.org/10.1021/cr300179f.
- (156) Barber, D. M.; Liu, S.-A.; Gottschling, K.; Sumser, M.; Hollmann, M.; Trauner, D. *Chem. Sci.* **2017**, *8*, 611–615, DOI: https://doi.org/10.1039/c6sc01621a.
- (157) Van der Berg, J.; Velema, W.; Szymański, W; Driessen, A.; Feringa, B. *Chem. Sci.* **2015**, *6*, 3593–3598, DOI: https://doi.org/10.1039/c5sc00215j.
- (158) Fissi, A.; Pieroni, O.; Balestreri, E.; Amato, C. *Macromolecules* **1996**, 29, 4680–4685, DOI: https://doi.org/10.1021/ma960280w.

- (159) Volgraf, M.; Gorostiza, P.; Numano, R.; Kramer, R. H.; Isacoff, E. Y.; Trauner, D. *Nat. Chem. Biol.* **2006**, *2*, 47–52, DOI: https://doi.org/10.1038/nchembio756.
- (160) Nevola, L.; Martín-Quirós, A.; Eckelt, K.; Camarero, N.; Tosi, S.; Llobet, A.; Giralt, E.; Gorostiza, P. Angew. Chem. Int. Ed. 2013, 52, 7704–7708, DOI: https://doi.org/10.1002/anie.201303324.
- (161) Albert, L.; Peñalver, A.; Djokovic, N.; Werel, L.; Hoffarth, M.; Ruzic, D.; Xu, J.; Essen, L.; Nikolic, K.; Dou, Y.; Vázquez, O. *ChemBioChem* **2019**, *20*, 1417–1429, DOI: https://doi.org/10.1002/cbic.201800737.
- (162) Dong, S.; Löweneck, M.; Schrader, T. E.; Schreier, W. J.; Zinth, W.; Moroder, L.; Renner, C. *Chem. Eur. J.* **2006**, *12*, 1114–1120, DOI: https://doi.org/10.1002/chem.200500986.
- (163) Doran, T. M.; Anderson, E. A.; Latchney, S. E.; Opanashuk, L. A.; Nilsson, B. L. *ACS Chem. Neurosci.* **2012**, *3*, 211–20, DOI: https://doi.org/10.1021/cn2001188.
- (164) Hoppmann, C.; Seedorff, S.; Richter, A.; Fabian, H.; Schmieder, P.; Rück-Braun, K.; Beyermann, M. Angew. Chem. Int. Ed. 2009, 48, 6636–6639, DOI: https://doi.org/10.1002/anie.200901933.
- (165) Schnölzer, M.; Kent, S. B. Science 1992, 256, 221–225, DOI: https://doi.org/10.1126/science.1566069.
- (166) Aemissegger, A.; Kräutler, V.; van Gunsteren, W. F.; Hilvert, D. *J. Am. Chem. Soc.* **2005**, *127*, 2929–2936, DOI: https://doi.org/10.1021/ja0442567.
- (167) Rück-Braun, K.; Kempa, S.; Priewisch, B.; Richter, A.; Seedorff, S.; Wallach, L. *Synthesis* **2009**, *24*, 4256–4267, DOI: https://doi.org/10.1055/s-0029-1217074.
- (168) Zbaida, S. Drug Metab. Rev. 1995, 27, 497–516, DOI: https://doi.org/10.3109/ 03602539508998333.
- (169) Boulègue, C.; Löweneck, M.; Renner, C.; Moroder, L. *ChemBioChem* **2007**, *8*, 591–594, DOI: https://doi.org/10.1002/cbic.200600495.
- (170) Zhu, J.; Guo, T.; Wang, Z.; Zhao, Y. *J. Control. Release* **2022**, *345*, 475–493, DOI: https://doi.org/10.1016/j.jconrel.2022.03.041.
- (171) Guo, X.; Liu, F.; Deng, J.; Dai, P.; Qin, Y.; Li, Z.; Wang, B.; Fan, A.; Wang, Z.; Zhao, Y. *ACS Nano* **2020**, *14*, 14715–14730, DOI: https://doi.org/10.1021/acsnano.0c00764.
- (172) Wong, A. D.; Güngör, T. M.; Gillies, E. R. *ACS Macro Lett.* **2014**, *3*, 1191–1195, DOI: https://doi.org/10.1021/mz500613d.
- (173) Mutlu, H.; Barner-Kowollik, C. *Polym. Chem.* **2016**, 7, 2272–2279, DOI: https://doi.org/10.1039/c5py01937k.
- (174) Klajn, R. *Chem. Soc. Rev.* **2014**, *43*, 148–184, DOI: https://doi.org/10.1039/c3cs60181a.
- (175) Kortekaas, L.; Browne, W. R. *Chem. Soc. Rev.* **2019**, *48*, 3406–3424, DOI: https://doi.org/10.1039/c9cs00203k.
- (176) Ali, A. A.; Kharbash, R.; Kim, Y. *Anal. Chim. Acta* **2020**, *1110*, 199–223, DOI: https://doi.org/10.1016/j.aca.2020.01.057.
- (177) Piard, J. J. Chem. Educ. **2014**, 91, 2105–2111, DOI: https://doi.org/10.1021/ed4005003.

- (178) Phillips, J.; Mueller, A; Przystal, F *J. Am. Chem. Soc.* **1965**, 87, 4020–4020, DOI: https://doi.org/10.1021/ja01095a067.
- (179) Ma, G.; Zhou, Q.; Zhang, X.; Xu, Y.; Liu, H. *New J. Chem.* **2014**, *38*, 552–560, DOI: https://doi.org/10.1039/c3nj01238g.
- (180) Shiraishi, Y.; Miyamoto, R.; Hirai, T. *Org. Lett.* **2009**, *11*, 1571–1574, DOI: https://doi.org/10.1021/o1900188m.
- (181) Wagner, K.; Byrne, R.; Zanoni, M.; Gambhir, S.; Dennany, L.; Breukers, R.; Higgins, M.; Wagner, P.; Diamond, D.; Wallace, G. G. J. Am. Chem. Soc. **2011**, 133, 5453–5462, DOI: https://doi.org/10.1021/ja1114634.
- (182) Raisch, M.; Genovese, D.; Zaccheroni, N.; Schmidt, S. B.; Focarete, M. L.; Sommer, M.; Gualandi, C. *Adv. Mater.* **2018**, *30*, 1802813, DOI: https://doi.org/10.1002/adma. 201802813.
- (183) Decker, H.; Felser, H. *Ber. Dtsch. Chem. Ges.* **1908**, *41*, 2997–3007, DOI: https://doi.org/10.1002/cber.190804102251.
- (184) Löwenbein, A; Katz, W *Ber. Dtsch. Chem. Ges.* **1926**, *59*, 1377–1383, DOI: https://doi.org/10.1002/cber.19260590704.
- (185) Dilthey, W; Wizinger, R *Ber. Dtsch. Chem. Ges.* **1926**, *59*, 1856–1858, DOI: https://doi.org/10.1002/cber.19260590830.
- (186) Dilthey, W; Berres, C; Hölterhoff, E; Wübken, H *J. Prakt. Chem.* **1926**, *114*, 179–198, DOI: https://doi.org/10.1002/prac.19261140108.
- (187) Irving, F. J. Chem. Soc. **1929**, 1093–1095, DOI: https://doi.org/doi.org/10.1039/JR9290001093.
- (188) Fischer, E.; Hess, O. *Ber. Dtsch. Chem. Ges.* **1884**, *17*, 454–462, DOI: https://doi.org/doi.org/10.1002/cber.188401701155.
- (189) Hirshberg, Y. J. Am. Chem. Soc. **1956**, 78, 2304–2312, DOI: https://doi.org/10.1021/ja01591a075.
- (190) Potisek, S. L.; Davis, D. A.; Sottos, N. R.; White, S. R.; Moore, J. S. *J. Am. Chem. Soc.* **2007**, *129*, 13808–13809, DOI: https://doi.org/10.1021/ja076189x.
- (191) Krysanov, S.; Alfimov, M. *Chem. Phys. Lett.* **1982**, *91*, 77–80, DOI: https://doi.org/10. 1016/0009-2614(82)87037-1.
- (192) Karube, I.; Nakamoto, Y.; Suzuki, S. *Biochim. Biophys. Acta* **1976**, *445*, 774–779, DOI: https://doi.org/10.1016/0005-2744(76)90127-3.
- (193) Smets, G; Braeken, J; Irie, M *Pure Appl. Chem.* **1978**, *50*, 845–856.
- (194) Sommer, M.; Komber, H. *Macromol. Rapid Commun.* **2013**, *34*, 57–62, DOI: https://doi.org/10.1002/marc.201200688.
- (195) Lukyanov, B.; Lukyanova, M. *Chem. Heterocycl. Compd.* **2005**, *41*, 281–311, DOI: https://doi.org/10.1007/s10593-005-0148-x.
- (196) Gruler, H; Vilanove, R; Rondelez, F *Phys. Rev. Lett.* **1980**, *44*, 590, DOI: https://doi.org/10.1103/PhysRevLett.44.590.
- (197) Shen, Q.; Cao, Y.; Liu, S.; Steigerwald, M. L.; Guo, X. J. Phys. Chem. C **2009**, 113, 10807–10812, DOI: https://doi.org/10.1021/jp9026817.

- (198) Levitus, M.; Glasser, G.; Neher, D.; Aramendía, P. F. *Chem. Phys. Lett.* **1997**, 277, 118–124, DOI: https://doi.org/10.1016/S0009-2614(97)00826-9.
- (199) Tyer Jr, N. W.; Becker, R. S. J. Am. Chem. Soc. 1970, 92, 1289-1294, DOI: https://doi.org/10.1021/ja00708a031.
- (200) Chen, J.; Zeng, F.; Wu, S. *ChemPhysChem* **2010**, *11*, 1036–1043, DOI: https://doi.org/10.1002/cphc.200900999.
- (201) Berton, C.; Busiello, D. M.; Zamuner, S.; Solari, E.; Scopelliti, R.; Fadaei-Tirani, F.; Severin, K.; Pezzato, C. Chem. Sci. 2020, 11, 8457–8468, DOI: https://doi.org/10.1039/d0sc03152f.
- (202) Such, G.; Evans, R. A.; Yee, L. H.; Davis, T. P. *J. Macromol. Sci., Part C: Polym. Rev.* **2003**, 43, 547–579, DOI: https://doi.org/10.1081/Mc-120025978.
- (203) McCoy, C. P.; Donnelly, L.; Jones, D. S.; Gorman, S. P. *Tetrahedron Lett.* **2007**, *48*, 657–661, DOI: https://doi.org/10.1016/j.tetlet.2006.11.110.
- (204) Hirshberg, Y.; Fischer, E. *J. Chem. Phys.* **1953**, *21*, 1619–1620, DOI: https://doi.org/10.1063/1.1699322.
- (205) Görner, H. *Phys. Chem. Chem. Phys.* **2001**, *3*, 416–423, DOI: https://doi.org/10.1039/B007708I.
- (206) Parthenopoulos, D. A.; Rentzepis, P. M. *Science* **1989**, 245, 843–845, DOI: https://doi.org/10.1126/science.245.4920.843.
- (207) Buback, J.; Nuernberger, P.; Kullmann, M.; Langhojer, F.; Schmidt, R.; Würthner, F.; Brixner, T. *J. Phys. Chem. A* **2011**, *115*, 3924–3935, DOI: https://doi.org/10.1021/jp108322u.
- (208) Hobley, J.; Pfeifer-Fukumura, U.; Bletz, M.; Asahi, T.; Masuhara, H.; Fukumura, H. *J. Phys. Chem. A* **2002**, *106*, 2265–2270, DOI: https://doi.org/10.1021/jp012564a.
- (209) Day, J. H. Chem. Rev. 1963, 63, 65-80, DOI: https://doi.org/10.1021/cr60221a005.
- (210) Wizinger, R; Wenning, H *Helv. Chim. Acta* **1940**, *23*, 247–271, DOI: https://doi.org/10.1002/hlca.19400230133.
- (211) Mustafa, A. Chem. Rev. 1948, 43, 509-523, DOI: https://doi.org/10.1021/cr60136a004.
- (212) Tian, W.; Tian, J. *Dyes Pigm.* **2014**, *105*, 66–74, DOI: https://doi.org/10.1016/j.dyepig.2014.01.020.
- (213) Roxburgh, C. J.; Sammes, P. G. *Dyes Pigments* **1995**, 27, 63–69, DOI: https://doi.org/Doi10.1016/0143-7208(94)00059-B.
- (214) Kortekaas, L; Chen, J.; Jacquemin, D; Browne, W. J. Phys. Chem. B **2018**, 122, 6423–6430, DOI: https://doi.org/10.1021/acs.jpcb.8b03528.
- (215) Li, M.; Zhang, Q.; Zhou, Y.-N.; Zhu, S. *Prog. Polym. Sci.* **2018**, *79*, 26–39, DOI: https://doi.org/10.1016/j.progpolymsci.2017.11.001.
- (216) Tipikin, D. Russ. J. Phys. Chem. A 2001, 75, 1720–1722.
- (217) Balmond, E. I.; Tautges, B. K.; Faulkner, A. L.; Or, V. W.; Hodur, B. M.; Shaw, J. T.; Louie, A. Y. *J. Org. Chem.* **2016**, *81*, 8744–8758, DOI: https://doi.org/10.1021/acs.joc.6b01193.
- (218) Knott, E. B. *J. Chem. SOc.* **1951**, 3038-3047, DOI: https://doi.org/10.1039/JR9510003038.

- (219) Palasis, K. A.; Abell, A. D. *Tetrahedron Lett.* **2024**, *138*, 154967, DOI: https://doi.org/10.1016/j.tetlet.2024.154967.
- (220) Rad, J. K.; Balzade, Z.; Mahdavian, A. R. *J. Photochem. Photobiol. C* **2022**, *51*, 100487, DOI: https://doi.org/10.1016/j.jphotochemrev.2022.100487.
- (221) Fagan, A.; Bartkowski, M.; Giordani, S. *Front. Chem.* **2021**, *9*, 720087, DOI: https://doi.org/10.3389/fchem.2021.720087.
- (222) Son, S.; Shin, E.; Kim, B.-S. *Biomacromolecules* **2014**, *15*, 628–634, DOI: https://doi.org/10.1021/bm401670t.
- (223) Del Canto, E.; Natali, M.; Movia, D.; Giordani, S. *Phys. Chem. Chem. Phys.* **2012**, *14*, 6034–6043, DOI: https://doi.org/10.1039/c2cp40275k.
- (224) Fujimoto, K.; Amano, M.; Horibe, Y.; Inouye, M. *Org. Lett.* **2006**, *8*, 285–287, DOI: https://doi.org/10.1021/ol0526524.
- (225) Qiu, Z.; Yu, H.; Li, J.; Wang, Y.; Zhang, Y. *Chem. Commun.* **2009**, 3342–3344, DOI: https://doi.org/10.1039/b822840j.
- (226) Hrebonkin, A.; Afonin, S.; Nikitjuka, A.; Borysov, O. V.; Leitis, G.; Babii, O.; Koniev, S.; Lorig, T.; Grage, S. L.; Nick, P. *Chem. Eur. J.* **2024**, *30*, e202400066, DOI: https://doi.org/10.1002/chem.202400066.
- (227) Strano, M. S.; Dyke, C. A.; Usrey, M. L.; Barone, P. W.; Allen, M. J.; Shan, H.; Kittrell, C.; Hauge, R. H.; Tour, J. M.; Smalley, R. E. *Science* **2003**, *301*, 1519–1522.
- (228) Cardano, F.; Del Canto, E.; Giordani, S. *Dalton Trans.* **2019**, *48*, 15537–15544, DOI: https://doi.org/10.1039/c9dt02092f.
- (229) Sommer, M. *Macromol. Rapid Commun.* **2021**, *42*, 2000597, DOI: https://doi.org/10. 1002/marc.202000597.
- (230) Stafforst, T.; Hilvert, D. *Chem. Commun.* **2009**, 287–288, DOI: https://doi.org/10.1039/b818050d.
- (231) Minkin, V. I. *Chem. Rev.* **2004**, *104*, 2751–2776, DOI: https://doi.org/10.1021/cr020088u.
- (232) Mühlberg, E.; Umstätter, F.; Kleist, C.; Domhan, C.; Mier, W.; Uhl, P. *Can. J. Microbiol.* **2020**, 66, 11–16, DOI: https://doi.org/10.1139/cjm-2019-0309.
- (233) Aibani, N.; da Costa, P. F.; Masterson, J.; Marino, N.; Raymo, F. M.; Callan, J.; Callan, B. *J. Control. Release* **2017**, 264, 136–144, DOI: https://doi.org/10.1016/j.jconrel.2017.08.013.
- (234) Lehn, J. *Angew. Chem. Int. Ed.* **1990**, 29, 1304–1319, DOI: https://doi.org/10.1002/anie.199013041.
- (235) Zhang, S. *Mater. Today* **2003**, *6*, 20–27, DOI: https://doi.org/10.1016/S1369-7021(03)00530-3.
- (236) Feynman, R. P. Engineering and Science **1960**, 23, 22–36.
- (237) Zhu, J.; Avakyan, N.; Kakkis, A.; Hoffnagle, A. M.; Han, K.; Li, Y.; Zhang, Z.; Choi, T. S.; Na, Y.; Yu, C.-J. Chem. Rev. 2021, 121, 13701–13796, DOI: https://doi.org/10.1021/acs.chemrev.1c00308.

- (238) Watson, H. *Essays Biochem.* **2015**, *59*, 43–69, DOI: https://doi.org/10.1042/bse0590043.
- (239) Weis, W. I.; Drickamer, K. *Annu. Rev. Biochem.* **1996**, *65*, 441–473, DOI: https://doi.org/10.1146/annurev.bi.65.070196.002301.
- (240) Ochman, H.; Lawrence, J. G.; Groisman, E. A. *Nature* **2000**, *405*, 299–304, DOI: https://doi.org/10.1038/35012500.
- (241) Perozo, E.; Cortes, D. M.; Sompornpisut, P.; Kloda, A.; Martinac, B. *Nature* **2002**, *418*, 942–948, DOI: https://doi.org/10.1038/nature00992.
- (242) Rajagopal, K.; Schneider, J. P. *Curr. Opin. Struct. Biol.* **2004**, *14*, 480–486, DOI: https://doi.org/10.1016/j.sbi.2004.06.006.
- (243) Jaradat, D. M. *Amino Acids* **2018**, *50*, 39–68, DOI: https://doi.org/10.1007/s00726-017-2516-0.
- (244) Lu, K.; Jacob, J.; Thiyagarajan, P.; Conticello, V. P.; Lynn, D. G. *J. Am. Chem. Soc.* **2003**, *125*, 6391–6393, DOI: https://doi.org/10.1021/ja0341642.
- (245) Zhang, S. *Interface focus* **2017**, 7, 20170028, DOI: https://doi.org/10.1098/rsfs. 2017.0028.
- (246) Kyle, R. A. *Br. J. Haematol.* **2001**, *114*, 529–38, DOI: https://doi.org/10.1046/j.1365-2141.2001.02999.x.
- (247) Sunde, M.; Serpell, L. C.; Bartlam, M.; Fraser, P. E.; Pepys, M. B.; Blake, C. C. *J. Mol. Biol.* **1997**, 273, 729–739, DOI: https://doi.org/10.1006/jmbi.1997.1348.
- (248) Westermark, P.; Andersson, A.; Westermark, G. T. *Physiol. Rev.* **2011**, *91*, 795–826, DOI: https://doi.org/10.1152/physrev.00042.2009.
- (249) Conway, K. A.; Harper, J. D.; Lansbury, P. T. *Biochemistry* **2000**, *39*, 2552–2563, DOI: https://doi.org/10.1021/bi991447r.
- (250) Tycko, R.; Wickner, R. B. *Accounts of chemical research* **2013**, *46*, 1487–1496, DOI: https://doi.org/10.1021/ar300282r.
- (251) Sipe, J. D.; Cohen, A. S. *J. Struct. Biol.* **2000**, *130*, 88–98, DOI: https://doi.org/10.1006/jsbi.2000.4221.
- (252) Benditt, E.; Eriksen, N; Hermodson, M.; Ericsson, L. *FEBS Lett.* **1971**, *19*, 169–173, DOI: https://doi.org/10.1016/0014-5793(71)80506-9.
- (253) Cohen, A. S.; Calkins, E. *Nature* **1959**, *183*, 1202–1203, DOI: https://doi.org/10.1038/1831202a0.
- (254) Alzheimer, A. Neurol. Central. 1906, 23, 1129–1136.
- (255) Chartier-Harlin, M.-C.; Kachergus, J.; Roumier, C.; Mouroux, V.; Douay, X.; Lincoln, S.; Levecque, C.; Larvor, L.; Andrieux, J.; Hulihan, M. *The Lancet* **2004**, *364*, 1167–1169, DOI: https://doi.org/10.1016/S0140-6736(04)17103-1.
- (256) Prusiner, S. B.; McKinley, M. P.; Bowman, K. A.; Bolton, D. C.; Bendheim, P. E.; Groth, D. F.; Glenner, G. G. Cell 1983, 35, 349–358, DOI: https://doi.org/10.1016/0092-8674(83)90168-x.
- (257) Sipe, J. D.; Benson, M. D.; Buxbaum, J. N.; Ikeda, S.-i.; Merlini, G.; Saraiva, M. J.; Westermark, P. *Amyloid* **2016**, *23*, 209–213, DOI: https://doi.org/10.1080/13506129.2016.1257986.

- (258) Iadanza, M. G.; Jackson, M. P.; Hewitt, E. W.; Ranson, N. A.; Radford, S. E. *Nat. Rev. Mol. Cell Biol.* **2018**, *19*, 755–773, DOI: https://doi.org/10.1038/s41580-018-0060-8.
- (259) Chiti, F.; Dobson, C. M. *Annu. Rev. Biochem.* **2017**, *86*, 27–68, DOI: https://doi.org/10.1146/annurev-biochem-061516-045115.
- (260) Otzen, D.; Riek, R. *Cold Spring Harb. Perspect. Biol.* **2019**, *11*, a033860, DOI: https://doi.org/10.1101/cshperspect.a033860.
- (261) Dobson, C. M. *Nature* **2003**, 426, 884–890, DOI: https://doi.org/10.1038/nature02261.
- (262) Li, J.; Uversky, V. N.; Fink, A. L. *Biochemistry* **2001**, *40*, 11604–11613, DOI: https://doi.org/10.1021/bi010616g.
- (263) Krone, M. G.; Baumketner, A.; Bernstein, S. L.; Wyttenbach, T.; Lazo, N. D.; Teplow, D. B.; Bowers, M. T.; Shea, J.-E. J. Mol. Biol. 2008, 381, 221–228, DOI: https://doi.org/10. 1016/j.jmb.2008.05.069.
- (264) Morilla, M. E.; Kocher, J.; Harmaty, M. *Ann. Intern. Med.* **2009**, *151*, 515–516, DOI: https://doi.org/10.7326/0003-4819-151-7-200910060-00017.
- (265) Imran, M.; Mahmood, S. *Virol. J.* **2011**, *8*, 1–9, DOI: https://doi.org/10.1186/1743-422X-8-559.
- (266) Chapman, M. R.; Robinson, L. S.; Pinkner, J. S.; Roth, R.; Heuser, J.; Hammar, M.; Normark, S.; Hultgren, S. J. *Science* **2002**, *295*, 851–855, DOI: https://doi.org/10.1126/science.1067484.
- (267) Claessen, D.; Rink, R.; de Jong, W.; Siebring, J.; de Vreugd, P.; Boersma, F. H.; Dijkhuizen, L.; Wösten, H. A. *Genes Dev.* **2003**, *17*, 1714–1726, DOI: https://doi.org/10.1101/gad. 264303.
- (268) Coustou, V.; Deleu, C.; Saupe, S.; Begueret, J. *Proc. Natl. Acad. Sci. U.S.A.* **1997**, *94*, 9773–9778, DOI: https://doi.org/D0I10.1073/pnas.94.18.9773.
- (269) Butko, P.; Buford, J. P.; Goodwin, J. S.; Stroud, P. A.; McCormick, C. L.; Cannon, G. C. *Biochem-Biophys. Res. Commun.* **2001**, 280, 212–215, DOI: https://doi.org/10.1006/bbrc.2000.4098.
- (270) Iconomidou, V. A.; Vriend, G.; Hamodrakas, S. J. FEBS Lett. 2000, 479, 141–145.
- (271) Kenney, J. M.; Knight, D.; Wise, M. J.; Vollrath, F. *Eur. J. Biochem.* **2002**, *269*, 4159–4163, DOI: https://doi.org/10.1046/j.1432-1033.2002.03112.x.
- (272) Fowler, D. M.; Koulov, A. V.; Alory-Jost, C.; Marks, M. S.; Balch, W. E.; Kelly, J. W. *PLoS Biology* **2006**, *4*, e6, DOI: https://doi.org/10.1371/journal.pbio.0040006.
- (273) Balistreri, A; Goetzler, E; Chapman, M *Microorganisms* **2020**, *8*, 1951, DOI: https://doi.org/10.3390/microorganisms8121951.
- (274) Levkovich, S. A.; Gazit, E.; Bar-Yosef, D. L. *Trends Microbiol.* **2021**, *29*, 251–265, DOI: https://doi.org/10.1016/j.tim.2020.09.005.
- (275) Maji, S. K.; Perrin, M. H.; Sawaya, M. R.; Jessberger, S.; Vadodaria, K.; Rissman, R. A.; Singru, P. S.; Nilsson, K. R.; Simon, R.; Schubert, D.; Eisenberg, D.; Rivier, J.; Sawchenko, P.; Vale, W.; Riek, R. *Science* 2009, 325, 328–332, DOI: https://doi.org/10.1126/science.1173155.

- (276) Bieler, S.; Estrada, L.; Lagos, R.; Baeza, M.; Castilla, J.; Soto, C. *J. Biol. Chem.* **2005**, 280, 26880–26885, DOI: https://doi.org/10.1074/jbc.M502031200.
- (277) Dueholm, M. S.; Petersen, S. V.; Sønderkær, M.; Larsen, P.; Christiansen, G.; Hein, K. L.; Enghild, J. J.; Nielsen, J. L.; Nielsen, K. L.; Nielsen, P. H. *Mol. Microbiol.* **2010**, 77, 1009–1020, DOI: https://doi.org/10.1111/j.1365-2958.2010.07269.x.
- (278) True, H. L.; Lindquist, S. L. *Nature* **2000**, *407*, 477–483, DOI: https://doi.org/10.1038/35035005.
- (279) Berchowitz, L. E.; Kabachinski, G.; Walker, M. R.; Carlile, T. M.; Gilbert, W. V.; Schwartz, T. U.; Amon, A. *Cell* **2015**, *163*, 406–418, DOI: https://doi.org/10.1016/j.cell.2015.08.060.
- (280) Wösten, H. A.; de Vocht, M. L. *Biochim. Biophys. Acta* **2000**, *1469*, 79–86, DOI: https://doi.org/10.1016/s0304-4157(00)00002-2.
- (281) Berthelot, K.; Lecomte, S.; Estevez, Y.; Coulary-Salin, B.; Bentaleb, A.; Cullin, C.; Deffieux, A.; Peruch, F. *PLoS One* **2012**, 7, e48065, DOI: https://doi.org/10.1371/journal.pone.0048065.
- (282) Antonets, K. S. et al. *Plos Biol.* **2020**, *18*, e3000564, DOI: https://doi.org/10.1371/journal.pbio.3000564.
- (283) Li, J.; McQuade, T.; Siemer, A. B.; Napetschnig, J.; Moriwaki, K.; Hsiao, Y.-S.; Damko, E.; Moquin, D.; Walz, T.; McDermott, A. *Cell* **2012**, *150*, 339–350, DOI: https://doi.org/10.1016/j.cell.2012.06.019.
- (284) Fowler, D. M.; Koulov, A. V.; Balch, W. E.; Kelly, J. W. *Trends Biochem. Sci.* **2007**, *32*, 217–224, DOI: https://doi.org/10.1016/j.tibs.2007.03.003.
- (285) Astbury, W. T.; Dickinson, S.; Bailey, K. *Biochem. J.* **1935**, 29, 2351, DOI: https://doi.org/10.1042/bj0292351.
- (286) Geddes, A.; Parker, K.; Atkins, E.; Beighton, E *J. Mol. Biol.* **1968**, *32*, 343–358, DOI: https://doi.org/10.1016/0022-2836(68)90014-4.
- (287) Eanes, E.; Glenner, G. J. Histochem. Cytochem. **1968**, 16, 673–677, DOI: https://doi.org/10.1177/16.11.673.
- (288) Bonar, L.; Cohen, A. S.; Skinner, M. M. *Proc. Soc. Exp. Biol. Med.* **1969**, *131*, 1373–1375, DOI: https://doi.org/10.3181/00379727-131-34110.
- (289) Eisenberg, D. S.; Sawaya, M. R. *Annu. Rev. Biochem.* **2017**, *86*, 69–95, DOI: https://doi.org/10.1146/annurev-biochem-061516-045104.
- (290) Knowles, T. P.; Vendruscolo, M.; Dobson, C. M. *Nat. Rev. Mol. Cell Biol.* **2014**, *15*, 384–396, DOI: https://doi.org/10.1038/nrm3810.
- (291) Serio, T. R.; Cashikar, A. G.; Kowal, A. S.; Sawicki, G. J.; Moslehi, J. J.; Serpell, L.; Arnsdorf, M. F.; Lindquist, S. L. Science 2000, 289, 1317–1321, DOI: https://doi.org/10.1126/science.289.5483.1317.
- (292) Chiti, F.; Webster, P.; Taddei, N.; Clark, A.; Stefani, M.; Ramponi, G.; Dobson, C. M. *Proc. Natl. Acad. Sci. U.S.A.* **1999**, *96*, 3590–3594, DOI: https://doi.org/10.1073/pnas.96.7.3590.
- (293) Eisenberg, D.; Jucker, M. *Cell* **2012**, *148*, 1188–1203, DOI: https://doi.org/10.1016/j.cell.2012.02.022.

- (294) Sicorello, A.; Torrassa, S.; Soldi, G.; Gianni, S.; Travaglini-Allocatelli, C.; Taddei, N.; Relini, A.; Chiti, F. *Biophys. J.* **2009**, *96*, 2289–2298, DOI: https://doi.org/10.1016/j.bpj. 2008.11.042.
- (295) Morris, A. M.; Watzky, M. A.; Finke, R. G. *Biochim. Biophys. Acta Proteins Proteom.* **2009**, 1794, 375–97, DOI: https://doi.org/10.1016/j.bbapap.2008.10.016.
- (296) Karamanos, T. K.; Kalverda, A. P.; Thompson, G. S.; Radford, S. E. *Prog. Nucl. Magn. Reson. Spectrosc.* **2015**, 88, 86–104, DOI: https://doi.org/10.1016/j.pnmrs.2015.05.002.
- (297) Meisl, G.; Kirkegaard, J. B.; Arosio, P.; Michaels, T. C.; Vendruscolo, M.; Dobson, C. M.; Linse, S.; Knowles, T. P. Nat. Protoc. 2016, 11, 252-272, DOI: https://doi.org/10.1038/nprot.2016.010.
- (298) Linse, S. *Biophys. Rev.* **2017**, *9*, 329–338, DOI: https://doi.org/10.1007/s12551-017-0289-z.
- (299) Tuite, M. F. Cell **2000**, 100, 289–292, DOI: https://doi.org/10.1016/S0092-8674(00) 80663-7.
- (300) Sebastiao, M.; Quittot, N.; Bourgault, S. *Anal. Biochem.* **2017**, *532*, 83–86, DOI: https://doi.org/10.1016/j.ab.2017.06.007.
- (301) LeVine III, H. In *Methods in Enzymology*; Elsevier: 1999, pp 274–284, DOI: https://doi.org/10.1016/S0076-6879(99)09020-5.
- (302) Wolfe, L. S.; Calabrese, M. F.; Nath, A.; Blaho, D. V.; Miranker, A. D.; Xiong, Y. *Proc. Natl. Acad. Sci. U.S.A.* **2010**, *107*, 16863–16868, DOI: https://doi.org/10.1073/pnas.1002867107.
- (303) Wetzel, R. *Acc. Chem. Res.* **2006**, *39*, 671–679, DOI: https://doi.org/10.1021/ar050069h.
- (304) Chun, S. Y.; Son, M. K.; Park, C. R.; Lim, C.; Kim, H. I.; Kwak, K.; Cho, M. *Chem. Sci.* **2022**, *13*, 4482–4489, DOI: https://doi.org/10.1039/d1sc06047c.
- (305) Zandomeneghi, G.; Krebs, M. R.; McCammon, M. G.; Fändrich, M. *Protein Sci.* **2004**, *13*, 3314–3321, DOI: https://doi.org/10.1110/ps.041024904.
- (306) Fränzl, M.; Thalheim, T.; Adler, J.; Huster, D.; Posseckardt, J.; Mertig, M.; Cichos, F. *Nat. Methods* **2019**, *16*, 611–614, DOI: https://doi.org/10.1038/s41592-019-0451-6.
- (307) Pinotsi, D.; Buell, A. K.; Galvagnion, C.; Dobson, C. M.; Kaminski Schierle, G. S.; Kaminski, C. F. *Nano Lett.* **2014**, *14*, 339–345, DOI: https://doi.org/10.1021/nl4041093.
- (308) Puchtler, H.; Sweat, F.; Levine, M *J. Histochem. Cytochem.* **1962**, *10*, 355–364, DOI: https://doi.org/10.1177/10.3.355.
- (309) Nilsson, M. R. *Methods* **2004**, *34*, 151–160, DOI: https://doi.org/10.1016/j.ymeth. 2004.03.012.
- (310) Adamcik, J.; Mezzenga, R. *Curr. Opin. Colloid Interface Sci.* **2012**, *17*, 369–376, DOI: https://doi.org/10.1016/j.cocis.2012.08.001.
- (311) Kühlbrandt, W. *Science* **2014**, *343*, 1443–1444, DOI: https://doi.org/10.1126/science. 1251652.
- (312) Li, Y.; Zhao, C.; Luo, F.; Liu, Z.; Gui, X.; Luo, Z.; Zhang, X.; Li, D.; Liu, C.; Li, X. *Cell Res.* **2018**, 28, 897–903, DOI: https://doi.org/10.1038/s41422-018-0075-x.

- (313) Tang, M.; Comellas, G.; Rienstra, C. M. *Acc. Chem. Res.* **2013**, *46*, 2080–2088, DOI: https://doi.org/10.1021/ar4000168.
- (314) Wälti, M. A.; Ravotti, F.; Arai, H.; Glabe, C. G.; Wall, J. S.; Böckmann, A.; Güntert, P.; Meier, B. H.; Riek, R. *Proc. Natl. Acad. Sci. U.S.A.* **2016**, *113*, E4976–E4984, DOI: https://doi.org/10.1073/pnas.1600749113.
- (315) Paschold, A.; Schäffler, M.; Miao, X.; Gardon, L.; Krüger, S.; Heise, H.; Röhr, M. I.; Ott, M.; Strodel, B.; Binder, W. H. *Bioconjugate Chem.* **2024**, *35*, 981–995.
- (316) Adamcik, J.; Castelletto, V.; Bolisetty, S.; Hamley, I. W.; Mezzenga, R. *Angew. Chem. Int. Ed.* **2011**, *50*, 5495–5498, DOI: https://doi.org/10.1002/anie.201100807.
- (317) Li, B.; Ge, P.; Murray, K. A.; Sheth, P.; Zhang, M.; Nair, G.; Sawaya, M. R.; Shin, W. S.; Boyer, D. R.; Ye, S. Nat. Commun. 2018, 9, 3609, DOI: https://doi.org/10.1038/s41467-018-05971-2.
- (318) Jacob, R. S.; Das, S.; Ghosh, S.; Anoop, A.; Jha, N. N.; Khan, T.; Singru, P.; Kumar, A.; Maji, S. K. *Sci. Rep.* **2016**, *6*, 23370, DOI: https://doi.org/10.1038/srep23370.
- (319) Jacob, R. S.; Anoop, A; Maji, S. K. In *Biological and Bio-inspired Nanomaterials. Advances in Experimental Medicine and Biology*, Perrett, S., Buell, A., Knowles, T., Eds.; Springer: Singapore, 2019, pp 265–290, DOI: https://doi.org/10.1007/978-981-13-9791-2\_8.
- (320) Nespovitaya, N.; Gath, J.; Barylyuk, K.; Seuring, C.; Meier, B. H.; Riek, R. *J. Am. Chem. Soc.* **2016**, *138*, 846–856, DOI: https://doi.org/10.1021/jacs.5b08694.
- (321) Gopalswamy, M.; Kumar, A.; Adler, J.; Baumann, M.; Henze, M.; Kumar, S. T.; Fändrich, M.; Scheidt, H. A.; Huster, D.; Balbach, J. *Biochim. Biophys. Acta Proteins Proteom.* **2015**, *1854*, 249–257, DOI: https://doi.org/10.1016/j.bbapap.2014.12.020.
- (322) Sachan, S.; Moya, C. G.; Voigt, B.; Köhn, M.; Balbach, J. *FEBS letters* **2023**, *597*, 995–1006, DOI: https://doi.org/10.1002/1873-3468.14587.
- (323) O'Nuallain, B.; Shivaprasad, S.; Kheterpal, I.; Wetzel, R. *Biochemistry* **2005**, *44*, 12709–12718, DOI: https://doi.org/10.1021/bi050927h.
- (324) Pashley, C. L.; Hewitt, E. W.; Radford, S. E. *J. Mol. Biol.* **2016**, *428*, 631–643, DOI: https://doi.org/10.1016/j.jmb.2016.01.009.
- (325) Voigt, B.; Bhatia, T.; Hesselbarth, J.; Baumann, M.; Schmidt, C.; Ott, M.; Balbach, J. *ChemPhysChem* **2023**, *24*, e202300439, DOI: https://doi.org/10.1002/cphc.202300439.
- (326) Urist, M. R.; Deutsch, N. M.; Pomerantz, G.; McLean, F. C. Am. J. Physiol. **1960**, 199, 851–855, DOI: https://doi.org/10.1152/ajplegacy.1960.199.5.851.
- (327) Guerreiro, P. M.; Renfro, J. L.; Power, D. M.; Canario, A. V. *Am. J. Physiol. Regul. Integr. Comp. Physiol.* **2007**, 292, R679–R696, DOI: https://doi.org/10.1152/ajpregu.00480.2006.
- (328) Zweifler, L. E.; Koh, A. J.; Daignault-Newton, S.; McCauley, L. K. *J. Bone Miner. Res.* **2021**, *36*, 1979–1998, DOI: https://doi.org/10.1002/jbmr.4389.
- (329) Aurbach, G. J. Biol. Chem. **1959**, 234, 3179–3181, DOI: https://doi.org/10.1016/S0021-9258(18)69644-9.
- (330) Goltzman, D. *Endocrinol. Metab. Clin. North Am.* **2018**, *47*, 743–758, DOI: https://doi.org/10.1016/j.ecl.2018.07.003.

- (331) Potts, J. T. *J. Endocrinol.* **2005**, *187*, 311–325, DOI: https://doi.org/10.1677/joe.1. 06057.
- (332) Shoback, D. New Engl. J. Med. **2008**, 359, 391-403, DOI: https://doi.org/10.1056/NEJMcp0803050.
- (333) Mihai, R.; Thakker, R. V. *Eur. J. Endocrinol.* **2021**, *184*, R165–R175, DOI: https://doi.org/10.1530/EJE-20-1367.
- (334) Kemper, B.; Habener, J. F.; Mulligan, R. C.; Potts Jr, J. T.; Rich, A. *Proc. Natl. Acad. Sci. U.S.A.* **1974**, *71*, 3731–3735, DOI: https://doi.org/10.1073/pnas.71.9.3731.
- (335) Wiren, K. M.; Potts Jr., J. T.; Kronenberg, H. M. *J. Biol. Chem.* **1988**, *263*, 19771–19777, DOI: https://doi.org/10.1016/S0021-9258(19)77701-1.
- (336) Meyer, D. I.; Krause, E.; Dobberstein, B. *Nature* **1982**, 297, 647–650, DOI: https://doi.org/10.1038/297647a0.
- (337) Vilardaga, J.-P.; Romero, G.; Friedman, P. A.; Gardella, T. J. *Cell. Mol. Life Sci.* **2011**, *68*, 1–13, DOI: https://doi.org/10.1007/s00018-010-0465-9.
- (338) Voigt, B.; Ott, M.; Balbach, J. *Macromol. Biosci.* **2023**, 23, 2200525, DOI: https://doi.org/10.1002/mabi.202200525.
- (339) Lauth, L. M.; Voigt, B.; Bhatia, T.; Machner, L.; Balbach, J.; Ott, M. *FEBS Lett.* **2022**, *596*, 2928–2939, DOI: https://doi.org/10.1002/1873-3468.14455.
- (340) Zraika, S.; Hull, R.; Verchere, C.; Clark, A; Potter, K.; Fraser, P.; Raleigh, D.; Kahn, S. *Diabetologia* **2010**, *53*, 1046–1056, DOI: https://doi.org/10.1007/s00125-010-1671-6
- (341) Kastritis, E.; Dimopoulos, M. A. *Br. J. Haematol.* **2016**, *172*, 170–186, DOI: https://doi.org/10.1111/bjh.13805.
- (342) Benilova, I.; Karran, E.; De Strooper, B. *Nat. Neurosci.* **2012**, *15*, 349–357, DOI: https://doi.org/10.1038/nn.3028.
- (343) Albert, L.; Vázquez, O. *Chem. Commun.* **2019**, *55*, 10192–10213, DOI: https://doi.org/10.1039/c9cc03346g.
- (344) Waldauer, S. A.; Hassan, S.; Paoli, B.; Donaldson, P. M.; Pfister, R.; Hamm, P.; Caflisch, A.; Pellarin, R. *J. Phys. Chem. B* **2012**, *116*, 8961–8973.
- (345) Deeg, A. A.; Schrader, T. E.; Kempter, S.; Pfizer, J.; Moroder, L.; Zinth, W. *ChemPhysChem* **2011**, *12*, 559–562, DOI: https://doi.org/10.1002/cphc.201001012.
- (346) Evgrafova, Z.; Voigt, B.; Baumann, M.; Stephani, M.; Binder, W. H.; Balbach, J. *ChemPhysChem* **2019**, *20*, 236–240, DOI: https://doi.org/10.1002/cphc.201800867.
- (347) Paschold, A.; Starke, N.; Rothemund, S.; Binder, W. H. *Org. Lett.* **2024**, *26*, 10542–10547, DOI: https://doi.org/10.1021/acs.orglett.4c03929.
- (348) Paschold, A.; Voigt, B.; Hause, G.; Kohlmann, T.; Rothemund, S.; Binder, W. H. *Biomedicines* **2022**, *10*, 1512, DOI: https://doi.org/10.3390/biomedicines10071512.
- (349) Ren, B.; Zhang, Y.; Zhang, M.; Liu, Y.; Zhang, D.; Gong, X.; Feng, Z.; Tang, J.; Chang, Y.; Zheng, J. J. Mater. Chem. B 2019, 7, 7267–7282, DOI: https://doi.org/10.1039/c9tb01871a.

- (350) Deike, S.; Rothemund, S.; Voigt, B.; Samantray, S.; Strodel, B.; Binder, W. H. *Bioorg. Chem.* **2020**, *101*, 104012, DOI: https://doi.org/10.1016/j.bioorg.2020.104012.
- (351) Nuti, F.; Gellini, C.; Larregola, M.; Squillantini, L.; Chelli, R.; Salvi, P. R.; Lequin, O.; Pietraperzia, G.; Papini, A. M. *Front. Chem.* **2019**, *7*, 180, DOI: https://doi.org/10.3389/fchem.2019.00180.
- (352) Murawska, G. M.; Poloni, C.; Simeth, N. A.; Szymański, W.; Feringa, B. L. *Chem. Eur. J.* **2019**, 25, 4965–4973, DOI: https://doi.org/10.1002/chem.201900090.
- (353) Sepehr, Z.; Nasr-Isfahani, H.; Mahdavian, A. R.; Amin, A. H. *J. Iran. Chem. Soc.* **2021**, *18*, 3061–3067, DOI: https://doi.org/10.1007/s13738-021-02253-5.
- (354) GALE, D. J.; WILSHIRE, J. F. *J. Soc. Dye. Colour.* **1974**, *90*, 97–100, DOI: https://doi.org/10.1111/j.1478-4408.1974.tb03188.x.
- (355) Tomasulo, M.; Kaanumal, S. L.; Sortino, S.; Raymo, F. M. *J. Org. Chem.* **2007**, *72*, 595–605, DOI: https://doi.org/10.1021/jo062004d.
- (356) Di Bella, S.; Consiglio, G.; Leonardi, N.; Failla, S.; Finocchiaro, P.; Fragalà, I. *Eur. J. Inorg. Chem.* **2004**, 2004, 2701–2705, DOI: https://doi.org/10.1002/ejic.200300959.
- (357) Laptev, A.; Lukin, A. Y.; Belikov, N.; Zvezdin, K.; Demina, O.; Barachevsky, V.; Varfolomeev, S.; Khodonov, A.; Shvets, V. *Russ. Chem. Bull.* **2014**, *63*, 2026–2035, DOI: https://doi.org/10.1007/s11172-014-0695-3.
- (358) Kollarigowda, R. H.; Braun, P. V. *J. Org. Chem.* **2021**, *86*, 4391–4397, DOI: https://doi.org/10.1021/acs.joc.0c02375.

## **Curriculum Vitae**

Vor- und Zuname André Paschold

Staatsangehörigkeit deutsch

#### **Schulische Ausbildung**

09/1999–07/2003 Staatliche Grundschule Probstzella

08/2003–06/2011 Erasmus-Reinhold-Gymnasium, Saalfeld (Saale)

#### **Akademische Ausbildung**

10/2011–09/2015 Bachelor of Science Chemie, Friedrich-Schiller-Universität Jena

Bachelorarbeit: "Synthese von On-Off-Sensoren auf Basis eines 1,3-

Thiazolgrundgerüsts"

Abschlussnote: 2.7

10/2015–03/2019 Master of Science Chemische Biologie, Friedrich-Schiller-Universität Jena

Masterarbeit: "Synthesis of Pseudomonas-derived secondary metabolites

and analogs"

Abschlussnote: 1,2

09/2019–heute Promotion zum Thema: "Photocontrol and Structural Analysis of

Amyloid Fibril Formation Using Azobenzene and Novel Spiropyran Photo-

switches"

Martin-Luther-Universität Halle-Wittenberg, Naturwissenschaftliche

Fakultät II, Institut für Chemie, Makromolekulare Chemie

#### Kentnisse & Fähigkeiten

· organische Synthese

· Entwicklung & Charakterisierung von Photoschaltern

- · Peptidchemie
- · Chemische Charakterisierung

**NMR** 

Optische Spektroskopie (UV/Vis, IR, Fluoreszenz)

Chromatographie (DC, LC, GPC)

Massenspektrometrie (MALDI, ESI)

- · Mikroskopische Charakterisierung (TEM, AFM)
- · Programmiersprachen

Wolfram Language, R, Python, Java, C#

#### Wissenschaftliche Veröffentlichungen

Publikationen

Klapper, M.; **Paschold, A.**; Zhang, S.; Weigel, C.; Dahse, H.-M.; Götze, S.; Pace, S.; König, S.; Rao, Z.; Reimer, L.; Werz, O.; Stallforth, P., Bioactivity and Mode of Action of Bacterial Tetramic Acids *ACS Chem. Biol.* **2019**, *14* (8), 1693–1697, DOI: https://doi.org/10.1021/acschembio.9b00388.

Klapper, M.; Schlabach, K.; **Paschold, A.**; Zhang, S.; Chowdhury, S.; Menzel, K.-D.; Rosenbaum, M. A.; Stallforth, P., Biosynthesis of Pseudomonas-Derived Butenolides *Angew. Chem. Int. Ed.* **2020**, *59* (14), 5607–5610, DOI: https://doi.org/10.1002/anie.201914154.

**Paschold, A.**; Voigt, B.; Hause, G.; Kohlmann, T.; Rothemund, S.; Binder, W. H., Modulating the Fibrillization of Parathyroid-Hormone (PTH) Peptides: Azo-Switches as Reversible and Catalytic Entities *Biomedicines* **2022**, 10 (7), 1512, DOI: https://doi.org/10.3390/biomedicines10071512.

Rupali, J. B.; Thomas, S.; Sen, N.; Paschold, A.; Binder, W. H.; Kumas, S., Bioinspired synthetic polymers-based inhibitors of Alzheimer's amyloid-β peptide aggregation, *Polym. Chem.* **2023**, *23*, 392–411 Polym Chem, 14 (2023), pp. 392-411, DOI: https://doi.org/10.1039/D2PY01217K

**Paschold, A.**; Schäffler, M.; Miao, X.; Gardon, L.; Krüger, S.; Heise, H.; Röhr, M. I. S.; Ott, M.; Strodel, B.; Binder, W. H., Photocontrolled Reversible Amyloid Fibril Formation of Parathyroid Hormone-Derived Peptides *Bioconjugate Chemistry* **2024**, 35 (7), 981–995, DOI: https://doi.org/10.1021/acs.bioconjchem.4c00188.

**Paschold, A.**; Starke, N.; Rothemund, S.; Binder, W. H., Spiropyran as building block in peptide synthesis and modulation of photochromic properties *Organic Letters* **2024**, 26 (49), 10542–10547, DOI: https://doi.org/10.1021/acs.orglett.4c03929.

Konferenzbeiträge

**Paschold, A.**; Voigt, B.; Rothemund, S.; Kohlmann, T.; Balbach, J.; Binder, W. H., Switchable  $PTH_{25-37}$  fibrillation via photoisomerization of an azobenzene motif, *Bordeaux Polymer Conference* **2022**, Poster.

André	Pascho	ld	

## **Appendix**

Supporting Information to: Modulating the Fibrillization of Parathyroid-Hormone (PTH) Peptides: Azo-Switches as Reversible and Catalytic Entities, *Biomedecines* **2022**, *10* (7), 1512, DOI: https://doi.org/10.3390/biomedicines10071512.

Supporting Information to: Photocontrolled Reversible Amyloid Fibril Formation of Parathyroid Hormone-Derived Peptides, *Biocon jugate Chemistry* **2024**, 35 (7), 981-995, DOI: https://doi.org/10.1021/acs.bioconjchem.4c00188.

Supporting Information to: Spiropyran as building block in peptide synthesis and modulation of photochromic properties, *Organic Letters* **2024**, 26 (49), 10542-10547, DOI: https://doi.org/10.1021/acs.orglett.4c03929.

# Modulating the fibrillization of parathyroid-hormone (PTH) peptides: azo-switches as reversible and catalytic entities.

Authors: André Paschold, Bruno Voigt, Gerd Hause, Tim Kohlmann, Sven Rothemund, and Wolfgang H. Binder

### **Table of content**

1. Sy	rnthesis of Fmoc-3,4'-AMPB	2
1.1.	Synthesis of (9 <i>H</i> -Fluoren-9-yl)methyl (4-aminobenzyl)carbamate 2	2
1.2.	Synthesis of Fmoc-3,4'-AMPB 5	2
2. Pe	ptide Characterisation	4
2.1.	Peptide sequences	4
2.2.	HPLC- and MALDI-ToF-data	4
2.3.	Photophysical properties of AzoPTH <sub>25-37</sub>	9
2.4.	Aggregation Kinetics of PTH <sub>25-37</sub> , trans-AzoPTH <sub>25-37</sub> , cis-AzoPTH <sub>25-37</sub> , and mix	tures 10
3. NN	MR-Spectra	12

#### 1. Synthesis of Fmoc-3,4'-AMPB

**Scheme S1:** Synthesis of Fmoc-protected 3,4'-AMPB 7. (a) Fmoc-ONSu, triethylamin, DMF/MeCN, 16 h, room temperature. (b) Oxone , DCM, water, 3 h, room temperature. (c) AcOH, DMSO, N<sub>3</sub>, 72 h, room temperature.

#### 1.1. Synthesis of (9H-Fluoren-9-yl)methyl (4-aminobenzyl)carbamate 2

4-Aminobenzylamine (1.85 mL, 16.4 mmol, 1 equiv.) was dissolved in a mixture of 12 mL THF and 1.5 mL aqueous 5% NaHCO<sub>3</sub> solution. A suspension of Fmoc-*N*-hydroxysuccinimide (Fmos-OSu) (5.52 g, 16.4 mmol, 1 equiv.) in 20 mL THF was added slowly and the reaction mixture was stirred for 18 h at ambient temperature. 500 mL of water were added and the suspension was filtrated. The precipitate was dissolved in THF and dried over Na<sub>2</sub>SO<sub>4</sub>. The solvent was removed *in vacuo* and **2** was obtained as a white solid (5.45 g, 15.3 mmol, 96% yield).

<sup>1</sup>**H-NMR** (400 MHz, DMSO- $d_6$ ) δ = 7.86 (d, J = 7.6 Hz, 2H,  $C_{ar}H$ ), 7.82 (d, J = 7.6 Hz, 2H,  $C_{ar}H$ ), 7.40 (td, J = 7.5 Hz, 1.2 Hz, 1H,  $C_{ar}H$ ), 7.32 (td, J = 7.5 Hz, 1.2 Hz, 1H,  $C_{ar}H$ ), 6.97 (t, J = 6.3 Hz, 1H, NH), 6.88 (d, J = 8.2 Hz, 2H,  $C_{ar}H$ ), 6.48 (d, J = 8.2 Hz, 2H,  $C_{ar}H$ ), 6.26 (s, 2H,  $C_{H_2}$ ), 4.88 (s, 2H,  $C_{H_2}$ ), 3.93 (d, J = 5.9 Hz, 1H,  $C_{H_2}$ ).

<sup>13</sup>C-NMR (100 MHz, DMSO- $d_6$ )  $\delta$  = 157.8 (C(O)N), 147.8 ( $C_{ar}$ N), 143.0 ( $C_{ar}$ ), 139.8 ( $C_{ar}$ ), 137.8 ( $C_{ar}$ ), 141.2 ( $C_{ar}$ ), 129.4 ( $C_{ar}$ H), 128.4 ( $C_{ar}$ H), 127.7 ( $C_{ar}$ ), 121.1 ( $C_{ar}$ H), 120.5 ( $C_{ar}$ H), 114.1( $C_{ar}$ H), 110.1 (CH<sub>2</sub>), 43.9 (CH<sub>2</sub>).

**MS** (ESI+):  $m/z = 383.11 \text{ [M+K]}^+$ .

Analytical data match reported literature values.[1]

#### 1.2. Synthesis of Fmoc-3,4'-AMPB 5

To a suspenison of 3-aminobenzoic acid (2.00 g, 14.6 mmol, 2 equiv.) in 36 mL DCM is a solution of Oxone® (8.80 g, 29.17 mmol, 4 equiv.) added dropwise. The reaction mixture is stirred at ambient temperature for 4 h. DCM is removed *in vacuo* and the formed precipitate is filtrated and washed with 100 mL water. The residue is dissolved in 175 mL DMSO and 175 mL of acetic acid are added. The solution is degassed for 30 min with N<sub>2</sub>. (9*H*-Fluoren-9-yl)methyl (4-aminobenzyl)carbamate **2** (2.51 g, 7.29 mmol, 1 equiv.) is added and the mixture is stirred for 72 h at ambient temperature. 100 mL water

and 400 mL EtOAc were added and the phases were separated. The aqueous phase is washed two times with 400 mL EtOAc and the combined organic phases were washed two times with 200 mL of a saturated aqueous NaCl solution. The organic phase was dried over Na<sub>2</sub>SO<sub>4</sub> and the solvent was removed *in vacuo*. The residue was purified by flash chromatography on normal phase silica gel (solvent: EtOAc + 0.1% FA) to obtain 5 as a mixture of the *E*- and the *Z*-isomer (1.51 g, 3.17 mmol, 43.5% yield).

<sup>1</sup>**H-NMR** (400 MHz, DMSO- $d_6$ ) *E:Z*-ratio = 29:11, *E*-isomer: δ = 13.27 (s, 1H, C(O)O*H* 8.37 (t, *J* = 1.9 Hz, 1H, C<sub>ar</sub>*H*), 8.15 – 8.08 (m, 2H, C<sub>ar</sub>*H*), 7.93 (t, *J* = 6.2 Hz, 1H, C<sub>ar</sub>*H*), 7.90 – 7.81 (m, 4H, C<sub>ar</sub>*H*), 7.76 – 7.66 (m, 3H, C<sub>ar</sub>*H*, N*H*<sub>2</sub>), 7.46 – 7.48 (m, 6H, C<sub>ar</sub>*H*), 4.38 (d, *J* = 6.7 Hz, 2H, C*H*<sub>2</sub>), 4.28 (d, *J* = 6.0 Hz, 2H, C*H*<sub>2</sub>), 4.24 (t, *J* = 6.8 Hz, 1H, C*H*), *Z*-isomer: 7.86 (d, *J* = 7.6 Hz, 2H, C<sub>ar</sub>*H*), 7.79 – 7.69 (m, 2H, C<sub>ar</sub>*H*), 7.66 (d, *J* = 7.5 Hz, 2H, C<sub>ar</sub>*H*), 7.46 – 7.35 (m, 4H, C<sub>ar</sub>*H*, C(O)N*H*), 7.28 (t, *J* = 7.5 Hz, 2H, C<sub>ar</sub>*H*), 7.08 (d, *J* = 8.0 Hz, 2H, C<sub>ar</sub>*H*), 6.99 (d, *J* = 7.8 Hz, 1H, C<sub>ar</sub>*H*), 6.81 (d, *J* = 8.2 Hz, 2H, C<sub>ar</sub>*H*), 4.36 (d, *J* = 6.6 Hz, 2H, C*H*<sub>2</sub>), 4.20 (t, *J* = 6.7 Hz, 1H, C*H*), 4.09 (d, *J* = 6.2 Hz, 2H, C*H*<sub>2</sub>).

<sup>13</sup>C-NMR (100 MHz, DMSO- $d_6$ ) *E*-isomer: δ = 167.2 (C(O)OH), 156.9 (C(O)N), 152.4 ( $C_{ar}$ N), 151.3 ( $C_{ar}$ N), 144.5 ( $C_{ar}$ ), 144.3 ( $C_{ar}$ ), 141.2 ( $C_{ar}$ ), 132.7 ( $C_{ar}$ H), 132.2 ( $C_{ar}$ H), 130.4 ( $C_{ar}$ ), 128.4 ( $C_{ar}$ H), 128.0 ( $C_{ar}$ H), 127.8 ( $C_{ar}$ H), 127.5 ( $C_{ar}$ H), 125.6 ( $C_{ar}$ H), 123.7 ( $C_{ar}$ H), 122.6 ( $C_{ar}$ H), 120.5 ( $C_{ar}$ H), 65.8 (CH<sub>2</sub>), 47.3 (CH), 44.0 (CH<sub>2</sub>) Z-isomer: δ = 167.1 (C(O)OH), 156.8 (C(O)N), 154.3 ( $C_{ar}$ N), 152.3 ( $C_{ar}$ N), 144.3 ( $C_{ar}$ ), 143.8 ( $C_{ar}$ ) 141.2 ( $C_{ar}$ ), 133.3 ( $C_{ar}$ ), 132.2 ( $C_{ar}$ H), 130.4 ( $C_{ar}$ H), 128.2 ( $C_{ar}$ H), 128.0 ( $C_{ar}$ H), 127.7 ( $C_{ar}$ H), 127.5 ( $C_{ar}$ H), 125.6 ( $C_{ar}$ H), 123.1 ( $C_{ar}$ H), 122.8 ( $C_{ar}$ H), 120.5 ( $C_{ar}$ H), 65.6 (CH<sub>2</sub>), 47.3 (CH), 43.5 (CH<sub>2</sub>).

**UV-Vis** *E*-isomer:  $\lambda_{\text{max}} = 291 \text{ nm}$ , 301 nm, 330 nm, 441 nm; *Z*-isomer:  $\lambda_{\text{max}} = 290 \text{ nm}$ , 301 nm, 434 nm; isobestic point (*E*:*Z*):  $\lambda_{\text{iso}} = 386 \text{ nm}$ .

**MS** (ESI+):  $m/z = 516.13 \text{ [M+K]}^+$ .

Analytical data match reported literature values. [2]

#### 2. Peptide Characterisation

#### 2.1. Peptide sequences

**Table S1:** Primary sequence and solubility in 50 mM Na<sub>2</sub>PO<sub>4</sub> buffer (pH 7.4) of peptides AzoPTH<sub>25-37</sub> and SP1-SP4.

peptide	primary sequence <sup>a</sup>	solubility $[\mu M]^b$
PTH <sub>25-37</sub>	H <sub>2</sub> N- <sup>25</sup> RKKLQ <sup>30</sup> DVHNF <sup>35</sup> VAL-OH	> 1000
AzoPTH <sub>25-37</sub>	$H_2N^{-25}RKKLQ^{30}D$ -Azo-HNF $^{35}VAL$ -OH	250
SP1	$H_2N-^{25}RKKLQ^{30}D\text{-}Azo\text{-}VHNF^{35}VAL\text{-}OH$	60
SP2	$H_2N-^{25}RKKLQ^{30}DV\text{-}Azo\text{-}HNF^{35}VAL\text{-}OH$	55
SP3	$H_2N^{-25}RKKLQ^{30}$ -Azo-VHNF $^{35}$ VAL-OH	35
SP4	$H_2N\hbox{-}^{25}RKKLQ^{30}\hbox{-}Azo\hbox{-}HNF^{35}VAL\hbox{-}OH$	25

<sup>&</sup>lt;sup>a</sup> Azo = 3,4'-AMPB; <sup>b</sup> maximum solubility was determined *via* UV-Vis absorption spectroscopy ( $\varepsilon$  = 49310 M<sup>-1</sup>cm<sup>-1</sup> at 205 nm for PTH<sub>25-37</sub>,  $\varepsilon$  = 13000 M<sup>-1</sup>cm<sup>-1</sup> at 327 nm for 3,4'-AMPB containing peptides).

#### 2.2. HPLC- and MALDI-ToF-data

AzoPTH<sub>25-37</sub>: MS (MALDI+): m/z calc. 1705.990 found 1706.254.

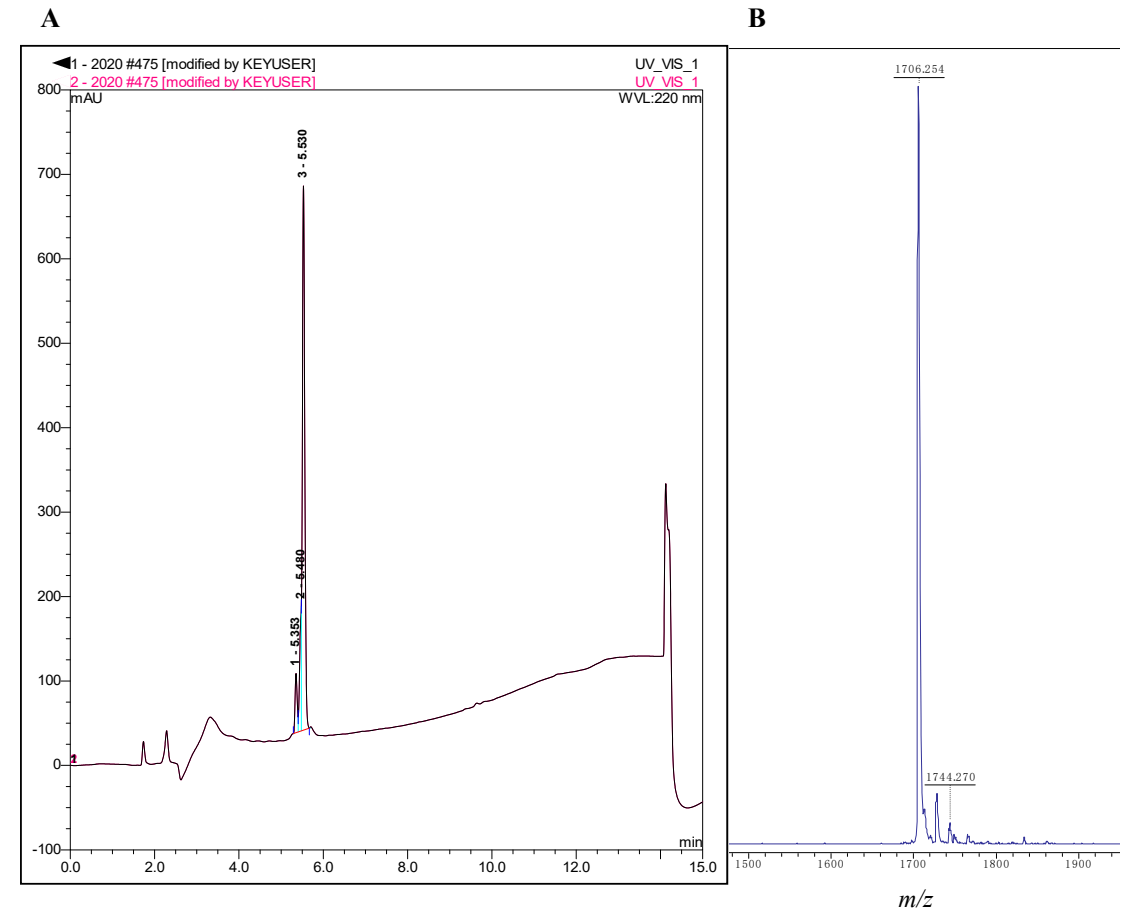


**Figure S1:** (A) HPLC-trace of AzoPTH<sub>25-37</sub> (*cis*-isomer at 5.353, *trans*-isomer at 5.530). (B) MALDI-spectrum of AzoPTH<sub>25-37</sub>.

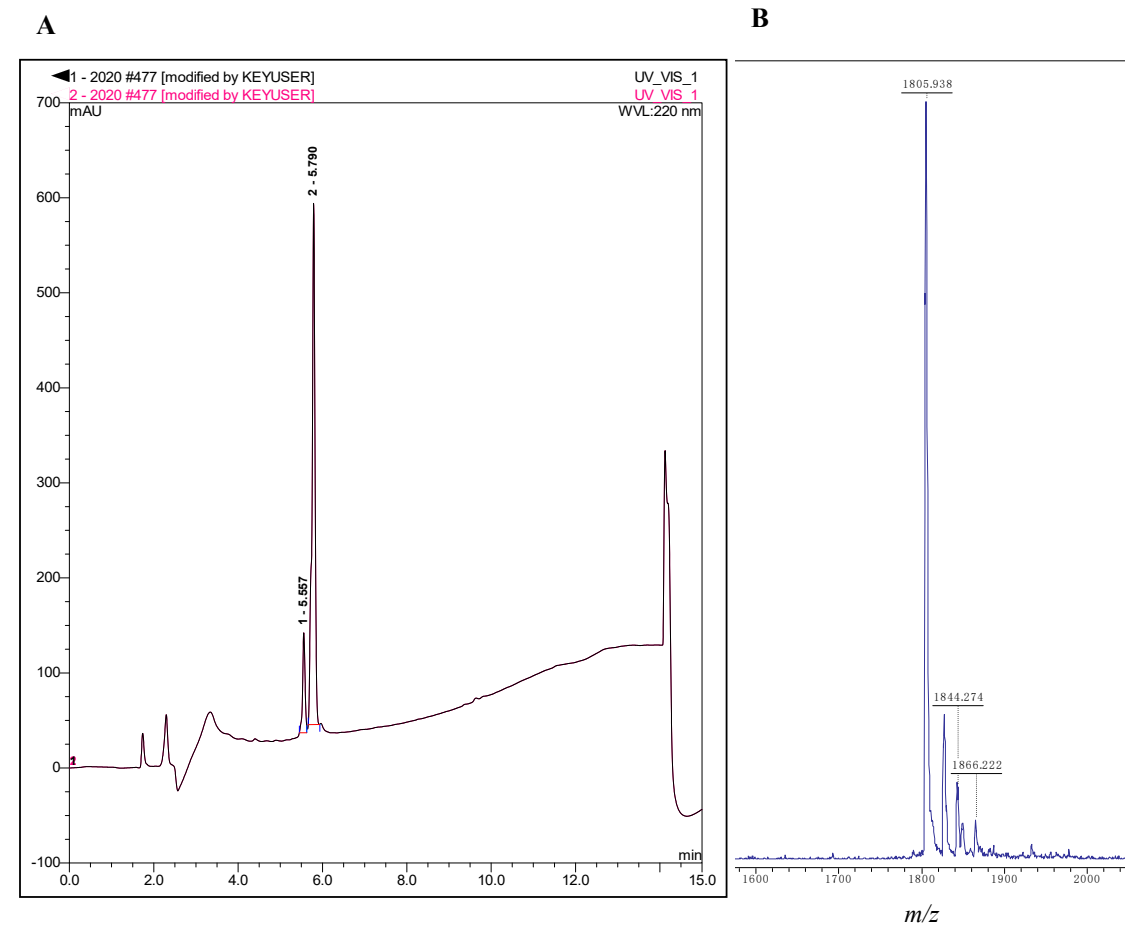


Figure S2: (A) HPLC-trace of SP1 (cis-isomer at 5.557, trans-isomer at 5.790). (B) MALDI-spectrum of SP1.

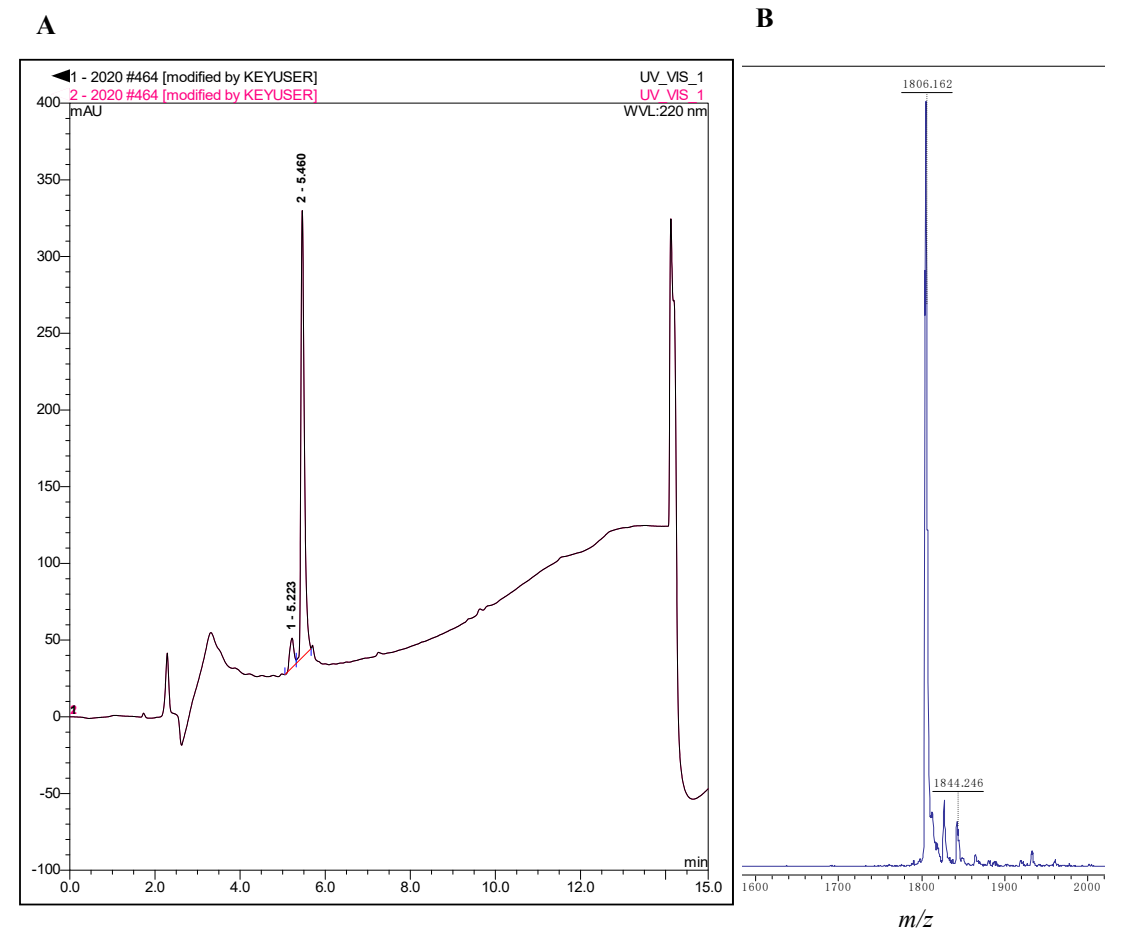


Figure S3: (A) HPLC-trace of SP2 (cis-isomer at 5.223, trans-isomer at 5.460). (B) MALDI-spectrum of SP2.

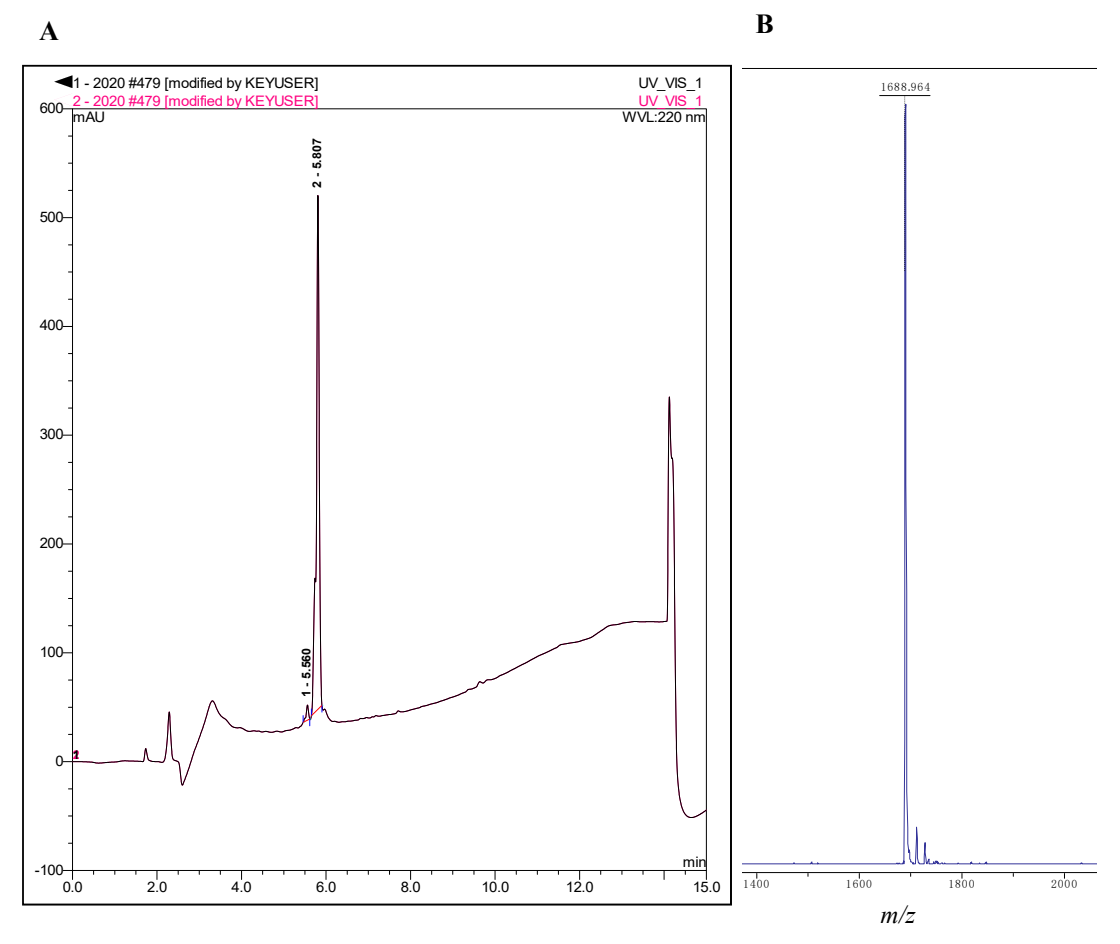


Figure S4: (A) HPLC-trace of SP3 (cis-isomer at 5.560, trans-isomer at 5.807). (B) MALDI-spectrum of SP3.

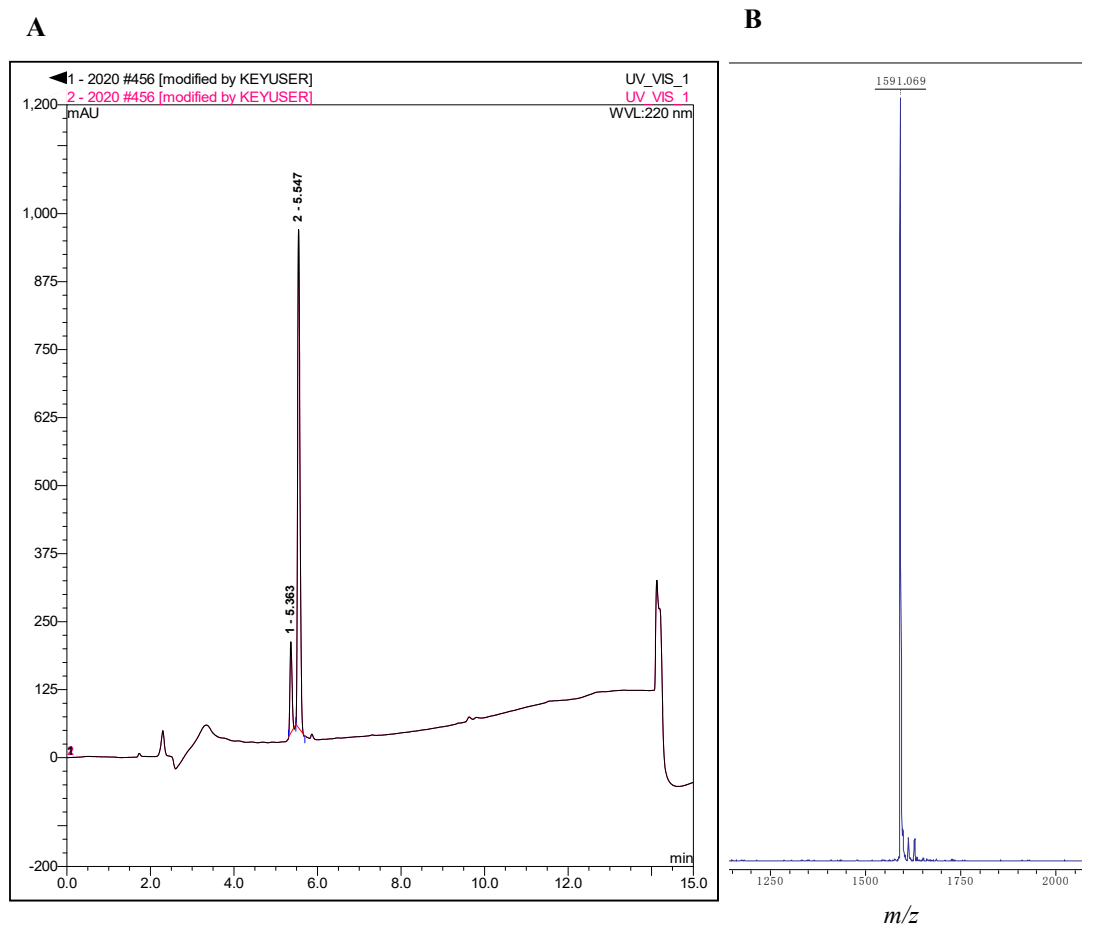
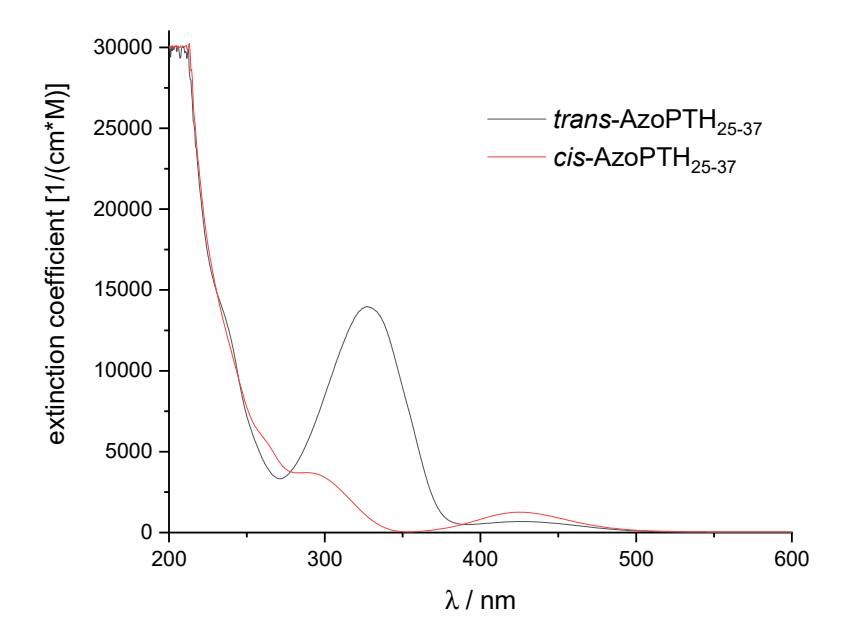
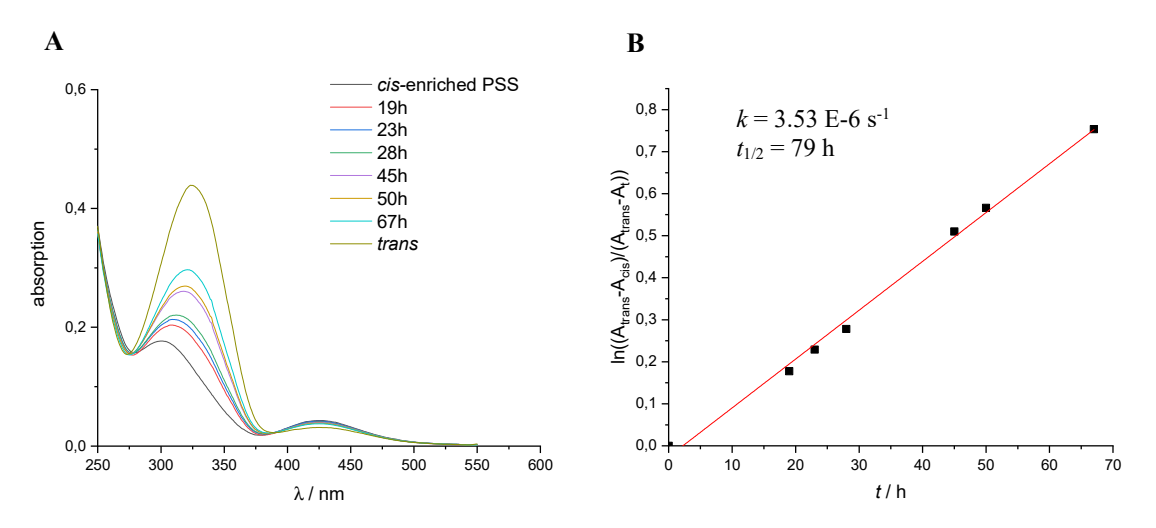


Figure S5: (A) HPLC-trace of SP4 (cis-isomer at 5.363, trans-isomer at 5.547). (B) MALDI-spectrum of SP4.

### 2.3. Photophysical properties of AzoPTH<sub>25-37</sub>



**Figure S6:** Separated UV/Vis-spectra of the pure isomers of AzoPTH<sub>25-37</sub>; spectra were separated with Wolfram Mathematica 12.2.



**Figure S7:** (**A**) UV/Vis-spectra of *trans*-isomer, *cis*-enriched PSS, and *cis*-enriched PSS sample after distinct time points in the dark. (**B**) logarithmic application of the absorption change over time to determine rate constant k and half-life time  $t_{1/2}$ .<sup>2</sup>

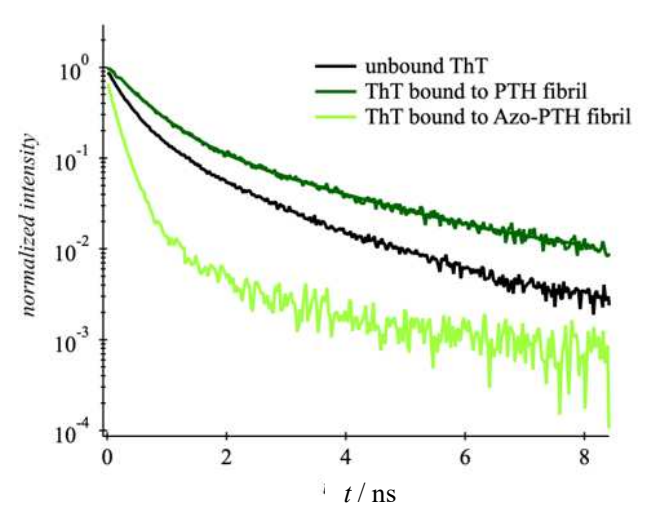


**Figure S8:** Time- resolved fluorescence measurement (excitation wavelength = 460 nm, emission wavelength = 480 nm) of unbound ThT (black), ThT bound to PTH<sub>25-37</sub> fibrils (dark green), ThT bound to *trans*-AzoPTH<sub>25-37</sub> fibrils (light green).

### 2.4. Aggregation Kinetics of PTH<sub>25-37</sub>, trans-AzoPTH<sub>25-37</sub>, cis-AzoPTH<sub>25-37</sub>, and mixtures

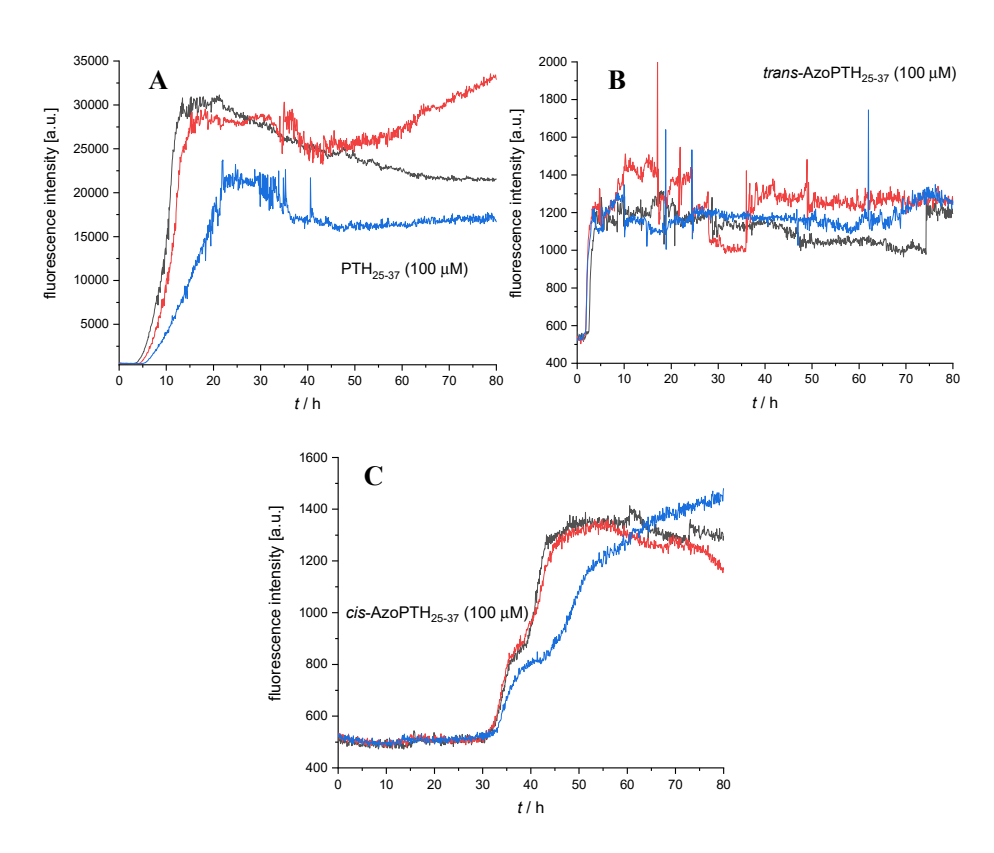


**Figure S9:** ThT monitored fibrillation assays ( $c = 100 \mu M$ , 37 °C, 50 mM Na<sub>2</sub>HPO<sub>4</sub>, pH7.4). (**A**) PTH<sub>25-37</sub>, (**B**) *trans*-AzoPTH<sub>25-37</sub>, (**C**) *cis*-AzoPTH<sub>25-37</sub>.

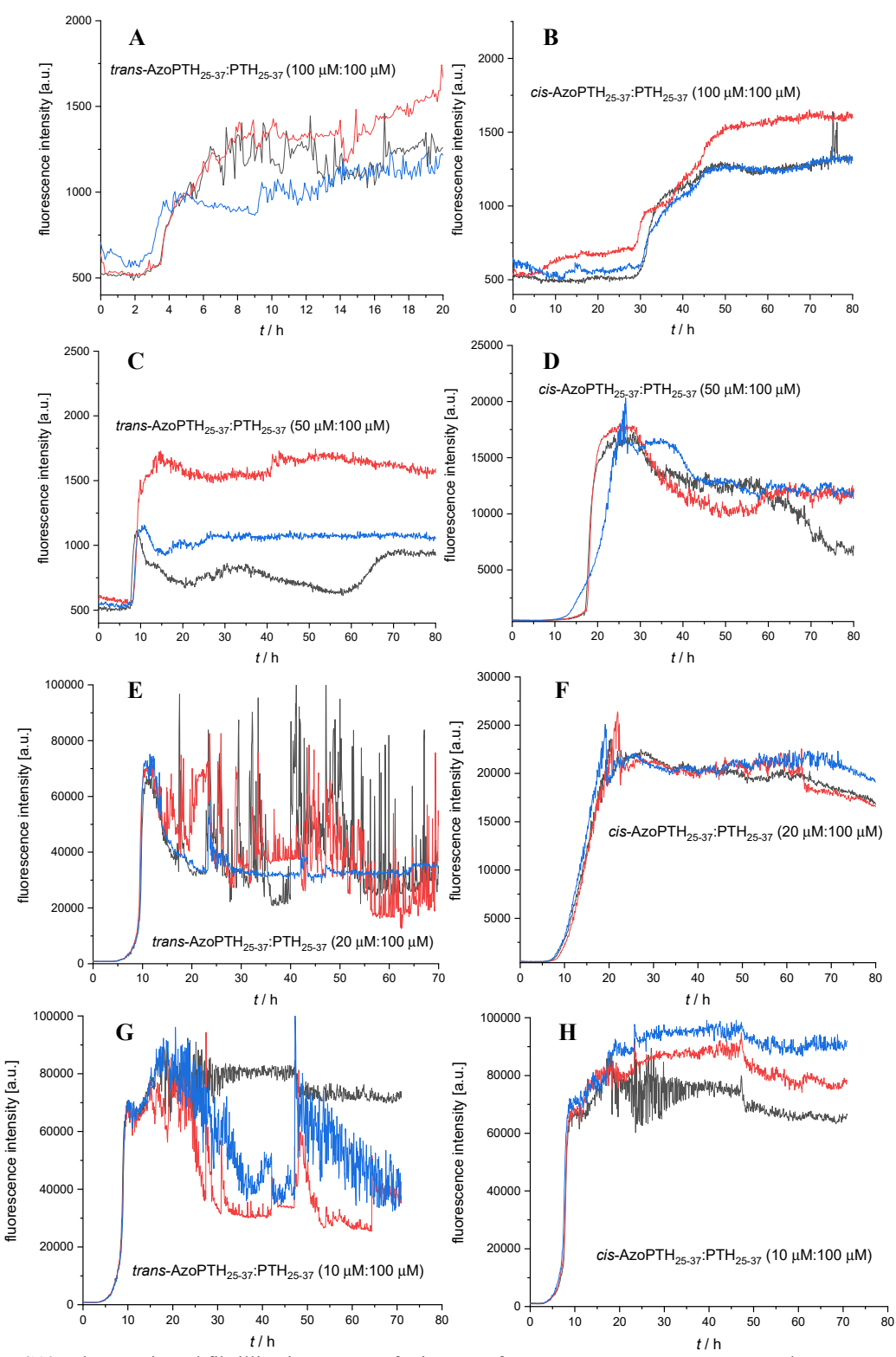
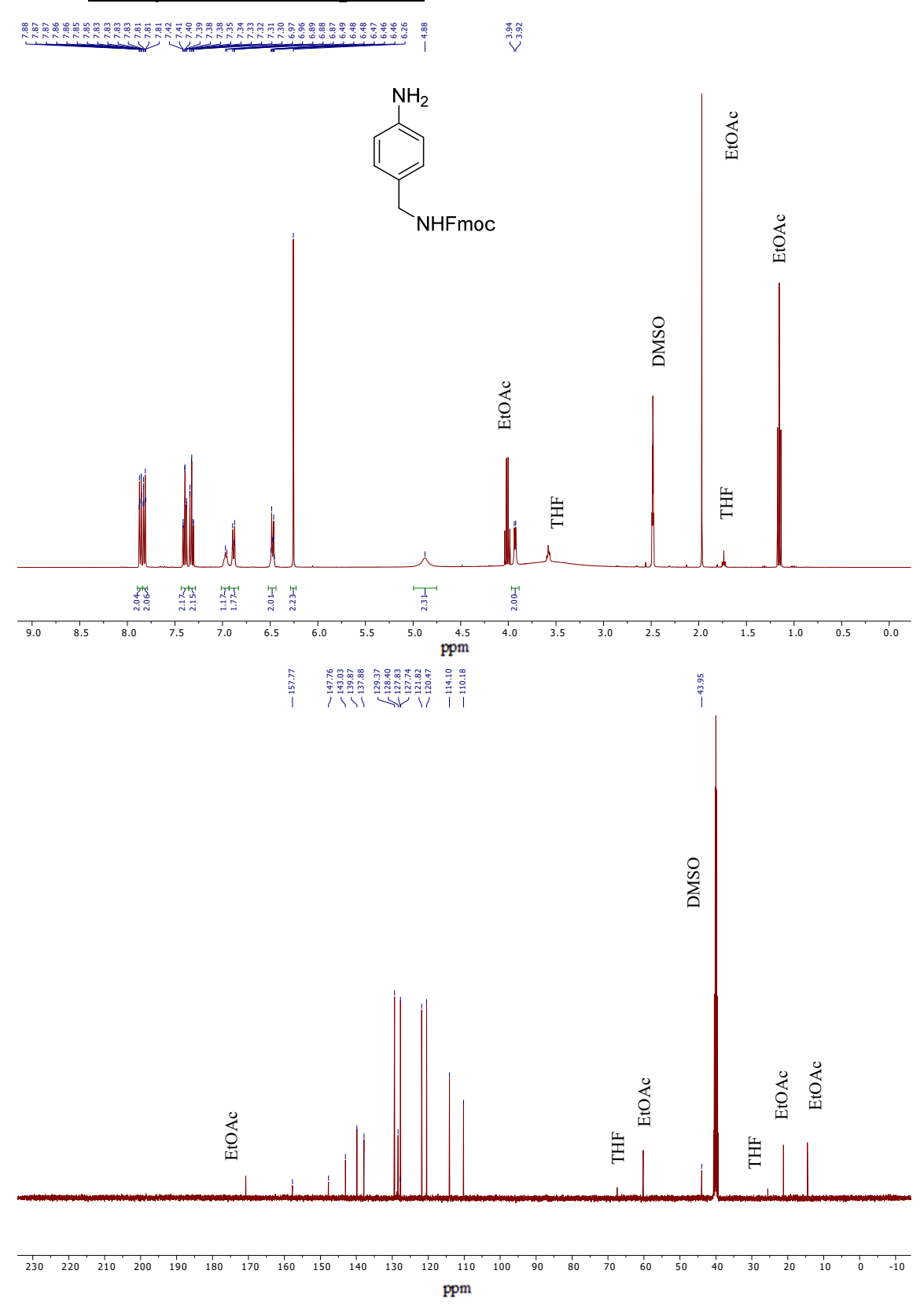
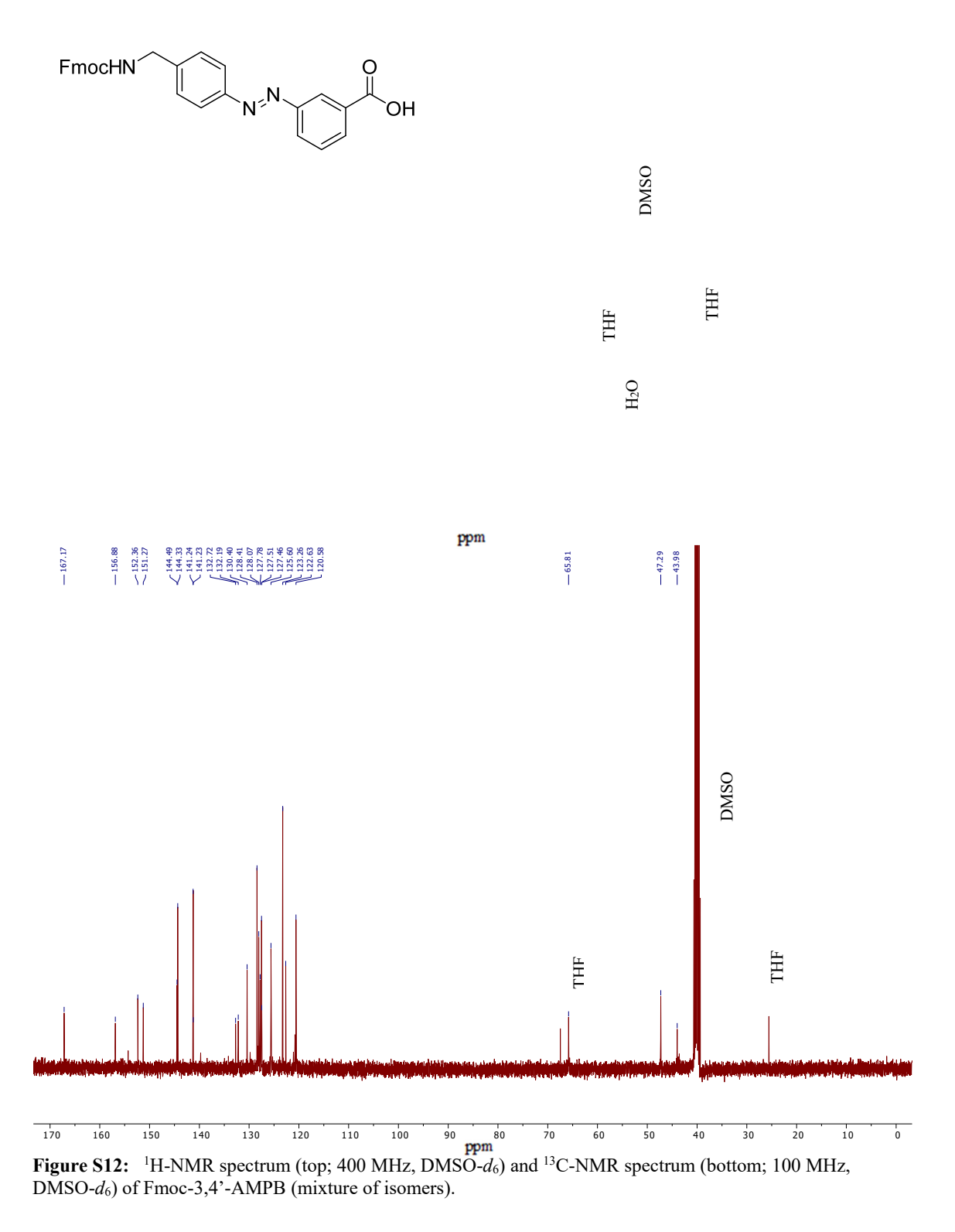


Figure S10: ThT monitored fibrillization assays of mixtures of PTH<sub>25-37</sub>, trans-AzoPTH<sub>25-37</sub>, and cis-AzoPTH<sub>25-37</sub> (37 °C, 50 mM Na<sub>2</sub>HPO<sub>4</sub>, pH7.4). (A) trans-AzoPTH<sub>25-37</sub>:PTH<sub>25-37</sub> (100 μM:100 μM), (B) cis-AzoPTH<sub>25-37</sub>:PTH<sub>25-37</sub> (100 μM:100 μM), (C) trans-AzoPTH<sub>25-37</sub>:PTH<sub>25-37</sub> (50 μM:100 μM), (D) cis-AzoPTH<sub>25-37</sub>:PTH<sub>25-37</sub> (50 μM:100 μM), (E) trans-AzoPTH<sub>25-37</sub>:PTH<sub>25-37</sub> (20 μM:100 μM), (F) cis-AzoPTH<sub>25-37</sub>:PTH<sub>25-37</sub> (10 μM:100 μM), (G) trans-AzoPTH<sub>25-37</sub>:PTH<sub>25-37</sub> (10 μM:100 μM).

## 3. Analytical NMR-Spectra



**Figure S11:**  $^{1}$ H-NMR spectrum (top; 400 MHz, DMSO- $d_{6}$ ) and  $^{13}$ C-NMR spectrum (bottom; 100 MHz, DMSO- $d_{6}$ ) of (9*H*-Fluoren-9-yl)methyl (4-aminobenzyl)carbamate.



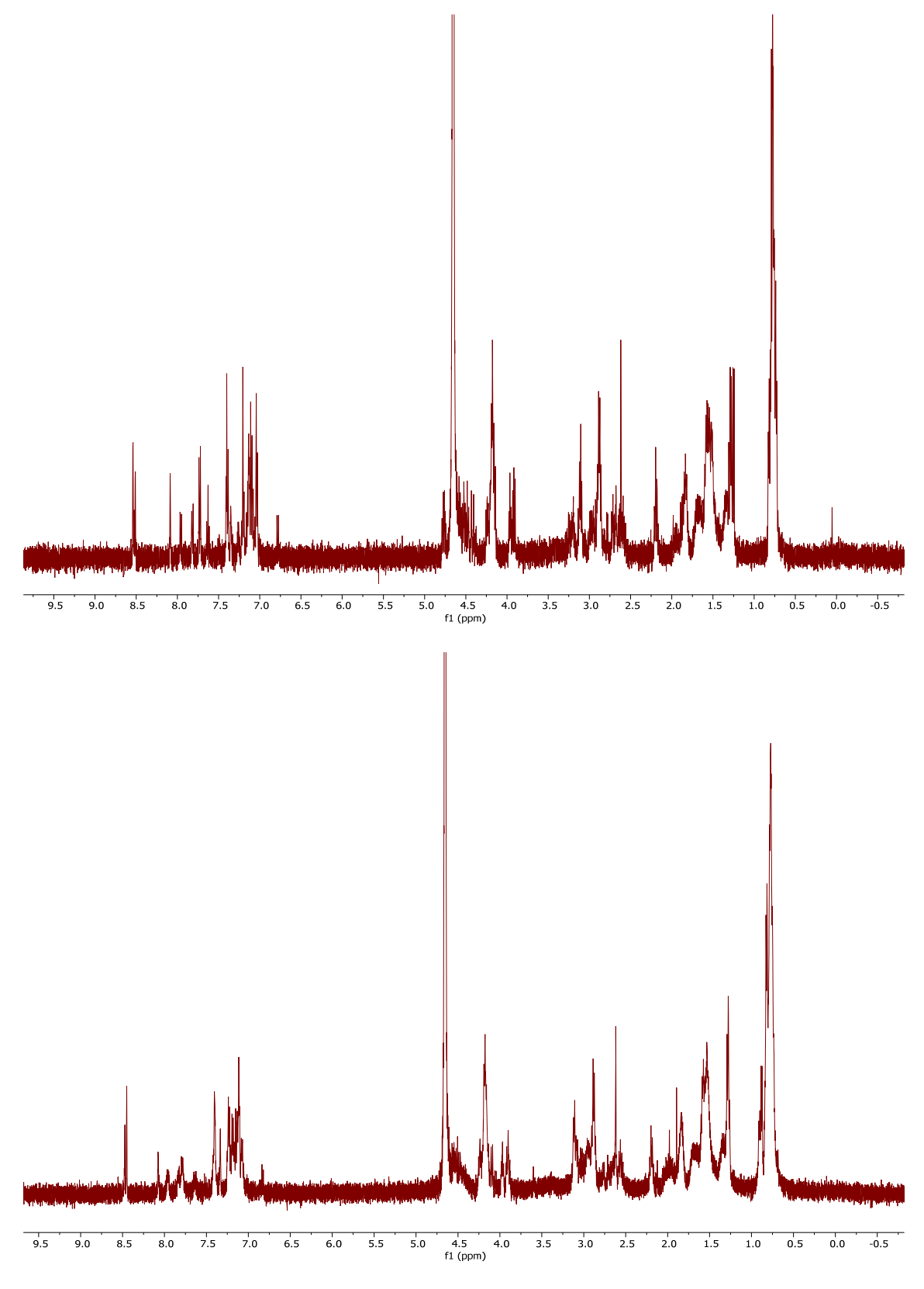


**Figure S13:** <sup>1</sup>H-NMR spectra (500 MHz, D<sub>2</sub>O) of AzoPTH<sub>25-37</sub> (top, *trans*-isomer) and SP1 (bottom, *trans*-isomer).

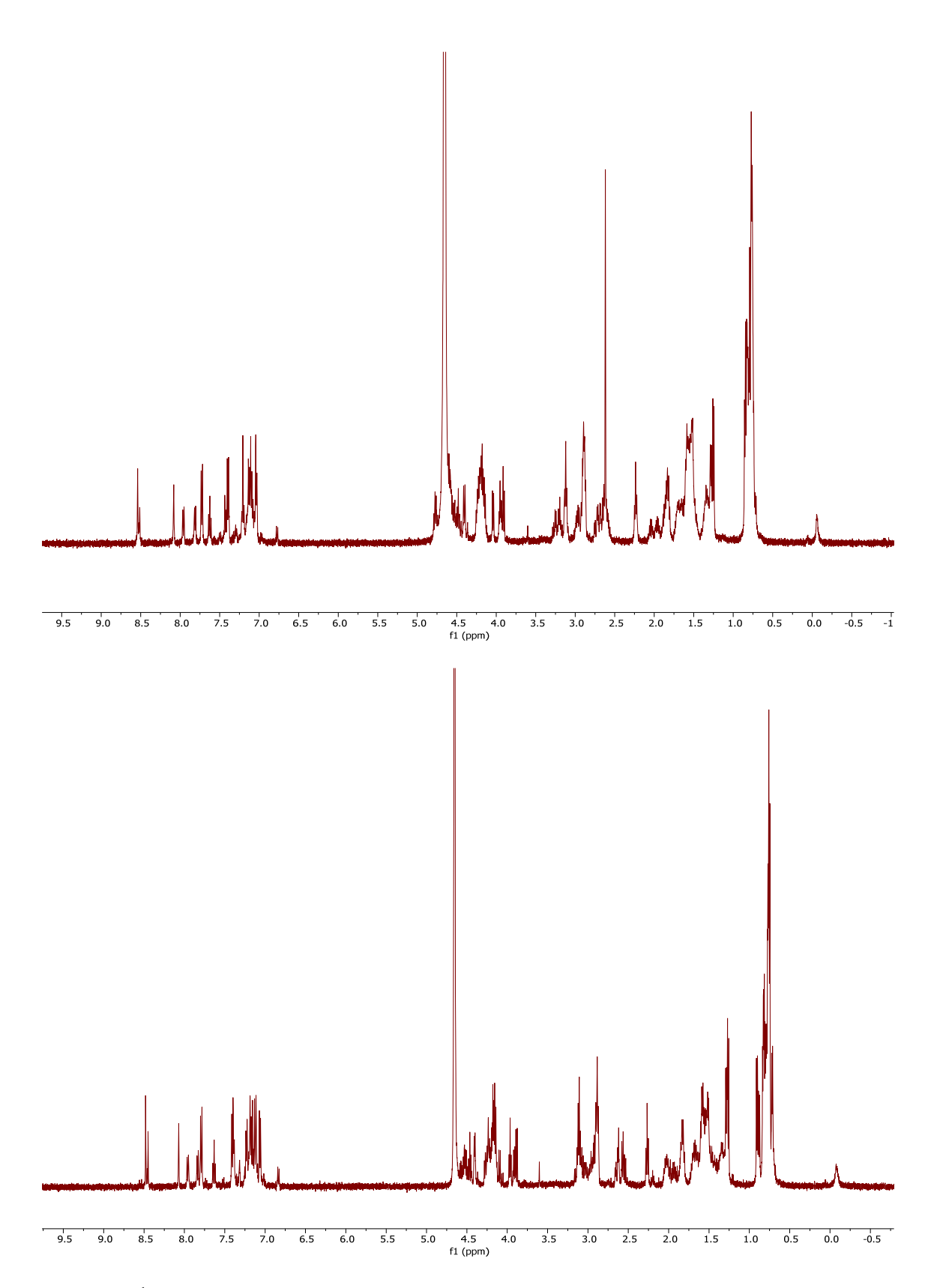


Figure S14: <sup>1</sup>H-NMR spectra (500 MHz, D<sub>2</sub>O) of SP2 (top, trans-isomer) and SP3 (bottom, trans-isomer).

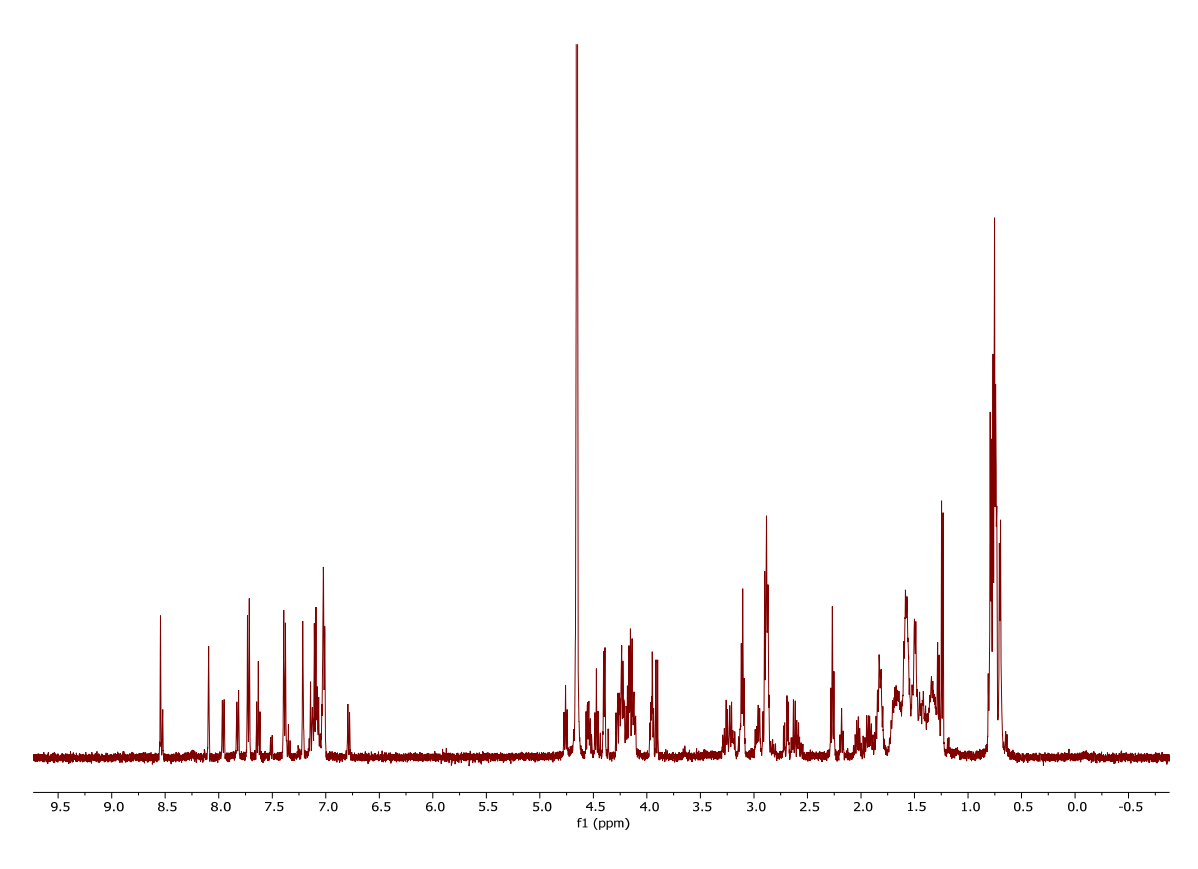


Figure S15: <sup>1</sup>H-NMR spectrum (500 MHz, D<sub>2</sub>O) of SP4 (*trans*-isomer).

- 1. Murawska, G. M.; Poloni, C.; Simeth, N. A.; Szymanski, W.; Feringa, B. L., Comparative Study of Photoswitchable Zinc-Finger Domain and AT-Hook Motif for Light-Controlled Peptide–DNA Binding. *Chemistry–A European Journal* **2019**, *25* (19), 4965-4973.
- 2. Rück-Braun, K.; Kempa, S.; Priewisch, B.; Richter, A.; Seedorff, S.; Wallach, L., Azobenzene-Based  $\omega$ -Amino Acids and Related Building Blocks: Synthesis, Properties, and Application in Peptide Chemistry. *Synthesis* **2009**, *24*, 4256-4267.

## **Supporting Information**

# Photocontrolled reversible amyloid fibril formation of parathyroid hormone-derived peptides

André Paschold<sup>1,#</sup>, Moritz Schäffler<sup>2,3,#</sup>, Xincheng Miao<sup>4</sup>, Luis Gardon<sup>2,5</sup>, Stephanie Krüger<sup>6</sup>, Henrike Heise<sup>2,5</sup>, Merle Insa Silja Röhr<sup>4</sup>, Maria Ott<sup>7</sup>, Birgit Strodel<sup>2,3\*</sup>, Wolfgang H. Binder<sup>1\*</sup>

#### **Contents**

1.	Supplementary figures	2
2.	Supplementary tables	. 19
3.	Peptide characterization after synthesis	. 21

<sup>&</sup>lt;sup>1</sup> Macromolecular Chemistry, Institute of Chemistry, Faculty of Natural Science II, Martin Luther University Halle Wittenberg, von-Danckelmann-Platz 4, 06120 Halle (Germany)

<sup>&</sup>lt;sup>2</sup> Institute of Theoretical and Computational Chemistry, Heinrich Heine University Düsseldorf, 40225 Düsseldorf, Germany

<sup>&</sup>lt;sup>3</sup> Institute of Biological Information Processing, Structural Biochemistry (IBI-7), Forschungszentrum Jülich, 52425 Jülich, Germany

<sup>&</sup>lt;sup>4</sup> Center for Nanosystems Chemistry (CNC), Theodor-Boveri Weg, Universität Würzburg, 97074 Würzburg, Germany

<sup>&</sup>lt;sup>5</sup> Institute of Physical Biology, Heinrich-Heine-Universität Düsseldorf, 40225 Düsseldorf, Germany

<sup>&</sup>lt;sup>6</sup> Biozentrum, Martin Luther University Halle-Wittenberg, Weinberweg 22, 06120 Halle (Germany)

<sup>&</sup>lt;sup>7</sup> Institute of Biophysics, Faculty of Natural Science I, Martin Luther University Halle-Wittenberg, Kurt-Mothes-Straße 3, 06120 Halle (Germany)

<sup>#</sup> These authors contributed equally to this work.

### 1. Supplementary figures

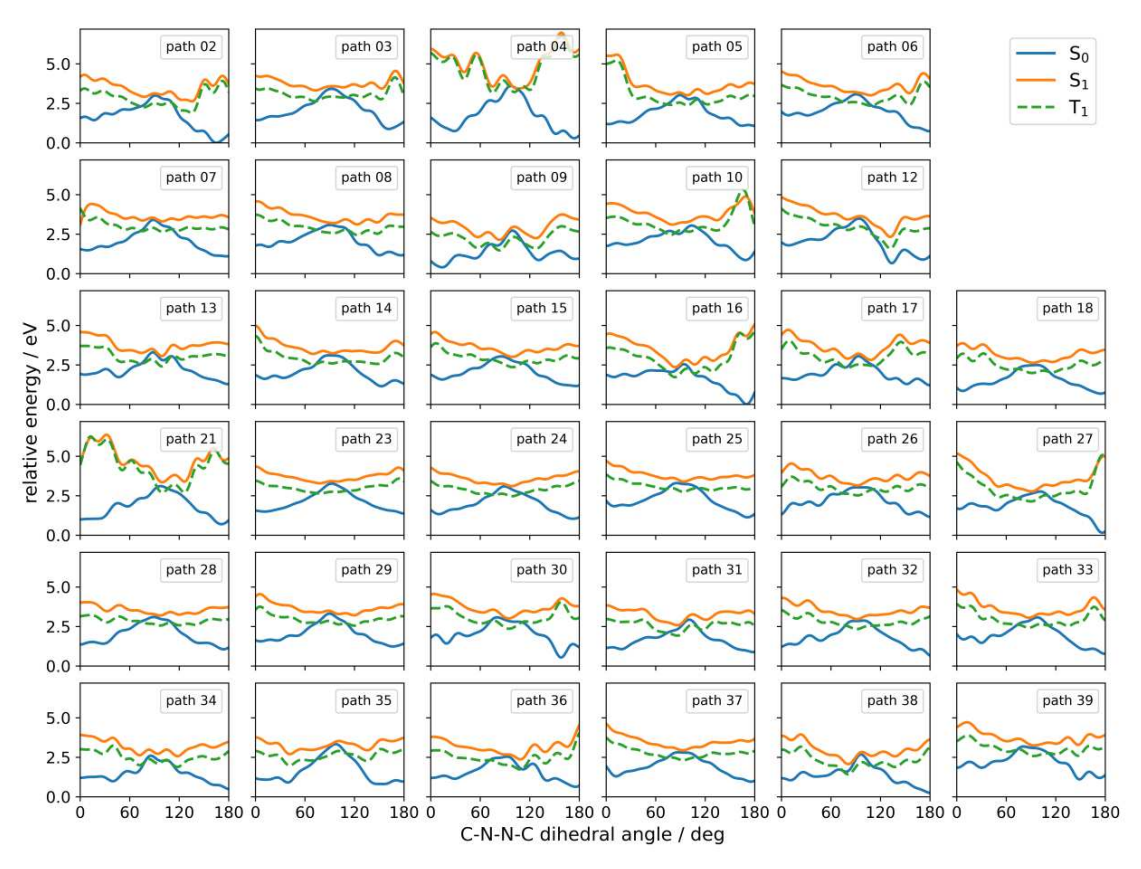
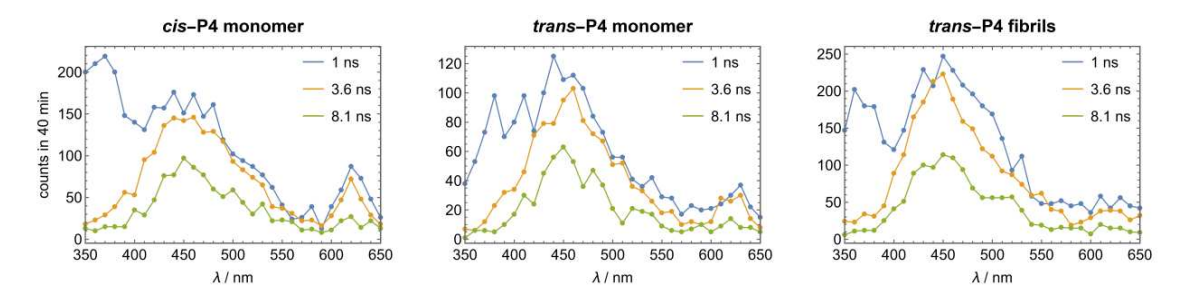
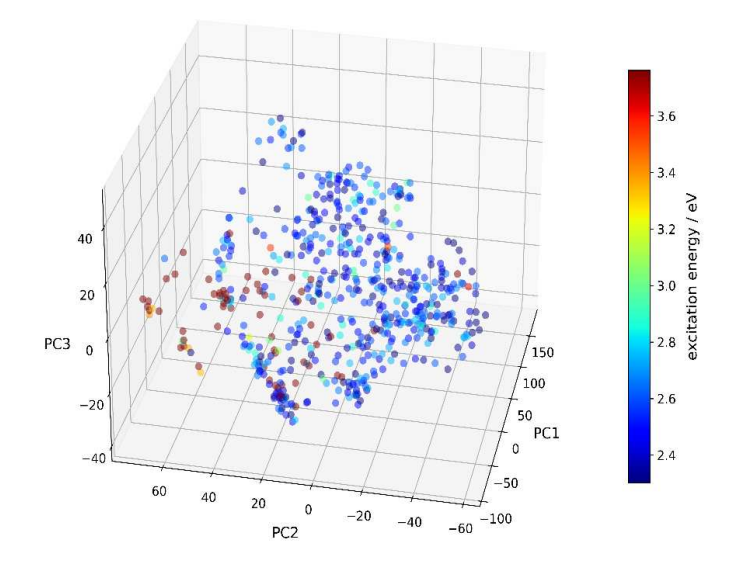


Figure S1. The smoothed potential energy curves from 34 converged  $cis \leftrightarrow trans$  isomerization paths. Single-point calculations are performed using NEVPT2(2,2)/xTB with implicit water through ALPB. The smoothing is carried out using Gaussian process regression. A subset of the paths has an energy barrier in the trans-cis-isomerization, notably paths 04, 10 and 21, with excitation energies before the barrier range from 2.5 to 3.0 eV. This correlates with the experimental fluorescence peak at 485 nm (Figure S2), albeit with an expected ipsochromic effect caused by the minimum active space considered in the calculations. We attribute the extended fluorescence lifetime, compared to azobenzene, to structures hindered by this barrier, preventing radiationless relaxation. These barriers predominantly arise from structures characterized by dihedral angles around 170°, which exhibit a heightened S0–S1 excitation energy in the scan.



**Figure S2.** Fluorescence life-time measurements. Fluorescence spectra measured at various points in time after the excitation pulse.



**Figure S3.** All geometries with dihedral angles near 170° projected on to the three-dimensional PCA space. The colors encode the S0–S1 excitation energies. The reduced three-dimensional space accounts for 86% of the total variance. Several clusters can be detected, notably one predominantly comprising structures with high excitation energies (visually represented in dark red in the lower left corner of the projection). This particular cluster is positioned at the negative extremity of the PC1-axis, advances towards the positive end of the PC2-axis and is situated approximately mid-way along the PC3-axis.

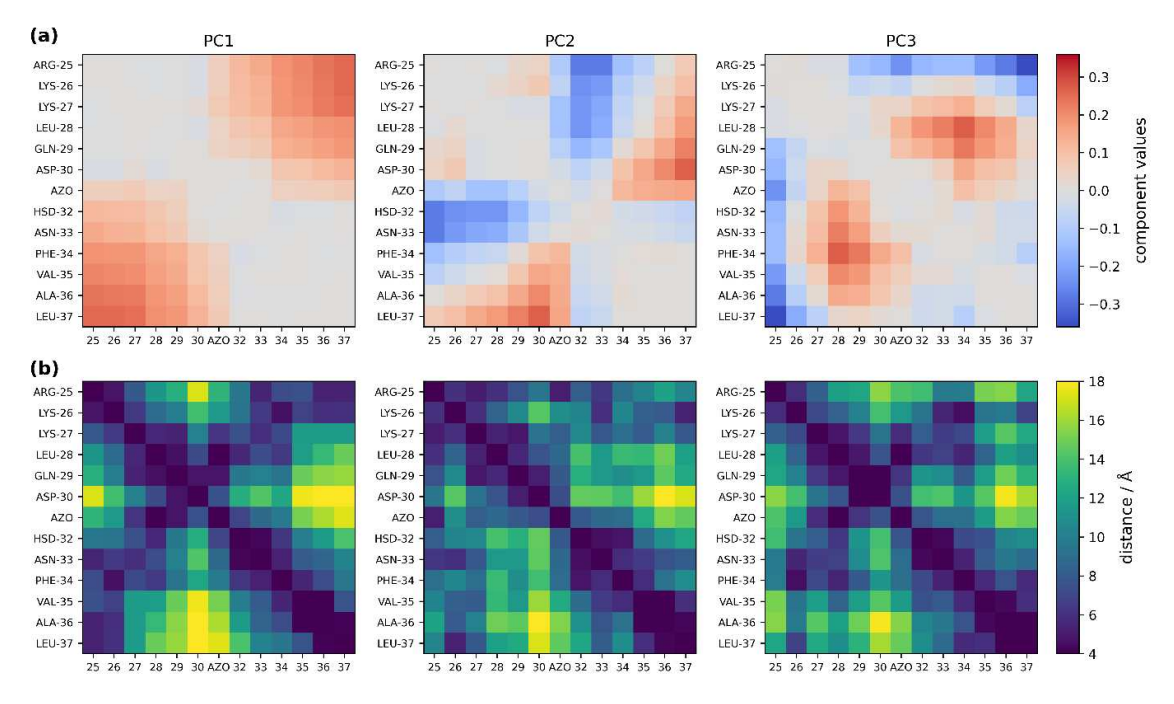


**Figure S4.** (a) The first three principal components represented in the distance matrix space. The first principal component signals a considerable separation between the residues R25 and A36/L37. Given this cluster's positioning at the PC1-axis's negative end, it implies that within these geometries, the distances between these residues are notably reduced. The second principal component reveals negative values for the separation between R25 and H32/N33, alongside positive distances between D30 and L37. The positive projection of this cluster on the PC2 suggests these distance matrix characteristics directly, without reversing the sign. With almost negligible projection on PC3, this component scarcely influences the distance matrices for structures within this cluster. (b) Distance matrices for clusters with high excitation energies. Despite originating from different paths, these matrices exhibit consistent patterns.

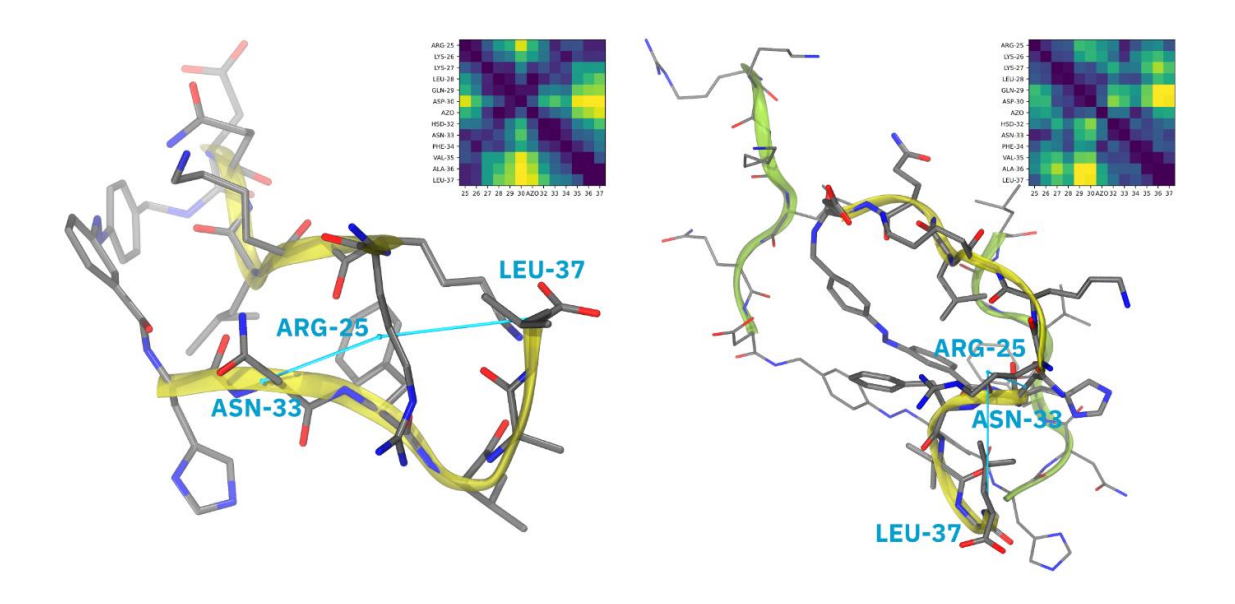


**Figure S5.** Selected monomer structure (left) with distance matrix shown in Figure S4b and dimer structure (right) with a similar distance matrix. The corresponding distance matrices are shown in the upper right corners. It can be seen that the simultaneous interactions of R25 with A36/L37 and H32/N33 potentially contribute to the S1-barrier during the *trans→cis* isomerization path, leading to longer fluorescence lifetimes. This structural motif is also found in the dimer, while their configurations stabilized by intermolecular interactions could also lead to an increased barrier.

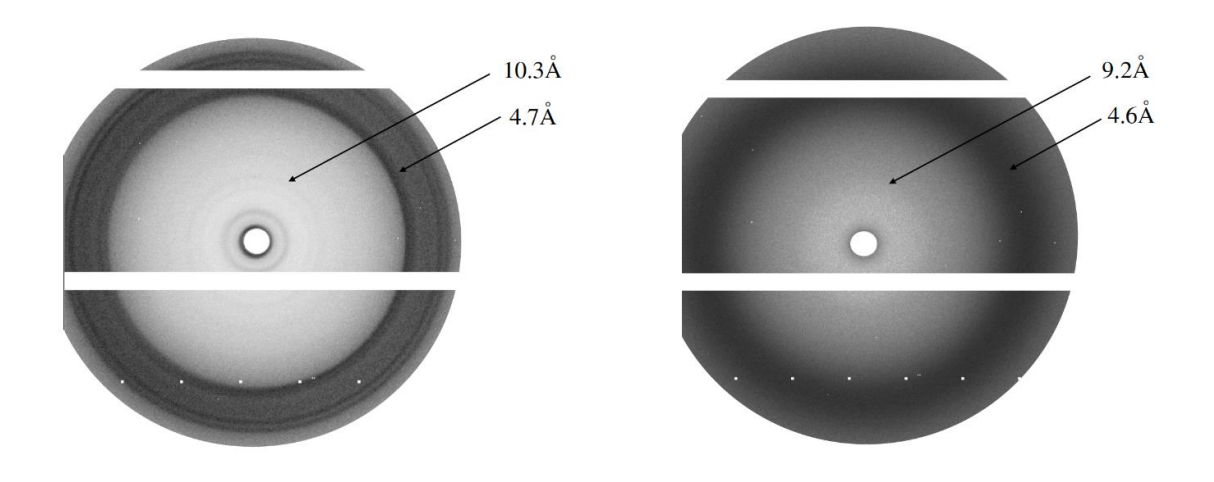


Figure S6: Wide-angle x-ray diffraction patterns from dried fibrillar samples of PTH<sub>25-37</sub> (left) and P4 (right).

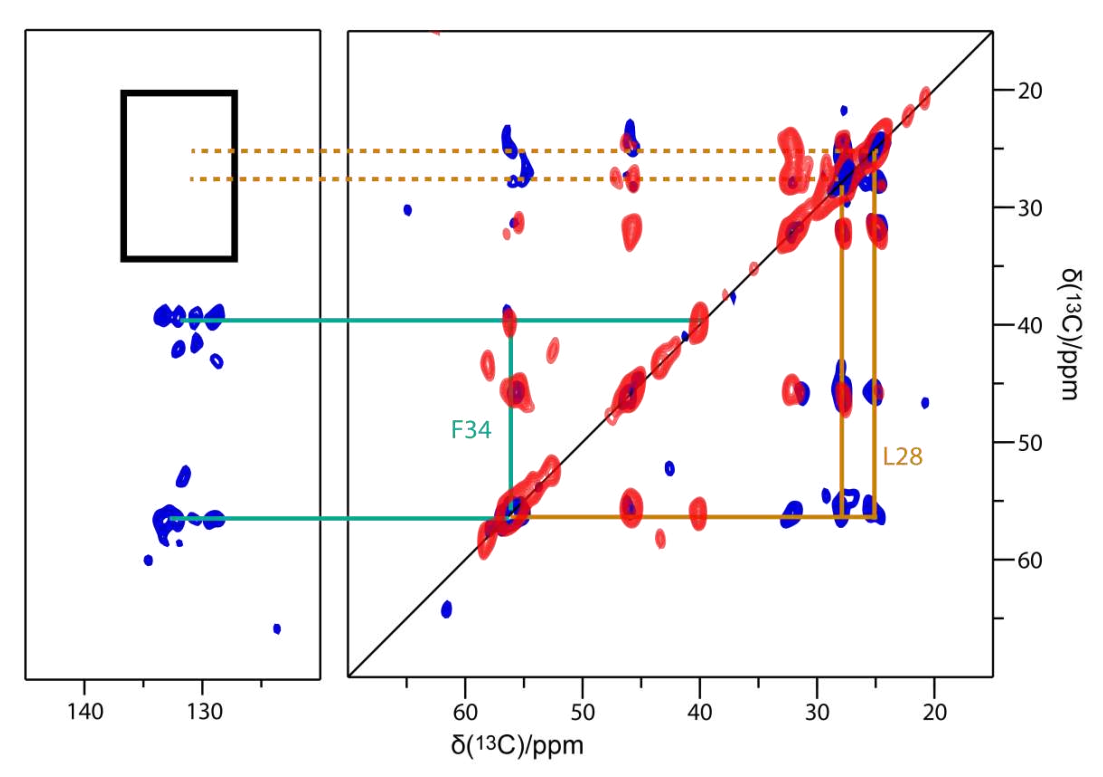
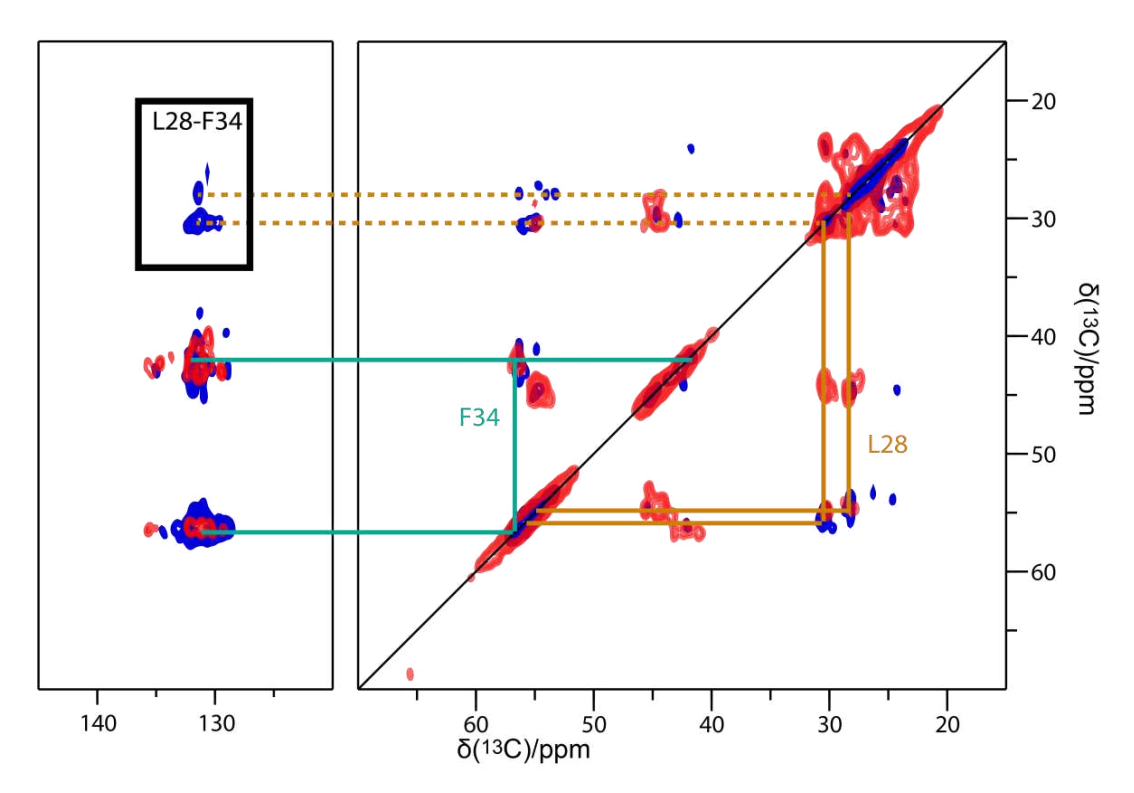
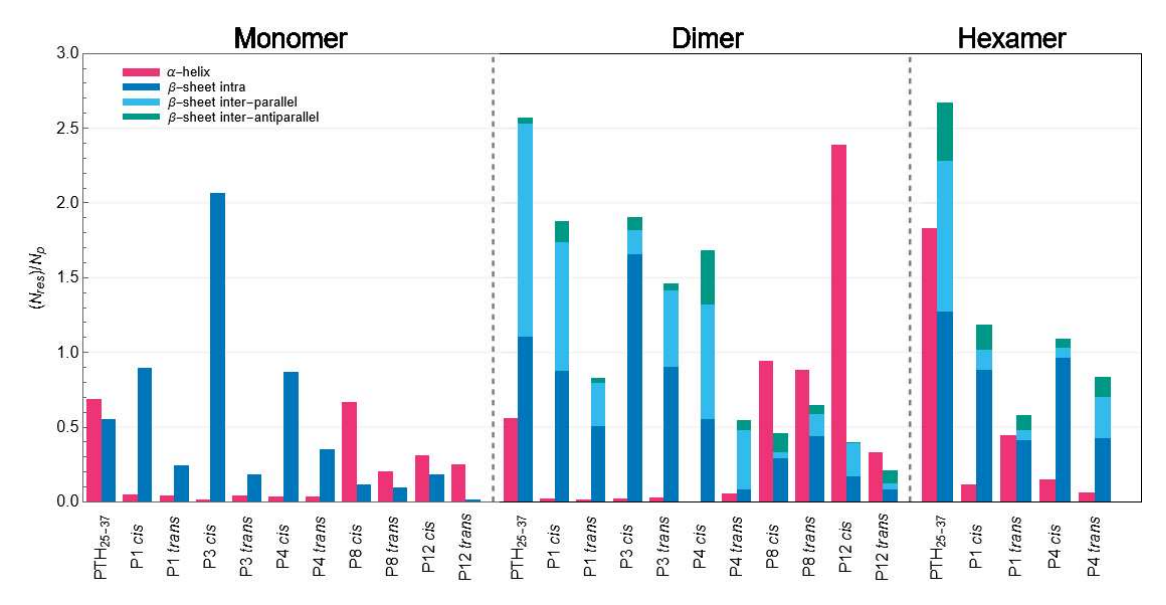


Figure S7. 2D  $^{13}$ C,  $^{13}$ C spin diffusion spectra of fibrils from PTH<sub>25-37</sub>, uniformly  $^{13}$ C labeled for L28 and F34, recorded under different conditions. Red: magnetic field strength 14.1 T (corresponding to 600 MHz  $^{1}$ H resonance frequency), spinning speed 11 kHz, mixing time 10 ms. Blue: magnetic fiels strength of 18.8 T (corresponding to 800 MHz  $^{1}$ H resonance frequency), spinning frequency of 20 kHz, mixing time 1 s. Figure S6 shows the 2D  $^{13}$ C,  $^{13}$ C spin diffusion spectra of fibrils from PTH<sub>25-37</sub>, uniformly  $^{13}$ C labeled for L28 and F34, recorded under different conditions. In the red spectrum, intraresidual cross-peaks between neighboring  $^{13}$ C sites of L28 and F34, respectively, are visible. At a longer mixing time of 1 s (blue), long-range correlations between all  $^{13}$ C spins within one residue are obtained. Spin systems of the labeled amino acids F34 (cyan) and L28 (brown) are marked by solid lines. Dashed lines show a possible contact between L28 Cγ/Cδ and an aromatic F34 carbon. The spinning speed of 20 kHz corresponds to the first order rotational resonance condition for resonances with a chemical shift difference of 100 ppm, leading to a recoupling of dipolar couplings between aromatic ring carbon atoms of F34 and aliphatic C<sub>γ</sub> and C<sub>δ</sub> signals of L28, facilitating magnetization transfer between those residues if the distance between these residues would not exceed 6 Å.  $^{20}$  The fact that no inter-residual cross-peaks between L28 and F34 can be observed is thus a strong indication against an antiparallel arrangement of β-strands within the β-sheet.



**Figure S8.** 2D  $^{13}$ C, $^{13}$ C spin diffusion spectra of fibrils from P4, uniformly  $^{13}$ C labeled for L28 and F34, recorded at a magnetic field strength of 18.8 T (corresponding to 800 MHz  $^{1}$ H resonance frequency) at a spinning speed of 20 kHz, corresponding to the first order rotational resonance condition for signals with a chemical shift difference of 100 ppm. Red: Mixing time of 50 ms. Blue: Mixing time of 1 s. See for more information in Fig. S6. Here, inter-residual cross-peaks between the aromatic ring signals of F and L C $\delta$  resonances are clearly visible for a mixing time of 1 s (blue spectrum).



**Figure S9.** Summary of all MD simulation results. The average numbers of residues  $\langle N_{\text{res}} \rangle$  forming secondary structure elements, divided into α-helical (magenta), intrapeptide β-sheets (blue), interpeptide parallel β-sheets (cyan) and interpeptide antiparallel β-sheets (green) are given. The average was taken over the number of frames of the simulation and normalized by the number of peptides  $N_P$  present in the corresponding simulation.

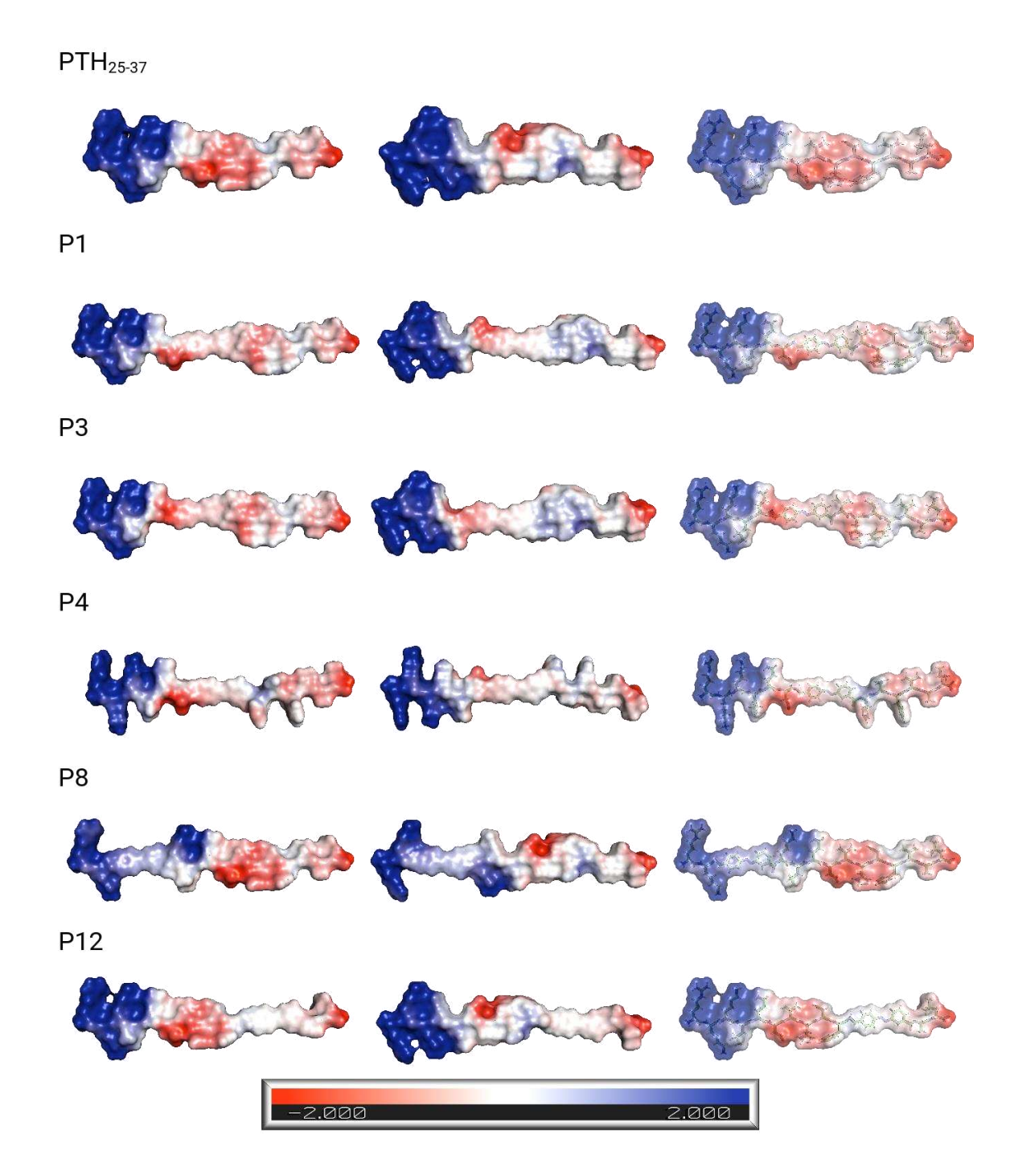


**Figure S10.** Electrostatic potential surface of PTH<sub>25-37</sub> and the peptides P1, P3, P4, P8, and P12, with values according to the color map at the bottom, ranging from -2 (red) to  $+2 \text{ kTe}^{-1}$  (blue). The electrostatic potential mapped to the molecular surfaces was calculated using the Adaptive Poisson-Boltzmann Solver (APBS<sup>1</sup>) plugin for the pymol<sup>2</sup> software package. For each peptide, the two views that are rotated by  $180^{\circ}$  around the backbone axis are shown, as well as a transparent front view.

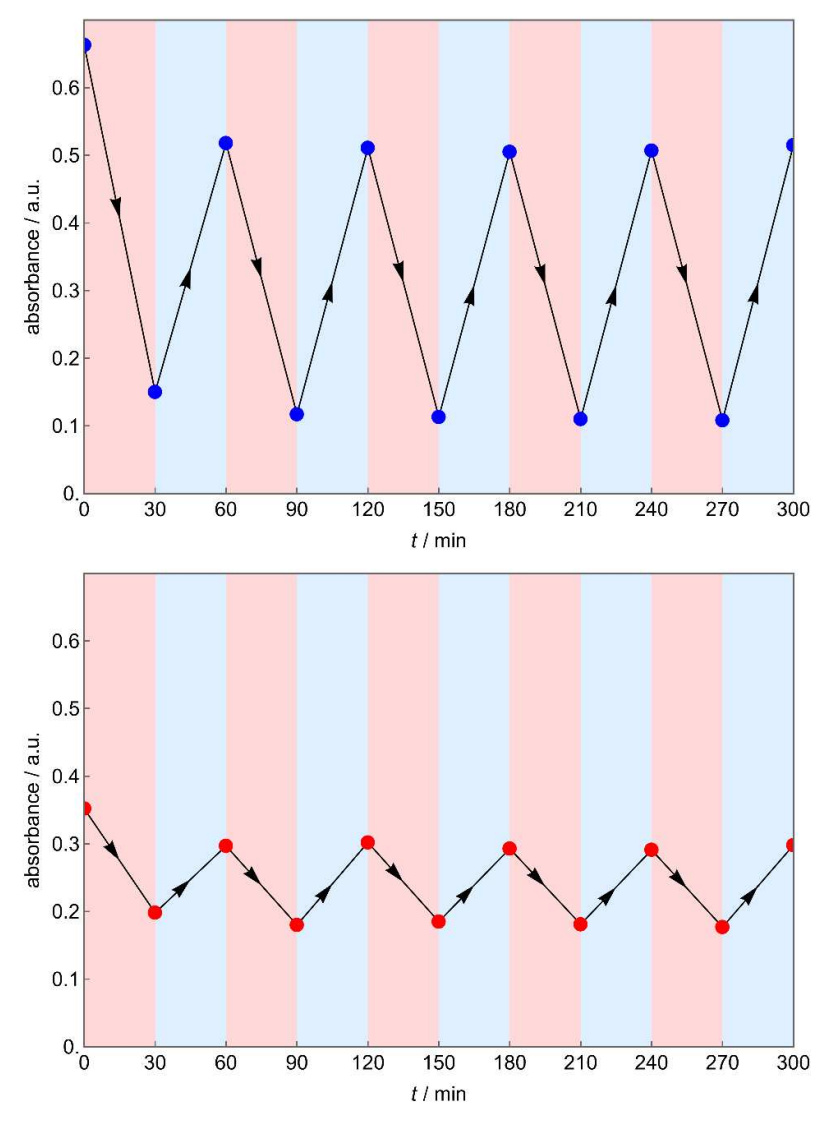


**Figure S11:** Control experiment to investigate photobleaching of the azobenzene unit during the photoisomerization. Absorption of P4 was measured after each isomerization step at 327 nm (top, blue dots) and 295 nm (bottom, red dots). Light red area corresponds to irradiation with light of 340 nm wavelength for 30 min to achieve *trans→cis* isomerization. Light blue area corresponds to irradiation with light of 405 nm wavelength for 30 min to achieve *cis→trans* isomerization.

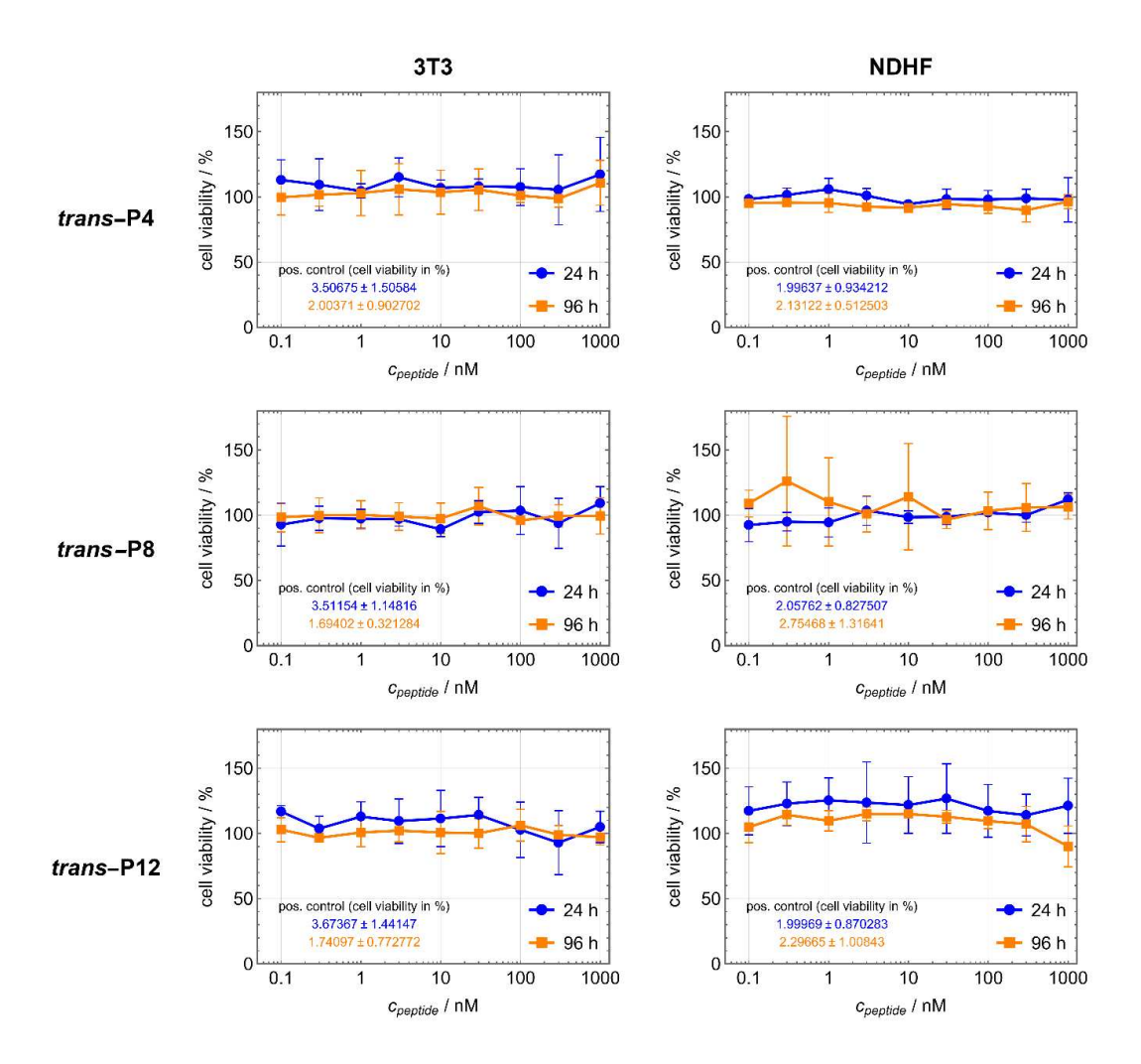


**Figure S12:** Cell viability assay of *trans*-P4, *trans*-P8, and *trans*-P12 on NHDF (human, adult, fibroblasts) and 3T3 (murine, embryonal, fibroblasts) cells after 24 h (blue) and 96 h (orange). 100% cell viability corresponds to the value of the negative, untreated control.

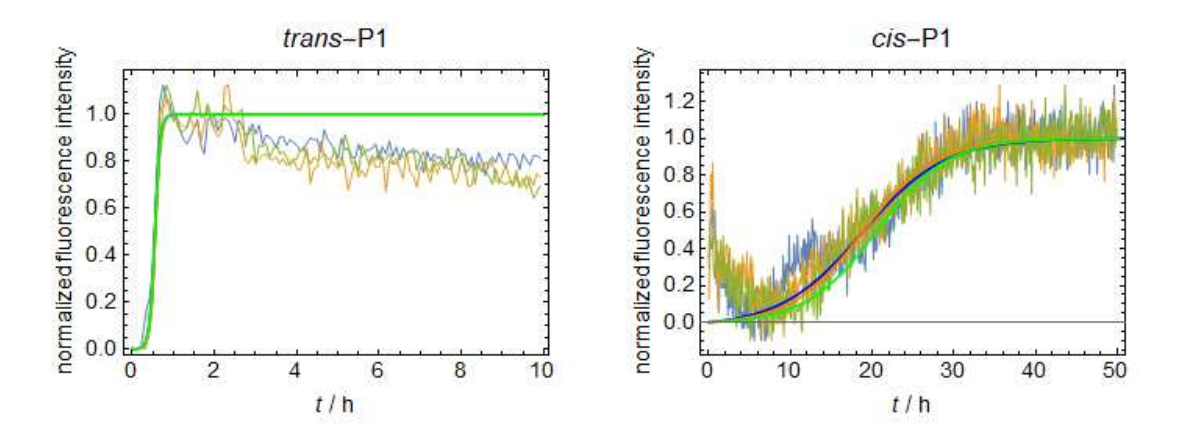


**Figure S13.** Fibrillization kinetics of 85  $\mu$ M P1 as *trans*- (left) and *cis*-isomer (right). Measured in a ThT-monitored fluorescence assay at 37 °C in 50  $\mu$ M Na<sub>2</sub>HPO<sub>4</sub> buffered aqueous solution (pH 7.4).

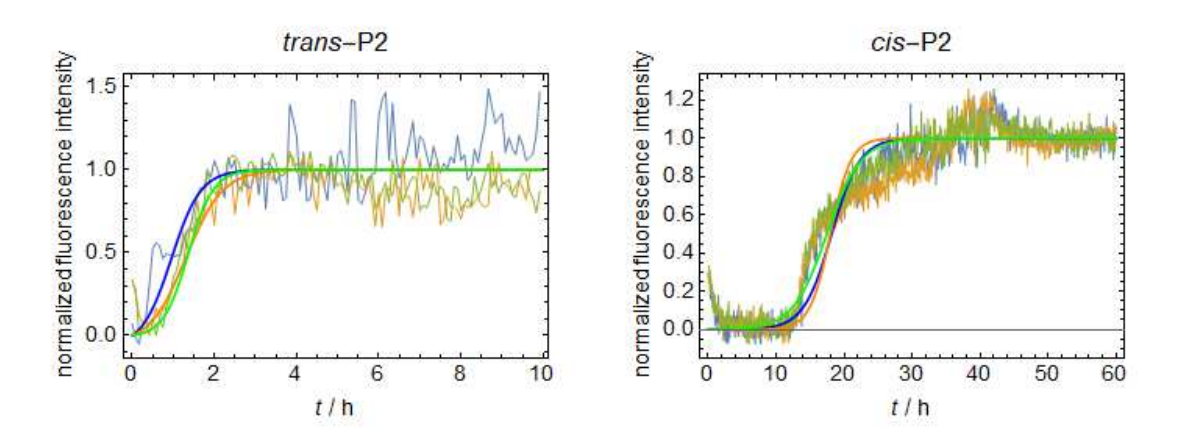


**Figure S14.** Fibrillization kinetics of 55  $\mu$ M P2 as *trans*- (left) and *cis*-isomer (right). Measured in a ThT-monitored fluorescence assay at 37 °C in 50  $\mu$ M Na<sub>2</sub>HPO<sub>4</sub> buffered aqueous solution (pH 7.4).

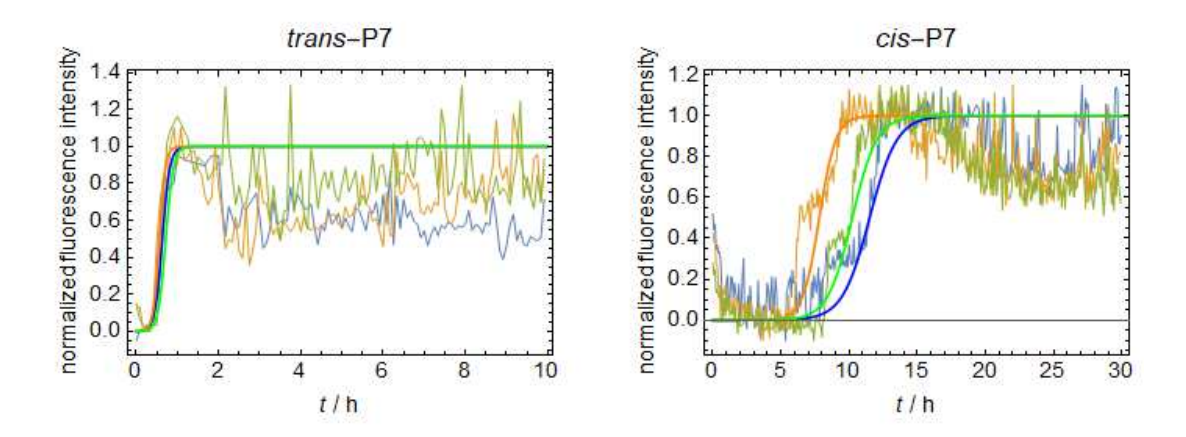


**Figure S15.** Fibrillization kinetics of 100  $\mu$ M P7 as *trans*- (left) and *cis*-isomer (right). Measured in a ThT-monitored fluorescence assay at 37 °C in 50  $\mu$ M Na<sub>2</sub>HPO<sub>4</sub> buffered aqueous solution (pH 7.4).

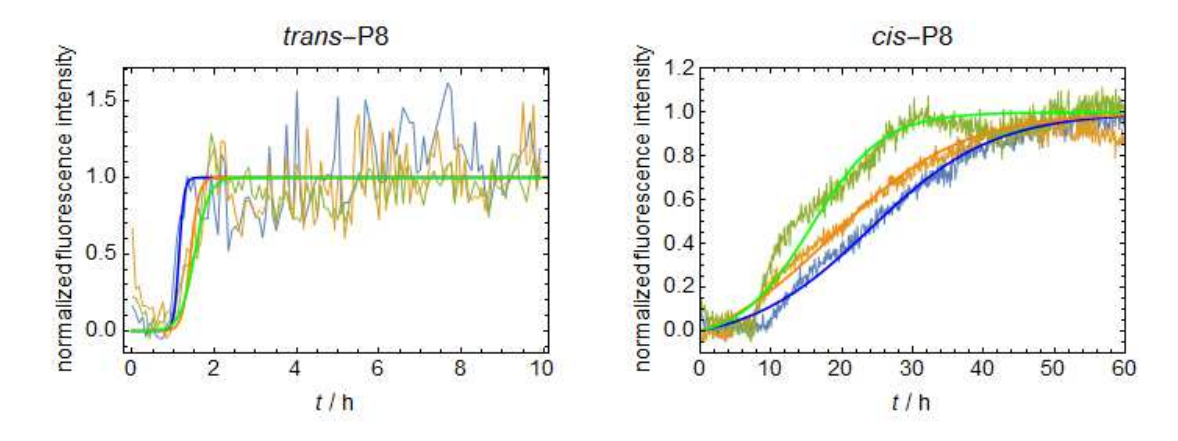


**Figure S16.** Fibrillization kinetic of  $100 \,\mu\text{M}$  P8 as *trans*- (left) and *cis*-isomer (right). Measured in a ThT-monitored fluorescence assay at 37 °C in  $50 \,\mu\text{M}$  Na<sub>2</sub>HPO<sub>4</sub> buffered aqueous solution (pH 7.4).

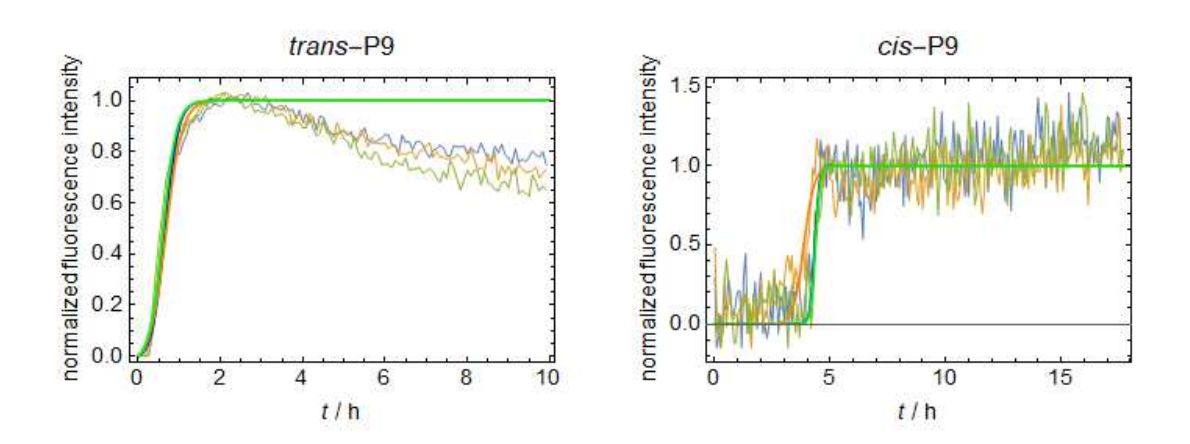


**Figure S17.** Fibrillization kinetics of  $100 \,\mu\text{M}$  P9 as *trans*- (left) and *cis*-isomer (right). Measured in a ThT-monitored fluorescence assay at 37 °C in  $50 \,\mu\text{M}$  Na<sub>2</sub>HPO<sub>4</sub> buffered aqueous solution (pH 7.4).

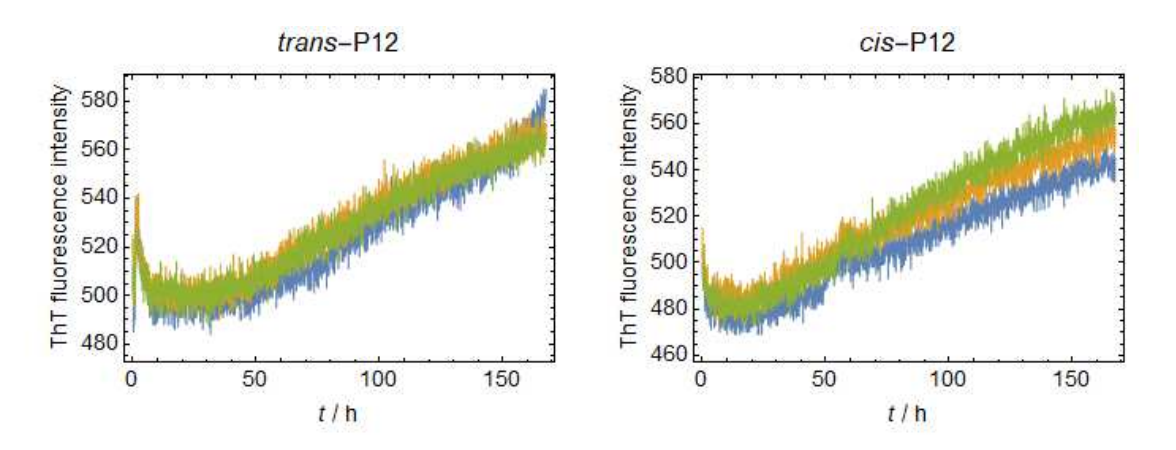


**Figure S18.** Fibrillization kinetics of  $100 \,\mu\text{M}$  P12 as *trans*- (left) and *cis*-isomer (right). Measured in a ThT-monitored fluorescence assay at  $37 \,^{\circ}\text{C}$  in  $50 \,\mu\text{M}$  Na<sub>2</sub>HPO<sub>4</sub> buffered aqueous solution (pH 7.4).

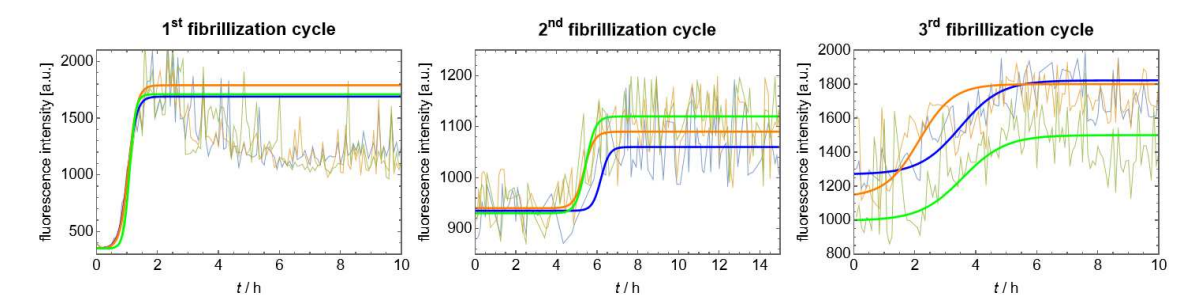


Figure S19. Fibrillization kinetics of P4 over three cycles of alternating fibrillization and fibril degradation through *trans* $\rightarrow$ *cis* isomerization measured in a ThT-monitored fibrillization assay at 37 °C in 50  $\mu$ M Na<sub>2</sub>HPO<sub>4</sub> buffered aqueous solution (pH 7.4).

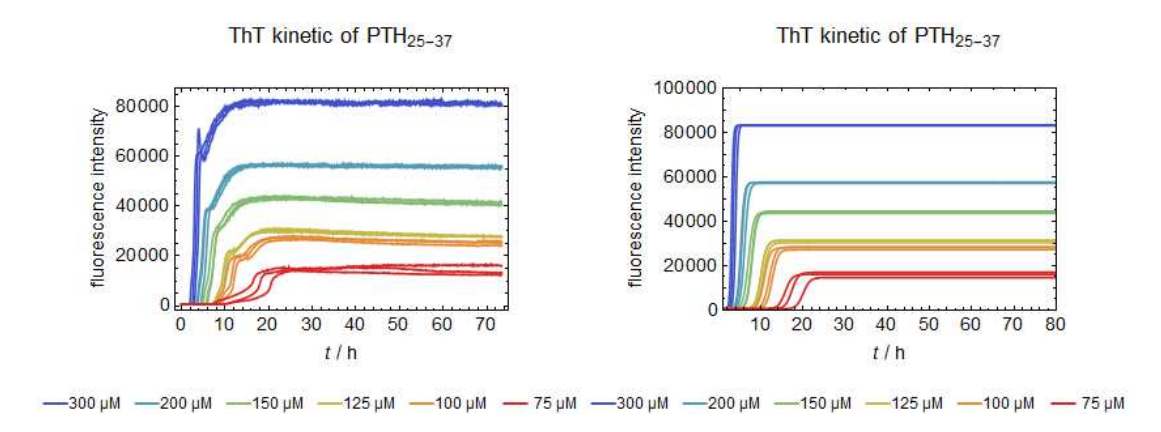


Figure S20. Fibrillization kinetics of PTH<sub>25-37</sub> in different concentrations measured in a ThT-monitored fluorescence assay at 37 °C in 50  $\mu$ M Na<sub>2</sub>HPO<sub>4</sub> buffered aqueous solution (pH 7.4); (left) raw data, (right) fitted data using Eq. (1).

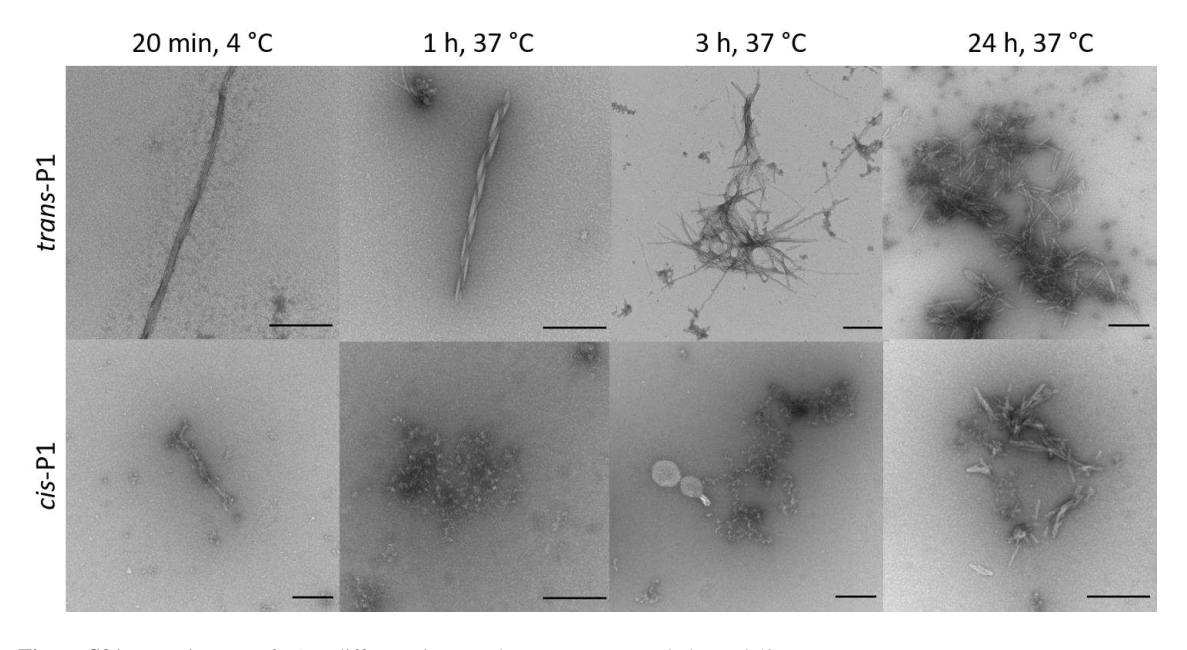


Figure S21. TEM images of P1 at different times and temperatures; scale bar = 250 nm.

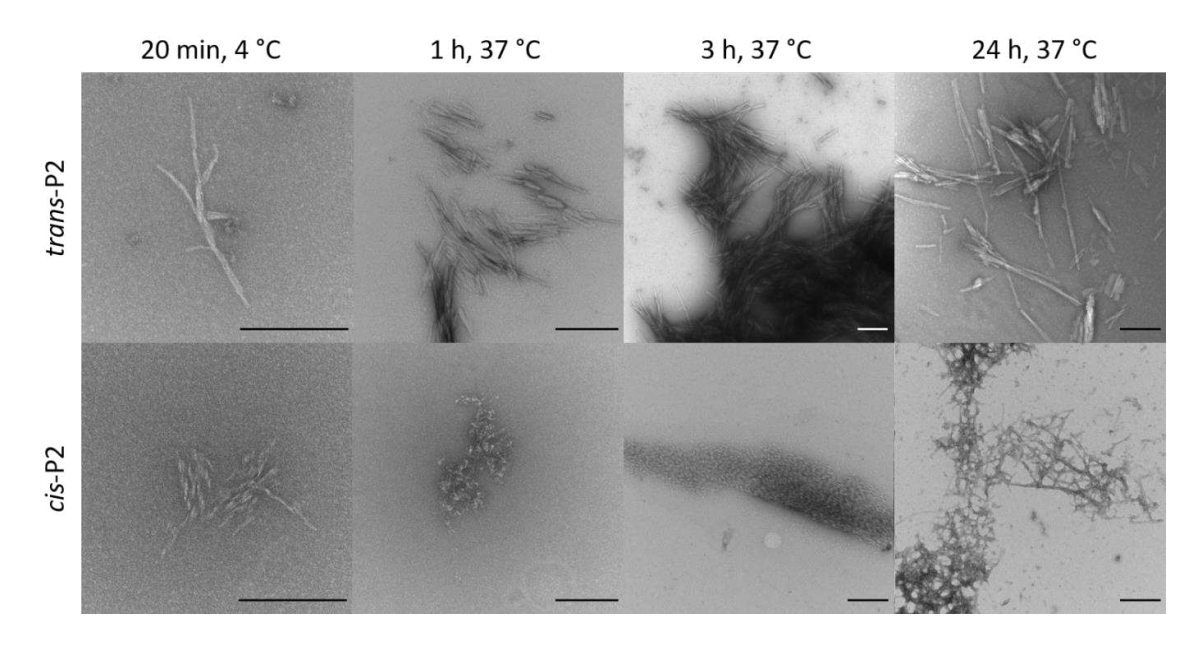


Figure S22. TEM images of P2 at different times and temperatures; scale bar = 250 nm.

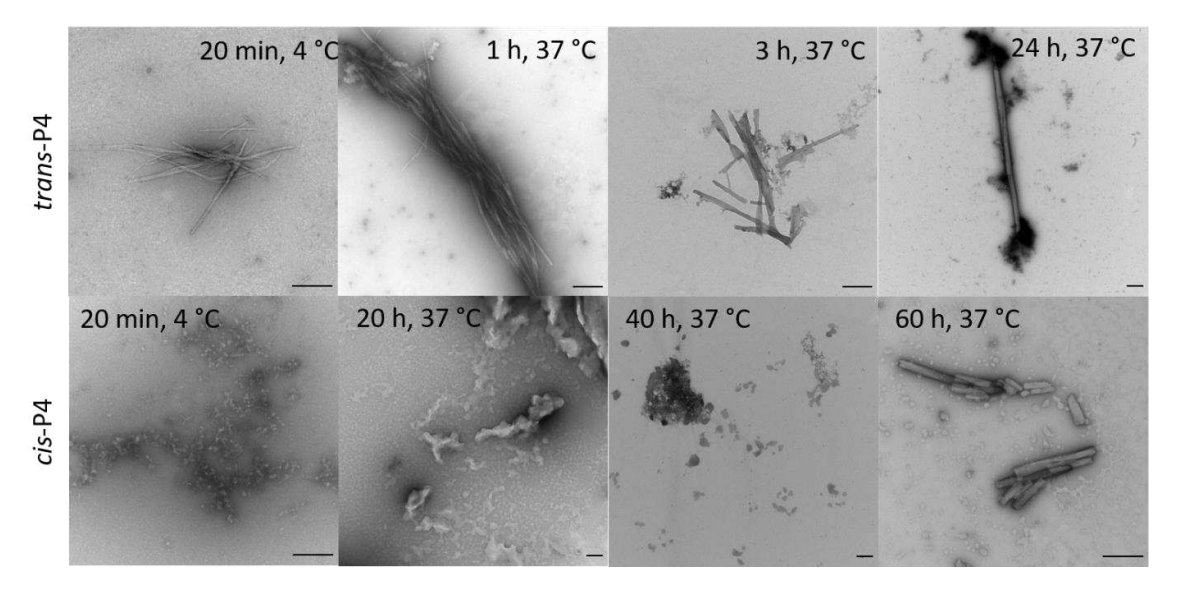
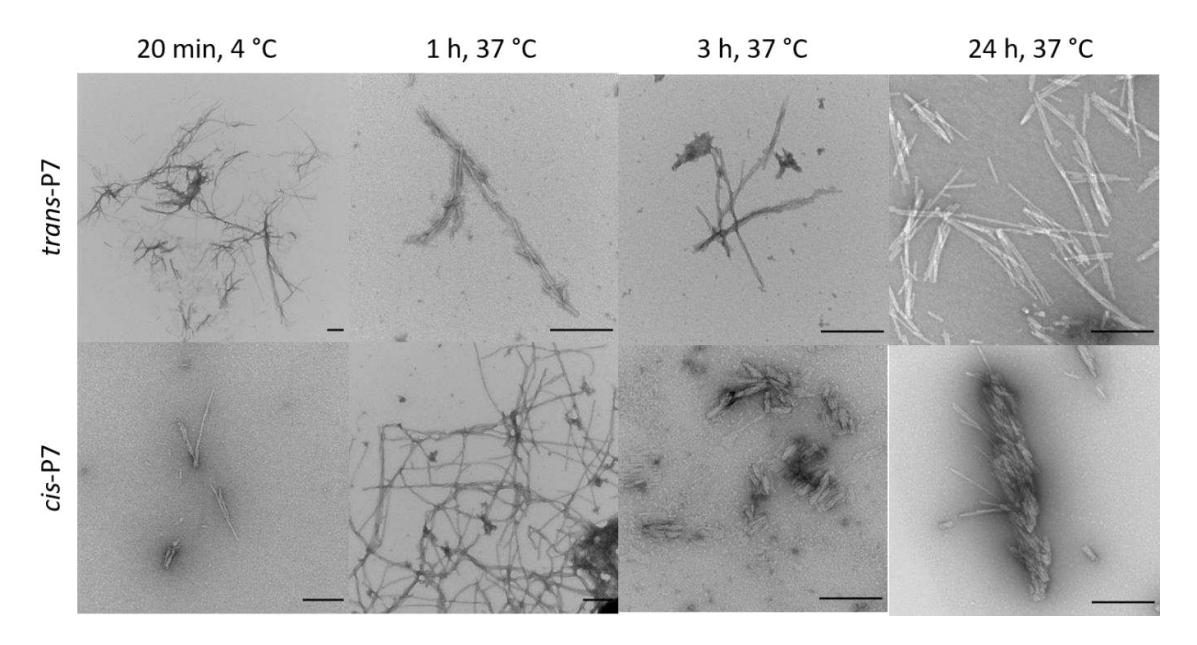
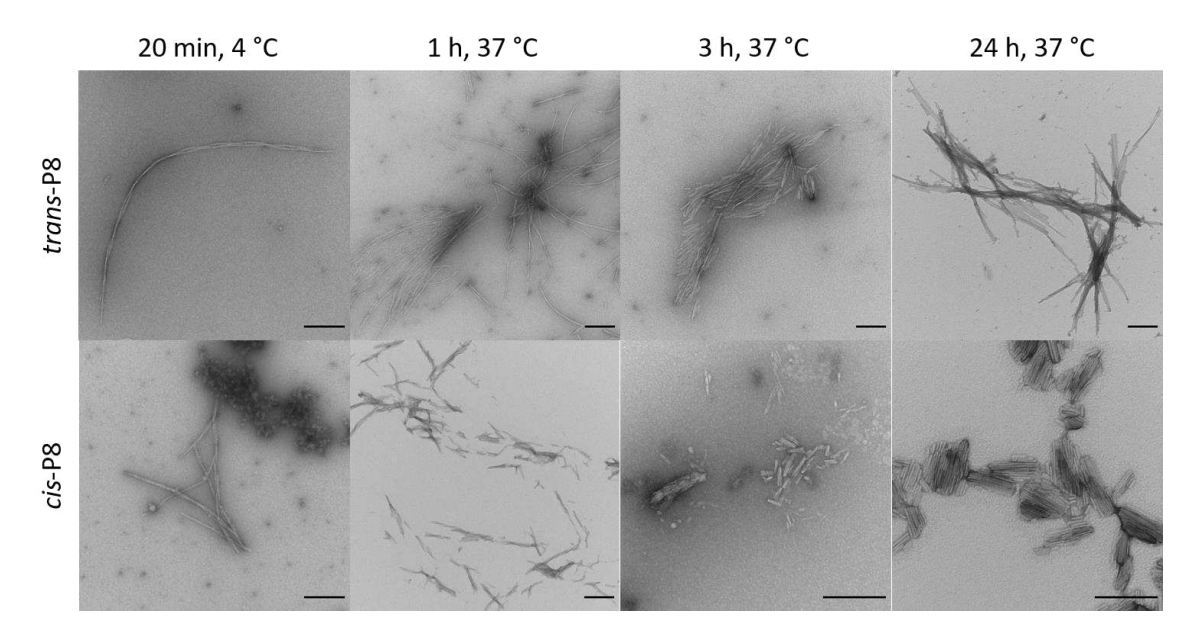


Figure S23. TEM images of P4 at different times and temperatures; scale bar = 250 nm.



**Figure S24.** TEM images of P7 at different times and temperatures; scale bar = 250 nm.



**Figure S25.** TEM images of P8 at different times and temperatures; scale bar = 250 nm.

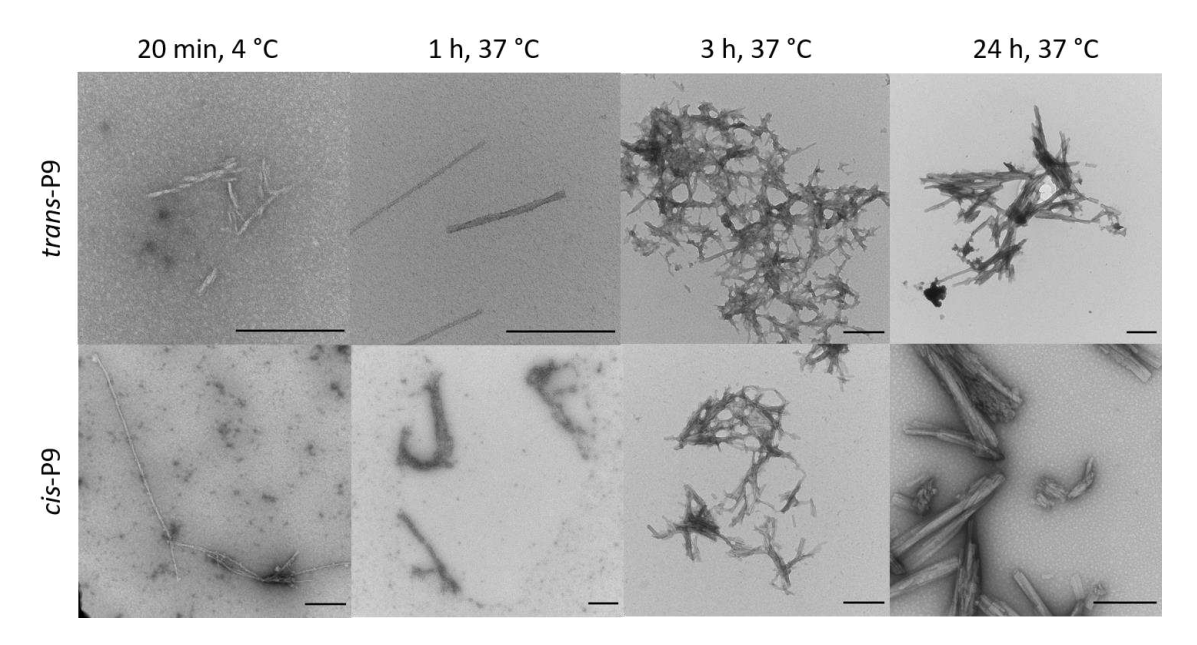


Figure S26. TEM images of P9 at different times and temperatures; scale bar = 250 nm.

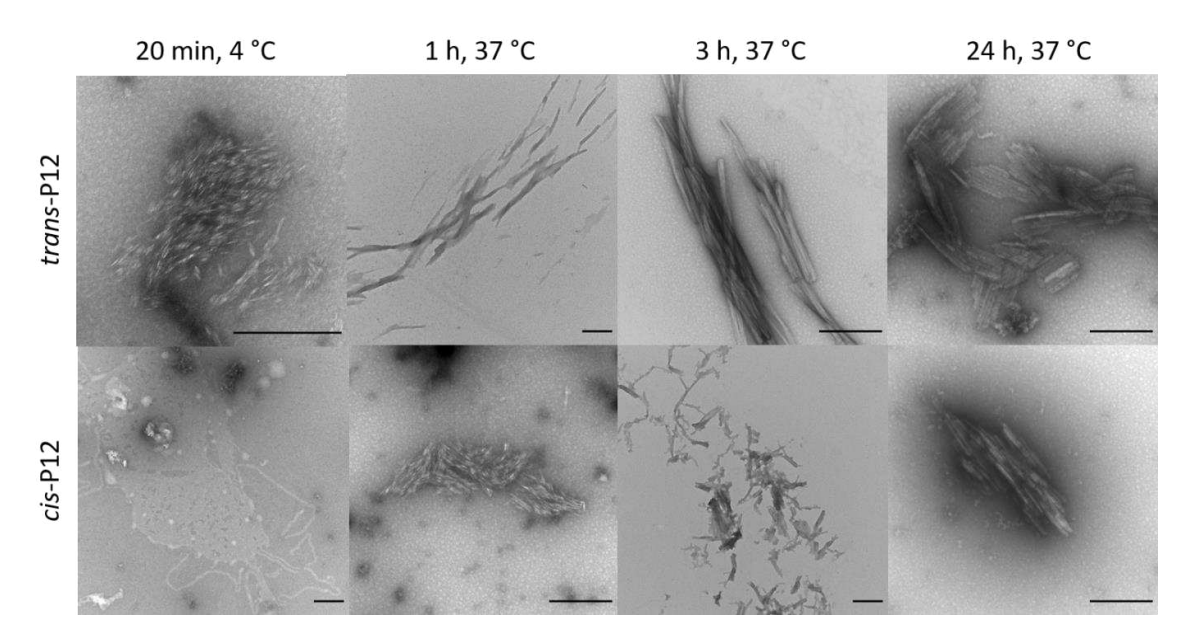
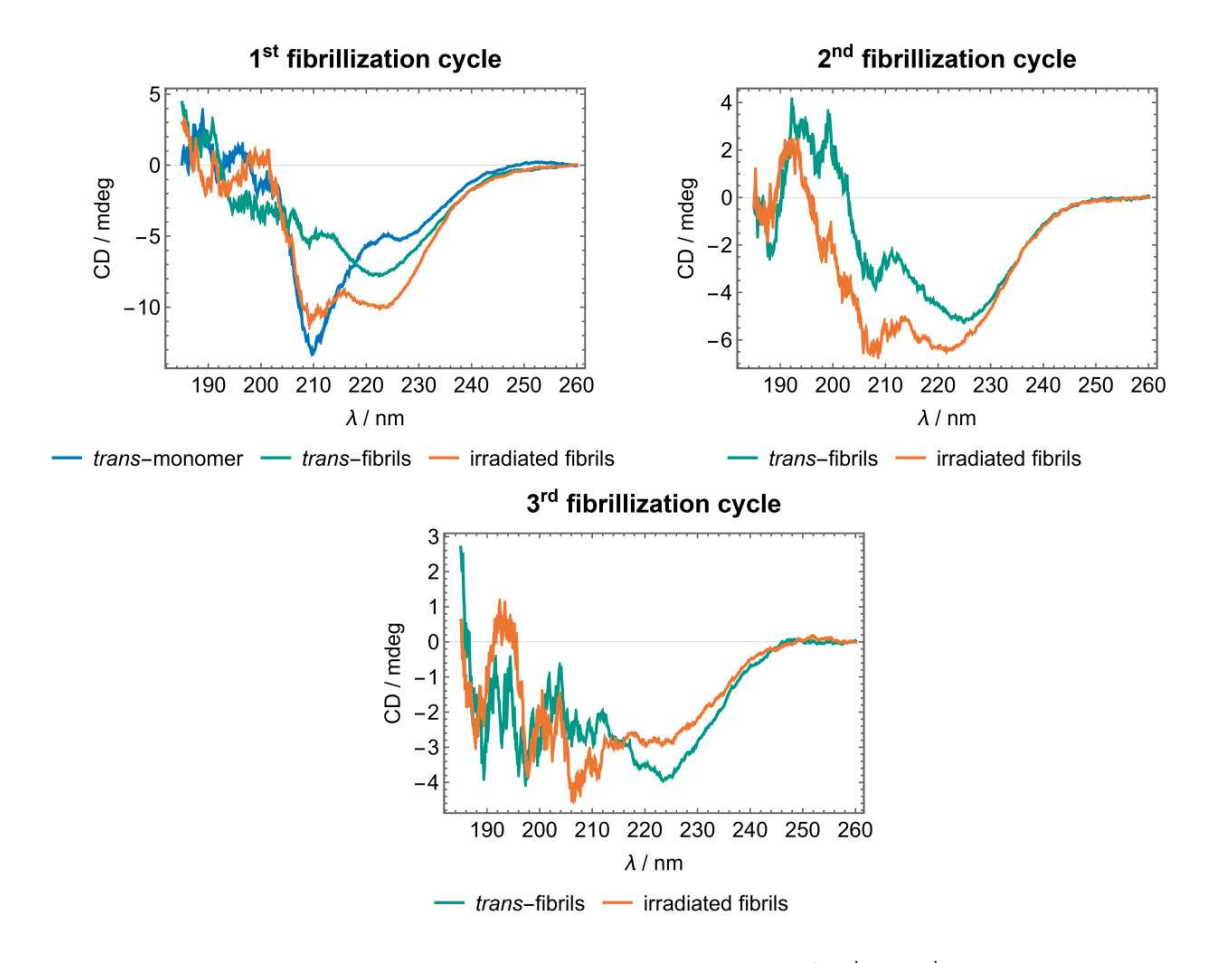
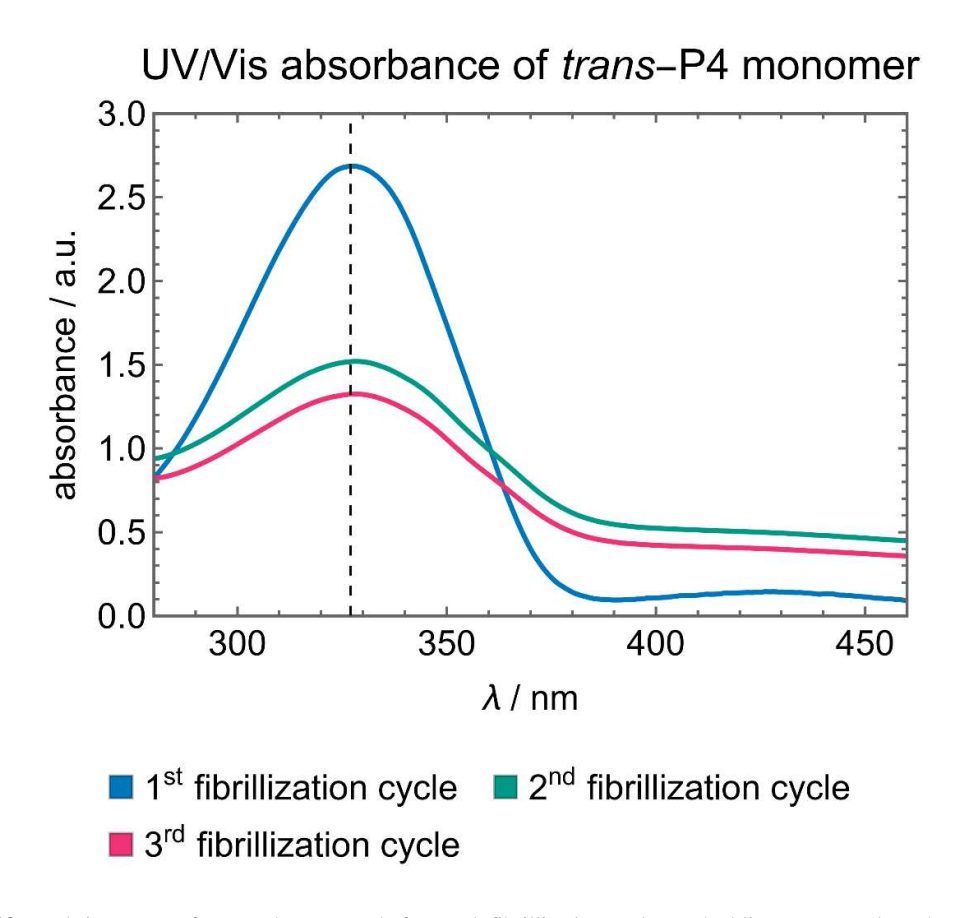


Figure S27. TEM images of P12 at different times and temperatures; scale bar = 250 nm.



**Figure S28:** CD-spectra of the reversible fibrillization of P4 over three cycles (1<sup>st</sup>, 2<sup>nd</sup>, and 3<sup>rd</sup>). *trans*-Isomer (blue) was measured directly after dissolving the peptide, *trans*-fibrils (green) were measured 20 h after reference sample reached the stationary phase, and irradiated fibrils (orange) were measured directly after irradiating the fibrils with 340 nm for 5 h.



**Figure S29:** UV/Vis-spectra of *trans*-P4 monomer before each fibrillization cycle. Dashed line corresponds to the absorption maxima of the *trans*-isomer at 327 nm.

# 2. Supplementary tables

Table S1. All Simulations performed, with their respective simulation time

Peptide	Simulation	Simulation Time [μs]
PTH <sub>25-37</sub>	Monomer/Dimer/Hexamer	3 systems x 10
P1	Monomer/Dimer/Hexamer - cis/trans	6 systems x 10
Р3	Monomer/Dimer - cis/trans	4 systems x 10
P4	Monomer/Dimer/Hexamer - cis/trans	6 systems x 10
P8	Monomer/Dimer - cis/trans	4 systems x 10
P12	Monomer/Dimer - cis/trans	4 systems x 10
PTH <sub>25-37</sub>	fibril	4 models x 1
P4	fibril	11 models x 1

**Table S2.** Sequence of PTH<sub>25-37</sub> and P1 – P12 and their respective solubility in buffered solution (50 mM aqueous Na<sub>2</sub>HPO<sub>4</sub>) with pH 7.4, the critical fibrillization concentration ( $c_{cr}$ ), and standard free energy of the fibrillization reaction  $\Delta G^0$ .

Peptide	Primary sequence	Solubility [µM]	$c_{cr}[\mu { m M}]$	$\Delta G^{\theta}$ [kJ/mol]
PTH <sub>25-37</sub>	PTH <sub>25-37</sub> <sup>25</sup> RKKLQ <sup>30</sup> DVHNF <sup>35</sup> VAL		42	26
P1	P1 <sup>25</sup> RKKLQ <sup>30</sup> D-Azo-VHNF <sup>35</sup> VAL		28	27
P2	<sup>25</sup> RKKLQ <sup>30</sup> DV-Azo-HNF <sup>35</sup> VAL 60 27		27	27
P3	<sup>25</sup> RKKLQ-Azo-VHNF <sup>35</sup> VAL	35	n.d.	n.d.
P4	<sup>25</sup> RKKLQ <sup>30</sup> D-Azo-HNF <sup>35</sup> VAL	370	23	28
P5	<sup>25</sup> RKKLQ-Azo-HNF <sup>35</sup> VAL	25	n.d.	n.d.
P6	<sup>25</sup> RKKLQ-Azo- <sup>30</sup> DVHNF <sup>35</sup> VAL	20	n.d.	n.d.
P7	<sup>25</sup> RKKL-Azo-Q <sup>30</sup> DVHNF <sup>35</sup> VAL	140	32	27
P8	<sup>25</sup> RK-Azo-KLQ <sup>30</sup> DVHNF <sup>35</sup> VAL	200	6	31
P9	<sup>25</sup> R-Azo-KLQ <sup>30</sup> DVHNF <sup>35</sup> VAL	130	26	27
P10	<sup>25</sup> RKKLQ <sup>30</sup> DVHN-Azo-F <sup>35</sup> VAL	7	n.d.	n.d.
P11	<sup>25</sup> RKKLQ <sup>30</sup> DVHNF <sup>35</sup> V-Azo-AL	20	n.d.	n.d.
P12	<sup>25</sup> RKKLQ <sup>30</sup> DVHNF-Azo-AL	135	-	-

n.d. - not determined

**Table S3.** Photophysical properties of P1, P2, P4, P7, P8, P9, P12 in buffered solution. *cis*-PSS – *cis*-photostationary state at 340 nm after 30 min. *trans*-PSS – *trans*-photostationary state at 405 nm after 20 min.

Peptide	$t_{1/2}$ (cis, 37 °C) [h]	after synthesis	cis-PSS	trans-PSS
		cis:trans ratio		
P1	90	5:95	86:14	19:81
P2	90	6:94	87:13	19:81
P4	97	3:97	82:18	24:76
P7	72	8:92	94:6	23:77
P8	89	6:94	85:15	23:77
P9	86	9:91	91:9	16:84
P12	63	4:96	90:10	19:81

**Table S4.** Fibrillization parameters of PTH<sub>25-37</sub>, P1, P2, P4, P7, P8, and P9 in buffered solution.  $t_{lag}$  - lag time.  $t_{char}$  - characteristic time.

Peptide	t <sub>lag</sub> (trans) [h]	t <sub>char</sub> (trans) [h]	t <sub>lag</sub> (cis) [h]	t <sub>char</sub> (cis) [h]
PTH <sub>25-37</sub>	7.770 ± 1.111	12.797 ±3.341	-	-
P1	$0.392 \pm 0.013$	$0.556 \pm 0.008$	$9.759 \pm 1.383$	19.640 ±0.842
P2	$0.482 \pm 0.207$	$1.247 \pm 0.208$	13.052 ±1.336	$17.867 \pm 0.360$
P4	$1.917 \pm 0.507$	$2.371 \pm 0.433$	29.525 ±0.558	$42.444 \pm 5.251$
P7	$0.381 \pm 0.056$	$0.627 \pm 0.078$	$8.014 \pm 1.643$	$9.875 \pm 1.881$
P8	$1.069 \pm 0.096$	$1.356 \pm 0.197$	5.524 ±1.781	$20.701 \pm 4.415$
P9	$0.267 \pm 0.019$	$0.653 \pm 0.040$	$3.833 \pm 0.458$	$4.188 \pm 0.290$

# 3. Peptide characterization after synthesis

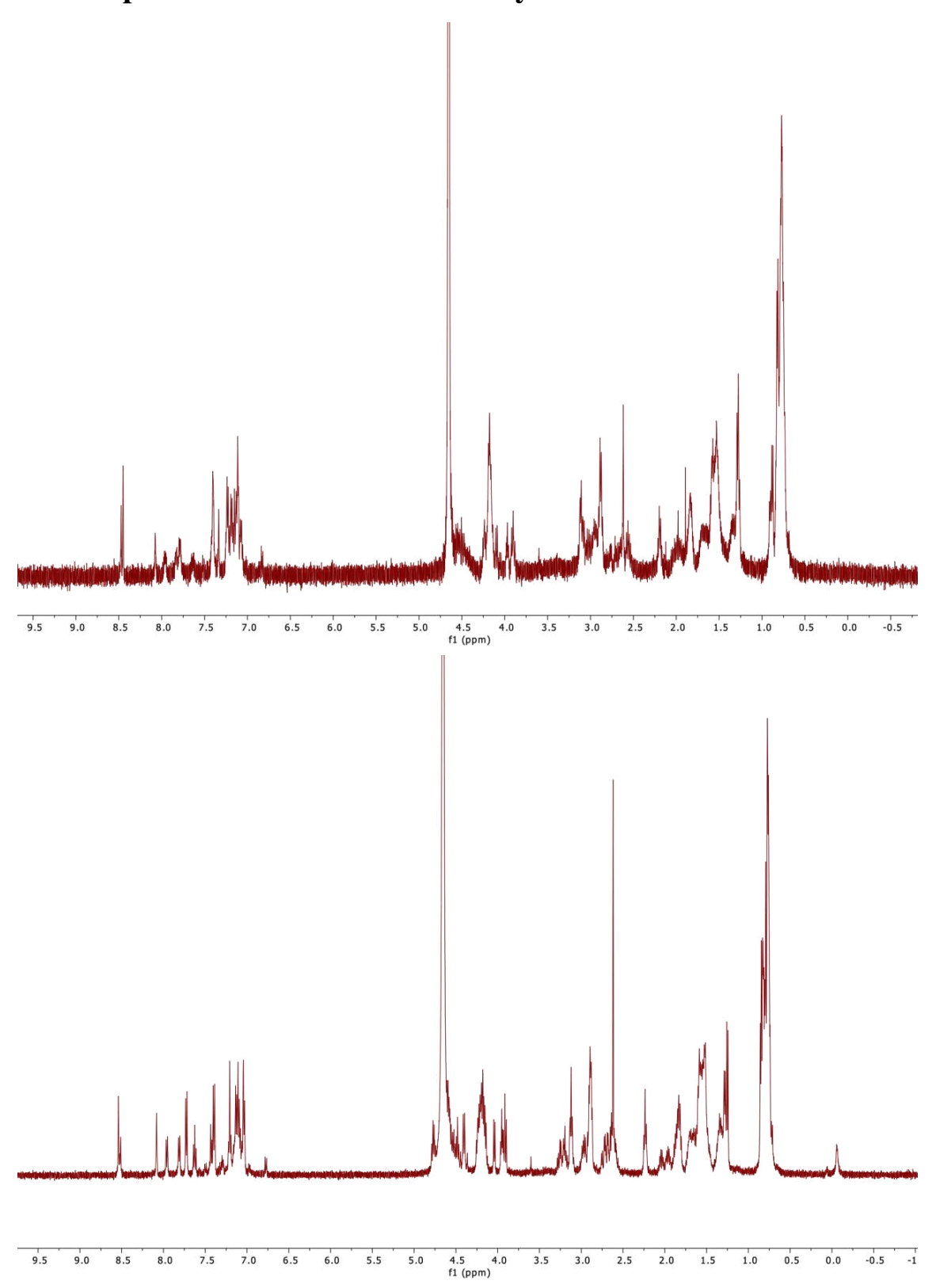


Figure S30: <sup>1</sup>H-NMR spectra (500 MHz, D<sub>2</sub>O) of P1 (top, trans-isomer) and P2 (bottom, trans-isomer).<sup>3</sup>

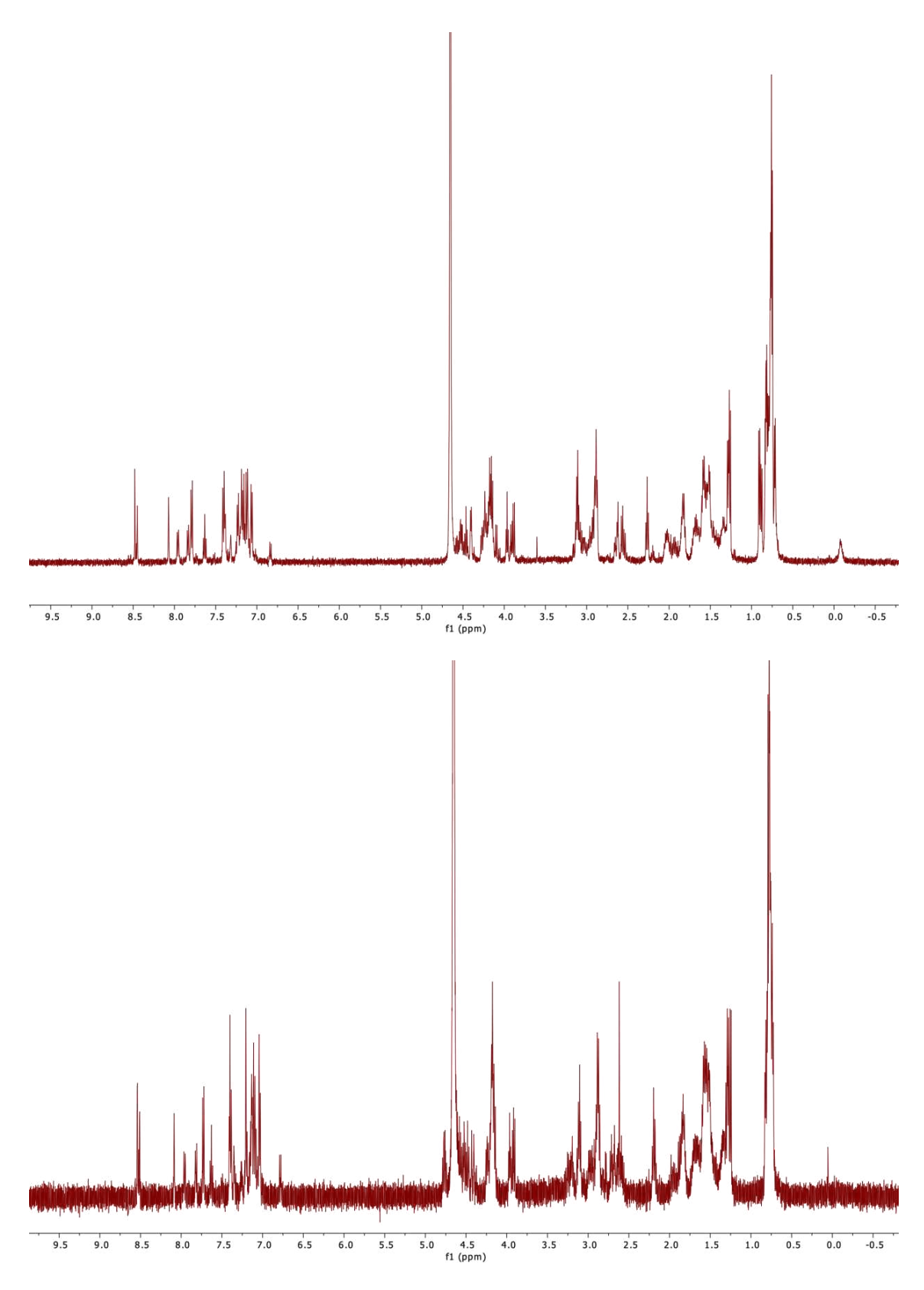


Figure S31: <sup>1</sup>H-NMR spectra (500 MHz, D<sub>2</sub>O) of P3 (top, trans-isomer) and P4 (bottom, trans-isomer).<sup>3</sup>

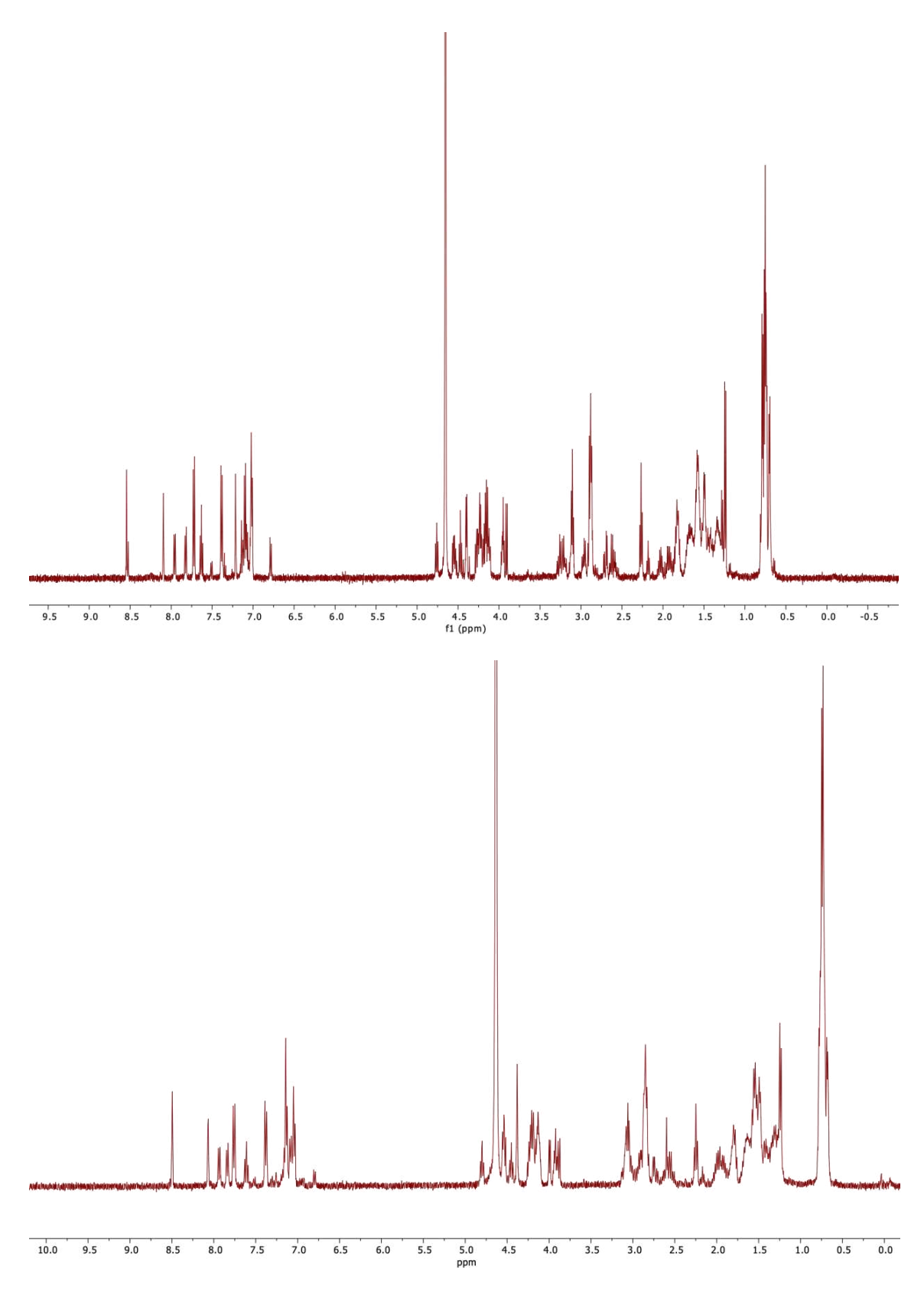


Figure S32: <sup>1</sup>H-NMR spectra (500 MHz, D<sub>2</sub>O) of P5 (top, *trans*-isomer)<sup>3</sup> and P6 (bottom, *trans*-isomer).

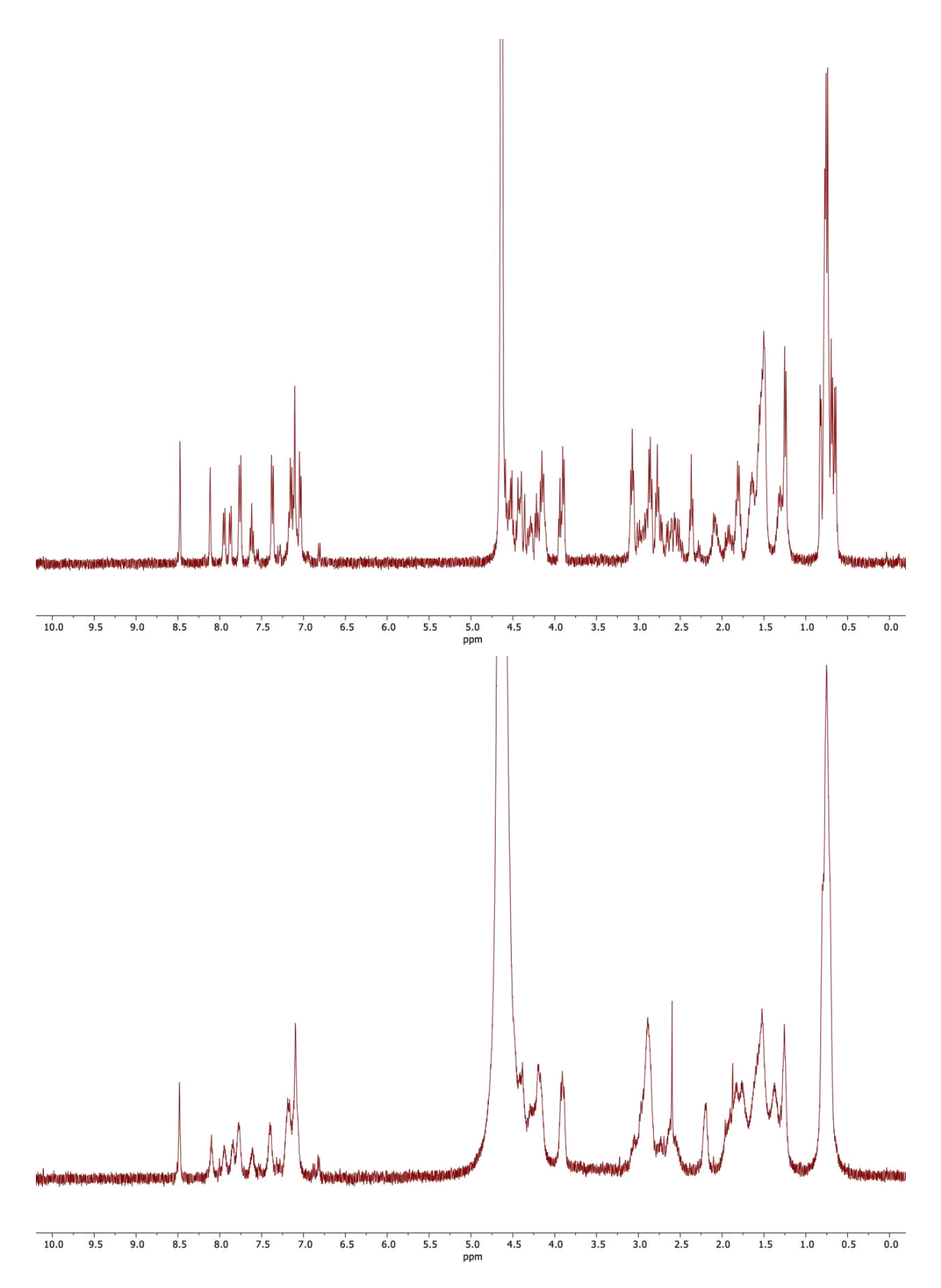


Figure S33: <sup>1</sup>H-NMR spectra (500 MHz, D<sub>2</sub>O) of P7 (top, *trans*-isomer) and P8 (bottom, *trans*-isomer).

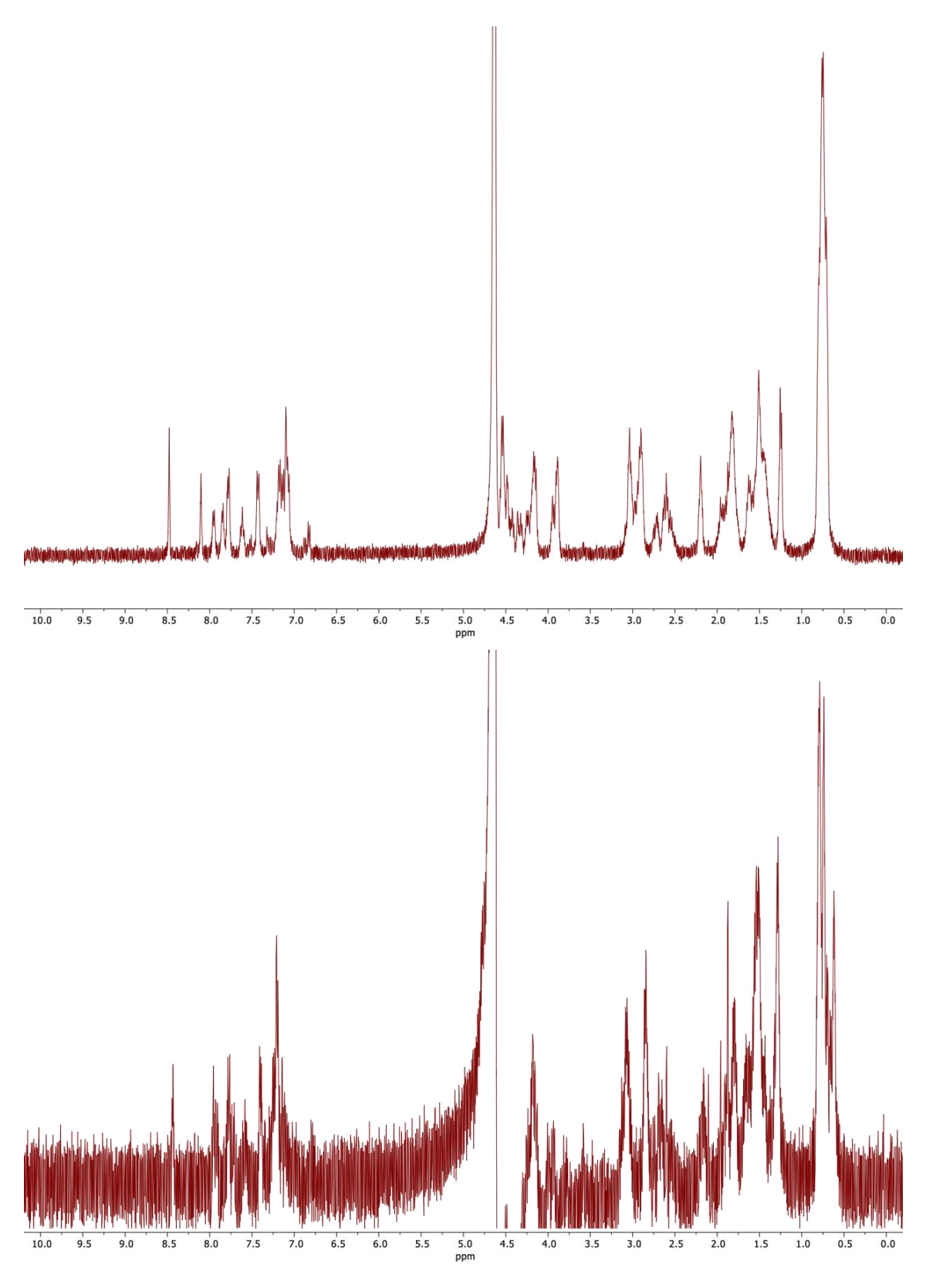
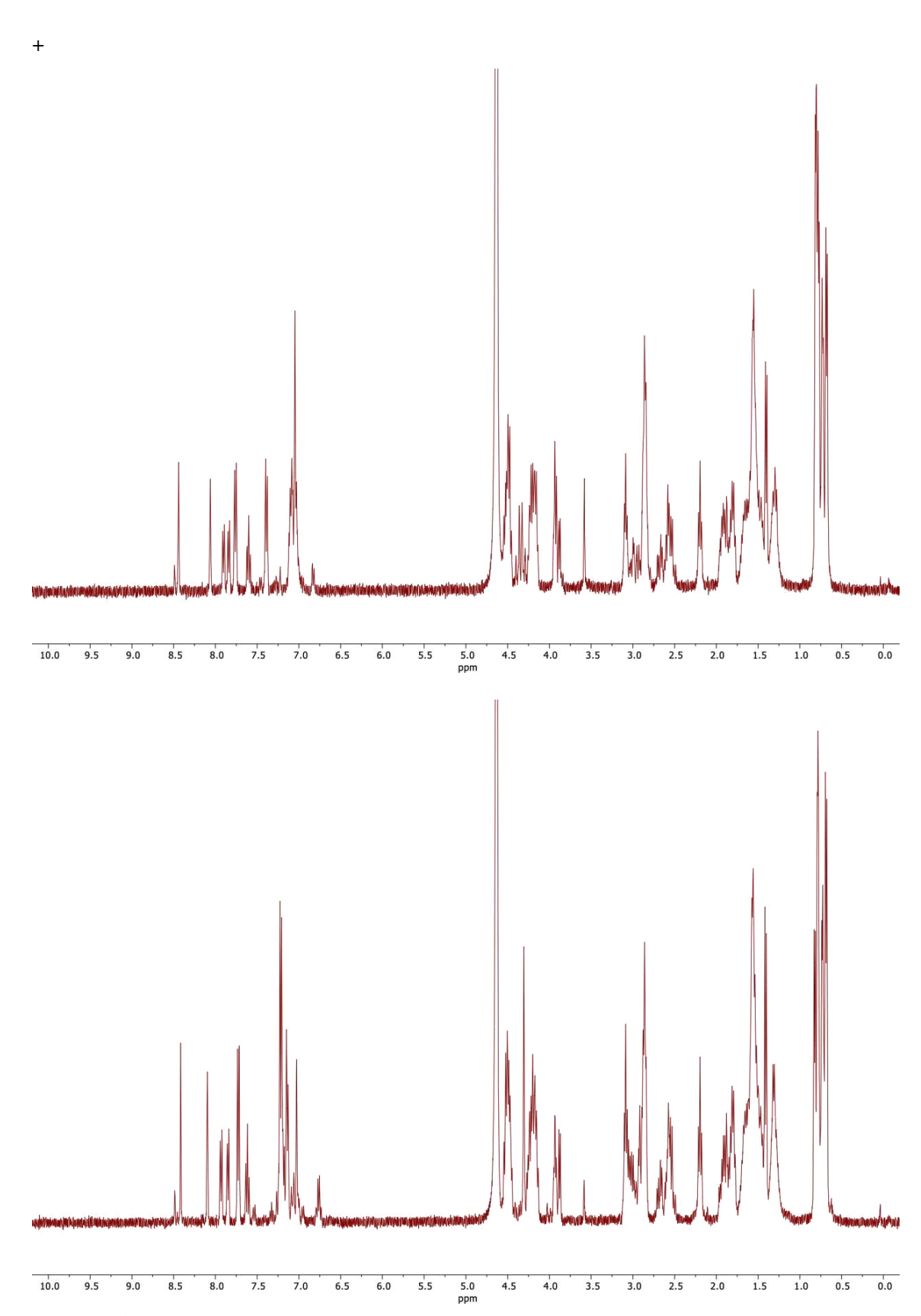


Figure S34: <sup>1</sup>H-NMR spectra (500 MHz, D<sub>2</sub>O) of P9 (top, *trans*-isomer) and P10 (bottom, *trans*-isomer).



 $\textbf{Figure S35:} \ ^{1}\text{H-NMR spectra (500 MHz, D}_{2}\text{O) of P11 (top, } \textit{trans-} \text{isomer) and P12 (bottom, } \textit{trans-} \text{isomer)}.$ 

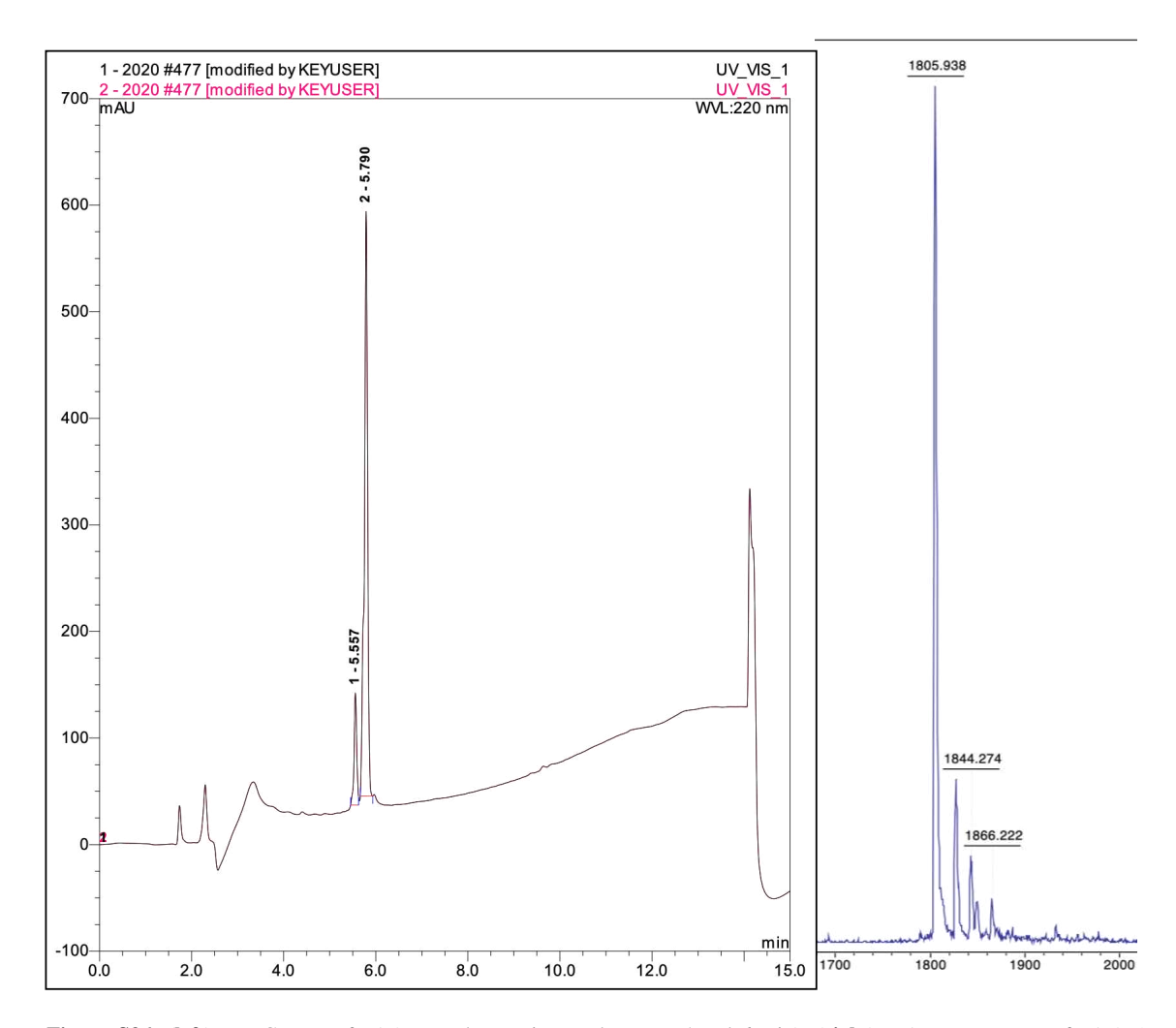
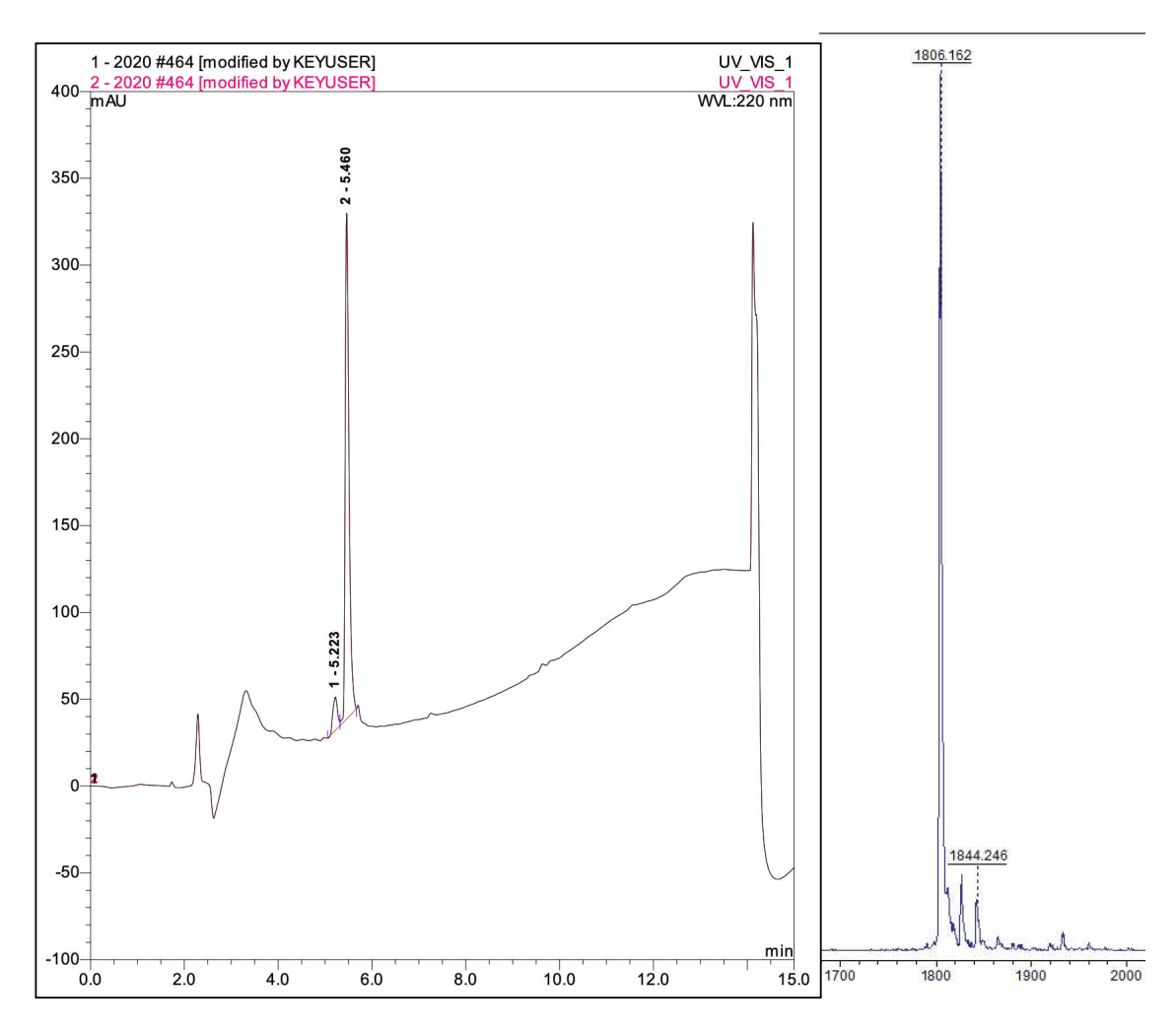
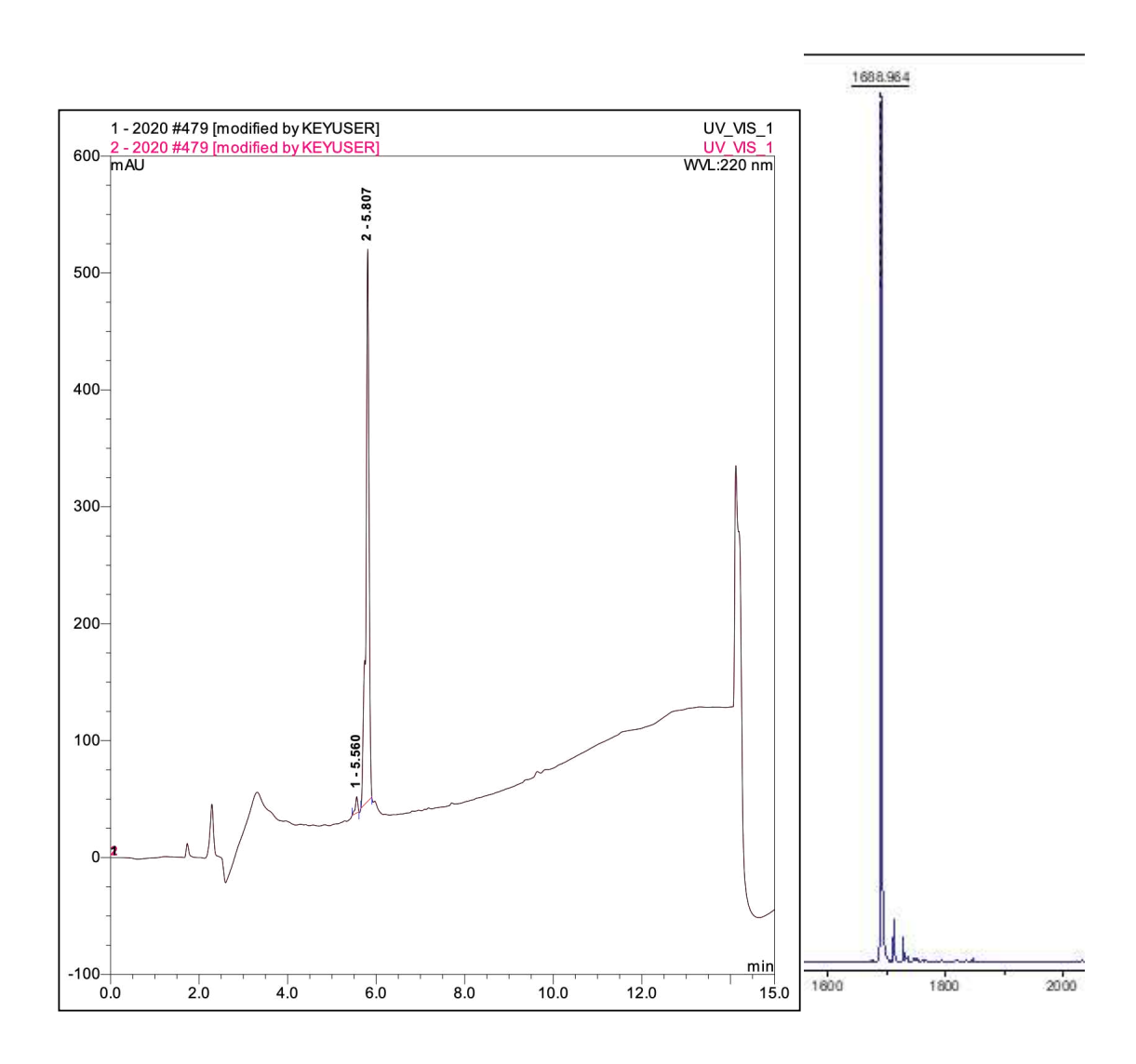


Figure S36: (left) HPLC-trace of P1 (cis- and trans-isomer between 5 and 6 min). (right) MALDI-spectrum of P1 (m/z calculated: 1805.00 found: 1805.938).<sup>3</sup>



**Figure S37:** (**left**) HPLC-trace of P2 (cis- and trans-isomer between 5 and 6 min). (**right**) MALDI-spectrum of P2 (m/z calculated: 1805.00 found: 1806.162).<sup>3</sup>



**Figure S38:** (left) HPLC-trace of P3 (cis- and trans-isomer between 5 and 6 min). (right) MALDI-spectrum of P3 (m/z calculated: 1689.97 found: 1688.964).<sup>3</sup>

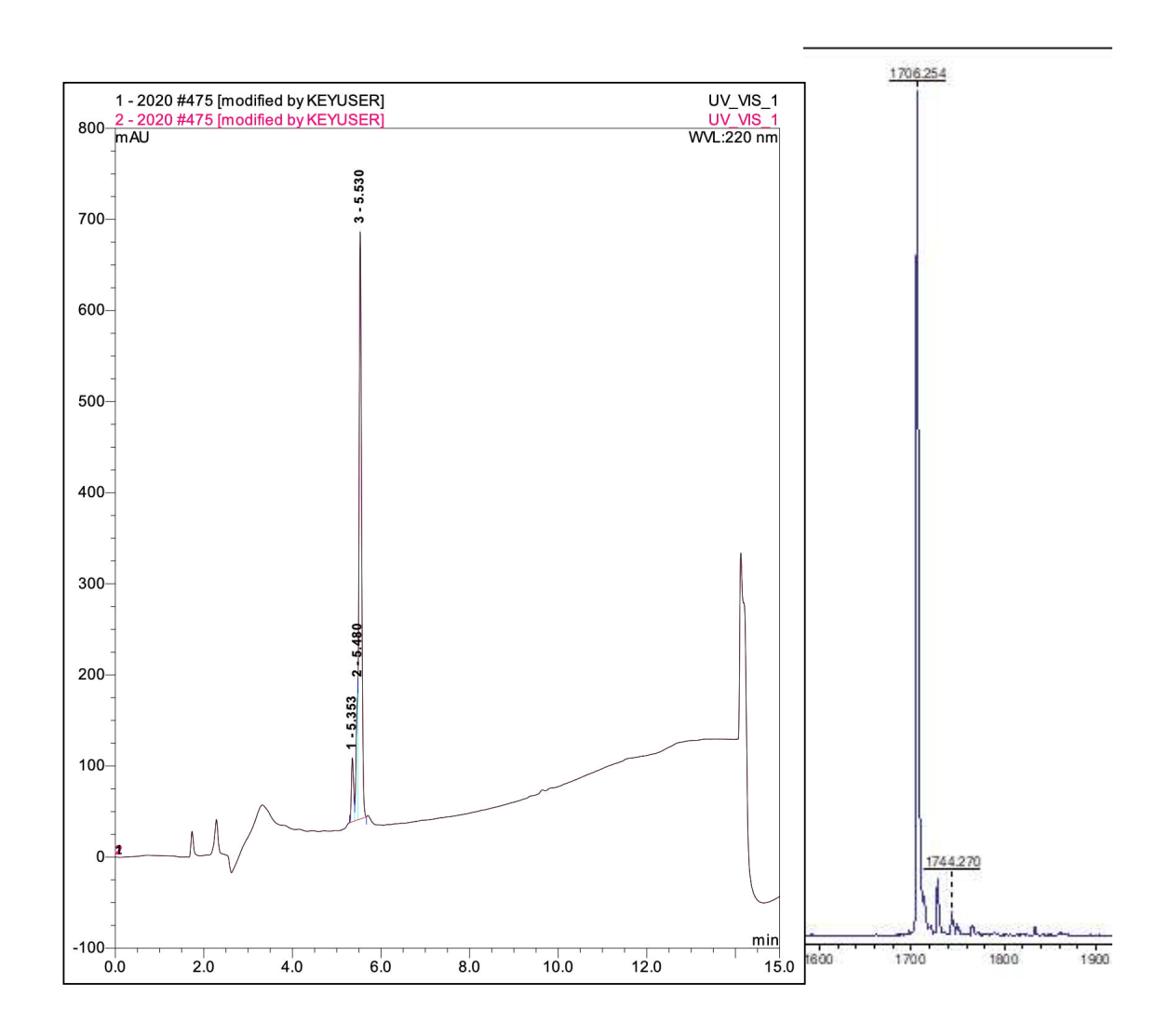


**Figure S39:** (**left**) HPLC-trace of P4 (cis- and trans-isomer between 5 and 6 min) (**right**) MALDI-spectrum of P4 (m/z calculated: 1705.93 found: 1706.254).<sup>3</sup>

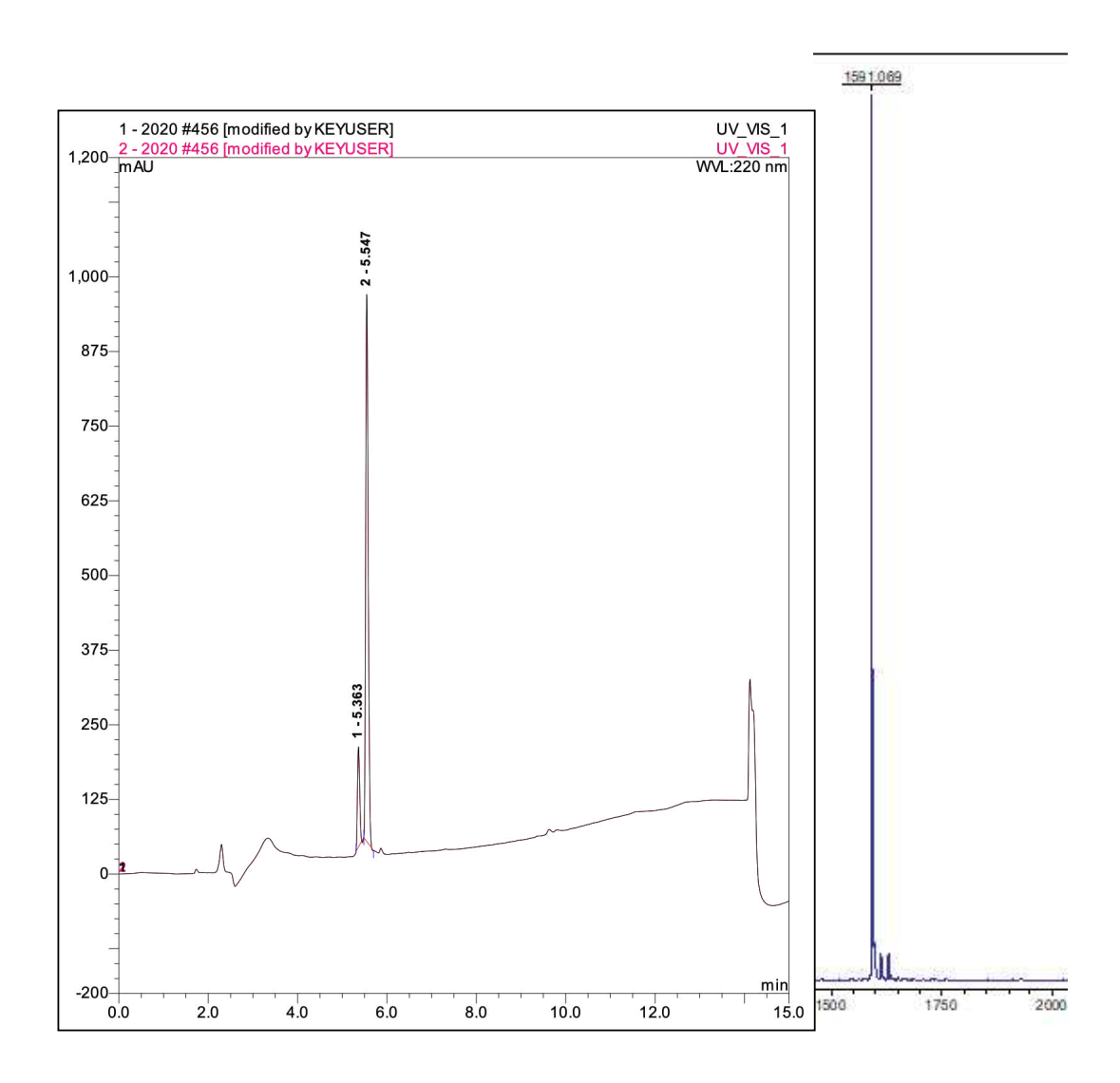


**Figure S40:** (**left**) HPLC-trace of P5 (cis- and trans-isomer between 5 and 6 min). (**right**) MALDI-spectrum of P5 (m/z calculated: 1590.90 found: 1591.069).<sup>3</sup>

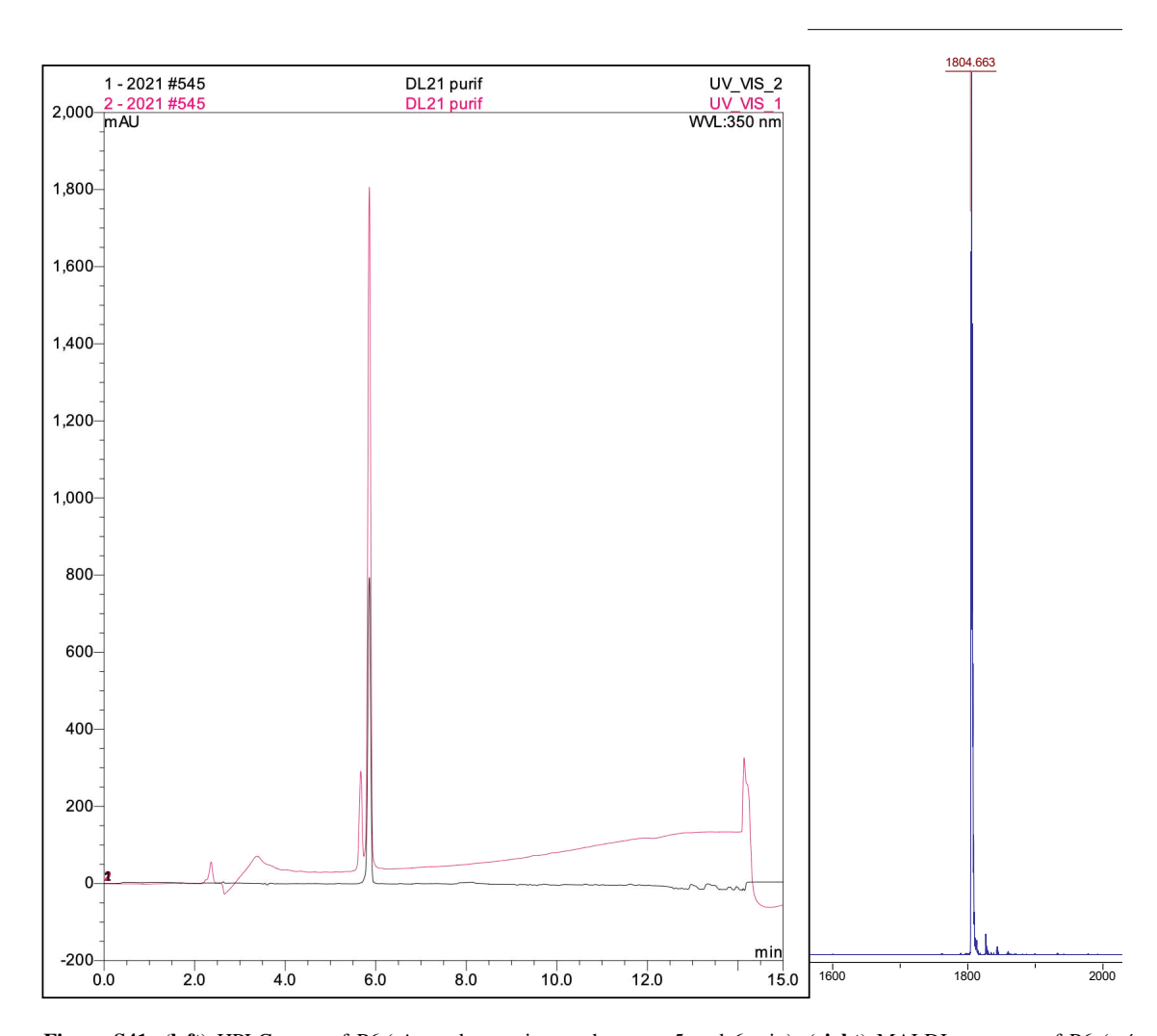


**Figure S41:** (**left**) HPLC-trace of P6 (*cis*- and *trans*-isomer between 5 and 6 min). (**right**) MALDI-spectrum of P6 (*m/z* calculated: 1805.00 found: 1804.663).

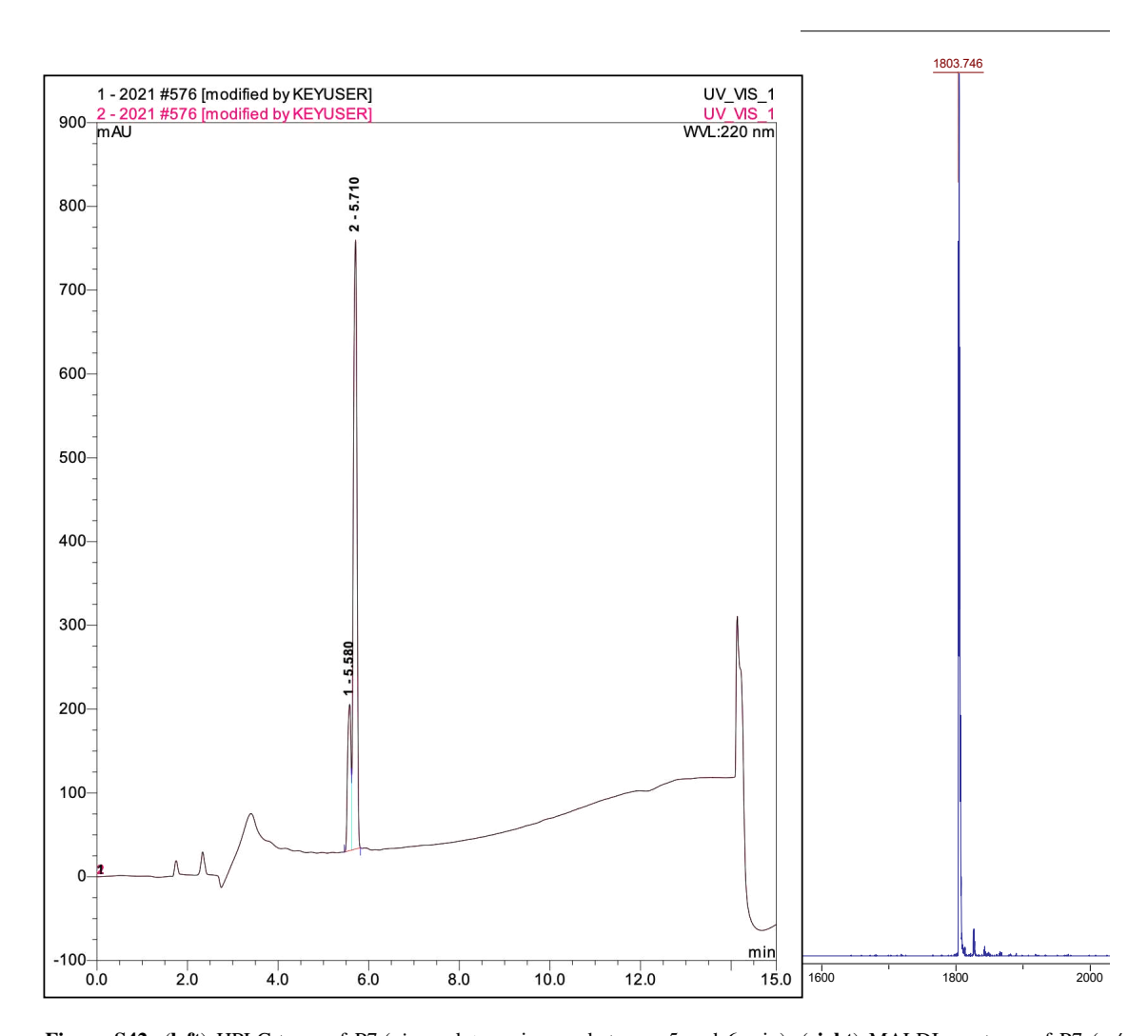


**Figure S42:** (**left**) HPLC-trace of P7 (*cis*- and *trans*-isomer between 5 and 6 min). (**right**) MALDI-spectrum of P7 (*m/z* calculated: 1805.00 found: 1803.746).

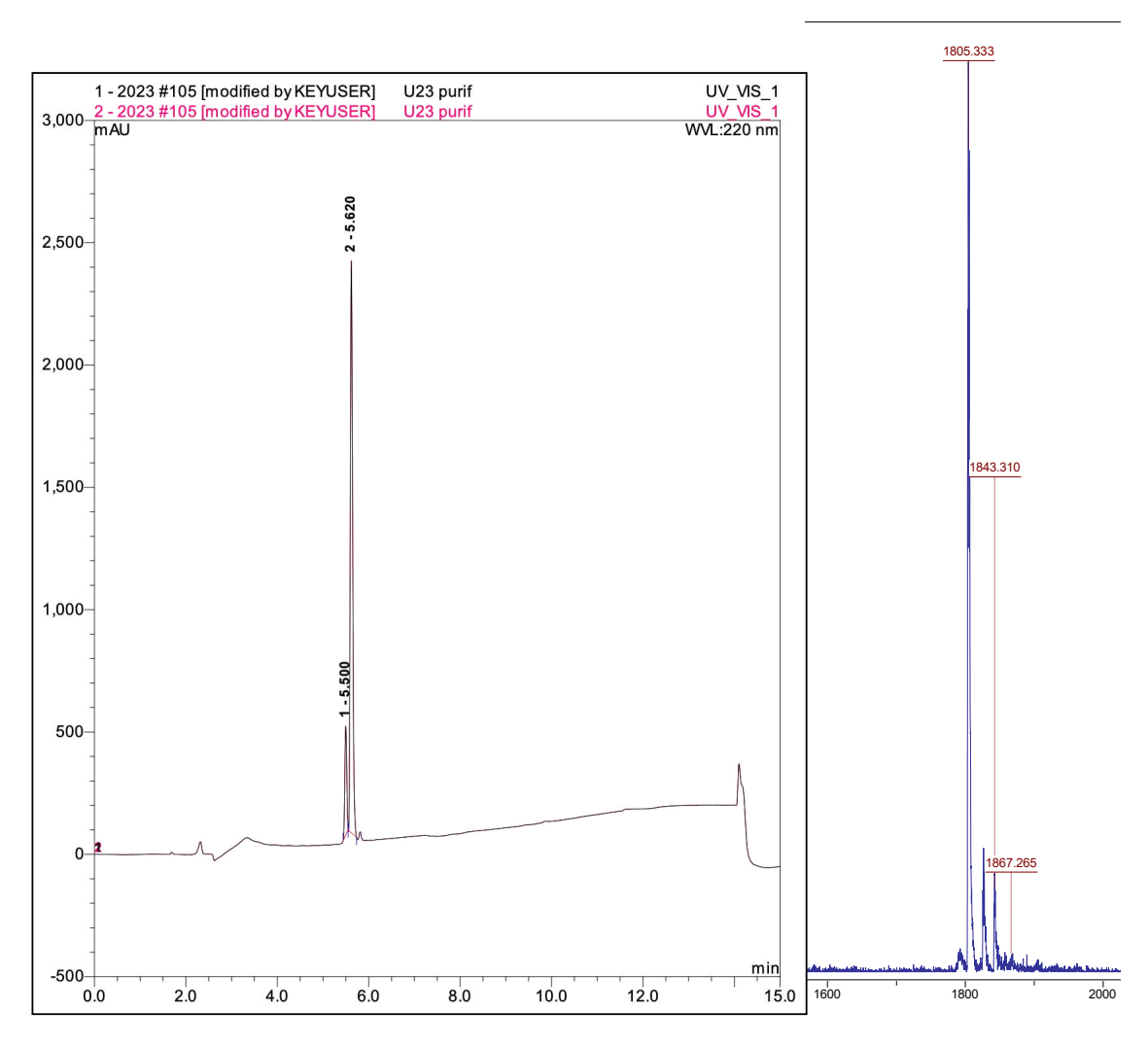


**Figure S43:** (**left**) HPLC-trace of P8 (*cis*- and *trans*-isomer between 5 and 6 min). (**right**) MALDI-spectrum of P8 (*m/z* calculated: 1805.00 found: 1805.333).

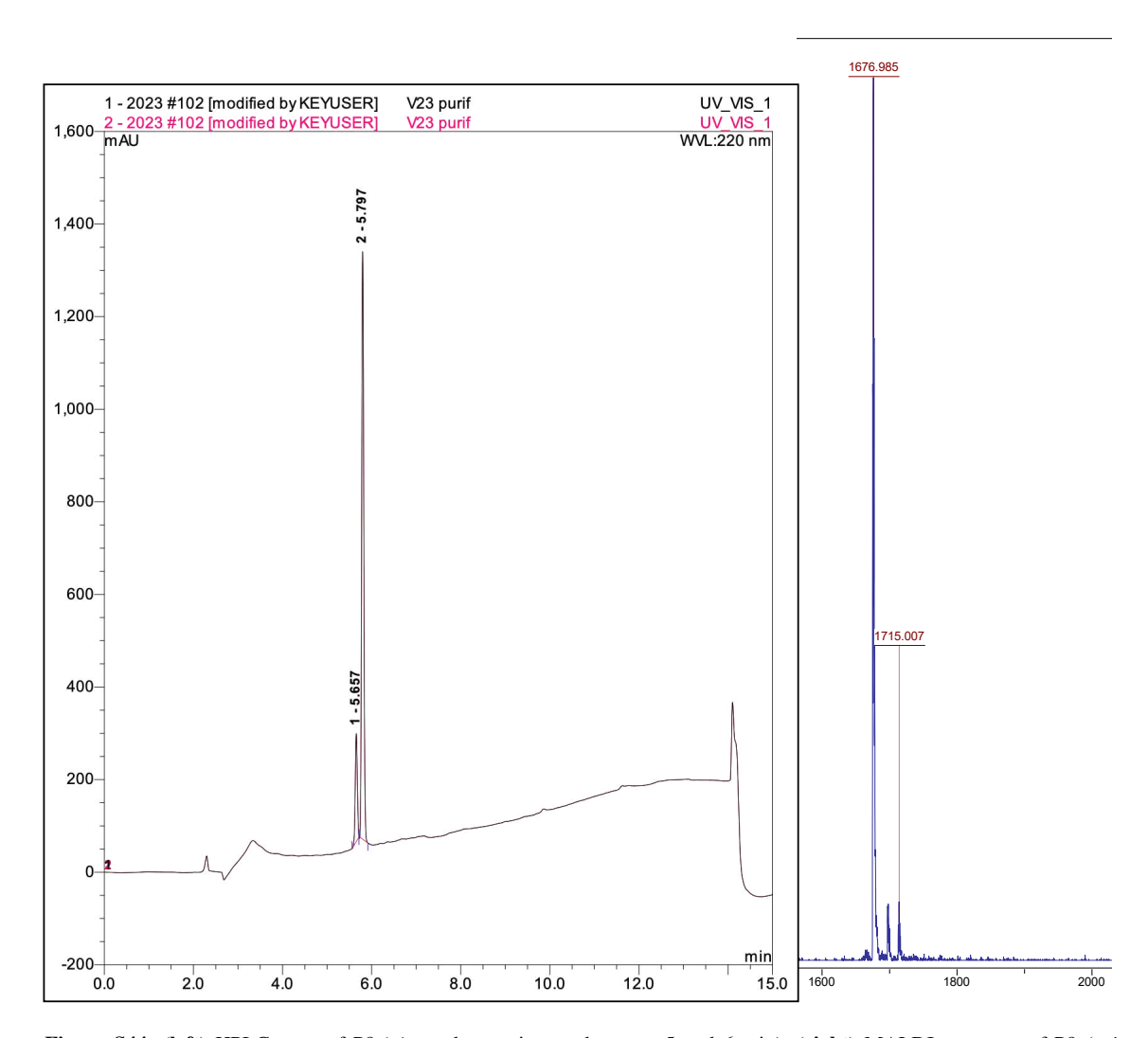


**Figure S44:** (**left**) HPLC-trace of P9 (*cis*- and *trans*-isomer between 5 and 6 min). (**right**) MALDI-spectrum of P9 (*m/z* calculated: 1676.90 found: 1676.985).

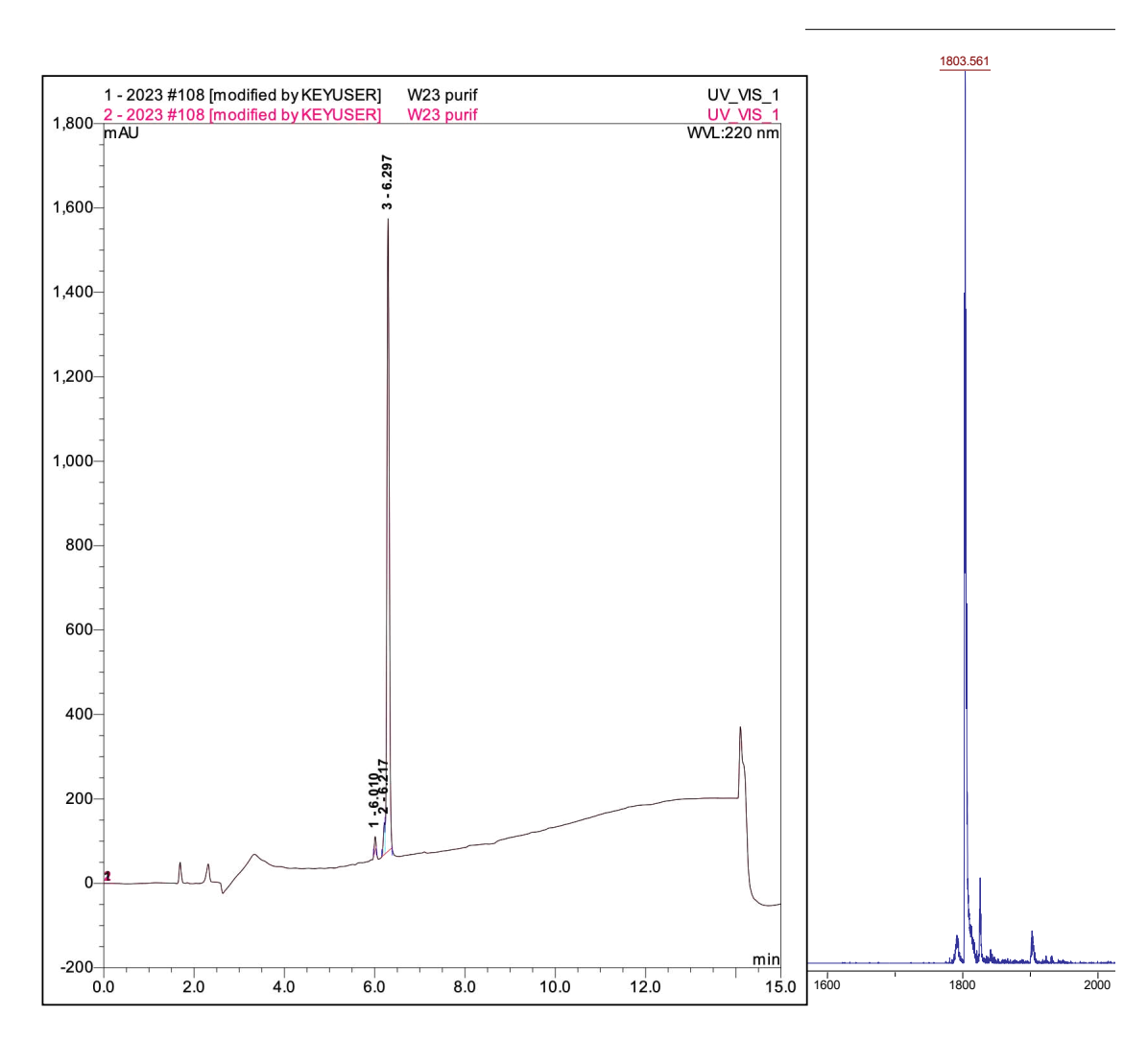


**Figure S45:** (**left**) HPLC-trace of P10 (*cis*- and *trans*-isomer between 6 and 7 min). (**right**) MALDI-spectrum of P10 (*m/z* calculated: 1805.00 found: 1803.561).

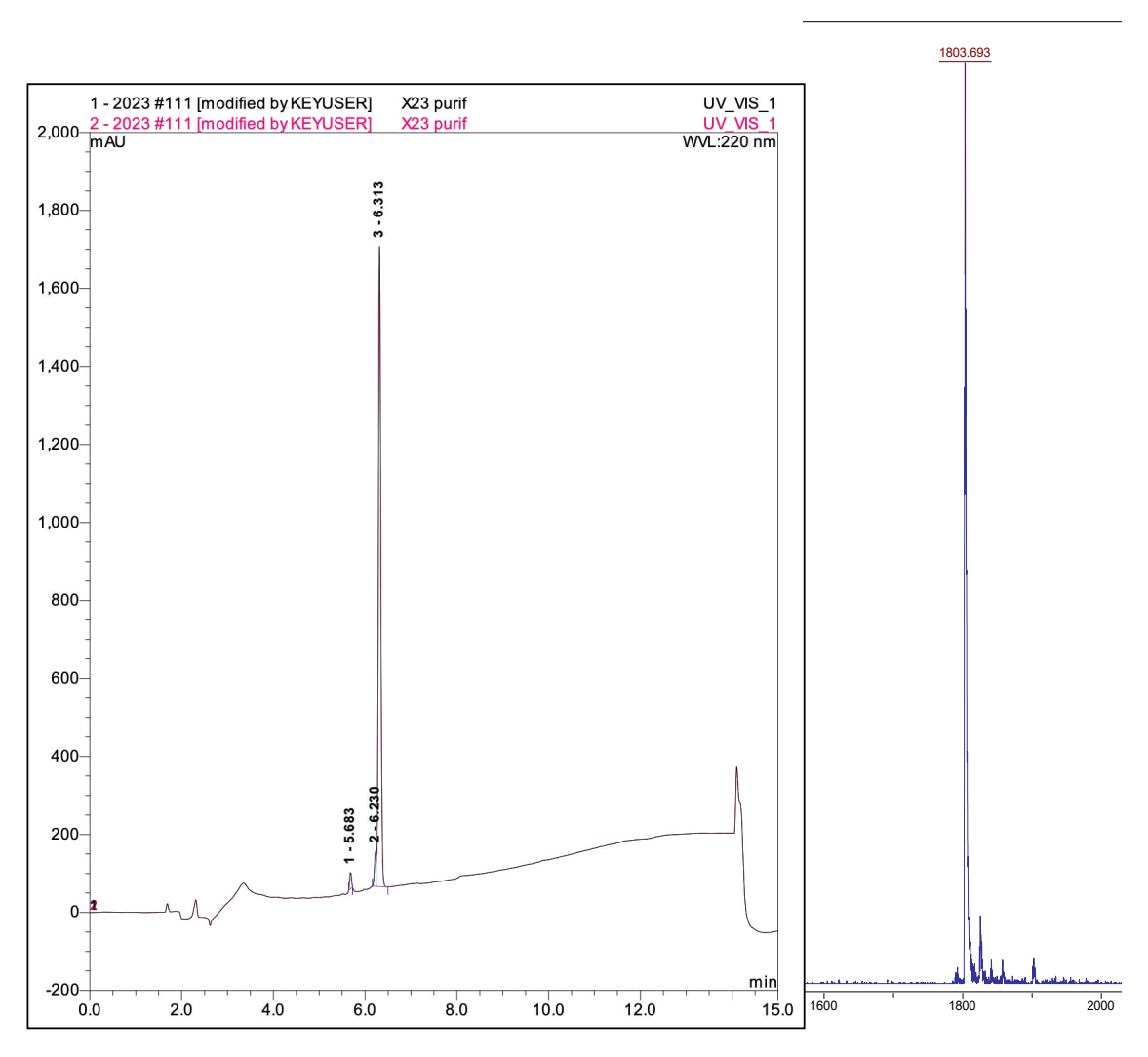


**Figure S46:** (**left**) HPLC-trace of P11 (*cis*- and *trans*-isomer between 6 and 7 min). (**right**) MALDI-spectrum of P11 (*m/z* calculated: 1805.00 found: 1803.693).

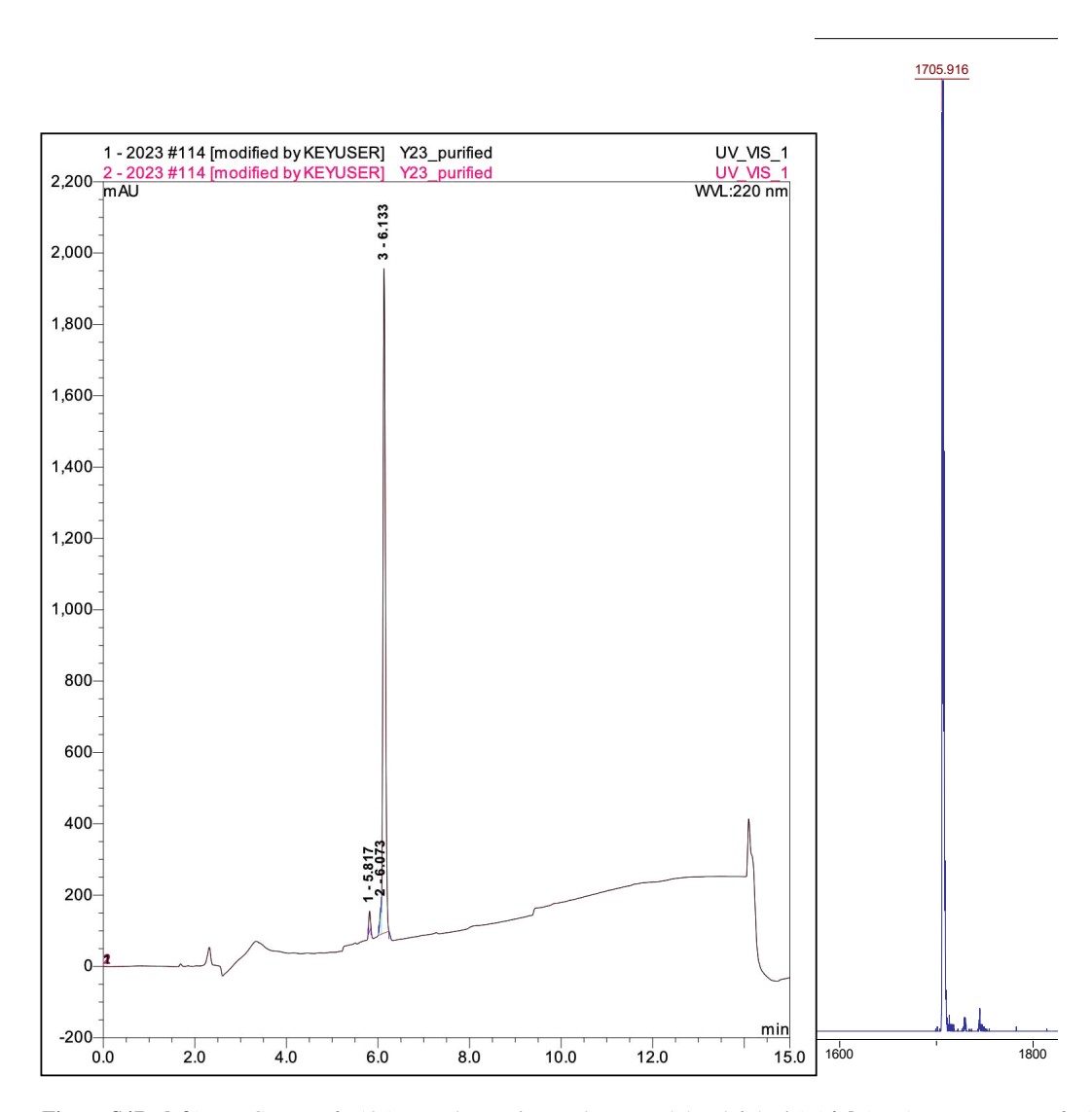


**Figure S47:** (left) HPLC-trace of P12 (*cis*- and *trans*-isomer between 5.5 and 6.5 min) (**right**) MALDI-spectrum of P12 (*m/z* calculated: 1705.93 found: 1705.916).

# References

- (1) Jurrus, E.; Engel, D.; Star, K.; Monson, K.; Brandi, J.; Felberg, L. E.; Brookes, D. H.; Wilson, L.; Chen, J.; Liles, K. Improvements to the APBS biomolecular solvation software suite. *Protein Sci.* **2018**, 27 (1), 112-128. DOI: 10.1002/pro.3280.
- (2) Schrödinger, L. The PyMOL Molecular Graphics System, Version 1.8. In (No Title), 2015.
- (3) Paschold, A.; Voigt, B.; Hause, G.; Kohlmann, T.; Rothemund, S.; Binder, W. H. Modulating the Fibrillization of Parathyroid-Hormone (PTH) Peptides: Azo-Switches as Reversible and Catalytic Entities. *Biomedicines* **2022**, *10* (7), 1512. DOI: 10.3390/biomedicines10071512.

# **Supporting Information**

# Spiropyran as building block in peptide synthesis and modulation of photochromic properties

André Paschold<sup>1</sup>, Niclas Starke<sup>1</sup>, Sven Rothemund<sup>2</sup>, Wolfgang H. Binder<sup>1</sup>

<sup>2</sup>Core Unit Peptide – Technologies, University of Leipzig Medical Center, Liebigstraße 21 04103 Leipzig (Germany)

wolfgang.binder@chemie.uni-halle.de

#### SUPPORTING INFORMATION

#### **Contents**

1.	Experimental procedures	2
	Supplementary tables	
	Synthetis procedures & analytical data	
4.	Supplementary figures	17
5.	NMR data of compounds and peptides and LC-MS of peptides	32

<sup>&</sup>lt;sup>1</sup> Macromolecular Chemistry, Institute of Chemistry, Faculty of Natural Science II, Martin Luther University Halle Wittenberg, von-Danckelmann-Platz 4, 06120 Halle (Germany)

# 1. Experimental procedures

#### 1.1. Chemicals

All technical solvents were distilled prior use. Air- and moisture- sensitive reactions were carried out in flame-dried glassware under atmospheric pressure of nitrogen. 1,3,3-Trimethyl-2-methylenindolin and 4-hydrazino benzoic acid were purchased from TCI Deutschland GmbH. NaOH and NaNO<sub>3</sub> were purchased from Gruessing GmbH. H<sub>2</sub>SO<sub>4</sub>Boc<sub>2</sub>O, iodomethane, citric acid, sodium citrate, NaH<sub>2</sub>PO<sub>4</sub>, 2-hydroxy-5-nitrobenzaldehyd, and PtO<sub>2</sub> were purchased from Sigma Aldrich. SnCl<sub>2</sub> and 3-methyl-2-butanone were purchased from Merck GmbH, triethlamin (TEA) and Na<sub>2</sub>HPO<sub>4</sub> from Alfa Aesar, Fmoc-Cl from Fluorochem, 3-fomyl-4-hydroxybezoic acid from abcr GmbH, Ac<sub>2</sub>O from VWR, and Celite® from Carl Roth GmbH.

The phosphate buffer for pH 7.4 was made as a mixture of an aqueous 50 mM Na<sub>2</sub>HPO<sub>4</sub> and 50 mM NaH<sub>2</sub>PO<sub>4</sub>-solution. The citrate buffer for pH 2.5 was made as a mixture of an aqueous 100 mM citric acid and a 100 mM sodium citrate solution. Each buffer solution was adjusted with a NaOH- and HCl-solution to the correct pH measured with a Titroline 7500 KF from SI Analytics.

#### 1.2. Instrumentation and Analysis

ESI-ToF-MS measurements were performed on a Bruker Daltonics microTOF via direct injection at a flow rate of 180  $\mu$ L h<sup>-1</sup> in positive mode with an acceleration voltage of 4.5 kV. Samples were prepared by dissolving in either LC-MS grade THF, LC-MS grade acetonitrile or LC-MS grade methanol or a mixture thereof. The instrument was calibrated using the ESI-L low concentration tuning mix from Agilent Technologies (product no. G1969-85000). The software Data Analysis (version 4.0) was used for data evaluation.

MALDI-ToF-MS measurements were performed on a Bruker Autoflex III system (Bruker Daltonics) using a nitrogen laser operating at a wavelength of  $\lambda = 337$  nm in reflection mode. The used matrix:analyte ratio was 1:1 and 1  $\mu$ L of the solution was spotted on the MALDI target. The peptide samples were either dissolved or suspended in MeCN + 0.1% trifluoroacetic acid (TFA) with a concentration of 20 mg/mL. Data evaluation was carried out via flexAnalysis software (3.4) and simulation of the isotopic pattern was performed by Data Analysis software (version 4.0).

*NMR* spectra were measured on an Agilent Technologies 400 MHz VNMRS and 500 MHz DD2 at 27°C. Chemical shifts ( $\delta$ ) are reported in ppm and referred to the solvent residual signal (CDCl<sub>3</sub> 7.26 ppm for <sup>1</sup>H and 77.0 ppm for <sup>13</sup>C, DMSO- $d_6$  2.50 ppm for <sup>1</sup>H and 39.52 ppm for <sup>13</sup>C, THF- $d_8$  1.72 and 3.58 ppm for <sup>1</sup>H and 67.2 and 25.3 ppm for <sup>13</sup>C, and D<sub>2</sub>O 4.66 ppm for 1H). The following abbreviations were used for <sup>1</sup>H- and <sup>13</sup>C-NMR peaks assignment: s = singlet, d = doublet, t = triplet, td = triplet of doublet, t = triplet.

ATR-IR spectra were measured on a Bruker Tensor Vertex 70 equipped with a Golden Gate Heated Diamond ATR Top-plate.

*UV/VIS-absorption* measurements were performed on a Perkin Elmer LAMBDA 365 UV/Vis Spectrophotometer using Helma analytics quartz glass cuvettes (d = 10 mm). Temperature control was achieved using the Perkin Elmer Peltier System L365. To describe the kinetic processes, the kinetic measurements were fitted according to a first-order reaction. In the measurements at 4 °C condensation of water occurred at the cuvette walls during the measurements. The respective parts during the kinetic measurements were excluded for the fit.

*MC-to-SP-isomerization* was achieved by irradiation of the respective peptide dissolved in a buffered aqueous solution in a quartz glass cuvette (d = 10 mm) under stirring with light with a distinct wavelength, whereby the light source was placed 1 cm away from the cuvette. Green light (peak at 525 nm) was generated using a LED (2 W, UHP-T-520-DI, Prizmatix) together with a driver (Ultra-High-Power LED Controller, Prizmatix). For light with a wavelength of 405 nm a mounted LED (1.3 W, M405L4, Thorlabs) was used together with a LED-driver (LEDD1B, Thorlabs).

High-performance liquid chromatography (HPLC) was performed on a Hitachi Chromaster (VWR) with the modules 5430 Detector, 5310 Column Oven, 5260 Autosampler, 5160 Pump. The mobile phases were water (eluent A) and acetonitrile (eluent B), respectively, each containing 0.1% formic acid. Samples were eluted for 60 min with a linear gradient, which had to be adjusted for each peptide individually. As column a Atlatis T3 5  $\mu$ m (Waters Corporation) was used. The oven temperature was set to 20 °C and the autosampler temperature to 4 °C.

Solid-phase peptide synthesis was utilized on an automated peptide synthesizer MultiPep RS (Intavis AG, Koeln, Germany) using standard Fmoc-chemistry and preloaded resin. Standard coupling of all protected natural amino acids were performed as single couplings in dimethylformamid (DMF) using 5 equivalents of amino acids and 2-(6-chloro-1-H-benzotriazole-1-yl)-1,1,3,3-tetramethylaminium hexafluorophosphate (HCTU) as coupling reagents and 10 equivalents of N-methyl-morpholine (NMM) as base for 1 h at room temperature. Special building groups, such as FASC-Fmoc 1a or SAFC-Fmoc 2a, were coupled with 3 equivalents using *N,N'*-diisopropylcarbodiimide (DIC) and N-Hydroxybenzotriazole (HOBT) in DMF/NMP at room temperature and with gentle shaking in the dark overnight. The N-terminal Fmoc protecting group was removed by washing the resin with 20% piperidine for 20 min. The final side chain deprotection and cleavage from the resin employed a mixture of trifluoroaceticacid and water (90:10 Vol%) with gentle agitation for 2h at room temperature.

The crude peptides were purified to >95% purity using preparative RP-HPLC (Gilson, Limburg, Germany). For both analytical and preparative use, the mobile phases were water (eluent A) and acetonitrile (eluent B), respectively, each containing 0.1% TFA. Samples were eluted with a linear gradient from 5% B to 95% B in 15 min for analytical runs and in 90 min for preparative runs on a

semipreprative PLRP-S column (Agilent Technologies, 300x25mm, 8um). Finally, all peptides were characterized by analytical HPLC Dionex Ultimate 3000 (Thermo Scientific, Germany) using a PLRP-S column (Agilent Technologies, 150x4.6mm, 3um) and MALDI-MS (Bruker Microflex LT, Bremen, Germany), which gave the expected [M+H]<sup>+</sup> mass peaks.

# 2. Supplementary tables

**Table S1.** Peptide primary sequences, the half-life time  $\tau_{1/2}$  and rate constant k of the thermal back-isomerization from SP-to-MC and, the half-life time  $\tau_{1/2}$  and rate constant k of the hydrolysis of the MC-form at different temperatures and pH values.

peptide	pН	T [°C]	thermal isomerization		decomposition	
			$ au_{1/2}$ [min]	k [min <sup>-1</sup> ]	$ au_{1/2}$ [min]	k [min <sup>-1</sup> ]
P1	7.4	37	$3.7 \pm 0.1$	0.185	$68.7 \pm 0.1$	0.101
		4	$171.4 \pm 0.3$	0.0040	$4418 \pm 11$	0.000156
•	2.5	37	$10.7 \pm 0.0$	0.0645	15620 ± 21	4.44 * 10 <sup>-5</sup>
		4	$1155 \pm 0$	0.000600	-	-
P2	7.4	37	$2.9 \pm 0.0$	0.237	$427.8 \pm 2.1$	0.00162
		4	$321.4 \pm 0.3$	0.00216	n.d.	n.d.
-	2.5	37	$11.3 \pm 0.0$	0.0613	18733 ± 10	3.70 * 10 <sup>-5</sup>
		4	$1151 \pm 2$	0.000602	n.d.	n.d.
P3	7.4	37	$6.0 \pm 0.1$	0.116	$75.3 \pm 0.2$	0.00921
		4	$358.9 \pm 0.2$	0.00193	n.d.	n.d.
-	2.5	37	$15.8 \pm 0.0$	0.440	n.d.	n.d.
		4	$2070 \pm 1$	0.000335	n.d.	n.d.
P4	2.5	37	$1.7 \pm 0.0$	0.429	$2072 \pm 1$	0.000334
-	1	37	$10.04 \pm 0.2$	0.0666	-	-
		4	$384.9 \pm 0.9$	0.00180	-	-

n.d. – not determined.

Table S2. Isomeric ratio in the thermal equilibrium and the SP-PSS at pH 2.5 (P1 – P3) and pH 1 (P4).

Peptide	ratio thermal equilibrium [MC:SP]	ratio PSS [MC:SP] (wavelength)
P1	98:2	4:96 (520 nm)
P2	98:2	3:97 (520 nm)
P3	98:2	5:95 (520 nm)
P4	98:2	49:51 (405 nm) 38:62 (520 nm)

# 3. Synthetis procedures & analytical data

# Synthesis strategy 1

Scheme S1. Synthesis pathway for spiropyrans 1a and 1b.

The overall yield over 4 steps was for **1a** 4% and for **1b** 18%, respectively. Especially **3-II**, **4a**, and **4b** are not completely stable at air and should therefore be processed faster.

#### Synthesis of 3-I

1,3,3-Trimethyl-2-methylenindolin (10 g, 57.7 mmol, 1 eq.) was slowly added to 60 mL concentrated  $H_2SO_4$  and cooled down to 0 °C. Sodiumnitrate (7.9 g, 63.5 mmol, 1.1 eq.) was added in small portions and the reaction mixture is stirred for 1 h. The solution was poured onto 100 g ice and neutralized with solid  $Na_2CO_3$ . The formed precipitate was filtrated and recrystallized (heated with an oil bath) in a mixture of acetone/water(1:1). **3-I** was obtained as a darkred solid. (7.3 g, 33.2 mmol, 58%).

Analytical data match reported literature values.<sup>1</sup>

 $R_f = 0.74$  (hexane:EE / 3:2).

<sup>1</sup>H-NMR (500 MHz, CDCl<sub>3</sub>):  $\delta$  = 8.12 (dd, J = 8.8, 2.3 Hz, 1H), 7.92 (d, J = 2.3 Hz, 1H), 6.51 (d, J = 8.8 Hz, 1H), 4.16–4.06 (m, 2H), 3.12 (s, 3H), 1.36 (s, 6H).

<sup>13</sup>C-NMR (125 MHz, CDCl<sub>3</sub>):  $\delta$  = 161.2, 151.5, 140.0, 138.2, 126.2, 118.1, 103.9, 78.9, 43.4, 29.7, 29.0. MS (ESI) m/z: [M+Li]<sup>+</sup> Calcd. for [C<sub>12</sub>H<sub>14</sub>N<sub>2</sub>O<sub>2</sub>Li]<sup>+</sup> 225.12; Found 225.12.

#### Synthesis of 3-II

**3-I** (2 g, 9.1 mmol, 1 eq.) and dry tin(II) chloride (10.4 g, 55 mmol, 6 eq.) were dissolved in 60 mL concentrated aqueous hydrogen chloride solution and refluxed (heated with an oil bath) for 2 h. The reaction solution was alkalinized and extracted three times with 60 mL  $Et_2O$ . The organic phases were combined and the solvent removed *in vacuo*. The residue was recrystallized in hexane (heated with an oil bath) and **3-II** was obtained as a green solid (1 g, 5.3 mmol, 58%).

Analytical data match reported literature values. <sup>2</sup>

 $R_f = 0.1$  (DCM:MeOH + 0.1% FA / 9:1).

<sup>1</sup>H-NMR (500 MHz, CDCl<sub>3</sub>):  $\delta = 6.56$  (d, J = 2.3 Hz, 1H), 6.51 (dd, J = 8.1, 2.3 Hz, 1H), 6.35 (d, J = 8.0 Hz, 1H), 3.79–3.72 (m, 2H), 3.35 (s, 2H), 2.99 (s, 3H), 1.33 (s, 6H).

<sup>13</sup>C-NMR (125 MHz, CDCl<sub>3</sub>):  $\delta$  = 163.4, 139.7, 138.9, 138.5, 114.1, 111.3, 105.1, 71.5, 44.4, 29.9, 29.0.

MS (ESI) m/z: [M+H]<sup>+</sup> Calcd. for [C<sub>12</sub>H<sub>17</sub>N<sub>2</sub>]<sup>+</sup> 189.14; Found 189.14.

#### Synthesis of 4a

To a mixture of **3-II** (0.5 g, 2.7 mmol, 1 eq.) and Fmoc-Cl (0.82 g, 3.2 mmol, 1.2 eq.) were added 4 mL water and the suspension was stirred at 60 °C (heated with an oil bath) for 2 h. The reaction suspension was neutralized with saturated aqueous NaHCO<sub>3</sub> solution and extracted three times with 60 mL DCM. The organic phases were combined and the solvent removed *in vacuo*. The residue was purified by flash chromatography on normal phase silica gel (solvent A: DCM + 0.1% FA, solvent B: MeOH + 0.1% FA, 95% A) and **4a** was obtained as a lightpurple solid. (0.38 g, 0.93 mmol, 35%).

 $R_f = 0.16$  (DCM:MeOH + 0.1% FA / 9:1).

<sup>1</sup>H-NMR (500 MHz, CDCl<sub>3</sub>):  $\delta$  = 7.78 (d, J = 7.5 Hz, 2H), 7.69–7.52 (m, 2H), 7.41 (t, J = 7.4 Hz, 2H), 7.37–7.29 (m, 2H), 7.24–7.15 (m, 1H), 7.05 (s, 1H), 6.52 (s, 1H), 6.45 (d, J = 8.3 Hz, 1H), 4.50 (d, J = 6.8 Hz, 2H), 4.28 (t, J = 6.9 Hz, 1H), 3.84 (q, J = 2.0 Hz, 2H), 3.02 (s, 3H), 1.34 (s, 6H). <sup>13</sup>C-NMR (125 MHz, CDCl<sub>3</sub>):  $\delta$  = 162.8, 154.1, 143.9, 143.2, 141.3, 138.3, 129.2, 127.7, 127.1, 125.0, 120.0, 119.2, 114.9, 104.6, 73.1, 66.7, 47.2, 44.3, 29.9, 28.9.

IR (ATR): v = 3303w, 2959w, 1697s, 1499s, 1208s cm<sup>-1</sup>.

UV/VIS (c = 0.06  $\mu$ mol mL<sup>-1</sup> in MeOH):  $\lambda_{max,1} = 289.2$ ,  $\lambda_{max,2} = 277.3$ ,  $\lambda_{max,3} = 265.3$  nm.

HR-MS (ESI) *m/z*: [M+H]<sup>+</sup> Calcd. for [C<sub>27</sub>H<sub>27</sub>N<sub>2</sub>O<sub>2</sub>]<sup>+</sup> 411.2106; Found: 411.2119.

#### Synthesis of 4b

**3-II** (585 mg, 3.1, mmol, 1 eq.) were dissolved in 40 mL THF. Boc<sub>2</sub>O (680 mg, 3.1 mmol, 1 eq.) and TEA (440  $\mu$ L, 3.1 mmol, 1 eq.) were added under a nitrogen atmosphere and the reaction mixture was stirred at ambient temperature for 18 h. The solvent was removed *in vacuo* and the residue was dissolved in 50 mL DCM. The solution was extracted three times with 50 mL of an aqueous solution with 5% acetic acid. The combined aqueous phases were washed two times with 50 mL Et<sub>2</sub>O and the solution was made alkaline (pH 9 – 10) with NaHCO<sub>3</sub>. The aqueous solution was extracted three times with 50 mL DCM. The combined organic phases were dried over Na<sub>2</sub>SO<sub>4</sub> and the solvent was removed *in vacuo*. The residue of **4b** (yellowish oil, 760 mg) was used without further purification.

 $R_f = 0.39 (DCM:MeOH / 19:1).$ 

<sup>1</sup>H-NMR (400 MHz, CDCl<sub>3</sub>)  $\delta$  = 7.17 (s, 1H), 7.02 – 6.90 (m, 1H), 6.41 (d, J = 8.3 Hz, 1H), 6.26 (s, 1H), 3.79 (q, J = 2.0 Hz, 2H), 2.99 (s, 3H), 1.49 (s, 9H), 1.31 (s, 6H).

<sup>13</sup>C-NMR (100 MHz, CDCl<sub>3</sub>)  $\delta$  = 163.0, 155.0, 142.7, 138.2, 129.7, 118.7, 114.7, 104.5, 79.6, 72.7, 44.3, 29.9, 28.9, 28.4.

MS (ESI) m/z: [M+H]<sup>+</sup> Calcd. for [C<sub>17</sub>H<sub>25</sub>N<sub>2</sub>O<sub>2</sub>]<sup>+</sup> 289.19; Found 289.19.

#### Synthesis of 1a

**4a** (0.3 g, 0.73 mmol, 1 eq.) and 3-formyl-4-hydroxybenzoic acid (0.16 g, 0.95 mmol, 1.3 eq.) were dissolved in 25 mL MeCN for 6 h and refluxed (heated with an oil bath) under a nitrogen atmosphere. The solvent was removed *in vacuo* and the residue was purified by flash chromatography on normal phase silica gel (solvent A: hexane + 0.1% FA, solvent B: EE + 0.1% FA, 60% A). **1a** was obtained as a redish solid (0.17 g, 0.3 mmol, 42%).

 $R_f = 0.45$  (hexane:EE + 0.1% FA / 3:2).

<sup>1</sup>H-NMR (500 MHz, DMSO- $d_6$ ): δ = 12.60 (s, 1H), 9.40 (s, 1H), 7.89 (d, J = 7.0 Hz, 2H), 7.79 (d, J = 2.2 Hz, 1H), 7.77 – 7.69 (m, 2H), 7.67 (dd, J = 8.5, 2.2 Hz, 1H), 7.41 (t, J = 7.4 Hz, 2H), 7.34 (t, J = 7.4 Hz, 2H), 7.23 (s, 1H), 7.15 (s, 1H), 7.10 (d, J = 10.5 Hz, 1H), 6.73 (d, J = 8.5 Hz, 1H), 6.49 (d, J = 8.3 Hz, 1H), 5.82 (d, J = 10.2 Hz, 1H), 4.41 (d, J = 6.9 Hz, 2H), 4.28 (t, J = 6.9 Hz, 1H), 2.60 (s, 3H), 1.17 – 1.07 (m, 6H).

<sup>13</sup>C-NMR (125 MHz, DMSO- $d_6$ ): δ = 167.2, 158.1, 154.2, 144.3, 141.2, 137.3, 136.9, 131.8, 131.2, 129.5, 129.0, 128.1, 127.6, 125.6, 123.2, 120.6, 120.2, 118.9, 118.0, 114.9, 107.3, 105.7, 65.9, 52.1, 47.2, 40.6, 40.4, 40.3, 40.1, 39.9, 39.8, 39.6, 29.2, 26.1, 20.1.

IR (ATR): v = 3338w, 2968br, 1693s, 1234m, 1208s cm<sup>-1</sup>.

UV/VIS (c = 0.46  $\mu$ mol mL<sup>-1</sup> in MeOH):  $\lambda_{max,1}$  = 443.7 nm.

HR-MS (ESI) *m/z*: [M+H]<sup>+</sup> Calcd. for [C<sub>35</sub>H<sub>31</sub>N<sub>2</sub>O<sub>5</sub>]<sup>+</sup> 559.2227; Found 559.2258.

#### Synthesis of 1b

The unpurified residue of  $7 (700 \text{ mg}, \sim 2.43 \text{ mmol}, 1 \text{ eq.})$  and 3-formyl-4-hydroxybenzoic acid (400 mg, 2.43 mmol, 1 eq.) were dissolved in 50 mL MeCN and the solution was refluxed (heated with an oil bath) for 4.5 h under a nitrogen atmosphere. The solvent was removed *in vacuo* and the residue was purified by flash chromatography in normal phase silica (solvent A: hexane + 0.1% FA, solvent B: EE + 0.1% FA, 60% A). **1b** was obtained as a redish solid (0.680 mg, 1.56 mmol, 64%).

 $R_f = 0.41$  (hexane:EE + 0.1% FA / 3:2).

<sup>1</sup>H-NMR (500 MHz, DMSO- $d_6$ ):  $\delta$  = 12.65 (s, 1H), 8.97 (s, 1H), 7.80 (d, J = 2.3 Hz, 1H), 7.68 (dd, J = 8.5, 2.3 Hz, 1H), 7.25 (s, 1H), 7.18 – 6.99 (m, 2H), 6.74 (d, J = 8.6 Hz, 1H), 6.48 (d, J = 8.3 Hz, 1H), 5.83 (d, J = 10.3 Hz, 1H), 2.61 (s, 3H), 1.46 (s, 9H), 1.17 (s, 3H), 1.10 (s, 3H).

<sup>13</sup>C-NMR (125 MHz, DMSO- $d_6$ ): δ = 166.7, 157.7, 153.1, 143.2, 136.3, 131.3, 129.0, 128.5, 122.7, 122.0, 119.8, 118.4, 117.5, 114.4, 113.6, 106.7, 105.3, 78.4, 51.6, 28.7, 28.2, 25.6, 19.7.

IR (ATR): v = 3319w, 3069w, 2973br, 1683s, 1158s cm<sup>-1</sup>.

HR-MS (ESI) m/z: [M+Na]<sup>+</sup> Calcd. for [C<sub>25</sub>H<sub>28</sub>N<sub>2</sub>O<sub>5</sub>Na]<sup>+</sup> 459.1890; Found 459.1909.

#### Synthesis strategy 2 || |0 6-I 6 OAc OAc $NO_2$ NO<sub>2</sub> O<sup>2</sup> AcO НО AcO AcO 8 8-I 8-II OAc NHR НО NHR AcO AcO **10a** R = Fmoc 9a R = Fmoc 2a R = Fmoc

Scheme S2. Synthesis pathway for spiropyrans 2a and 2b.

2b R = Boc

The overall yield over 6 consecutive steps was for 2a 4% and for 2b 3%, respectively. Especially 8-II, was not completely stable at air and should therefore be processed faster. Furthermore, the actual indole precursor was generated in the last step from 7 in situ through deprotonation. A more convenient method could be to produce and isolate the respective indole precursor in an additional step.

**10b** R = Boc

**9b** R = Boc

#### Synthesis of 6-I

4-Hydrazinobenzoic acid 6 (5 g, 33 mmol, 1 eq.) and 3-methyl-2-butanone (5 ml, 59 mmol, 1.8 eq.) were added to 50 mL acetic acid and refluxed (heated with an oil bath) for 16 h. The solvent was removed in vacuo, the residue redissolved in 50 mL DCM and neutralized with saturated aqueous NaHCO<sub>3</sub>solution. The combined organic phases were dried over Na<sub>2</sub>SO<sub>4</sub> and the solvent was removed in vacuo to obtain 6-I as an orange solid (1.3 g, 6.4 mmol, 19%).

Analytical data match reported literature values.<sup>3</sup>

 $R_f = 0.74 \text{ (DCM:MeOH} + 0.1\% \text{ FA} / 9:1).$ 

<sup>1</sup>H-NMR (500 MHz, CDCl<sub>3</sub>):  $\delta$  = 12.76 (s, 1H), 7.97 (d, J = 1.6 Hz, 1H), 7.90 (dd, J = 8.1, 1.5 Hz, 1H), 7.49 (dd, J = 8.0, 1.2 Hz, 1H), 2.23 (s, 3H), 1.25 (s, 6H).

<sup>13</sup>C-NMR (125 MHz, CDCl<sub>3</sub>):  $\delta$  = 192.1, 167.9, 157.9, 146.6, 130.0, 127.7, 123.2, 119.6, 53.9, 22.7, 15.8.

MS (ESI) m/z: [M+H]<sup>+</sup> Calcd. for [C<sub>12</sub>H<sub>14</sub>NO<sub>2</sub>]<sup>+</sup> 204.10; Found 204.10.

#### Synthesis of 7

**6-I** (5 g, 25 mmol, 1 eq.) was dissolved in 70 mL toluene and 35 mL MeCN under nitrogen atmosphere. Iodomethane (1.8 ml, 30 mmol, 1.2 eq.) was added and the reaction mixture was refluxed (heated with an oil bath) for 16 h. The formed precipitate was separated, washed with hexane and cold ethanol and dried. **7** was obtained as an orange-pinkish solid (2.9 g, 8.4 mmol, 34%).

Analytical data match reported literature values. <sup>3</sup>

 $R_f = 0.21$  (DCM:MeOH + 0.1% FA / 9:1).

<sup>1</sup>H-NMR (400 MHz, DMSO- $d_6$ ):  $\delta = 8.35$  (s, 1H), 8.17 (d, J = 8.4 Hz, 1H), 8.02 (d, J = 8.4 Hz, 1H), 3.98 (s, 3H), 2.80 (s, 3H), 1.55 (s, 6H).

<sup>13</sup>C-NMR (100 MHz, DMSO- $d_6$ ): δ = 199.5, 166.9, 145.7, 142.4, 132.0, 130.8, 124.7, 115.8, 54.7, 35.5, 21.9, 15.0.

MS (ESI) m/z: [M-I]<sup>+</sup> Calcd. for [C<sub>13</sub>H<sub>16</sub>NO<sub>2</sub>]<sup>+</sup> 218.12; Found 218.12.

#### Synthesis of 8-I

2-Hydroxy-5-nitrobenzaldehyd 8 (2.5 g, 15 mmol, 1 eq.) was dissolved in 50 mL acetic anhydride. Three drops of concentrated  $H_2SO_4$  were added and the solution was stirred for 1 h under nitrogen atmosphere at ambient temperature. The reaction mixture was poured in 500 mL water and stirred for 30 min. The formed precipitate was separated, washed with water and dried. 8-I was obtained as white crystals (3.57 g, 11.5 mmol, 76%).

Analytical data match reported literature values.4

 $R_f = 0.23$  (hexane:EE/ 8:2).

<sup>1</sup>H-NMR (400 MHz, CDCl<sub>3</sub>):  $\delta$  = 8.53 (d, J = 2.8 Hz, 1H), 8.29 (dd, J = 8.9, 2.8 Hz, 1H), 7.93 (s, 1H), 7.35 (d, J = 8.9 Hz, 1H), 2.38 (s, 3H), 2.13 (s, 6H).

<sup>13</sup>C-NMR (100 MHz, CDCl<sub>3</sub>):  $\delta$  = 168.3, 168.2, 152.7, 145.6, 129.6, 125.8, 124.4, 123.8, 84.1, 20.8, 20.6.

MS (ESI+, MeCN/MeOH):  $m/z = 318.081 \text{ [M+Li]}^+$ . 318.0801

MS (ESI) m/z: [M+Li]<sup>+</sup> Calcd. for [C<sub>13</sub>H<sub>13</sub>NO<sub>8</sub>Li]<sup>+</sup> 318.08; Found 318.08.

#### Synthesis of 8-II

**8-I** (1.5 g, 4.8 mmol, 1 eq.) was dissolved in 40 mL ethanol and  $PtO_2$  (109 mg, 480  $\mu$ M, 0.1 eq.) was added. The reaction suspension was stirred for 12 h under a hydrogen atmosphere (5 bar) at ambient temperature. The suspension was filtrated over Celite® and the solvent of the filtrate was removed *in vacuo*. The residue was purified by flash chromatography on normal phase silica gel (solvent A: hexane, solvent B: EE, 60% A) and **8-II** was obtained as a yellowish solid (0.95 g, 3.4 mmol, 70%).

Analytical data match reported literature values.<sup>4</sup>

 $R_f = 0.4$  (hexane:EE / 1:1).

<sup>1</sup>H-NMR (500 MHz, CDCl<sub>3</sub>):  $\delta$  = 7.79 (s, 1H), 6.95–6.83 (m, 2H), 6.69 (dd, J = 8.7, 2.8 Hz, 1H), 3.72 (s, 2H), 2.30 (s, 3H), 2.10 (s, 6H).

<sup>13</sup>C-NMR (125 MHz, CDCl<sub>3</sub>):  $\delta$  = 170.1, 168.4, 144.6, 140.1, 128.1, 123.8, 117.0, 113.5, 85.4, 20.8, 20.7.

MS (ESI) *m/z*: [M+Li]<sup>+</sup> Calcd. for [C<sub>13</sub>H<sub>15</sub>NO<sub>6</sub>Li]<sup>+</sup> 288.11; Found 288.11.

#### Synthesis of 9a

**8-II** (2 g, 7.1 mmol, 1 eq.) and Fmoc-Cl (2.2 g, 8.5 mmol, 1.2 eq.) were suspended in 10 mL water and stirred for 2h at 60 °C (heated with an oil bath). The reaction mixture was extracted three times with 60 mL EE and the combined organic phases were dried over Na<sub>2</sub>SO<sub>4</sub>. The solvent was removed *in vacuo* 

and the residue was purified by flash chromatography on normal phase silica gel (solvent A: hexane, solvent B: EE, 80% A) to obtain **9a** as transparent crystals (1.45 g, 2.9 mmol, 41%).

 $R_f = 0.12$  (hexane:EE / 4:1).

<sup>1</sup>H-NMR (500 MHz, CDCl<sub>3</sub>):  $\delta$  = 7.85 (s, 1H), 7.79 (d, J = 7.6 Hz, 2H), 7.68 (s, 1H), 7.61 (d, J = 7.5 Hz, 2H), 7.44–7.40 (m, 3H), 7.33 (t, J = 7.4 Hz, 2H), 7.05 (d, J = 8.8 Hz, 1H), 6.74 (s, 1H), 4.56 (d, J = 6.6 Hz, 2H), 4.28 (t, J = 6.5 Hz, 1H), 2.32 (s, 3H), 2.09 (s, 6H).

<sup>13</sup>C-NMR (125 MHz, CDCl<sub>3</sub>):  $\delta$  = 169.5, 168.4, 153.2, 143.8, 143.6, 141.4, 135.8, 128.4, 127.8, 127.2, 124.9, 123.8, 120.8, 120.1, 117.8, 85.0, 67.0, 47.1, 20.8, 20.7.

IR (ATR): v = 3399m, 1749s, 1727s, 1543m, 1195s cm<sup>-1</sup>.

UV/VIS (c = 0.05  $\mu$ mol mL<sup>-1</sup> /MeOH):  $\lambda_{max,1} = 300$ ,  $\lambda_{max,2} = 289$ ,  $\lambda_{max,1} = 264$ ,  $\lambda_{max,1} = 244$  nm.

HR-MS (ESI) *m/z*: [M+Li]<sup>+</sup> Calcd. for [C<sub>28</sub>H<sub>25</sub>NO<sub>8</sub>Li]<sup>+</sup> 510.1740; Found 510.1724.

#### Synthesis of 9b

**8-II** (1 g, 3.6 mmol, 1 eq.) and Boc<sub>2</sub>O (1.55 g, 7 mmol, 2 eq.) were dissolved in 10 mL DCM and stirred at ambient temperature for 12 h under a nitrogen atmosphere. The solvent was removed *in vacuo* and the residue was purified by flash chromatography on normal phase silica gel (solvent A: hexane, solvent B: EE, 80% A) to obtain **9b** as a transparent gel (0.57 g, 1.5 mmol, 42%).

Analytical data match reported literature value.4

 $R_f = 0.63$  (hexane:EE / 3:2).

<sup>1</sup>H-NMR (400 MHz, CDCl<sub>3</sub>):  $\delta$  = 7.84 (s, 1H), 7.64 (d, J = 2.5 Hz, 1H), 7.41 (d, J = 8.8, 2.7 Hz, 1H), 7.03 (d, J = 8.8 Hz, 1H), 6.52 (s, 1H), 2.31 (s, 3H), 2.09 (s, 6H), 1.52 (s, 9H).

<sup>13</sup>C-NMR (100 MHz, CDCl<sub>3</sub>):  $\delta$  = 169.6, 168.4, 152.5, 143.3, 136.5, 128.2, 123.7, 120.7, 117.6, 85.1, 80.9, 28.3, 20.8, 20.7.

MS (ESI) *m*/*z*: [M+Li]<sup>+</sup> Calcd. for [C<sub>18</sub>H<sub>23</sub>NO<sub>8</sub>Li]<sup>+</sup> 388.16; Found 388.16.

#### Synthesis of 10a

**9a** (0.1 g, 0.2 mmol, 1 eq.) was dissolved in 20 mL ethanol and 1 mL of concentrated H<sub>2</sub>SO<sub>4</sub> was added. The solution was refluxed (heated with an oil bath) for 2 h and neutralized with a saturated aqueous NaHCO<sub>3</sub>-solution. The solution was extracted three times with 50 mL Et<sub>2</sub>O and the combined organic phases were dried over Na<sub>2</sub>SO<sub>4</sub>. The solvent is removed *in vacuo* and **10a** was obtained as beige crystals (52 mg, 0.14 mmol, 73%).

 $R_f = 0.28$  (hexane:EE / 4:1).

<sup>1</sup>H-NMR (400 MHz, THF- $d_8$ ): δ = 10.58 (s, 1H), 9.91 (s, 1H), 8.82 (s, 1H), 7.88 (s, 1H), 7.79 (d, J = 7.5 Hz, 2H), 7.67 (d, J = 7.3 Hz, 2H), 7.51 (s, 1H), 7.36 (t, J = 7.5 Hz, 2H), 7.28 (t, J = 7.4 Hz, 2H), 6.85 (d, J = 8.9 Hz, 1H), 4.55 (d, J = 6.3 Hz, 2H), 4.26 (t, J = 6.2 Hz, 1H).

<sup>13</sup>C-NMR (100 MHz, THF- $d_8$ ): δ = 196.8, 157.8, 154.3, 145.0, 142.2, 132.8, 128.2, 128.0, 127.6, 125.5, 122.6, 121.5, 120.5, 118.0, 66.6, 48.1.

IR (ATR): v = 3294m, 1693s, 1658s, 1243s, 732m cm<sup>-1</sup>.

UV/VIS (c = 0.07  $\mu$ mol mL<sup>-1</sup> /MeOH):  $\lambda_{max,1} = 356$ ,  $\lambda_{max,2} = 256$ ,  $\lambda_{max,3} = 235$  nm.

HR-MS (ESI) m/z: [M+Na]<sup>+</sup> Calcd. for [C<sub>22</sub>H<sub>18</sub>NO<sub>4</sub>Na]<sup>+</sup> = 382.1055; Found 382.1052.

#### Synthesis of 10b

**9b** (0.5 g, 1.3 mmol, 1 eq.) was dissolved in 10 mL methanol and 5 g NaOH dissolved in 5 mL water were added. The solution was refluxed (heated with an oil bath) for 3 h and neutralized with an aqueous 1 M HCl-solution. The solution was extracted three times with 20 mL EE and the combined organic phases were dried over Na<sub>2</sub>SO<sub>4</sub>. The solvent was removed *in vacuo* and the residue was purified by flash chromatography on normal phase silica gel (solvent A: hexane, solvent B: EE, 90% A) to obtain **10b** as a yellow solid (0.21 g, 890 μmol, 45%).

Analytical data match reported literature values.<sup>4</sup>

 $R_f = 0.45$  (hexane:EE / 4:1).

<sup>1</sup>H-NMR (400 MHz, CDCl<sub>3</sub>):  $\delta$  = 10.76 (s, 1H), 9.86 (d, J = 0.5 Hz, 1H), 7.83 (s, 1H), 7.29 (dd, J = 8.9, 2.7 Hz, 1H), 6.92 (d, J = 8.9 Hz, 1H), 6.45 (s, 1H), 1.52 (s, 6H).

<sup>13</sup>C-NMR (100 MHz, CDCl<sub>3</sub>):  $\delta$  = 196.5, 157.6, 153.0, 130.8, 128.4, 123.3, 120.2, 118.0, 80.9, 28.3.

MS (ESI) *m*/*z*: [M+Li]<sup>+</sup> Calcd. for [C<sub>12</sub>H<sub>15</sub>NO<sub>4</sub>Li]<sup>+</sup> 244.12; Found 244.11.

#### Synthesis of 2a

**10a** (0.3 g, 0.83 mmol, 1 eq.) and **7** (0.58 g, 1.7 mmol, 2 eq.) were dissolved in 100 mL ethanol under a nitrogen atmosphere and TEA (0.47 mL, 3.3 mmol, 4 eq.) was added slowly. The solution was refluxed (heated with an oil bath) for 3 h and neutralized with an aqueous 1 M HCl-solution. The solution was extracted three times with 60 mL EE and the combined organic phases were dried over Na<sub>2</sub>SO<sub>4</sub>. The solvent was removed *in vacuo* and the residue was purified by flash chromatography on normal phase silica gel (solvent A: DCM, solvent B: MeOH, 98% A) to obtain **2a** as a red solid (0.12 g, 0.21 mmol, 26%).

 $R_f = 0.41 (DCM:MeOH / 19:1).$ 

<sup>1</sup>H-NMR (400 MHz, THF- $d_8$ ):  $\delta$  = 12.83 (s, 1H), 8.64 (s, 1H), 7.87 (dd, J = 8.2, 1.7 Hz, 1H), 7.80 (d, J = 7.6 Hz, 2H), 7.72 (d, J = 1.7 Hz, 1H), 7.68 (d, J = 7.4 Hz, 2H), 7.43 – 7.34 (m, 3H), 7.29 (td, J = 7.4, 1.2 Hz, 2H), 7.10 (d, J = 8.7 Hz, 1H), 6.93 (d, J = 10.2 Hz, 1H), 6.58 (d, J = 8.7 Hz, 1H), 6.53 (d, J = 8.2 Hz, 1H), 5.76 (d, J = 10.2 Hz, 1H), 4.51 (d, J = 6.5 Hz, 2H), 4.27 (t, J = 6.4 Hz, 1H), 2.77 (s, 3H), 1.33 (s, 3H), 1.17 (s, 3H).

<sup>13</sup>C-NMR (100 MHz, THF- $d_8$ ): δ = 167.6, 154.2, 152.6, 150.5, 145.1, 142.2, 137.3, 133.3, 131.6, 130.6, 128.1, 127.6, 125.6, 123.8, 122.3, 120.5, 119.8, 119.4, 117.5, 115.3, 106.2, 104.8, 66.5, 51.8, 48.2, 28.7, 25.9, 20.3.

IR (ATR): v = 3303br, 3064br, 1671s, 1583s, 1199s cm<sup>-1</sup>.

UV/VIS (c = 0.09  $\mu$ mol mL<sup>-1</sup> /MeOH):  $\lambda_{max,1} = 474$ ,  $\lambda_{max,2} = 378$ ,  $\lambda_{max,3} = 299$ ,  $\lambda_{max,4} = 264$  nm. HR-MS (ESI) m/z: [M+H]<sup>+</sup> Calcd. for [C<sub>35</sub>H<sub>31</sub>N<sub>2</sub>O<sub>5</sub>]<sup>+</sup> 559.2227; Found: 559.2207.

#### Synthesis of 2b

**10b** (0.5 g, 2.1 mmol, 0.5 eq.) and **7** (1.45 g, 4.2 mmol, 2 eq.) were dissolved in 100 mL ethanol under a nitrogen atmosphere and TEA (1.2 mL, 8.4 mmol, 4 eq.) was added slowly. The solution was refluxed (heated with an oil bath) for 3 h and neutralized with an aqueous 1 M HCl-solution. The solution was

extracted three times with 60 mL EE and the combined organic phases were dried over Na<sub>2</sub>SO<sub>4</sub>. The solvent was removed *in vacuo* and the residue was purified by flash chromatography on normal phase silica gel (solvent A: hexane, solvent B: EE, 20% A) to obtain **2b** as a pink solid (0.3 g, 0.7 mmol, 33%).

 $R_f = 0.35 (DCM:MeOH / 19:1).$ 

<sup>1</sup>H-NMR (400 MHz, DMSO- $d_6$ ):  $\delta$  = 12.25 (s, 1H), 9.10 (s, 1H), 7.76 (dd, J = 8.2, 1.7 Hz, 1H), 7.61 (d, J = 1.6 Hz, 1H), 7.34 (s, 1H), 7.04 (dd, J = 8.8, 2.4 Hz, 1H), 6.98 (d, J = 10.2 Hz, 1H), 6.59 (dd, J = 8.4, 6.2 Hz, 2H), 5.75 (d, J = 10.2 Hz, 1H), 2.70 (s, 3H), 1.44 (s, 3H), 1.21 (s, 3H), 1.08 (s, 3H).

<sup>13</sup>C-NMR (100 MHz, DMSO- $d_6$ ):  $\delta$  = 167.9, 153.4, 153.0, 149.3, 136.8, 132.9, 131.1, 130.2, 123.3, 121.4, 120.9, 119.5, 118.6, 117.4, 114.8, 106.3, 104.0, 79.2, 51.3, 28.9, 28.6, 26.0, 20.2.

IR (ATR): v = 3448w, 2980m, 1724s, 1667s, 1155s cm<sup>-1</sup>.

UV/VIS (c = 0.03  $\mu$ mol mL<sup>-1</sup> /MeOH):  $\lambda_{max,1} = 301$ ,  $\lambda_{max,2} = 233$  nm.

HR-MS (ESI) *m/z*: [M+Li]<sup>+</sup> Calcd. [C<sub>25</sub>H<sub>28</sub>N<sub>2</sub>O<sub>5</sub>Li]<sup>+</sup> 443.2158; Found: 443.2121.

# 4. Supplementary figures

#### UV/Vis-spectra

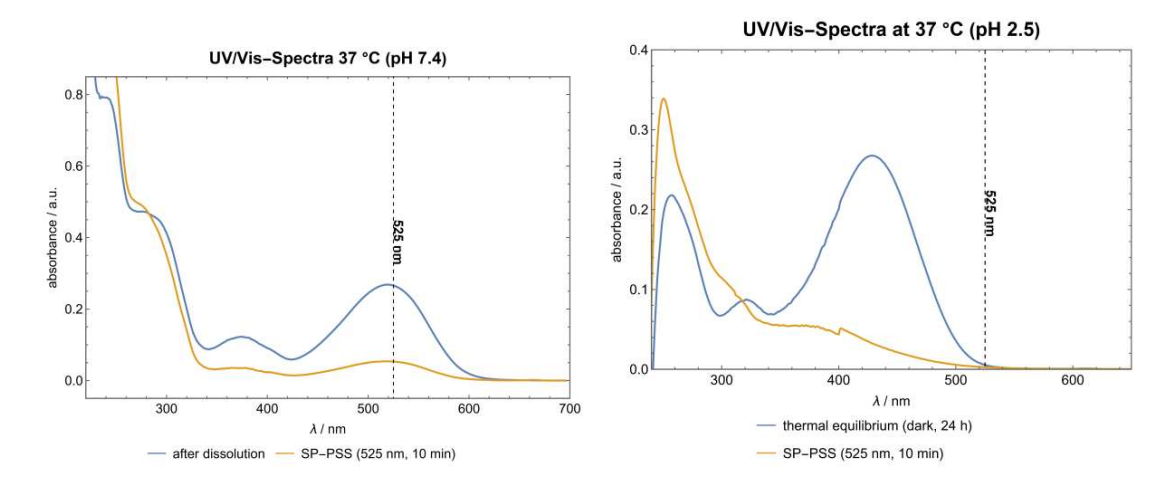


Figure S1. UV/Vis-spectra of P1 at 37 °C and different pH values: pH 7.4 (left, 55 μM), pH 2.5 (right, 13 μM).

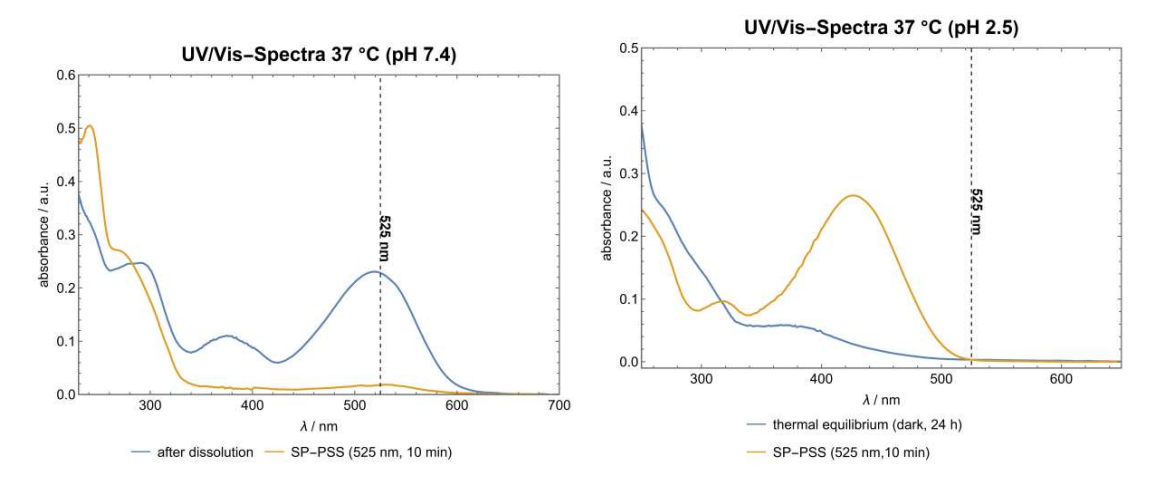


Figure S2. UV/Vis-spectra of P2 at 37 °C and different pH values: pH 7.4 (left, 30 μM), pH 2.5 (right, 16 μM).

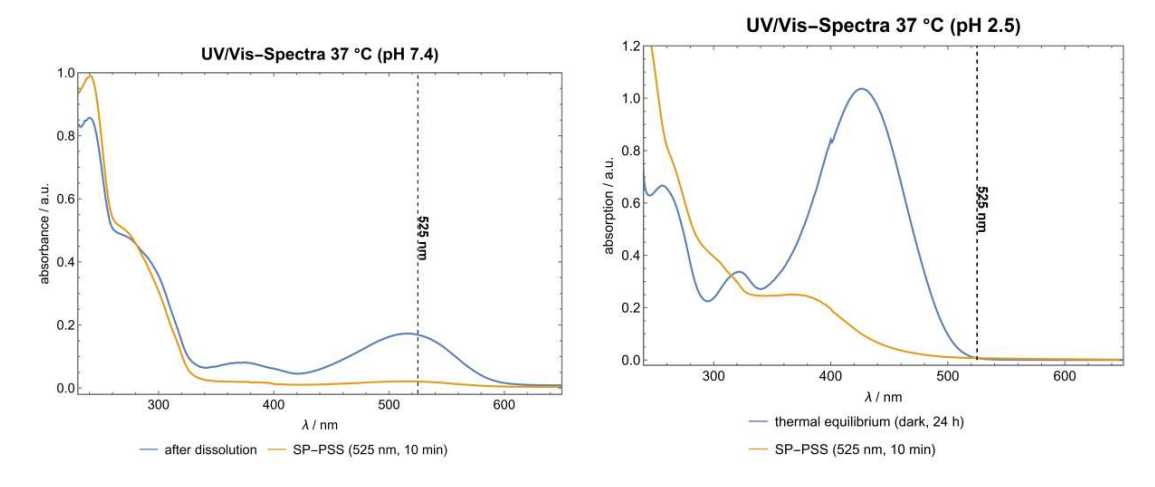


Figure S3. UV/Vis-spectra of P3 at 37 °C and different pH values: pH 7.4 (left, 50  $\mu$ M), pH 2.5 (right, c = 55  $\mu$ M).

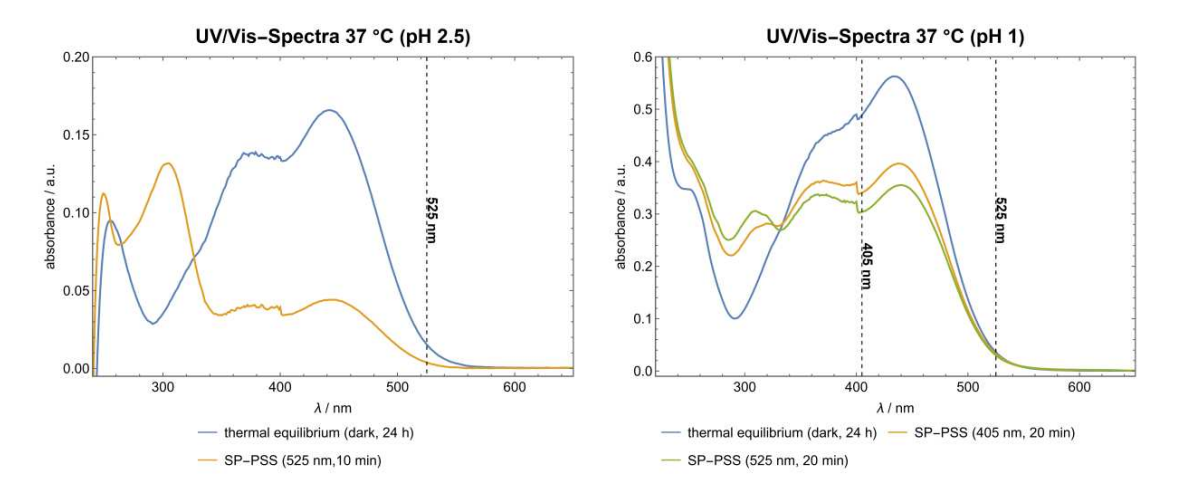
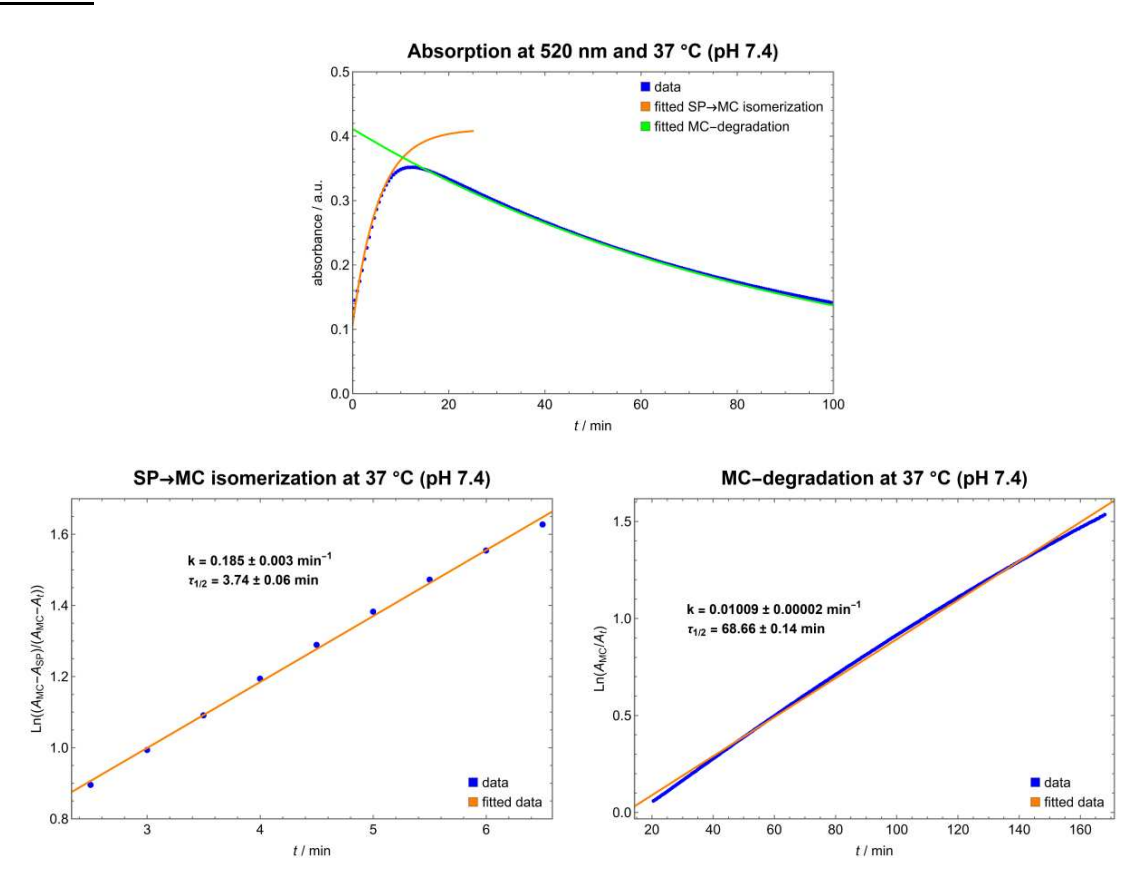
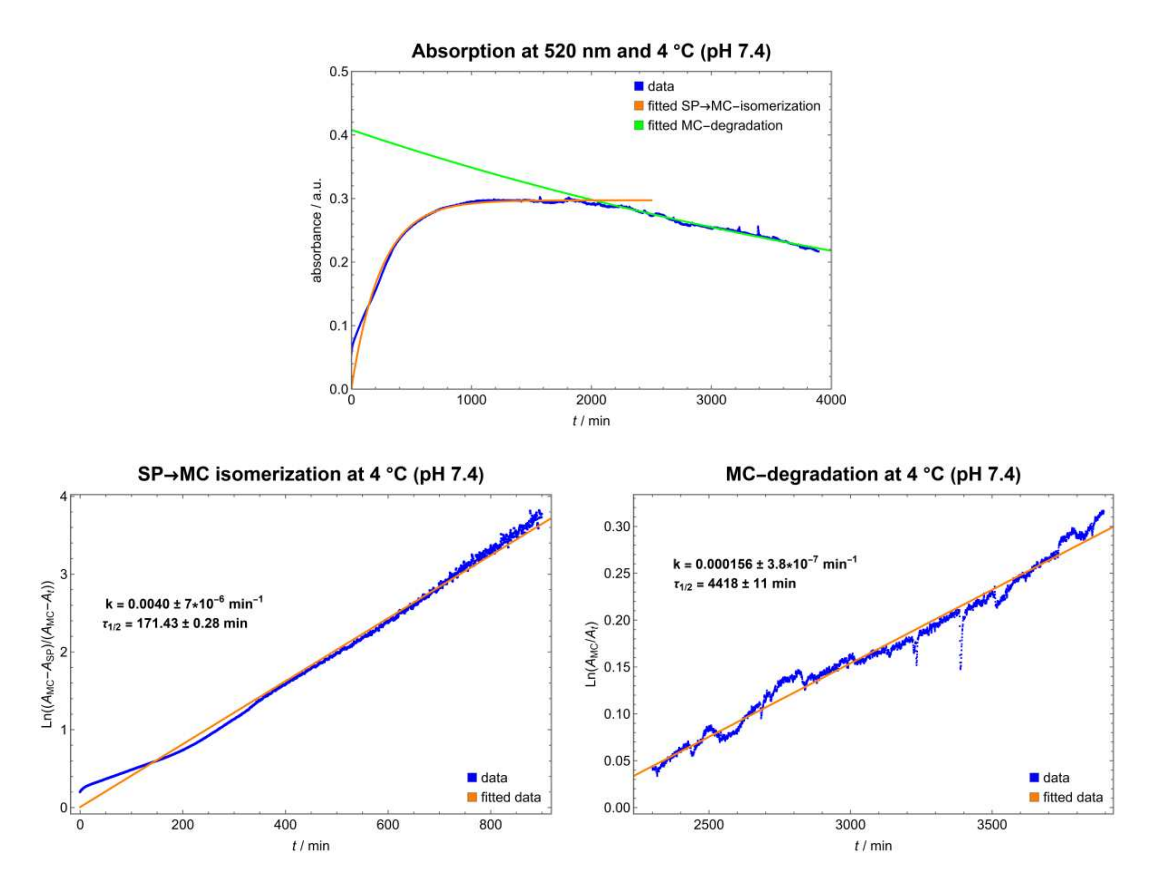


Figure S4. UV/Vis-spectra of P4 at 37 °C and different pH values: pH 2.5 (left, 15  $\mu$ M), pH 1 (right, 44  $\mu$ M).

#### **Kinetics**



**Figure S5.** Kinetic measured at 520 nm (top) of SP-to-MC isomerization (rate constant k, lower left) and hydrolysis (rate constant k, lower right) of **P1** (55  $\mu$ M) at pH 7.4 and 37 °C.



**Figure S6.** Kinetic measured at 520 nm (top) of SP-to-MC isomerization (rate constant k, lower left) and hydrolysis (rate constant k, lower right) of **P1** (40  $\mu$ M) at pH 7.4 and 4 °C.

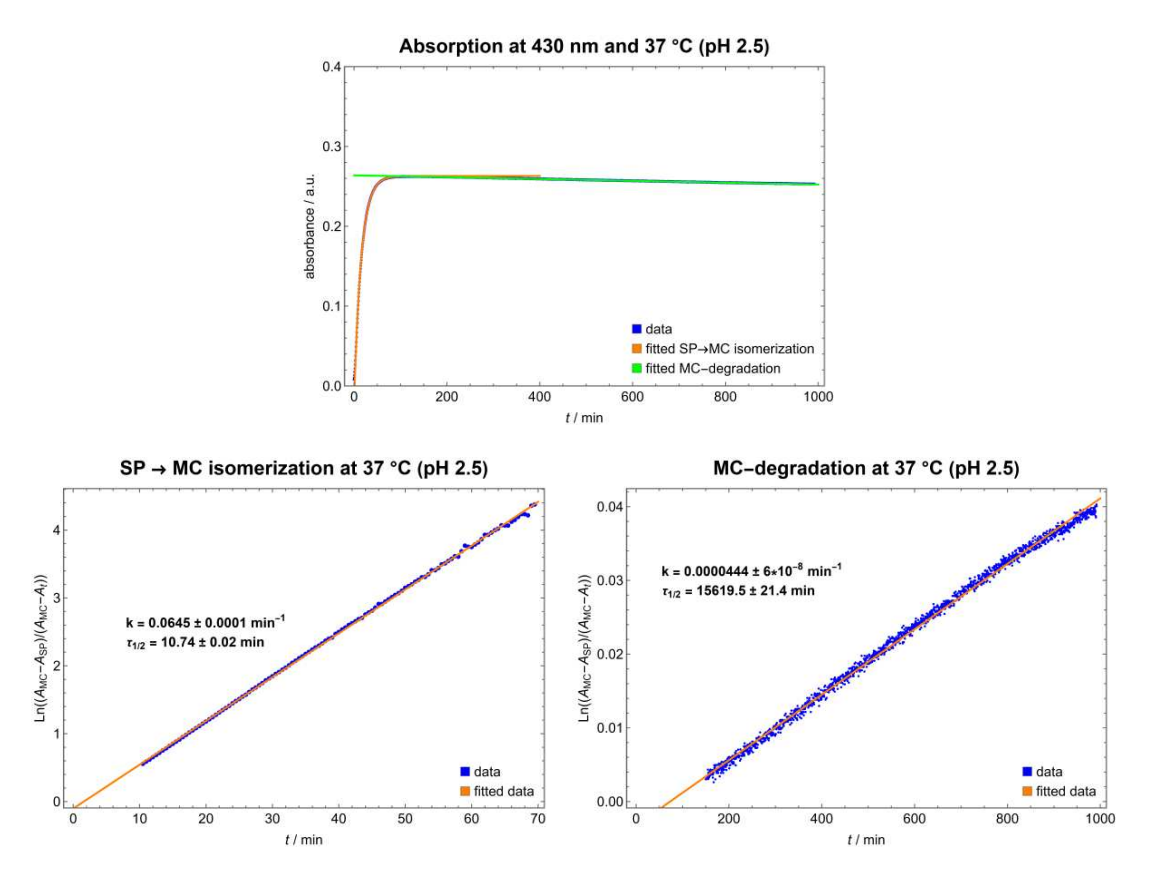


**Figure S7.** Kinetic measured at 430 nm (top) of SP-to-MC isomerization (rate constant k, lower left) and hydrolysis (rate constant k, lower right) of **P1** (13  $\mu$ M) at pH 2.5 and 37 °C.

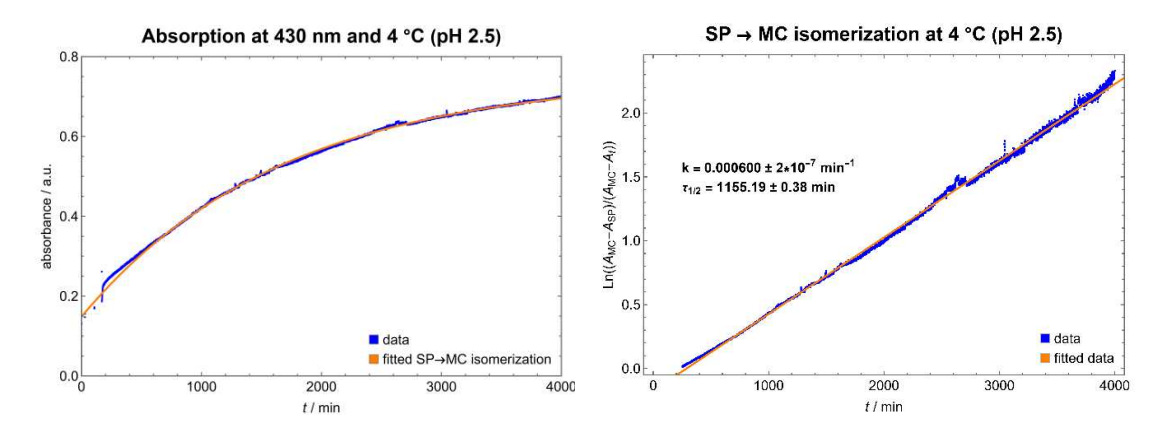


**Figure S8.** Kinetic measured at 430 nm (left) of SP-to-MC isomerization (rate constant k, right) of **P1** (13  $\mu$ M) at pH 2.5 and 4 °C.

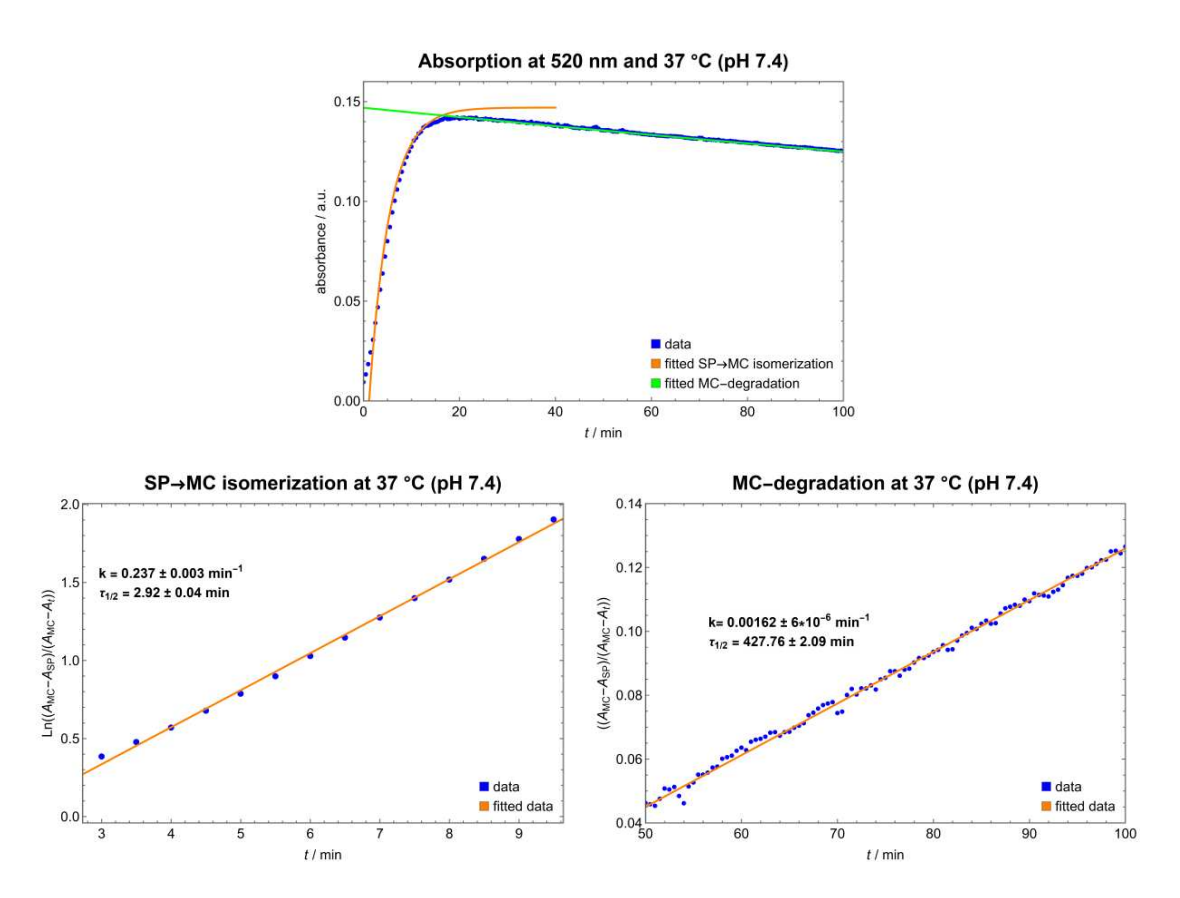


**Figure S9.** Kinetic measured at 520 nm (top) of SP-to-MC isomerization (rate constant k, lower left) and hydrolysis (rate constant k, lower right) of **P2** (20  $\mu$ M) at pH 7.4 and 37 °C.

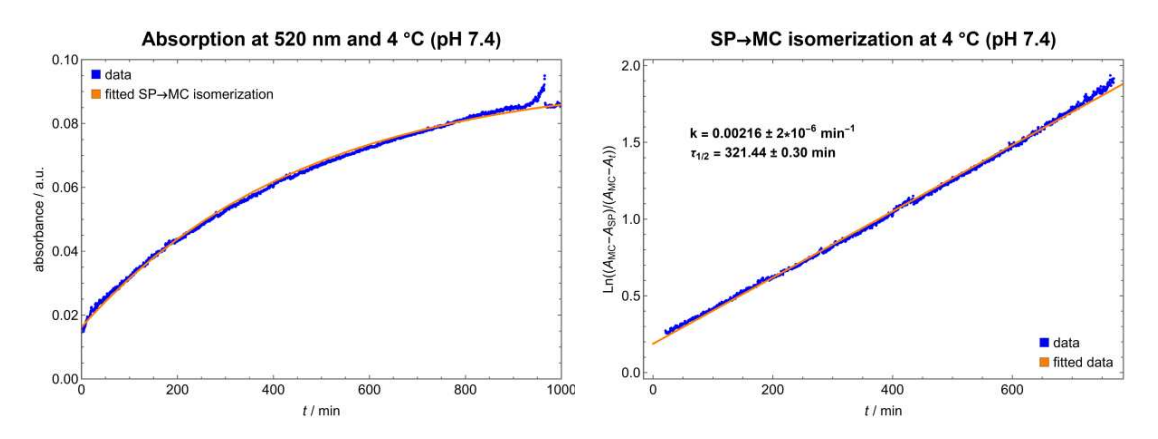


**Figure S10.** Kinetic measured at 520 nm (left) of SP-to-MC isomerization (rate constant k, right) of **P2** (12  $\mu$ M) at pH 7.4 and 4 °C.

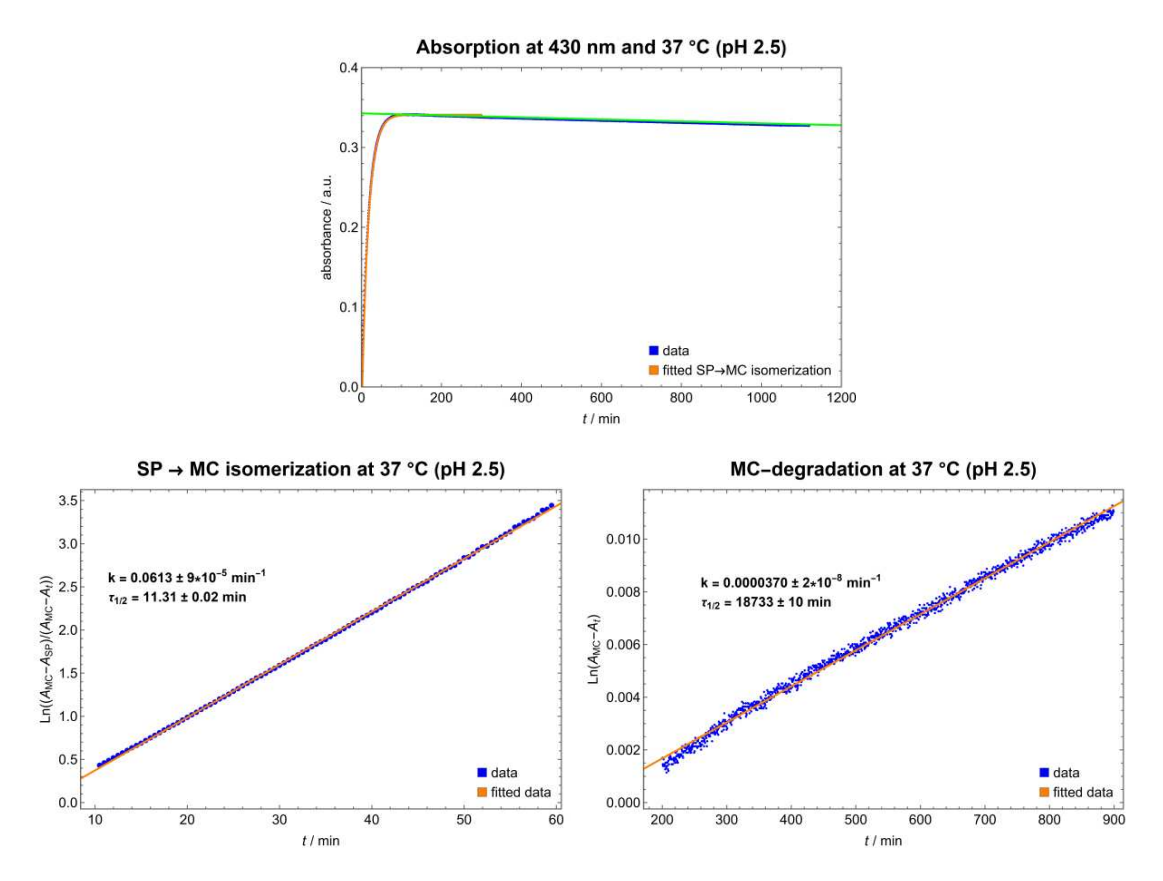


**Figure S11.** Kinetic measured at 430 nm (top) of SP-to-MC isomerization (rate constant k, lower left) and hydrolysis (rate constant k, lower right) of **P2** (16  $\mu$ M) at pH 2.5 and 37 °C.

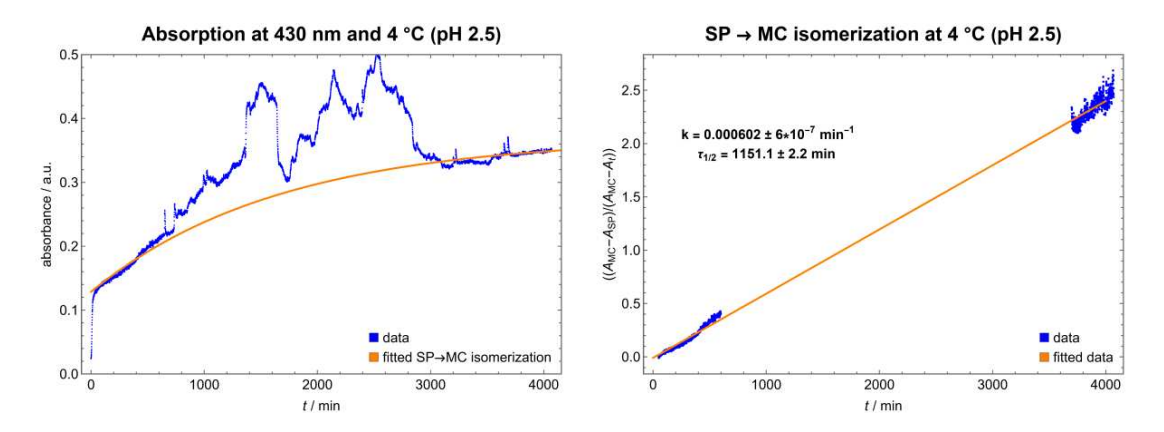


**Figure S12.** Kinetic measured at 430 nm (left) of SP-to-MC isomerization (rate constant k, right) of **P2** (16  $\mu$ M) at pH 2.5 and 4 °C.

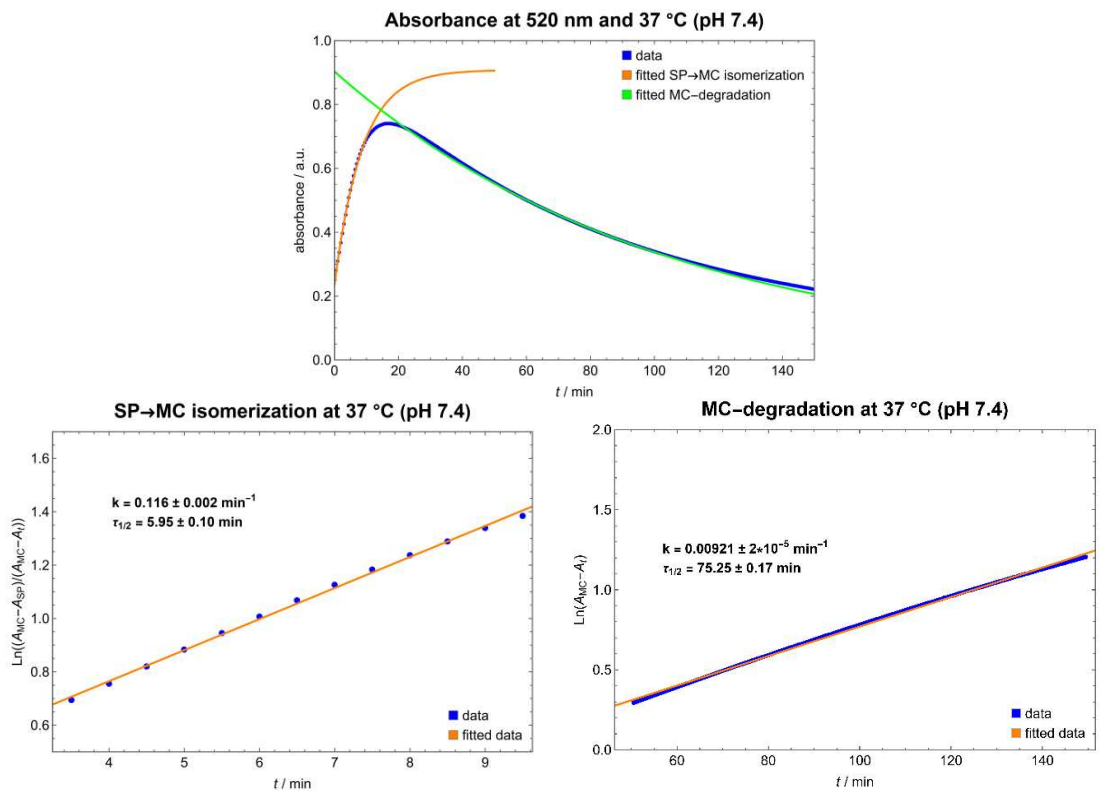


**Figure S13.** Kinetic measured at 520 nm (top) of SP-to-MC isomerization (rate constant k, lower left) and hydrolysis (rate constant k, lower right) of **P3** (120  $\mu$ M) at pH 7.4 and 37 °C.

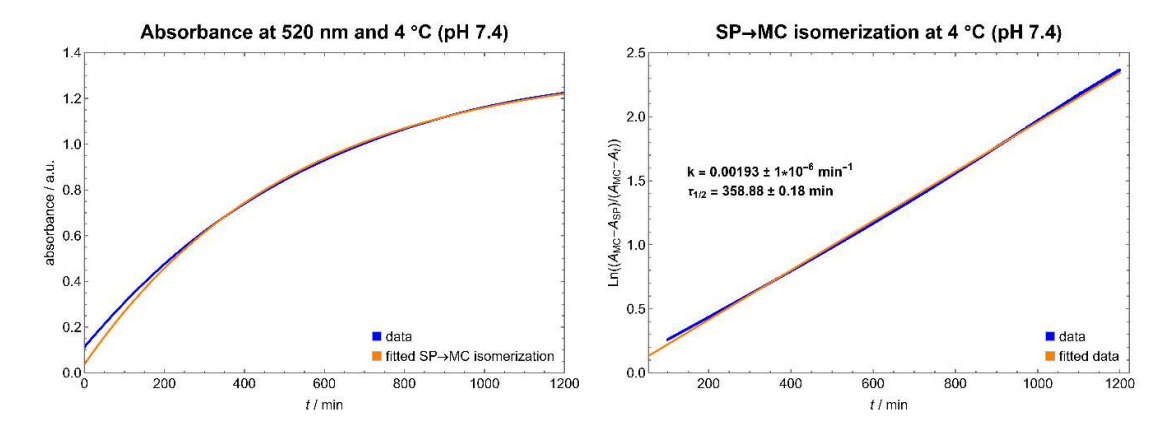


**Figure S14.** Kinetic measured at 520 nm (left) of SP-to-MC isomerization (rate constant k, right) of **P3** (160  $\mu$ M) at pH 7.4 and 4 °C.

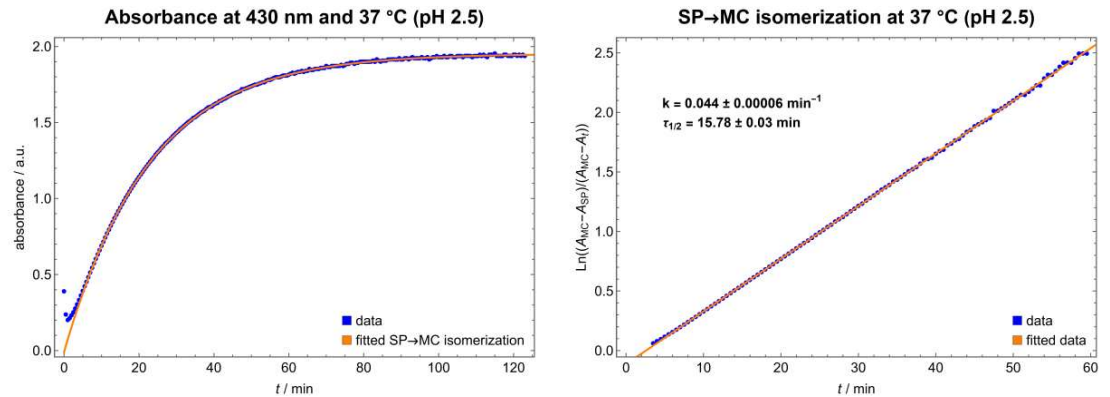
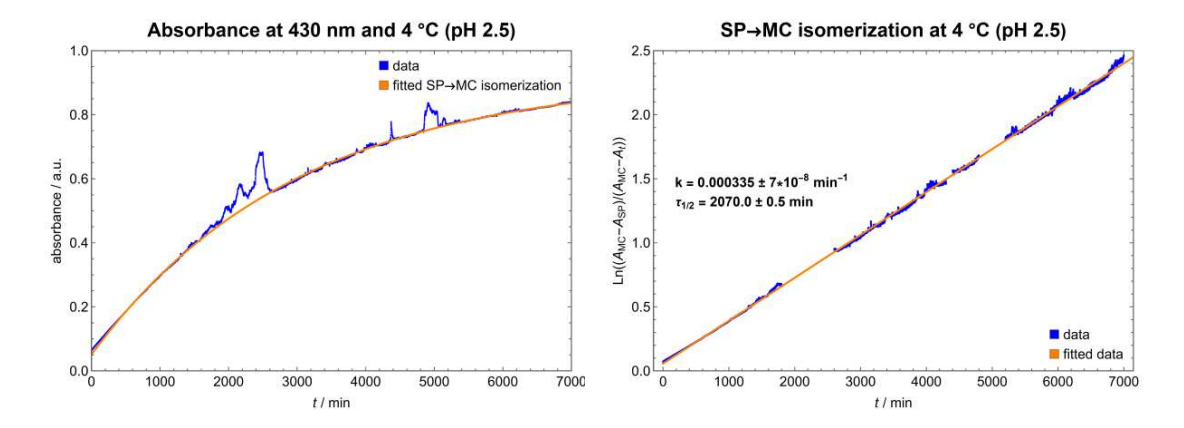
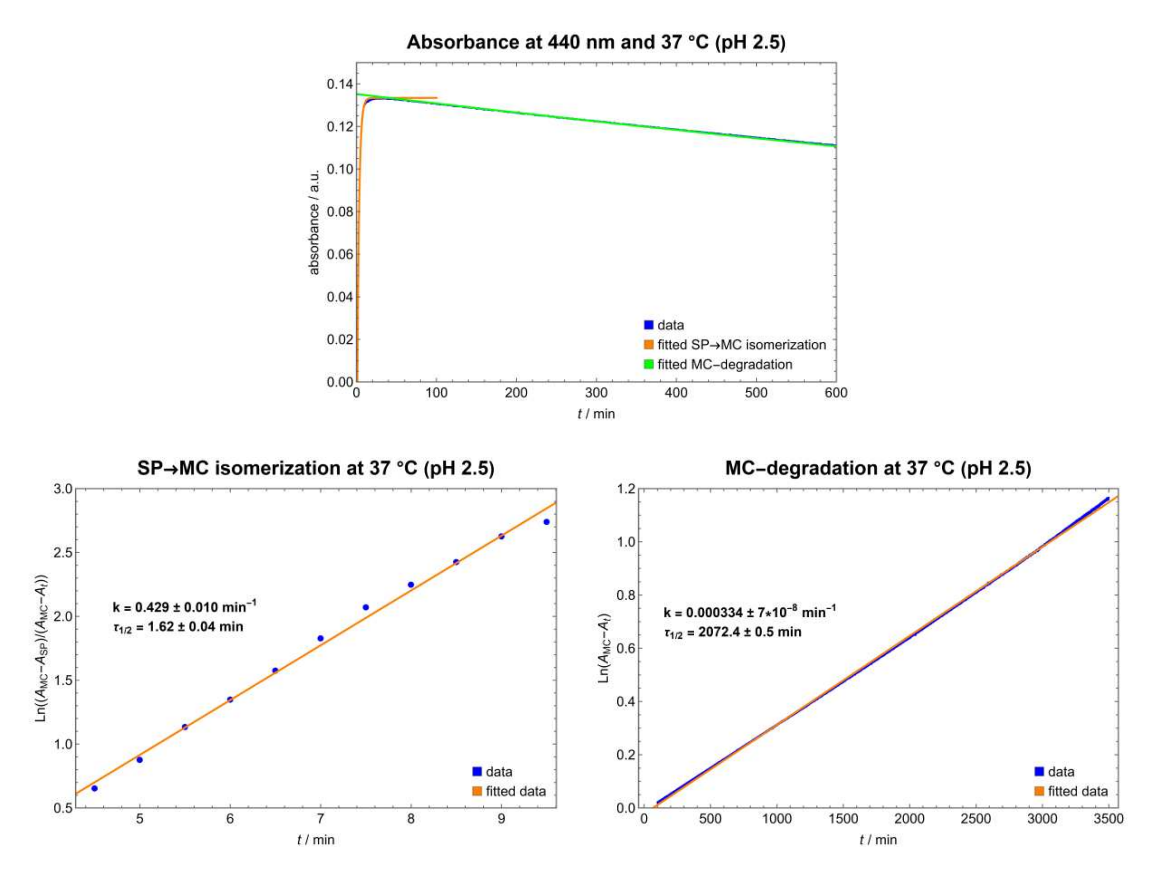


Figure S15. Kinetic measured at 430 nm (left) of SP-to-MC isomerization (rate constant k, right) of P3 (100  $\mu$ M) at pH 2.5 and 37 °C.



**Figure S16.** Kinetic measured at 430 nm (left) of SP-to-MC isomerization (rate constant k, right) of **P3** (50  $\mu$ M) at pH 2.5 and 4 °C.



**Figure S17.** Kinetic measured at 440 nm (top) of SP-to-MC isomerization (rate constant k, lower left) and hydrolysis (rate constant k, lower right) of **P4** (15  $\mu$ M) at pH 2.5 and 37 °C.

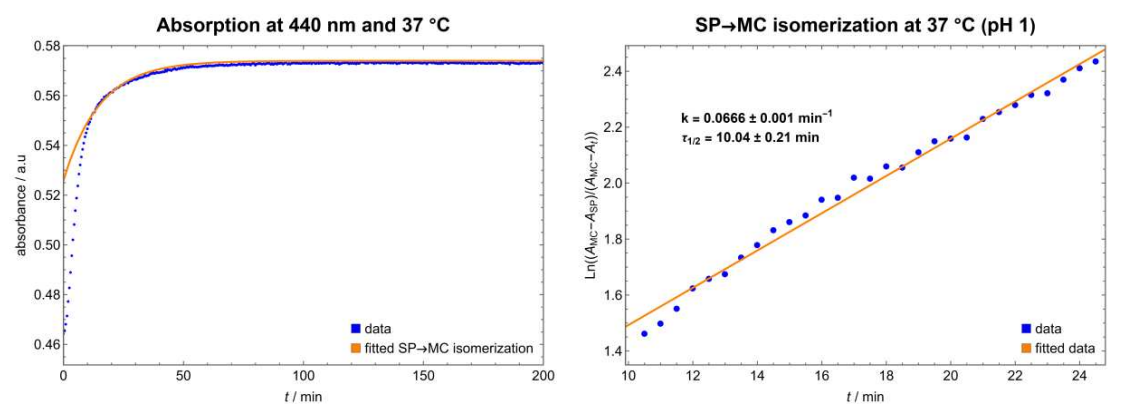


**Figure S18.** Kinetic measured at 440 nm (left) of SP-to-MC isomerization (rate constant k, right) of **P4** (44  $\mu$ M) at pH 1 and 37 °C.

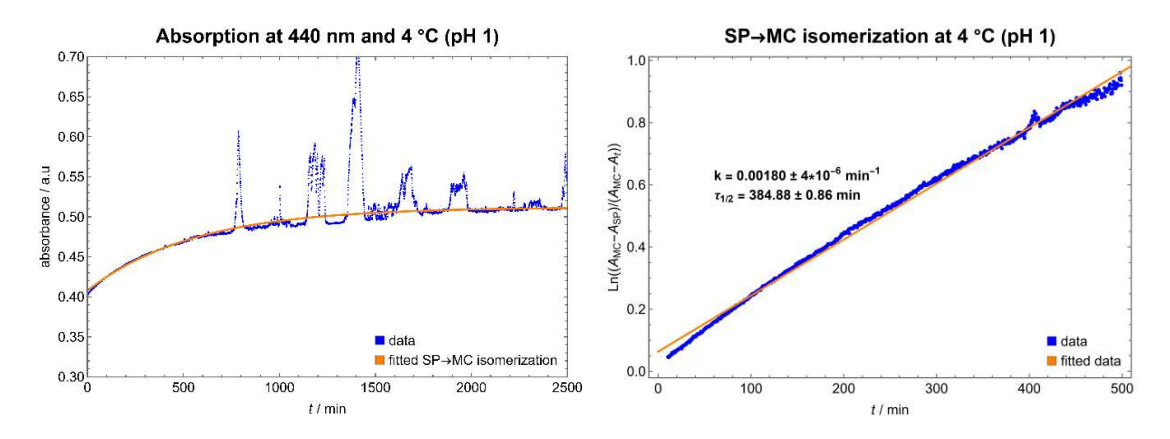


**Figure S19.** Kinetic measured at 440 nm (left) of SP-to-MC isomerization (rate constant k, right) of **P4** (39  $\mu$ M) at pH 1 and 4  $^{\circ}$ C.

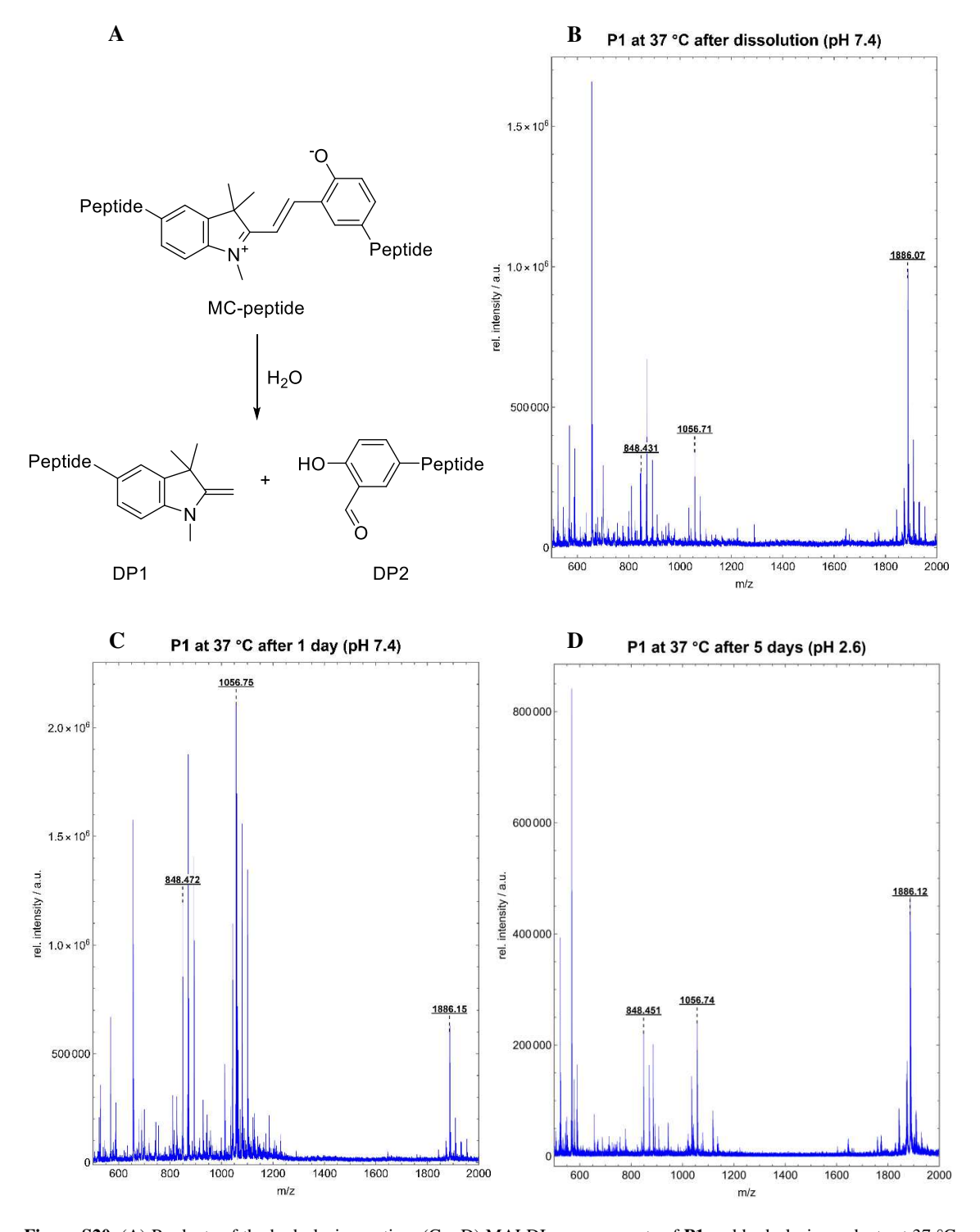


**Figure S20.** (A) Products of the hydrolysis reaction. (C - D) MALDI-measurements of **P1** and hydrolysis products at 37 °C after dissolution at pH 7.4 (B), after 1 day at pH 7.4 (C), and after 5 days at pH 2.6 (D). Calculated mass of **P1**+H $^+$ : 1886.0435, calculated mass for DP1+H $^+$ : 1056.6600, calculated mass for DP2+H $^+$ : 848.3997.

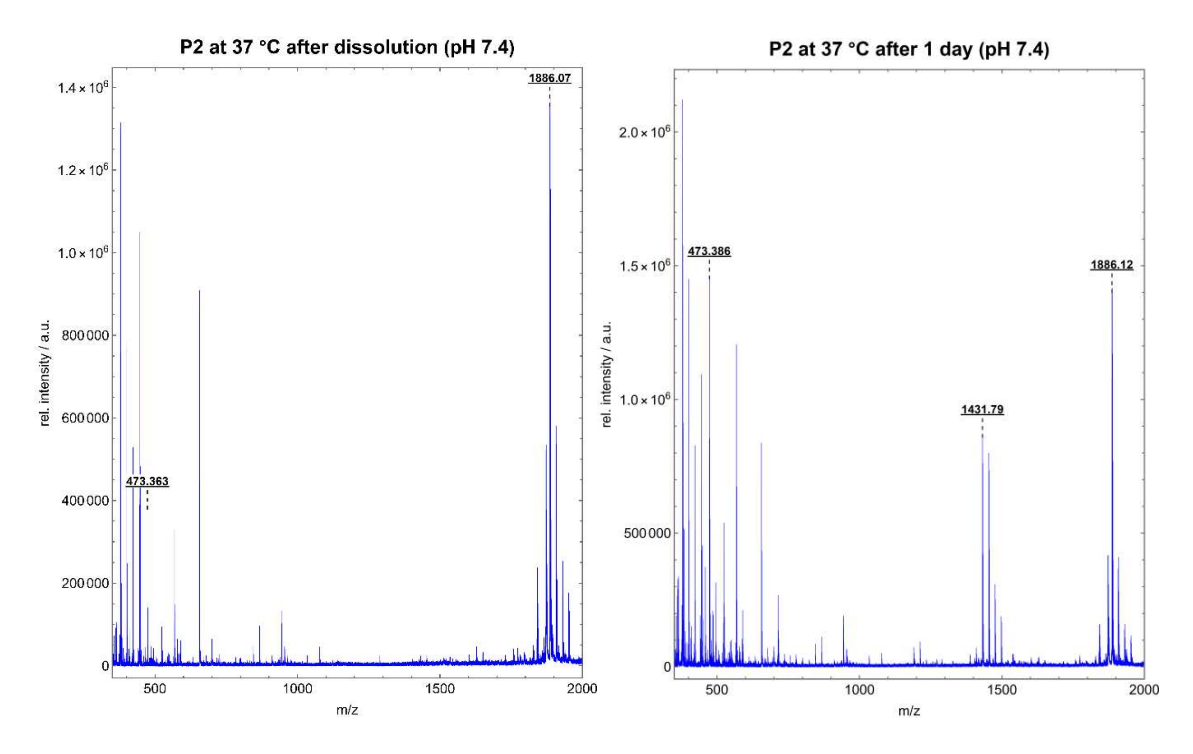


**Figure S21.** MALDI-measurements of **P2** and hydrolysis products at 37 °C after dissolution at pH 7.4 (left) and after 1 day at pH 7.4 (right). Calculated mass of **P2**+H<sup>+</sup>: 1886.0435, calculated mass for DP1+H<sup>+</sup>: 473.3347, calculated mass for DP2+H<sup>+</sup>: 1431.7267.

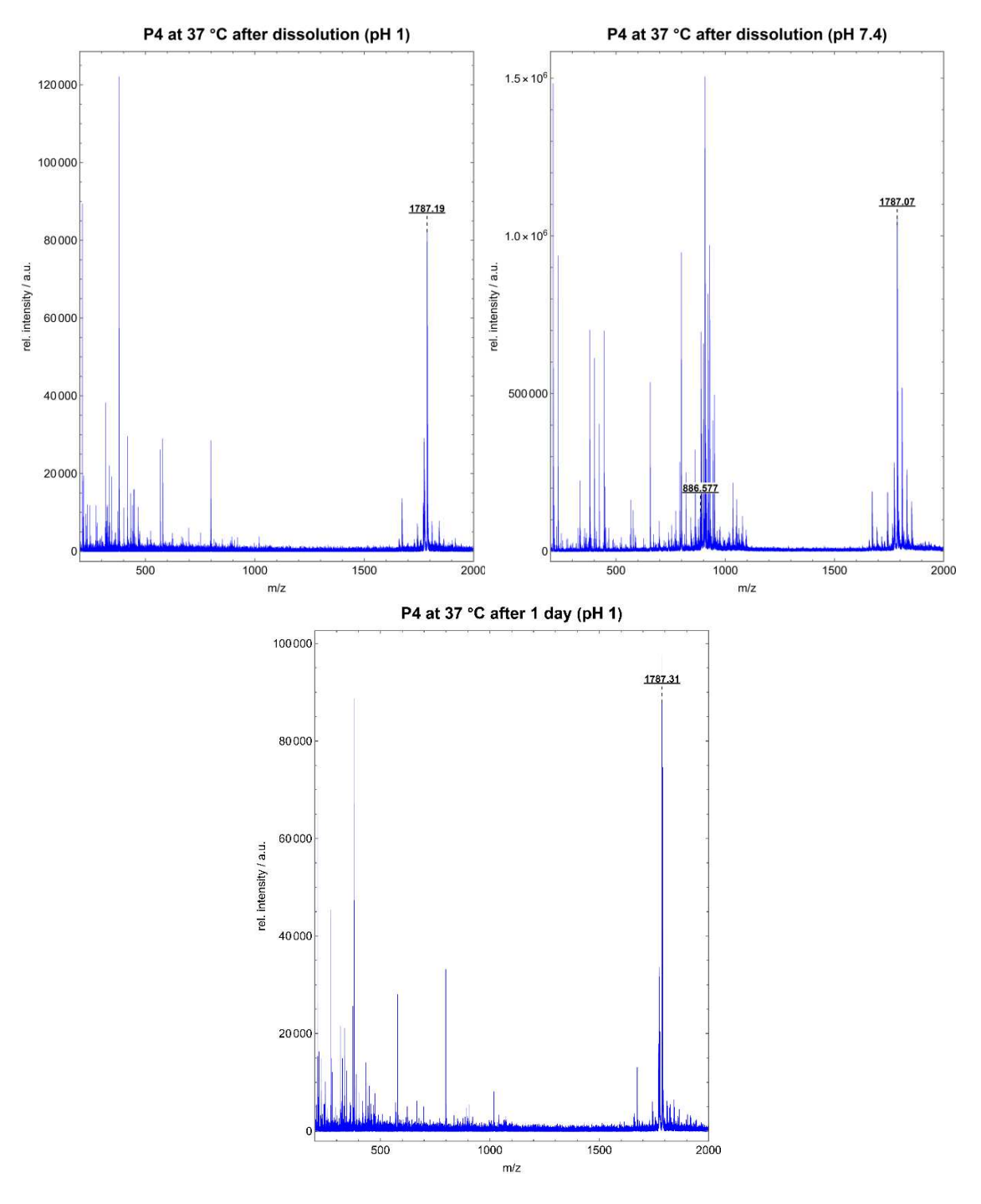


**Figure S22.** MALDI-measurements of **P4** and hydrolysis products at 37 °C after dissolution at pH 7.4 (top, left), after dissolution at pH 1 (top, right), and after 1 day at pH 1 (bottom). Calculated mass of **P4**+H<sup>+</sup>: 1786.9571, calculated mass for DP1+H<sup>+</sup>: 886.4934, calculated mass for DP2+H<sup>+</sup>: 919.4996.

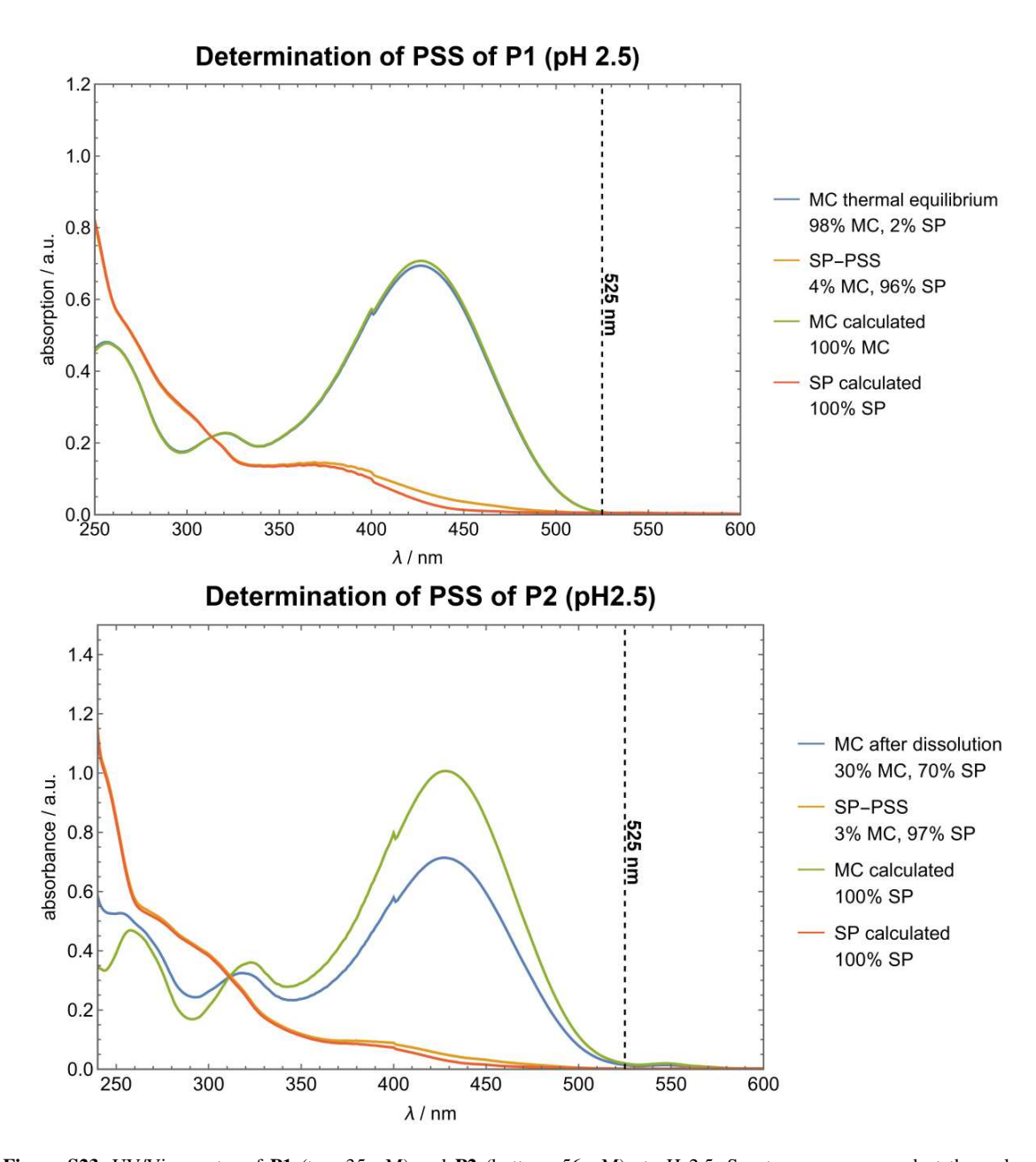


Figure S23. UV/Vis-spectra of P1 (top, 35  $\mu M$ ) and P2 (bottom, 56  $\mu M$ ) at pH 2.5. Spectra were measured at thermal equilibrium (P1), after dissolution (P2) and in the SP-PSS (after irradiation with green light for 10 min). SP:MC ratio was analyzed with HPLC and the spectra of the pure MC- and SP-form were calculated using Mathematic 13.3.1.0.

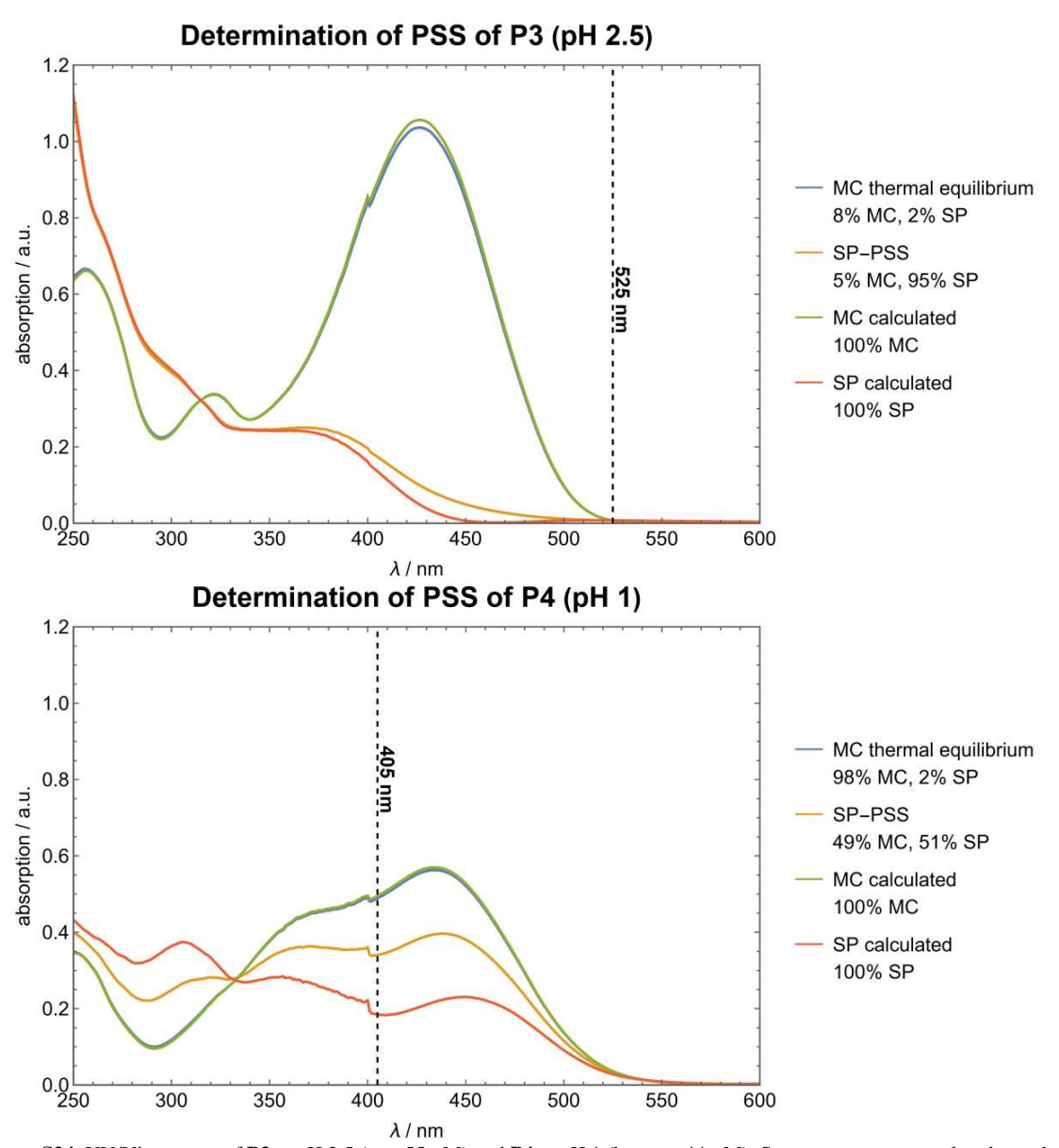


Figure S24. UV/Vis-spectra of P3 at pH 2.5 (top, 55  $\mu$ M) and P4 at pH 1 (bottom, 44  $\mu$ M). Spectra were measured at thermal equilibrium and in the SP-PSS (for P3 after irradiation with green light for 10 min, for P4 after irradiation with 405 nm for 10 min). SP:MC ratio was analyzed with HPLC and the spectra of the pure MC- and SP-form were calculated using Mathematic 13.3.1.0.

## 5. NMR data of compounds and peptides and LC-MS of peptides

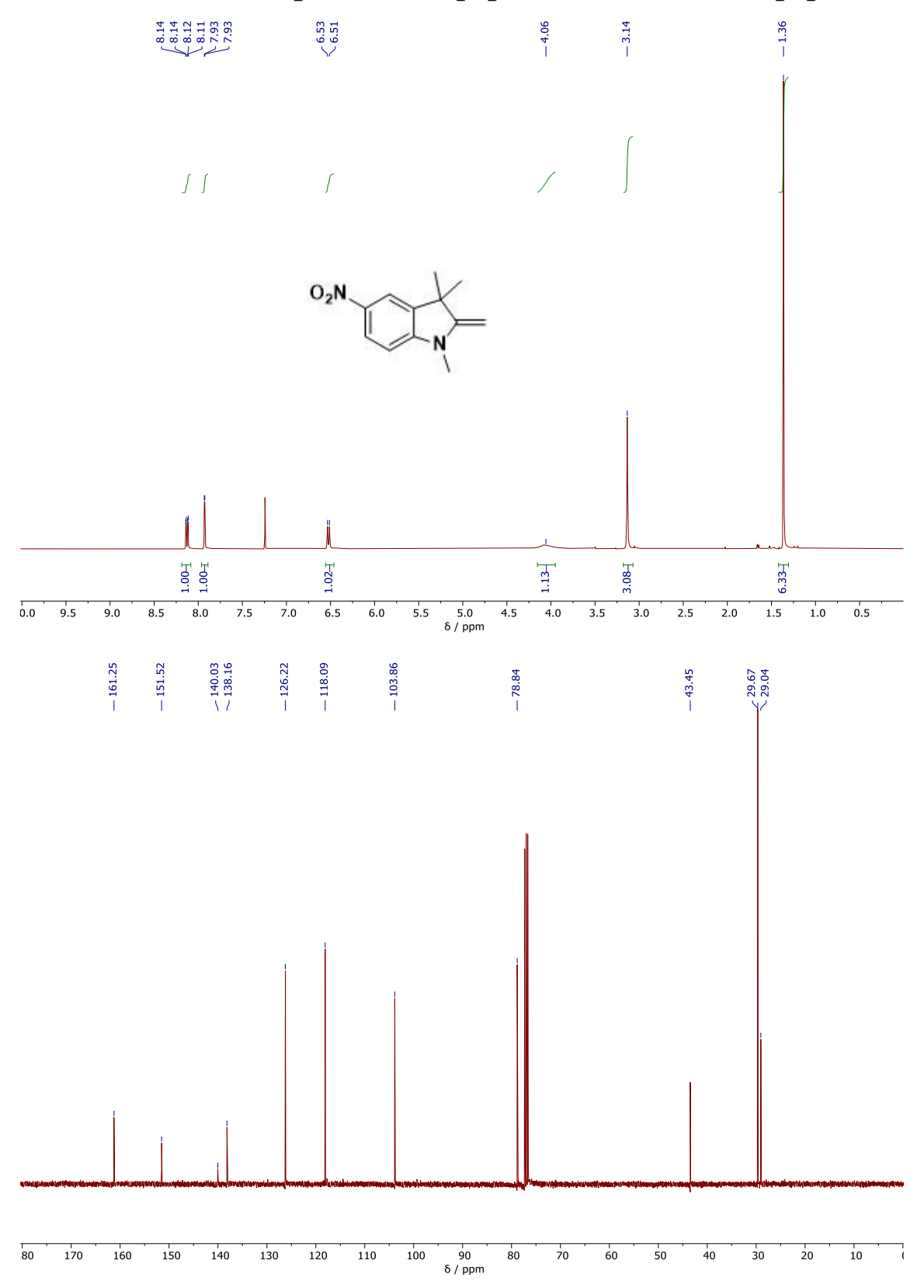


Figure S25.  $^{1}$ H-NMR (top, 500 MHz) and  $^{13}$ C-NMR (bottom, 125 MHz) in CDCl<sub>3</sub> of 3-I.

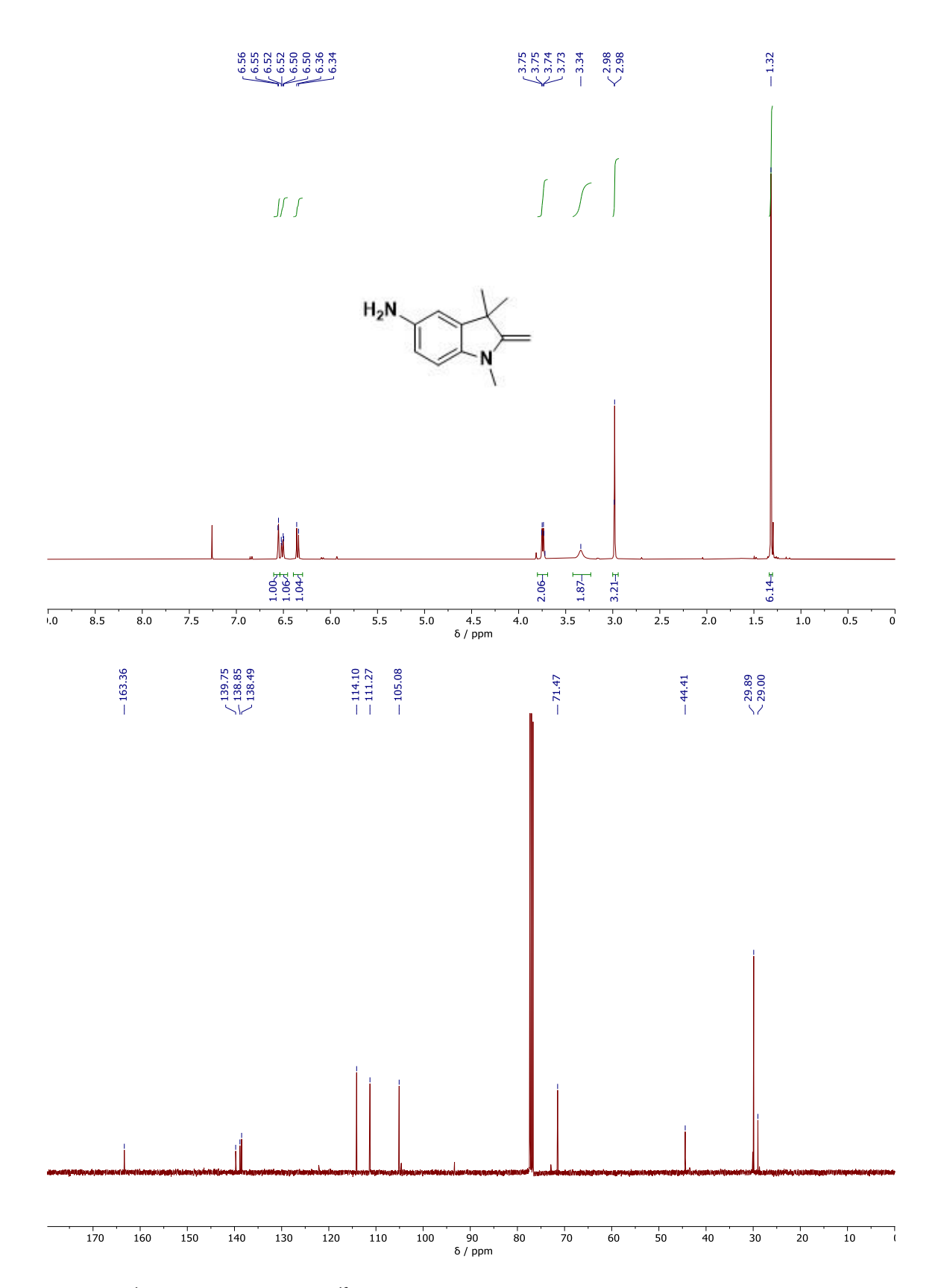


Figure S26.  $^1$ H-NMR (top, 500 MHz) and  $^{13}$ C-NMR (bottom, 125 MHz) in CDCl<sub>3</sub> of 3-II.

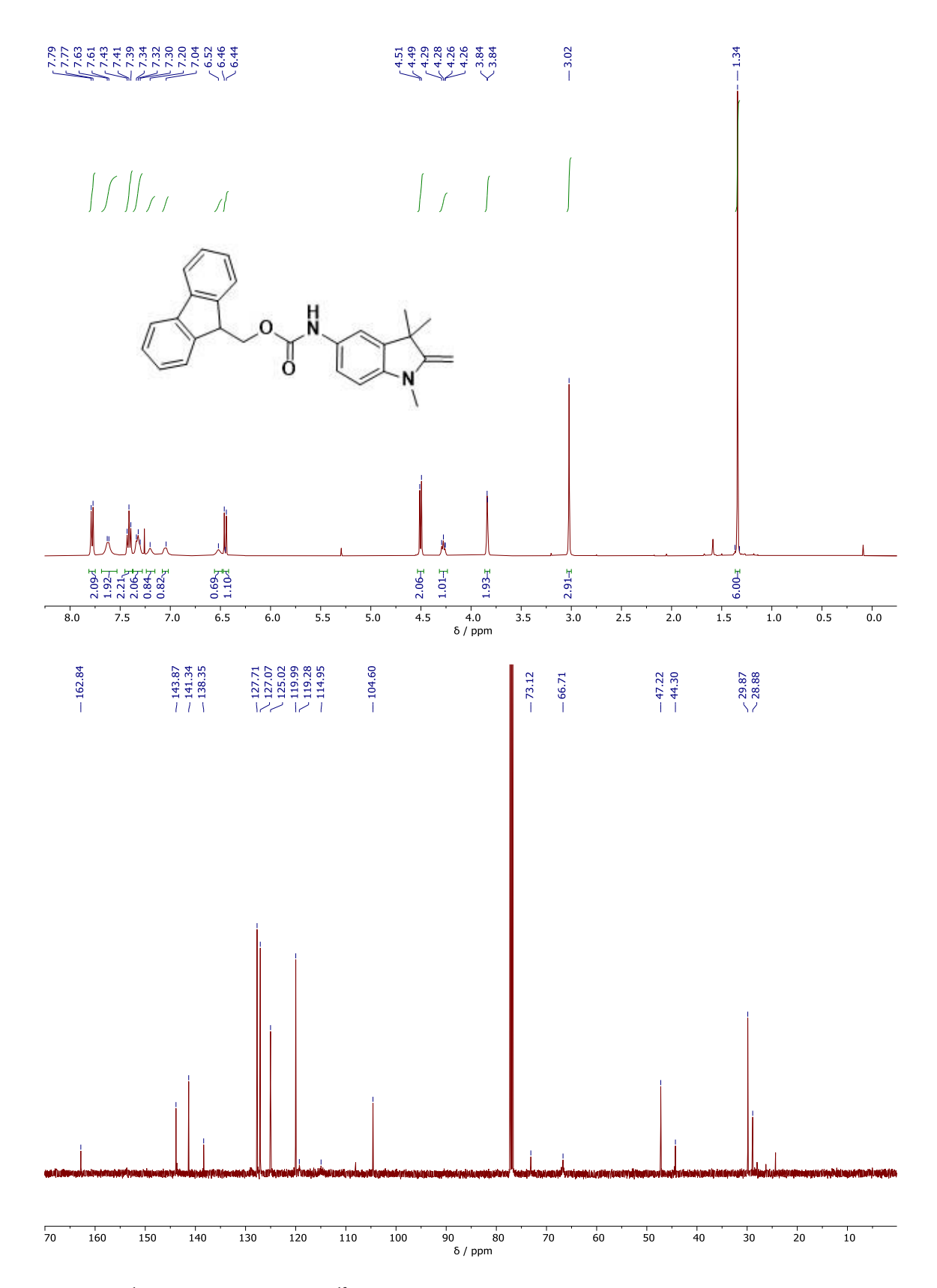


Figure S27.  $^1$ H-NMR (top, 500 MHz) and  $^{13}$ C-NMR (bottom, 125 MHz) in CDCl<sub>3</sub> of 4a.

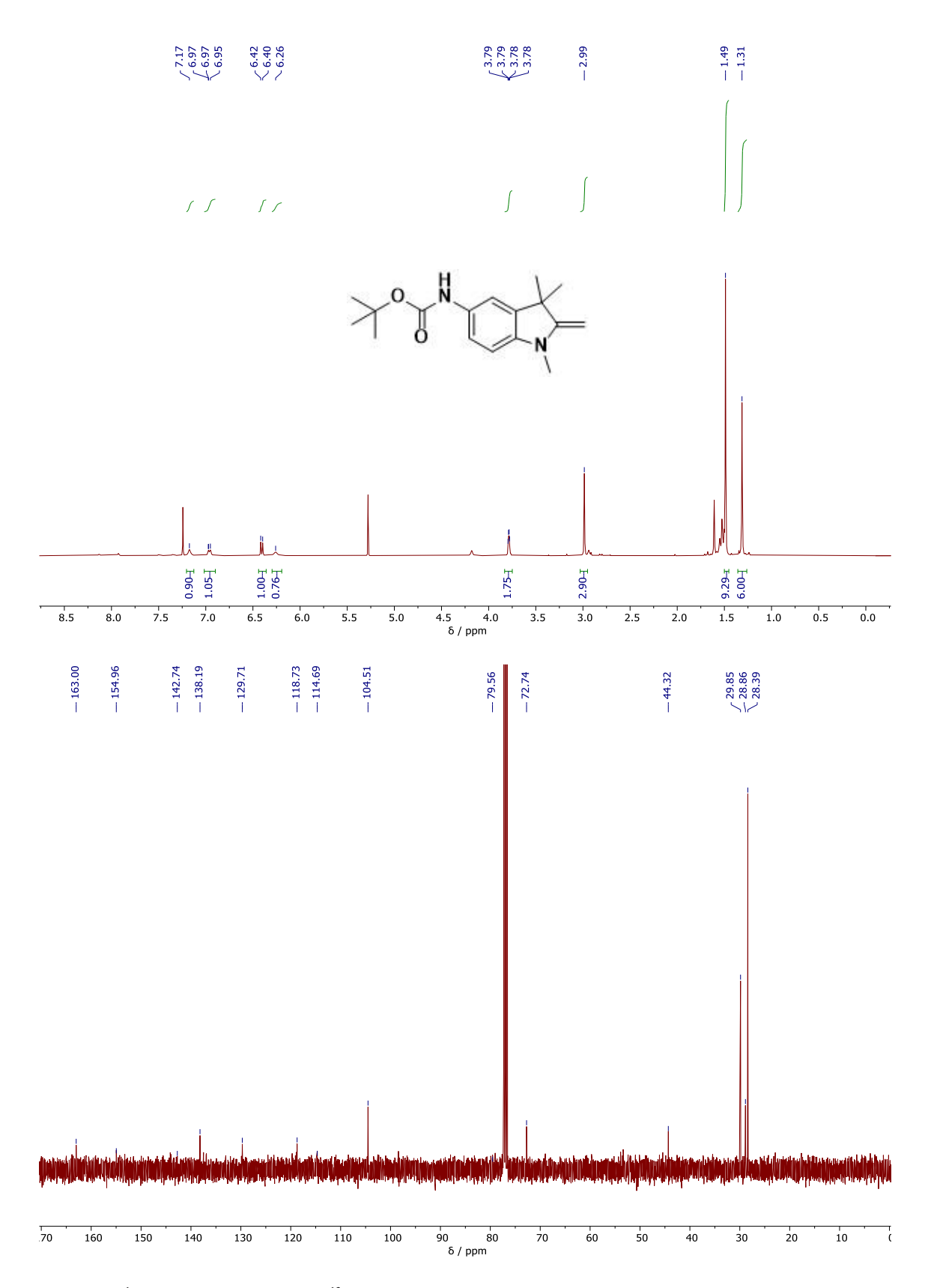


Figure S28.  $^1$ H-NMR (top, 400 MHz) and  $^{13}$ C-NMR (bottom, 100 MHz) in CDCl<sub>3</sub> of 4b.

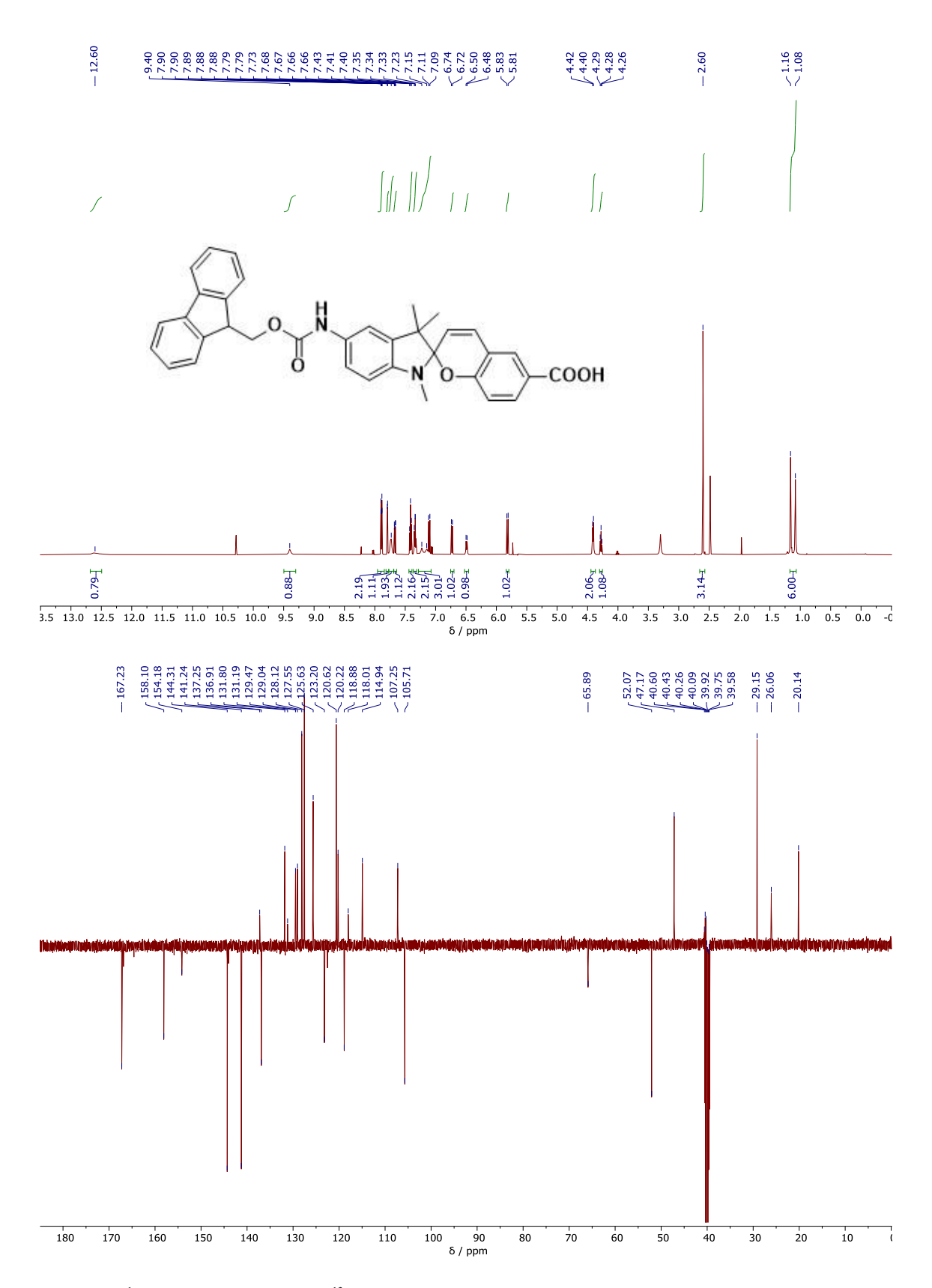
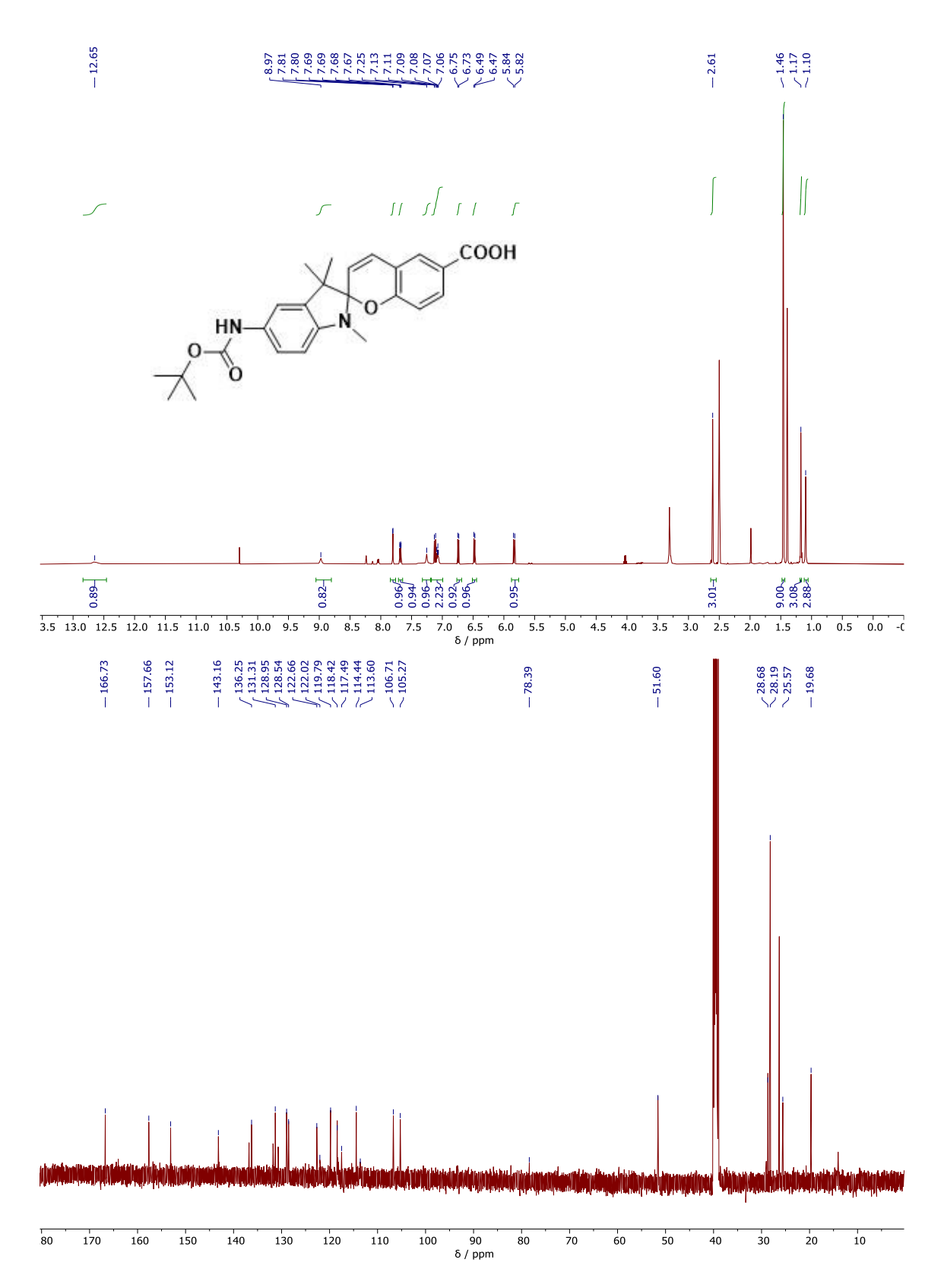


Figure S29.  $^1\mathrm{H}\text{-}\mathrm{NMR}$  (top, 500 MHz) and  $^{13}\mathrm{C}\text{-}\mathrm{NMR}$  (bottom, 125 MHz) in DMSO- $d_6$  of 1a.



**Figure S30.**  $^{1}$ H-NMR (top, 500 MHz) and  $^{13}$ C-NMR (bottom, 125 MHz) in DMSO- $d_6$  of **1b**.

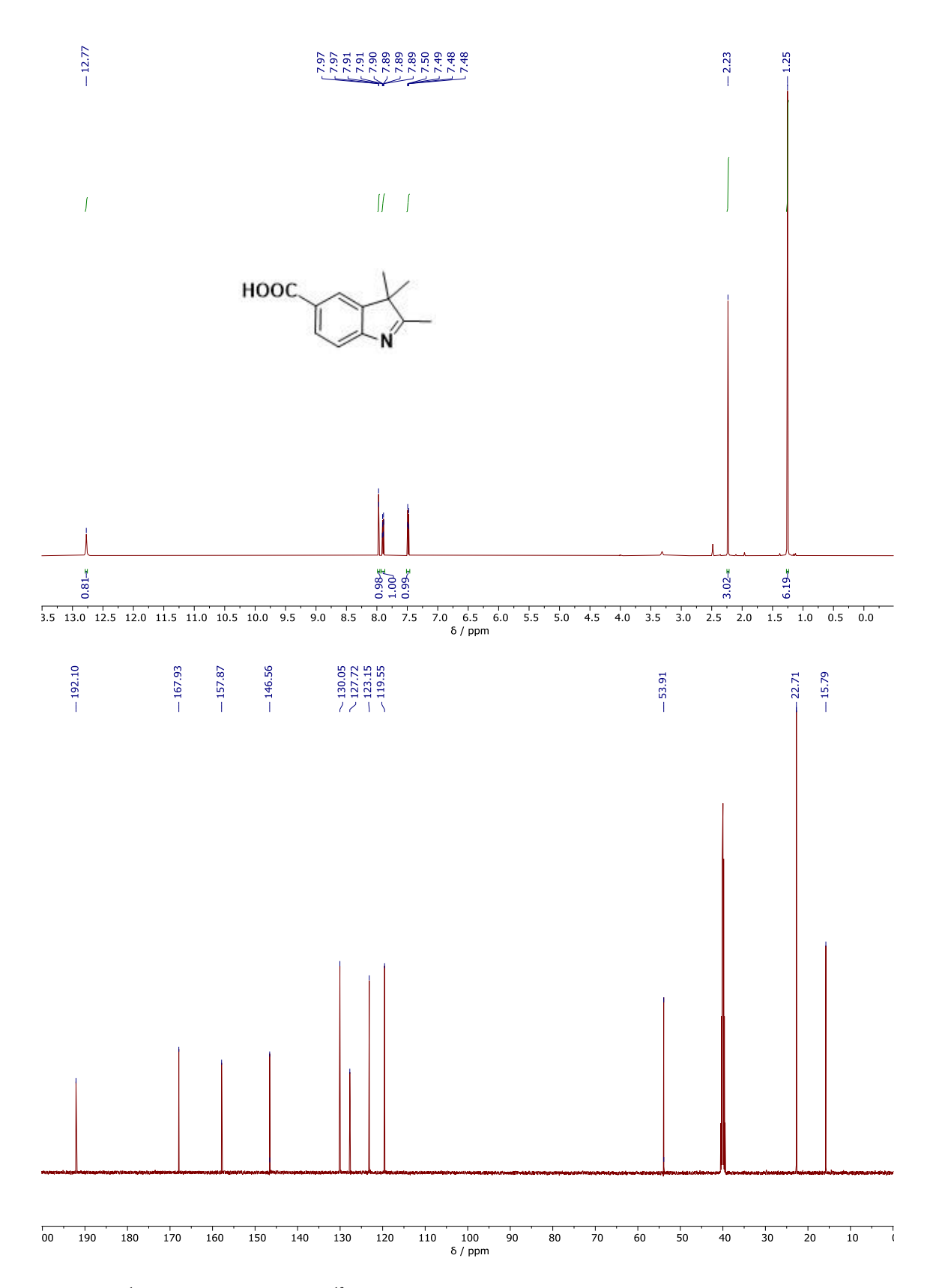


Figure S31.  $^{1}$ H-NMR (top, 500 MHz) and  $^{13}$ C-NMR (bottom, 125 MHz) in CDCl<sub>3</sub> of 6-I.

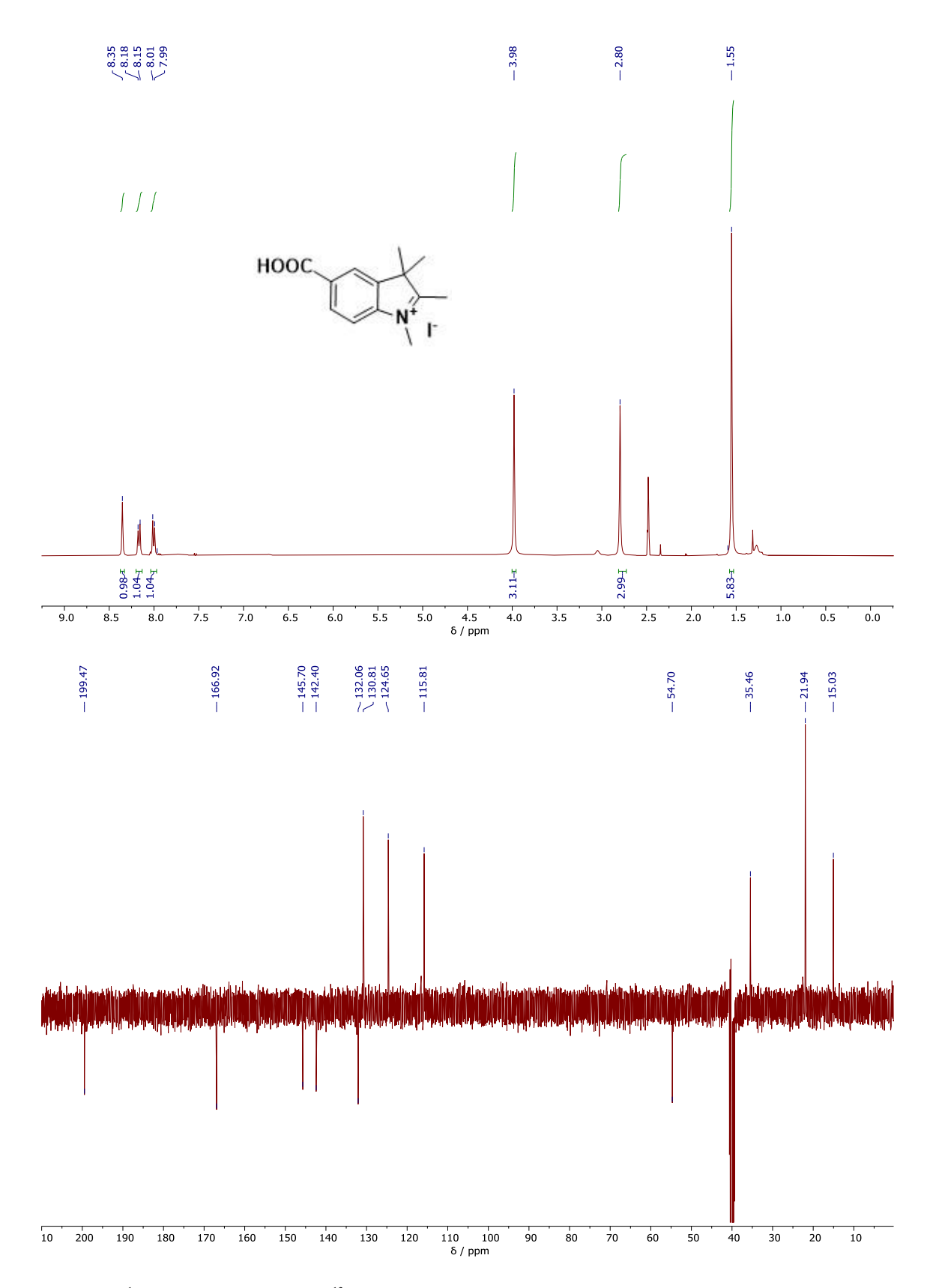


Figure S32.  $^1\text{H-NMR}$  (top, 400 MHz) and  $^{13}\text{C-NMR}$  (bottom, 100 MHz) in DMSO-d6 of 7.

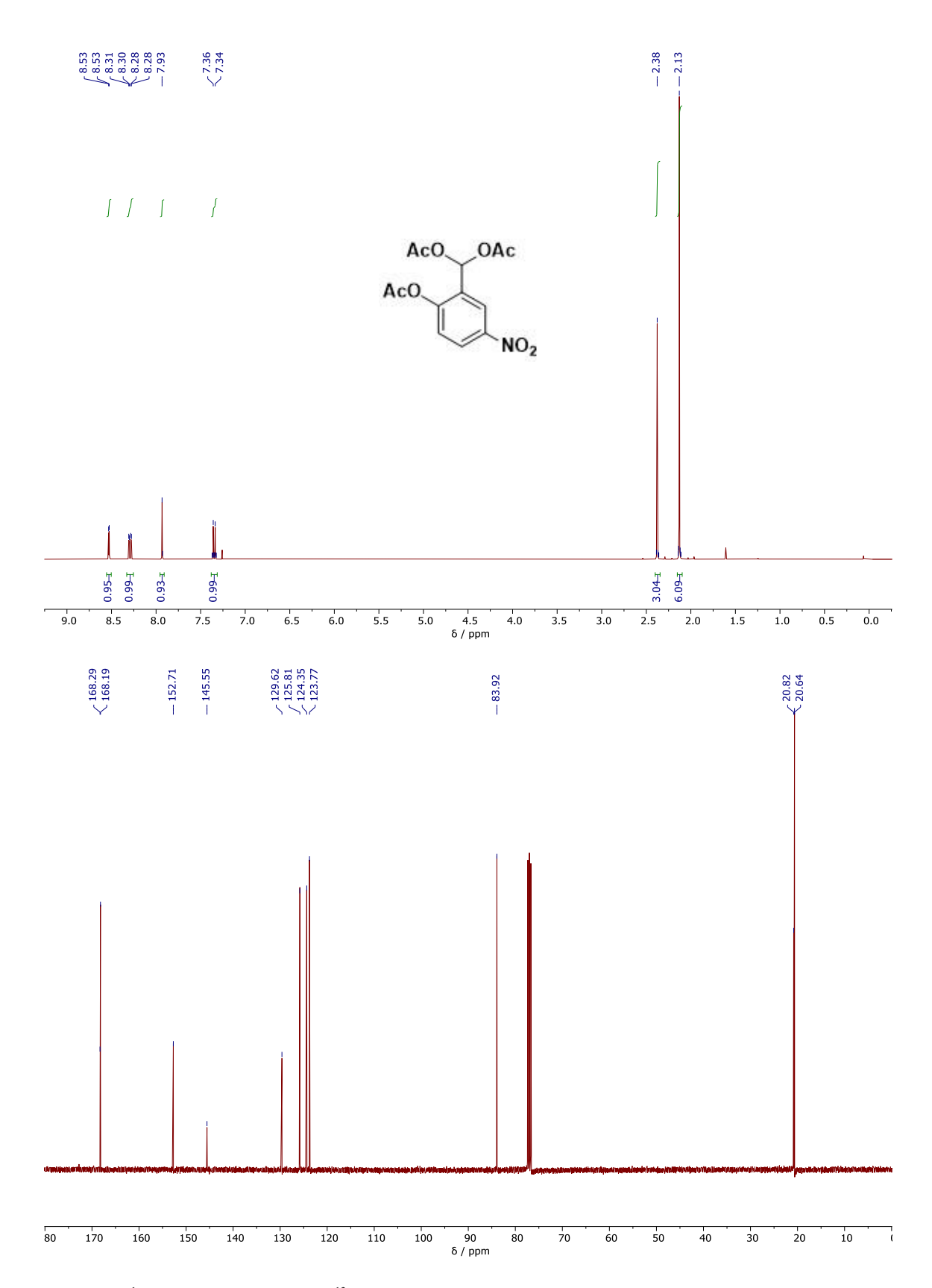


Figure S33. <sup>1</sup>H-NMR (top, 400 MHz) and <sup>13</sup>C-NMR (bottom, 100 MHz) in CDCl<sub>3</sub> of 8-I.

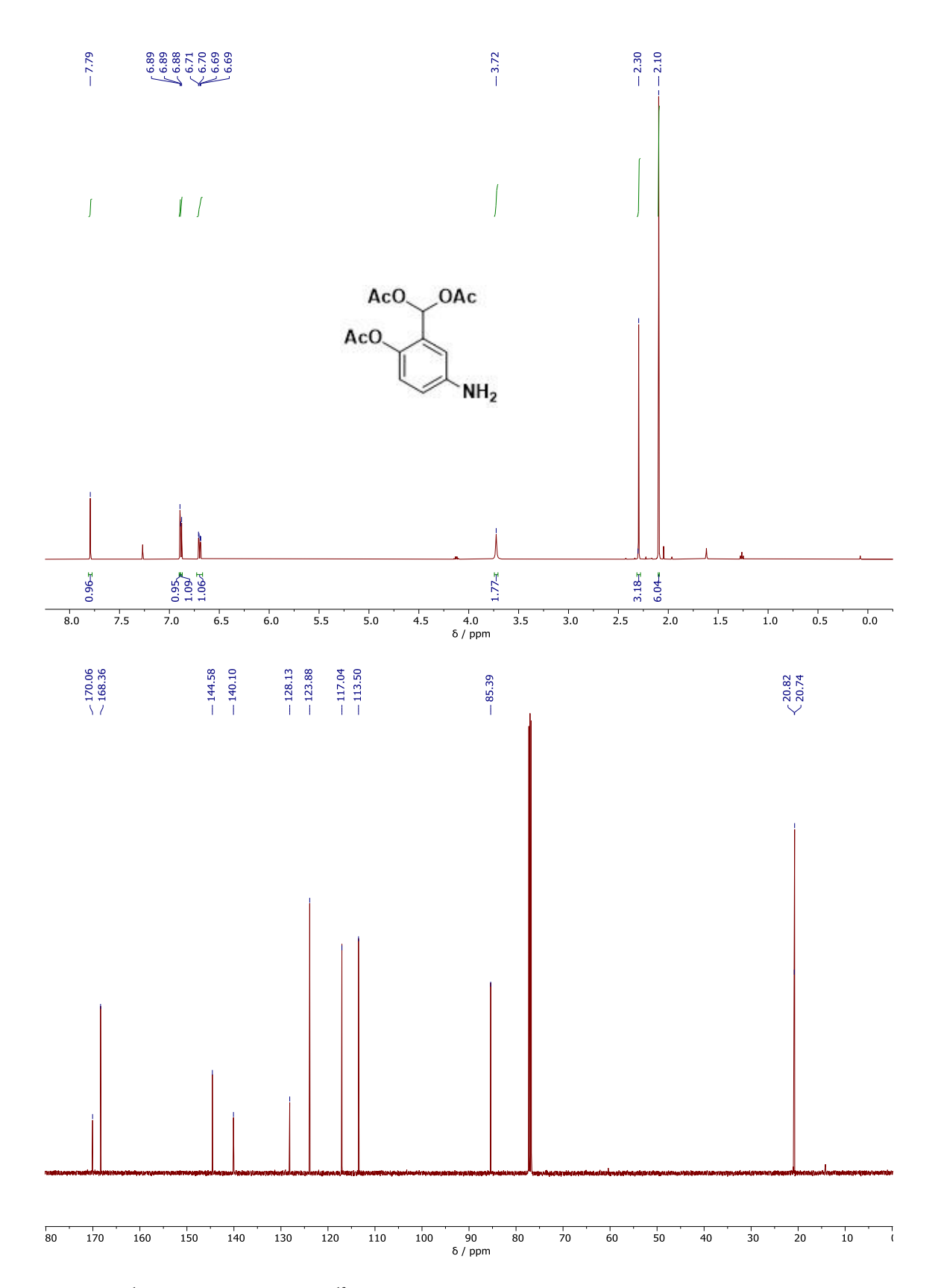


Figure S34.  $^1$ H-NMR (top, 500 MHz) and  $^{13}$ C-NMR (bottom, 125 MHz) in CDCl<sub>3</sub> of 8-II.

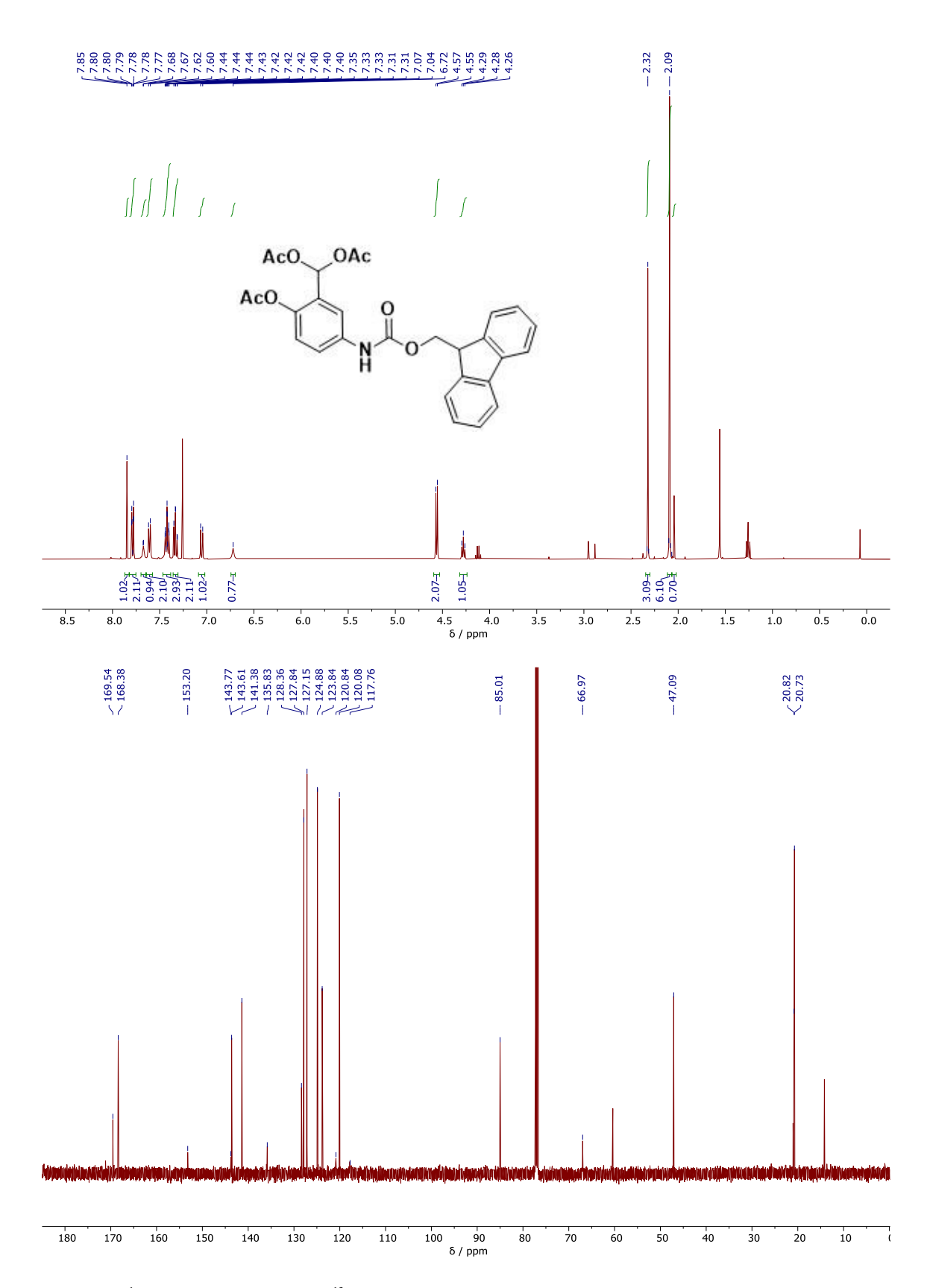


Figure S35.  $^1\text{H-NMR}$  (top, 500 MHz) and  $^{13}\text{C-NMR}$  (bottom, 125 MHz) in CDCl<sub>3</sub> of 9a.

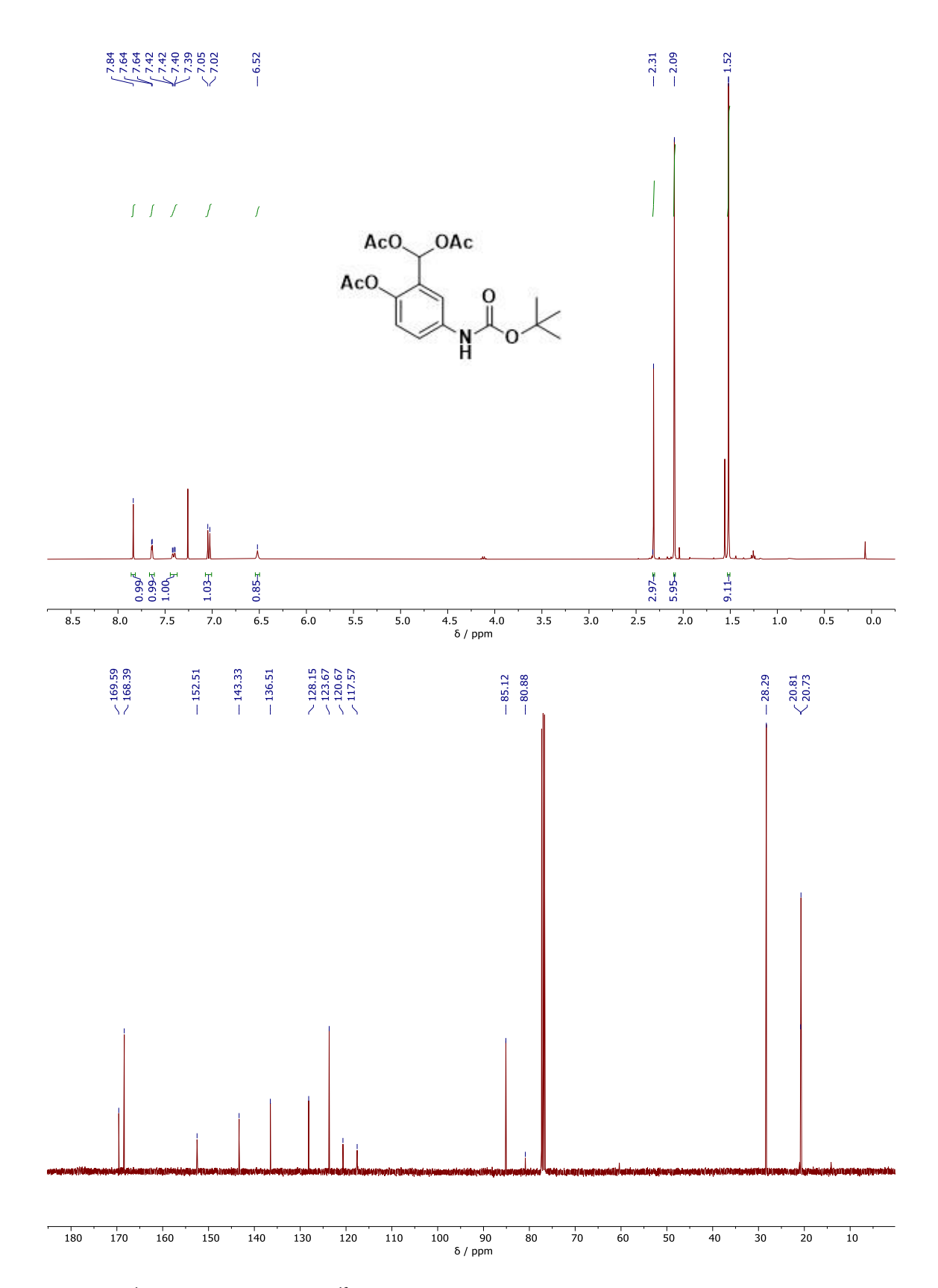
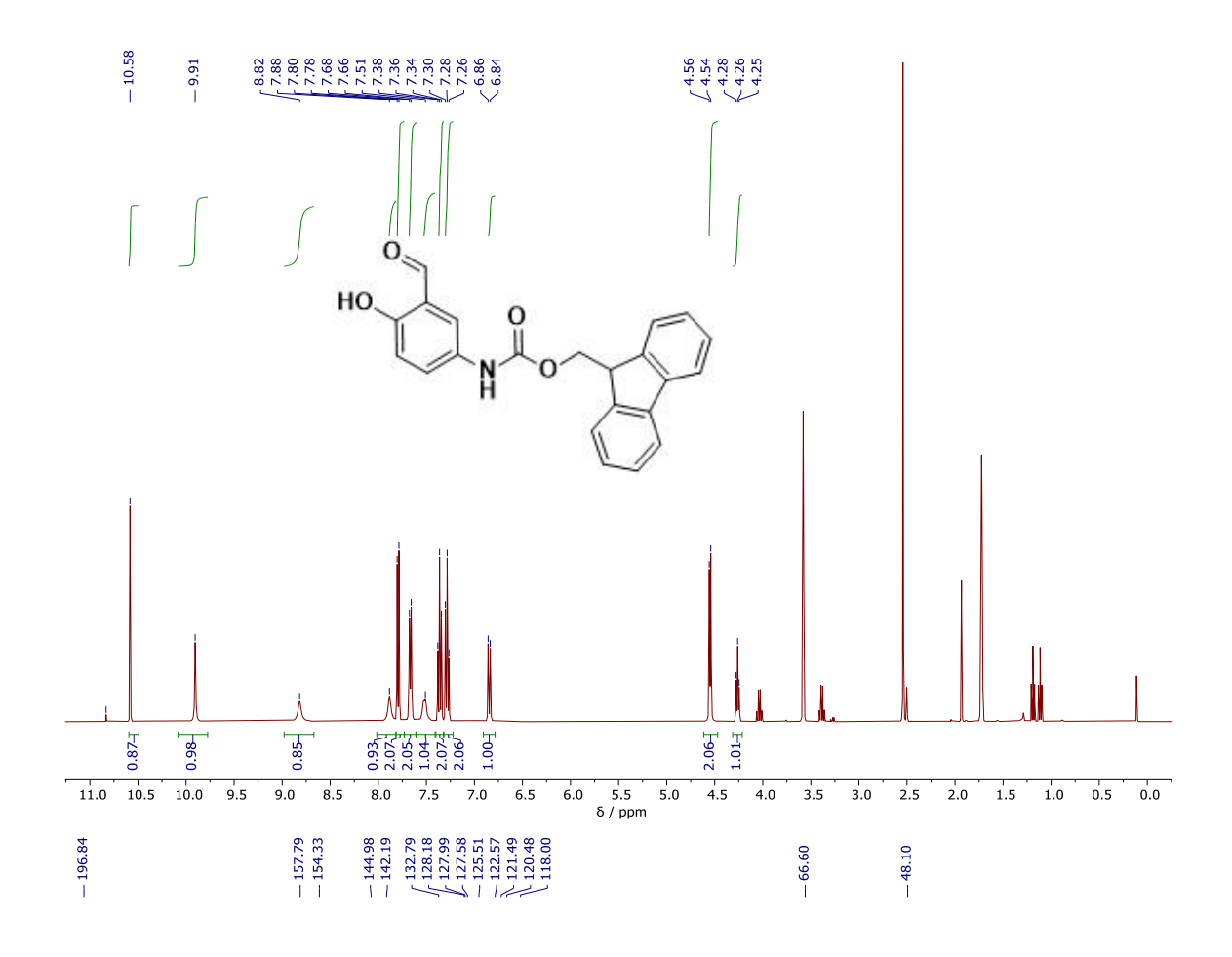


Figure S36. <sup>1</sup>H-NMR (top, 400 MHz) and <sup>13</sup>C-NMR (bottom, 100 MHz) in CDCl<sub>3</sub> of 9b.



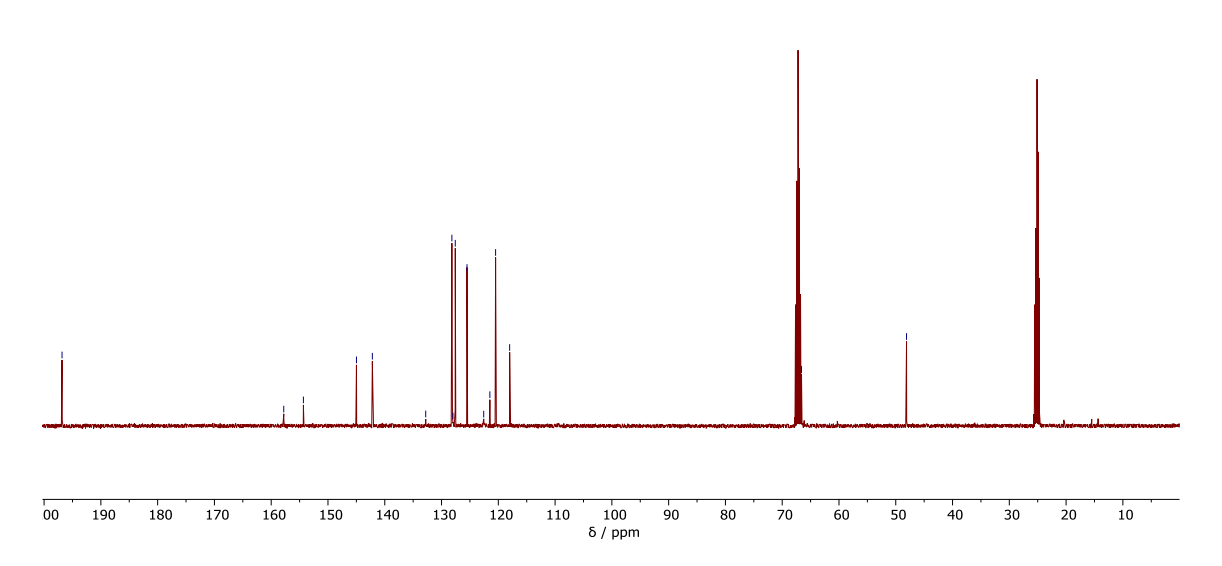


Figure S37.  $^{1}$ H-NMR (top, 400 MHz) and  $^{13}$ C-NMR (bottom, 100 MHz) in THF- $d_8$  of 10a.

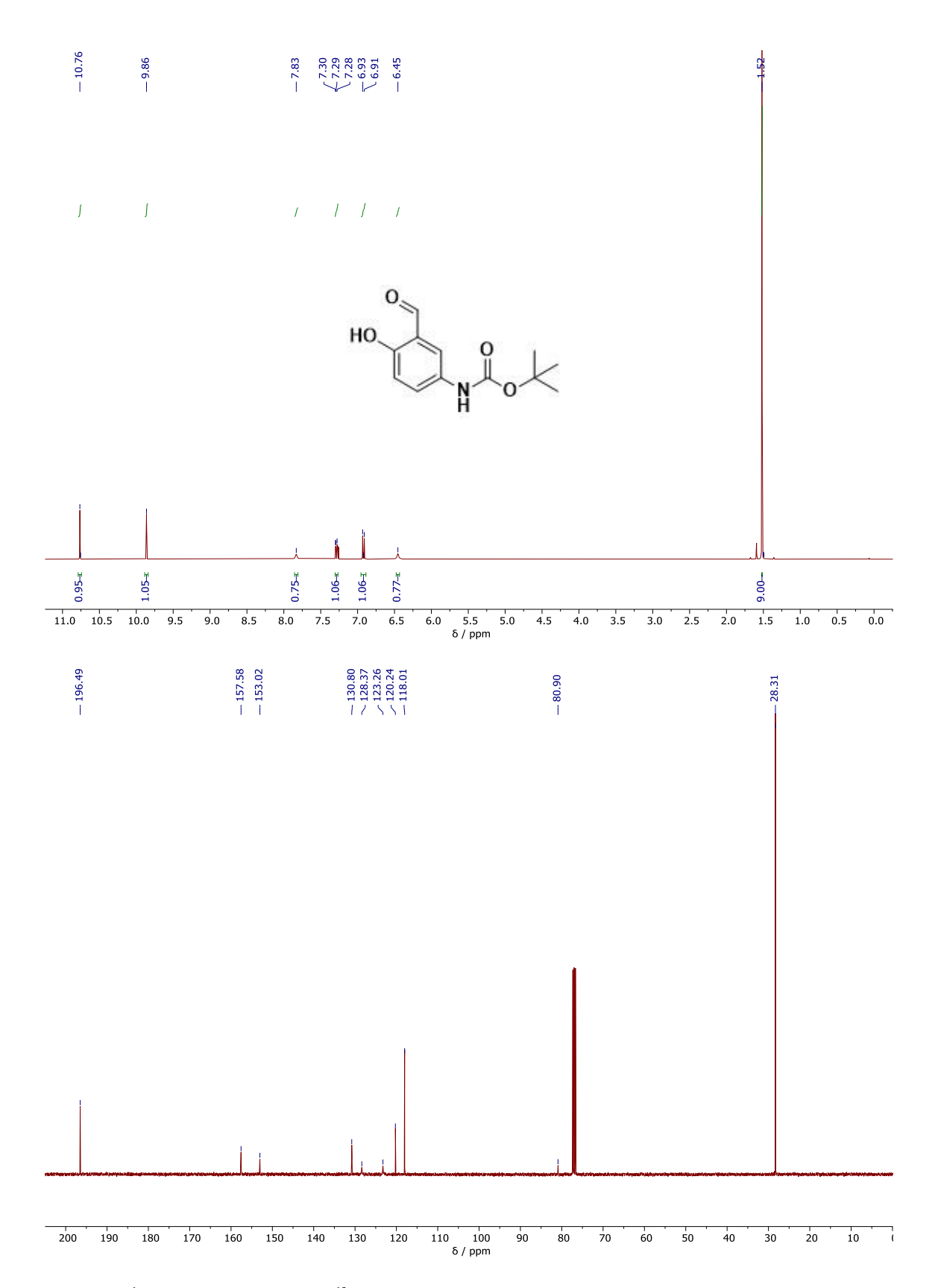


Figure S38. <sup>1</sup>H-NMR (top, 400 MHz) and <sup>13</sup>C-NMR (bottom, 100 MHz) in CDCl<sub>3</sub> of 10b.

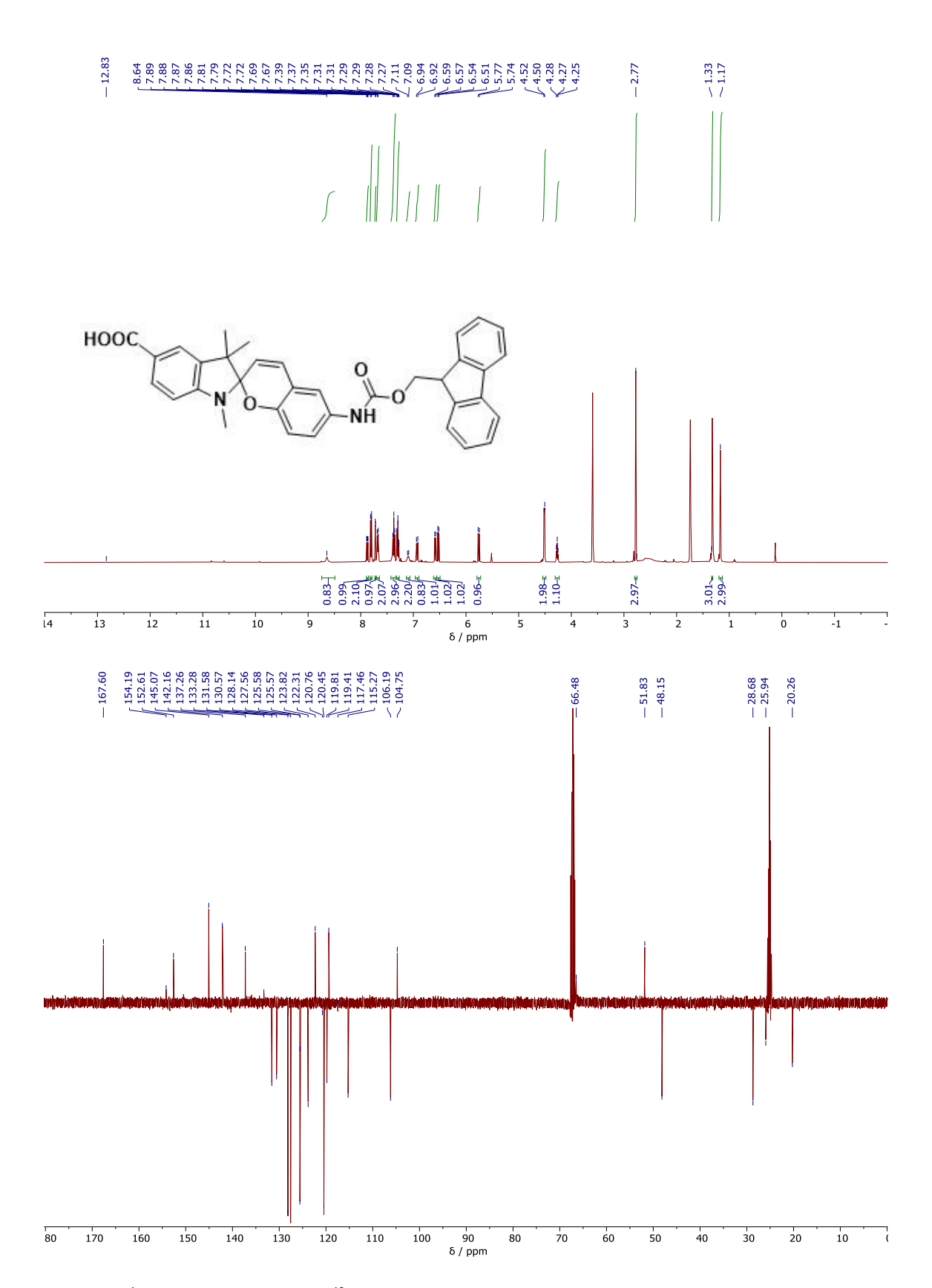
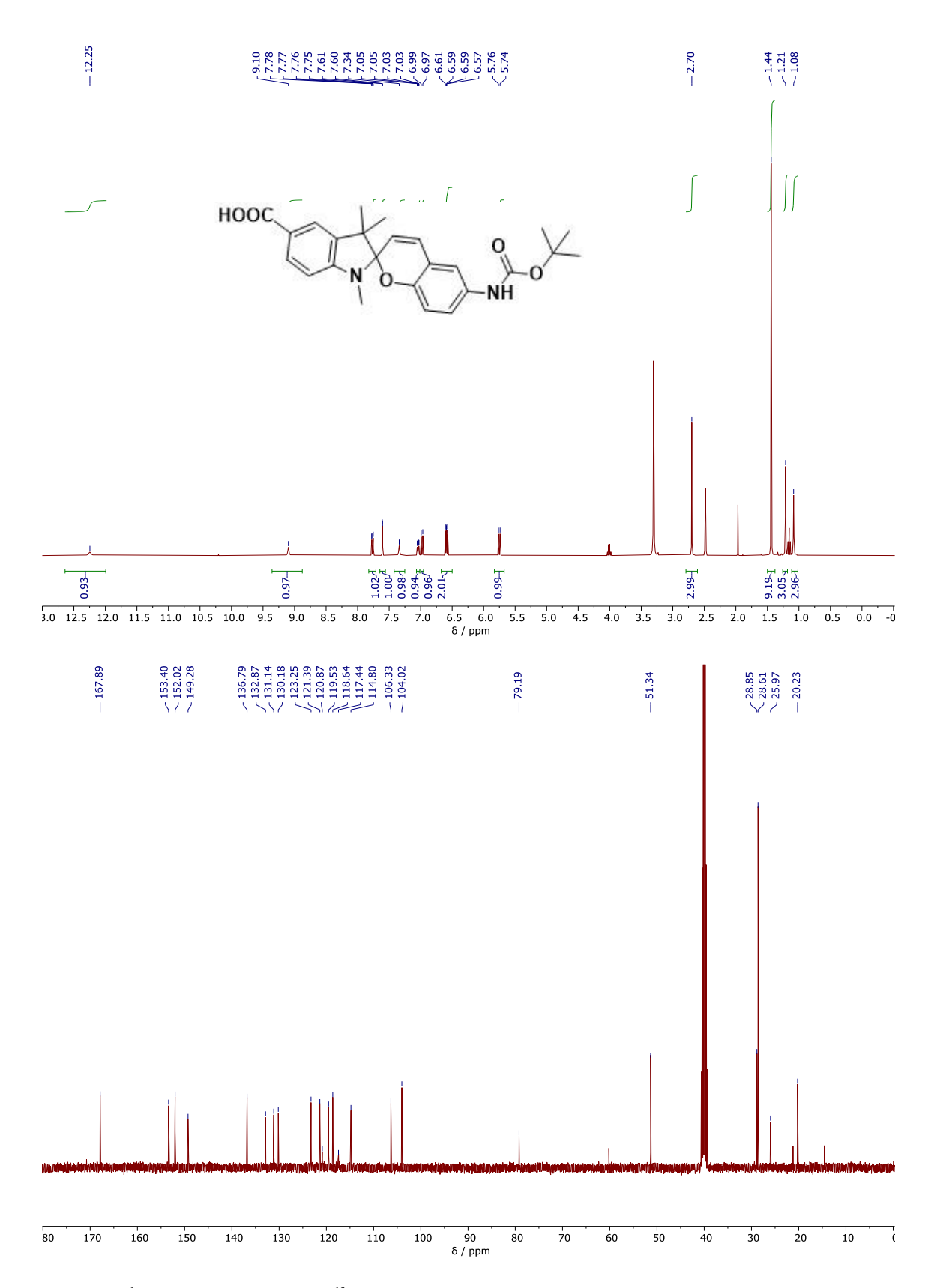


Figure S39.  $^1$ H-NMR (top, 400 MHz) and  $^{13}$ C-NMR (bottom, 100 MHz) in THF- $d_8$  of 2a.



**Figure S40.**  $^{1}$ H-NMR (top, 400 MHz) and  $^{13}$ C-NMR (bottom, 100 MHz) in DMSO- $d_6$  of **2b**.

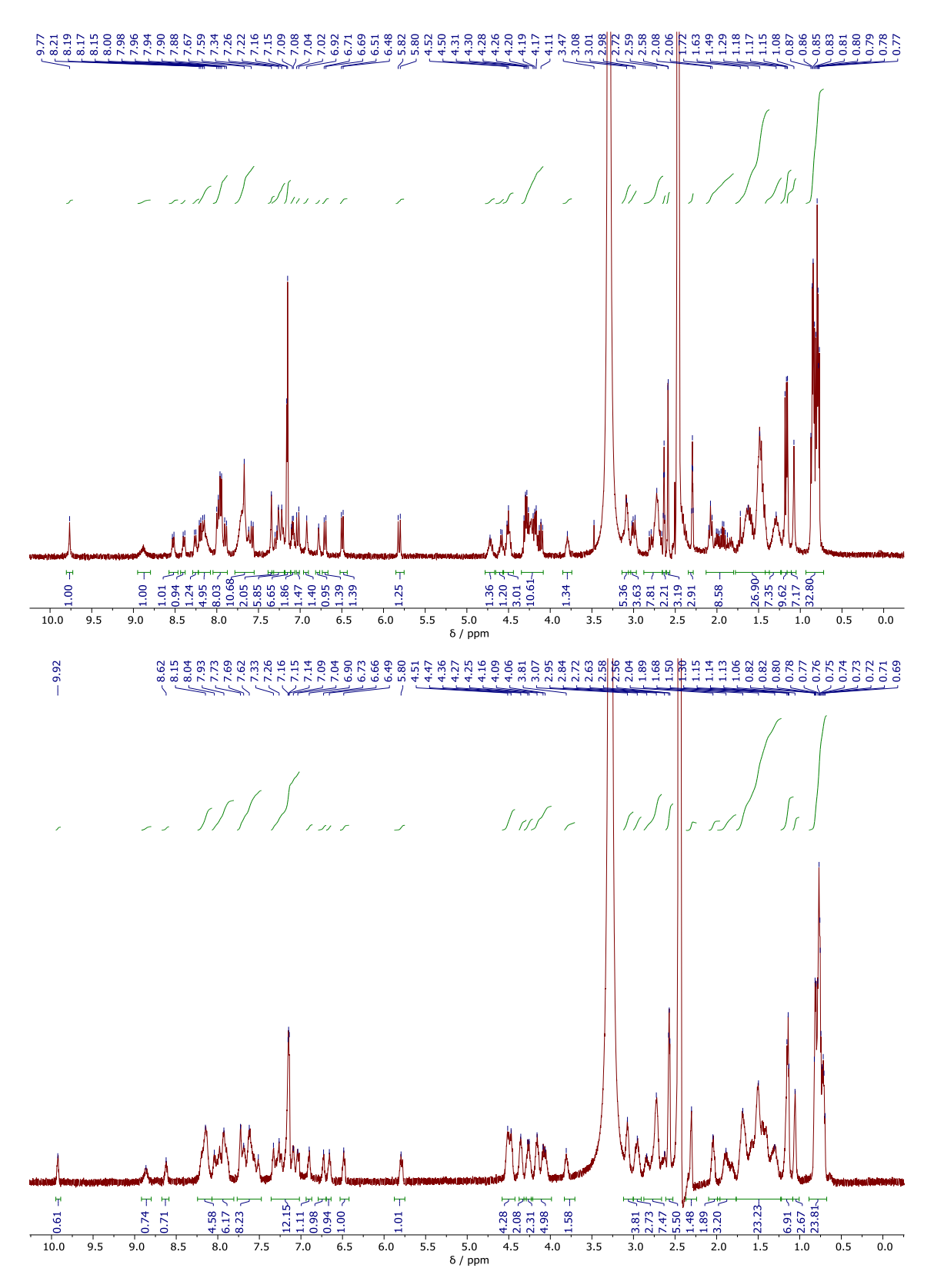


Figure S41: <sup>1</sup>H-NMR spectra (400 MHz, DMSO-*d*<sub>6</sub>) of P1 (top, mixture of isomers) and P2 (bottom, mixture of isomers).

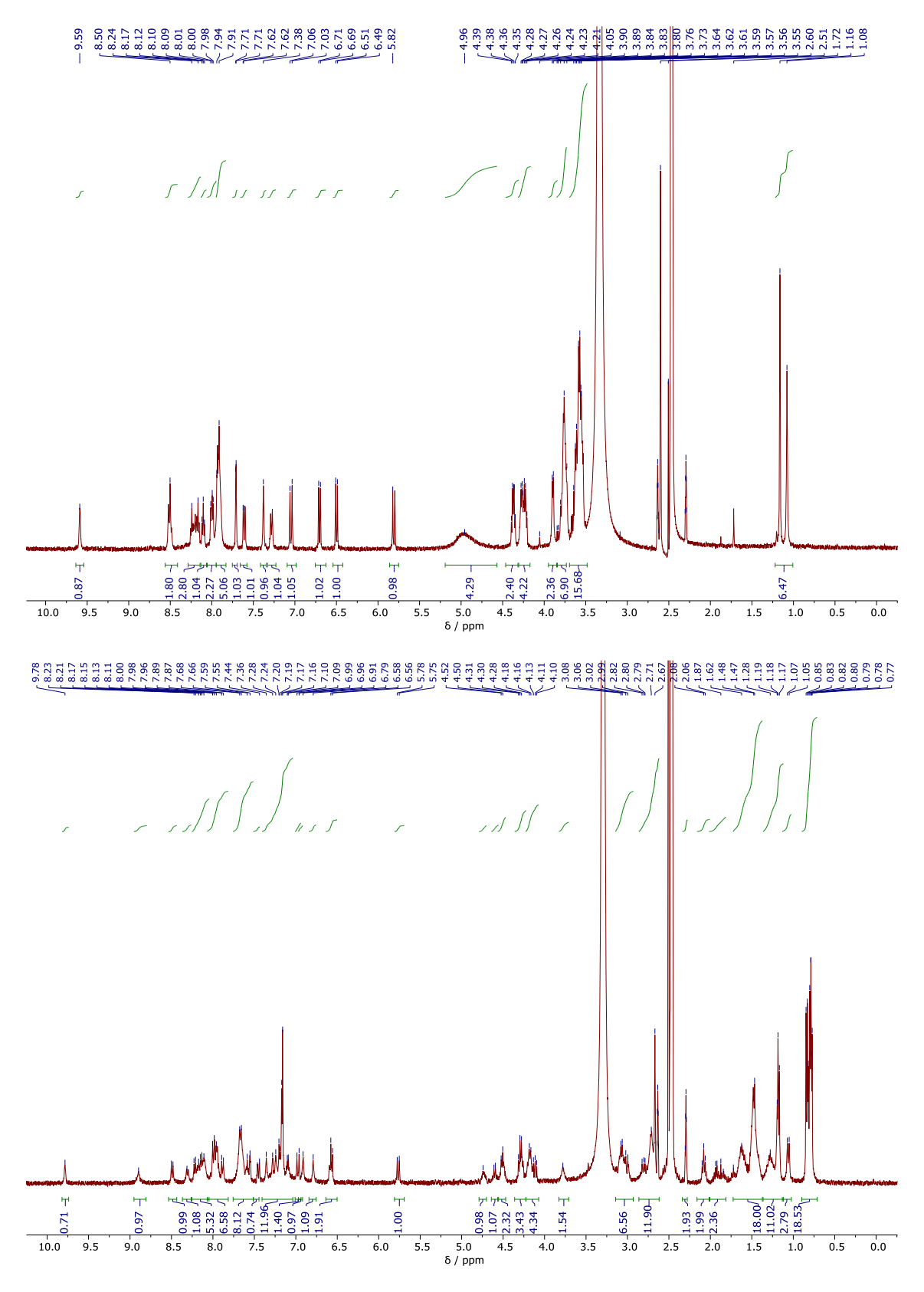
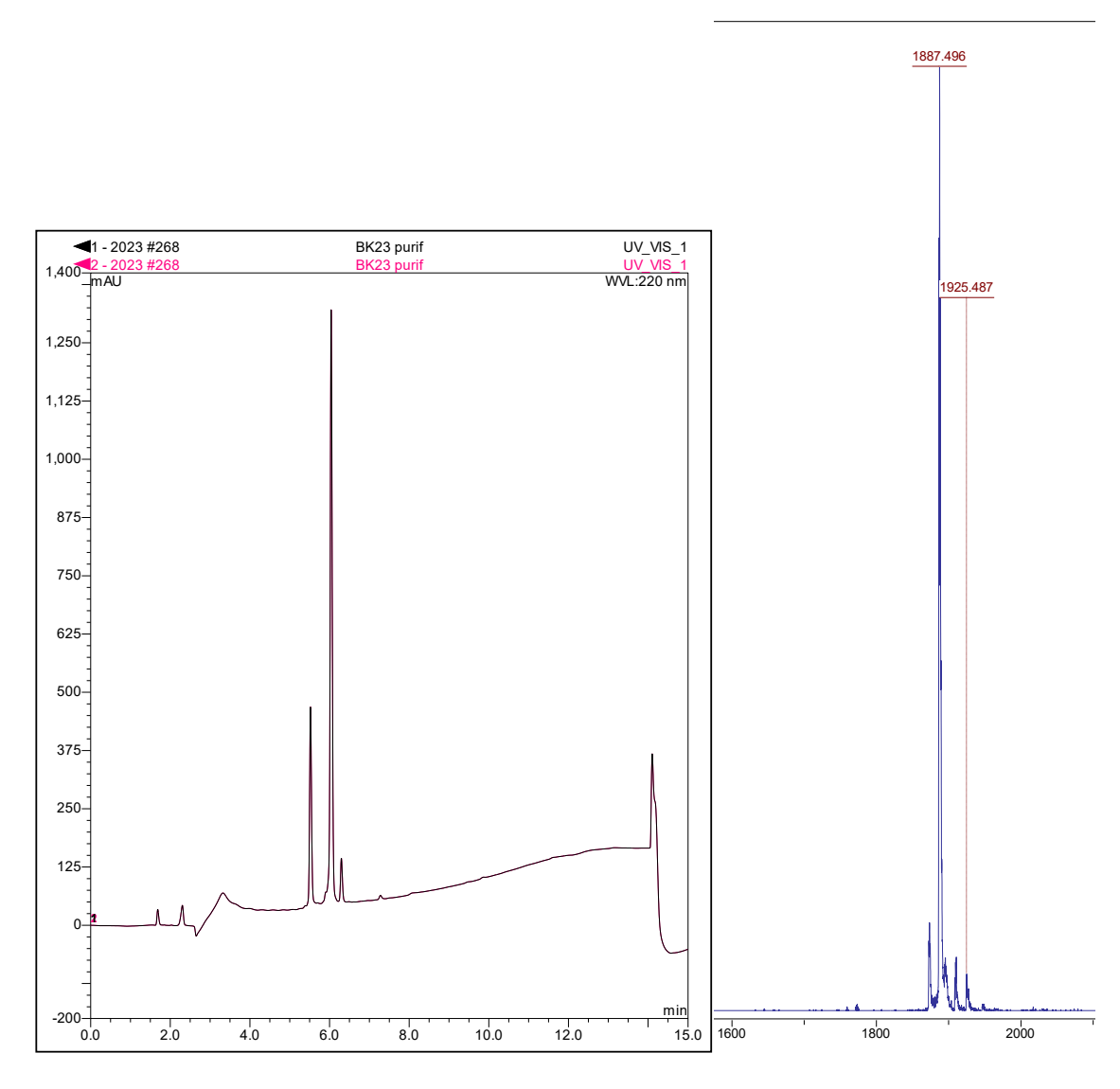
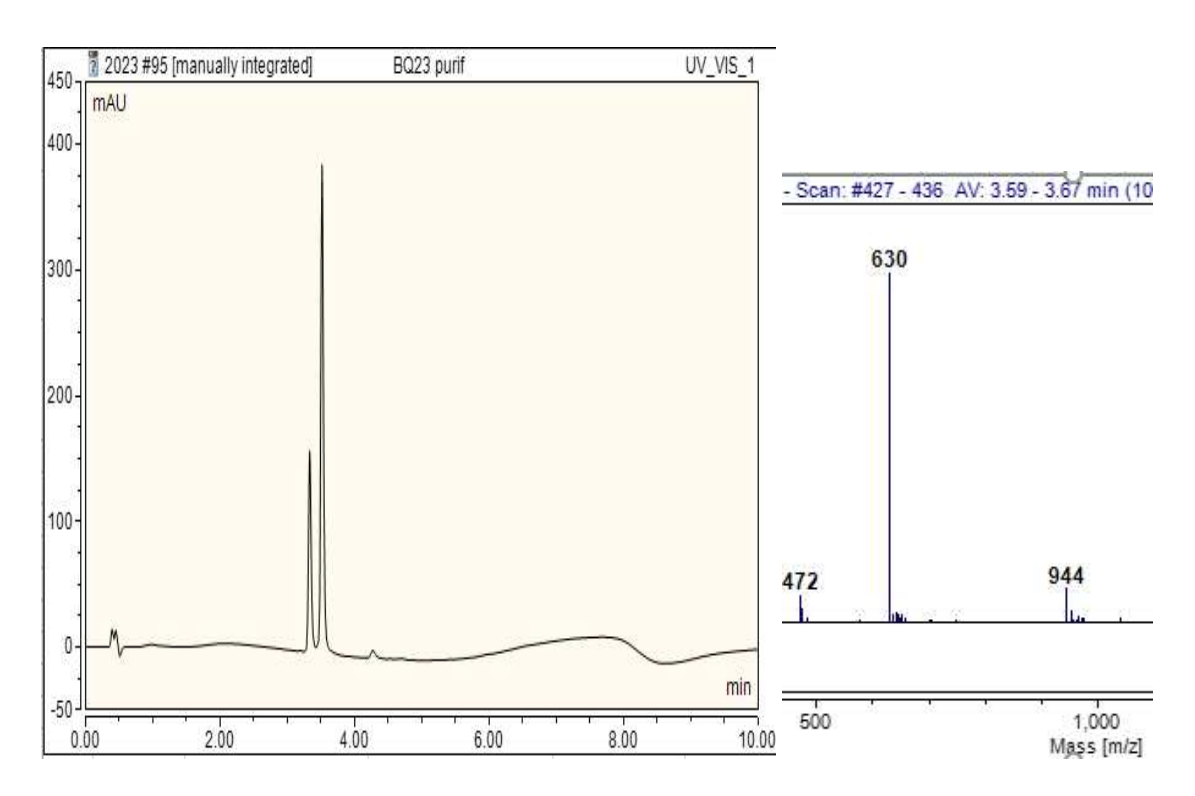


Figure S42: <sup>1</sup>H-NMR spectra (400 MHz, DMSO-*d*<sub>6</sub>) of **P3** (top, mixture of isomers) and **P4** (bottom, mixture of isomers).



**Figure S43:** (**left**) HPLC-trace of P1 (MC- and SP-isomer between 5 and 7 min). (**right**) MALDI-spectrum of **P1** (*m/z* calculated: 1886.0435 found: 1887.496).



**Figure S44:** (left) HPLC-trace of P2 (MC- and SP-isomer between 3 and 4min). (right) LC-MS spectrum of P2 (m/z calculated [M+2H]<sup>2+</sup>: 945 found 945; calculated [M+3H]<sup>3+</sup>: 630 found 630).

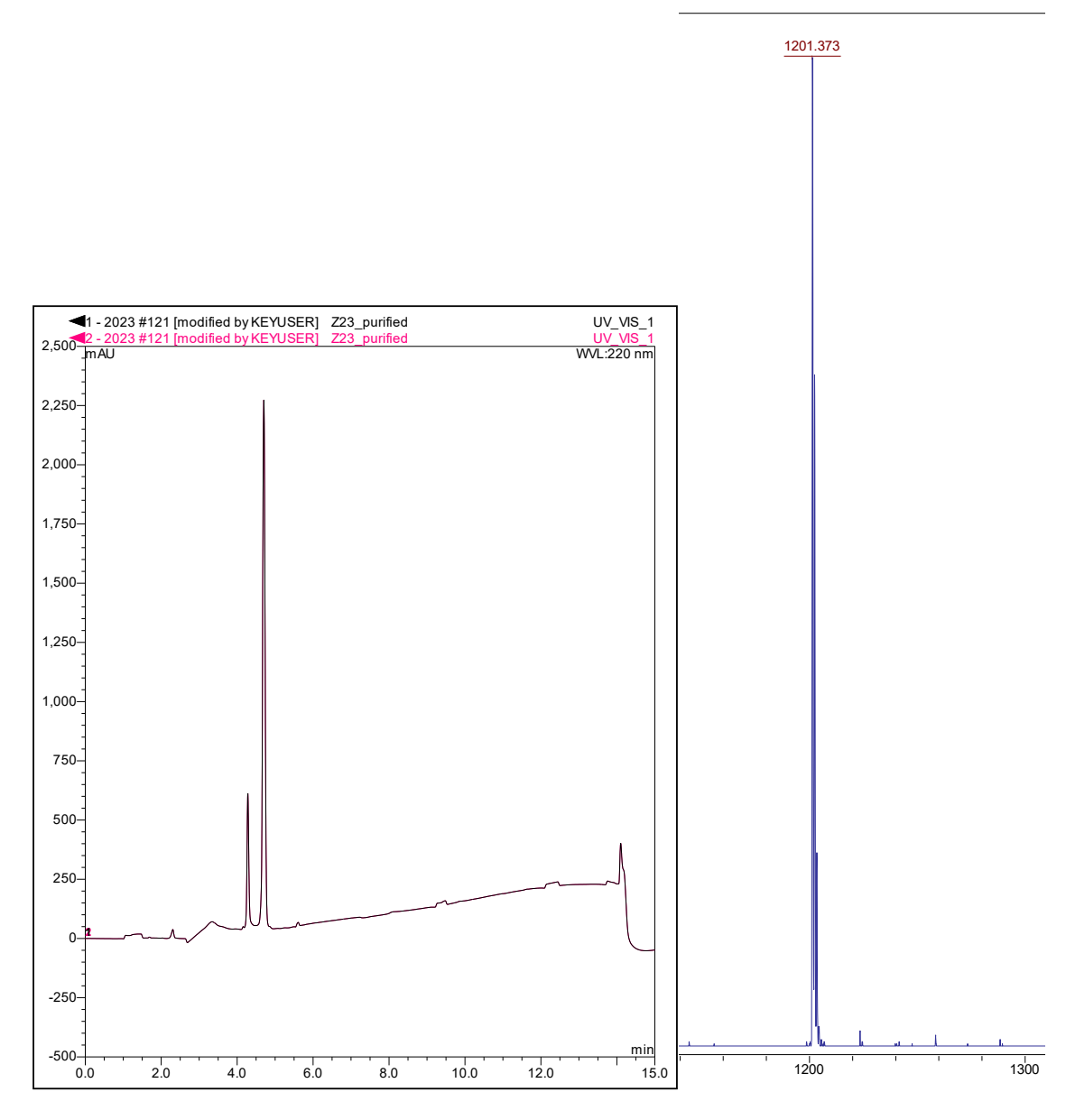


**Figure S45:** (left) HPLC-trace of P3 (MC- and SP-isomer between 4 and 5 min). (right) MALDI-spectrum of P3 (m/z calculated: 1201.4756 found: 1201.373).

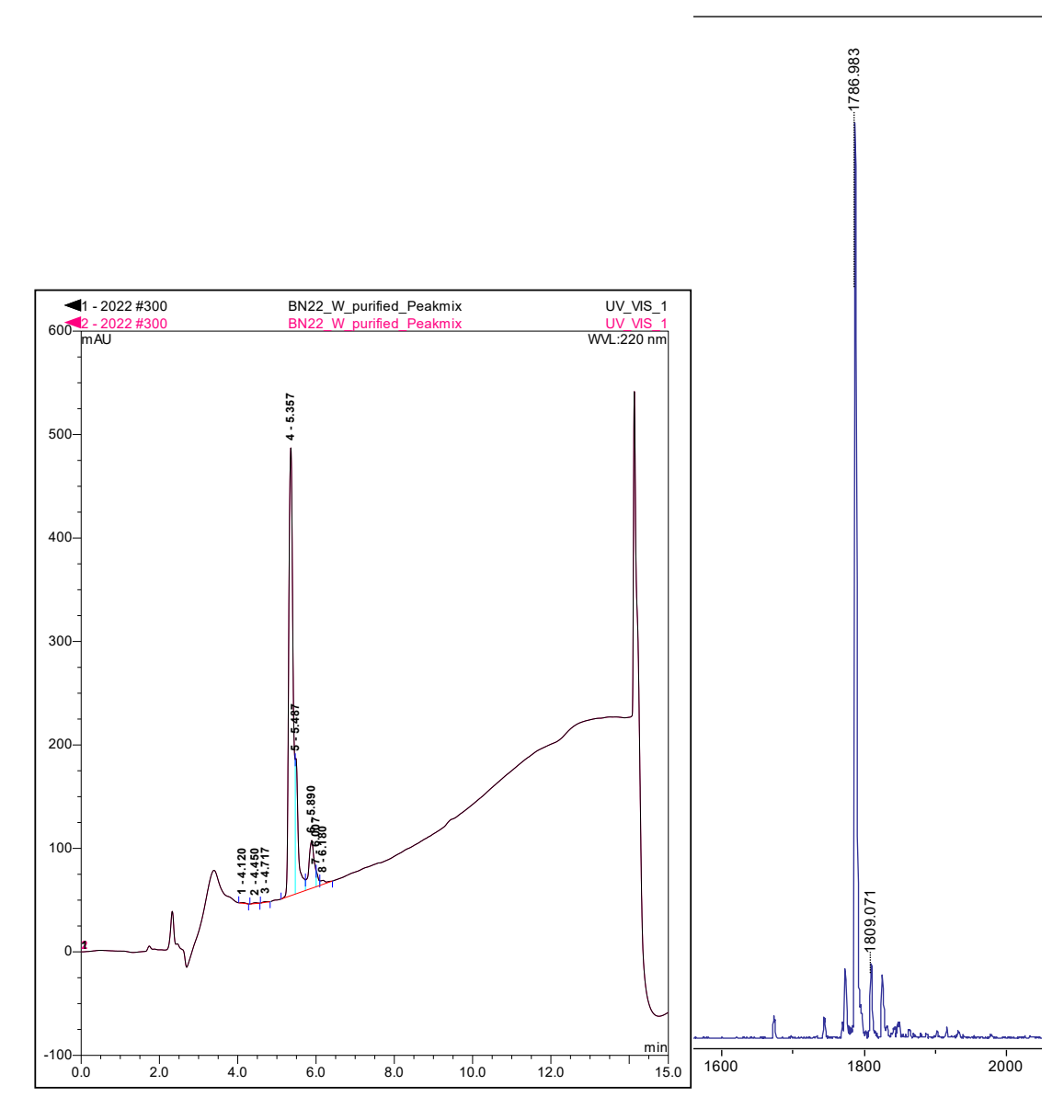


**Figure S46:** (left) HPLC-trace of P4 (MC- and SP-isomer between 6 and 7 min). (right) LC-MS spectrum of P4 (m/z calculated [M+H]<sup>+</sup>: 1787 found 1787).

- (1) Sepehr, Z.; Nasr-Isfahani, H.; Mahdavian, A. R.; Amin, A. H. Synthesis, characterization, and UV–visible study of some new photochromic formyl-containing 1', 3', 3'-trimethylspiro [chromene-2, 2'-indoline] derivatives. *J. Iran. Chem. Soc.* **2021**, *18* (11), 3061-3067. DOI: 10.1007/s13738-021-02253-5.
- (2) GALE, D. J.; WILSHIRE, J. F. Fibre–reactive Basic Dyes I–Polymethine Dyes Containing the N–Chloroacetyl Group. *J. Soc. Dye. Colour.* **1974**, *90* (3), 97-100. DOI: 10.1111/j.1478-4408.1974.tb03188.x.
- (3) Tomasulo, M.; Kaanumal, S. L.; Sortino, S.; Raymo, F. M. Synthesis and properties of benzophenone– spiropyran and naphthalene– spiropyran conjugates. *J. Org. Chem.* **2007**, *72* (2), 595-605. DOI: 10.1021/jo062004d.
- (4) Di Bella, S.; Consiglio, G.; Leonardi, N.; Failla, S.; Finocchiaro, P.; Fragalà, I. Film polymerization—a new route to the synthesis of insoluble polyimides containing functional nickel (II) schiff base units in the main chain. *Eur. J. Inorg. Chem.* **2004**, 2004 (13), 2701-2705. DOI: https://doi.org/10.1002/ejic.200300959.